MME 2011

22ND Micromechanics and Microsystems Technology Europe Workshop

PROCEEDINGS

editorial team
Agne Johannessen
Per Øhlckers
Erik Johannessen
Mehdi Azadmehr
cover art
Bjørn Jensen

optimized for screen

MME 2011

Proceedings of the 22nd Micromechanics and Microsystems Technology Europe Workshop

19-22 June 2011 Tønsberg, Norway

ISBN 978-82-7860-224-9

editorial team

Agne Johannessen
Per Øhlckers
Erik Johannessen
Mehdi Azadmehr

Department of micro and nano systems technology
Vestfold University College, Norway

Table of Content

Invited Speakers

Papers

MICRO ENERGY HARVESTING AFTER THE FIRST DECADE: FROM BASIC RESEARCH TO PRACTICAL APPLICATION

P. Woias

Albert-Ludwig-University Freiburg, Dept. of Microsystems Engineering, Lab. for Design of Microsystems, Freiburg, Germany

***Abstract* — Research on energy harvesting has seen a tremendous up-rise in the last decade, not only in MEMS but also in other industrial and academic sectors. It is interesting to watch how the scope of research changes after this so-called first decade. In the beginning the primary focus has been on the development of micro and mesoscale generators. In the meantime, that energy storage and electronic power management are also recognized in their importance and studied in more depth. Finally, energy harvesting is no longer taken as a primary goal in itself, but as an enabling technology for energy-autonomous embedded systems. Their operation in an application-specific environment with a potentially high variability of ambient energy and low levels of available power set the requirements on the energy harvesting sub-system in use. These boundary conditions are not new: Natural environments provide the same preconditions for all their "embedded systems". As a consequence, more recent research on energy harvesting shows a trend towards biologically-like features, like e.g. the adaptivity of harvesting concepts to different or highly variable energy resources. This publication will show a few examples of this trend and give also a comparison of the current state of the art of technology with requirements of a low-power embedded system.**

***Keywords :* Energy harvesting, piezoelectric generators, energy storage, power management, biologically inspired systems**

I - Introduction

Although this may not be obvious on the first sight, we are surrounded by a high diversity of distributed, decentralized and embedded systems today. Visible pilot applications are easily identified with mobile phones, notebooks and PDAs. However, distributed systems, often based on MEMS devices, have meanwhile - and much more secretly for their users - penetrated not only the IT sector but almost every area of our daily living. Examples are the steadily growing application in cars, distributed sensor and actuator systems in buildings and industrial fabrication, distributed MEMS devices in medical care and, recently, MEMS-RFID tags in transport and logistics. For embedded sensor systems with mutually communicating nodes the topic "wireless sensor network (WSN)" is common today. As a consequence, also energy-autonomous embedded systems are no longer considered as a vision, but as an upcoming reality.

II – State of the art and requirements

While RF communication may serve for a flexible data communication within an embedded system, the energy is - in many cases - still supplied by wires or batteries. Fig. 1 shows, as one prominent example, the growing number of electronic control units (ECUs) in cars [1]. As a consequence, a modern mid-size passenger car carries approximately 3 km of wires for the supply of all electric components and for internal data communication via specific on-board networks [2]. This requires complicated and error-prone power grids, that are fabricated and installed by hand, not easily maintained and, over all, do provide a substantial cost factor.

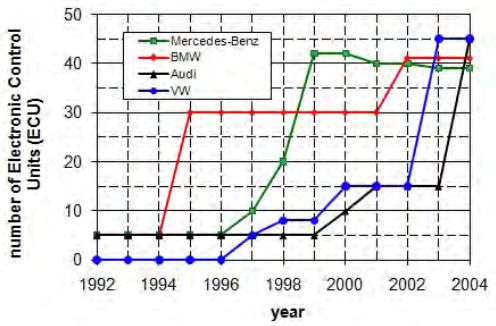

Figure 1*: Annual statistics on the up-rise of electronic control units (ECUs) in German passenger cars from the mid 1990s on, data taken from [1]*

Consequently, recent studies on the world-wide consumption of copper state that approximately 5% of the global copper market does fall on the wiring in cars, compared to 3% used in electronic circuit boards or IC housings and 13% used for the global water supply [3].

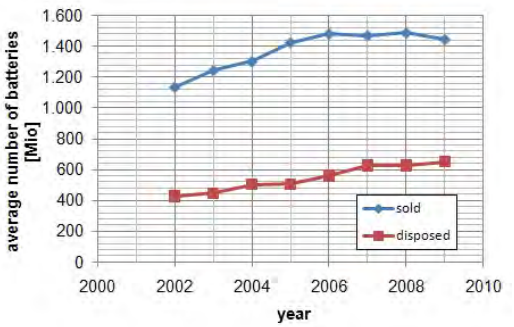

Figure 2*: Annual statistics on the battery sale and disposal in Germany, provided from the German battery recollection system GRS [4]*

Batteries and other exhaustible energy sources are restricted to low power embedded systems that have to be easily accessible for service. Moreover, environmen-

tal concerns arise from the growing numbers of batteries in use. For that aspect Fig. 2 shows statistical data from the largest German battery recollection system [4]. In 2006 this sales and recollection chain alone counted a total sale of approximately 1.4 billion of batteries. One third of this number has been recollected and disposed environmentally friendly in the same year, which is a good result in a world-wide comparison, but may still not be considered as sufficient.

Micro Energy Harvesting, i.e. the conversion of ambient energy into an embedded system's electrical power supply, promises a much better approach for operating a fully embedded system, as it would make the nodes truly energy-autonomous and avoid the problems described above. We use energy harvesting in the macro world by employing wind, solar or water power as "renewable" forms of energy, with all associated problems like varying energy supply, the need to bridge power-down phases and the environmentally friendly design of the power stations.

These challenges multiply if we tackle the field of "micro energy harvesting". A simple replacement of the battery or the power cord by a "micro power plant" will not solve the task. In contrary, micro energy harvesting relies on a thorough design of the whole embedded system. Micro energy converters have to be provided with a size and function compatible to the respective application site. The varying availability of ambient energy will require an efficient intermediate storage to bridge phases of low supply, as a back-up power grid is not available. An efficient energy management has to transfer the electrical energy between all subsystems in an optimal way. Finally, the energy consumption of the system node itself, and, as a consequence its operation profile, has to be optimized to a high extent by appropriate design and system control measures.

III – Bioinspiration - a step towards application?

In the meantime a large number of review publications are available that summarize the principles, technologies and potential applications of energy harvesting, in many cases with a focus on generators [5], sometimes with additional remarks on energy storage [6] or, more recently, with a treatment of energy-efficient wireless communication [7]. This paper will not summarize these contents again, but intends to give some ideas on future research directions for energy harvesting. For that it is important to point out that the application of embedded systems can be much more "nature-like" as one might accept. The typical boundary conditions of a living being in its natural environment are set by a highly variable power supply from the ambient, e.g. by shift between day and night or summer and winter. For a technical system the equivalent would be the on-off time of its technical and non-technical environment producing variable temperatures, vibration amplitudes, frequency spectra or irradiation levels. Like in nature, the necessity to bridge low-energy and brown-out phases is given, e.g. for continuously monitoring WSNs. This will require, in association to biological systems, the introduction of different levels of reduced activity, duty cycles and ultra low-power sleep modi. Also, an embedded system will exhibit a highly variable and rapidly changing internal power consumption, reaching from low-power sensing activities over average-power signal processing up to high-power wireless communication. This calls for storage concepts with a low internal leakage, comparable to the fat reserve of an animal, and a flexible capability to deliver power via the activation of an electrical analogon to blood glucose. Finally, undesirable environmental influences from temperature, humidity or vibration have to be tolerated to a certain extent. This altogether can be summarized into three global requirements on energy harvesting, storage, energy management and system operation:

1. high adaptivity
2. efficient and flexible energy storage
3. „wise" system management and operation

In the following a few examples of recent research will be given that try to follow these prerequisites. Also, a survey of selected state-of-the-art techniques will be performed, concerning their ability to fulfill the requirements given above.

IV – Energy Conversion

A. Parallelized and multi-resource energy harvesting

A living being is, either from good reason or due to its biological concept, dependent from several ambient energy resources. Haematocryal animals require a certain temperature level, hence a certain income of thermal energy, to start their activity. Omnivores take their food from many resources to ensure a sufficient income of nutrition. In an energy-autonomous system this would mean to tap different ambient energy sources in parallel, as one source may show longer brown-out phases that can be bridged with energy from another, complementary source. Also, the use of different conversion principles for one type of resource (e.g. vibrations) allows for a more flexible design concerning the generator properties or the conversion ranges. Today, this idea is mostly followed by building block strategies integrating individual and separate generators into a hybrid design.

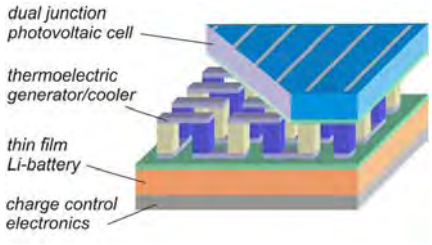

Figure 3*: Schematic of a solar-thermoelectric „power tile"[8]*

The so-called „power tile" is an example of a hybrid solar-thermoelectric generator for space applications [8] using this building-block philosophy. The device

combines a photovoltaic (PV) cell, a thermoelectric generator (TEG) and a thin-film battery in a flat multi-layer stack (Fig. 3). The PV cell harvests energy from solar irradiation, while the temperature gradient between the illuminated cell surface and the shaded backside is converted via the TEG. Both generators feed into the thin film battery via an integrated power management circuit. The TEG is also intended to be used as a Peltier heat pump to keep the battery within its allowed temperature range.

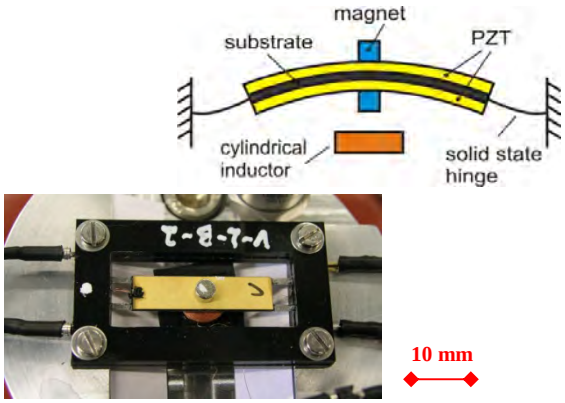

Figure 4: *Piezo-electromagnetic vibration harvester [9]: schematic (top, with upper coil removed) and photograph (bottom, with upper coil removed)*

A hybrid parallel harvester has been developed in our research team to harvest from vibrations with two different conversion principles in one device [9]. The device is built according to the well-known principle of mechanoelectric generators [5]: A seismic mass is mounted onto a spring and set under vibrations from a host system. The movement of the seismic mass with respect to the generator frame is used to either deform a piezoelectric material integrated into the spring or to induce a varying magnetic field into a coil mounted nearby, the latter by means of a magnet mounted onto the seismic mass. The piezo-electro-magnetic generator demonstrated here uses a bimorph piezo cantilever as a spring with two magnets attached and two coils mounted on top and on the bottom. (see Fig. 4).

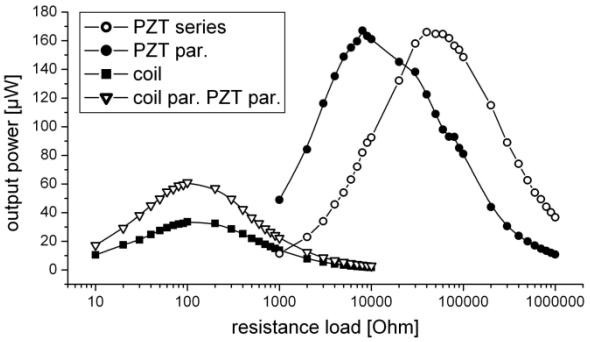

Figure 5: *Output power of the hybrid generator shown in Fig. 4 under resonant excitation (peak acceleration: 10 mm/s²) and as a function of the respective load resistances [9]*

As a result the generator provides two power sources with different output voltages and source resistances: While the piezogenerator will develop high voltages at low currents, the electromagnetic part will deliver higher currents at much lower voltages. Also the piezoelectric and the electromagnetic generators can be switched into various parallel and serial configurations to obtain an optimal impedance matching and power output (Fig. 5).

B. Broadband and frequency-adaptive piezogenerators

Vibration is a highly attractive power source due to its widespread availability, although it shows, as a general drawback, a high variability of its frequencies and amplitudes. Common mono-resonant mechanoelectric generators will only harvest from vibrations in an optimal way when the external host frequency matches exactly with their own resonance frequency. As this is not the case for a variable excitation frequency, wide-band generators or frequency-adaptive generators are favorable for a more realistic application scenario.

In recent time, several concepts have been studied to overcome this problem. One solution is the use of mechanical oscillators with a non-linear spring that changes its stiffness with the actual position and speed of the seismic mass. Better known as the so-called Duffing oscillator, such a non-linear resonator shows a broadband excitability over a certain frequency range [10, 11]. However, as this device is essentially a bistable oscillator an unstable oscillation behavior is found for certain excitation conditions. The oscillator may fall back into a non-favorable oscillation behavior with low power output and is only relinquished from this state via a mayor change of the input conditions. Nevertheless, the concept is promising and leaves a wide space for optimization.

An active tuning of a generator's resonance frequency is the alternative to the quasi self-tuned Duffing concept. In the past years, several attempts have been made to achieve this goal [12], mostly with tunable piezogenerators and as stand-alone tests of various tuning concepts. This leaves out of sight that a certain amount of energy is required for a tuning operation and has to be harvested continuously. The Duffing oscillator performs this redistribution between harvested power and tuning power in a quasi-automatic way, i.e. his output power will always be smaller than the output power of a similar, linear generator operating at resonance. Therefore, a frequency-tunable mechanoelectric generator with low requirements on the tuning power would provide the capability to harvest almost the total power available at resonance over a larger frequency range.

Fig. 6 shows a frequency-tunable piezogenerator that has been realized as a fully self-sustaining broadband vibration harvester. The converter is based on multi-layered piezoelectric beams as described in an earlier publication [13]. One part of these piezoelectric beams is used to generate electrical power, whereas another part is employed as an actuator to change the stiffness and therefore the spring constant of the resonator. In

combination with a low-power microcontroller, a self-sufficient frequency-tunable energy harvester system is obtained.

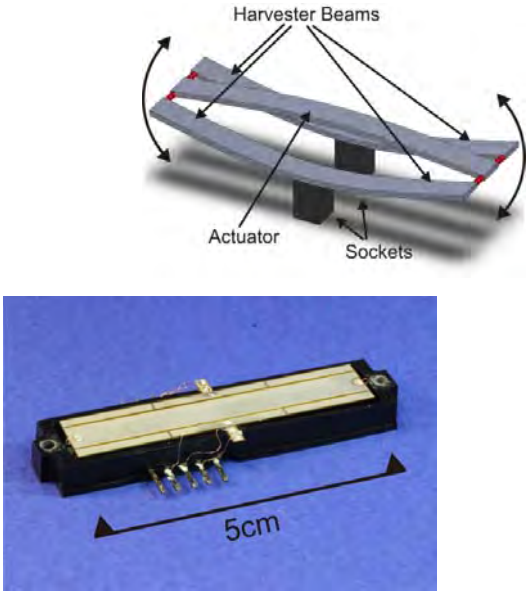

Figure 6: *Frequency-tunable piezogenerator [13]: schematic (top) and photograph (bottom)*

Fig. 6 shows a frequency-tunable piezogenerator that has been realized as a fully self-sustaining broadband vibration harvester. The converter is based on multi-layered piezoelectric beams as described in an earlier publication [13]. One part of these piezoelectric beams is used to generate electrical power, whereas another part is employed as an actuator to change the stiffness and therefore the spring constant of the resonator. In combination with a low-power microcontroller, a self-sufficient frequency-tunable energy harvester system is obtained.

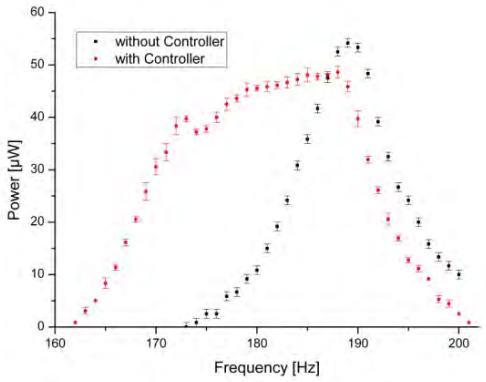

Figure 7: *Output power of a frequency-adaptive piezogenerator system with and without adaptive tuning (sinusoidal excitation with an amplitude of 0.6 G, tuning interval: 20 s)*

In Figure 7 the power output of this scavenger is shown with and without frequency tuning. The active tuning generates a nearly constant output power over a frequency range that is approximately 4 times wider than the power bandwidth of the un-tuned generator. Every 20 s the microcontroller in the system detects the actual host frequency and readjusts the actuator voltage via a step-up converter. The completion of the tuning operation is checked via a voltage measurement at the piezoactuator. The power for the microcontroller and all associated electronics (step-up converter, actuator voltage measurement) is harvested from the generator The tuned peak power is therefore 5 to 25 µW lower than the peak power of the static, un-tuned resonance curve. A similar system is currently under development for the piezoelectric resonance-tuning of an electromagnetic harvester [14]. Within this parallel study it could be demonstrated that piezoactuators, once charged to a fixed voltage level, retain their strain, even under vibration, for a certain period of time. Therefore, it is sufficient - and power-efficient - to activate the control system in regular time intervals only.

Compared to state-of-the-art in broad-band energy harvesters, this system allows to harvest over a wide frequency range without suffering from a poor quality factor. It is also capable to compensate other disturbing factors, e.g. the influence of temperature on the resonance behavior of the mechanical generator structure. Furthermore, the already present microcontroller can be used for other tasks, at the cost of a marginally higher power consumption.

V – Energy Storage

A. Electrical capacitors

Depending on the power requirements of the embedded system electrical capacitors may be the best storage concept up to a medium-time power supply. In comparison to rechargeable batteries they exhibit a longer lifetime and a much higher flexibility concerning operational voltages and currents. However, the application of electrical capacitors in conjunction with a low-power microgenerator and a low-power embedded system requires a close attention at all potential power losses during charge, discharge, operation and idle times. The result is somewhat surprising and shall be discussed here briefly using data and citations from an own previous publication [15]. These effects are not important, predominant or visible at all in conventional applications of capacitors, but will be appear as soon as the field of low-power systems is addressed:

For a long operational lifetime a solid-state dielectric capacitor would, as a first guess, be an optimal choice over electrolytic capacitors. These capacitors are capable to deliver acceptably high currents in short periods of time, e.g. to buffer a higher power draw due to the start of wireless communication. Today, multilayer ceramic capacitors (MLCCs) are available with a volumetric capacitance up to 12 µF/mm³. This has been achieved via a continuous shrinkage of the thickness of the ceramic dielectric layer, down to values in the range of 1 µm and below. However, together with this size reduction, the insulation resistance R_P of the dielectric material becomes important as a power loss factor. In general, the parasitic resistance of a dielectric capacitor is inversely proportional to its capacitance C and de-

pends on the specific resistance ρ and the permittivity ε of the dielectric material:

$$R_p \propto \frac{\rho \cdot \varepsilon}{C}$$

Consequently, a 100 µF MLCC will exhibit an insulation resistance of only 5 MOhm [16]. An embedded system with a typical operational power consumption of 50 µW and a low-power sleep modus at 5 µW, both at a supply voltage of 2.3 V, may be taken as a practical application scenario. At 2.3 V one 100 µF MLCC used in this system will continuously draw a leakage power of 1 µW which is 2% of the maximal system power. Such a power drain can be considered as critical or non-critical, depending on the energy supply from the generator. In power down, however, this leakage path will draw 20% of the required power, thus compromising the low-power sleep modus in an unacceptable way.

In comparison, a properly selected low-leakage electrolytic capacitor turns out as a better choice. The leakage current I_L of electrolytic capacitors is falling rapidly from an initially high to a much smaller small continuous value. According to standardized test procedures [17], its typical corner values are described according to:

$$I_L(t = 2\,\mathrm{min})[\mu A] < (\alpha \cdot U_R[V] \cdot C_R[\mu F]) + I_0\,[\mu A]$$
$$I_L(t = 5\,\mathrm{min})[\mu A] < (\beta \cdot U_R[V] \cdot C_R[\mu F]) + I_0\,[\mu A]$$

The factors α and β take typical values around 0.01 and 0.001, respectively, while the continuous leakage current I_0 may amount a few µA, all values depending on the electrical capacitance value C_R at the rated voltage. Taking the embedded system given above, a suitable 100 µF capacitor with a rated voltage of 10V would show a much smaller continuous power loss in the range of 80 nW. This calculation takes into account that the continuous leakage current of an electrolytic capacitor decreases, in addition to the temporal effects, with the applied voltage. Here, a 10V-rated device is used for the buffering of the 2.3 V system voltage.

Finally, so-called “super-caps” or “Gold-caps” range at the upper scale of the capacitance range, with a power density close to rechargeable batteries. These capacitors use the build-up of electrochemical double layers at solid-electrolyte interfaces within liquid, organic or polymer electrolytes. A double layer thickness in the nm-range and electrode materials with effective areas up to 2000 m²/g allow for large electrical capacitances in the Farad-range.

However, it should be recognized, that these capacitors represent a bridge between electrochemical, rechargeable batteries and electrolytic capacitors. They may need a minimal charging current to accept power and will also show a higher leakage current, as they possess no insulating dielectric layer. This requires an energy harvester with a high-enough output current at a suitable output voltage level. As soon as the current drops below the values required by the capacitor, the “storage” system turns into a power dissipation system. Nevertheless, this type of capacitor is capable to deliver electrical power over long periods and with an acceptable leakage rate. With the 50µW example system used here, a typical 0.15 F super-cap would show a continuous leakage around 0.5 µW. With this leakage rate 50 % of the energy stored in the capacitor would be dissipated within 168 hrs, i.e. 7 days.

B. Rechargeable batteries

Today, rechargeable batteries are indispensible for the long-term operation of highly miniaturized energy-autonomous embedded systems. Among a large variety of battery chemistries the Li-Ion system offers the highest volumetric and gravimetric energy density and accepts charging and discharging under all state-of-charge (SOC) conditions. This meets well with the severe boundary conditions of energy harvesting, as the in-flow and out-flow of electrical energy are not predictable and will lead to large variations of the SOC. In comparison the NiCd or NiMH systems show a certain memory effect upon an only partial charge and discharge and cannot be regenerated easily in the field, as this would require several controlled full charge and discharge cycles.

For a long-term application it should be kept in mind that the electrochemistry of the Li-Ion battery is based on a forward and backward shift of Li^+ ions between the battery anode and cathode. Therefore, a periodic volume increase and decrease occures in both battery compartments during every charge and discharge cycle. The result is a mechanical ageing accompanied by a loss of capacity over time. The resulting - always limited - battery lifetime has to be considered in conjunction with the required system’s operational lifetime. This may range between several month, e.g. for an application in logistics and 10 years, e.g. for a tire pressure sensor or an in-door light sensor. As another downturn these batteries require a tight control of the charging conditions, do not tolerate trickle or overcharge and will suffer severely from a single deep discharge.

As a consequence of the ageing process described above the lifetime capacity, i.e. the product of discharge level and discharge cycle number, remains almost constant before the non-avoidable on-set of ageing and degradation. Therefore, the operational lifetime of a Li-ion battery can be prolonged via a flat charge-discharge strategy [15]: While only 100 cycles can be performed with a 100% discharge and recharge rate, 1000 cycles can be performed with an only 10% discharge and recharge rate. Hence, a Li-ion battery with a sufficient over-capacity that is only charged and discharged in small percentages of its total available capacity, is a good choice for a long operational lifetime. In many cases this “too large” battery does not increase the size of an embedded system over acceptable levels. Especially low power systems are operable with coin batteries, whose volume is dominated by packaging.

In any case, the integration of batteries, capacitors and energy harvesters requires a specific power management circuit to distribute the harvested energy in an optimal way. This circuit would monitor the energy in-

flow and out-flow, supply the embedded system with its required power, either from the battery or from the generator, and transfer all surplus energy into a long-term storage unit.

VI – Energy management

The electronic energy management in an energy-autonomous embedded system has to fulfill a large variety of tasks. This may include a step-up operation to generate a higher output voltage from a generator delivering low input voltages, like, e.g., a PV cell or a thermoelectric generator [18]. A step-down operation may be required to reduce the high output voltage, e.g. of a piezoelectric generator, to acceptable values. Electrostatic or piezoelectric harvesters, depend on [19] or benefit from [20, 21] synchronous charge extraction techniques to deliver maximal power. Other tasks, like battery management or power distribution have already been mentioned before. In all cases the power consumption of the power management itself should be as low as possible. Also, low operation voltages or low start-up voltages may be required [18].

While these functions are obvious, depending on the generators in use, other attributes are not clearly visible and will only appear in low-power embedded systems or under true low-power conditions. This will be taken as a more elaborated example here:vIn power-critical applications an embedded system will operate either in a duty cycle mode, i.e. with ultra low power sleep phases between short periods of activity, or fall totally dead without any remaining energy in its internal storage. In the latter case a controlled start-up and dead-fall has to be performed to reestablish the system function, to recharge the internal buffer storage and to avoid undetermined states during power-down. If this is not performed properly, a deadlock situation may occur during start-up, where the system's storage unit, e.g. a capacitor, remains only partially charged and the system stays non-functional. Fig. 8 illustrates this critical state with the load curve of a piezoelectric generator and the start-up voltage-current relationship of a temperature sensor module. When starting from zero voltage the piezogenerator is first - and heavily - loaded with a small effective resistance provided by the empty storage capacitor. In this operation set-point, the generator is not capable to deliver its optimal power, i.e. the recharging of the storage capacitor will happen slowly. As a second drawback, the CMOS electronics used in the system may show a so-called sub-threshold behavior. A high current draw is observed in this voltage range below the operational set-point. Both effects together can overload the generator and prevent a rise of the system voltage to nominal values.

A simple, yet necessary solution for this problem is a power-on switch that blocks the connection between the generator-storage unit and the system electronics until the sub-threshold voltage range is overcome and the capacitor voltage is at nominal values. This can either be done with commercial electronic building blocks [23] or with discrete voltage monitor circuits [22]. In both cases the voltage monitor itself has to be free from sub-threshold behavior, has to start from low voltages and is not allowed to draw significant power.

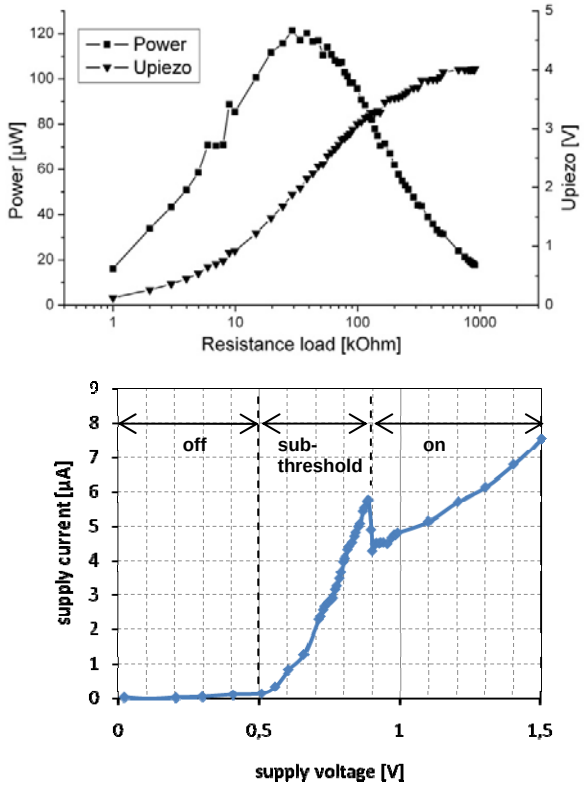

Figure 8: *Typical power curve of a piezoelectric generator as a function of the load resistance [22], with the optimal load point at 2 V (top) and sub-threshold current surge of a 1.5 V temperature sensor module during start- up [15] (bottom)*

VI – Summary and conclusions

Within this publication a brief outline of future research directions for energy harvesting and energy-autonomous embedded systems is given. One common idea was the "biology-like" aspect of a robust and reliable operation under power constraints and highly variable environmental conditions. Adaptivity and flexibility of energy harvesting principles have been discussed with frequency-adaptive and frequency-tunable piezogenerators as premier example. Both concepts offer promising degrees of freedom for a further optimization. The general idea could also be transferred into other conversion principles. Energy storage is still an open question with respect to the severe boundary conditions in a low-power embedded system. This demands a thorough reduction of all power leakages and a wise design-in and operation of the available capacitors or rechargeable batteries. Finally, the electronic power management used in an energy-autonomous embedded system has to be functional from low voltages with a minimum power drain. Although first commercial products are available that were designed specifically for energy harvesting applications, this is also - still - a wide field for further research.

In general, these research directions outline the concept of an energy-autonomous distributed system that will change the operation philosophy of distributed and embedded systems as such in a rather drastic way. Although not outlined here, a growing part of the actual research is already focused on this novel subject. Again, biology is delivering the obvious blueprint: We will have to shift from the "function first" operation strategy that is still valid in most applications today to a strict "energy first" paradigm. We will also have to consider novel control and management strategies, e.g. by using probability procedures in the central control station ("When is node x of the embedded system likely to give a message ?"), power-efficient wake-up strategies for individual nodes, a power-saving data transfer in the distributed system, e.g. by node hopping and, last, redundant system control strategies that are tolerant against the brown-out of individual nodes.

Despite the complexity of this venture the reward would be manifold: We would, ultimately, receive "quasi-living" systems with an unprecedented level of autonomy and reliability that can be operated in almost every environment, at remote sites and without any technical service. This vision is, hopefully, a tempting driver for progress in this pioneering research area and for a widespread future commercial success.

References

[1] J. Leohold, Communication Requirements for Automotive Systems, keynote talk at the 5th IEEE Workshop on Factory Communication Systems, Vienna, Sept. 22-24, 2004, *retrieved from http://www.ict.tuwien.ac.at/wfcs2004/downloads/*

[2] N. Navet, Y Song, F Simonot-Lion, C Wilwert, Trends in Automotive Communication Systems, *Proc. IEEE* 93 (6), pp. 1204-1223, June 2005.

[3] G. Angerer, A. Mohring, F. Marscheider-Weidemann, M. Wietschel, Kupfer für Zukunftstechnologien, project study of the FhG-ISI, Karlsruhe, Germany, 2010, *retrieved from http://www.isi.fraunhofer.de/isi-de/e/projekte/kufperstudie_fsem_314536_wi.php.*

[4] Annual reports 2002 to 2009 of the German battery recollection system GRS, *retrieved from http://www.grs-batterien.de*

[5] S P Beeby, M J Tudor, N M White, Energy harvesting vibration sources for microsystems applications, *Meas. Sci. Technol.* 17, 2006, R175–R195.

[6] K.A Cook-Chennault, N. Thambi, A.M. Sastry, Powering MEMS portable devices - a review of non-regenerative and regenerative power supply systems withspecial emphasis on piezoelectric energy harvesting systems, *Smart Mater. Struct.* 17, 2008, 043001 (33pp).

[7] W.K.G. Seah, A.T.S. Chan, Challenges in Protocol Design for WirelessSensor Networks Powered by Ambient Energy Harvesting, *Technical report series, University of Wellington, Victoria, Australia*, Febr. 2011 (ISSN 1179-4259).

[8] http://www.techbriefs.com/index.php?option=com_staticxt&staticfile=/Briefs/Jan04/NPO30433.html, *last access in June 2011*.

[9] M. Wischke, M. Masur, F. Goldschmidtboeing, P.Woias, A hybrid generator for vibration energy harvesting, *IEEE Transducers 2009*, Denver, Co, USA, *Digest of Techn. Papers*, 2009, pp. 521-524.

[10] B P Mann, N D Sims, Energy harvesting from the nonlinear oscillations of magnetic levitation, *Journ. Sound Vibr.* 319 (1-2), 2009, pp. 515-530.

[11] S. C. Stanton, C. C. McGehee, B. P. Mann, Nonlinear Dynamics for Broadband Energy Harvesting: Investigation of a Bistable Piezoelectric Inertial Generator, *Physica D* 239, 2010, pp. 640-653.

[12] D. Zhu, J. Tudor, S. Beeby, Strategies for increasing the operating frequency range of vibration energy harvesters: a review, *Measurement Science and Technology* 21 (2), 2010. pp. 022001.

[13] C Eichhorn, F Goldschmidtboeing, P Woias, Bidirectional frequency tuning of a piezoelectric energy converter based on a cantilever beam, *J. Micromech. Microeng*. 19 (6), 2009, 094006.

[14] M. Wischke, M. Masur, F. Goldschmidtboeing, P. Woias, Electromagnetic vibration harvester with piezoelectrically tunable resonance frequency, *J. Micromech. Microeng.* 20 (3), 2010, 035025.

[15] P. Woias, C. Eichhorn, Martin Wischke, F. Goldschmidtböing, Micro Energy Harvesting: Research after the first decade, *Proc. VDE-Kongress 2010*, Leipzig, Germany, 2010, no page numbers av.

[16] http://www.murata.com/products/capacitor/faq/mlcc/index.html#q03, *last access in June 2011*.

[17] IEC 60384-4 and EN 130 300.

[18] J. M. Damaschke, Design of a Low-Input-Voltage Converter for Thermoelectric Generator, *IEEE Trans. on Industry Applications* 33 (5), Sept/Oct. 1997, pp. 1203-1207.

[19] S. Meninger, J. O. Mur-Miranda, R. Amirtharajah, A. P. Chandrakasan, J. H. Lang, Vibration-to-Electric Energy Conversion, *IEEE Trans. on VLSI Systems 9* (1), Febr. 2001, pp. 64-71.

[20] E. Lefeuvre, A. Badel, C. Richard, D. Guyomar, Piezoelectric Energy Harvesting Device Optimization by Synchronous Electric Charge Extraction, *J. Intel. Mat. Structures* 16, 2005, pp. 865-876.

[21] T. Hehn, Y. Manoli, Highly efficient CMOS-integrated Circuit for Piezoelectric Generators, *Proc. PowerMEMS 2009*, Wash. DC, 2009, pp. 431-434.

[22] P. Woias, M. Wischke, C. Eichhorn, B. Fuchs, An Energy-autonomous Wireless Temperature Monitoring System powered by Piezoelectric Energy Harvesting, *Proc. PowerMEMS 2009*, Washington DC, USA, 2009, pp. 209-212.

[23] Torah R N, Glynne-Jones P, Tudor M J, Beeby S P 2007 Energy-aware wireless microsystem powered by vibration energy harvesting, *Techn. Dig. PowerMEMS 2007, Freiburg, Germany, 2007,* pp. 323-326.

HIGH PERFORMANCE THERMAL IMAGING FPA BASED ON SI/SIGE QUANTUM WELL THERMISTORS IN COMBINATION WITH NOVEL 3D WAFER LEVEL INTEGRATION CONCEPTS

T. Kvisterøy[1]

[1]*Sensonor Technologies AS; Horten, Norway*

***Abstract* — A new 3D integration concept for the fabrication of uncooled infrared bolometers using low temperature oxide-oxide wafer bonding to transfer the detector material from a sacrificial carrier wafer to a CMOS ROIC wafer has been developed at Sensonor. The legs supporting the bolometer pixels and connecting them to the ROIC are built underneath the pixel membrane. Mono crystalline Si/SiGe quantum wells with high TCR and low 1/f noise are used for temperature sensing. A second wafer level bonding step, based on Cu-Sn solid liquid inter diffusion soldering, are used for the vacuum encapsulation of the FPA.**

***Keywords :* Heterogeneous 3D integration, Quantum well thermistor, Non-conductive transfer bonding, Wafer level vacuum encapsulation, SiGe, MEMS, Micro bolometer, FIR focal plane array**

I - Introduction

Bolometers are detectors that convert a minute temperature change induced by incoming electromagnetic radiation into a measurable electrical signal. The uncooled infrared bolometers usually refer to resistive micro bolometers in which the temperature change is converted into a resistance change that can be measured and interpreted as image information. The progress achieved in the last years in the area of uncooled infrared bolometer technology has made it possible to reach performance levels that previously were only possible with cooled infrared photon detectors. Most of the reported uncooled bolometers are fabricated by building up a focal plane array (FPA), consisting of a multitude of pixels, directly on top of the pre-manufactured read out integrated circuit (ROIC) using thin layer deposition and patterning. This monolithic integration is limited to materials and processes that are compatible with the CMOS "substrate". Processing temperatures above 400-450°C are prohibited and therefore the choices for the infrared sensitive material (the thermistor) are limited to materials that can be obtained by processing at such low temperatures. Vanadium oxide (VOx) and amorphous silicon (α-Si) are examples of such monolithically integrated bolometer materials. VOx has demonstrated good performance, but it is a somewhat exotic material and difficult to make. Amorphous silicon is compatible with CMOS fabrication, but it exhibits inferior material characteristics to VOx resulting in more modest detector performance.

II – Technology

A novel noncooled micro bolometer, SB100, has been developed at Sensonor. It uses Si/SiGe quantum wells as temperature sensitive material. See Figure 1.

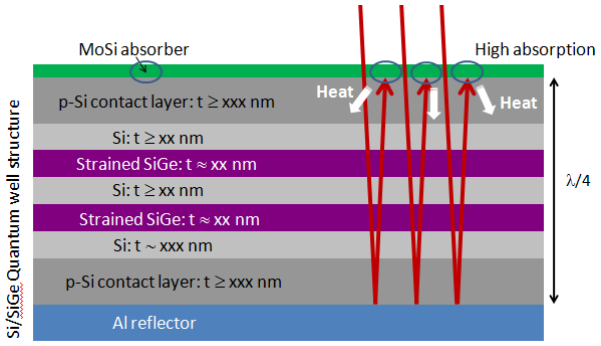

Figure 1*: Si/SiGe Quantum Well thermistor structure*

The thermistor material is transferred from a handle wafer to the CMOS wafer by low temperature oxide-oxide wafer bonding. Transfer bonding allows the use of high quality crystalline material for the temperature sensing. The pixel definition is completed after the removal of the sacrificial carrier wafer by deposition and etching processes that are compatible with the pre-fabricated ROIC. See Figure 2.

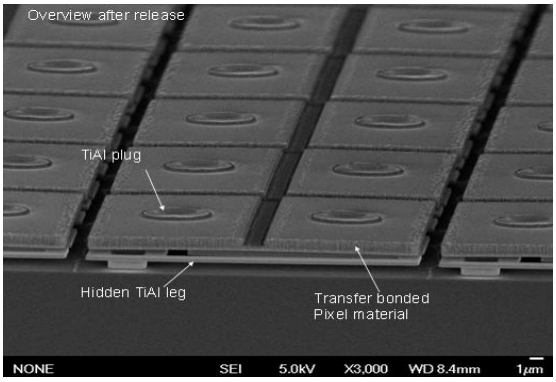

Figure 2*: Released Si/SiGe Quantum Well thermistor pixels with supporting legs underneath*

The advantage of this heterogeneous 3D integration resides in the improved performance of the thermistor layer and consequently of the FPA. High TCR (higher than 3% / K) and low 1/f noise together with an optimized pixel design lead to improved bolometer performances compared to those of existing devices. The legs that connect the pixels to the ROIC are fabricated prior to the transfer bonding and they are therefore situated

under the pixels enabling high fill factors. The pixels are subsequently released by anhydrous vapor HF of the sacrificial oxide layer. Finally the ROIC wafer containing the released FPA is bonded in vacuum with a silicon cap wafer providing the needed low pressure and hermetic encapsulation at low cost. Antireflection coatings and a thin getter layer are deposited on the cap wafer prior to bonding. See Figure 3.

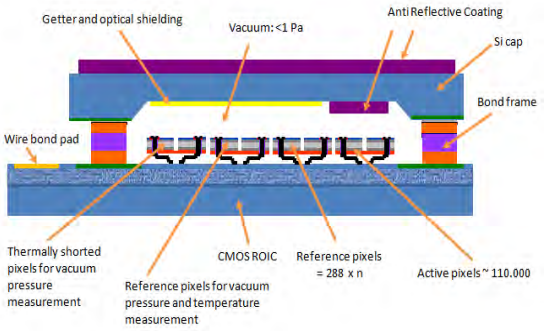

Figure 3*: The SB100 wafer level packaged micro bolometer-with Si/SiGe Quantum Well thermistor pixels*

II – Micro bolometer function

The SB100 consists of 384*288 pixels. It converts the projected LWIR (Long Wave IR) image to a digital data stream of image frames. No part of the SB100 is thermally controlled. The SB100 is intended used with a dedicated controller (FPGA or digital ASIC) acting as a provider of FPA configuration data as well as video frame readout timing master and frame data receiver on a per-line basis. The controller is assumed to implement per-pixel image correction functions based on static correction terms and relative temperature data from the SB100. To aid dynamic NUC (Non Uniformity Correction) the use of a mechanical shutter is assumed. See Figure 4.

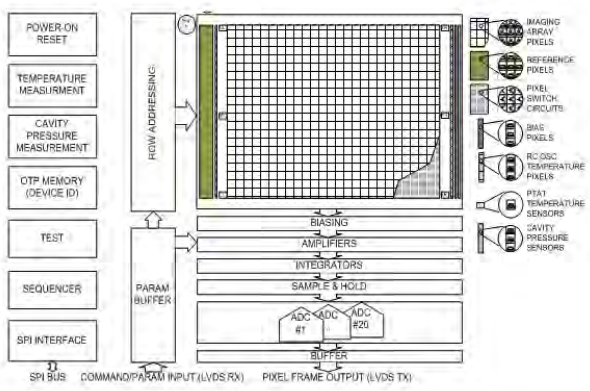

Figure 4*: SB100 micro bolometer functional block diagram*

MEMS RELIABILITY: A FAILURE MECHANIMS PERSPECTIVE

W. M. van Spengen[1,2], W.M.vanSpengen@tudelft.nl

Invited paper

[1]*Delft University of Technology ; 3mE-PME-MNE, Mekelweg 2, 2628CD Delft, The Netherlands*
[2]*Also with Falco Systems, Gelderlandplein 75L, 1082LV, Amsterdam, The Netherlands*

***Abstract* —Reliability is the property of a MEMS device to perform its intended function under stated conditions for a stated amount of time. Proper assessment of the reliability in an early stage of the design is desirable, as is shown using a number of examples (the digital micromirror device (DMD), radio frequency (RF-) MEMS switches and MEMS accelerometers). Typical failure mechanisms of MEMS are presented shortly, and four of them discussed in more detail. These are: charging in RF MEMS switches, adhesion, friction and wear, and fatigue of microscopic silicon structures. Both important state of the art knowledge and 'loose ends' are presented. Proper reliability assessment is not only scientifically interesting but can also bring you a competitive advantage, because the evolution from a first prototype MEMS device to a fully reliable product typically takes years.**

***Keywords :* MEMS reliability, charging, adhesion, friction, fatigue**

I - Introduction

Many MEMS devices do not make it from the laboratory to the marketplace because their reliability is insufficient for commercial applications. The reason is twofold: on one hand, our scientific knowledge of the physical and chemical processes that govern the long-term stability and degradation of microscopic devices and surfaces is still incomplete; on the other hand, the knowledge that is available is often not taken into account early in the design phase.

In this paper, the main concepts of MEMS reliability are introduced. Three important cases are discussed as examples, where the reliability of the devices played a key role. These are the Texas Instruments Digital Micromirror Device (DMD), RF MEMS switches, and MEMS accelerometers. Then, some general statistical tools to assess the reliability and failures over time are introduced. The main failure mechanisms in MEMS devices are presented afterwards. Of these, four, on which I have worked myself, are discussed in more detail: charging of dielectrics in capacitive RF MEMS switches, adhesion, friction and wear, and fatigue of silicon microstructures. Presented is both 'common knowledge' and a number of 'loose ends' where more research is desirable.

II – MEMS reliability: device case studies

A. The Digital Micromirror Device (DMD)

The Texas Instruments (TI) DMD is an example of a device where the reliability of the individual functional units has to be extreme. It consists of a memory chip, with a moving mirror above each cell, arranged in a regular matrix. The mirrors are mounted in torsional hinges made of an aluminum alloy. Every mirror serves as a pixel in an image projection system, and one single dysfunctional mirror results in a dead pixel, and hence an unusable chip.

When TI started the first development of the DMD in 1987, they obtained a functional device fairly soon [1]. However, the mirrors would sometimes fail, due to adhesion (the two positions that the mirrors can take are defined with stoppers that physically touch the moving device). This was aggravated by the fact that the aluminum alloy springs would suffer from creep under the heat of the high-power projection lamp.

The quest was to make creep-resistant springs. It was finally solved with a special alloy, making TI patent in the process all binary, ternary and quaternary aluminum alloys for micromachine use [2]. In addition, the adhesion was mitigated by making the mirror land on little springs that could aid the release process when the mirror has to move to its other position. Also, an organic compound was added inside the package, which partly evaporates when the lamp is switched on, and redeposits a low-adhesion layer on the touching structures every time the device is used. The aluminum alloy springs and the spring stoppers are visible in Fig. 1.

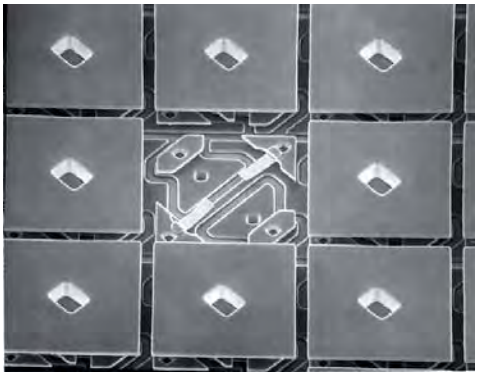

Figure 1*: Close-up of a number of DMD mirrors, with one mirror removed to see the aluminum alloy springs, and the spring-based stoppers. Image courtesy of Texas Instruments.*

Years were spent optimizing the device for reliability. Only in the year 2000, one could finally consider it to be a fully mature product. For a full account, see [3]. For a commercial product, this is an incredible development time, and chances are that TI would have never embarked on the DMD development process if this had been clear from the start. Issues regarding reliability are not only a nuisance, though. Know-how of how to solve them can be of considerable commercial value, especially when your competitors do not have this knowledge. TI is now market leader in DMD-type projection chips.

B. RF- (Radio Frequency) MEMS switches

It has been envisioned for at least 15 years now, that MEMS-based microscopically small switches would be beneficial over transistor switches in many applications. Examples are their use as low insertion loss transceiver switches, reconfigurable GHz range antenna arrays [4], and, recently, even as a replacement of conventional semiconductor amplifiers in harsh environments using pulse-width modulation (PWM) [5].

The first MEMS membrane switch was conceived in 1979 [6], and research intensified from halfway the nineties onward, when their merits for use as low insertion loss switching devices in the GHz range became apparent. However, despite many articles and numerous patents, there are hardly any commercial devices available today. The ones which are, like the Radant MEMS switch range [7], still have severe limitations in terms of maximum voltage and power switched, and number of operation cycles until failure occurs. This state of affairs is mainly due to the degradation of the metal-to-metal contact with repeated switching. This degradation of contact metals is also an issue in macroscopic relays, but is aggravated by the fact that the contact forces in MEMS are necessarily small.

Many of the refinements developed for normal relays have not yet been applied in microfabrication processes. Examples are special alloys for every switching power and voltage, contacts which scrape over one another to ensure a good contact even in the presence of a thin insulating surface layer, high contact forces, and enclosures sealed with gas mixtures dedicated to the particular switch type. These are all areas where MEMS switch designers have not yet been successful. To combat this problem, capacitive RF MEMS switches have been introduced, which employ a variable capacitor instead of a metal-to metal contact to switch high-frequency signals only. They come with their own set of reliability problems, notably the charging of the thin dielectric between the capacitor plates. This phenomenon will be discussed in more detail later, in section V. The first company to produce a cheap, easy to use and fully reliable RF MEMS switch may see a huge market all for itself, but no one is there yet.

C. MEMS accelerometers for space

Acceleration sensing is one of the areas where micro-machining has been applied extremely successfully. MEMS-based accelerometers can be found from car airbag system sensors (*they* have to be extremely reliable!) to modern cellphones.

These accelerometers typically consist of a small moving mass held by springs. Acceleration causes the mass to move, and its displacement is sensed e.g. capacitively or piezoresistively. The device can be either a parallel plate capacitor or a comb drive structure, or both (for sensitivity in different orientations).

A complication if one wants to use them in space is that they should be rad-hard (in fact the same holds for MEMS switches). It was found [8,9] that under the influence of ionizing radiation, typical accelerometers failed, because the dielectric below the moving part was charged, causing erratic motion or even a total collapse of the moving part (Fig. 2a). The obvious solution was to remove the dielectric entirely, after which the devices could stand an increase in radiation dose up to the point where the structural materials themselves degraded purely mechanically.

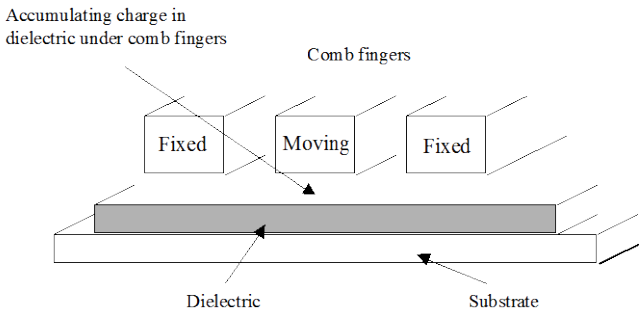

Figure 2a*: A typical accelerometer suffers from charging when subjected to ionizing radiation*

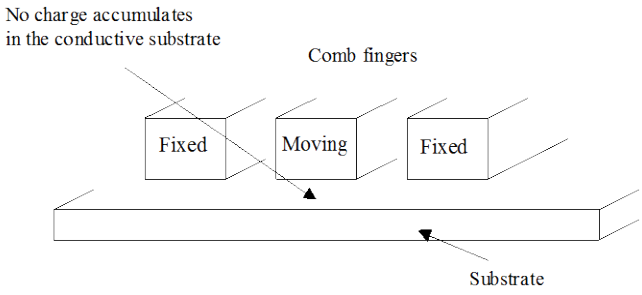

Figure 2b*: A similar device without dielectric survives a far higher radiation dose*

D. Discussion of the device case studies

These examples show that reliability of MEMS devices needs to be taken very seriously. The typical time span to bring a completely new, fully reliable MEMS technology to the market is on the order of ten years. This means that it poses a considerable threat to commonplace concepts like ‘short-time-to-market’ and

'return-on-investment'. However: do the reliability assessment better than your competitors, and your chances of long-term success are also large.

III – MEMS reliability: definition and statistics

Reliability is the property of an object to perform its intended function under stated conditions for a stated period of time. In that sense, the reliability assessment of an object is much more than the characterization of the functionality. It explicitly deals with long-term correct behavior under the influence of external perturbations.

During their operational life 'in the field', MEMS devices may fail. Individual failures occur 'randomly' and typically follow Poisson statistics. The chance *P* of having *n* failures until time *t* is given by

$$P(n,t) = \frac{(\lambda(t)\cdot t)^n}{n!}\exp\left[-\lambda(t)\cdot t\right].$$

Closely related are the reliability function *R(t)*, giving the probability of having *0* failures until time *t*,

$$R(t) = P(n=0,t) = \exp\left[-\lambda(t)\cdot t\right],$$

and the failure distribution function *f(t)*, giving the amount of devices left times how fast they fail,

$$f(t) = R(t)\lambda(t).$$

In these equations, the crucial factor is the failure rate $\lambda(t)$, which can be time dependent. An example of a time-dependent failure rate is the often encountered 'bath tube curve' (Fig. 3). It is divided in an early stage where the failure rate is high (the 'infant mortality regime'), the useful life region with a (preferably) low, constant failure rate, and an 'end of life' region, typically associated with wear-out failures, where the failure rate goes up again.

The failure distribution function *f(t)* in the infant mortality region is often described well by a Weibull distribution (many independent sources cause the failures), while the *f(t)* in the end of life region if often described by a lognormal distribution, indicating that a single failure mechanism dominates.

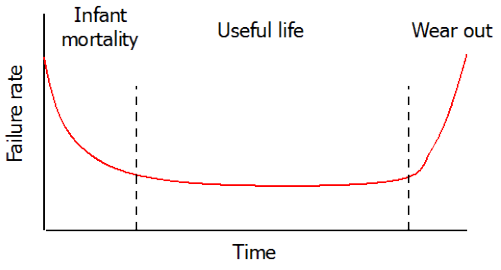

Figure 3*: The bath tube curve failure rate graph*

IV – Failure modes and failure mechanisms

MEMS reliability can be assessed purely statistically (how many failures under which conditions?), at the level of failure modes (what's wrong?), or at the level of failure mechanisms (how come?). The failure mode is the description of the apparent error. The failure mechanism is the process that caused the failure to occur. As an example, in Fig. 4, the failure mode of the electrostatic comb drive is a partly molten device. There can be several failure mechanisms associated with this error. A high-current high-voltage driver was connected to the actuation electrodes. Somehow, the moving part has touched the stationary part. This can be due to simply rough handling, or overvoltage stress, but in this particular case, it happened while the device was actuated in the SEM (scanning electron microscope), so it can also be that charge building up on an unconnected electrode or on a dielectric caused the device to move erratically, causing the short circuit that partly vaporized it.

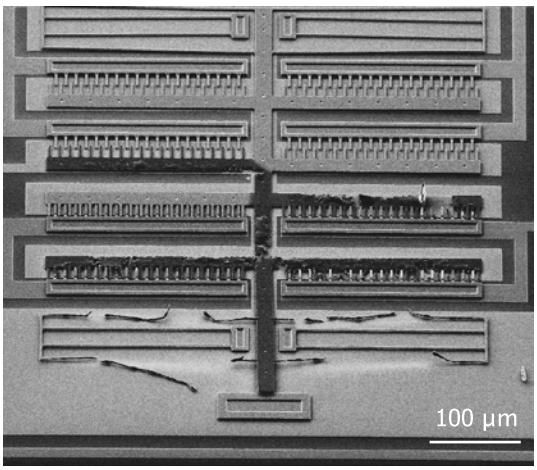

Figure 4*: The failure mode of this partly molten comb drive is clear, but the failure mechanism needs further study.*

Table 1: *Typical failure mechanisms in MEMS devices*

Fracture	Wear
Overload	Adhesive
Fatigue	Abrasive
	Corrosive
Creep	
Applied stress	Degradation of dielectrics
Intrinsic stress	Charging
Thermal stress	Leakage
	Breakdown
Adhesion	
Capillary forces	Delamination
Molecular forces	Contamination
Electrostatic forces	Melting
	Electrostatic discharge
Electromigration	(……)

Because the failure mechanism tells us something about the root cause of the failure and how to prevent it, the most important thing to do in reliability research is to characterize these failure mechanisms, that means to characterize the e.g. physical, chemical or mechanical processes that ultimately lead to failures in microscopic devices. This knowledge can then be used to create predictive (fundamental physics/chemistry based, or purely phenomenological) models. The main failure mechanisms encountered in MEMS are listed in table 1.

Of these failure mechanisms dielectric charging, adhesion, friction/wear, and fatigue fracture will now be covered concisely as examples, providing both part of what is already known, and some open questions.

V – Examples of failure mechanisms research

A. Charging of dielectrics

Capacitive RF MEMS switches were thought to be the answer to the reliability problems that metal-to-metal contact micro-switches had due to their deteriorating contacting surfaces. A basic capacitive RF MEMS switch is a two state variable capacitor, where a free-standing bridge can collapse under the influence of an actuation voltage onto a high dielectric constant insulator (Fig. 5). In the free-standing position, the capacitance is low, and a RF signal is basically unaltered, while in the pulled-in position, the capacitance is high and the RF signal is blocked.

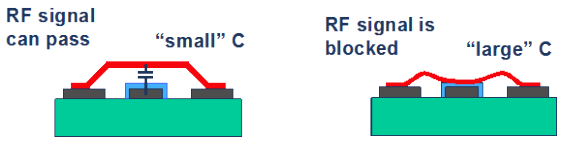

Figure 5*: Operating principle of a capacitive RF MEMS shunt switch*

Upon pull-in, the high actuation voltage is present over the dielectric and causes charge accumulation, resulting in stiction failures (Fig. 6)

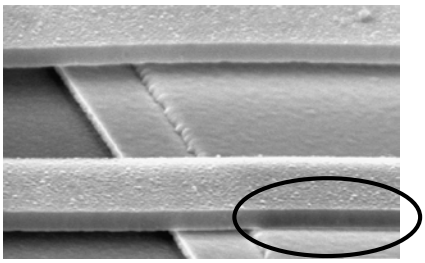

Figure 6*: The typical failure mode of a capacitive RF MEMS switch is the bridge adhering to the dielectric below it.*

The actual process leading to this failure mode is rather intricate [10]. Effectively, the charged dielectric behaves as if there were a built-in voltage present, which shifts the capacitance versus actuation voltage curve. Fig. 7a shows the curve that describes the capacitance change of the switch caused by the pull-in behavior with no built-in charge. The curve is symmetric around 0 V, as both positive and negative actuation voltages V cause an attractive force *F* due to the relation $F \sim V^2$. Together with the linear restoring spring force of the deformed bridge, and the fact that the force becomes higher as the bridge comes closer to the electrode below the dielectric, a general curve can be calculated that describes when the bridge is pulled in and pulled out at two different voltages, indicated with the this line.

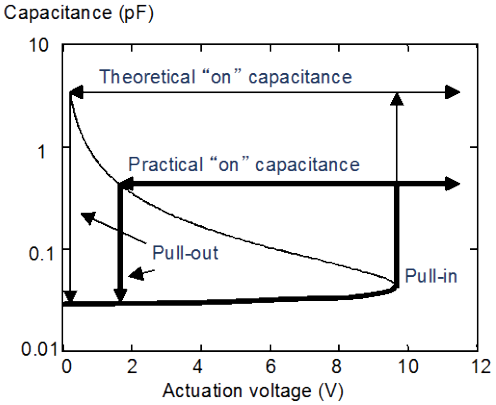

Figure 7a*: Pull-in and pull-out cause a capacitance change. The points of pull-in and pull-out are dictated by the general curve (thin line, only positive half drawn). The capacitance is less then the theoretical value due to the surface roughness lowering the maximum attainable capacitance. The bold line shows the actual switching behavior when the voltage is changed [10].*

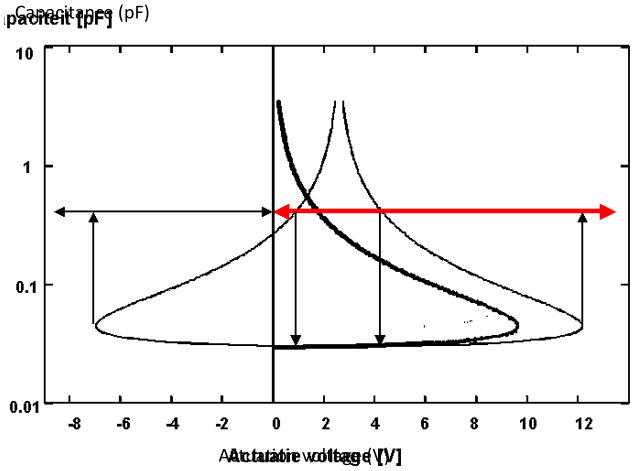

Figure 7b: *The whole curve shifts under the influence of charge building up, and the motion becomes erratic. The red arrow shows the behavior when the switch is actuated with a square wave: it stays closed [10].*

This general curve is displaced when charge builds up in the dielectric due to a voltage overstress condition. As a result the pull-in and pull-out voltage shift (Fig. 7b). When the voltage is slowly varied, the switch will move up and down as before, but at different voltage. Also a smaller negative voltage will be required to pull the bridge in. The situation changes if the switch is actuated with a square wave with 0 V and a voltage above the pull-in voltage as its two states and fast rising and falling edges, as is often used. The bridge will move

in when the actuation voltage is applied, but will be still be pulled-in when the actuation voltage has returned to 0 V due to the limited response time (it will not move faster than the mechanical resonance frequency). This will result in the peculiar situation that we cross the general curve a second time, but now for the negative branch. Because the switch itself does not know whether it came from a situation where it was pulled-in by a positive or a negative actuation voltage, it will remain stuck at 0 V. In real life this manifests itself as a switch that works well when tested slowly in the lab, even though the pull-in and pull-out voltage change somewhat, while if fails to function properly in a real application with square wave actuation.

Full failure mechanism assessment of the stiction failure mode also involves the investigation of the charge trapping physics as a function of layer deposition parameters [11]. Current conduction was proposed to take place by Poole-Frenkel conduction or Fowler-Nordheim tunneling. Charge trapping may occur at unsaturated sites of a non-stochiometric dielectric. High-*k* dielectrics, desirable because they make it possible to achieve a high capacitance change in the switch, tend to have severe problems with charge retention. Both very leaky dielectrics, where the charge cannot stay for a long time, and perfect dielectrics with no trapping can be a solution. The non-uniformity of the charge trapping also needs to be taken into account [12]. The dielectric can also be dispensed with altogether [5, 13, 14]

The voltage overstress charging issue is not the only reliability threat to reckon with in capacitive RF MEMS switches: others include creep and fatigue of the bridge, long-term leak-tightness of a protective encapsulation, shock resistance, susceptibility of the dielectric to ionizing radiation (as in the case of the accelerometers), adhesion changes of the contacting bridge and dielectric; these are all effects to keep in mind as well during the design.

B. Adhesion between microscopic structures

Adhesion of MEMS devices has been a regular problem ever since the technology was developed. Typical 'stiction' failures during drying after the sacrificial layer etch have been largely eliminated by the application of self assembled monolayer (SAM-) coatings and the use of CO_2 and cyclohexane supercritical point drying.

The adhesion forces between microscopic surfaces due to capillary condensation, molecular van der Waals and Casimir forces, trapped surface charge and direct chemical bonding are a reliability concern. They can be relatively large on this scale (scaling as x^2 with the dimension while most other forces scale as x^3), depend on the environment, and are not always constant over time. The failure mode is again stuck parts, but the root cause is in the details of interaction of the two contacting surfaces rather than just bulk or surface charge as in the case of capacitive RF MEMS switches.

The effect has been extensively modeled over the last 10 years, with models widely differing in scope and sophistication, e.g. [15-18]. Most of them take into account some or all of the following:

- A (mostly statistical) description of the roughness of the individual surfaces, often including the shape of the highest asperities
- A description of how the highest asperities behave upon contact with the other surface (elastic, plastic, adhesive, Hertzian, and with analytical and finite element simulations, …)
- A description of the distribution of the distance between the surfaces
- A description of the forces acting between the surfaces (capillary, molecular, electrostatic, cold welding, reactions, third body species, …)
- A description of the contact type: continuous, intermittent, external force, environment e.g., temperature, humidity, …)
- A description of the maximally available restoring spring force (can be time and environment dependent too!) dictating how much adhesive force can be tolerated.

An easy to grasp way to look at adhesion of microscopically rough surfaces is the two contacting surfaces depicted in Fig. 8. The highest points contact each other, and how far the surfaces will be driven into one another depends on the externally applied force, the adhesion force itself, and the properties of the asperities (hardness, elasticity, elasticity of the bulk redistributing the stress, and so on).

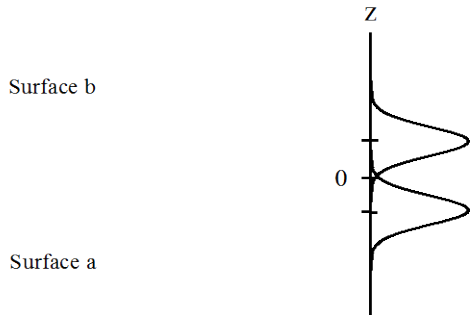

Figure 8*: Geometry of two rough surfaces in contact. The adhesion force is highest where the surfaces are closest together. The graph shows the two surface position distribution functions.*

If the distance dependency of the surface forces is known (parts of the surface near to the other surface will contribute more than surfaces far away from each other), one can estimate the total adhesive force per unit area. This calculation can be done mostly independently for capillary, molecular, Casimir, and electrostatic forces.

By assessing also the maximally available restoring force to separate the surfaces, a prediction can be made of whether the surfaces will tend to adhere or not. Most adhesion models are usable up to this point. They do not take into account that the surface interaction can change considerably upon repeated contact, which has recently

been demonstrated for O_2 plasma cleaned polysilicon adhesion sensor devices (Fig. 9) [19]. Also ageing due to long-term contact, a reliability threat because adhesion typically increases in this case [20], has not been thoroughly assessed theoretically. Another issue in real applications is that the surfaces often do not directly contact each other, but touch with the contamination layers on their surfaces only, which can change the adhesive forces completely, even though they do not change the geometry of the contact significantly.

Measurements like those presented in Fig. 9 are made with dedicated MEMS adhesion sensors, such as the one shown in Fig. 10. It is a comb drive actuator with a head which touches a counter-surface when the displacement exceeds 2.0 µm. Reducing the voltage again after the contact has been made results in a pulling force on the contact, and when the adhesion is overcome, the comb drive jumps out of contact. The jump length quantifies the adhesive force present.

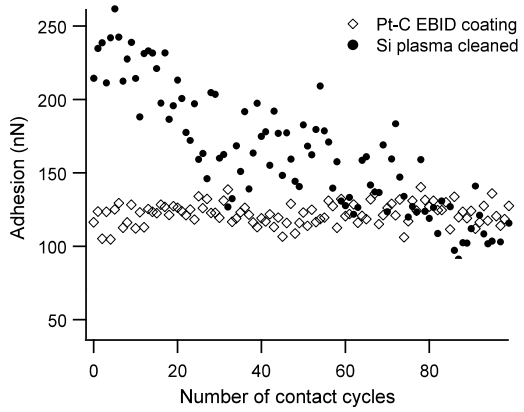

Figure 9*: Typical MEMS adhesion models do not take into account the evolution of the surface chemistry upon repeated contact, as is demonstrated in this recent measurement [19].*

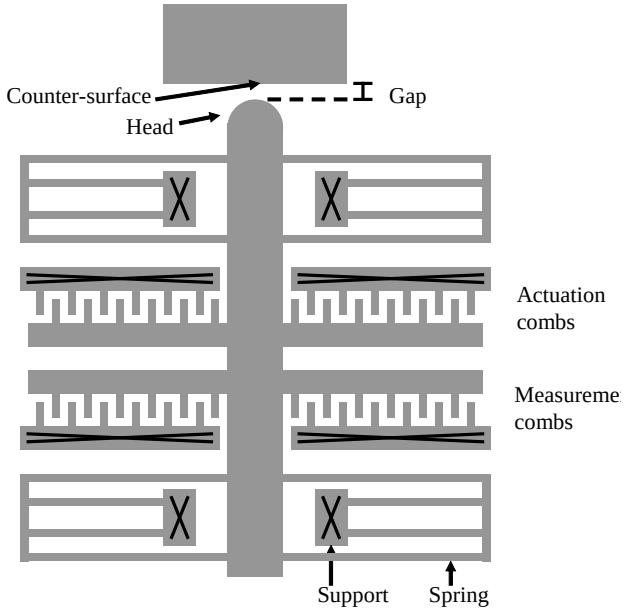

Figure 10: *MEMS adhesion sensor [21]*

Adhesion problems can be solved by applying anti-stiction coatings like SAM-layers, or plasma deposited fluorocarbon coatings. Roughening the surface also helps, at least temporarily. Durability of these coatings is an issue. Hermetic packaging can prevent the strongest of all adhesion forces, capillary condensation, to be present, but it is no easy job to guarantee the water-tightness of a microscopic encapsulation for 10 years or more, even if getter materials are used. This is another major reliability concern.

C. Friction and wear on the micro-scale

Surfaces contacting each other and then sliding laterally pose their own set of problems, besides adhesion. Friction and wear are so problematic in microsystems, that most designs avoid the use of sliding surfaces altogether. Typical macroscopic wear solutions like lubrication with oil are often not applicable in MEMS due to the resulting viscous drag [22]. We are left with surfaces that directly contact each other during sliding, in the presence of third bodies between the surfaces such as contamination and wear debris. The situation is aggravated by the fact that silicon, often used in MEMS, although it otherwise has very good mechanical properties, is tribologically a poor material: it wears easily, especially under the influence of water from the environment. Silicon wear in MEMS was studied extensively by Sandia National Laboratories [23, 24] and others [24, 26]. The application of SAMs as an anti-friction/anti-wear coating is much less successful than in the case of adhesion reduction, as the layer is simply too thin and rubbed away too easily, exposing the bare silicon (native oxide) surface after some sliding has taken place [27].

Where adhesion modeling already has the tendency to get out of hand in terms of complexity because of the many phenomena that play a role, this holds even more for the fundamentals of friction and wear. A complete physics community, the field of nanotribology, is studying the effects that take place in a sliding contact at the nanometer scale. This research has gained a lot of momentum after the invention of the AFM (atomic force microscope) and the FFM (friction force microscope – an AFM sensitive to lateral forces).

It was found hat the basis of friction can be led back to a number of irreversible nanometer scale processes that consume energy. The first is atomic scale stick-slip, where a hard tip slides in little hops over an atomic lattice. FFM experiments really show this single-atom hopping well-resolved [28]. The other processes have to with the movement of third bodies between the surfaces, the displacement of surface atoms (the beginning of wear), and chemical reactions between the surfaces and of the surfaces with the third bodies.

The scale of MEMS is somewhere between the macroscopic treatment of friction (which is largely phenomenological), and the fundamental processes at the nm scale. As such, it can be expected that certain nanotribo-

logical principles can be 'scaled-up' to be used in MEMS, while on the other hand MEMS themselves can be used to investigate until what scale typical nm-scale effects such as the almost complete disappearance of friction due to lattice mismatch (superlubricity) [29] and temperature-assisted hopping (thermolubricity) [30] can survive.

MEMS devices that allow the same kind of investigations as performed with the FFM have been pioneered by Senft and Dugger [31]. A recent example is the MEMS tribometer [32], a two-dimensional adhesion sensor with which also rubbing experiments can beperformed (Fig. 11). With it, more refined experiments with optimized readout can be performed, which show stick-slip behavior on the order of the surface roughness of the MEMS devices.

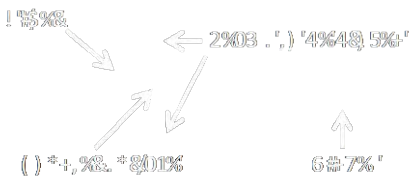

Figure 11*: The head of the MEMS tribometer friction sensor. The slider can be moved in three dimensions by two comb drive actuators (outside the view, they can be the same as in Fig 10) and a pad to pull the head down. The head slides against the counter-surface. The little beams of the counter-surface can be broken, the structure then flipped upright and secured in position. This allows access to the sidewall surface with a conventional AFM to assess the sidewall surface roughness after the experiment [33].*

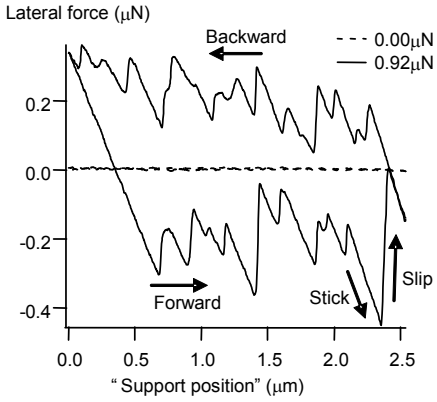

Figure 12*: Irregular, but repeatable stick-slip of a MEMS device with sliding contacts [32].*

Figure 12 shows the stick-slip behavior of a MEMS 'head' sliding against a counter-surface with the sidewalls touching in a 'friction loop'. The vertical axis represents the lateral force experienced by the slider (the friction force). The horizontal axis shows where the slider would have been when it had not been hindered due to the interaction with the other surface. Such plots are common to plot the results of FFM experiments at the atomic scale as well.

To describe stick-slip friction on the atomic scale, in the nanotriblogy community the Prandtl-Tomlinson model is used [33, 34]. A periodic potential describing the surface lattice, and a quadratic potential describing the AFM tip spring constant are used to calculate the atomic scale hopping, and the effect that play a role. Recently, it was shown that the model can be modified to include a stochastic term to describe MEMS surfaces, and that this phenomenological 'stochastic Prandtl-Tomlinson model' can be used to simulate measurements like shown in Fig.12. The result is convincing with only a small overestimation of small-scale stick slip (Fig. 13).

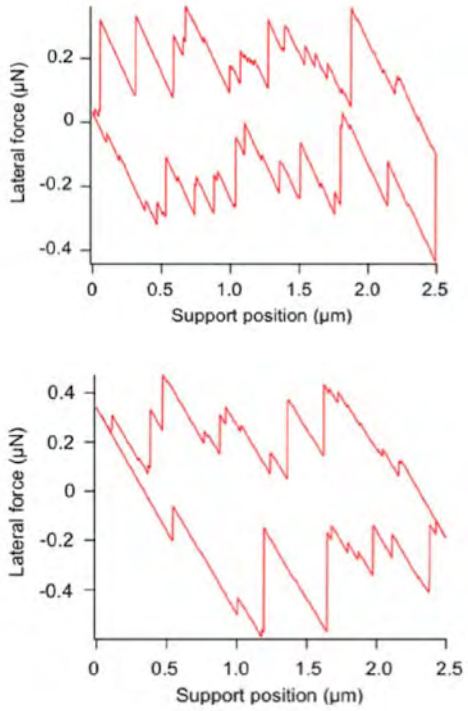

Figure 13*: Simulations of the measurement of Fig. 10 with the stochastic Prandtl-Tomlinson model, using the stochastic parameters of the surface roughness as input [35].*

Extensive quantitative measurements on wear at the nano-scale were performed in the context of the Millipede project for writing data with an AFM tip [36]. Such a tip for data storage has to survive siding over a very long distance. In the course of this research, it was shown that reaction rate theory provides a good basis to describe atomic scale wear [37, 38].

Recent developments in wear reduction include dither (high frequency vibrations to lower friction in MEMS [39, 40]), Diamon-Like Carbon (DLC) coatings [41], and Vapor Phase Lubrication (VPL) [42]. The latter is a very promising technology in which pentanol vapor capillary condenses at the contact points, just like water does in normal adhesion. When the surfaces slide, the pentanol molecules are physically ripped apart

(tribochemistry), and form a hard, wear-resistant layer on the surface of which not yet much is known but the fact that it contains carbon [43]. The obvious advantage of VPL is that it automatically lubricates all the points in contact, also at difficult to reach locations, where DLC, which is a line of sight deposition technique, is difficult to apply universally.

D. Fatigue fracture in silicon micromachines

Fatigue fracture in silicon microstructures has been a concern ever since it was discovered in 1992 [44]. Macroscopic silicon does not show fatigue, because it is an ideally brittle material. Microscopic structures made of silicon do show fatigue, though.

Several explanations have been brought forward, being stress corrosion cracking (SCC) in the surface oxide layer [45], surface oxide growth due to periodic stress followed by fracturing of the oxide, named reaction layer fatigue (RLF) [46], and fully mechanical explanations involving wedging of cracks, or small-scale dislocation mobility [47].

Although the common view has been for some time that a cyclic component of the stress is required to initiate fatigue crack growth in silicon, this has been challenged lately [48, 49]. Indeed, the pure SCC mechanism will also take place in continuously tensile stressed SiO_2, such as is known from optical fiber deterioration [50].

Using the SCC theory used for optical fibers, it is possible to describe the measured fatigue data very well (Fig. 14), but a static crack growth has to be assumed, which is not generally accepted.

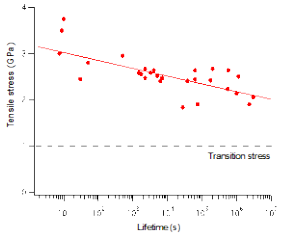

Figure 14*: Measurement of the delayed fracture in silicon microstructures due to fatigue [51] and SCC model [49].*

More refined fatigue measurements are required to solve the riddle and find out what is really happening. What is important to take into account in the discussion on fatigue in silicon microstructures, is that the phenomenon occurs only at stresses which are a fair fraction of the stress required for immediate fracture. Most MEMS devices are operated far from this point, and hence will not be affected at all.

VI - Conclusion

MEMS reliability is an important topic that is often neglected, especially early in the design phase. The study and the optimization of the reliability of a completely new MEMS technology typically change the development time to a commercial product to 10 years (instead of the 1 - 2 years that are typically needed for a working prototype).

It has been shown that proper assessment of the failure mechanism that can occur leads to new scientific knowledge, which has been demonstrated by examples. However, it also brings in a huge competitive advantage. Do your reliability assessment well, and you can bring your MEMS product to a commanding position in a defensible market segment, and stay there for a long time.

Acknowledgements

The MME organizing committee is thanked for kindly inviting me to present this work. Most of this text describes a short overview of prior work of the author. In this context, the Dutch STW foundation is thanked for financial support in the ‘Veni and ‘Vidi’ programs.

References

[1] Douglass, M.B., DMD reliability: a MEMS success story, *Proc. SPIE* Vol. 4980, pp. 1 - 11, 2003

[2] Tregilgas, J.H., Micromechanical device having an improved beam, Texas Instruments Inc., *US patent* no 5,552,924, 1996

[3] Sontheimer, A.B., Digital Micromirror Device (DMD) hinge memory lifetime reliability modeling, *Proc. International Reliability Physics Symposium (IRPS)*, Dallas, pp. 118 - 121, 2002

[4] Rebeiz, G.M., RF MEMS: Theory, design, and technology, *John Wiley & Sons*, Hoboken, 2003

[5] Van Spengen, W. M., S.B. Roobol, W.P. Klaassen, T.H. Oosterkamp, The MEMSamp: using (RF-)MEMS switches for the micromechanical amplification of electronic signals, *J. Micromech. Microeng.* Vol. 20, pp. 125011-1 – 125011-10, 2010

[6] Petersen, K.E., Microemechanical membrane switches on silicon, *IBM J. Res. Develop*. Vol. 23, pp. 367 - 359, 1979

[7] SPST RF-MEMS switch DC to 12 GHz RMSW101, Radant MEMS datasheet, retrieved from www.radantmems.com on May 17, 2011

[8] Knudson, A.R., S. Buchner, P. McDonald, W.J. Stapor, A.B. Campbell, K.S. Grabowski, D.L. Knies, The effects of radiation on MEMS accelerometers, *IEEE Trans. Nucl. Sci.* Vol. 43, pp. 3122 - 3126, 1996

[9] Lee, C.I., A.H. Johnston, W.C. Tang, C.E. Barnes, Total dose effects on microelectromechanical systems (MEMS): accelerometers, *IEEE Tran. Nucl. Sci.* Vol. 43, pp. 3127 - 3132, 1996

[10] Van Spengen, W.M., R. Puers, R. Mertens, I. De Wolf, A comprehensive model to predict the charging and reliability of capacitive RF MEMS switches, *Micromech. Microeng.* Vol. 14, pp. 514 – 521, 2004
[11] Daigler, R., E. Papandreou, M. Koutsoureli, G. Papaioannou, J. Papapolymerou, Effect of deposition conditions on charging processes in SiNx: Application to RF-MEMS capacitive switches, *Microelectron. Eng.* Vol. 86, pp. 404 - 407, 2009
[12] Rottenberg, X., I. De Wolf, B.K.J.C. Nauwelaers, W. De Raedt, H.A.C. Tilmans, Analytical model of the DC actuation of electrostatic MEMS devices with distributed dielectric charging and nonplanar electrodes, *J. Microelectromech. Syst.* Vol 16, pp. 1243 - 1253, 2007
[13] Blondy, P., A. Crunteanu, C. Champeaux, A. Catherinot, P. Tristant, O. Vendier, J.L. Cazaux, L. Marchand, Dielectric less capacitive MEMS switches, *IEEE MTT-S Int. Microw. Symp. Dig.* Vol. 2, Limoges, pp. 573 - 576, 2004
[14] Ekkels, P., X. Rottenberg, P. Czarnecki, H. Philipsen, R. Mertens, R. Puers, H.A.C. Tilmans, Air gap-based MEMS switch technology using nickel surface micromachining, *Sens. Act. A* Vol. 166, pp. 256 - 263, 2011
[15] Van Spengen, W.M., R. Puers, I. De Wolf, A physical model to predict stiction in MEMS, *J. Micromech. Microeng.* Vol. 12, pp. 702 – 713, 2002
[16] De Boer, M.P., Capillary adhesion between elastically hard rough surfaces, *Exp. Mech.* Vol. 47, pp. 171 - 183, 2007
[17] Zhao Y.P., L.S. Wang, T.X. Yu, Mechanics of adhesion in MEMS - a review, *J. Adhesion Sci. Technol.* Vol. 17, pp. 519 - 546, 2003
[18] D.B. Asay, M.P. de Boer, S.H. Kim, Equilibrium vapor adsorption and capillary force: extract Laplace-Young equation solution and circular approximation approaches, *J. Adhesion Sci. Technol.* Vol. 24, pp. 2363 - 2382, 2010
[19] Van Spengen, W.M., Hints of atomic scale phenomena in adhesion and friction measurements with MEMS devices, *Tribology* Vol. 4, pp. 115 – 120, 2010
[20] Liu H., B. Bhushan, Adhesion and friction studies of microelectromechanical systems/ nanoelectromechanical systems materials using a novel microtriboapparatus, *J. Vac. Sci. Technol.* A, Vol. 21, pp. 1528 - 1538, 2003
[21] Van Spengen, W.M., E. Bakker, J.W.M. Frenken, A 'nano-battering ram' for measuring surface forces - Obtaining force-distance curves and sidewall stiction data with a MEMS device, *J. Micromech. Microeng.* Vol. 17, pp. S91 – S97, 2007
[22] Deng, K., G.P. Ramanathan, M. Mehregany, Micromotor dynamics in lubricating fluids, *J. Micromech. Microeng.* Vol. 4, pp. 266 - 269, 1994
[23] Miller, S.L., J.J. Sniegowski, G. LaVigne and P.J. McWorther, Friction in surface micromachined microengines, *Proc. SPIE* Vol. 2722, pp. 197 - 204, 1996
[24] Flater, E.E., A.D. Corwin, M.P. de Boer, R.W. Carpick, In situ wear studies of surface micromachined interfaces subject to controlled loading, *Wear* Vol. 260, pp. 580 - 593, 2006
[25] Gabriela, K.J., F. Behia, R. Mahadevana, M. Mehregany, In situ friction and wear measurements in integrated polysilicon mechanisms, *Sens. Act. A* Vol. 21, pp. 184 - 188, 1990
[26] Williams, J.A., H.R. Le, Tribology and MEMS, *J. Phys. D* Vol. 39, pp. R201 – R214, 2006
[27] Hook, D.A., S.J. Timpe, M.T. Dugger, J. Krim, Tribological degradation of fluorocarbon coated silicon microdevice surfaces in normal and sliding contact, *J. Appl. Phys.* Vol. 104, pp. 034303-1 - 034303-6, 2008
[28] Mate, C.M., G.M. McClelland, R. Erlandsson, S. Chiang, Atomic scale friction of a tungsten tip on a graphite surface, *Phys. Rev. Lett.* Vol. 59, pp. 1942 - 1945, 1987
[29] Dienwiebel, M., G.S. Verhoeven, N. Pradeep, J.W.M. Frenken, Superlubricity of Graphite, *Phys. Rev. Lett.* Vol. 92, pp. 126101-1 - 126101-4, 2004
[30] Gnecco, E., R. Bennewitz, T. Gyalog, Ch. Loppacher, M. Bammerlin, E. Meyer, H.-J. Güntherodt, Velocity dependence of atomic friction, *Phys. Rev. Lett.* Vol. 84, pp. 1172 - 1175, 2000
[31] Senft D.C., M.T. Dugger, Friction and wear in surface micromachined tribological test devices, *Proc. SPIE* Vol. 3224, pp. 31 - 38, 1997
[32] Van Spengen W.M., J.W.M. Frenken, The Leiden MEMS tribometer: real time dynamic friction loop measurements with an on-chip tribometer, *Trib. Lett.* Vol. 28, pp. 149 – 156, 2007
[33] Prandtl, L., Ein Gedankenmodell zur kinetischen Theorie des festen Körper, *Z. Angew. Math. Mech.* Vol. 8, pp. 85 - 106, 1928
[34] Tomlinson, G.A., A molecular theory of friction, *Philos. Mag.* Vol. 7, pp. 905 - 939, 1929
[35] Van Spengen. W.M., V. Turq, J.W.M. Frenken, The description of friction of silicon MEMS with surface roughness: virtues and limitations of a stochastic Prandtl-Tmlinson model and the simulation of vibration-induced friction reduction, *Beilstein J. Nanotechnol.* Vol. 1, pp. 163 – 171, 2010
[36] Vettiger, P., G. Cross, M. Despont, U. Drechsler, U. Durig, B. Gotsmann, W. Haberle, M.A. Lantz, H.E. Rothuizen, R. Stutz, G. K. Binnig, The "millipede" - Nanotechnology entering data storage, *IEEE Trans. Nanotechnol.* Vol. 1, pp. 39 - 55, 2002
[37] Gotsmann B., M.A. Lantz, Atomistic Wear in a Single Asperity Sliding Contact, *Phys. Rev. Lett.* Vol. 101, pp. 125501-1 – 125501-4, 2008
[38] Jacobs, D.B.T., B. Gotsmann, M.A. Lantz, R.W. Carpick, On the Application of Transition State Theory to Atomic-Scale Wear, *Tribol. Lett.* Vol. 39, pp. 257 – 271, 2010
[39] Lantz, M.A., D. Wiesmann, B. Gotsmann, Dynamic superlubricity and the elimination of wear on the nanoscale, *Nature Nanotechnol.* Vol. 4, pp. 586 –

591, 2009
[40] Van Spengen, W.M., G.H.C.J. Wijts, V. Turq, J.W.M. Frenken, Microscale friction reduction by normal force modulation in MEMS, *J. Adhesion Sci. Technol.* Vol 24, pp. 2669 – 2680, 2010
[41] Smallwood, S.A., K.C. Eapen, S.T. Patton, J.S. Zabinski, Performance results of MEMS coated with a conformal DLC, *Wear* Vol. 260 pp. 1179 – 1189, 2006
[42] Asay, D.B, M.T. Dugger, S.H. Kim, In-situ vapour-phase lubrication of MEMS, *Tribol. Lett.* Vol. 29, pp. 67 - 74, 2008
[43] Asay, D.B., M.T. Dugger, J.A. Ohlhausen, S.H. Kim, Macro- to nanoscale wear prevention via molecular adsorption, *Langmuir* Vol. 24, pp. 155 - 159, 2008
[44] Connally, J.A., S.B. Brown, Slow crack growth in single-crystal silicon, *Science* Vol. 256, pp. 1537 - 1539, 1992
[45] Van Arsdell W.W, S.B. Brown, Subcritical crack growth in silicon MEMS, *J. Microelectromech. Syst.* Vol. 8, pp. 319 - 327, 1999
[46] Muhlstein, C.L., E.A. Stach, R.O. Ritchie, A reaction-layer mechanism for the delayed failure of micron-scale polycrystalline silicon structural films subjected to high-cycle fatigue loading, *Acta Mater.* Vol. 50, pp. 3579 - 3595, 2002
[47] Kahn, H., L. Chen, R. Ballarini, A.H. Heuer, Mechanical fatigue of polysilicon: effects of mean stress and stress amplitude, *Acta Mater.* Vol. 54, pp. 667 - 678, 2006
[48] Baumert, E.K., P.O. Theillet, O.N. Pierron, Investigation of the low-cycle fatigue mechanism for micron-scale monocrystalline silicon films, *Acta Mater.* Vol. 58, pp. 2854 - 2863, 2010
[49] Van Spengen, W.M., Static Crack growth and fatigue modelling for silicon MEMS, *Proc. Micromechanics Europe*, Enschede, pp. 285 - 288, 2010
[50] Wiederhorn, S.M., E.R. Fuller Jr., R. Thomson, Micromechanisms of crack growth in ceramics and glasses in corrosive environments, *Met. Sci.* Vol 14, pp. 450 - 458, 1980
[51] Muhlstein, C.L., S. B. Brown, R. O. Ritchie, High cycle fatigue and durability of polycrystalline silicon thin films in ambient air, *Sens. Act. A* Vol. 94, pp. 177 - 188, 2001

Integration of meso- and nano-scale objects by capillary assembly and adhesive transfer

Cyrill Kuemin[1,2], Lea Nowack[1,2], Cathrein Hueckstaedt[1,2], Emanuel Loertscher[1], Antje Rey[1,3], Nicholas D. Spencer[2], Heiko Wolf[1*]

[1]*IBM Research – Zurich, Säumerstr. 4, 8803 Rüschlikon, Switzerland*
[2]*Laboratory for Surface Science and Technology, Department of Materials, ETH Zurich, Wolfgang-Pauli-Strasse 10, 8093 Zürich, Switzerland*
[3]*Nanotechnology Group, Department of Mechanical and Process Engineering, ETH Zurich, Tannenstrasse 3, 8092 Zürich, Switzerland*

The special properties of micro- and nanoscale objects, such as metal and semiconductor nanoparticles, nanowires, nanotubes, or functionalized polymer particles make them promising building blocks for novel optical, electronic, or biosensing devices. Often, these small objects are prepared as colloidal suspensions or can be dispersed in a liquid to form a stable suspension. Thus, the fabrication of devices requires methods for efficient and accurate integration of particles from the liquid phase onto a solid surface. More complex device architectures may, in addition, entail the selective assembly of several different types of small objects at pre-defined locations or demand an assembly with the correct orientation when such objects are non-spherical.

We describe a technique that uses a combination of capillary assembly and printing with elastomeric stamps to fabricate defined particle arrays with high yield and accuracy. Capillary assembly is performed from an aqueous colloidal suspension onto a patterned template. The template is a silicone elastomer replica of a 3D-structured silicon master. In a subsequent transfer step, the assembled particles are printed onto the target substrate.

During capillary assembly, the meniscus of a colloidal particle suspension is dragged over the 3D-structured elastomer template (Figure 1)[1]. Particles get trapped and positioned at predefined geometric features of the template by capillary forces. The actual deposition process during capillary assembly is very sensitive to the geometry of the assembly traps. By going beyond particle deposition into simple holes, to fabricating templates with arrays of posts of specific shape and geometry instead, it was possible to assemble sub-micrometer polymer particles in a size-selective manner (Figure 2)[2].

Even non-spherical nano-objects, such as gold nanorods, lend themselves to capillary assembly in sparse arrays with single-particle resolution. In order to obtain high assembly yields, it is essential to reach high particle concentrations in a narrow zone directly at the meniscus (the accumulation zone). At a given colloid concentration, this can be achieved by controlling the temperature of the colloid and thus the evaporation rate at the meniscus. Under optimized conditions, assembly yields of more than 90% could be reached (Figure 3)[3].

When using short linelets (shallow holes with dimensions close to those of the nanorods) as assembly sites it is possible to control the position as well as the orientation of the assembled nanorods (Figure 4). Thus, these rod-shaped nanoparticles could be positioned in large numbers with unprecedented accuracy.

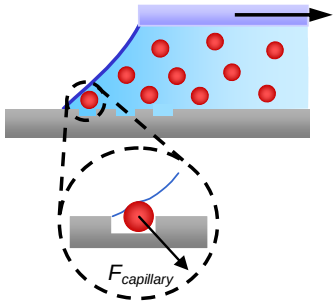

Figure 1: Schematic view of the capillary assembly step. The template consists of a patterned silicone elastomer. The meniscus of the colloidal particle suspension is dragged over the template, filling topographical structures with particles.

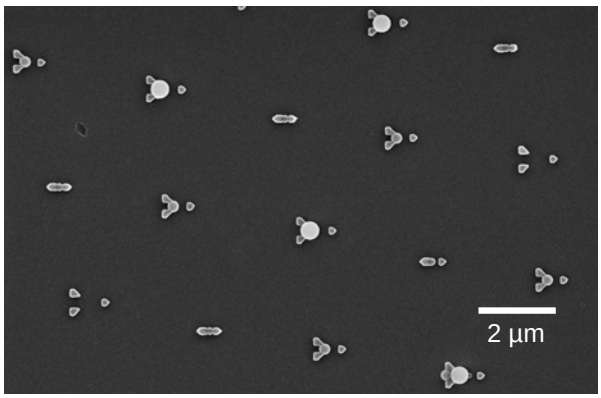

Figure 2: Scanning electron microscope (SEM) image of polystyrene spheres of different sizes, assembled sequentially into their corresponding assembly sites on a PDMS template.

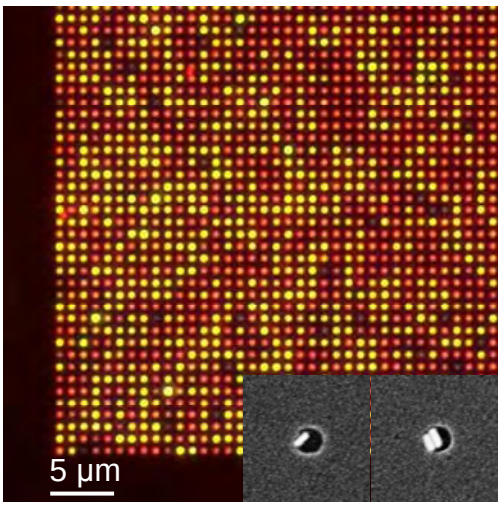

Figure 3: Dark-field optical micrograph of 25 nm x 74 nm Au nanorods assembled onto an elastomer template consisting of an array of circular holes (120 nm diameter, 40 nm deep). The inset shows SEM images of individual holes filled with Au nanorods.

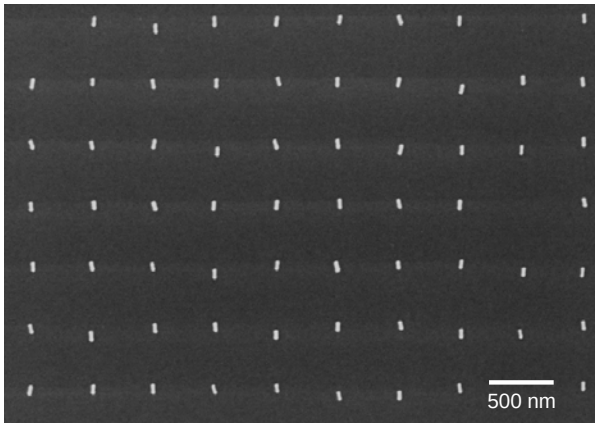

Figure 4: SEM image of an array of Au nanorods (25 nm x 80 nm) printed onto a Si substrate from a template with 37-nm deep linelets (50 nm x 120 nm) acting as assembly sites.

References

[1] Malaquin, L.; Kraus, T.; Schmid, H.; Delamarche, E.; Wolf, H. "Controlled Particle Placement through Convective and Capillary Assembly" Langmuir **2007**, *23*, 11513-11521

[2] Kuemin, C.; Hueckstaedt, K. C.; Lörtscher, E.; Rey, A.; Decker, A.; Spencer, N.D.; Wolf, H. "Selective Assembly of Sub-Micrometer Polymer Particles" *Adv. Mater.* **2010**, *22*, 2804-2808

[3] Kuemin, C.; Stutz, R.; Spencer, N.D.; Wolf, H. "Precise Placement of Gold Nanorods by Capillary Assembly" *Langmuir* **2011**, *27*, 6305-6310

High Temperature Micro Sensors: Structure and Circuit

Jijun Xiong[a, 1]

North University of China, Taiyuan City , China

Micro sensors with high temperature tolerance can be widely used in the fields such as automotive, aviation & aerospace industries. For example, high temperature pressure sensors are the key devices for the function and health control system of jet engine, re-entry capsule, and deep space probe. Now the design and manufacture technologies of traditional room-temperature silicon-based piezoresistance micro sensors have been advanced developed. But these devices will be damaged at elevated temperature for three main problems. One is the leakage problem of the PN junction at high temperature (>150^{o}C). Another problem is that when the temperature is higher than 500^{o}C, the silicon membrane become ductile and the stress will result in unrecoverable deformation. The third one is the stability problem of leads of circuit as the temperature is higher than 600^{o}C.

New piezoresistive micro sensors have been developed by using new materials with better high temperature properties. The typical materials are some wide band gap semiconductors, (for example, GaN, SiC etc.). The SiC based micro pressure sensors have been proven that operate properly for hundreds hours at 600^{o}C. But at higher temperature, the sensitivity of the piezoresistive sensors drops severely. The contact resistance between metal and semiconductor will changed related to the co-diffusion phenomenon at high temperature. The diffusion of impurities become more obviously as well. Therefore, the irreversible change of resistive parameter is avoidable if the device work long time at high temperature.

In order to develop micro sensors with much higher temperature tolerance, ceramic and some wide band gap semiconductors are usually used to fabricate a stress-sensitive inductor-capacitor (LC) structure. A series of new devices based on the wireless passive operating mode have been introduced. In those kinds of micro sensors, the frequency shift of the sensor induced by the pressure, acceleration, will be remotely read out by a RF coil which can be safely fixed up at a normal temperature region. The core sensitive structure of passive sensors is a variable capacitor. Colloidal forming or low temperature co-fired of ceramics, and SiCN are experienced to fabricate LC structures. The membranes of those structures maintain their elasticity even at temperature higher than 1000^{o}C.

Wireless circuits instead of Wheatstone bridge with electrical leads are employed as readout parts for passive micro sensors. The simple force sensitive capacitor and LC structure have excellent high temperature stability. Meanwhile, the signal processing circuits of the micro sensors are protected by absolutely isolation from high temperature environment. Obviously, the distance between LC structure and readout circuit is a key part to design this kind of sensors. Other key factors for the design of passive micro sensors include the high temperature elastic parameter variety of the sensing capacitive and the remote readout parameters such as RF frequency, Q factor of LC circuit, antenna shape and orientation etc. Hopefully, those kind of high temperature wireless passive micro sensors have the high potential to work in higher temperature more than 1000^{o}C.

[1] Xiongjj@263.net

Fig.1 LTCC cavity structure for variable capacitance

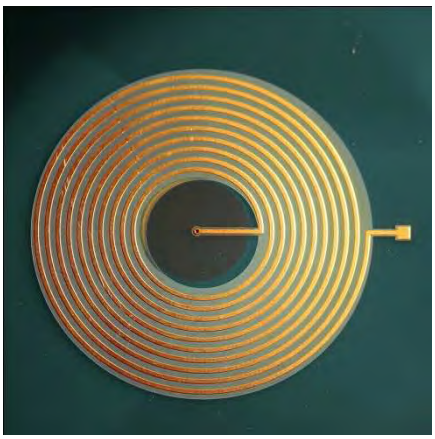

Fig.2 Top-view image of PCB base LC pressure sensor

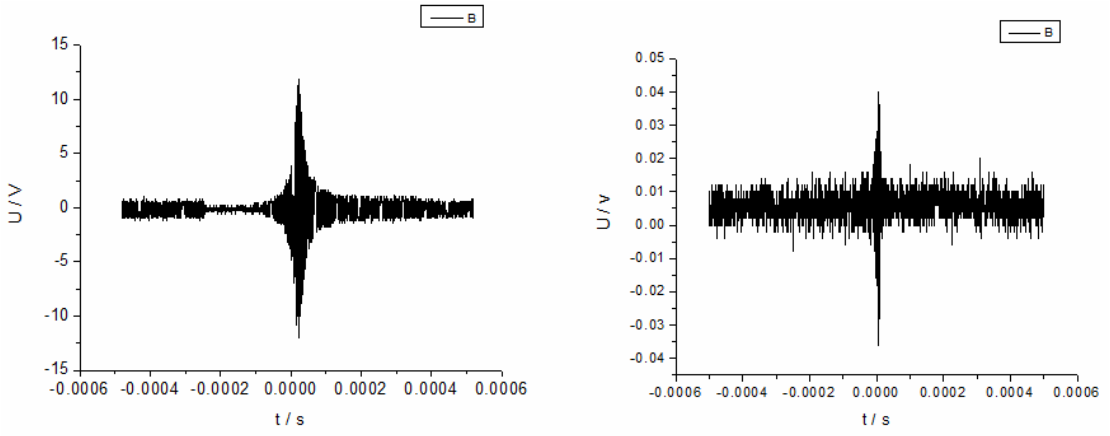

(a) (b)

Fig.3 Comparison of the signal intensity between that of PCB LC pressure sensors with different metal thickness, (at 10mm distance from readout antenna), a. 75 μ m metal layer; b. 10 μ m metal layer;

CHEMICAL, MECHANICAL AND VISCOELASTIC PROPERTIES OF BIO-DEGRABLE POLYMERS (PLLA & PCL) UPON DEGRADATION FOR PACKAGING APPLICATION

C.M. Boutry[1] and C. Hierold[1]

[1]*Group of Micro and Nanosystems, Department of Mechanical and Process Engineering, ETH Zurich, CH-8092 Zurich, Switzerland*

***Abstract* — The biodegradable polymers PLLA and PCL are potentially good candidates for the packaging of a new generation of all biodegradable sensors implanted inside the body. The chemical properties of the polymers upon degradation were evaluated through GPC, DSC, oxygen and water vapor permeability, and water contact angle measurements. The mechanical properties were measured by mean of tensile and compression tests, and the viscoelastic properties were assessed with DMTA and relaxation tests. As a conclusion PCL exhibits higher long-term mechanical stability, while PLLA has the lowest permeability and both materials will be suitable for different kind of applications.**

***Keywords :* Biodegradable polymers, packaging, PLLA, PCL, *in-vitro* degradation, viscoelasticity**

I - Introduction

The vision of this project is to fabricate an all-biodegradable RLC resonator made of biodegradable conductive polymer, from which the resonance frequency will be measured remotely for sensing application inside the body. Packaging the passive electronic circuit is necessary to protect the circuit from degradation during the period of use. Two biodegradable polymers (polylactide PLLA and polycaprolactone PCL) are evaluated for this purpose through an *in-vitro* degradation study. The samples fabrication was described elsewhere [1], and the present paper summarizes the main results of the *in-vitro* study with a detailed analysis of the chemical, mechanical and viscoelastic properties of the polymers upon degradation.

II - Experimental Details

After being produced by compression molding, the samples were annealed, sterilized, weighted and fully immersed in Phosphate Buffered Saline solution (pH 7.4, Medicago). The samples were stored in an incubator at 37°C with 5% CO_2. The pH of PBS was controlled weekly and the solutions were regularly renewed to prevent significant changes of pH. After 0, 4, 8, 12, and 16 months, 14 PLLA and 14 PCL tensile samples (ISO 527 #4, gauge 0.5x6.3x12.5mm), 20 PLLA and 20 PCL cylinders (ø3.7x8mm), 15 PLLA and 15 PCL stripes (0.5x5x20mm), and 4 PLLA and 4 PCL membranes (0.5mmx5cm^2) were removed from incubator. Figure 1 shows the visual aspect of PLLA upon degradation. 10 cylinders and 7 tensile samples of both materials were tested directly in water for tensile, compression, and relaxation tests. The other samples were removed from PBS, washed in DI water, dried with towel and air jet, and the weight and thickness were measured immediately. Then the samples were dried in vacuum oven at 40°C during 48 hours, and measured again. Between the tests the samples were stored under nitrogen.

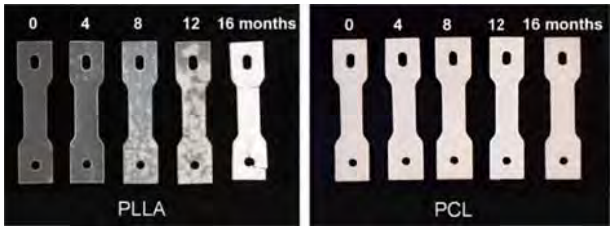

Figure 1*: In-vitro degradation study: PLLA tensile samples after 4, 8, 12 and 16 months of* in-vitro *degradation*

III - Results and Discussion

A. Samples weight

All the samples used later for other tests are weighted after 0, 4, 8, 12 and 16 months of incubation. Figure 2 shows the variation of weight for all the PCL samples (tensile samples, cylinders, stripes, and membranes), and it can be observed that the mass decreases when increasing the incubation duration. Similar results are measured for PLLA, except that larger error bars are obtained. The reason is the brittle nature of the PLLA samples which start to partially disintegrate already after 8 months of incubation (see figure 1).

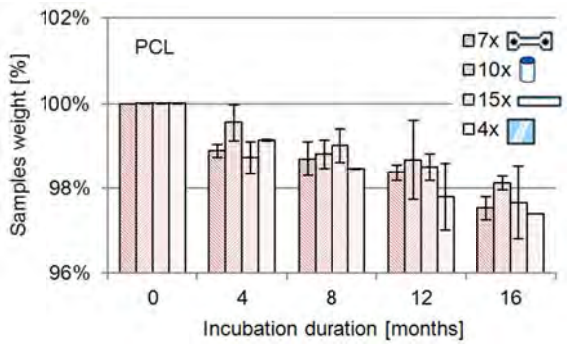

Figure 2*: Variation of the PCL samples weight upon degradation (after drying 48h in oven at 40°C in vacuum) including the tensile samples, cylinders, stripes and membranes that will be later used for the other chemical and mechanical tests*

B. Gel permeation chromatography (GPC)

The influence of *in-vitro* degradation on the length of the backbone molecular chain of the polymers is evaluated with GPC measurements. As shown in figure 3-top, the number average molecular weight Mn de-

creases for PLLA to reach 28% of its initial value after 12 months of degradation. On the opposite, for PCL, Mn does not significantly vary over the 16 months of incubation. Moreover, the ratio Mw/Mn (Mw is the weight average molecular weight) describes the distribution of lengths of polymer chains (figure 3-bottom), and it does not vary significantly for PLLA and PCL over 16 months.

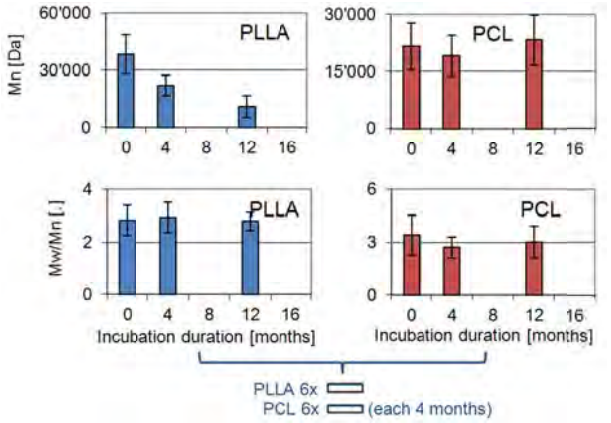

Figure 3*: GPC measurements on PLLA and PCL stripe samples. Top: Number average molecular weight (Mn). Bottom: ratio of Mw (weight average molecular weight) over Mn*

C. Differential scanning calorimetry (DSC)

Figure 4-top shows the DSC thermographs of PLLA and PCL and the influence of the incubation duration on the melting temperature Tm, the crystallization temperature Tc and the glass transition temperature Tg. For PLLA (figure 4-top-left), the crystallization peak decreases after 4 and 8 months of incubation, indicating that the saturation crystallization is progressively reached (~57%). This result is confirmed by the calculation of the crystallization from the area of the melting peak (figure 4-bottom). The same observation is made for PCL: The percentage of crystalline phase increases in the first months of incubation and then reaches its saturation value (~64%). The crystallization is calculated from the heat of fusion, taken to be 93 J/g for a 100% crystalline PLLA and 135 J/g for 100% crystalline PCL [2].

D. Oxygen and water vapor permeability

The polymer permeability has a strong impact on the choice of the appropriate material for a packaging application: It indicates when the active device inside the packaging will be exposed to water and will start to degrade. Water vapor permeability and oxygen permeability were measured upon degradation for PLLA and PCL, and the results are given in figure 5. It was not possible to measure the PLLA samples after 12 and 16 months since the samples were too fragile and had cracks preventing the measurements. For both PLLA and PCL membranes, a decrease of the water vapor and oxygen permeability is observed in the first 8 months of incubation. Later, between 8 and 16 months of *in-vitro* degradation, the permeability for PCL reaches a stable value and doesn't vary anymore significantly.

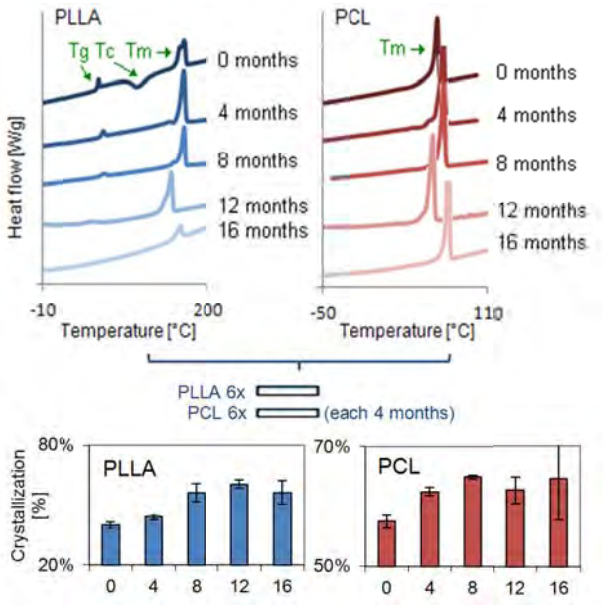

Figure 4*: DSC measurements on PLLA and PCL stripe samples. Top: Thermographs (first heat, 10°C/min). Bottom: Variation of polymer crystallization upon degradation*

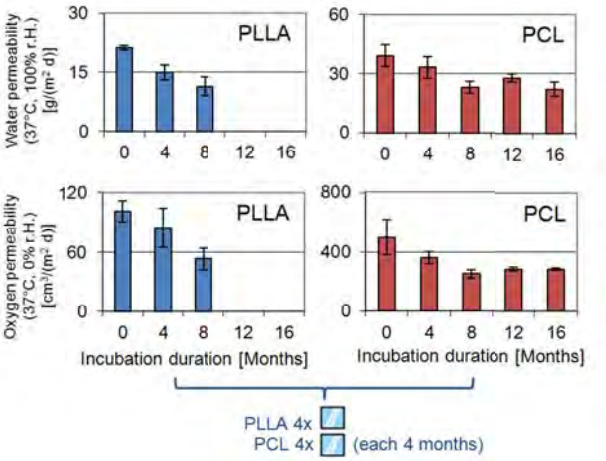

Figure 5*: Permeability measurements on PLLA and PCL membrane samples after 4, 8, 12 and 16 months. Top: Water vapor permeability. Bottom: Oxygen permeability*

E. Water contact angle

The influence of the *in-vitro* degradation on the hydrophilic nature of the polymer is observed by measuring the water contact angle on PLLA and PCL membranes after carefully cleaning the surface with deionized water. As shown in figure 6, there is a slight decrease of the water contact angle for both polymers, corresponding to an increase of the hydrophilicity upon degradation.

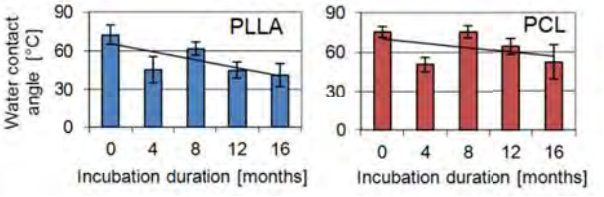

Figure 6*: Water contact angles measured on PLLA and PCL membranes after 4, 8, 12 and 16 months of incubation*

F. Tensile tests

The tensile measurements were performed according to ISO 527, with a strain rate of $0.001s^{-1}$. For PLLA the tensile modulus slightly increases until 8 months of incubation, before strongly decreasing after 12 months (figure 7-top). For PCL the tensile modulus increases when the incubation duration increases, to reach approximately +38% of its initial value after 12 months of incubation.

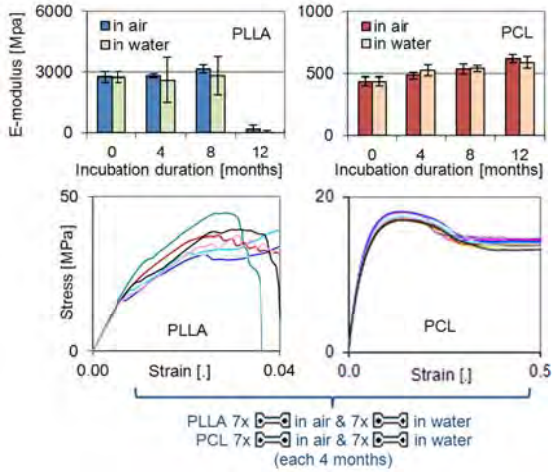

Figure 7*: Tensile tests on PLLA and PCL tensile samples after 4, 8, 12 and 16 months of* in-vitro *degradation. Top: Tensile E-modulus. Bottom: typical curves measured for the brittle PLLA samples (left, $T_{measurement}<Tg_{PLLA}$, $Tg_{PLLA}\approx 60°C$) and the ductile PCL sample (right, $T_{measurement}>Tg_{PCL}$, $Tg_{PCL}\approx -60°C$)*

G. Compression tests

For the compression measurements, a strain of 0.25 was applied on the PLLA and PCL cylinder samples (strain rate $0.001s^{-1}$). The measured compression moduli are shown in figure 8. The compression modulus decreases strongly for PLLA after 12 months of incubation (-90%), while an increase is observed for the PCL samples (+30% after 12 months in PBS).

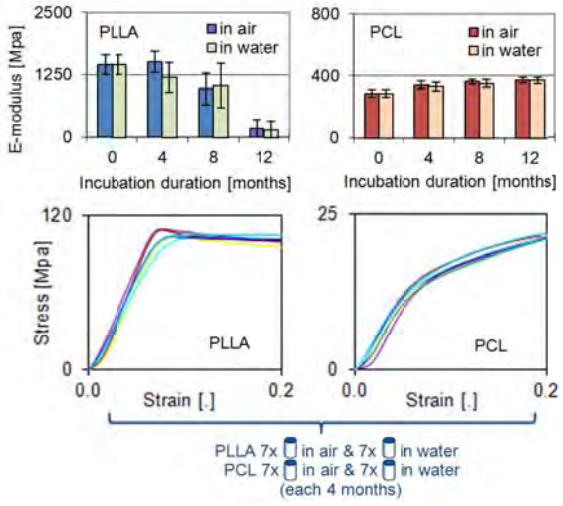

Figure 8*: Compression tests on PLLA and PCL cylinder samples. Top: Compression E-modulus. Bottom, typical curves measured for PLLA (left) and PCL (right)*

H. Dynamic Mechanical Thermal Analysis (DMTA)

The viscoelastic properties are evaluated with creep tests performed by DMTA. An oscillating load is applied on stripe samples and the strain is recorded while varying the temperature (figure 9-top). The storage compliance E' and loss compliance E" curves are used to calculate the glass transition Tg, which can be compared with Tg measured by DSC. The DMTA and DSC measurements for PLLA are in good agreement (figure 9-bottom), with Tg decreasing in average by 20% after 12 months of incubation.

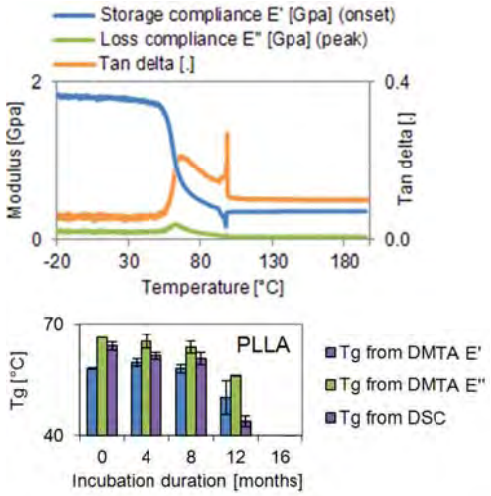

Figure 9*: DMTA measurements on PLLA stripe samples. Top: Storage compliance E', loss compliance E'' and tan delta. Bottom: Variation of Tg upon degradation: Comparison of Tg calculated from the onset of E' with Tg calculated from the maximum peak of E'', and with Tg measured with DSC*

I. Viscoelastic measurement: Relaxation tests

The viscoelasticity is evaluated by relaxation measurements: Several strain levels, ranging from 0.01 to 0.04, are applied on PLLA and PCL cylinders and the stress is recorded as a function of time. Before the measurements, the samples are preconditioned at the maximal strain to allow reproducible results. The measured stress curves are evaluated using the modified superposition model of Findley, adapted from the Fung model [3] (figure 10-bottom). In the model of Findley, the relaxation depends on time and strain level: $\sigma(\varepsilon,t) = \sigma_0 t^{-B}$. The average relaxation coefficient B and the average initial load σ_0 for PLLA and PCL samples as a function of incubation duration are plotted in figure 10. It can be seen that B and σ_0 do not change significantly for PCL during 12 months of incubation (figure 10-middle), while for PLLA the degradation of the mechanical properties and the effect on the viscoelastic parameters B and σ_0 is clearly noticed (figure 10-top).

IV - Discussion

It is observed that the weight of the samples decrease upon degradation for both PLLA and PCL. The GPC measurements show that the length of the molecular chain does not significantly vary for PCL after 16 months of incubation. For PLLA, the chain length decreases, indicating that the polymer is starting to degrade. Typically the polymer degrades by chemical hydrolysis in two steps [4]: First the water penetrated the polymer bulk and attacks the amorphous phase. The

long polymer chains are converted into shorter fragments which are water-soluble. Mn decreases but the mechanical properties are not affected since the crystalline phase is responsible for the polymer matrix stability. In a second step, the crystalline phase starts to degrade, and a loss of mechanical properties is observed. The DSC measurements indicate that the percentage of crystalline phase increases for both PLLA and PCL during the first months of incubation, and stabilizes afterwards. This is explained by two phenomena happening simultaneously: a) The aging of the polymer samples, where the chains in the amorphous phase slowly rearrange themselves into a crystalline phase. b) The degradation of the amorphous phase in a first time, where the water-soluble short fragments are removed. It is also observed that the water vapor and oxygen permeability decrease during the first 8 months of incubation for both PLLA and PCL, reaching later an equilibrium value. This result can be explained by the percentage of crystalline phase in the material measured by DSC: When the crystallinity increases, the permeability decreases. The water contact angle decreases for both PLLA and PCL upon degradation, corresponding to a rise in hydrophilic nature of the samples. The results of tensile and compression mechanical tests are in good agreement with the chemical tests: The tensile and compression moduli increase at the beginning of the incubation for both PLLA and PCL, which can be explained by the rise of the percentage of crystalline phase in the samples. For PLLA, the samples become brittle and start to lose their mechanical properties after 8 months (cylinders) and 12 months (tensile samples), while the PCL samples keep their mechanical strength over the all study. The viscoelastic DMTA measurements are in good agreement with the DSC results, and permit to determine Tg which decreases significantly after 12 months of incubation. Moreover the modified superposition model of Findley was successfully applied to the viscoelastic relaxation tests. The extracted parameters are in good agreement with the mechanical tests, indicating a decrease of the PLLA mechanical strength after 8 months of incubation while the PCL samples show no significant decrease after 12 months.

V - Conclusion

The chemical, mechanical and viscoelastic properties of the biodegradable polymers PLLA and PCL upon *in-vitro* degradation were investigated. Depending on the final packaging application, both materials can be considered as suitable: The results of this study show that PCL is more appropriate if a long-term mechanical stability is required. On the other hand, PLLA exhibits lower water and oxygen permeability than PCL. PLLA can therefore be considered as a good packaging material for shorter period of use if the packaged device has to be protected from external fluids e.g. inside the body.

Acknowledgments: Many thanks to Thomas Schweizer, Stephan Busato, Oliver Schneider and Gioele Balmelli for their kind help in the GPC, DSC, permeability measurements and samples preparation.

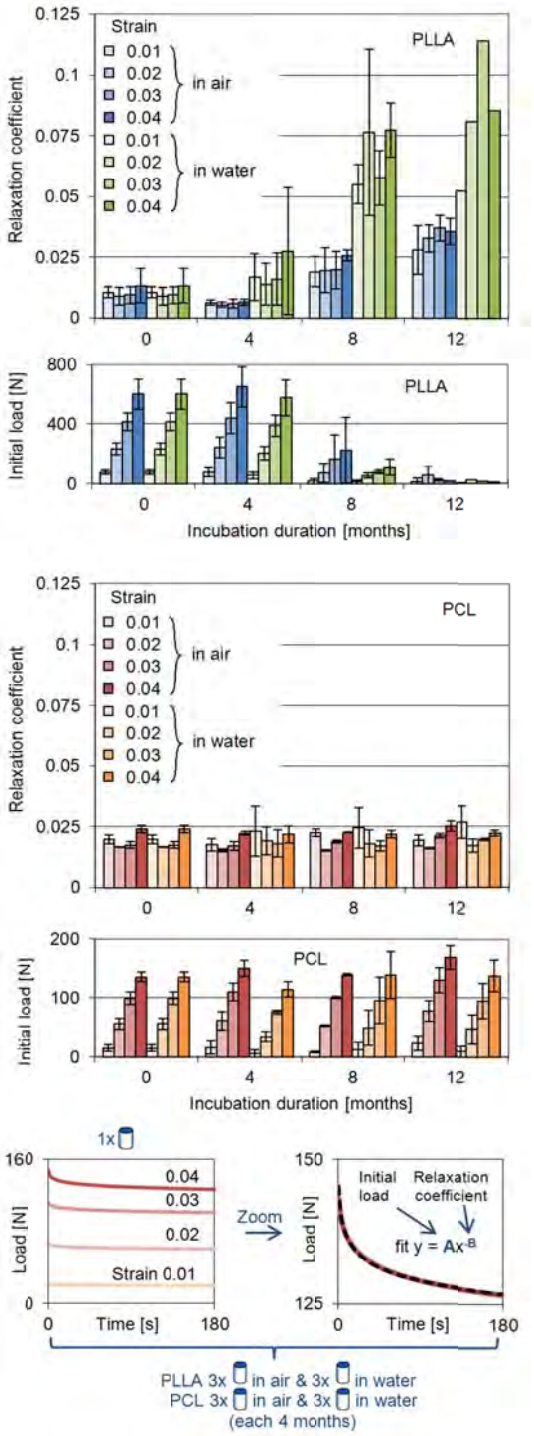

Figure 10*: Relaxation tests on PLLA and PCL cylinder samples. Top: PLLA relaxation coefficient and Initial load upon degradation. Middle: Same for PCL. Bottom: Description of measurement and fitting process.*

References

[1] C.M. Boutry, G. Balmelli, and C. Hierold, *MME*, Toulouse, September 20-22, 2009.

[2] G.L. Siparsky, K.J. Voorhees, J.R. Dorgan, and K. Schilling, *J. Environ. Polym. Degr.* 5-3, pp. 125-136, 1997.

[3] P.P. Provenzano, R.S. Lakes, D.T. Corr, and R.Vanderby Jr., *Biomechan. Model. Mechanobiol.* 1, pp 45-57, 2002.

[4] J.C. Middleton, A.H. Tipton, *Biomaterials* 21, pp. 2335-2346, 2000.

BURIED MICROCHANNELS IN SILICON WITH PLANAR SURFACE

Z. Fekete[1], A. Pongrácz[1], Á. Szendrey[1], P. Fürjes[1]

[1] *Research Institute for Technical Physics and Materials Science - MFA, H-1525 Budapest P.O. Box 49, Hungary*

***Abstract* — The fabrication of microchannels using MEMS technology always attracted the attention of reserachers and designers of microfluidic systems. Our group focused on realizing buried fluidic channels in silicon substrates involving Deep Reactive Ion Etching (DRIE). To meet the demands of today's complex microsystems, our aim was to create passive microfluidics in the bulk Si substrate well below the surface, while retaining planarity of the wafer. Therefore additional lithographic steps, i.e. the formation of continual wires of integrated circuits, are still possible on the chip surface. In this work, the so-called Buried Channel Technology is enhanced by a selective edge-masking in order to eliminate under-etching phenomenon at the top of the trenches to be filled. The effect of Al protection on the subsequent etch steps are also discussed. Applying the proposed masking method, we successfully demonstrated the planarity by SEM abd AFM characterisation. The concept makes the micromachining of channels having relatively large cross-section and located deeply below the silicon substrate surface possible as well..**

***Keywords :* buried microchannel, microfluidics, deep reactive ion etching**

I - Introduction

Realization of buried channels in silicon substrates is still highly motivated by the rapid development of embedded microfluidic systems. Evolution in micromachining technologies has induced resarches into novel fabrication methods. Several attempts has been made to integrate closed channels in silicon-based MEMS fluidic applications. Surface micromachining techniques [1] as well as wet chemical etching processes [2] and wafer bonding [3] solutions have been elaborated for this purpose. The advent of highly anisotropic dry etching techniques supported the alternative micromachining technique of the so-called Buried Channel Technology (BCT) which was first presented by de Boer et al [4]. Based on the concept, a range of applications has been proposed by other authors [5-8] usually focused on microneedle topics.

However, the original process flow open the door to more efficient use of the substrate itself, a disadventageous feature of that has not been eliminated yet. Under-etching phenomenon (see Figure 1.a) directly by the substrate wafer typically restricts the possibility of realizing microchannels with large diameters, since its dimension follows the isotropic etch profile performed during microchannel formation.

The aim of our experiment is to investigate on methods for the protection of maskedges in order to reduce the unevenness (see Figure 1.b.) on the surface above the microchannel filled by thin film. If substantially planar surfaces are formed, further lithography steps can be taken. Therefore patterned conductive layers (even crossing the axis of microchannels) can be established on the same wafer which is milestone of integrating BCT in todays advanced microprobe applications [9-10]. The success of our experimental design is shown in Figure 1.b.

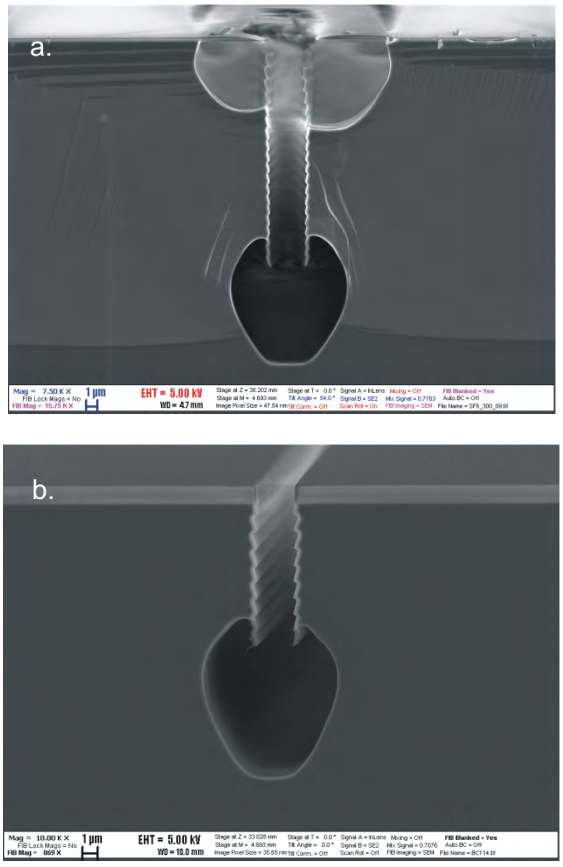

Figure 1: *SEM view of the microchannels before trench-filling demonstrating the effect of under-etching (a.) and its elimination using selective edge passivation by aluminium evaporation (b.).*

II - Experimental Details

The fabrication method of the buried microchannels in single crystalline silicon wafer is based on the process sequence (detailed in Figure 2.) first reported in [4]. As an oxid mask layer is formed and patterned on the

surface of the <100> oriented Si wafer (step 1.), the sample is exposed to anisotrope dry Si etching using Bosch recipe (step 2.). For DRIE micromachining Oxford Plasmalab System 100 was utilized. After a subsequent thin oxid (100nm) formation for sidewall passivation (step 3.), a e-beam evaporation (Varian) of 100nm aluminum was performed (step 4). Microloading during DRIE etch process is also indicated on the figures. A DRIE recipe for anisotrope dry SiO_2 etching was applied in order to remove both the oxide and the aluminum layer from the bottom of the trenches (step 5). The microchannel itself is then formed by an isotropic dry Si etching in SF_6 plasma (step 6). Finally the trench is filled and sealed by poly-silicon deposition (step 7.). The etching parameters of DRIE are intended to be published in the final paper.

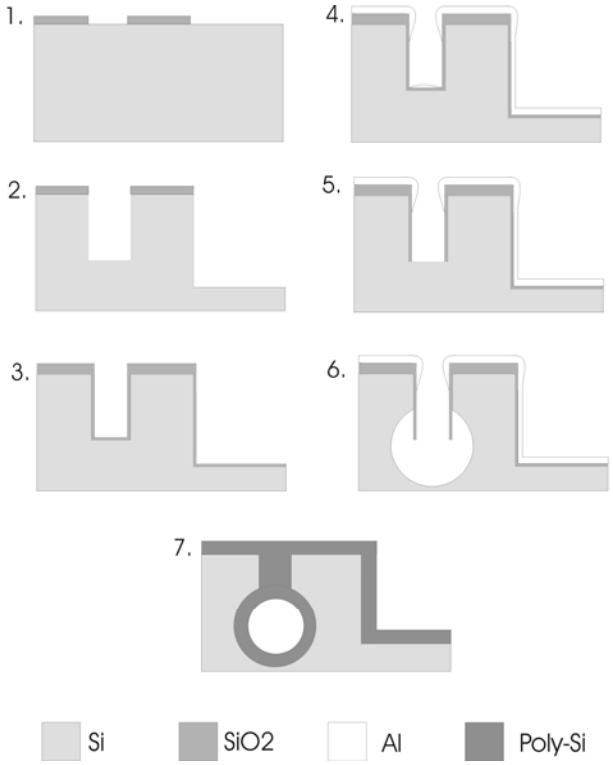

Figure 2: *Process sequence of buried channel fabrication*

III - Results and Discussion

The concept of 3D passivation of trench edges was first examined by Silvaco simulation. The results of the planetary model for 100nm Al deposition are clearly shown in Figure 3. However, the step coverage of evaporated Al is beneficial for the passivation of the critical edges, a thin layer of Al is also present at the bottom of the trenches (Figure 3.b).

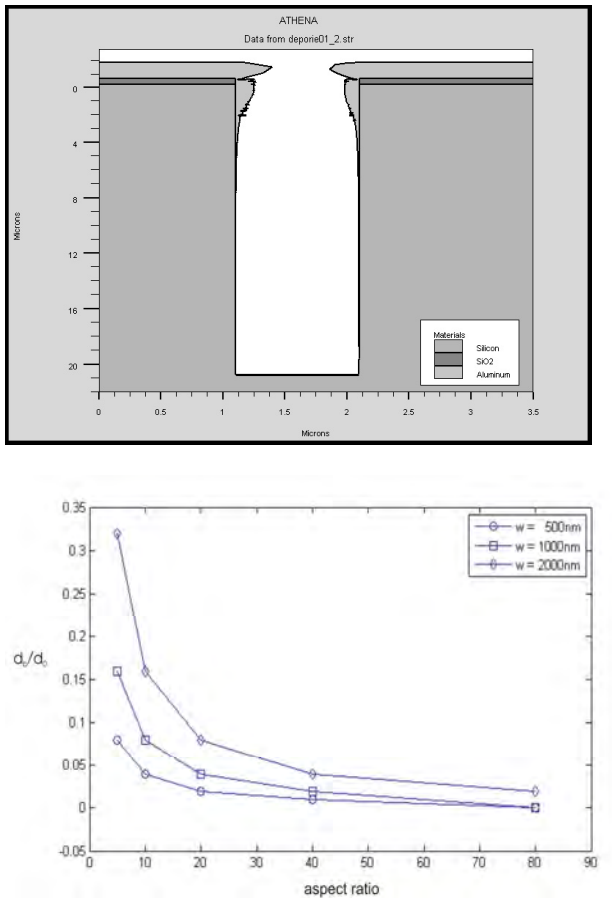

Figure 3: *Typical step coverage (a.) of a trench (width: 1µm, depth: 20µm). The thickness of Al layer deposited at the bottom of the trench is strongly depends on the width (w) and the aspect ratio of that (b.) – Al thickness on the plane wafer surface and at the bottom of the trench is denoted by d0 (100nm) and db respectively.*

a.) One can notice that as aspect ratio of the trenches increases, the Al layer thickness at the bottom decreases. This means that etch time of the anisotrope SiO2 etching (step 5) should be increased as far as Al is deposited in the trench (see Figure 3.b).

b.) If the aspect ratio of the trench increases the etch rate of step 5 decreases. The chemical component (CHF_3) of the etchant becomes less effective and ion bombardment of Ar is supposed to be more dominant in the etching mechanism. The Al masking layer on the surface lowers the exposed SiO2 area to the etchant, therefore improves the removal of by-products from the trenches. In this case, the decrease in etch rate at higher aspect ratio is moderate.

c.) However, the selectivity of step 5 (anisotropic dry SiO2 etch) to Al is reported as 1:30, an increasing aspect ratio can significantly lower that parameter.

d.) Remarkable change in the isotropic Si etching (step 6) of trenches was also noticed. Etch rate increased by almost 100%, when the wafer surface is protected by aluminum instead of SiO_2. We assume electrostatic and/or thermal conditions are responsible for the effect,

however, further experiments should be carried out to understand the phenomenon in depth.

e.) The etch rate of the Al/SiO_2 double-layer is very difficult to estimate in deep trenches, since the selectivity of SF6 etchant to SiO_2 is not negligible (~10nm/min). The formation of channels does not mean obviously that step 5 removed both Al and SiO_2 entirely.

For the above reasons, a safety margin for each etch cycle is recommended to set up to ensure the formation of the desired microchannel. However, the experimental determination of such safety margin is beyond the scope of this work, some important change in process parameters can be expressed if aspect ratio of the trenches is altered. Since the aspect ratio defines the location of the channel axis inside the silicon substrate, it is essential to know how to tune etch cycle times when such etch protection is applied.

The final microstructure after isotropic Si etch of the sample is shown in Figure 4. a & b.

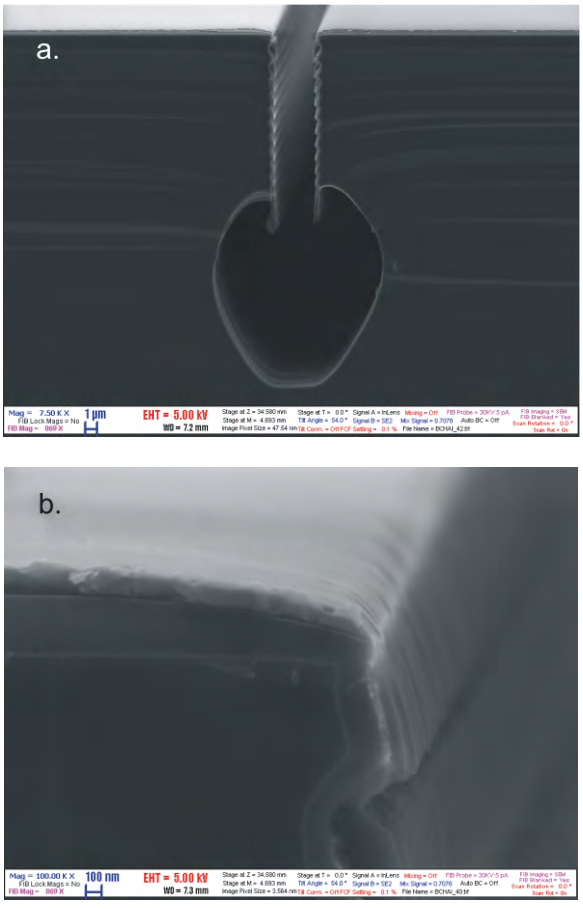

Figure 4: *Open channels after Si isotrope etch of the Al passivated sample (a.).Close SEM view of the edges (b). Complete protection of the oxide boundary is apparent at the edges.*

Some unique features of the proposed method of edge passivation can be concluded:

1. Structures of larger feature size (characteristic dimension is at least twice as great) on the wafer are substantially protected by the aluminium layer from being etched during isotrope etching in SF6 plasma. The effect of this property can be clearly observed on Figure 5.

2. Further advantage of this passivation method is that long etch time, and therefore the formation of channels buried deeply below substrate surface are possible because of the high selectivity of both the anisotropic dry oxide etch and the isotropic dry Si etching [11] to aluminium mask layer.

3. While under-etching is practically disappeared from the vicinity of the edges, the unevennes of the surface topography is restricted into the submicron range (see Figure 6.a.).

Resulted surface topography was investigated by evaluating AFM profiles above the filled trenches (Figure 6.b). Average depth of the remaining trenches is between 400-500nm, which is adequate for taking further litography steps (i.e. wiring).

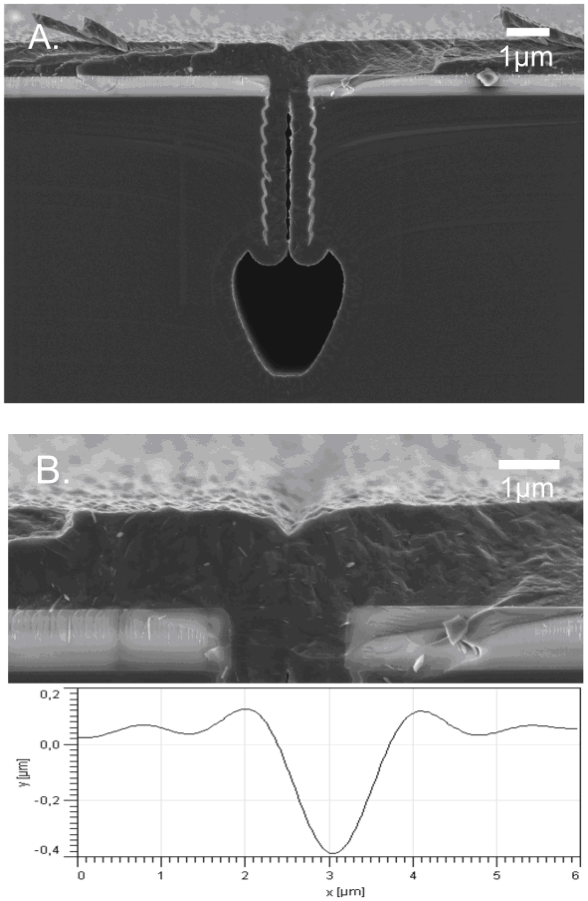

Figure 6: *Cross-section of a buried microchannel (a.), and close view with surface profile above the sealing (b.)*

IV - Conclusion

Our research group aimed to make improvements in the microfabrication technology of silicon buried microchannels. The edge protection of the trenches before anisotropic dry oxide etch was achieved by

simple aluminum evaporation step, which finally resulted in excellent surface planarity above the sealed microchannels. Due to the moderate step coverage, the aluminum masking layer passivated only the larger features and the edges of the thin trenches, which is typically affected by under-etching during isotropic Si etch. The reduced planarity was successfully demonstrated through surface profile measurements.

The influence of the Al passivation step on both the anisotropic SiO_2 etch and isotropic Si etch is remarkable. Therefore etch cycles should be carefully defined if Al is present both at the bottom of the DRIE etched trenches and throughout the wafer surface. The proposed development can contribute to the fabrication of hollow microprobes for i.e neural recording applications, where either the needle width or the electrode density can be improved on account of the removal of under-etching phenomenon.

Acknowlegdements

The partial supports of the ENIAC JTI and the National Innovation Office (NIH) via CAJAL4EU project, the Hungarian National Research Found (OTKA) via NF69262 and the János Bolyai fellowship of the Hungarian Academy of Sciences (recipients: Anita Pongrácz and Péter Fürjes) are gratefully acknowledged.

References

[1] L. Lin, A. P. Pisano, *J. Microelectromech. Syst.* Vol. 8 No. 1. pp. 78-84, 1999

[2] J. Chen, K. D. Wise, J. F. Hetke, S. C. Bledsoe, IEEE Trans. on Biomed. Eng. Vol. 44 No. 8. pp. 760-769, 1997

[3] B. L. Gray, D. K. Lieu, S. D. Collins, R. L. Smith, A. I. Barakat, *Biomedical Microdevices* 4:1 pp. 9-16, 2002

[4] M. J. de Boer, R. W. Tjerkstra, J. W. Berenschot, H. V. Jansen, G. J. Burger, J. G. H. Gardeniers, M. Elwenspoek, A. van den Berg, *J. Microelectromech. Syst.* Vol. 9 No. 1. pp. 94-103, 2000

[5] M. Dijkstra, M. J. de Boer, J. W. Berenschot, T. S. J. Lammerink, R. J. Wiegerink, M. Elwenspoek, *J. Micromech. Microeng.* 17 pp. 1971–1977, 2007

[6] A. Agarwal, N. Ranganathan, W. L. Ong, K. C. Tang, L. Yobas, *Sens. & Act. A* 142 pp. 80–87, 2008

[7] S. J. Paik, S. Byuna, J. M. Lima, Y. Park, A. Lee, S. Chung, J. Changa, K. Chuna, D. Choa, *Sens. & Act. A* 114 pp. 276–284, 2004

[8] C. Rusu, R. van't Oever, M. J. de Boer, H. V. Jansen, J. W. Berenschot, M. L. Bennink, J. S. Kanger, B. G. de Grooth, M. Elwenspoek, J. Greve, J. Brugger, A. van den Berg, *J. Microelectromech. Syst.* Vol. 10 No. 2. pp. 238-245, 2001

[9] K. Seidl, S. Spieth, S. Herwik, J. Steigert, R. Zengerle, O. Paul, P. Ruther, *J. Micromech. Microeng.* 20 105006, 2010

[10] T. Stieglitz, *Int. J. Micro-Nano Scale Transport* Vol. 1 No. 2 pp. 139-158, 2010

[11] B. A. Ganji, B.Y. Majlis, *IEEE Int. Conf. on Semiconductor Electronics*, pp. 41 – 47, 2006

QUICK FLOW SENSOR INSENSITIVE TO FLUID PROPERTIES

Y. Di[1,2], C. Gerhardy[1], W.K. Schomburg[1]

[1]*RWTH Aachen University, Konstruktion und Entwicklung von Mikrosystemen (KEmikro), Steinbachstraße 53 B, 52074 Aachen, Germany*
[2]*East China University of Science & Technology, School of Mechanical & Power Engineering, Meilong Road 130, 200237 Shanghai，P.R. China*

***Abstract* — A sensor measuring the time a heat pulse needs to flow downstream which is equipped with a flow parallel wire (FPW) shows a characteristic curve which is only a weak function of fluid properties. A FPW has been combined with a fast flow sensor based on measuring the pressure drop over a narrow channel. That way, the advantages of both sensors were obtained and their specific drawbacks have been avoided.**

***Keywords:* flow sensor, time of flow, polymer, flow parallel wire, FPW**

I - Introduction

Micro flow sensors are usually based on either the heat taken away from a hot wire by the flow or the pressure drop over a capillary or aperture [1]. Both principles show the disadvantage that the characteristic curve needs to be calibrated before use with the fluid the flow of which shall be measured. If the fluid is not known, it is not possible to obtain a reliable measurement of the flow.

There are only a few measurement principles which avoid this problem. One possibility is to measure the real volume which passes through the sensor by detecting the deflection of a membrane moved by the flow periodically back and forth [2]. Another approach is based on the Coriolis force on a mass flow inside of a micro channel [3]. Both principles require a comparatively complex micro fluidic design.

A third attempt to develop a flow sensor which is not a function of the properties of the fluid was producing a heat pulse in the fluid and measuring when this heat pulse arrives at a certain position [4-6]. The heat pulse typically is generated by an electrical current through a wire crossing the flow channel. The arrival of the heat pulse is then measured with a downstream sensor wire. A small constant electrical current is supplied to the sensor wire. Since the resistance of the sensor wire is rising with temperature, the voltage drop over the wire is a function of temperature, and, this way, the temperature is measured.

Usually the time is measured between generating the heat pulse and arriving of the maximum of the temperature peak at the sensor wire. The temperature peak is decreasing and broadening while traveling downstream, but at a first glance no reason is found why in the center of the channel the time of flow of the peak should not coincide with the time of flow of the fluid. As a consequence, the reciprocal of the flow time should be proportional to the mean flow velocity no matter what fluid is inside of the channel.

Measurements of the flow time show that it is a weaker function of fluid properties than e.g. an anemometric flow sensor. However, considerable changes of the characteristic curves of time of flow sensors as a function of fluid have been observed [5, 7].

Recently a time of flow sensor has been developed which shows an even smaller influence of so different fluids such as water, ethanol, and oil on the characteristic curve [7]. This sensor employs a sensor wire in the center of the channel which is arranged parallel to the channel and the upstream and downstream parts of the wire are combined to a half bridge (Fig. 1). Therefore, this sensor is called a flow parallel wire (FPW).

The disadvantage of all time of flow sensors including the FPW is a long response time caused by the need to wait until the heat pulse reaches the sensor wire. Response time can be reduced if the distance between the heater and the sensor wire is small. However, this reduces also measurement accuracy. Therefore, a FPW has been combined with a quick flow sensor measuring the pressure drop over a capillary.

II - Sensor design

Figure 1 shows the combined sensors schematically. The pressure drop over a capillary, 0.3 mm × 0.3 mm × 9 mm in height, width, and length, respectively, is measured. The pressure sensor is able to measure pressure changes within milli seconds.

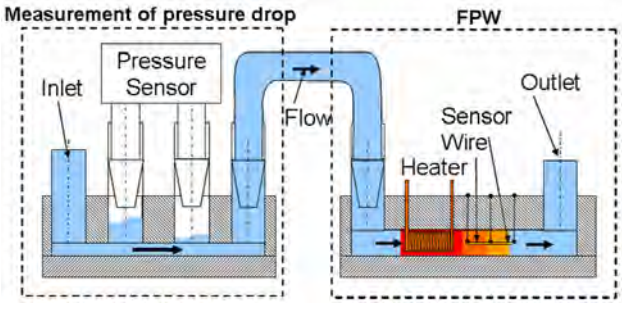

Figure 1: *Design of the combination of a sensor for the pressure drop over a micro channel and a FPW.*

In principle the pressure drop Δp generated over a capillary consists of two terms describing the friction due to the viscosity η of the fluid in the channel and the energy loss required to accelerate the fluid in the narrower part of a flow channel:

$$\Delta p = -32 \frac{\eta L}{D_h^2} v - \frac{\rho}{2} v^2 \quad (1)$$

In the above equation L, D_h, ρ, and v are length of the capillary, its hydraulic diameter, density of the fluid, and mean flow velocity, respectively. The first term of Eq. 1 is linear in the flow velocity. Therefore, it is preferred when the first term dominates the characteristic curve of the sensor. This is achieved by a long capillary with a small hydraulic diameter which is calculated from height H and width W of the capillary as:

$$D_h = 2 \frac{H\,W}{H + W} \quad (2)$$

Thus for a narrow and long channel the first term in Eq. 1 dominates. The characteristic curve of the sensor then is a linear function of the mean flow velocity v and the viscosity η of the fluid. The characteristic curve is shown in Fig. 2 for water, ethanol, and the oil Fina M2. It is clearly seen that it is a strong function of the fluid and that a calibration curve is required for each fluid. It is also seen that the capillary is narrow and long enough to result in a nearly linear relationship between pressure difference and flow.

Viscosity in general is a function of temperature. As a consequence, the pressure drop over a capillary is also a function of temperature (Fig. 3).

The FPW shown in Fig. 1 consists of a heater coil and two sensor wires arranged in the center of the capillary and parallel to it. The heater coil, 8 mm and 0.8 mm in length and outer diameter, respectively, was made of an insulated copper wire with a diameter of 100 µm. 2 mm downstream of the coil there is starting the sensor wire. It is 10 mm long. In the middle of the sensor wire there was soldered an electrical connection allowing combining the two parts of the sensor wire in a bridge circuit. The sensor wire is made of gold and its diameter is 17.5 µm.

Figure 5 shows a typical bridge signal as a function of time. When a heat pulse arrives at the sensor wire, its upstream part is heated first and the signal of the bridge is rising because the resistance of a heated wire is increased. With the continuing flow of the heat pulse the signal is rising because a larger part of the upstream part of the sensor wire is heated. When the heat pulse arrives at the downstream part of the sensor wire, the bridge signal is reducing. The arrival time of the peak of the bridge signal is a function of flow velocity, geometry of the coil, and heating parameters but only a weak function of the properties of the fluid [7].

The quick response time of measuring the pressure drop over a capillary was combined with the reliable characteristic curve of the flow parallel wire by calibrating the characteristic curve of the pressure sensor every 5 s with the signal from the flow parallel wire. The mean value of the output voltage of the pressure sensor was calculated for 5 s and then the slope of its characteristic curve was calculated from the flow velocity known from the FPW.

III - Experiments

The characteristic curves of both measuring the pressure drop over a capillary and the FPW were first taken individually and afterwards the behavior of the combination of the two sensors was investigated.

A. Pressure drop over capillary

A constant flow was generated with a syringe pump through the capillary described above and the pressure drop over the capillary was measured as a function of flow velocity.

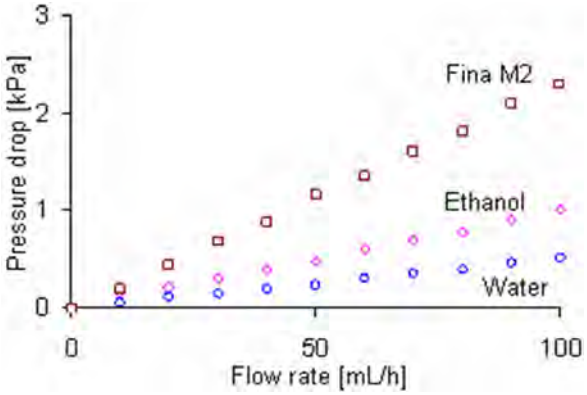

Figure 2: *Pressure drop over the capillary described in the text as a function of flow rate and the fluid used.*

These experiments were performed with different fluids (cf. Fig. 2) and with water at different temperatures in a climatic cabinet (cf. Fig. 3). The entire syringe pump and the sensor were placed into the climatic cabinet to ensure that the water was at the same temperature as the environment in the chamber.

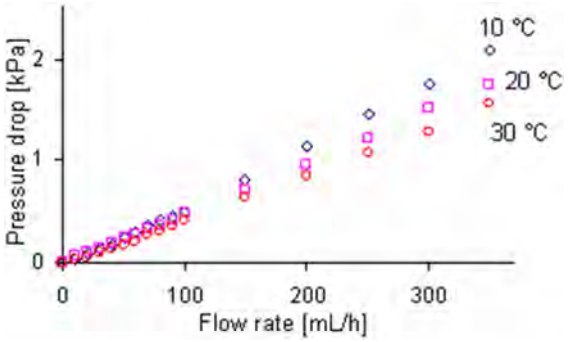

Figure 3: *Pressure drop measured over the capillary described in the text as a function of temperature when water is fed through it.*

To avoid discontinuities in the flow attributed to the syringe pump, the mean value of 10 measurements was calculated for every data point. The pressure drop as a function of flow rate was measured at room temperature for water, ethanol and oil. In Fig. 2 it is clearly seen that the characteristic curve of this sensor is a strong function of the employed fluid.

The results in Fig. 3 show that the characteristic curve of the pressure drop over the capillary is a function of temperature although the change of the

viscosity of water as a function of temperature is small compared to other fluids such as oil.

B. Flow parallel wire

When the FPW shown in Fig. 1 is employed to measure the time a heat pulse needs to travel from the heater to the sensor wire, the characteristic curve is only a weak function of the fluid. Water, ethanol, and oil all show similar time of flow as shown in Fig. 4.

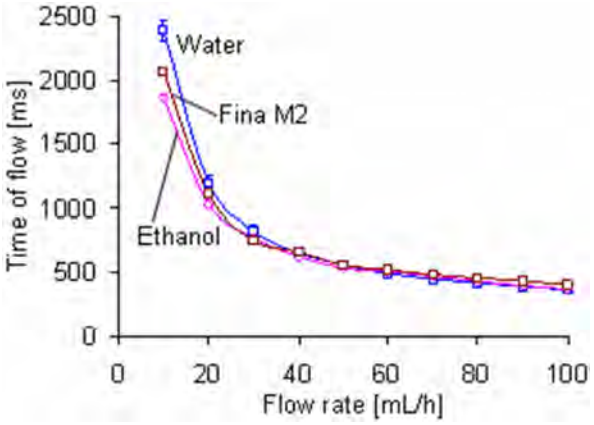

Figure 4: *Time between the start of the heater pulse and the arrival of the maximum at the sensor wire of a FPW as a function of flow rate.*

The heater was driven with 100 ms long current pulses of 2 A. In Fig. 4 there are shown the times between the start of the heater pulse and the maximum of the bridge output. The bridge output as a function of time is shown in Fig. 5 for flow rates and mean flow velocities of 30 mL/s and 60 mL/s and 8.3 mm/s and 16.6 mm/s, respectively.

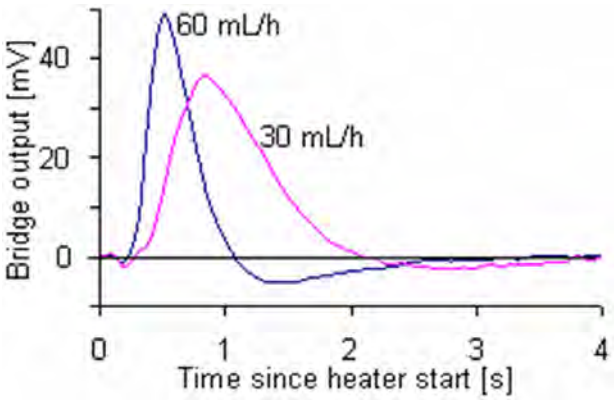

Figure 5: *Output of a FPW as a function of time and flow.*

C. Combination of pressure sensor and FPW

The measurement of the pressure difference over a capillary has been combined with a FPW by calibrating the pressure sensor every 5 s with the measurement from the FPW. Thus a change in temperature or the composition of the fluid results in a recalibration of the pressure sensor after not more than 5 s. In Fig. 6 there are shown the sensor outputs of the pressure sensor calibrated for water, the FPW, and the combination of both sensors (i.e. the pressure sensor is recalibrated by the FPW). The times when the pressure sensor was recalibrated are marked with a dashed line in the figure. A 20 cm long hose filled with water was connected on one side to the combined sensors as shown in Fig. 1 and on the other side to the outlet of a syringe filled with ethanol. A syringe pump delivered an average flow of 40 mL/h. Therefore, the change from water to ethanol was driven through the sensors.

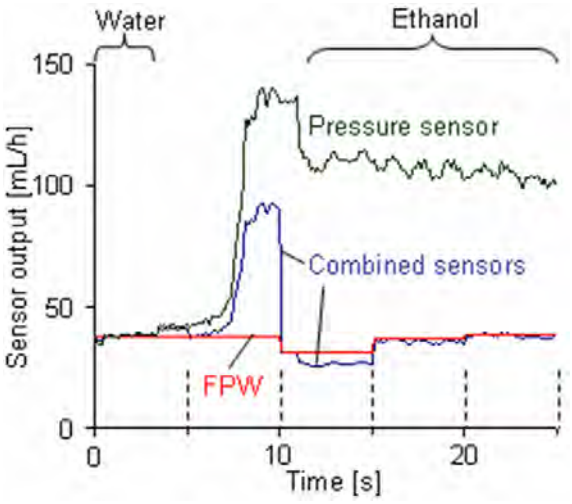

Figure 6: *Calibrated and not calibrated output of the pressure sensor when the fluid is changed from water to ethanol.*

Due to diffusion at the interface of water and ethanol there is a soft start of ethanol appearing in the pressure sensor at 4 s in Fig. 6. The larger viscosity of ethanol results in a rising signal of the pressure sensor. At 5 s the small rise of the signal of the combined sensors was taken down to 40 mL/h again. The same happens at 10 s, and after 15 s the combined sensors show the correct flow although the pressure sensor alone has a much larger output. On the other hand, the quick changes generated by the not steady flow of the syringe pump are shown by the combined sensors and not by the FPW with its large response time.

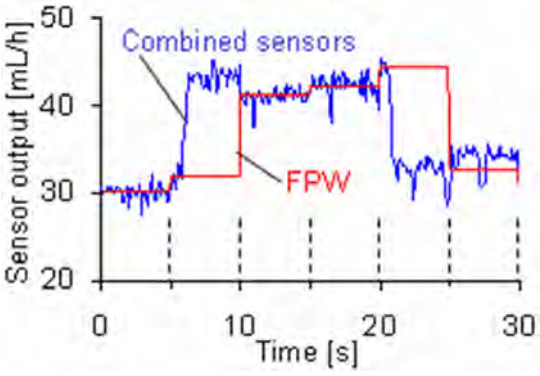

Figure 7: *Output of the combined sensors when the flow generated by the syringe pump is changed from 30 mL/h to 40 mL/h and back.*

In another experiment it was shown that a quick response is obtained from the combination of the two sensors because the pressure sensor shows a short response time. As shown in Fig. 7, the output signal of the combined sensor reacts immediately when the flow is changed from 30 mL/h to 40 mL/h. The observed reaction time of the sensor is 250 ms. This reaction time is not attributed to the sensor but to the switching time of the syringe pump.

The fluctuations of the FPW signal at nearly constant flow are due to the limited accuracy (approximately ±5 %) of the flow time measurement.

IV - Conclusions

A quick flow sensor has been calibrated periodically with a flow parallel wire (FPW). The output of the FPW is only a weak function of the properties of the fluid. This arrangement of a quick sensor with a FPW combines the advantages of both sensors. The combined sensor is only weakly affected by the characteristics of the fluid (approximately 20 % at small flow rates) and it is as quick as the sensor with the short response time.

Besides this, disadvantages of the quick sensor such as a changed characteristic curve when the capillary is partly closed by particles in the fluid or a cross sensitivity of the pressure senor on temperature changes, are also overcome by recalibrating with the FPW.

Instead of the pressure measurement over a capillary there could also be employed another quick sensor e.g. an anemometer with a small heat capacity.

When a quick flow sensor is calibrated with a fluid and it is known that its composition does not change, there is no need for a combination with a FPW. However, when the fluid properties are not exactly known, the combination of a quick sensor with a FPW will provide both a short response time and accuracy as good as the FPW.

References

[1] N.T. Nguyen, "Micromachined flow sensors - a review", Flow Measurement and Instrumentation **8** (1997) 7 - 16.

[2] P. Shao, Z. Rummler, W.K. Schomburg, “Dosing system for the nano liter range, fabricated with the AMANDA process”, J. Micromech. Microeng. (2003) 85-90.

[3] P. Enoksson, G. Stemme, E. Stemme, “A Coriolis Mass Flow Sensor Structure in Silicon”, Proc. MEMS (1996) 156 – 161.

[4] T.E. Miller, H. Small, “Thermal Pulse Time of Flight Liquid Flow Meter”, Anal. Chem. **54** (1982) 907 – 910.

[5] M. Ashauer, H. Glosch, F. Hedrich, N. Hey, H. Sandmaier, W. Lang, „Thermal flow sensor for liquids and gases“, Proc. MEMS (1998) 351 - 355, ISBN 0-7803-4412-X.

[6] S. Ćerimović, A. Talić, F. Kohl, R. Beigelbeck, J. Schalko, A. Jachimowicz, ”Micromachined flow sensors enabling electrocalorimetric and TOF transduction”, Proc. Eurosensors XXIII, Procedia Chemistry **1** (2009) 132 - 135.

[7] C. Gerhardy, W.K. Schomburg, “Flow sensing insensitive to fluid properties with a flow parallel wire”, to be published at Eurosensors 2011.

DESIGN AND ANALYSIS OF TWO TYPES OF MEMS DC-DC STEP UP VOLTAGE CONVERTERS

R. Gleeson, N.M. White and M. Kraft

Electronics and Computer Science, University of Southampton, Southampton SO17 1BJ, UK

***Abstract* — This paper presents a comprehensive analysis of novel voltage step-up converters for energy harvesting and other low-power applications. The step-up operation is based on isolating the charge of a mechanically variable capacitor and varying the gap between the electrodes by an appropriate method of providing an actuation force. Two devices are presented; a bi-stable device and a resonant device, specifically designed for solar and vibration energy harvesting respectively. The bi-stable device introduces a separate electrostatic actuator element to manipulate the variable capacitor electrodes, whereas, in the case of the resonant device, ambient vibrations provide the necessary actuation force. System-level Multisim models have been developed and verified using 3D FEM Coventorware and MEMS+ simulations.**

Keywords : **Mechanically Variable Capacitor, Energy Harvesting, Voltage Step up Conversion**

I - Introduction

As miniaturization and portability of modern electronic devices becomes an increasingly important issue, so does the need for these devices to operate from lower supply voltages. An issue exists, however, in matching the supply voltage to the level required for the intended application. Self-sufficient devices, which eliminate the need for an external voltage source, are also becoming a popular area of interest. Much research has and is being done in the field of energy harvesting devices and some are now commercially available e.g. vibration harvesters, solar panels etc. However, these harvesters produce relatively low voltages and are often cascaded in series to achieve the desired voltage range. To address these issues in voltage discrepancies, various voltage multiplication techniques have been introduced. Currently, charge pump circuits are the most common multiplication technique used for DC voltage step-up conversion, however, in addition to being generally energy inefficient, these circuits can be quite area consuming for large multiplication factors as they must be cascaded in series to reach the desired level of multiplication.

Within the past two decades, a significant amount of research has been conducted in the field of Micro-Electro Mechanical systems (MEMS). It is now possible to resolve issues that would have previously been impossible to achieve with standard design techniques. Accelerometers and gyroscopes have been popular areas of research during this time. In such devices, ambient acceleration causes a displacement of a proof mass, which may be represented as a capacitor electrode, thus causing a change in capacitance. The same methodology of mechanically varying levels of capacitance has been further developed as a method of creating a new form of MEMS voltage converter. The operation on which these converters are based on is relatively straightforward; if a mechanically variable capacitor is kept at a constant charge, Q, and its electrodes are displaced by an external force, the voltage, V, across the capacitor, C will increase according to Q=C*V.

There have been several previous theoretical investigations [1-4] into these devices with few real devices being fabricated and little information regarding power efficiency, which is a critical factor for energy harvesting. In this paper, two single-stage multiplier devices are presented; a bi-stable and a resonant device. These have been specifically designed for the purpose of integration with solar and vibration energy harvesters [5]. The bi-stable device features an electrostatic actuation element while the resonant device relies on ambient vibrations to provide the actuation force. For energy harvesting, it is of the utmost importance that the end devices are designed to exhibit high levels of power efficiency and relatively low levels of parasitic capacitance to compete with existing charge pumps circuits. This is the focus of this research.

A theoretical analysis of these devices is presented in addition to system level and FEM simulations which have been used to create initial device prototype masks. These devices are to be fabricated using a novel dicing-free Silicon-on-Insulator (SOI) process developed at the Southampton Nanofabrication Centre [6].

II – Principle of Operation

The operation of a MEMS DC converter is based on a mechanically variable capacitor. A circuit level representation for this device is shown in fig.1. Initially, switch S1 is closed and the capacitor electrodes are brought to a distance g_{min} resulting in maximum capacitance C_{max} as it charges up to the input voltage. The capacitor is then isolated by opening both switches to prevent discharging of the capacitor. While isolated, an external actuation force pulls apart the capacitor electrodes until an electrode distance g_{max} with minimum capacitance C_{min} is reached. This action increases the voltage across the capacitor. Switch S2 is then closed to allow for the capacitor to discharge to the load. The cycle then repeats. The multiplication factor of the device is given as a ratio of the maximum and minimum capacitances i.e. $M = C_{max}/C_{min}$. The switches S1 and S2 are represented as ideal switches in the diagram; however, choosing an appropriate method of switching is

not trivial. In [3] it was reported that the use of 1N4148 diodes would contribute too much loss to the system through relatively high diode capacitance (≈4pF) and forward voltage drop (≈1V). For this work, various switching methods were investigated and 1N4149 diodes were chosen as the most convenient method of isolation for the simulations in this paper. These diodes have a lower value of diode capacitance (≈2pF) than their previously suggested counterpart. In future, it may be possible to replace these diodes with an ohmic MEMS switch which would offer low off and on state capacitances, low forward voltage drop and good electrical isolation. Currently, there are no existing commercial ohmic MEMS switches which can be operated at a low enough voltage.

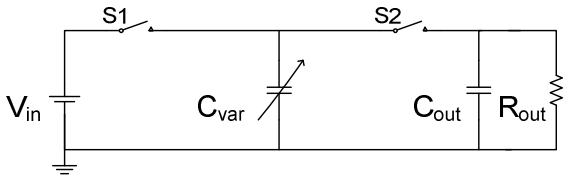

Figure 1*: Converter circuit overview. C_{var} is the mechanically varying capacitor driven by non overlapping switches S1 and S2.*

III – System level Modeling

The initial modeling of the converters was conducted in SIMULINK using similar models to those developed by Hass and Kraft [1]. For the current work, the general functionality of the models was verified and they were replicated in Multisim, which is a SPICE-based simulator having a large electronic internal component library.

A. Bi-stable Device

In this design, a parallel plate actuator is used to drive apart the electrodes of a comb drive capacitor. The 2nd order equation dictating this motion is given by:

$$mg'' + bg' + k(x_0 - x) = F_{EL} \qquad (1)$$

Where k represents the spring constant, b is the damping co-efficient, x is the displacement, x_0 is the "at rest" gap, m is mass and $F_{EL}$is the electrostatic force which is given as a difference between the force generated by the capacitor and the actuator. The formulae for the forces generated by capacitor and actuator are given as follows:

$$F_{el\_cap} = \frac{Nt\varepsilon_0 V^2}{x} \qquad (2)$$

$$F_{el\_act} = \frac{\varepsilon_0 A V^2}{2x^2} \qquad (3)$$

Here, N is the number of comb fingers, t is the thickness of the electrodes, A is electrode area and V is the input voltage. The bi-stable device has been designed with the intention of integration with solar energy harvesters. For this reason, the input voltage is assumed to be 24V, which is a typical output for such generators. While both capacitor and actuator share the same supply voltage, they are both "switched on" at different times; this is illustrated in fig. 2.

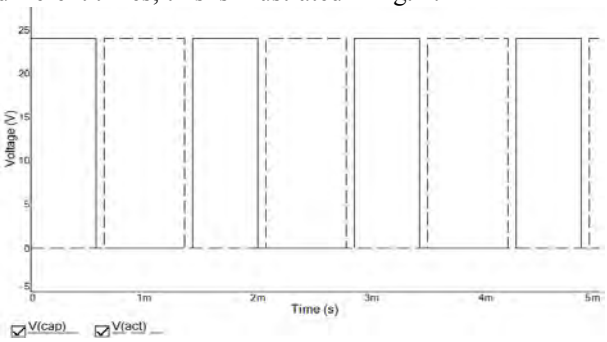

Figure 2*: On and off times for capacitor and actuator in the bi-stable device*

The Multisim model for the mass-spring-damper system is shown in fig. 3. Electrostatic forces from the capacitor and actuator (F_elec_cap and F_elec_act) are input to the system and displacement (X_out) is generated. Integrators convert acceleration to velocity to displacement. The stopper block checks to see if a point of maximum or minimum displacement has been reached, and if it has, the acceleration is reset to zero, this is the same functionality of a mechanical stopper.

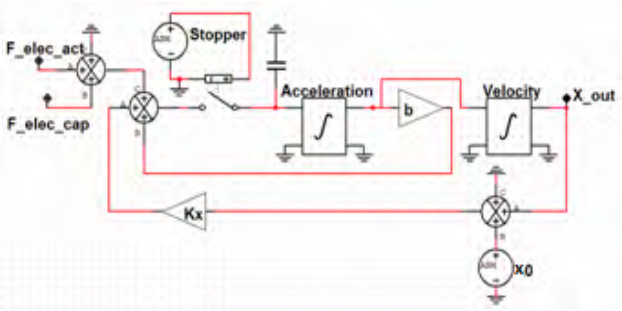

Figure 3*: Multisim model of mass-spring-damper system for bi-stable device.*

The capacitance of the comb drive is calculated using the formula:

$$C_{COMB} = \frac{2Ntg\varepsilon_0}{g} \qquad (4)$$

Where g is the spacing between comb finger electrodes.

B. Resonant Device

The actuator element in the bi-stable device consumes power and thus degrades the maximum electrical efficiency that can be achieved by the system; this will be discussed later. Vibration energy harvesters output low levels of power (≈1mW) and voltage (<1V); therefore, it was necessary to design a converter which could improve on the bi-stable design's efficiency.

By replacing the electrostatic actuator element in the previous design with a proof mass, the system can make use of ambient vibrations to provide actuation. The resonant frequency of the mechanical system can be

tuned to match the frequency of vibration using the formula:

$$\omega_0 = \sqrt{\frac{k}{m}} \qquad (5)$$

Where $\omega_0 = 2\pi f_0$ and f_0 is the resonant frequency. The chosen frequency for the design is ≈170Hz as it is low enough to closely match the resonant frequency of vibration harvesters. The mechanical model of the resonant system is similar to that in fig. 3, however, now the input force to the system is a vibration of certain magnitude (i.e. acceleration), thus F = ma. The level of acceleration determines the amount of multiplication achieved.

There is no need to switch the capacitor voltage on and off as it will generate such a low electrostatic force in comparison to the actuating vibration. It is necessary though to use diodes to isolate the charge as discussed earlier. In this case, the output of the vibration energy harvester is so low (≈0.5Vac) that regular PIN diodes cannot be used. The obvious choice is Schottky diodes, however, the frequency of the AC source is low enough to prevent the variable capacitor from holding a charge from one cycle to the next without discharging though the diodes. Therefore diodes are not suitable and the possibility of using inertial switches is being investigated.

III – Finite Element Modeling

System level simulations present an ideal model of operation where $M = C_{max}/C_{min} = g_{max}/g_{min}$. FEM simulations provide more realistic results as they take into account non-ideal factors, in particular, parasitic capacitances which affect the multiplication factor that can actually be achieved by the device. For the comb capacitor, this is mainly due to fringing fields between electrodes and by increasing the overlap distance between electrodes, the effect of the fringing fields can be reduced. For this work, the 3D designs shown in figures 4 and 5 were developed using MEMS+ and transferred to Conventorware for analysis. Table 1 shows that for an ideal multiplication factor of 5, as the minimum gap increases, so does the value of multiplication.

g_{min} (µm)	C_{min} (pF)	C_{max} (pF)	M
2	.06868	.1237	1.8
7	.15	.475	3.16
10	.188	.65	3.45
20	.4	1.69	4.25
30	.58	2.57	4.43
40	.72	3.286	4.56

Table 1*: Effect that minimum gap between electrodes has on multiplication factor. Results obtained from Conventorware simulations.*

While choosing 40µm as the value for minimum gap, this would mean a maximum gap of 200µm; this is difficult to design as the capacitor and actuator in the bi-stable system would require a large area to produce enough electrostatic force to move this distance. For this work, a value of 7µm was selected for g_{min} in the bi-stable device as it gives a reasonable multiplication factor without being too area consuming. The minimum gap can be larger in the resonant device as long as the proof mass has been designed to move the required distance under a given acceleration.

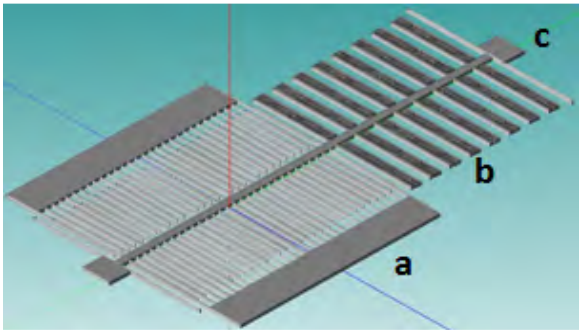

Figure 4*: MEMS + model of bi-stable device (a) parallel plate actuator, (b) comb drive capacitor, (c) anchor and spring.*

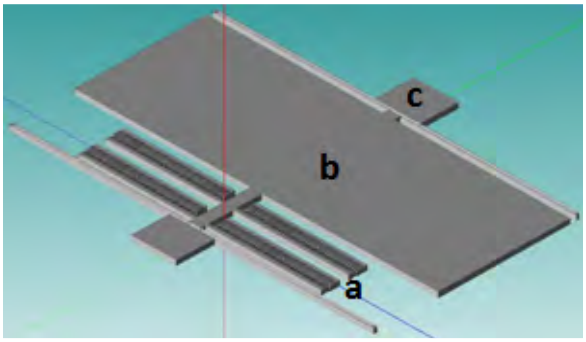

Figure 5*: MEMS + model of resonant device (a) comb drive capacitor, (b) proof mass, (c) anchor and spring.*

III - Results and Discussion

A. Output Voltage

Figure 6 and 7 shows the actual output of the bi-stable and resonant devices versus the ideal output.

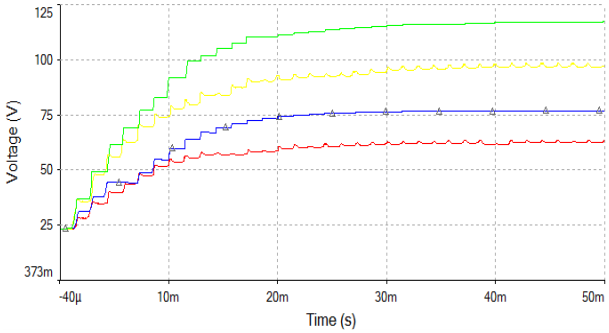

Figure 6*: Voltage output of bistable device. (green) ideal model of variable capacitor (C_{var}) and ideal diodes used in control circuit of fig. 1, (yellow) ideal model of C_{var} with 1N4149 diodes, (blue) non-ideal model of C_{var} (M≈3.2) with ideal diodes, (red) non-ideal model of C_{var} with 1N4149 diodes.*

As discussed earlier, there are currently no suitable realistic switching elements for the resonant device. However, it is possible to simulate the device using ideal diodes which have an infinite "off state" resistance to prevent current leaking away from the variable capacitor.

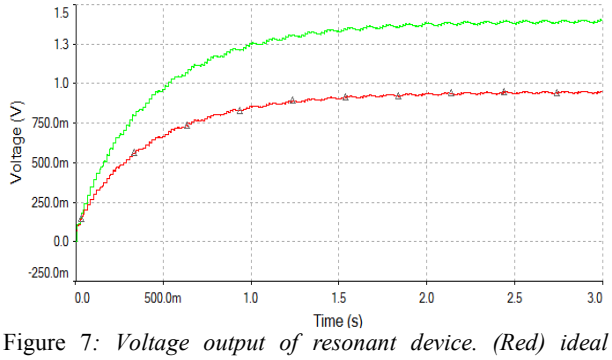

Figure 7*: Voltage output of resonant device. (Red) ideal diodes and C_{var} in control circuit, (Green) non ideal C_{var} model in circuit.*

The input to the circuit is 428mV RMS so it is expected that the output voltage would be slightly higher. This "attenuated" output is due to the 0.2V drop across the ideal diodes.

B. Power Efficiency

The power efficiency of the bi-stable system is calculated using the following formulae:

$$P_{IN} = P_{ACT} + P_{CAP} \quad (6)$$

$$P_{CAP/ACT} = \frac{CV^2}{2t} \quad (7)$$

$$\eta = \frac{P_{OUT}}{P_{IN}} \quad (8)$$

Where η is electrical efficiency and t is the time during which the relevant capacitor is switched on. Tables 2 and 3 shows a comparison of the average electrical power efficiencies achieved in the bi-stable and resonant devices respectively.

C_{var}	Diodes	Average P_{IN}	Average P_{OUT}	Average η
Ideal	Ideal	5.97µW	3.31µW	67%
Ideal	1N4149	5.97µW	1.95µW	42%
Non-ideal	Ideal	5.3µW	1.38µW	31%
Non-ideal	1N4149	5.3µW	830nW	18.5%

Table 2*: Average power efficiencies for bi-stable device based on varying capacitor models and control circuit arrangements*

For the resonant device, since there is no electrical actuator element, the efficiency can be written as follows:

$$\eta = \frac{P_{OUT}}{P_{CAP}} \quad (9)$$

C_{var}	Diodes	Average P_{IN}	Average P_{OUT}	Average η
Ideal	Ideal	12pW	3.8pW	55%
Non-ideal	Ideal	7.3pW	1.8pW	36.5%

Table 3*: Average power efficiencies for resonant device based on varying capacitor models.*

IV – Future Work and Conclusion

Two voltage converters for energy harvesting applications have been presented and analyzed in terms of their outputs and efficiency. Through FEM and system level simulations, it was shown that the parasitic capacitance of the variable capacitor device coupled with the total capacitance of the switching diodes contribute an attenuation factor to output voltage and efficiency. The removal of the electrostatic actuator element for the resonant device results in a greater ideal maximum efficiency (≈95%) compared to the bi-stable device (≈75%) but the bi-stable has a greater average. It was not possible to conduct a complete analysis of the resonant device as current leakage made it difficult to find suitable switch components for charge isolation. While these circuit analyses are important, the focus of this work for the future will be on the fabrication of the devices presented; then a real world approach to the circuit analysis can be undertaken.

References

[1] C. Haas and M. Kraft, "Modeling and analysis of a MEMS based approach to a voltage step-up conversion", *J.Micromech. Mircoeng.*, vol. 14, pp. 114-22, 2003.

[2] S. Ghandour, G. Despesse and S. Basrour, "Theoretical analysis of a new MEMS approach to build a high efficiency fully integrated DC-DC converter", *Proc. MME,* 2009.

[3] C. O' Mahoney and M. Hill, "Modeling and performance evaluation of a MEMS DC/DC converter", *J. Mircomech. Microeng.,* vol. 16, pp. 149–55, 2006.

[4] L. Li, M. Begbie and D. Uttamchandani, "Single-input, dual-output MEMS DC/DC converter", *Electronics Letters*, vol. 43, No. 15, 2007

[5] M. El Hami, P. Glynne-Jones, N.M. White, S. Beeby, E. James, A.D. Brown and J.N. Ross, "Design and fabrication of a new vibration-based electromechanical power generator", *Sensors and Actuators A,* vol. 92, pp. 335-42, 2001

[6] I. Sari, I. Zeimpekis and M. Kraft, "A full wafer dicing free dry release process for MEMS devices" *Proc. Eurosensors XXIV,* Linz, Austria, September 5-8, 2010.

ENHANCED ELECTRO-MECHANICAL PERFORMANCE OF TIO2 NANO-PARTICLE MODIFIED POLYDIMETHYLSILOXANE (PDMS) AS ELECTROACTIVE POLYMERS

Guangmin Ouyang, Kaiying Wang, and Xuyuan Chen

Vestfold University College, Horten 3179, Norway

Abstract —This paper reports a polymer nano-composite with enhanced electro-mechanical performance by mixing TiO2 nano-particles into polydimethylsiloxane (PDMS) matrix. The nano-composites with TiO2 concentration up to 30 wt% were synthesized by in-situ polymerization. High energy ball milling and surfactant polyethylene glycol was used to reduce the agglomeration and ensure a stable dispersion. The properties of nano-composites, i.e. transmittance, elastic modulus, response time and dielectric constant, can be tuned by controlling the TiO2 concentration. The nano-composites were applied in tunable gratings and showed reduced driving voltage and response time, comparing with traditional electroactive polymers (EAPs).

Keywords : **Nano-composite, Electro-mechanical, EAP, PDMS, Tunable gratings.**

I – Introduction

Electroactive polymers (EAP) have recently attracted considerable interests in applications of electro-mechanical actuators and sensors, thanks to its lightweight, reliability, durability and easily processing [1]. They have been employed in spatial light modulation, sound generation, ultrasonic transduction and precision driving [2]. In these applications, EAPs deform by electric field. The strain of polymers is originate from both the Maxwell stress, arising from Coulomb electrostatic interactions among free charges on electrodes, and the electro-strictive stress, arising from strain-induced permittivity change of the material [3]. Though most of EAPs show their capability of high-level actuating performance, two effects limit their application areas. First, a high voltage, typically in the order of kilovolts, is needed to drive the EAPs [4, 5]. Second, due to the viscoelastic property of polymers, the EAP based device normally has slow response time (in a range of millisecond to second) than traditional silicon based device [6].

In order to broaden the application area of EAPs, improvements of their electro-mechanical properties are necessary. Recently, nano-particles have been widely employed as fillers to reinforce the physical and/or chemical properties of EAPs. Attribute to their high specific surface area of more than 1000 m2/g, small amount of nano-particles bring significant improvements of mechanical, electrical, and thermal properties to EAPs [7]. Various kinds of nano-particles, such as zinc oxide [8], carbon nanotube [9], lead magnesium niobate-lead titanate [10], have been applied in EAPs.

In this work, polydimethylsiloxane (PDMS) was chosen as the host polymer because of its remarkable durability and resistance to temperature, UV radiation and weathering [11]. Titanium dioxide particles were used as filling material owing to its relatively high permittivity, chemical inertness, non-toxicity and easily dispersed in silicone matrix [1]. The nano-composites were synthesized and characterized by their transparency, elastic modulus, response time and dielectric constant. Comparing with pure PDMS, the nano-composites proposed in this work showed enhanced electro-mechanical performance which is important for using EAPs in applications of MEMS sensors and actuators.

II - Experimental

Three dimensional PDMS network was cross-linked by hydrosilylation reaction. Linear vinyl-terminated PDMS reacts with cross-linkers, which were trimethylsiloxy-terminated methyhydrosiloxane- dimethylsiloxane copolymer, to form a three dimensional network. They were purchased from Gelest, Inc. The cross-linking process was catalyzed by platinum complex previously dissolved in xylene, which were from UCT Specialties, LLC, at room temperature. The titanium dioxide nano-particles were purchased from Sigma-Aldrich Co., with primary size of 25 nm.

The synthesize method of nano-composite is in-situ polymerization. Firstly, the TiO2 nano-particles (with weight percentage from 1% to 30%) were mixed with linear vinyl-terminated PDMS in the presence of polyethylene glycol (PEG). The PEG was one fifth of the nano-particles by weight. These components were intensively mixed by high energy ball-milling for 24 hours. Secondly, the cross-linker and catalyst were added into the solution one after another, followed by manual stirring for 2 min. The amount of the linear PDMS and the cross-linker were 9:1 by weight and the catalyst has 0.1 wt%. Finally, samples were cured at room temperature for a couple of hours.

Light transmittance measurements were carried out for 10 μm thick nano-composite films which were deposited on glass plates. Hitachi U-1100 spectrophotometer was used for the measurements. The elastic modulus and response time was measured using home-made measurement systems as described in [12]. The static dielectric constant was obtained by measuring the capacitance of cylindrical samples, in which the edge effect was taken into consideration.

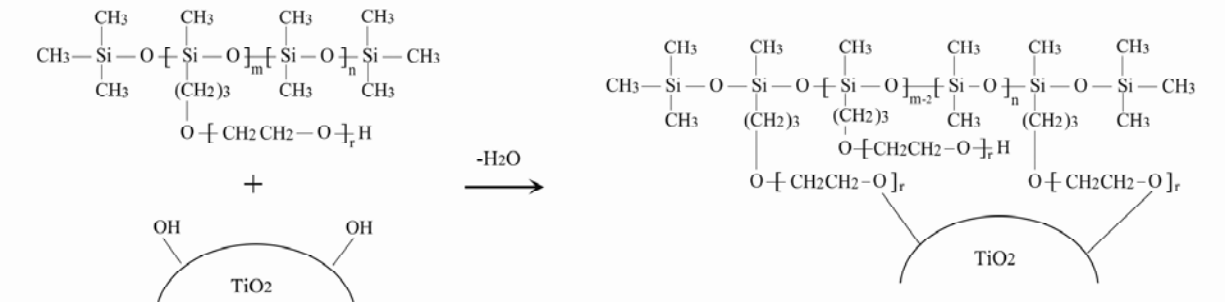

Figure 1. Chemical reaction between surfactant polyethylene glycol (PEG) and TiO2 nano-particles.

II - Results and Discussion

The inhomogeneous dispersion due to the pronounced agglomeration tendency of nano-particles is the biggest technical obstacle for synthesizing a polymer nano-composite [13]. Two techniques were applied in this work to reduce the agglomerations. First, high-energy ball-milling was used during mixing. It provided high impact and shear fields to break the agglomerates. Second, PEG was used as a surfactant to achieve a homogenous dispersion and avoid the re-agglomeration. PEG is a good surfactant for dispersing TiO2 into silicones. It has branched polyethlene chains which can bond to the OH group on TiO2 surface. The reaction formula is shown in Fig. 1, where two polyethlene chains are bonded to the TiO2 surface. PEG itself can mix well with PDMS since they have the same backbone structure. After ball milling of TiO2 and PDMS dispersions, TiO2 nano-particles were attached to the PEG by chemical bonding and the PEG (with TiO2 attached) were physically suspended in the linear PDMS solution. The TiO2 nano-particles in PDMS solution with or without the presences of PEG are compared in Fig. 2. A phase separation is clearly seen when no surfactant was used, indicating an unstable and inhomogeneous dispersion. The microstructure of the nano-composite is checked by SEM, as shown in Fig. 3. The nano-particles are evenly dispersed in polymer matrix with diameter below 500 nm.

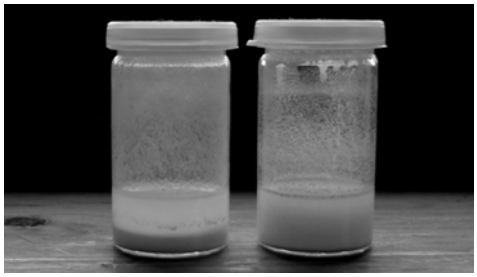

Figure 2. Comparison between TiO2 in PDMS solution without (left) and with (right) the presences of PEG. The mixture is left in room temperature of 24 hours after ball milling.

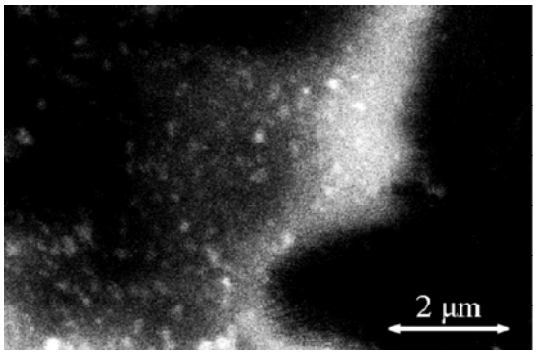

Figure 3.SEM image of dispersed TiO2 nano-particles in PDMS matrix. The white spots are nano-particles.

Nano-composites with varied TiO2 concentration were characterized. Light transmittance of the nano-composites is shown in Fig. 4. The transmittance decreases to 0.8 when TiO2 concentration reaches 5 wt%, and this value drops to almost zero when the TiO2 concentration reaches to 20 wt%. The loss of the transmittance is due to the relatively large particle size. It is very difficult to disperse the TiO2 in polymer matrix with diameter below 100 nm, even with high energy ball milling. Agglomeration is inevitable due to the high surface energy of nano-particles. The scattering of the light due to the particles lead to the transmittance loss when light pass through the nano-composite film.

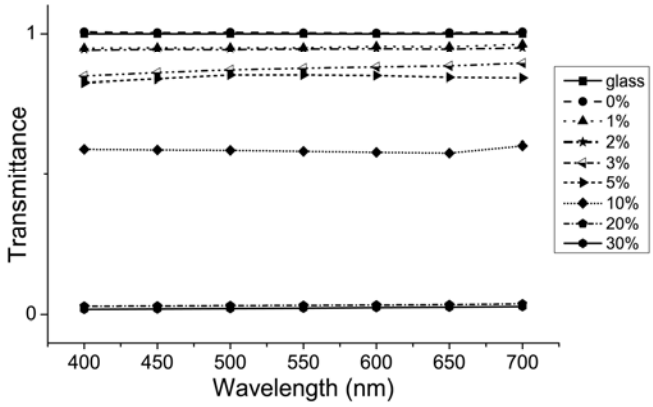

Figure 4. The transmittance of nano-composites with varied TiO2 concentration.

The influence of nano-particles to elastic modulus and response time is shown in Fig. 5. The elastic modular of the nano-composite decreases with increasing particle concentration for low particle concentration. Once the particle concentration increases to more than 5

wt%, the elastic modulus increases. The influence of nano-particles to the elastic modulus is attributed to two factors: softening effects due to the interfering of cross-linking (major effect for TiO2 concentration lower than 5 wt%) and hardening effects due to the intrinsic high elastic modulus of TiO2 (major effect for TiO2 concentration higher than 5 wt%). At 5 wt% of particle concentration, the two effects balance with each other, and the elastic modulus is more or less the same with the pure PDMS elastomer. The changing of elastic modulus with regard to particle concentration was also reported by other research groups [1, 14] which used high particle concentration (above 20 wt%). It was reported that the elastic modulus increased continuously with TiO2 concentration due to the intrinsic high elastic modulus of TiO2 particles. The deterioration of the cross-linking process by particles was not mentioned. However, the interfering of cross-linking is inevitable when the particle have diameter comparable with the length between cross-linking site of PDMS. It is also observed that the cross-linking process was prolonged by introducing nano-particles. The curing time of nano-composite increased with the particle concentration. This could be due to the interface effect between particles and polymer, which slowed down the cross-linking process. Meanwhile the catalysis was also influenced by nano-particles. The changing of response time with regard to particle concentration is plotted in Fig. 5. Pure PDMS had response time of 9 μs, while the response time reached to 3 μs when 30 wt% nano-particles were added. The relationship between elastic modulus and response time can be roughly fitted to "Voigt-Kelvin model". In brief, the elastic modulus is inverse proportional to the response speed [15].

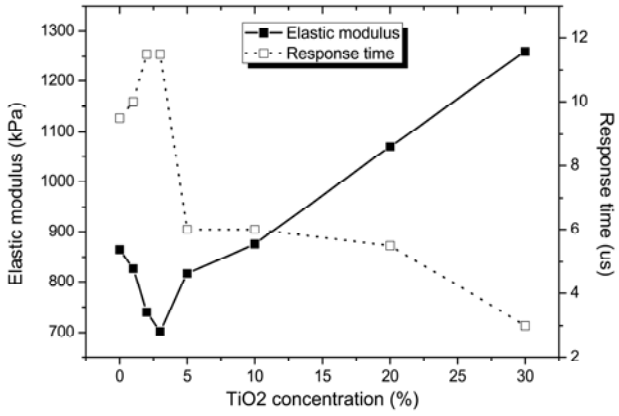

Figure 5. The elastic modulus (solid line) and response time (dashed line) of nano-composites with varied TiO2 concentration.

The dependence of static dielectric constant on particle concentration is shown in Fig. 6. A sharp increase of the dielectric constant from 2.9 to 3.9 was observed when the weight fraction of TiO2 nano-particles increased from 0% to 5%. Thereafter, the dielectric constant gradually increased to 4.4 with nano-particles concentration increasing to 30 wt%. The two phases of increasing tendency of dielectric constant could be due to the particle bridging or flocculation at high particle concentration. The detailed mechanism about this phenomenon will be investigated in future works. The increased dielectric constant gives an advantage of increased electric force acting on EAPs, therefore reduce the requirement of the driving voltage.

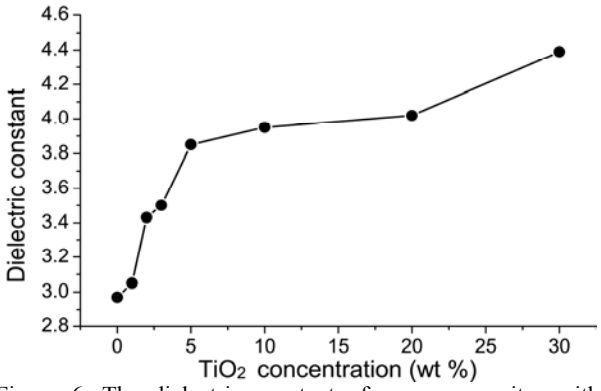

Figure 6. The dielectric constant of nano-composites with varied TiO2 concentration.

From measurement results, properties of nano-composite can be tuned by modifying the TiO2 concentration in polymer matrix. An enhanced electro-mechanical performance of the nano-composite is achieved for different applications. In applications where a low dirving voltage is the top consideration, the nano-composite should be as soft as possible, i.e. using TiO2 concentration around 3 wt%. Since the strain increase with reduced elastic modulus of the actuation material under same stress, the requirement for driving voltage is reduced for a certain amout of strain. Though nano-composites with high TiO2 concentration have higher dielectric constant (meaning higher stress under same driving voltage), the elastic modulus increase much faster with nano-particles comparing with increasing of dielectric constant, therefore constrain the deformation amplitude of nano-composite. In appplications where the response time is the mostly desired, the material should be made with high TiO2 concentration. In such case, 3 μs response time is obtained. It need higher voltage to actuate, nevertheless the increased dielectric constant can relief the requirement of high voltage to some extend.

IV - Application

Nano-composite with 5 wt% TiO2 was applied in a tunable polymer grating. The elastic modulus of nano-composite is more or less the same with pure PDMS elastomer. However, dielectric constant is increased and the response speed is improved. The structure of the tunable polymer grating as well as the fabricated tunable grating chip is shown in Fig. 7. In this device, the PDMS-TiO2 nano-composite (5 μm thick) is sandwiched between a top gold electrode (50 nm thick) and bottom interdigital electrodes (150 nm thick). When no voltage is applied, the nano-composite has a flat surface, working as a reflective mirror. When voltage is applied,

a sinasodual phase grating is generated on nano-composite surface as shown in Fig. 8. More details of the EAP based tunable gratings are referred to [6]. In order to ensure the diffraction efficiency, 230 V DC voltage and ±100 V AC voltage was applied to the top and bottom electrodes, respectively. The peak-to-peak deformation was measured as 190 nm, giving 90% first order diffraction efficiency for the light with 633 nm wavelength. The response time of the device was the same as the response time of the nano-composite, which was 6 μs, indicating that the time lag due to RC circuit in the device is negligiable.

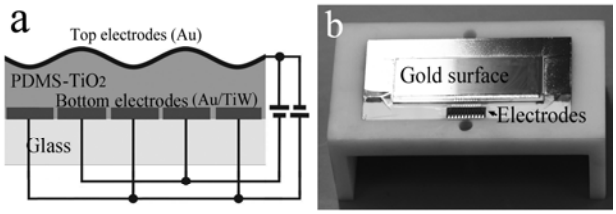

Figure 7. Tunable grating chip with nano-composite utilized as EAP to create the gratings. a) Schematic of the chip and electrical connection. b) The fabricated tunable grating chip.

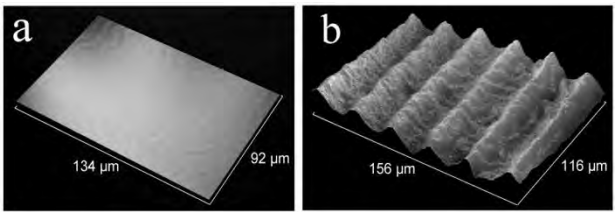

Figure 8. The profile of nano-composite grating. a) When no voltage is applied, the surface is flat. b) When voltage is applied, the grating profile is observed.

V – Conclusion

TiO2 nano-particles with concentration up to 30 wt% were dispersed into PDMS matrix, forming nano-copmposites. Agglormaration of nano-particles was broken and the TiO2 partices were evenly dispersed in polymer with sizes below 500 nm. At 30 wt% of TiO2 particle concentration, the nano-composite became opque and the elastic modulus, the resposne time, dielectric cosntant of the nano-composite reached to 1.26 MPa, 3 μs and 4.4, respectively. The nano-composite with 5 wt% TiO2 was applied in tunable gratings. Comparing with traditional technology [13], where pure polymer was used as acutaion material, the requirement for driving voltage is reduced from 250 V to 230 V and the resposnse speed is improved from 9 μs to 6 μs. To further reduce the requirement of the driving voltage, nano-particles, such as metallophthalocyanine, copper-phthalocyanine, can be used. The dielectric constant of these polymer nano-composite is expected to be higher due to the extrmely high dielectric constant of the paticles.

Acknowledgments

The authors are grateful to Dr. M. N. Akram, Dr. L. Henriksen and Dr. V. Kartashov for fruitful discussions. This research work is funded by the Research Council of Norway under grant BIA-286 project number 182667 and poLight AS.

References

[1] F. Carpi and D.D. Rossi, IEEE T Dielect El In, Vol.12, No.4, pp.835-843, 2005.
[2] H. S. Nalwa, Marcel Dekker, New York, NY 1995.
[3] T. Yamwong, A. M. voice and G. R. Davies, J. Appl. Phys., Vol. 91, pp.1472-1476, 2002.
[4] R. Pelrine, R. Kornbluh, J. Joseph, R. Heydt, Q. Pei and S. Chiba, Mater. Sci. Eng. C, Vol. 11, pp. 89-100, 2000.
[5] F. Carpi and D. De Rossi, Mater. Sci. Eng. C, Vol. 24, pp. 555-562, 2004.
[6] G. Ouyang, K. Wang, L. Henriksen, M.N. Akram, X.Y. Chen, Sensor Actuat A-Phys, Vol.158, pp. 313-319, 2010.
[7] X. L. Wang, I. K. Oha, J. B. Kim, Compos Sci Technol, Vol. 69, pp.2098-2101, 2009.
[8] M. Sato, A. Kawata, S. Morito, Y. Sato, I. Yamaguchi, Eur Polym J, Vol. 44, pp.3430-3438, 2008.
[9] J. N. Coleman, U. Khan, W. J. Blau, Y. K. Gun'ko, Carbon, Vol. 44, pp.1624-1652, 2006.
[10] G. Gallone, F. Carpi, D. D. Rossi, G. Levita, A. Marchetti, Mater. Sci. Eng. C, Vol. 27, pp. 110-116, 2007.
[11] V. Kartashov, L. Henriksen, J. H. Ulvensøen, B. Svardal, T. Svortdal, R. Berglind, and G. Hedin, J. Soc. Inf. Disp. Vol.17, pp.581-587, 2009.
[12] Ouyang G, Wang K, Akram MN, Henriksen L, Chen XY, Appl Phys A – Mater, pp. 1-8, 2011.
[13] Federico Carpi, Giuseppe Gallone, Fabia Galantini, and Danilo De Rossi, Adv Funct Mater, Vol. 18, pp.235-342, 2008.
[14] X.Q.Zhang, M.Wissler, B, Jaehne, R.Broennimam, G.Kovacs, Proc. SPIE, Vol.5385, 12.540888, 2004.
[15] J. M. G. Cowie and V. Arrighi, Boca Raton: CRC press, 2007.

HIGH SENSITIVITY AND FAST RESPONSE ELECTROACTIVE POLYMER VIA NETWORK SWELLING

Guangmin Ouyang [1], Kaiying Wang [1], Lars Henriksen[2], and Xuyuan Chen [1]

[1] Vestfold University College, Horten 3179, Norway
[2] PoLight AS, Horten 3179, Norway

***Abstract* — Three dimensional cross-linked PDMS network was swollen by mixing linear PDMS and cross-linker with high mobility silicone oils, to improve the sensitivity and response time of the polymer. Elastic modulus and response time of this electroactive polymer were investigated using mechanical and optical measurement systems. The change of the elastic modulus and response time were analyzed based on the network topology, i.e. the cross-link density, the entanglements, the chain confirmation. Optimized PDMS with swollen network can have elastic modulus around 200 kPa and response time around 30 µs. De Gennes theory was applied to predict the elastic modulus with regard to polymer concentration in highly swollen PDMS networks and the experimental results showed agreements with the theory. This optimized electroactive polymer can be a promising candidate in applications such as MEMS spatial light modulators and tunable gratings.**

***Keywords :* PDMS; Swelling; EAP; Elastic modulus; Response time.**

I – Introduction

Electroactive polymers (EAPs) represent today one of the most performing classes of material in Mircro-electro-mechanical (MEMS) devices, attributing to its flexibility, durability, light weight, easy fabrication and low production cost [1]. As one of the widely used EAPs, Poly(dimethylsiloxane) (PDMS) shows its durability, resistance to high temperature, UV radiation and chemical attack [2]. It has been applied in MEMS tunable gratings [3-5], spatial light modulators [6, 7] and artificial muscles [2]. In these applications, the most important performance of PDMS is its mechanical deformation under electric force, which can be characterized by its sensitivity and response time. When PDMS is applied in a spatial light modulator as actuation material, for example, fast response time is required to obtain high frame rate while high sensitivity is necessary to achieve high diffraction efficiency [8]. General problems with polymer actuators are that they are not quiet sensitive, therefore need very high voltage to activate, and the response time is relatively slow [1,6, 9].

Typically, a cross-linked PDMS has a three dimensional network, formed by linear vinyle-terminated PDMS reacting with multifunctional cross-linker, which is expressed as Eq. (1).

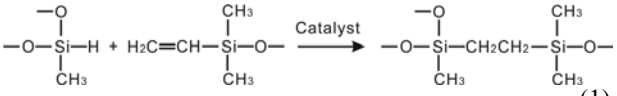

(1)

The physical-mechanical properties of the cross-linked PDMS are determined by its network topology, i.e. the cross-linking density, the entanglements, the residual chemical groups, etc. In order to increase the sensitivity, polymers with small elastic modulus are expected. Classic rubber theories predict that a network with low elastic modulus is easy to achieve by increasing the chain length between cross-links, in another words, by decreasing the cross-link density (the average number of cross-links per unit volume). However, there are two limitations by using this method. First, when the molecular weight of the chain between cross-link is increased above the entanglement length, the network is dominated by the entanglements rather than cross-link density. In such case, it is impossible to further decrease the elastic modulus by modifying the cross-link density [10]. Second, the response time of the cross-linked PDMS was sacrificed due to the increased inter-chains entanglements [8].

Since both the response time and elastic modulus of PDMS are essential, in this work, the elastic modulus of PDMS is reduced by swelling of the network. Short chain miscible solvent was mixed with linear PDMS and cross-linkers. Because of the difference in mobility of the solvent and the PDMS molecular, the interaction between solvent and PDMS network, the movement and conformation of PDMS networks are changed. By optimization of PDMS network via swelling, the synthesized PDMS elastomer can have elastic modulus around 200 kPa and response time around 30 µs. Comparing with other techniques [1, 6, 9], where the PDMS have elastic modulus bigger than 700 kPa and response time longer than 2 ms, the PDMS optimized in this work show improvements in both sensitivity and response time.

II - Experimental

Linear vinyl-terminated PDMS and cross-linkers (trimethylsiloxy-terminated methyhydrosiloxane-dimethylsiloxane copolymer), with molecular weight of 9400 g/mol and 1950 g/mol, respectively, were purchased from Gelest, Inc. The cross-linking process was catalyzed by platinum complex previously dissolved in xylene, which were from UCT Specialties, LLC, at room temperature. The solvents are silicone oils, purchased from Sigma-aldrich, with molecular weight of 700 and 1000, respectively.

The PDMS were optimized by swelling of the network with polymer concentration from 10% to 100%. The solvent was added into linear PDMS solution and stirred for 3 min. Then, the cross-linker and catalyst were added into the mixture, followed by stirring thoroughly for 5 min. At last, the samples were debubbled in room temperature then cured in oven at 60°C. The molar ratio between function groups of linear PDMS (C=C) and cross-linkers (Si-H) were set as C=C : Si-H = 1 : 1.2 to achieve a PDMS network with minimum dangling or pendant chains [8]. The presence of extra Si-H function group was necessary due to inevitable oxidation/hydrolysis side reactions. By introducing solvent into PDMS network, the polymers were swollen. The polymer chains between cross-links uncoil to some extent in order to keep the solvent molecules inside the network, and the volume of the network increase.

The response time of the PDMS elastomer was measured using an optical measurement system. In the measurement setup, the testing PDMS is deposited on a prism coated with an indium tin oxide layer (works as one electrode). A metal needle (works as another electrode) is suspended closely to the PDMS film. When the voltage is applied to electrodes, a small spot on the PDMS (the area under the needle) experience an electric force and start to deform. The deformation leads to light diffraction and scattering, which is detected by the photo-detector. The response time is obtained by comparing the detected signal to applied voltage in oscilloscope.

The elastic modulus of the PDMS elastomer is obtained by Hertz equation using a mechanical measurement system. In this setup, a metal probe with sphere indenter is fixed with a load cell. The probe is controlled to move perpendicular to the PDMS surface by a control stage. When the indenter contacts to the PDMS surface, the contacting force is obtained by the load cell. According to the Hertz equation, there is a linear relationship between indentation depth of power 3/2 and the force on indenter. The elastic modulus is a function of the gradient and can be obtained by plotting indentation depth with regard to detected force. More details of the measurement setups are refer to [8].

III - Results and Discussion

Elastic modulus and response time of swollen PDMS with varied polymer concentration are plotted in Fig. 1, where silicone oil of molecular weight (MW) 700 and 1000 were used as solvents. From experiments, there are not much difference between PDMS swollen by MW 700 solvent and MW 1000 solvent. The unswollen PDMS has elastic modulus of 601 kPa and response time of 9 μs. This kind of PDMS has a very fast response time, however, the sensitivity is relatively low, i.e. need high voltage to actuate. By introducing the solvent into the network, the elastic modulus decrease, meaning a promoted sensitivity. Though the response time increases at the same time, the increase rate is relatively low. For PDMS swollen by silicone oil of MW 700, when polymer concentration decrease from 100% to 10%, the elastic modulus decrease from 601 kPa to 12 kPa and response time increase from 9 μs to 164 μs; while for PDMS swollen by silicone oil of MW 1000, the elastic modulus decrease from 601 kPa to 13 kPa and response time increase from 9 μs to 166 μs. To show the advantage of this optimization method, the properties of PDMS via swelling are compared with the results published in [8], in which the PDMS properties are tuned by modifying the cross-link density. As shown in Fig. 2, in order to obtain a PDMS with same sensitivity, the one optimized by swelling the network have much faster response time. For example, if a PDMS elastomer with elastic modulus of 200 kPa is required, the PDMS tuned via swelling has a response time of 34 μs while the PDMS tuned via decreasing the cross-link density has a response time of 500 μs.

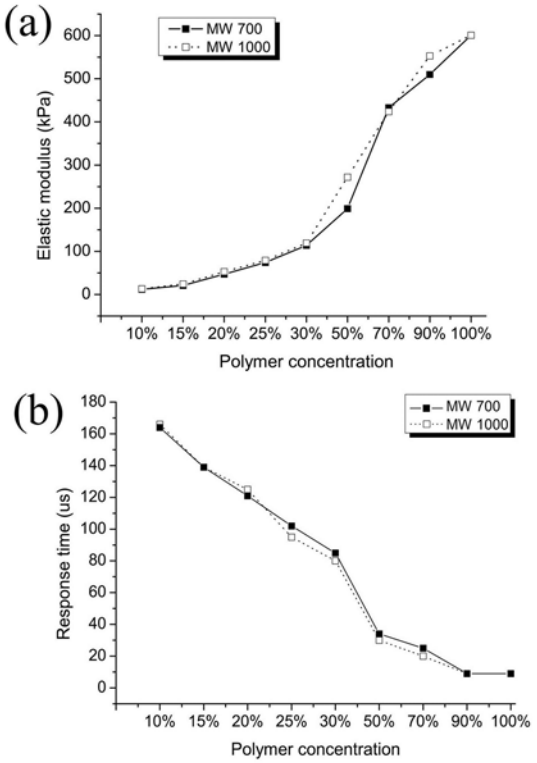

Figure 1: Variation of PDMS properties with regard to polymer concentration. (a) Changing of response time; (b) Changing of elastic modulus.

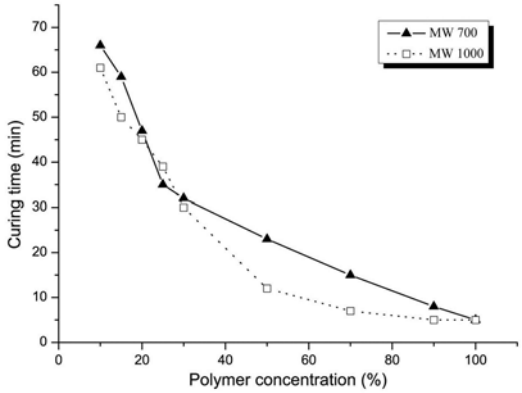

Figure 2: Comparison of PDMS properties tuned by modifying the cross-link density and by swelling.

The change of the response time of swollen PDMS is attributed to three aspects. First, the number of trapped entanglements between networks chains are lowered, attributing to the extended network. The reduced entanglements contribution in PDMS structure makes the PDMS respond faster to the applied force [8]. Second, because polymer chains are surrounded by high mobility solvents, the movements of the structure elements of PDMS and the change in conformation of the network are promoted, leading to a fast response PDMS. Third, since the cross-link density is inverse proportional to the volume of network, the swollen network decrease the cross-link density therefore prolong the response time. According to the experiments, the delay of polymer chain movements introduced by the decreased cross-link density is compensated by the lowered entanglements and easy movements of polymer chains. Only a slight increase of the response time is observed in a swollen PDMS network. Comparing with other technologies, where PDMS with elastic modulus of 1MPa and response time of 2 ms [1], PDMS with elastic modulus of 1.8 MPa and response time around 10 ms [6], and PDMS with elastic modulus around 700 kPa and response time of 3 s [9] are utilized in MEMS modulators and actuators, the optimized PDMS using the proposed technique are improved from both sensitivity and response time.

PDMS with swollen network needs more time to cure compare with unswollen PDMS. As shown in Fig. 3, the curing time increase with decreased polymer concentration in swollen PDMS.

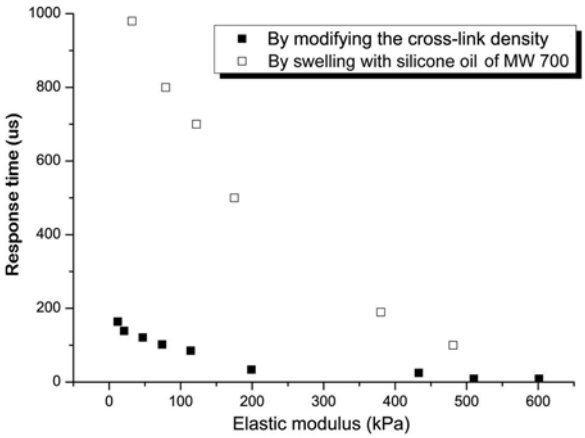

Figure 3: The curing time of PDMS with swollen network.

Classical rubber theories describe the unswollen polymer network in terms of shear modulus by: [11, 12]

$$G = \left(1 - \frac{2}{f}\right)\frac{\rho}{M}RT + G_N^0 T_E \quad (2)$$

where G is the shear modulus equal to $E/3$ in the case of the incompressible polymer, f is the functionality of the cross-linker, ρ is the density, M is the molecular weight, R is the gas constant, T is the temperature, G_N^0 is the plateau modulus of the melt of uncross-linked polymer and T_E is the trapping factor. The first term in Eq. (2) is the modulus contributed from chemical cross-links, while the second term is from entanglements. When solvent is added to the reaction mixture, there is no simple scaling of Eq. (2) to describe the modulus change, because the solvents effect the entanglements and chemical cross-links in different ways. De Gennes described the properties of swollen polymer networks based on the analogy found between the swollen network and semidiluted polymer solution [13].

$$G = B(\varphi/N) \quad (3)$$

$$\varphi \propto N^{1-3\nu} \quad (4)$$

where B is a constant which depends on the polymer/solvent system, φ is the polymer concentration, N is the degree of polymerization between cross-link points and ν is the excluded volume component. In the case of good solvent, the value of ν is around 0.6. From Eq. (3) and Eq. (4), it follows that:

$$G \propto B\varphi^{3\nu/(3\nu-1)} \quad (5)$$

From Eq. (5), there is a linear relationship between *logG* and *logφ* with gradient of *2.25*. Eq. (5) is only valid when polymer is considered as an infinitely thin chain, i.e. possessing length but not volume. At high polymer concentration, the finite volume of the structural elements may no longer be neglected. The elastic modulus with regard to polymer concentration above 70% is plotted in Fig. 4 together with the theory prediction. The gradient for silicone oil of MW 700 and MW 1000 were calculated as 2.02 and 2.06 respectively by linear fitting using least mean square method. These results show agreements with the theory prediction which is 2.25 in this case. The small deviation can be due to some effects not taken into account in the theory, e.g. increase loop formation due to increased distance between cross-links, higher mobility of polymer chains, hindering of cross-linking process by the presence of large amount of solvent.

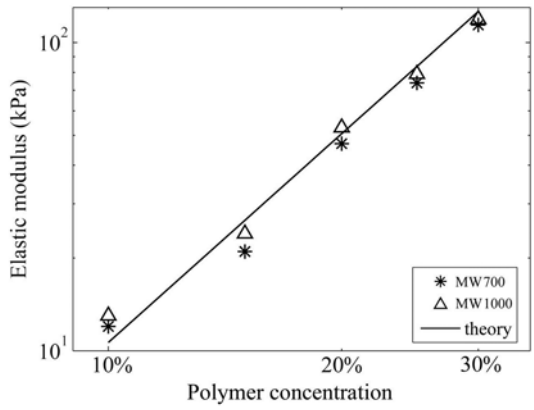

Figure 4: The elastic modulus of highly swollen PDMS network.

IV - Conclusion

Highly sensitive and fast response PDMS were successfully synthesized by swelling of the three dimensional network. The high sensitivity of PDMS is because of the decreased cross-link density, while the improved response time is attributed to the reduced trapped entanglements and easy move-

ments/conformation of polymer chains. The elastic modulus of highly swollen PDMS was investigated using de Gennes theory. A linear relationship between *logG* and *logφ* was observed with a gradient of 2.02 and 2.06 for solvent with MW 700 and MW 1000, respectively. These results agreed with the theory, which gives a gradient of 2.25. Comparing with other techniques, the optimized PDMS via swelling has achieved both higher sensitivity and faster response time. This PDMS can be a promising candidate as electroactive polymer material for applications such as MEMS spatial light modulators, tunable gratings and artificial muscles.

Acknowledgments

The authors are grateful to Dr. M. N. Akram and Dr. V. Kartashov for fruitful discussions. This research work is funded by the Research Council of Norway under grant BIA-286 project number 182667 and poLight AS.

References

[1] Pelrine R, Kornbluh R, Joseph J, Heydt R, Pei Q, Chiba S. Mat Sci Eng C – Bio S, Vol. 11, pp. 89-100, 2000.
[2] Clarson SJ and Semlyen JA. Siloxane polymers. Prentice Hall, Englewood Cliffs, N.J., 1993.
[3] Aschwanden M and Stemmer A. Polymeric, Opt Lett , vol. 11, pp. 2610-2612, 2006.
[4] Ouyang G, Wang K, Henriksen L, Akram MN and Chen XY, Sensor Actuat A – Phys, vol. 158, pp. 313-319, 2010.
[5] Ouyang G, Tong Z, Akram MN, Wang K, Kartashov V, Yan X, and Chen XY, Opt Lett, vol. 35, pp. 2852-2854, 2010.
[6] Sakarya S, Vdovin G, Sarro PM, Sensor Actuat A – Phys, vol. 108, pp. 271-275, 2003.
[7] Sakarya S, Vdovin G, Sarro PM, Sensor Actuat A – Phys, vol. 97, pp. 468-472, 2002.
[8] Ouyang G, Wang K, Akram MN, Henriksen L, Chen XY, Appl Phys A – Mater, pp. 1-8, 2011.
[9] Xuequn Z, Wissler, M, Jaehne B, Breonnimann R, Kovacs G, Proc. SPIE, vol. 5385, pp. 78-86, 2004.
[10] Larsen AL, Larsen PS, Proc. SPIE, vol. 5385, pp. 108-117, 2004.
[11] Langley NR, Macromolecules vol. 1, pp. 348-352, 1968.
[12] Dossin LM and Graessley WW, Macromolecules, vol. 12, pp. 123-130, 1979.
[13] deGennes PG, Scaling Concepts in Polymer Physics, Cornell, Ithaca, NY, 1979.

ENHANCED WET ETCHING PROCESS OF PZT/ZRO2 THIN FILMS FOR RF MEMS CAPACITIVE SWITCHES

D. Min, N. Hoivik and U. Hanke

Vestfold University College, Institute of Micro and Nano Systems Technology, 3103 Tønsberg, Norway

***Abstract* — A wet etching process of PZT/ZrO_2 thin films suitable as the dielectric layer in RF MEMS capacitive switches was investigated. PZT thin films are typically etched using buffered HF (BHF) and HCl acids. In order to increase the etch rate, a nichrome etchant (10-30% ($(NH_4)_2Ce(NO_3)_6$) + 1-5% CH_6COOH + 70-90% H_2O) was applied at ~43°C prior to BHF etching. The etching results indicate that the use of a nichrome etchant effectively increases the etching rate of PZT film with proper undercutting. The temperature and time of the nichrome etchant affected the etching rate and quality of the PZT/ZrO_2 films as well.**

***Keywords :* PZT, ZrO_2, wet etching, nichrome**

I - Introduction

Radio frequency (RF) microelectromechanical system (MEMS) capacitive switches, which will be key microwave devices in the near future, have been extensively developed for application in switching matrices and phase shifters. Large RF isolation related to down-state capacitance of switches is a key factor in determining RF performance of the device. Thus, the use of a high dielectric constant material has been considered. In this work, we have chosen both ferroelectric PZT and ZrO_2 thin films to form a double layer dielectric film. PZT is a well-known ferroelectric and piezoelectric with a large dielectric constant, and ZrO_2 is an excellent dielectric with a large breakdown field strength and high dielectric constant (>25). Dielectric properties of combined PZT/ZrO_2 thin films perform better than single PZT thin film in terms of current leakage, breakdown field strength, and dielectric losses at microwave frequencies [1, 2].

In order to pattern a PZT film on the switch bottom electrode, wet etching based on buffered HF (BHF) and HCL is typically used instead of dry etching, mainly due to low cost, good selectivity, and high etch rate [3]. However, PZT etch rate can wary a lot depending on the PZT deposition process and etchant concentration.

For dual layers of PZT/ZrO_2 deposited on the TiW adhesive layer prepared by the chemical solution deposition (CSD) method [4], it was observed that the etching rate of the PZT and ZrO_2 films was quite slow when only using BHF and HCL, making it difficult to correctly pattern the film. To an extent, it even caused etching of the SiO_2 layer underneath the TiW adhesive layer. Thus, it was necessary to increase the etch rate of the PZT film with proper undercutting, and avoiding SiO_2 etching. In this report we suggest an alternate process to improve PZT etching that uses a nichrome etchant consisting of 10-30% ($(NH_4)_2Ce(NO_3)_6$) + 1-5% CH_6COOH + 70-90% H_2O) at a much higher temperature,~43°C,than the usual temperature of 25-26°C, and we discuss the etching results for different etching processes.

II - Experimental Details

The substrate material used was a 300 µm thick high resistivity Si wafer. A coplanar waveguide (CPW) was patterned on the sputtered 300 nm Au/15 nm TiW layers deposited on a 500 nm thick thermal SiO_2 layer. In our switch fabrication, both PZT and ZrO_2 thin films were prepared by the chemical solution deposition (CSD) method on a15 nm thick TiW layer. The final thicknesses of the PZT and ZrO_2 films were 280 nm and 100 nm, respectively. The PZT thin film was coated with AZ4562 photoresist using a standard lithography process to form the etching masks. To etch the PZT and ZrO_2 films, two different etchants with several compositions were prepared. Table 1 shows the wet etching process with etchants used in this experiment. Figure 1 shows the microscope image after deposition of the PZT/ZrO_2 films and a schematic view of the cross-section indicating each layer of the structure.

Table 1: *Two-step etching process for PZT/ZrO_2 film patterning*

Etchant	Process
1	10-30% ($(NH_4)_2Ce(NO_3)_6$) + 1-5% CH_6COOH + 70-90% H_2O at 43°C for 4 minutes
2	1BHF (7:1)+2HCl+4H_2O at room temperature for 9 minutes

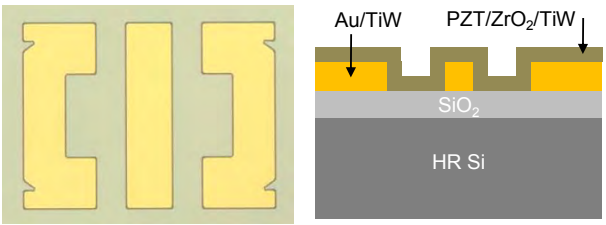

Figure 1: *Microscope images of PZT/ZrO2/TiW films deposited on CPW (a) and schematic cross section (b)*

III - Results and Discussion

Figure 2 shows the microscope images (top view) of the obtained PZT/ZrO_2 pattern after etching using BHF (7:1) and 2HCl+H_2O separately at room temperature [5]. It was observed that the etch rate of PZT and ZrO_2 was low. Figure 2(a) shows the etching results after 3.5 minutes. Figure 2(b) shows the etching results after 11 minutes. When the etching process became long, the dielectric layers underneath the photoresist were cracked. As seen in figure 2(c), the dielectric layers fell off after removing the photoresist layer due to the long etching time of 20 minutes. Some residues that may possibly induce adhesive failure with an upper layer and increase RF insertion loss were still seen on the CPW.

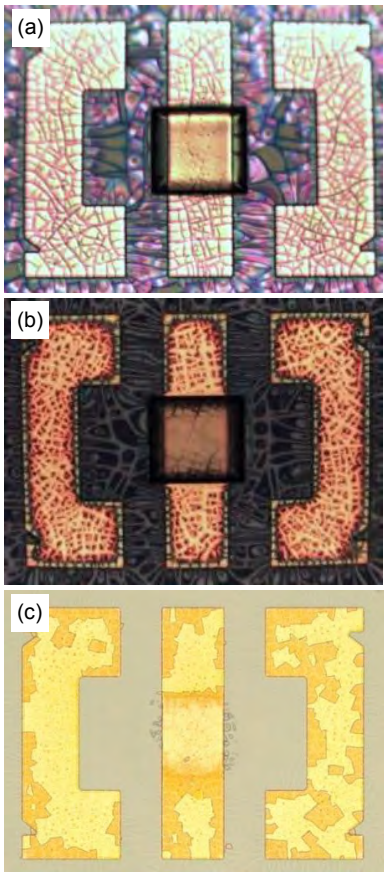

Figure 2: *Microscope images of the obtained PZT pattern over different etching using conventional etching; (a) 3.5 minutes (b) 11 minutes (c) 20 minutes*

In order to resolve the low etch rate, we used a nichrome etchant before BHF etching (step 2 in table 1). It is typically used to etch Cr adhesive layers. However, it was experimentally found that a PZT thin film can be gradually etched by a nichrome etchant as time passes. The temperature of the etchant was increased up to ~43°C in order to accelerate the reaction with PZT. Figure 3 shows the PZT patterns after 3 minutes of 1BHF+2HCL+4H_2O etching in two sequential steps. It can be seen that the PZT/ZrO_2 films were patterned. However, some residues were still left over on the CPW. It was also observed that the color of the SiO_2 layer changed depending on the BHF etching time, which is attributed to SiO_2 etching by BHF. The TiW layer was placed to improve adhesion between the ZrO_2 and SiO_2 layers and also to protect the SiO_2 against BHF. However, the SiO_2 layer was unexpectedly etched. Figure 4 shows the PZT/ZrO_2 pattern after 9 minutes of etching in step 2. Dielectric layers were patterned, but undercutting occurred due to the longer etching time. However, compared to the etching results in figure 3, very small residues were observed in this etching result. The dielectric layer did not fall off after etching, which is compared to the results in figure 2(c). The color of the SiO_2 layers are also compared with the etching results in figure 3 due to the different etching times in step 2. When the temperature of the nichrome etchant was lower than ~36°C, the PZT film was not etched as much as at ~43°C. On the other hand, when the time of step 1 was increased to 10 minutes, it was seen that the PZT/ZrO_2 pattern was easily fallen off during BHF etching. Thus, it seems that the time and temperature of the nichrome etchant significantly affected the etching results. How PZT etching is influenced by a nichrome etchant in terms of chemical reaction is being investigated. The thin lines observed on the dielectric layers in figure 3(a) and 4(a) may be attributed to cracks in the dielectrics and are being investigated as well. Table 2 shows the summary of the etching experiments.

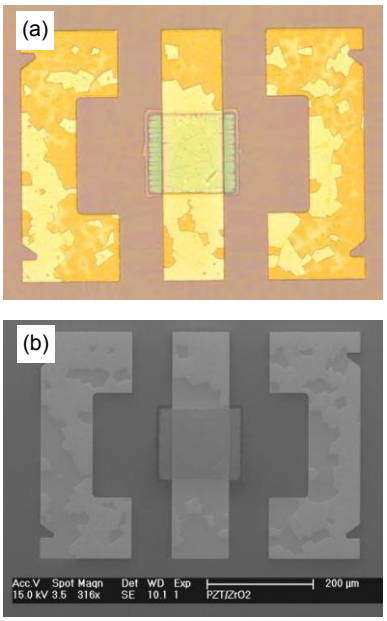

Figure 3: *microscope (a) and SEM (b) images of the obtained PZT/ZrO2 patterns after etching in two sequential steps: step 1 for 5 minutes and step 2 for 3 minutes*

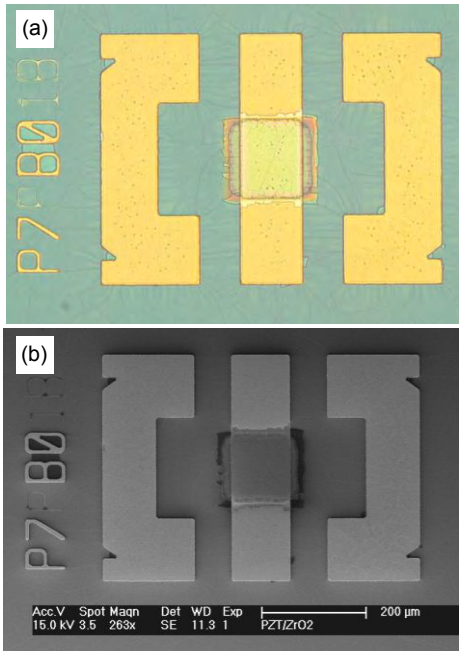

Figure 4: *microscope (a) and SEM (b) images of the obtained PZT/ZrO2 patterns after etching in two sequential steps: step 1 for 4 minutes and 20 seconds and step 2 for 9 minutes*

Table 2: *Summary of wet etching experiments*

Process	Process	Remark
1	Step 1 at 36°C for 3 minutes Step 2 at room temperature for 3.5 minutes	Slow etching; the etching results are the same as seen in figure 2
2	Step 1 at 43°C for 4-5 minutes. Step 2 at room temperature for 9 minutes	Properly patterned (Figure 4)
3	Step 1 at 43°C for 10 minutes Step 2 at room temperature for 2 minutes	PZT/ZrO_2 falls off

IV - Conclusion

In order to fabricate RF MEMS capacitive switches, correct patterning of the dielectric layers is needed. In this experiment, CSD PZT/ZrO_2 thin films were chosen and etched for the dielectric layer. We found that PZT and ZrO_2 films were etched slowly in BHF solution, and during the etching process the SiO_2 layer underneath the TiW adhesive layer was etched as well. In order to pattern dielectrics, a nichrome etchant was applied at ~43°C before BHF etching. It was clearly observed that PZT thin film can be etched faster with a nichrome etchant than without it, and that the SiO_2 etching rate is also decreased. This method of etching PZT/ZrO_2 thin films appears to be effective and may also be useful in developing further PZT etching processes. We are currently working on the cracks found on the dielectrics after long etching process.

Acknowledgement

The authors wish to acknowledge the assistance and support of Zekija Ramic at VUC, SINTEF ICT and SINTEF Materials and Chemistry, Oslo. This work is partially funded by the Norwegian Research Council under Grant No. 181712/I30 "Microtechnological Research Platform".

References

[1] T. Kim, A.I. Kingon, J.P. Maria and R.T. Croswell *J. Am. Ceram. Soc.*, vol. 89, pp. 3426-30, 2006
[2] D. Min, N. Hoivik, G. U. Jensen and U. Hanke *Microwave Conference (EuMC), 2010 European*, pp. 1579-82, 2010
[3] K. Zheng, J. Lu and J. Chu *Jpn. J. Appl. Phys. Part 1 - Regul. Pap. Short Notes Rev. Pap.*, vol. 43, pp. 3934-7, 2004
[4] F. Tyholdt, F. Calame, K. Prume, H. Raeder and P. Muralt *J. Electroceram.*, vol. 19, pp. 311-4, 2007
[5] L.-P. Wang, R. Wolf, Q. Zhou, S. Trolier-McKinstry and R.J. Davis *MRS Online Proceedings Library*, vol. 657, pp. null-null, 2000

ANALOG DRIVER FOR SYNCHRONIZED QUASI-STATIC MOEMS MIRRORS

M. Lenzhofer[1], A. Tortschanoff[1]

[1]*Carinthian Tech Research AG, Villach, Austria*

***Abstract* — In this paper we present for the first time an analog control loop for positioning micro optical mechanical system (MOEMS) mirrors. The measured results are compared to the characteristics of the devices when driven in open loop mode. MEMS mirrors achieve more and more interest in miniaturized applications for example spectrometers and scanner devices. To obtain better physical properties, especially an increased aperture in scanning devices, several devices have to be synchronized to each other. This represents a major challenge because the MOEMS elements show a spread in their mechanical properties like resonance frequency and response curve. When using this control loop circuit presented in this paper, synchronization for each mirror can be achieved very easily, because the parameters are adjusted individually for each device. Consequently the same set-point signal leads to the same mirror deflections. In this contribution we present the principle of the quasi-static driver concept and show the experimental results achieved with a 470 Hz quasi-static mirror, which demonstrates its capabilities but also show its limitations.**

***Keywords :* MOEMS mirror, MEMS device, quasi-static mirror, analog control loop, position control, MEMS driver**

I - Introduction

A number of MOEMS based projection displays[1], imaging devices, barcode readers[2], spectrometers[3] and infrared imaging cameras have been developed for industrial, medical and consumer market. Especially for scanner products one fast oscillating mirror axis or even two axes to project a 2D raster pattern are necessary. To achieve a larger aperture an array of synchronized micromechanical devices can be used. Quasi-static mirrors can follow arbitrary trajectories and as such have several advantages.

The advantage of driving MEMS mirrors is that high mirror deflection angles can be achieved at relatively low driving voltages and minimal energy consumption. Additionally they are shock and vibration resistant and feature high scanning rates caused by the low mass of the mirror element.

To guarantee proper functionality, meaning stable well-defined amplitudes even under varying environmental conditions, it is essential to implement a closed loop control[4]. Our driver position feedback is obtained by integrating a PSD device to detect the position of the mirror element. The advantage of performing one controller stage for each mirror element is that they can be supplied with the same input signal and thus are automatically synchronized because they lock onto the same reference signal.

In this contribution we present our driver circuit for a quasi-statically driven mirror device including the feedback scheme, and show first experimental results with a quasi-static mirror. While our circuit is specially designed and adjusted to control a specific device, the basic concept is viable for all kind of quasi-static micro actuators.

II - MOEMS Device and driving Principle

The quasi-static micromechanical mirrors used for our development are commercially available devices from Mirrorcle Technologies Inc.®[5]. Figure 1 shows a photograph of the device we used. The MEMS actuator is fabricated in monolithic single crystal silicon and consists of 2-dimensional, gimbal-less vertical comb driven structures[6]. The mirror plate is fabricated in a separate SOI process and metalized before it is bonded to the actuator. The MOEMS mirror achieves a maximal amplitude of approximately 6.56° at 123 V. The resonant frequency depends on the used axis and is between 466 Hz and 470 Hz.

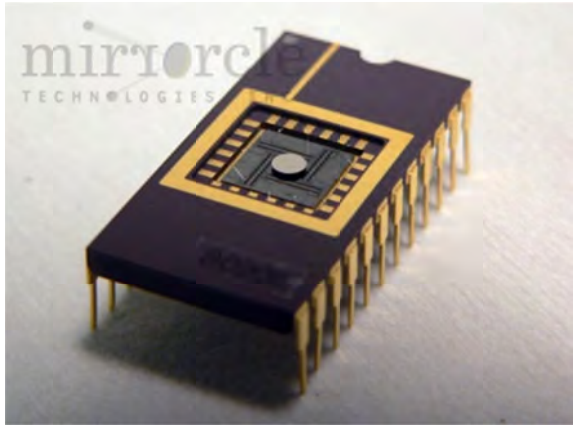

Figure 1: *Photograph[5] of the quasi-static mirror used to test our driving concept.*

To drive this MOEMS device a differential high voltage scheme with an additional bias voltage is used, which can be adjusted to prevent damage of the device. The advantage of this method is that it linearizes the device characteristic and provides smooth transitions when moving from one quadrant to the other. Figure 2 shows the basic diagram of this driving method and the characteristic curve of the device.

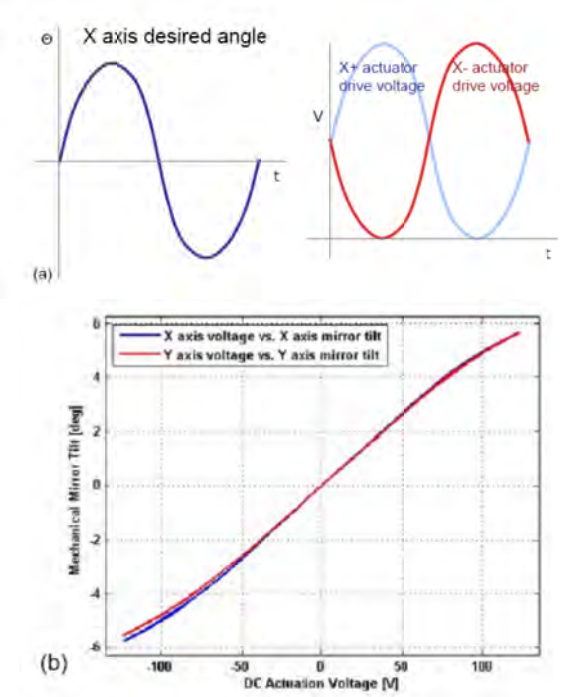

Figure 2: *a) Deflection angle of the mirror plate with the linearized 4-quadrant driving scheme. b) Mirror deflection angle dependent on the applied driving voltage*[5].

III - System Integration and Results

Figure 3 shows the developed driver box that contains two independent high voltage drivers in order to synchronize two quasi-static mirror devices. For the feedback path two dimensional PSD circuits are used, which generate an output voltage of ±3 V depending on the power of the reference laser diode. Because of the fact that the implemented high voltage driver board accepts levels of approximately ±9 V to achieve the maximal output voltage of up to +140 V, an additional power supply was inserted that supplys the output amplifiers. The set-point signal for the PID controller is applied to the Sub-D plug. All other signals are just supply wires and indicator lines from the PSD device to achieve the possibility to monitor or adjust the optical configuration.

Figure 3: *Photograph of the developed high voltage driver box to drive two synchronized quasi-static mirrors.*

To control the quasi-static axis, an analog PID controller was designed. Figure 4 shows the realized circuit. It consists of a first order input filter followed by an input amplifer, which can be configured very flexibly, either to use it as inverting or non inverting amlifier or impedance amplifier. This flexibility was necessary to achieve the possibility to use different laser modules, which lead to higher or lower signals on the PSD. The next stage is an adder circuit that substracts the actual value from the desired set point value. Afterwards the difference is weighted by three independent stages representing the integral, the diffrential and the proportional value of the PID controller. The feature to adjust all the values independently is very important, because every MOEMS miror has sligtly different parameters. The transfer function of the implemented controller is given by:

$$F(j\omega) = K_R\left[1 + \frac{1}{j\omega \cdot T_N} + \frac{j\omega \cdot T_V}{1 + j\omega \cdot T_1}\right]$$

with

$$K_R = \frac{R_{11}}{R_{4,14,20}},\ T_N = R_3 \cdot C_1,\ T_V = R_{17} \cdot C_5$$

and

$$T_1 = R_{19} \cdot C_5 .$$

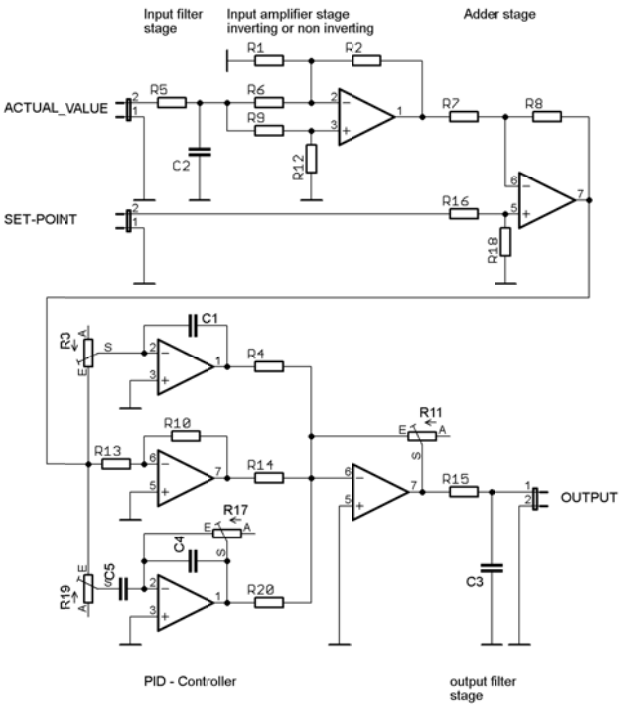

Figure 4: *Schematic of the realized PID control loop.*

Before starting the adjustment of the PID controller the step response signal of the quasi-static mirror was measured. Figure 5 shows the measured signals.

a)

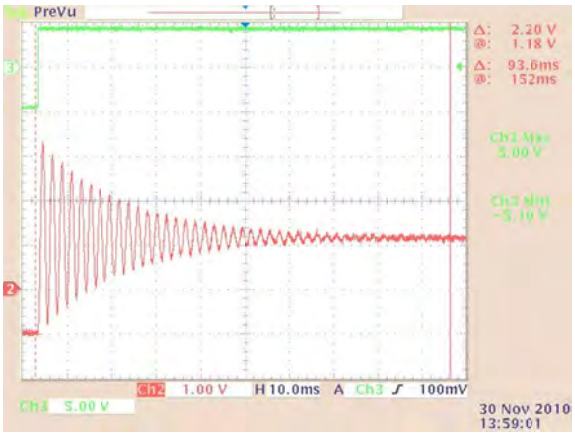

b)

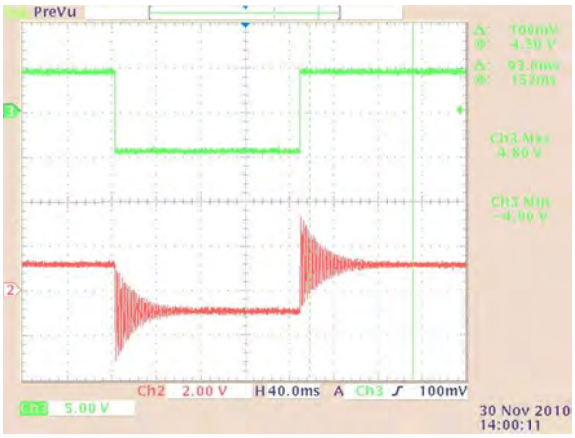

Figure 5: *a) Detailed zoom of the step response signal. The mirror oscillates with its eigenfrequency of about 80 ms before reaching a quasi-stationary position. b) The mirror response is identical on both, raising and falling slope of the control signal.*

In the next step the PID controller parameters were adjusted, so that the following optimized signal curves could be measured, figure 6.

For a scanner application, where the movement of the mirror could define the vertical deflection, a constant linear variation would be of interest. Therefore the input signal form was changed from a rectangular waveform to a triangular one. Figure 7 illustrates the measurement results with this trajectory.

a)

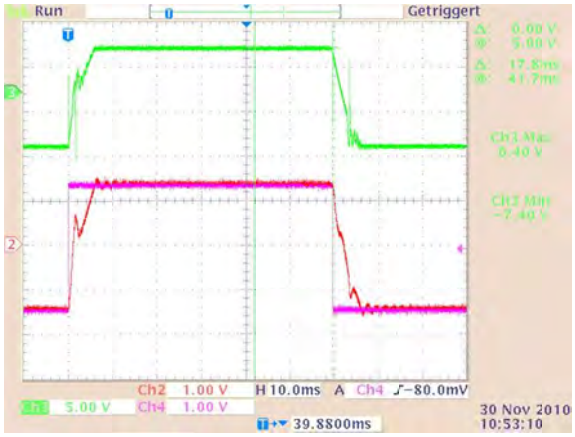

b)

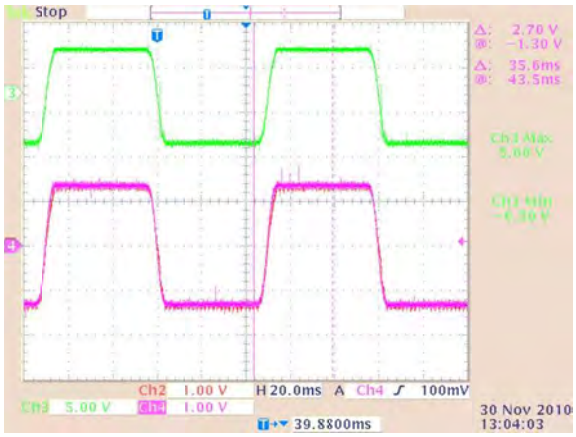

Figure 6: *a) This diagram shows the achieved step response of the mirror when implementing it into the PID control loop. The speed of reaching the maximum deflection could be increased so that the mirror now just requires 8 ms anymore to reach a quasi-stationary position. b) Measurement when driving the mirror in open loop, where the rectangular control signal is filtered by a Bessel low-pass with a bandwidth of about 180 Hz.*

a)

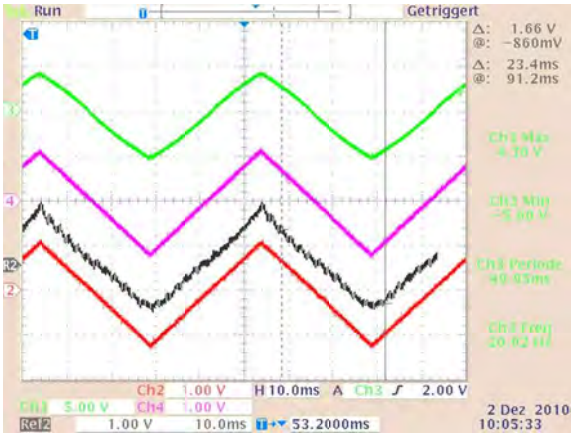

b)

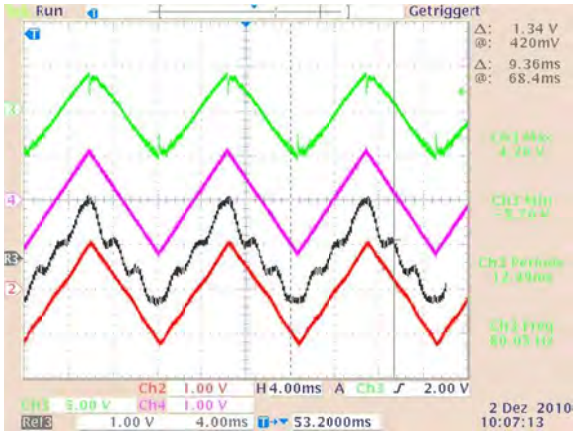

Figure 7: *a) Signal 4 is the input signal, which sets the position of the mirror. Signal 3 represents the output of the PID circuit that controls the HV stage. Signal 2 indicates the mirror movement measured by the PSD. R2 is the signal of the PSD when driving the mirror in open loop. The measurement was done at a frequency of 20 Hz. b) The signals are still the same, but the measurements were done with a frequency of 80 Hz.*

At higher frequencies it can be seen, that the resonance frequency of the mirror leaks into the measured position signal, if driving the mirror element in open loop. The reason is that every abrupt change in the control signal leads to an excitation of the eigenfrequency of the mirror. The effect is stronger if the frequency gets closer to its eigenfrequency. This means that it is very important to use a controlled driver design to achieve higher scanning frequencies and also much more precision.

CONCLUSIONS

In this article we presented a novel unit for closed-loop control of electrostatically driven quasi-static MOEMS mirrors, which will significantly improve the performance of these components.

The experimental results prove the possibility to drive quasi-static mirror elements within a PID control loop. The control circuit leads to a 10 times faster position reaching than just driving the mirror in an open loop circuit and even much more precision. When using a PID controller it is also possible to achieve higher control frequencies. As long as the set-point signal's frequency is 6 times lower than the mirror's eigenfrequency the given trajectory is followed perfectly.

This control concept is perfectly convenient to synchronize more mirror elements, because after connecting them in parallel, every mirror controller locks onto the same input frequency or analog signal. We expect it to provide significant impact for applications of these MOEMS mirrors e.g. in compact projection devices.

ACKNOWLEDGEMENTS

Funding and cooperation with all scientific and industrial partners involved in the 7th framework project "TACO" (grant agreement n°248623) is gratefully acknowledged.

References

[1] A. D. Yalcinkaya, H. Urey, D. Brown, T. Montague, R. Sprague, *Two-axis electromagnetic microscanner for high resolution displays*, IEEE J. Microelectromechanical Systems 15, pp. 786-794, 2006.

[2] M. H. Kiang, O. Solgaard, R. S. Muller, K. Y. Lau, *Micromachined polysilicon microscanners for barcode readers*, IEEE Photon. Technol. Lett. 8, pp. 1707–1709, 1996.

[3] F. Zimmer, H. Grueger, A. Heberer, A. Wolter, H. Schenk, *Development of a NIR micro spectrometer based on a MOEMS scanning grating*, Proc. SPIE, 5455, Vol. 9, 2004.

[4] A. Tortschanoff, M. Lenzhofer, A. Frank, M. Wildenhain, T. Sandner, H. Schenk, W. Scherf, A. Kenda, *Position encoding and phase control of resonant MOEMS mirrors*, Sensors and Actuators A 162, pp. 235–240, 2010.

[5] *Gimbal-less Two-Axis Scanning Micromirrors*, Datasheet of mirrorcle Technologies Inc., www.mirrorcletech.com, 2009.

[6] V. Milanovic, *Multilevel-Beam SOI-MEMS Fabrication and Application*, IEEE/ASME Journal of Micromechanical Systems, Vol. 13, No. 1, pp. 19-30, February, 2004.

COST-EFFECTIVE PROCESSING OF A PIEZORESISTIVE MEMS CANTILEVER SENSOR

I. Clausen, S.T. Moe, A. Vogl
SINTEF ICT, Dep. of Microsystems and Nanotechnology, Oslo, Norway

***Abstract* — In this paper cost-effective methods for fabrication of a piezoresistive cantilever sensor for industrial use are focused. The intended use of the presented cantilever is a medical application. A closer description of the cantilever design is given. The low-cost processing sequence is presented and each processing step is explained in detail. Results from electrical probing and mechanical strength test are given. The results demonstrate that the chosen low-cost processing route results in high yield and a mechanical robust device.**

***Keywords :* MEMS Processing, Micro Cantilever, Medical Sensor**

I - Introduction

In this paper we focus on cost-effective methods for fabrication of a piezoresistive sensor element for industrial use. The production of a great many MEMS devices described in research papers has the aim of proof of concept to demonstrate a sensor, or an actuator principle, or to verify a new processing step or processing route. For this purpose the main interest is to get some - or at least one - working device. When developing a working device for the industry, however, a cost-effective production method with high yield is demanded.

For high-end products the costs are not necessarily critical; the obvious advantages of MEMS with small size, low energy consumption and reliable characteristics are often crucial, and the willingness to pay may be high to achieve these characteristics. For products in the low-end range, however, the MEMS industry has to compete with other engineering solutions, where price-per-element is the most critical factor.

One of the first MEMS elements ever realized for industrial use was a cantilever sensor developed by SI, Norway (now SINTEF), in the 1960s [1]. The cantilever sensor presented in this paper is designed for medical applications with respect to size and measurement range. However, MEMS cantilever devices have a number of application areas;

- measurement of mechanical properties as position, pressure, force, and acceleration [2-3]
- detection of attachment of biomolecules and DNA strands for use in biosensors [4-7]
- detection of changes in resonance frequency [8]
- actuating element [9]

For all the above mentioned application fields, alternative solutions do however exist. To ensure commercial success for MEMS cantilever devices, cost-effective fabrication methods and process flow are therefore necessary.

II - Cantilever Design

The presented device is a piezoresistive Si/glass cantilever die used as a position sensor (Figure 1). The die consists of two parts; the silicon cantilever with integrated piezoresistors, and the glass support, which is bonded to the cantilever for assembly and easier handling. To obtain a mechanically robust device, the die is designed with a beveled transition area between the support and the cantilever arm for reduced stress-concentration (Figure 2).

Outer dimensions of the Si/glass cantilever die are (length, width, height): 6450 µm × 1040 µm × 1055 µm. Detailed measures of the die are given in Figure 3. The size is determined by the specific medical application. Reduced consumption of Si, and thereby reduced price-per-chip, is also a motivation for making the device very small. On a 6” Si wafer there are 1536 active dies.

Figure 1*: A piezoresistive silicon/glass cantilever die for position sensing*

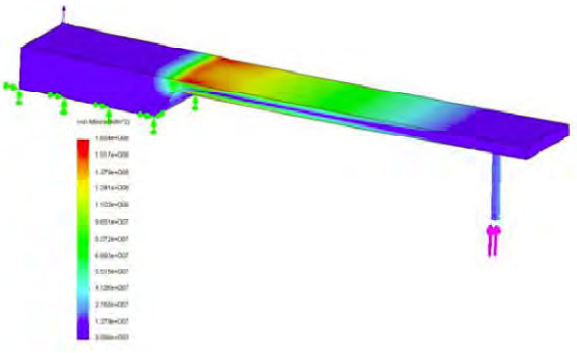

Figure 2: *FEM simulation of cantilever design. Red color indicates area with high stress concentration*

Four p-type piezoresistors form a Wheatstone bridge configuration. The nominal resistor values are 5 kΩ, and the bridge is designed for a 5 V bias voltage. A resistor equal to the bridge resistors is placed on the support of the cantilever and is not sensitive to strain induced in the cantilever. This resistor can be used for compensation of temperature induced effects. The bond pads and conductors are made of Al. The conductors stop 130 µm from the p-doped resistors to minimize tension induced by thermal expansion of the metal. The cantilever is designed for a maximum deflection of ± 70 µm.

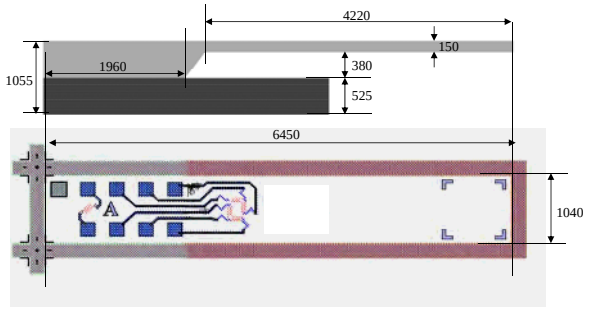

Figure 3: *Outline of the Si/glass cantilever die with a Wheatstone bridge and a fifth resistor for temperature compensation.*

When making the wafer design, the dies were arranged with every second column rotated 180 degrees. This gave the densest positioning of the dies on the wafer. To ensure the mechanical stability of the wafer during processing, a row across the wafer was not removed in TMAH etch.

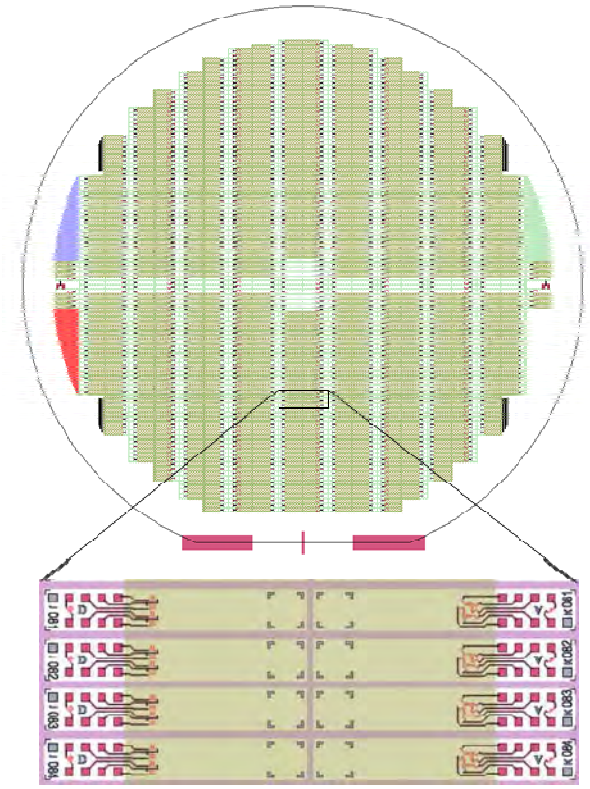

Figure 4: *Wafer design showing the die distribution on the wafer.*

III – Fabrication and Characterization

The silicon dies were fabricated on 6" BSOI wafers composed of a 150 µm n-type silicon device layer, a 500 nm buried oxide (BOX) layer and a 380 µm handle wafer. The processing sequence was as follows:

1. Ion implantation of resistors (moderately doped p-type)
2. Ion implantation of conductors (highly doped p-type)
3. Reactive ion etch (RIE) of backside oxide
4. Opening of contact holes
5. Metallization (Al)
6. Definition of the cantilever arm by anisotropic TMAH etch
7. Bonding of silicon wafer to glass wafer
8. Electrical probe test
9. Dicing

With this process flow, steps 1-6 could be done as standard batch processing, and only the bonding and the dicing were done on single wafers.

After step 6) the oxide thickness was 370 nm on both sides of the wafer. The back side oxide was patterned and used as mask for the TMAH etch. The thickness of the cantilever arm was precisely defined by the device layer as the BOX layer worked as an effective stop layer for the TMAH etch process.

To avoid damage on the already present metal pads and lines during the TMAH etch, a front side protection was required. The polymeric protective coating ProTEK™ (Brewer Science), which allows for batch processing, was chosen. The ProTEK™ was spin-coated on the wafer surface.

The oxidized silicon device wafer and the glass substrate were laminated by anodic bonding. This process is compatible with metallized wafers and provides high resulting bond strength. Anodic bonding was performed using a SB6e substrate bonder from SUSS MicroTec. The device wafer was bonded to a 525 µm thick, double-sided polished glass wafer (Pyrex 7740) by applying a bias of 1000 V at 400 °C for 2.5 min.

Before dicing, the wafers were electrically probed using a TSK A-PM-90A automatic probe station with a dedicated probe card. The cantilever dies were characterized electrically by measuring the resistor values, the bridge breakdown voltage, the bridge offset and the leakage current. The measurements were performed in a dark environment at room temperature.

Individual Si/glass cantilever dies were released by dicing. Due to the glass support wafer underneath the Si structure, a multi-step dicing process was required. The glass support was formed by dicing through the glass-wafer from the back side, removing the glass under-

neath the movable cantilever (Figure 5, 1). Subsequently, the individual dies were released by dicing (from the Si front side) through the full thickness of the bonded wafer stack (Figure 5, 2).

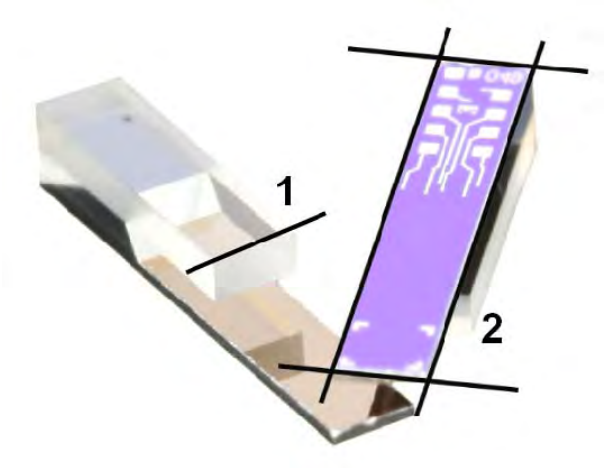

Figure 5: *Illustration of the multi-step dicing process of the silicon-glass stack for release of individual units*

Mechanical strength was tested in a test jig where assembled cantilever components were deflected until breakage (Figure 6). Both upwards and downwards deflection was tested.

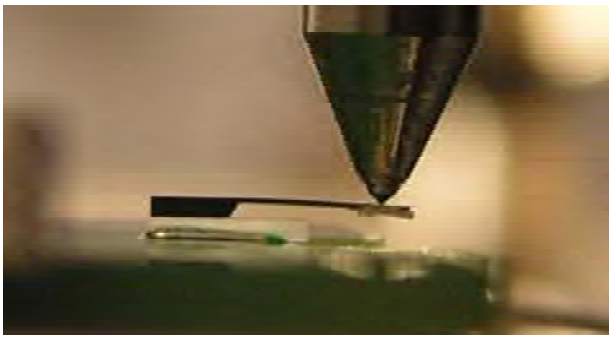

Figure 6: *Test of mechanical strength of an assembled cantilever component*

IV - Results and Discussion

A. Electrical Characteristics

The results of electrical probing together with acceptance criteria are shown in Table 1. A total yield of 90.5 % was obtained for dies from 4 wafers.

Table 1: *Results of electrical probing*

Parameter	**Specifications**		**Measured**		**unit**
	min	**max**	**avg.**	**std.**	
$V_{breakdown}$ @ -100 nA	30	-	50.9	3	V
$I_{leakage}$ @ -15 V	-	- 2	- 0.0075	0.2	nA
Bridge resistance	3.5	6.5	5.05	0.1	kΩ
Zero Bridge	-50	+50	13.6	13	mV

B. Mechanical Strength

The results of mechanical strength tests are shown in Table 2.

Table 2: *Results of mechanical strength test*

	Deflection [µm]
Max downwards deflection before breakage	127
Max upwards deflection before breakage	98

C. Cost-effective Fabrication

The process sequence for the cantilever was carefully selected for low-cost production. All photo lithography steps were done before the TMAH etching and wafer bonding; hence the wafers could be batch processed without special care during the photo steps.

Forming the cantilever arm by anisotropic TMAH etch with stop on buried oxide, removed the need for other tuning of the etch depth. The device layer formed the cantilever, and the thickness was precisely defined by the wafer producer.

Another benefit from the anisotropic TMAH etch was a mechanically robust device with a beveled transition area achieved through the highly orientation-dependent etch rate in Si. The test results of mechanical breakage showed that the cantilevers could withstand a load causing a deflection substantially larger than the requirement specification of ±70 µm.

The use of a dry front side single wafer holder was an alternative method to ProTEK™ for protection of the wafer front side during the TMAH etching. However, a dry front side holder does not allow for TMAH batch processing. The ProTEK™ coating displayed good protective properties. One wafer was etched in TMAH for 60 hours (more than 2 x nominal etching time) and no defects on the wafer front side were observed.

Anodic bonding was successful, i.e. a positive net voltage appeared on the Si surface even though several oxide layers were present in the Si wafer.

The first back side dicing could have been replaced by pattering of the glass wafer by e.g. etching or sand blasting prior to the wafer bonding. However, dicing is a less expensive method. Dicing also allows the anodic bonding to be done without alignment of the (un-patterned) glass wafer to the silicon wafer before bonding.

The release of the cantilever itself could have been done with e.g. DRIE from the front side. With the chosen design and processing route, the mechanical element was however released in the same dicing process as the final die dicing. Again, the dicing is cost effective and a final dicing process is unavoidable to attain individual devices.

V – Conclusion

A cost-effective processing route for a piezoresistive MEMS cantilever sensor element was described. The presented device was designed for medical applications, but MEMS cantilever devices have a wide range of application areas

The cantilever die was processed on 6” BSOI wafers. Anisotropic TMAH etch was used to form the cantilever arm with automatic termination of the etch process against the oxide layer. ProTEK™ provided sufficient protection of the front side metal lines and metal pads during the TMAH etch. A glass support die wafer was anodic bonded to the device wafer through several oxide layers (box layer and backside oxide) present on the device wafer. The final release of individual elements was done by a multi-step dicing process. Electrical probing of fabricated units showed a yield of 90.5%. Mechanical strength test showed that the cantilever die was a robust design.

References

[1] P. Ohlckers and H. Jakobsen, *Microelectronics Journal*, vol. 29, pp. 587-600, Sep 1998.
[2] P. Grabiec, *et al.*, *Bioelectrochemistry*, vol. 66, pp. 23-28, Apr 2005.
[3] R. Raiteri, *et al.*, *Sensors and Actuators B-Chemical*, vol. 79, pp. 115-126, Oct 2001.
[4] C. Ziegler, *Analytical and Bioanalytical Chemistry*, vol. 379, pp. 946-959, Aug 2004.
[5] L. G. Carrascosa, *et al.*, *Trac-Trends in Analytical Chemistry*, vol. 25, pp. 196-206, Mar 2006.
[6] R. Marie, *et al.*, *Ultramicroscopy*, vol. 91, pp. 29-36, May 2002.
[7] K. W. Wee, *et al.*, *Biosensors & Bioelectronics*, vol. 20, pp. 1932-1938, Apr 2005.
[8] F. M. Battiston, *et al.*, *Sensors and Actuators B-Chemical*, vol. 77, pp. 122-131, Jun 2001.
[9] W. E. Booij, *et al.*, *Journal of Electroceramics*, vol. 19, pp. 387-393, Dec 2007.

A MODIFIED BOSCH PROCESS FOR SMOOTH SIDEWALL ETCHING

Feng Gao, Sami Ylinen, Markku Kainlauri, Markku Kapulainen
VTT Technical Research Centre of Finland, Tietotie 3, Espoo, Finland

***Abstract* — This paper presents a method to etch smooth silicon sidewalls. The so called modified Bosch process combines a passivation step, a breakthrough step and a continuous etch step within one etch cycle. This method offers much smoother sidewall than a typical Bosch process while higher aspect ratio than a standard continuous process. The sidewall of a 5 µm deep silicon waveguide structure etched by this method has a root mean square (RMS) roughness below 10 nm while a peak-to-valley (P–V) roughness below 60 nm. The same method can be applied to etch interconnect via through the SOI layer, which extends the etching aspect ratio to more than 15:1 with small undercut and smooth sidewalls.**

***Keywords:* DRIE, Bosch process, MOEMS, MEMS, Sidewall roughness**

1 Introduction

Scalloping or sidewall ripple is a common feature of the Bosch process in DRIE [1-4]. Sidewall roughness of the etched structures by a typical Bosch process is normally in a few hundred nanometers range [2]. This roughness is not so critical for most of the MEMS applications where the high aspect ratio mechanical structures are more important [5]. However, for many MOEMS applications, smoother silicon sidewalls are needed [6-8]. In silicon microphotonics, for example, silicon is used as a medium for light propagation. Waveguide structures are fabricated on the silicon or SOI substrate to propagate light of the certain wavelengths. Light propagation in the waveguide is strongly affected by the roughness of the waveguide sidewalls [9]. High roughness increases light scattering in the waveguide leading to high propagation losses.

Obtaining low sidewall roughness directly from dry etching is quite challenging. Solehmainen et al. [6] developed continuous SF_6/C_4F_8 etch process with parameter ramping and achieved much better sidewall roughness than the Bosch process. Juan and Pang [7] used Cl_2 plasma by an electron cyclotron resonance (ECR) source and achieved silicon sidewall roughness of 29.95 nm. To further smoothen the sidewalls of the etched structures, post-etch treatments are often applied to achieve the final smoothness. Yun et al. [8] proposed a method using KOH etching at low concentration and low temperature to smoothen the vertical sidewall of (110) SOI (silicon-on-insulator) wafer after DRIE. Lee et al. [10] demonstrated that sidewall scalloping can be dramatically reduced by hydrogen annealing.

In this paper, a modified Bosch process combining switched steps and continuous SF_6/C_4F_8 etching is developed to achieve vertical and smooth sidewalls in silicon. This process demonstrates better sidewall roughness control than most of the other DRIE processes and has the potential to etch high aspect ratio structures. As used in many others applications [9, 11], thermal oxidation and oxide removal are also applied to further smoothen the surface for silicon waveguide applications. Comparisons between waveguides etched by this process and by another DRIE process showed remarkable improvement in propagation loss.

2 Experimental Details

A modified Bosch process was developed in a DRIE tool: Aviza Dsi. The recipe consists of 3 steps within a repeatable loop: a deposition step, a breakthrough step and a continuous etch step. The main parameters in the recipe are listed in *Table 1*. The combination of the *Dep* and *Break* is meant to form strong and uniform sidewall passivation layer while keeping the bottom of the etched structures open. The *Etch* uses both etching (SF_6) and passivation (C_4F_8) chemistry. The additive O_2 in the *Etch* step is used to improve etching uniformity across the 150 mm wafer. The source power and platen power are supplied at 13.56MHz. The platen power is pulsed at 150Hz with 20% duty cycle to prevent notching when etching to the buried oxide of the SOI substrates.

Table 1. *Process parameters of the modified Bosch process*

	Dep	Break	Etch
Time (sec)	1.5	1	5
Pressure (mT)	15	20	20
Source power (W)	2500	2500	2500
Platen power (W)	100	250	150
Platen pulsing	150Hz (20%)	150Hz (20%)	150Hz (20%)
Platen temp (°C)	10	10	10
O_2 (sccm)	1	200	50
Ar(sccm)	50	50	1
C_4F_8 (sccm)	300	1	180
SF_6 (sccm)	1	1	270
Loops	30		
Time (min)	3.75		

A single side polished <100> silicon wafer with 1 µm SiO_2 mask layer was first patterned and etched with the developed recipe for 30 loops (3.75 min). Then the second lithography was applied and an additional etch was performed with a standard Bosch process. This is to enlarge the measurement area allowing measurements with a conventional AFM. The wafer was then cleaved near to the edge of the additional etch to prepare the AFM sample as sketched in *Figure 1*.

For comparison purpose, another AFM sample was prepared with the same sequence of processes but the

first etch was done with a STS ASE tool using the same continuous process as in Solehmainen et al. [6]. The AFM measurements were then carried out with a Veeco DI Dimension 3100.

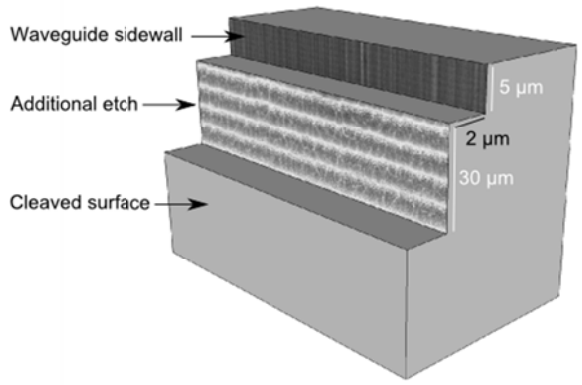

Figure 1. *A sketch of a test sample for AFM measurements (dimensions are not in scale). Waveguide sidewall height was approximately 5 µm and the additional etch step to 30 µm. The additional etch sidewall is separated from waveguide sidewall with approximately 2 µm*

In order to prove that the newly developed etching process can improve the performance of microphotonic devices, rib-type silicon waveguides were fabricated on SOI wafers. The SOI substrate has an active silicon layer of 3.7 µm and a buried oxide layer of 2 µm in thickness. The rib height was defined by timing the waveguide etch to around 2 µm depth (*Figure 2*). After dry etching of the rib waveguide structure, a thermal oxide of 500 nm was grown by wet oxidation at 1050°C and was removed by BHF etching. A TEOS oxide layer of 500 nm was then deposited with LPCVD on the waveguide structure to work as a cladding oxide.

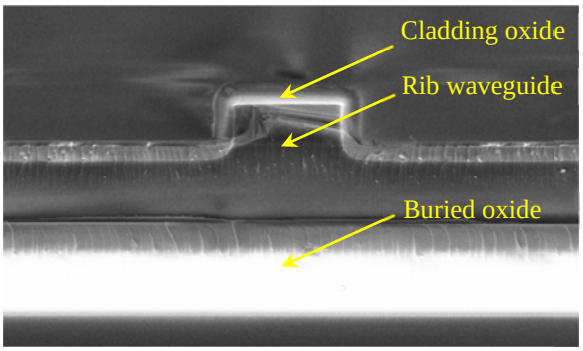

Figure 2. *SEM cross-section of a rib-waveguide structure fabricated on SOI wafer*

To demonstrate the usage of the etch process for other applications (such as TSV), a silicon wafer with via hole patterns was etched using the same recipe in the Aviza Dsi for 200 loops (25 min) and then cross-section was examined with SEM.

3 Results and Discussion

A. SEM and AFM measurements

SEM images in *Figure 3* shows the detailed profile of the silicon sidewalls etched by the modified Bosch process. The fairly faint ripples created by the switched process are still noticeable but the peak-to-valley variations are small, i.e. less than 20 nm. The average silicon etch rate of this process is around 1.5 µm/min for feature openings larger than 10 µm. Oxide etch rate is about 50 nm/min, which gives a selectivity to silicon of 30. The etching uniformity across the 150 mm wafer is less than ±3% which is good enough for most of the MEMS and MOEMS applications. The roughness of the waveguide sidewalls (the first etched sidewalls) was evaluated by AFM. *Figure 4* presents the AFM measurement results aside with the SEM cross-sections of the etched samples.

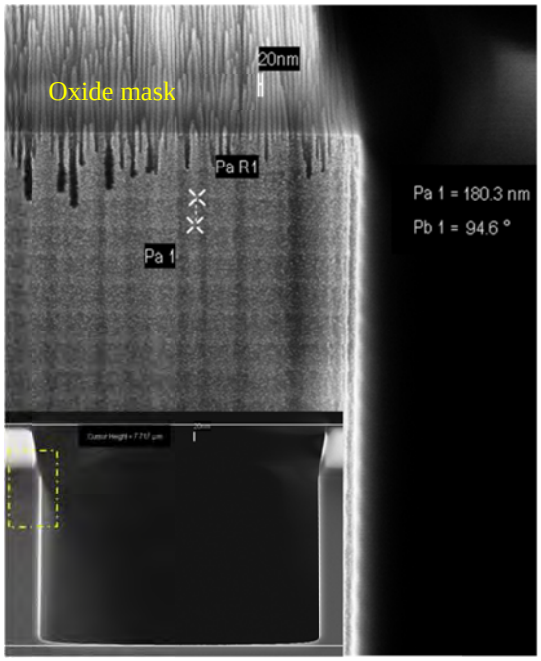

Figure 3. *SEM image of the sidewall profile etched by the modified Bosch process*

By comparing the AFM measurement results listed in *Table 2*, the modified Bosch process has almost the same root mean square (RMS) roughness and horizontal analysis result as the continuous process. However, the improvement in the vertical analysis is significant. It indicates that both etching processes will keep the horizontal variation inherited from the mask but the modified Bosch process has less change in roughness level from the top to the bottom. This also reflects the purpose of the recipe, which is to give more uniform and strong passivation to the sidewalls. From the SEM images, the top part of the sidewall etched with the modified Bosch process looks rough. But in AFM scanning, the waviness is not as rough as they look like in the SEM image. The waviness is most probably generated during the lithography steps where the trilayer resist technique reported by Juan and Pang [7] should help to minimize it.

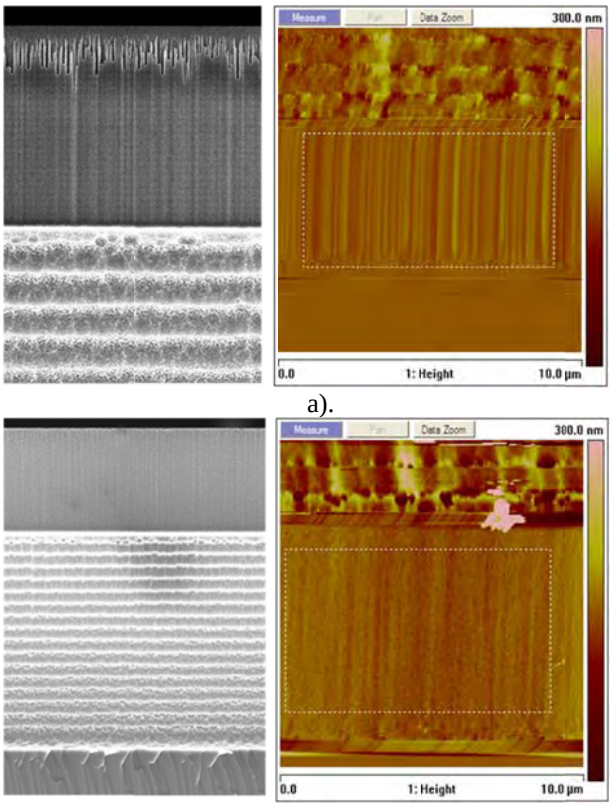

Figure 4. *SEM (on the left) and AFM (on the right and upside-down) images of the etched samples:* ***a)*** *was first etched with the modified Bosch process and* ***b)*** *was first etched with the continuous process*

Table 2. *AFM measurement results of the two DRIE processes*

	Modified Bosch	Continuous
RMS roughness [nm]	8.02	8.08
P-V roughness [nm]	55.0	68.5
Horizontal analysis RMS [nm]	5.57	7.29
Vertical analysis RMS [nm]	1.54	4.81

B. SOI waveguide measurements

The silicon waveguides fabricated on SOI substrate with both etching processes were measured and the results were compared. The propagation loss was measured from a 54.2 cm long spiral-shaped waveguide with a bending radius of 4 mm. The waveguide input and output facets were polished to optical quality using diamond lapping films. Propagation loss from waveguide etched with continuous process gave 0.14 ± 0.01 dB/cm for TE and 0.20 ± 0.01 dB/cm for TM. While the results from waveguide etched with modified Bosch process gave less propagation loss, 0.08 ± 0.01 dB/cm for TE, 0.07 ± 0.01 dB/cm for TM respectively. Total internal reflection waveguide mirrors were also inspected to compare the result of the two etching processes. In a waveguide mirror, the mirror surface needs to be as smooth as possible, but in addition to that, the mirror surface needs to be vertical. Losses per mirror were measured from three 2 cm long waveguides, each containing a different amount of mirrors. Average value from measurement was calculated, obtaining a loss value per mirror. Mirrors etched with the continuous process gave a loss values of 1.0 dB/mirror TE, and 1.2 dB/mirror TM, whereas mirrors etched with the modified Bosch process gave significantly better loss values of 0.3 dB/mirror TE, and 0.2 dB/mirror TM.

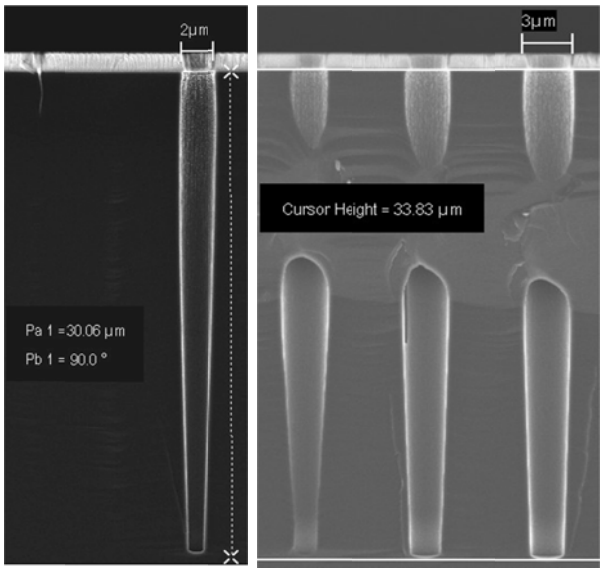

Figure 5. *SEM corss-section of 2-3 µm vias etched by the modified Bosch process*

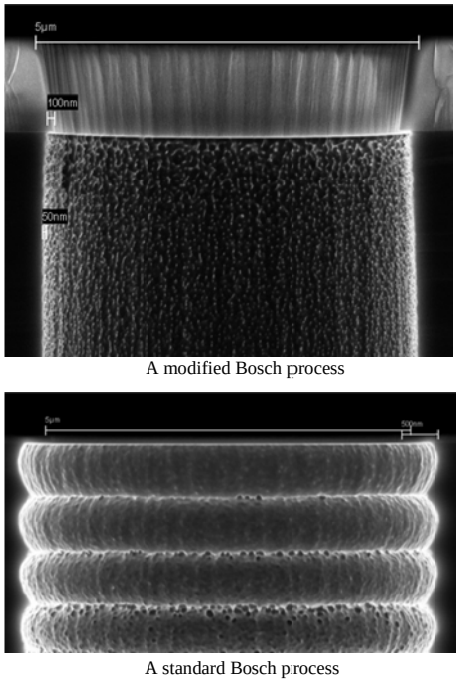

Figure 6. *Comparison of the under mask sidewall profile of the modified Bosch process and a standard Bosch process in etched 5 µm via holes*

C. Via etching results

The active top silicon layer of the SOI wafers used for MEMS applications are normally thicker than 1um and even up to more than 100um depending on the device design. Via holes are sometimes needed to penetrate the top silicon and the buried oxide layer to perform certain functions [12]. Small undercut and smooth sidewalls of the via holes are often preferred for those applications. In this test, a silicon wafer was etched with the pattern of circular holes 1-10 µm in diameters. The cross-section SEM images of 2-3 µm holes are shown in *Figure 5* and profiles for 5 µm holes under the mask are compared in *Figure 6*.

The etched 2 µm holes have an aspect ratio of 15:1 and the slight tapered profile is especially preferred for polysilicon or metal filling process. The results of this test give the evidence that the modified Bosch process can extend its application to higher aspect ratio structures beyond the range of the continuous process. Meanwhile, the sidewall roughness level is comparable with the etched waveguide structures and the undercut from the mask is smaller than 100 nm. These demonstrate extraordinary improvement to a standard Bosch process while compromising the overall etch rate and selectivity.

4 Conclusions

A modified Bosch process has been successfully developed to etch smooth silicon sidewalls. By combining the passivation, the breakthrough and the continuous etch step into a repeatable loop, the process is capable to keep the same roughness level through the top to the bottom of the etched sidewalls. The sidewall roughness etched by this process is well maintained below 10 nm RMS which is suitable for most of the MOEMS applications. Silicon waveguides fabricate on SOI wafers with this process showed less propagation loss compare to the ones etched by the continuous process. High aspect ratio structures like the interconnecting vias were also etched with the same process, which extended its application to aspect ratio up to 15:1.

References

1. Robert Bosch Gmbh, patents 4855017 and 4784720 (USA), and 4241054C1 (Germany), 1994
2. A. A. Ayon, R. Braff, C. C. Lin, H. H. Sawin, and M. A. Schmidt, “Characterization of a time multiplexed inductively coupled plasma etcher”, J. Electrochem. Soc., vol. 146, pp. 339 - 349 , 1999
3. C.H. Lee, K. Jiang, G.J. Davies, “Sidewall roughness characterization and comparison between silicon and SU-8 microcomponents”, Mater Charact., 58(2007), pp.603–609
4. R. Agarwal, S. Samson, S. Kedia, S. Bhansali, “Fabrication of integrated vertical mirror surfaces and transparent window for packaging MEMS devices”, Journal of Microelectromechanical systems, Vol. 16, Issue 1, pp. 122-129, Feb. 2007
5. B. Wu, A. Kumar, and S. Pamarthy, “High aspect ratio silicon etch: A review”, Journal of Applied Physics, Volume 108, Issue 5, pp. 051101 (2010)
6. K. Solehmainen, T. Aalto, J. Dekker, M. Kapulainen, M. Jarjanne, K. Kukli, P. Heimala, K. Kolari and M. Leskela, “Dry-etched silicon-on-insulator waveguides with loss propagation and fiber-coupling losses”, J. Lightwave Technol. 23 (2005), pp. 3875–3880
7. W. H. Juan and S. W. Pang, “Controlling sidewall smoothness for micromachined Si mirrors and lenses”, J. Vac. Sci. Technol., vol. B 14, pp.4080 - 4084 , 1996
8. S.S. Yun, S.K. You, J.H. Lee, “Fabrication of vertical optical plane using DRIE and KOH crystalline etching of (110) silicon wafer”, Sensors and Actuators A 128 (2006), pp. 387-394.
9. D. K. Sparacin, S. J. Spector and L. C. Kimerling, “Silicon waveguide sidewall smoothing by wet chemical oxidation”, J. Lightw. Technol., vol. 23, p.2455 , 2005
10. M.M. Lee, M. Wu, “Thermal annealing in Hydrogen for 3D profile transformation on silicon on insulator and sidewall roughness reduction”, Journal of Microelectromechanical systems, vol.15 (2006), pp. 338-343.
11. N. C. H. Le , D. V. Dao , R. Yokokawa , J. C. Wells and S. Sugiyama, “Fabrication of optically smooth, through-wafer silicon molds for PDMS total internal reflection (TIR)-based devices”, Microsystem Technologies (2009) 15:1845–1853
12. J. Kiihamäki, J. Dekker, P. Pekko, H. Kattelus, T. Sillanpää, T. Mattila, “Plug-up – a new concept for fabricating SOI MEMS devices”, Microsystem Technologies (2004) 10:346–350

NANOIMPRINTING POLYIMIDE AND POLYMER MULTILAYERS

Kolari K., Haatainen T., Ylinen S., Aalto T.

VTT Technical Research Centre of Finland, Tietotie 3 02150 Espoo, Finland

***Abstract* — This paper presents realization of controlled features in polyimide and PMMA, which are of interest in microfabrication, by using nanoimprint lithography with a silicon stamp. The observations highlight the importance of layer thickness, imprint temperature and local pressure in order to achieve required features in a polymer.**

***Keywords :* Nanoimprint lithography, polyimide**

I - Introduction

Imprinting submicron-scale features has been studied almost two decades during and after the pioneer work of Chou [1]. Nanoimprint lithography (NIL) is one of the nanopatterning methods, in addition to e-beam, extreme UV-, X-ray and holography lithography [2-3].

Most importantly, nanoimprinting is studied due to its potential to minimize or completely avoid using any expensive equipment while maintaining the required accuracy and resolution known in VLSI technology. On one side, nanoimprinting tries to continue the trend of increasing packing density of miniaturized electrical and optical devices beyond optical methods, i.e. below the 22 nm node. On the other hand, the tediousness of e-beam and X-ray lithography, and their low throughput, can be overcome by utilizing nanoimprinting as the means to transfer large scale patterns on a desired substrate. Such substrate can be e.g. silicon, III-V semiconductor, ceramic, glass, polymer roll-to-roll polymer web or metal foil.

The issues and obstacles in taking the full advantage of this method into use include the requirement for levelling and aligning the stamp into the substrate, wear and clogging of the stamp, and controlling of reflow of the imprinted material during the patterning.

Nanoimprinting is divided into two material categories; UV-NIL and thermal NIL. Since the cross-linking of polymers can alter the viscosity of UV-curable polyimide as much as with any other polymer, it is not studied here. Also, soft molding [4] is not feasible with hard and non-permeable stamps. Cui [5] showed two more approaches feasible for obtaining about 100 nm wide and 100 nm high trenches, in addition to imprinting into polyimide in its non-cured state; pattern transfer with reactive ion etching and the focus of this paper; direct imprinting at about T_g of polyimide.

More precisely, this paper concentrates on controlling the features imprinted into thermally curable polyimide and more precisely, on the pressure-temperature regime where imprinting becomes challenging.

II - Experimental Details

The imprinting tool used was a NPS 300 nanoimprinting stepper by Smart Equipment technologies SAS. The patterning of polyimide film was done using a sequential method in which a small stamp is used to imprint wafer-sized substrates step-by-step. The temperature was varied between 200 and 350 °C in 50 °C steps, while the imprinting force was 20 or 140 N and imprinting time and cooling time were kept constant both at 1 minute.

The polyimide used in the experiments was a thermally curable Evotek P84™, diluted with (N-ethyl-2-pyrrolidone) NEP. The boiling point of NEP is 202 °C and the glass transition temperature of the polyimide is 250-300 °C.

It was observed that diluting the polyimide below 8 w% resulted in the edges of 150 mm silicon wafer having no longer full coverage of polyimide after spinning. The ripping edges were also observed above 8 w% when using spin speeds above 1750 rpm. Baking at 82 °C improved the edges slightly by re-dissolving the polyimide into NEP and allowing for better surface wetting of the solution compared to room temperature.

In Table 1 the resulting thickness at centre of the Si wafer and at 40 mm from the centre is given with respect to dilution and spin speed. Dispensing was done at 300 rpm and immediately after that 100 rpm/s acceleration was used until the top speed, where 30 s was spent. During the spinning the polyimide turned turbid but after baking at 80 °C for 2 min the tabulated values for roughness and optical quality were achieved. Total evaporation of NEP is achieved by baking at about 200 °C, leading to 10-20 % reduction in thickness.

Before NIL, polyimide was baked at 80-200 °C for 5 minutes, however the only difference between the extreme values were observed when the 80 °C sample de-adhered partially from the substrate after NIL at 350 °C. Also, the substrate material was observed to have an impact on the adhesion and final thickness of the polyimide layer, but here only Si and poly-methyl-

metacrylate (PMMA) with similar adhesion properties were used as underlaying materials.

Table 1: *Thickness of polyimide with respect to dilution level and spin speed (rpm), and rms roughness (nm).*

Dilution	Spin	Centre	40 mm	Rms
6,5 w%	1250	580	710	20
6,5 w%	2000	350	460	20-200
8,5 w%	1000	1205	1220	15
8,5 w%	1750	605	760	20
10,5 w%	1600	1325	1525	20
10,5 w%	2250	845	1050	25

For further analysis, three layers of polyimide were chosen; the thinnest measured about 600 nm (6,5 w%), the medium 1,2 µm (8,5 w%) and a double layer of 10,5 w% measured about 2,8 µm.

The analysis of 3 µm wide and 1,07 µm high trench pairs 150 µm apart from each other, the trench separation being 4 µm within the pair, was done by using reflectometer FilmTek 4000, profile scanner Dektak and atomic force microscope (AFM) Nanoscope. The stamp size was 1,3 x 1,3 mm on an elevated mesa of 30 µm height, for total area of imprinted features about 0,1 mm^2.

The poly-methylmetacrylate (PMMA) was diluted in toluene as a solid powder to 10 w-%. After dispensing at 1000 rpm and spinning at 2500 rpm for 20 s, and baking at 120 °C for 5 min, a 2,8 µm film was achieved.

III – Polyimide

The NIL trace assumed rectangular shape when the layer thickness and imprinting force were sufficiently high. The trace started to lag from the full depth when 1,2 µm layer was imprinted with 20 N force below 300 °C. A feature imprinted into the 600 nm thick polyimide is shown in Fig. 1 at 350 °C with 2000 bar calculated pressure (20 N) at the imprinted trenches. The largest height difference observed between the trench bottoms and the banks is 700 nm, while the periphery is halfway of the value.

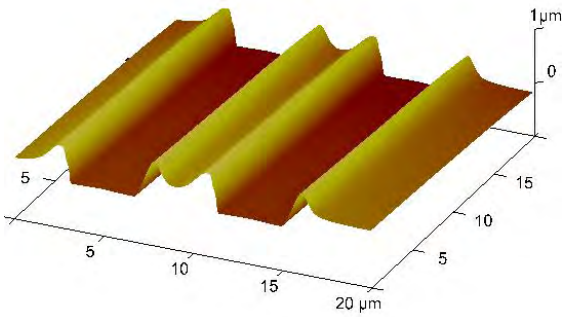

Figure 1: *Initially 600 nm thick polyimide reflows from under the imprinting ridges in stamp, making trenches into polyimide, to less than 2 µm distance.*

The side banks and the central ridge with its banks visible in Fig. 1 are explained in Fig. 2 and their topographic measurements tabulated in Table 2, for 1,2 µm and 2,8 µm polyimide patterned with 20 N and 140 N NIL force, respectively.

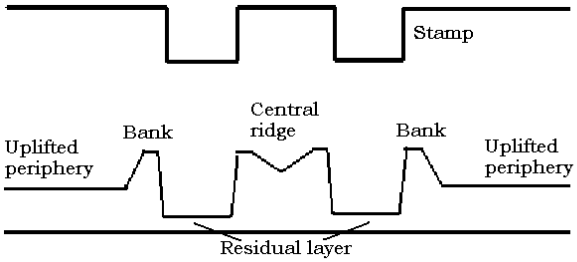

Figure 2: *Schematics of NIL pattern.*

Table 2: *Average uplift (nm) of polyimide at peripheral regions between trench and the height of banks compared to the level of periphery.*

Temp	Uplift	Banks	Uplift	Banks
	2,8 µm	2,8 µm	1,2 µm	1,2 µm
200°C	-10	130	10	240
250°C	40	80	0	400
300°C	90	40	-20	500
350°C	110	0	-30	550

It is observed that the banks vanish at high temperatures for 2,8 µm, while their absolute elevation is about 120 nm and independent on temperature. The peripheral regions lift up with the temperature (Fig. 3).

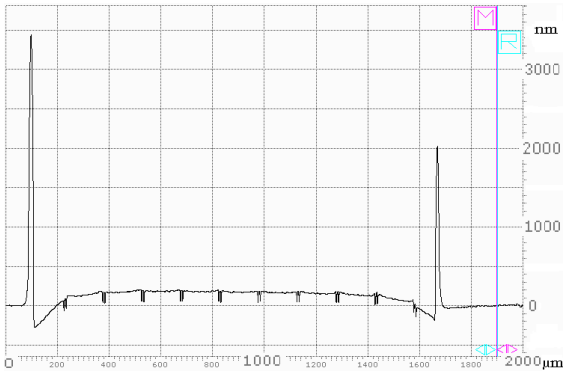

Figure 3: *Radially inhomogenous uplift after NIL at 350 °C into 2,8 µm polyimide.*

For 1,2 µm polyimide essentially no uplift is observed, but the thickness of the stamped area does not substantially decrease either. The side banks are higher than for 600 nm polyimide in Fig. 1, which can be explained by the amount of polyimide available to build up the ridges. The central ridges grow even higher than the side banks until the stamp height is reached above 300 °C (Fig. 4).

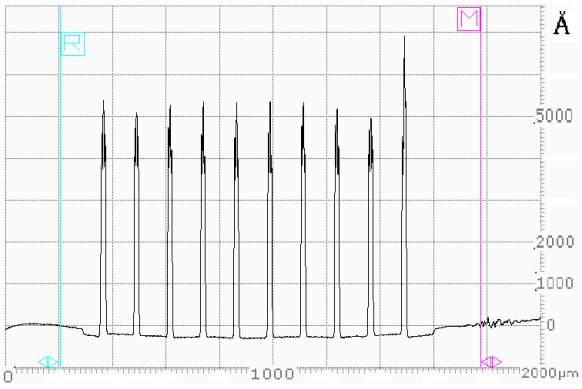

Figure 4: *The height of ridges is 500 nm after imprinting at 300 °C into 1,2 µm thick polyimide.*

By intuition, the flow is first directed upward next to the imprinted trenches. Then, if the imprinting force is sufficient and there is enough material to push, the whole stamp will squeeze material sideways from below the stamp, decreasing the remaining thickness of polyimide and causing negative uplift. While having 6 % filling factor in our case, the results contradict with intuition for thick polyimide with positive uplift.

The thickness difference of the stamped peripheral polyimide compared to intact polyimide outside the stamp was also measured with reflectometer shown in Table 3. It is seen that generally the reflectometer gives even higher values than the profiler. For example, after imprinting at 300 °C the 2,8 µm polyimide top surface assumed in average 130 nm higher level next to the imprinted features (at the banks) while further away, at 70 µm distance from the closest trench pairs, the level was 40 nm lower, indicating the ridge height. This gives a 90 nm uplift far from the closest trench pairs, while the value given by reflectometer was in average 145 nm.

Table 3: *Comparison of lift of 2,8 µm polyimide surface (nm) after NIL as measured by reflectometer and profile at different temperatures.*

Temp	Center	Outside	Ref.diff.	Profiler
200°C	2810	2790	20	-10
250°C	2900	2825	75	40
300°C	2980	2835	145	90
350°C	2950	2785	165	170

From the filling factor of the ridges on the stamp making trenches into the polyimide, for full depth (1,07 µm) features and full contact of the stamp into the polyimide (resulting no banks), 70 nm can be expected as the average uplift. The measured uplift for 2,8 µm polyimide was less than that at 200-250°C, but more than that at 300-350 °C. However, as shown in Fig. 3, the radial non-uniformity made an accurate calculation difficult.

For 1,2 µm polyimide, the measured uplift was 35 nm at 200 °C, but at 250-350 °C in close agreement with the estimated 70 nm.

IV – PMMA and Polyimide on PMMA

PMMA was significantly easier to imprint at 200 °C, when the full height of the stamp was transferred into the polymer by using 10 times larger stamps. Elevated temperature did not cause deformation of PMMA until 300 °C was exceeded. Polyimide was discovered to spin slightly thinner on PMMA as on Si with same spin speed and baking temperature.

With 2,6 µm PMMA underlayer, NIL of 1,2 µm polyimide assumes more radial non-uniformity. In addition to trench formation at the edges of the stamp (Fig. 3), the filling of the area between trench pairs and the absolute elevation of the banks depend on location within the imprinted region. Also, the central ridge formed between the two trenches (Fig. 2) was observed to be lower at the centre of the imprinted region. At the centre of the imprinted area, the central ridge is already 200 nm lower than the side ridges after NIL at 250 °C (Fig. 5), but the difference increases to 600 nm at 300 °C. Further from the centre the height difference between central ridge and the side banks become lower in general.

It appears as if the counterforce acting on the stamp were lower at the centre of the stamp leading to poorer filling of the stamp and, at the same time, the 4 µm wide central ridges were too narrow for the underlaying PMMA to flow under the central ridge. Instead, PMMA escapes underneath the trench pairs to the 140 µm wide area between the trench pairs, and on the stamp scale to the edges of the imprinted area. This radial effect is even stronger at 300 °C (Fig. 6), where the edges of the imprinted area assume ideal NIL result, but the centre of the imprinted area has large side ridges and central ridges pushed far below the initial surface level. The maximum elevation of the banks above the initial level before NIL is about 150 nm independent of temperature.

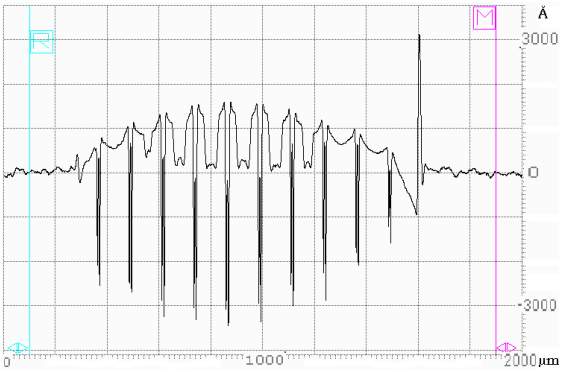

Figure 5: *The height of central ridges between the two high side banks after NIL of polyimide on PMMA at 250 °C.*

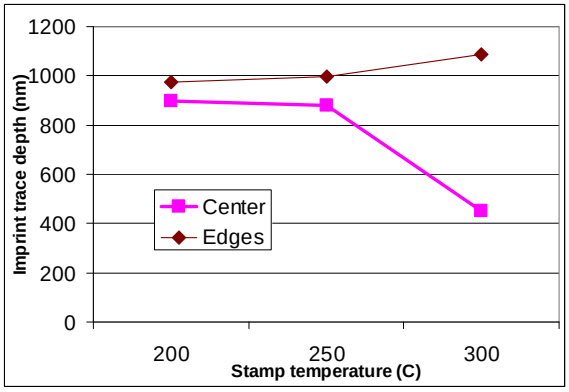

Figure 6: *The bank height measured from the bottom of the imprinted trenches at centre and off-centre of the stamped region.*

IV - Conclusion

Thick polyimide climbs about 120 nm the stamp wall building banks in the studied 200-350 °C regime while a higher temperature improves filling the stamp. 1,2 µm polyimide climbs further depending on temperature, but the counterforce from the <700 nm compressed polyimide under the stamp ridges prevent filling the stamp more than about 1/5 of the area with the used 20 N force. 0,6 µm polyimide climbs again slightly less indicating the limited amount of material, and the about 350 nm compressed polyimide carries the stamp on its ridges alone. The reason for difference between reflectometric and profiler data for, as well as the radial inhomogeneity, is unknown but an increase in refractive index or formation of solvent gas pocket can be suspected. Also, the variable background level may cause an error in profiler measurements.

When a soft sublayer is used, polyimide trace is prevented from reaching the full stamp depth due to penetration of polyimide into the lower layer. Especially attempts toward narrow features may encounter severe limitations due to this effect. Also, the stiffer polyimide may bounce back after the stamp is withdrawn, even though the full depth was achieved during NIL, due to relaxation of compressed one of the films.

As polyimide is often used for harsh environments for its chemical resistance and physical hardness, and as an optical medium, such as waveguides and claddings, the results show that after finding a suitable combination between the imprint pattern area and height, temperature and thickness of the polyimide, NIL can be used for obtaining three-dimensional features into it.

Acknowledgements

The authors acknowledge European Commission project FP7-ICT4-P3SENS (248304) and VTT Technical Research Centre for funding the work described in this paper.

References

[1] Chou S. Y. et al., *Appl. Phys. Lett.* 67, vol. 21, pp. 3114-6, 1995.
[2] Haatainen T. et al., *Phys. Scr.* 67, vol. 4, pp. 357-60, 2003.
[3] Haatainen T., *Doctoral thesis*, VTT Publications, 2011.
[4] Pai I. et al., *J. Microm. Microeng.* 16, pp. 2192-6, 2006.
[5] Cui B. et al., *Microelec. Eng.* 83, pp. 906-9, 2006.

CNT BUNDLES AS ELECTRODES FOR ECL SENSORS

A. Sanginario[1], D. Demarchi[1], M. Giorcelli[2], M. Castellino[2], A. Tagliaferro[3] and P. Civera[1]

[1] *Politecnico di Torino, Department of Electronics, Torino, Italy*
[2] *Politecnico di Torino, Department of Physics, Torino, Italy*
[3] *Politecnico di Torino, Department of Materials Science and Chemical Engineering, Torino, Italy*

***Abstract* — The present application is based on the use of carbon nanotubes (CNTs) as electrodes for electrochemiluminescence (ECL) detection technique used for biomolecules sensing. For this purpose we have grown self standing cylinder-shaped blocks of multi-wall CNTs (MWCNTs) by means of a catalytic chemical vapour deposition system, fed by camphor and ferrocene gases. The blocks were post processed, for their use as electrodes for the sensing of $Ru(bpy)_3^{2+}$. A custom potentiostat and related software has been designed, realized and utilized for the experiments. It has been observed a periodical light emission that lasts for hundreds of cycles, likely due to the CNTs structure and properties. Thanks to a data-processing algorithm, integrated into the software, which exploits this behavior, the experiments show that it is possible to obtain a great increase in detection limit as compared to the common working metal electrodes.**

***Keywords:* CNT, ECL, electrode, electrochemiluminescence, scientific software**

I – Introduction

Carbon NanoTubes (CNTs) have attracted tremendous interest since their discovery [1]. Their electronic properties in combination with mechanical and chemical ones suggest that they can be used as a very promising electrode material for electrochemical experiments [2]. We used Multi Walled CNTs (MWCNTs) as electrode material for ECL experiments and in particular in these pages is described their application for the detection of tris (2,2'-bipyridyl) ruthenium (II) ($Ru(bpy)_3^{2+}$). ECL is based on the same concept of PhotoLuminescence (PL), see figure 1, but it has some important advantages that make it more attractive than PL. In ECL, as the stimulus is a voltage, the only photons reaching the photodetector are those generated by the electrochemiluminescent molecules and not also from the light source as in the case of PL. Moreover ECL instrumentation is less expensive, easier to scale down to micro and nano scale and intrinsically less noisy. ECL is mostly used for the detection of biomolecules such as DNA, proteins, etc. The present work aims to exploit the positive characteristics of CNT behavior and ECL efficiency. Our challenge is to engineer this powerful method in order to design more sensitive biosensors and thus to create a reliable and low-cost biosensor. For these reasons an electrode based on a CNT bundle has been realized and used as Working Electrode (WE) in a standard electrochemical cell, with a gold Counter Electrode (CE) and a silver Reference Electrode (RE). Results have been compared with a gold WE of the same dimensions and working in the same experimental conditions, used as a benchmark.

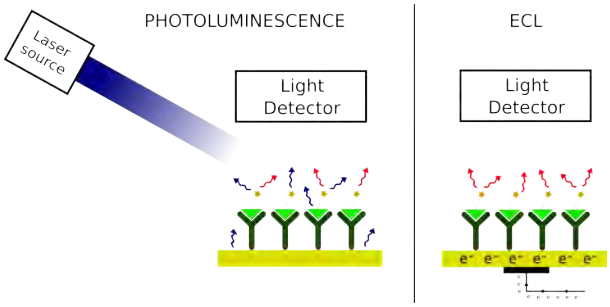

Figure 1: *Differences between PL and ECL*

II – Experimental Details

Carbon nanotubes cylinders deposition and growth

Thermal-CVD process for growing multi-wall carbon nanotubes (MWCNTs) was performed at 850°C in a horizontal quartz tube housed in a cylindrical furnace. An inert gas flow (N_2) carried the gas mixture of carbon precursor (commercial camphor) and metal catalyst (ferrocene 98% purity in weight, Aldrich) after their evaporation. The mix, in a 20/1 mass ratio (precursor/catalyst) has been carried towards the centre of the furnace, where the gases pyrolysis led to the deposition of a CNTs layer on the silicon patterned substrate. For growth parameters and details see [3] and [4]. The geometry of the cylindrical electrodes has been drawn on silicon surface using the photolithography technique. Positive photoresist (HPR 504, Fujifilm) thin layer (1.4μm thick) has been masked, exposed to UV light and removed with its proper solution, leaving resist pillars on the silicon surface. The substrate has been subsequently covered with a double metal layer (5 nm of titanium as adhesion layer, and 100 nm of copper) using the thermal evaporation technique in high vacuum ($\sim 10^{-7}$ torr).

Resist has been subsequently removed with a lift-off procedure in acetone, leaving round metal-free areas of the desired geometry on the substrate, prior to CNTs deposition. During the deposition CNTs grow vertically respect to the silicon surface and can reach heights of few millimeters, fig. 2 shows a CNTs column fallen

Figure 2: *Side view of CNT bundles rows.*

down on a silicon substrate.

Preparation of CNT electrodes

In order to use CNTs bundles as electrodes in a standard electrochemical cell, it is necessary to perform the steps depicted in figure 3. When CNT pillars are still attached to the silicon substrate, as shown in figure 2, a copper wire is glued on their upper face with a conductive paste, figure 3(b) and (c), aimed to collect the voltammetric current. Then, the CNT bundle and the electrical contact are covered with epoxy resin to insulate them and give them mechanical stability for a better handiness, figure 3(d) and (e). After the epoxy resin has been cured, everything is covered with the exception of the lower face still in contact with the silicon (figure 3(f)). The electrode is now mechanically detached from the surface (figure 3(g)), so that the lower face is the only one that will be in contact with the solution. Counter and reference electrode were prepared in a similar way: a gold and a silver wire were contacted from one side and covered with epoxy resin. A drawing of the three electrodes is shown in figure 4.

Reagents

Stock solution is composed by 50 ml of tris (2,2'-bipyridyl) ruthenium (II) [5] $Ru(bpy)_3^{2+}$, with a concentration of 10^{-4} M and 60 μl of TriPropilAmmine (TPA) dissolved into 50 ml of Phosphate Buffer Solution (PBS) whose concentration is 10^{-1} molar. The ruthenium complex used as electrochemiluminescent label was purchased from Cyanagen S.r.l. PBS was prepared by dissolving 13.6 mg of KH_2PO_4 with 871 mg of K_2HPO_4, in 50 ml of deionized water. Both TPA and phosphates were purchased by Sigma-Aldrich.

Electrochemical system setup

A custom potentiostat and software have been developed to perform all electrochemical experiments.

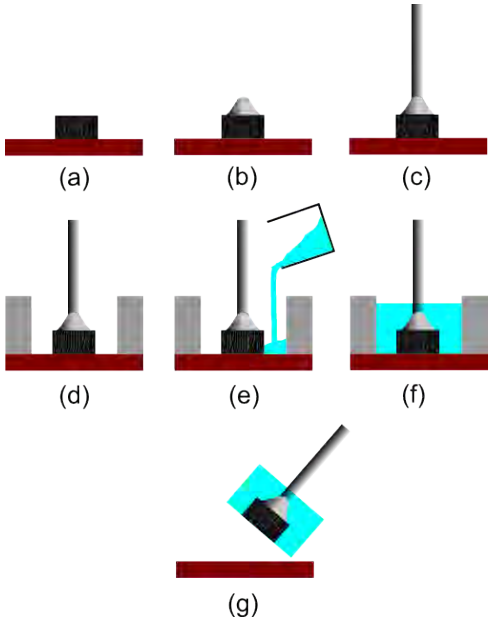

Figure 3: *Production steps of the CNT electrodes: a) cylindrical pillar (few millimeters height and diameter) of CNTs has been grown onto a silicon wafer. b) A drop of conductive glue is deposited onto the column. c) A copper wire is dipped into the glue until it hardens. d) An hollow structure is positioned around the CNT column. e) Epoxy resin is poured into the mold. f) The whole CNT column and its connection with the wire is covered with epoxy and left to harden. g) Once the mold has been removed, the whole structure is mechanically detached from the silicon surface thus leaving only one face of the cylindrical CNT pillar free.*

The software, written in Python language, can handle different experiments and waveforms, while the potentiostat has been designed to generate stable cell driving potentials and to collect the very small currents from the voltammetric signal. Our system scheme is shown in figure 4, where the three electrodes are indicated: the Reference in silver, the Counter in gold and the Working in CNTs. Five hundreds μl of solution are spotted into a small glass container placed on the top of a Photo Multiplier Tube (PMT), an Hamamatsu H9306-03, then the three electrodes are dipped in and a suitable voltage sweep is applied to induce ECL reaction. At its emitting potential, the chemical solution starts to emit photons that are collected and amplified by the underneath PMT, which transfer a voltage to the control system proportional to the intensity of the collected light.

III – Results and Discussion

A. Comparison between two types of electrode response

Experiments were performed both with a CNT working electrode and with a gold working electrode of the same diameter of 2 mm, for different dilutions of the stock solution. A crucial difference was recorded

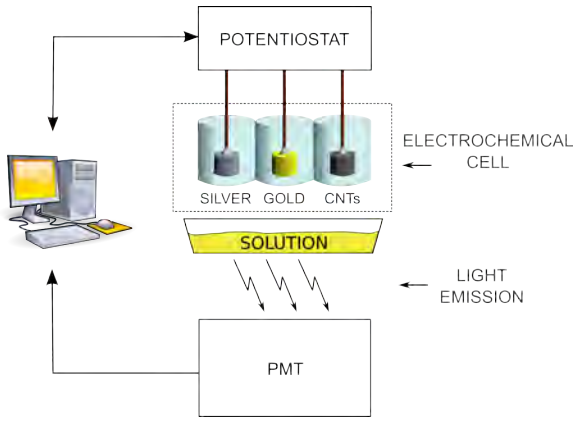

Figure 4: *The electrochemical system*

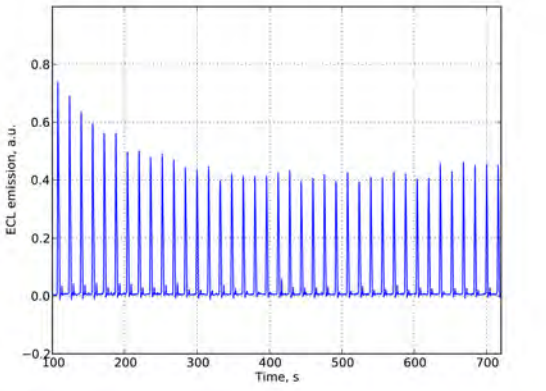

Figure 6: *Periodic emission from CNT Working Electrode*

between CNT and gold electrode. Indeed gold electrode showed a decreasing light response over time (i.e. over voltammetry cycles) that rapidly decreased under the level of background noise (figure 5), this is due to the increasing passivation of the electrode during the experiment. On the contrary, CNT electrodes were able to maintain a constant light response for hundreds of voltammetric cycles, as demonstrated in figure 6. This stability could be ascribed to the carbon property of forming gaseous oxides that, going away, could refresh the solution around the surface and thus acting as a sort of mixer. We exploited this behavior to extract light signal, even when buried in background noise, by applying a custom algorithm based on methods used for analysis and detection of periodic signals and obtaining a great improvement in detection limit and SNR ratio.

B. The custom algorithm

As previously mentioned, a new method was developed, as described in the authors' patent [6], in order to increase the SNR of the detected signal. The method was based on the customization of the algorithm called averaging. The averaging is one of the most powerful algorithms for periodic signal management and so its customization

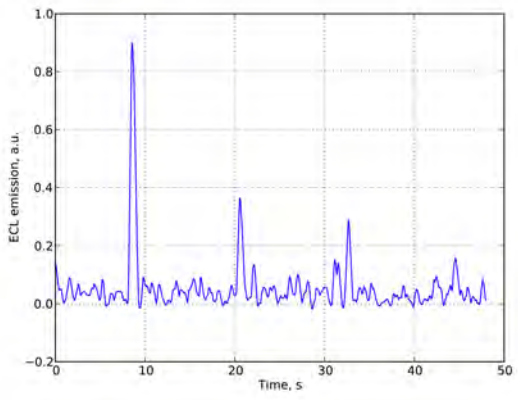

Figure 5: *Emission from gold Working Electrode*

to the presented sensor gave the significant SNR increase. The key point of the considerable improvement obtained is that the light emission occurs always at the same potential, hence after a fixed amount of seconds in the time domain, producing a periodic emission signal. By averaging over many cycles of light emission we are able to pull down the noise and consequently to extract weak light emission signals buried into the background noise. Fig. 7(a) shows a portion of raw data before they are processed by our algorithm. As, in this case, the concentration of Ru compound is very low, the wanted signal is buried into the noise because only few photons reached the PMT. Thanks to our data treatment it has been possible to extract the low signal from that noise thus consequently to detect very low amount of chemical analyte (fig. 7(b)). As said before, in our case, the detection limit of the standard electrochemical cell with a gold working electrode was a dilution of 1:50 (fig. 8). Using CNT working electrode, associated to our customized algorithm, it was possible improve the SNR and to reach dilutions up to 1:1000 and even more, as can be seen in fig. 7(b), where for a diluition of 1:1000 the signal is perfectly extracted from the noise and clearly detectable.

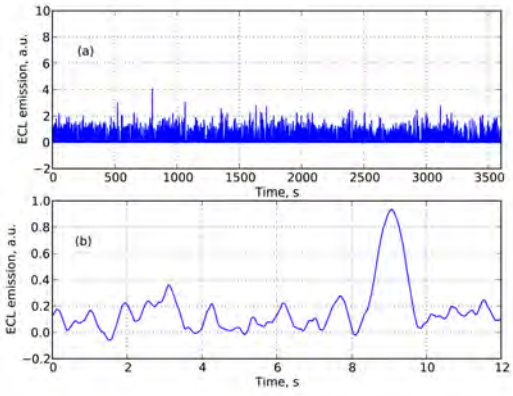

Figure 7: *(a) CNT emission raw signal and (b) signal resulting after custom algorithm application*

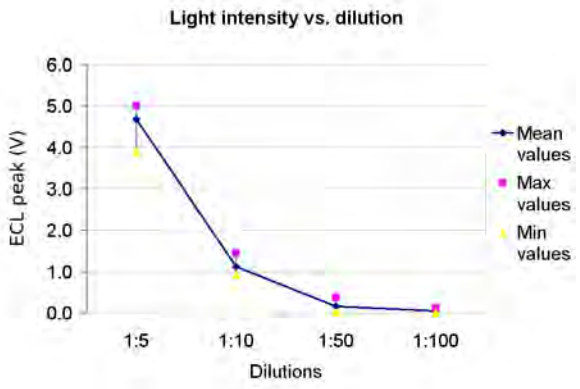

Figure 8: *Relation between dilution and emitted signal*

This diluition, considering the concentration of the stock solution used, corresponds to a ruthenium concentration of 80 $pg/\mu l$ (i.e. a $10^{-7}M$ molar detection level).
Figure 9 shows the detection limits obtained by 50 different CNT WEs after data processing. It was decided to determine the detection limit using the heuristic method of having the signal of a double intensity in respect to the background noise. The fact that at least 10% of CNTs emissions reached a detection limit of 1:2000, corresponding to a ruthenium concentration of 40 pg/μl (i.e. a 10^{-7}M molar detection level), is worth noting. Moreover, almost all of the CNT WEs tested had a lower detection limit than the gold ones, that reached the lowest detection limit of about 1:200 (i.e. a 10^{-6}M molar detection level).

IV – Conclusion and future works

Obtained results show that CNTs can be used in ECL and voltammetry devices as electrodes, and that their use lead to an improvement in detection limit. Such electrodes present an unexpected behavior of constant signal emission likely due to their large surface area and their disordered-matrix shape. This effect has been exploited to obtain a great improvement of the minimum signal noticeable, having a gain of at least 20 times. This improvement is essential for detection of biomolecules such as DNA or proteins and it will give the possibility to realize more efficient and precise biomedical diagnostic devices.

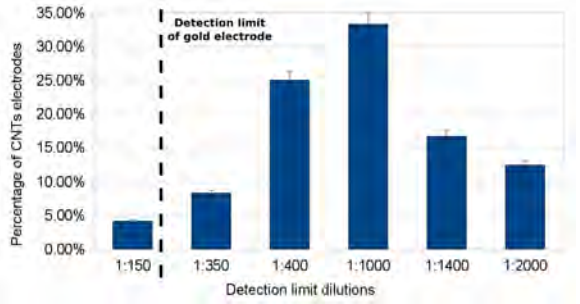

Figure 9: *Detection limits of 50 CNT electrodes tested*

Next step in order to build a biosensor of micro- and nano-metric dimensions is the integration of electrodes onto a silicon chip with standards surface micromachining technologies.

References

[1] S. Iijima, Nature 314:56, 1991

[2] Z. Xu, X. Chen, X. Qu, J. Jia, S. Dong, Biosens. Bioelectron. 20:579, 2004

[3] S. Musso, S. Porro, M. Rovere, A. Chiodoni, A. Tagliaferro, Diamond and Related Materials, 16:1174-1178, 2007

[4] S. Musso, S. Porro, M. Giorcelli, A. Chiodoni, C. Ricciardi, A. Tagliaferro, Carbon / Letters to the Editor, 45:1133-1136, 2007

[5] A. J. Bard, "Electrogenerated chemiluminescence", Marcel Dekker, New York, 2004

[6] D. Demarchi, P. Civera, A. Sanginario, R. Canova, M. Turturici, L. Della Ciana, Patent Number: TO201000212, 19/03/2010

VACUUM FORMATION OF SOLDER VIAS

Jiebin Gu[1], W. T. Pike[1]

[1]*Imperial College London, SW7 2AZ, UK*

***Abstract* — In this paper we present a solder filling technique for through-silicon vias that using a low vacuum approach. This rather simple technique can be used to fabricate solder-filled vias with high aspect ratios.**

***Keywords :* Through-silicon via, solder ball, advanced packaging**

I - Introduction

Through-silicon via (TSV) technology has wide applications in advanced packaging, such as 3D interconnects, silicon interposers and MEMS packaging. In RF IC's, TSV can also be used to form an embedded Faraday cage for parasitic insulation [1]. Conventional via-filling techniques mainly involve electroplating of copper or CVD of polysilicon [2-6], which limits both speed of fabrication and resistivity.

Although solder is widely used in electronic packaging, filling the through-silicon via with solder is challenging because liquid solder is unwettable to silicon, or as well as the common oxide and nitride dielectrics. To date, two solder filling techniques have been studied. The first approach is to immerse wafers with holes or trenches into a pool of molten solder in a sealed container, pumping to high vacuum [7]. In the high vacuum environment, liquid solder can easily overcome surface tension and flow into the through-wafer hole or trenches. However immersion of the whole wafer/device into molten solder excludes any prior metallization on the devices. Another approach involves our previous studies of a solder-pump technique, which employs surface tension to drive liquid solder into the via holes [8, 9]. However this Gibbs-Thomson-effect-based solder-pump technique can only allow solder flow from smaller to larger holes, which limits its application to fabricate high-aspect-ratio through-silicon vias: diameters of about 300 µm and aspect ratios of about not much less than two have been demonstrated. It is not currently possible to achieve vias less than 100 µm in diameter given the minimum available size of solder balls.

In this paper, a practical method is proposed and demonstrated for filling vias with liquid solder using a low vacuum to drive liquid solder into otherwise unwettable via holes less than 100 µm in diameter. No moving parts are involved inside the set-up, which makes it practical for various potential applications.

II – Concept and Mechanism

The concept in Figure 1 shows the assembled device structure and reflow rig. The substrate where vias will be formed is place on top of a feed substrate, with feed hole and via vertically aligned. These feed holes are initially loaded with solder balls held by a supporting frame incorporated into the bottom of the feed substrate. The feed hole should be round in order to be blocked when the solder balls reflow. The feed substrate not only serves as a solder reservoir for the via substrate above, but also forms the top surface of an inner sealable cavity underneath the solder balls. The whole structure is placed in a sealed reflow chamber connected to a vacuum pump.

The reflow processes can be divided into 5 main steps: purging, heating, melting, pumping/filling, and cooling:

A. Purging

The purging step removes the oxygen from reflow the chamber with a nitrogen flow, thus minimizing oxidation during reflow. To ensure the inner cavity is also purged, the feed hole is made slightly larger than the size of solder balls, as shown in Figure 2 (a).

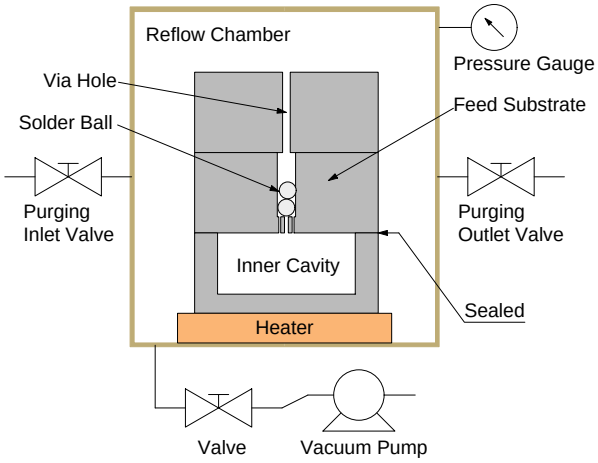

Figure 1: The concepts of the low vacuum solder filling method (not in scale).

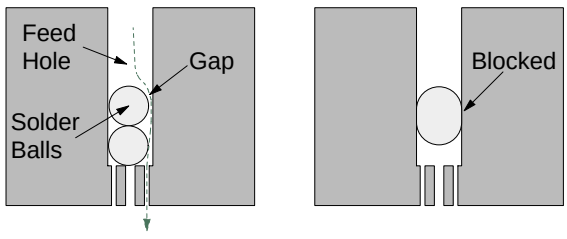

(a) (b)

Figure 2: (a) Before melting, the gap between the solder balls and the feed hole allow purging of the inner cavity. (b)After

melting, the feed hole is blocked by the molten solder, thus seals the inner cavity.

B. Heating

After purging, the reflow chamber is sealed under nitrogen and then heated. As the temperature of the nitrogen rises, the chamber and cavity pressure increases to about 1.6 bar, as shown in Figure 3.

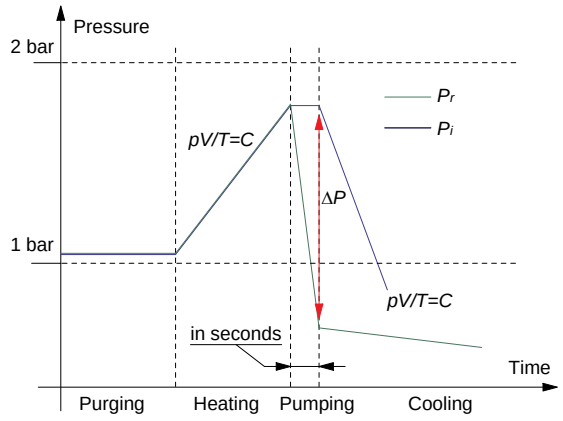

Figure 3: pressure change through all the reflow stages. P_i and P_r is the pressure in the inner cavity and the reflow chamber respectively.

C. Melting

Once melting point is reached, the solder balls in the feed hole melt and combine. The diameter of the feed hole is designed to be large enough to allow the loading of the solder balls, but also small enough to be blocked by the combined solder volume, which requires a minimum of two solder balls as shown in Figure 2 (b). Once the feed hole is blocked, the inner cavity is sealed from the reflow chamber.

To ensure the combined volume should be able to block the feed hole, there is a constraint on the diameter of the feed hole (d_{feed}).

$$d_{ball} < d_{feed} < \sqrt[3]{N} d_{ball} \quad (1)$$

where d_{ball} is the diameter of the solder ball, N is the number of solder balls loaded in each feed holes.

D. Pumping & Filling

In order to push the liquid solder into the via hole, the pressure on the inner cavity should be higher than that of the reflow chamber, which is achieved by pumping down the reflow chamber once the feed hole is blocked and the inner cavity is sealed. From Figure 4, the created pressure differential across the solder volume (ΔP) should meet the following condition:

$$\Delta P = P_i - P_r > \frac{2\gamma}{r_{via}} - \frac{2\gamma}{r_{feed}} \quad (2)$$

where P_i and P_r is the pressure in the inner cavity and the reflow chamber respectively, γ is surface tension of the liquid solder, r_{feed} and r_{via} is the radii of the feed and via hole respectively. If we assume that $r_{feed} \gg r_{via}$, we can neglect the pressure generated in the feed hole and formula (2) becomes

$$\Delta P = P_i - P_r > \frac{2\gamma}{r_{via}} \quad (3)$$

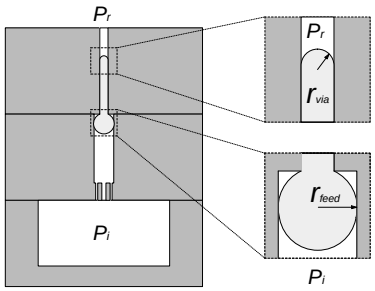

Figure 4: After pumping down the reflow chamber, liquid solder is pushed into the via hole by pressure differential between inner cavity and reflow chamber.

Table 1 lists the pressure differential required for various via hole diameters, which shows that only a rough vacuum is needed to drive the liquid solder. For the size of the reflow chamber (about 0.02 m^3) we use, it should take only a few seconds for a conventional pump to achieve the required pressure. Because the pressure is already about 1.6 bar before pumping, the required pressure differential (ΔP) should be achievable with even a pressure differential of more than 1 bar possible.

Table 1: Pressure differential vs. via hole diameter.

d_{via}(μm)	180	120	100	50	20
ΔP (bar)	0.12	0.18	0.21	0.43	1.08

During the filling process, it is expected that there will be leakage in the inner cavity results in an inevitable decrease in pressure differential. However, because reflow is fast, less than one second in our experiments, the pressure differential only needs to be maintained briefly. Therefore a slight leakage of the inner cavity will not hinder the filling process.

E. Cooling

Once reflow is completed, the chamber is cooled down to solidify the solder in the via holes. Thereafter, the pressure differential between the inner cavity and chamber will gradually decrease due to leakage while the pressure in the reflow chamber will itself decrease as the temperature decreases. Figure 3 shows schematically the pressure change in both the inner cavity and reflow chamber through all the stages.

III – Demonstration

A. Design

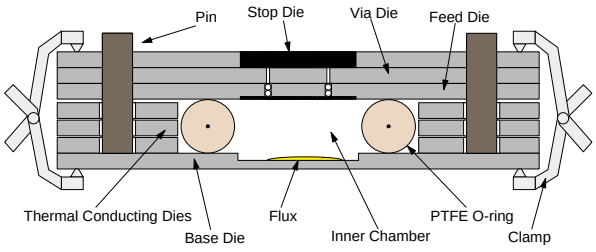

(a)

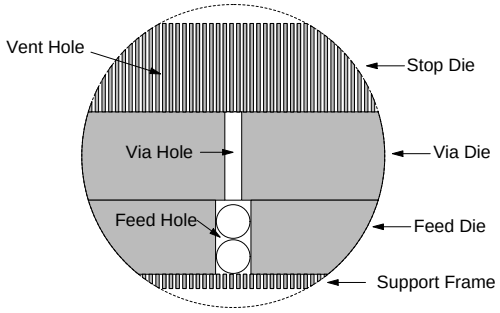

(b)

Figure 5: (a) Cross-section schematic of the assembled structure. (b) Close-up schematic of the feed hole, via hole and the support frame.

Figure 5(a) shows the cross-section schematic of the demonstration structure, composed mainly of silicon dies. The inner cavity is formed by a base die, an O-ring and a feed die, which then are secured by clamps. The O-ring provides a better seal than direct silicon-silicon contact. The O-ring is made of PTFE, which can bear a relative high temperature, up to 300°C. A small amount of flux is placed on the bottom of the base silicon die to help combat oxidation during reflow. Because reflow relies on thermal conductivity between the heating stage below the structure, a stack of micromachined silicon dies is placed between the base die and the feed die to provide a thermal short. Vertical alignment is achieved using metal pin-dowels, as shown in Figure 6(b).

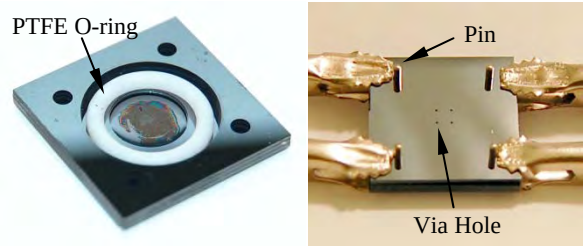

(a) (b)

Figure 6: (a) partially assembled inner cavity, formed by base die, thermal conducting dies and PTFE O-ring. (b) Top view of the fully assembled structure(without stop die).

In order to prevent the liquid solder being pushed right out of the via hole, a porous stop die containing vent holes much smaller than the via holes is used as a top cover, as shown in Figure 5(b). These vent holes ensure the via hole can be easily evacuated during the pumping process, while the generated pressure differential is not sufficient to push the liquid solder through the narrow vent holes.

B. Fabrication of Silicon Dies

All the silicon parts, including the base die, feed die, via die, the stop die and the thermal conducting dies are fabricated on a standard 100 *mm* double-side polished silicon wafer by DRIE (deep reactive-ion etching). The fabrication of the feed die used both-side etching, and the fabricated structure is shown in Figure 7.

All the dies are 20 *mm* square. The PTFE O-ring is 13.6*mm* across with a cross-section diameter of 1.78*mm*. The fabricated vent holes are hexagonal and 40 µm across.

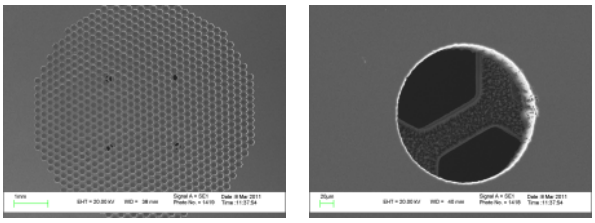

(a) (b)

Figure 7: (a) backside view of the feed die; (b) close-up view of the feed hole.

C. Reflow Process

Before reflow, the manually assembled structure is placed on the heating stage of the reflow chamber. The chamber is first nitrogen purged for 15 minutes and then brought up to reflow temperature. Due to the limited thermal pathway, the maximum temperature of the stage is set above the reflow temperature of 220 °C by a margin of 50 °C. When maximum temperature is reached, the reflow chamber is vacuum pumped and the chamber pressure monitored, although the inner cavity pressure cannot be measured.

IV- Results and Discussion

The initial geometry tested used two 300-μm solder balls, a 525-µm height by 180-µm diameter via hole, and a 312 µm diameter feed hole. Theoretically, a ΔP of 0.12 *bar* is required. In our experiment, the chamber pressure drops from 1.2*Bar* to 0.8*Bar* in seconds on evacuation. Figure 8 shows the SEM image of the solder cylinder formed in the via hole after removal of the via die for inspection. During the reflow, it was confirmed that the filling process takes less than one second. It was also found that the pumping speed is crucial to the success of this approach: too slow pumping cannot generate enough pressure differential to move the liquid solder. Furthermore, although the DRIE-fabricated sidewall of the feed hole is not perfectly smooth, the roughness of the sidewall does not affect the filling process.

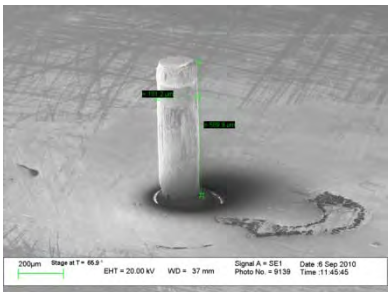

Figure 8:2 × 300 µm solder balls are pushed into a 180 µm diameter via hole. Notice the via die is forcedly removed.

In the second demonstration, two 170-µm solder balls were loaded to attempt to fill a via hole of 525-µm height by 120-µm diameter, with a feed hole 200 µm in diameter. For $d_{via} = 120\mu m$, theoretically, ΔP of 0.18 bar is required. We observed a chamber pressure drop of 0.4 *bar*. A 2×2 array of vias was tested. 3 out of the 4 vias completed reflow as designed. Figure 9 shows the SEM image of the top and bottom solder cap formed in one of the via holes. Figure 10 shows the cleaved view of the solder cylinder formed in the silicon die.

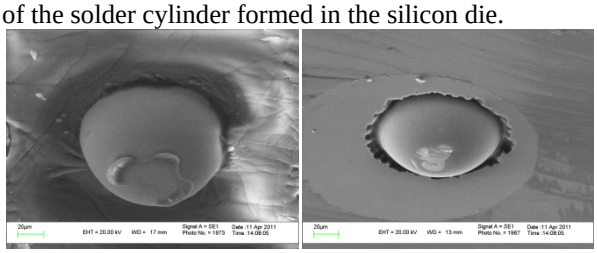

(a) (b)

Figure 9:2 × 170 µm solder balls are pushed into a 120 µm diameter via hole. (a)Top view of the solder formed in the via hole, (b)Bottom view of the solder formed in the via hole.

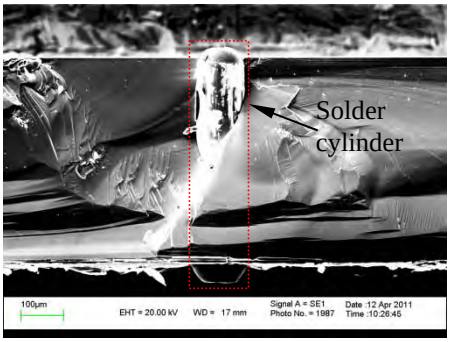

Figure 10: cleaved view of the solder cylinder in the solder die of 120 µm in diameter. The thickness of the silicon die is 525 µm.

IV - Conclusion

We have successfully demonstrated a simple method for via filling with solder. The proposed method has several advantages: (a) in contrast to the solder-pool method, only an easily achievable, very rough vacuum is needed; (b) because of the possible large pressure differential, vias close to 100 µm in diameter can be achieved; (c) the self-sealing approach avoids any further mechanisms in the process, making the technique easy to implement.

References

[1] J. Jozwiak. Integrating through-wafer interconnects with active devices and circuits. *Advanced Packaging, IEEE Transactions on [see also Components, Packaging and Manufacturing Technology, Part B: Advanced Packaging, IEEE Transactions on*, 31(1):4-13, 2008.

[2] C. Patrick Yue, Anthony Mccarthy, Changsup Ryu, Thomas H.LEE, S. Simon Wong, and Calvin F. Quate. Ultra-low resistance, through-wafer via (twv) technology and its applications in three dimensional structures on silicon. *Japanese journal of applied physics.Pt.1, Regular papers & short notes*, 38(4):2393-2396, Apr. 1999.

[3] Zheyao Wang, Lianwei Wang, N. T. Nguyen, W. A. H. Wien, H. Schellevis, P. M. Sarro, and J. N. Burghartz. Silicon micromachining of high aspect ratio, high-density through-wafer electrical interconnects for 3-d multichip packaging. *Advanced Packaging, IEEE Transactions on*, 29(3):615-622, 2006.

[4] Mark G Allen Chang-Hyeon Ji, Florian Herrault. A metallic buried interconnect process for through-wafer interconnection. *J. Micromech. Microeng.* Vol. 18, Number 8, 2008.

[5] M. Saadaoui. Local sealing of high aspect ratio vias for single step bottom-up copper electroplating of through wafer interconnects. In *Sensors, 2007 IEEE*, pages 974-977, 2007.

[6] N. T. Nguyen, E. Boellaard, N. P. Pham, V. G. Kutchoukov, G. Craciun, and P. M. Sarro. Through-wafer copper electroplating for three-dimensional interconnects. *J. Micromech. Microeng.*, 12(4):395-399, 2002.

[7] S. Yamamoto, K. Itoi, T. Suemasu, and T. Takizawa. Si through-hole interconnections filled with au-sn solder by molten metal suction method. In *Micro Electro Mechanical Systems, 2003. MEMS-03 Kyoto. IEEE The Sixteenth Annual International Conference on*, pages 642-645, 2003.

[8] Jiebin Gu, W. T. Pike and W. J. Karl: A novel capillary-effect-based solder-pump structure and its potential application for through-wafer interconnection, 2009, *J. Micromech. Microeng*, Issue 7, Vol.19, pp 074005.

[9] Jiebin Gu, W. T. Pike and W. J. Karl: Solder Pump Technology for Through-Silicon via Fabrication, Microelectromechanical Systems, Journal of, vol.PP, no.99, pp.1-3, 0 doi: 10.1109 /JMEMS.2011.2127460.

.

INFLUENCE OF VISCOUS AIR DAMPING ON OPERATION OF VIBRATION-TO-ELECTRICITY CONVERTER FOR POWERING OF WIRELESS MEMS SENSORS

R. Dauksevicius[1], G. Kulvietis[1], V. Ostasevicius[2], I. Milasauskaite[2]

[1]*Department of Information Technologies, Vilnius Gediminas Technical University, Vilnius, Lithuania*
[2]*Institute for High–Tech Development, Kaunas University of Technology, Kaunas, Lithuania*

***Abstract* — The presented study deals with numerical modeling and dynamic analysis of vibration-to-electricity converter based on piezoelectric cantilever-type microstructure, which purpose is to function as a micropower generator for wireless MEMS sensors. The paper describes the developed multiphysical finite element model of the converter, which couples mechanic, piezoelectric and fluidic domains. The fluid-structure interaction is modeled in the form of squeeze-film damping that is governed by nonlinear compressible isothermal Reynolds equation. Results of modal, harmonic and transient analyses are reported, which demonstrate the influence of the air damping on dynamical and electrical performance of the micropower generator as a function of ambient pressure and air-film thickness.**

Keywords : **Harvesting, Piezoelectric, Micropower generator, Modeling, Squeeze-film damping**

I - Introduction

The increasing need for completely self-powered MEMS-based sensing systems has triggered active research of micropower harvesting technologies during the last 15 years. Rapid progress in microfabrication and low-power microelectronics accelerated the development of a wide range of battery-powered portable, implantable or embedded devices including autonomous wireless sensor networks with their expected pervasive monitoring applications within industrial, civilian, healthcare, environmental, agri-food, security, defense and other sectors. These sensors are usually deployed at remote and/or hardly accessible locations therefore replacement of depleted batteries can become very troublesome and costly, particularly with sensors increasing in number and decreasing in size. These issues can be alleviated or even eliminated by means of energy harvesting approach – capturing ambient kinetic or thermal energy, light or RF radiation, acoustic noise, etc. and converting into usable electrical energy. Harnessing mechanical motion for this purpose is particularly attractive since: a) potential power density levels are fairly attractive, b) structural vibrations are encountered around most machines, structures or biological systems. Therefore kinetic energy harvesting is a highly promising solution for powering autonomous sensors that are embedded, for example, in civil structures for *in situ* structural health monitoring. The main complication in this case is that ambient vibrations vary widely in frequency and amplitude (e.g. common sources, such as household appliances and manufacturing equipment generate vibrations with amplitudes of 0.2 – 10 m/s^2 at frequencies of 60 – 200 Hz). Piezoelectric and electromagnetic transduction principles are considered to be the most promising for vibration-based harvesters, while electrostatic devices are presently limited by their high impedance and output voltages, which reduce the amount of available current. Piezoelectric conversion has an advantage of higher energy density levels with respect to the electromagnetic and electrostatic transduction mechanisms. Piezoelectric micropower generators (PMPGs) also benefit from relatively simple geometry and fewer peripheral components. Moreover, it is not difficult to integrate microelectronic circuits on the same chip because the process for depositing both thin and thick piezoelectric films is a fairly mature technology [1-4].

However, the majority of current micro-scaled PMPGs do not generate sufficient energy to directly power most electronics including MEMS-based sensors. Significant research efforts are currently focused on two principal approaches for improving efficiency of these generators: a) development of hybrid micropower supply units comprising both on-board storage and energy harvesting from environmental vibrations, optimization of energy generation and accumulation subsystems; b) improvement of charge density via material and structural enhancements including expansion of operating frequency range of the devices by means of tuning their resonant frequency or widening the bandwidth [2-5].

The purpose of this study is to investigate the modeling and design of a piezoelectric vibration-to-electricity converter to be used as a micropower source. The focus of the paper is on modeling and simulation of viscous air damping in order to evaluate its influence on dynamic and electrical characteristics of the PMPG.

II - PMPG Modeling

A. Description of Finite Element Model

The design of analyzed PMPG is based on bi-layer cantilever structure with proof mass at the free end (figure 1 and table 1). The supporting cantilever layer and the proof mass are made from silicon, while PZT-5A is used for piezoelectric layer, which is positioned on the top of the supporting layer and is poled along the thickness (*z(3)* axis) direction resulting in transverse

("d_{31}") operation mode. Cantilever configuration is chosen since: a) for the given loading it produces the highest average strain, which directly determines the power output; b) cantilever-type fixing condition results in the lowest resonance frequency for a given device size, which is required in targeted applications of the vibrational PMPGs, i.e. powering of autonomous wireless sensors installed in industrial or civil structures.

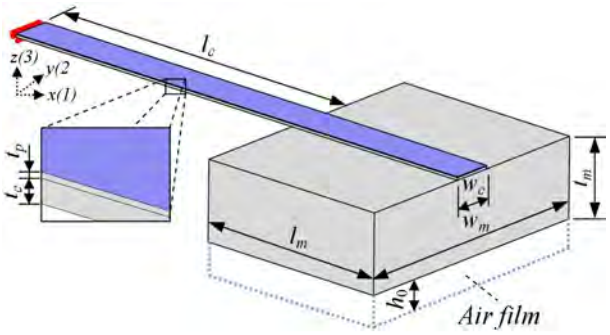

Figure 1: *Schematic representation of the modeled PMPG, which consists of a double-layer cantilever structure (composed of supporting Si layer t_c and piezoelectric layer t_p atop) with proof mass at the free end. Air film of thickness h_0 is present between an imaginary fixed ground surface and the bottom boundary of the proof mass (drawn not to scale).*

Table 1: *Design parameters of the considered PMPG.*

Description and symbol	Value	Unit
Length of uniform cantilever l_c	2500	μm
Length of proof mass l_m	1500	μm
Width of cantilever w_c	300	μm
Width of proof mass w_m	3000	μm
Thickness of cantilever supporting layer t_c	20	μm
Thickness of piezoelectric layer t_p	20	μm
Thickness of proof mass t_m	1000	μm
Young's modulus of supporting layer and proof mass (Si) E_{Si}	200	GPa
Density of supporting layer and proof mass (Si) ρ_{Si}	2330	kg/m^3
Poisson's ratio of supporting layer and proof mass (Si) ν_{Si}	0.33	-

Finite element model of the PMPG was realized within COMSOL Multiphysics by employing the "Piezoelectric Application" mode. Piezoelectric layer has got electrodes on its bottom and top faces, which are perpendicular to *z(3)* axis. Due to low thickness mechanical behavior of the electrodes may be neglected. Their electrical behavior is evaluated by imposing proper electrostatic boundary conditions: the bottom face is grounded, while the top one is set to "Floating potential" condition. For the rest of faces of the piezoelectric layer the condition of "Zero charge/Symmetry" is applied. Input vibrations are assumed to be acting only along *z(3)* axis.

B. Squeeze-film Damping

When designing micro-scaled PMPGs with bulky proof mass at the end of the cantilever structure one should consider a possibility of manifestation of a specific case of viscous air damping phenomenon referred to as squeeze-film damping, which occurs when a structure of large lateral dimensions, that is in a relatively close proximity to a fixed surface, vertically moves towards this nearby rigid surface with a thin air-film in-between. Thus, if the bottom face (boundary) of the proof mass is located relatively close to some stationary ground surface, then during transverse motion of the mass its fairly small displacement in normal direction would compress (or pull back) a significant amount of air out of (or into) the narrow gap. However, the viscosity of the air will limit the flow rate along the gap, and thus the pressure will be increased inside the gap and act against the structure. The squeezed air-film between the mass and ground surface will likely to have a significant effect on PMPG dynamic behavior due to the induced counter-reactive pressure force that is exerted on the vibrating cantilever structure [6].

Nonlinear compressible isothermal Reynolds equation is usually used for modeling of squeeze-film damping occurring in micro-scale [7]:

$$\frac{\partial}{\partial x}\left(h^3 P\frac{\partial P}{\partial x}\right)+\frac{\partial}{\partial y}\left(h^3 P\frac{\partial P}{\partial y}\right)=12\mu_{eff}\left(h\frac{\partial P}{\partial t}+P\frac{\partial h}{\partial t}\right), \quad (1)$$

$$\mu_{eff}=\frac{\mu}{1+9.638\left(\frac{L_0 P_a}{p_0 h_0}\right)^{1.159}}. \quad (2)$$

Here the total pressure in the gap P and the gap thickness h are functions of time and position (x, y). μ is the dynamic viscosity of the gas, μ_{eff} is the effective viscosity coefficient, which is used to account for gas rarefaction effects (a model of T. Veijola [8] is used here; it is adopted by the COMSOL Multiphysics as one of the optional approaches), p_0 is the initial (ambient) pressure in the gap, L_0 is the mean free path of air particles at atmospheric pressure P_a, and h_0 is the initial air-film thickness. For the P_a = 101325 Pa, $L_0 \approx 65$ nm. Total pressure in the gap is equal to $P = p_0 + \Delta p$, where Δp is an additional air pressure variation due to the squeezed air-film effect.

"Film Damping Application" mode, which makes use of (1) and (2), was added to the piezoelectrical model in order to perform dynamic simulations of the PMPG taking into account the effect of squeeze-film damping (a linearized version of (1) is used for harmonic analysis).

III - Results and Discussion

A. Modal Analysis

Numerical study of the PMPG finite element model started from the determination of the natural frequencies and the associated vibration mode shapes (figure 2(a,b)). Performed modal analysis indicates that the fundamental frequency of the PMPG is equal to 184 Hz.

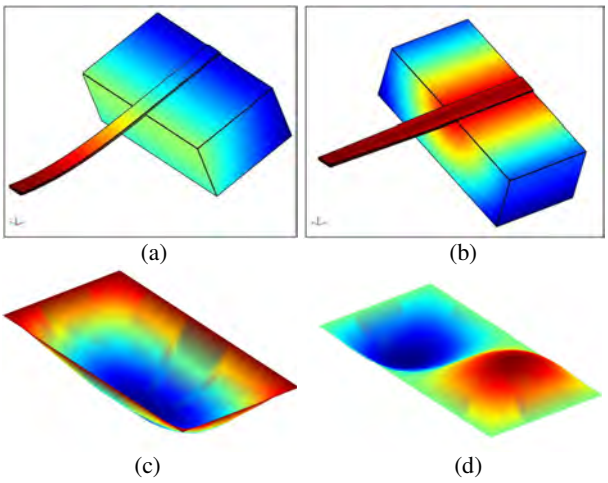

Figure 2: *The first two vibration modes of the analyzed PMPG: (a) the 1st out-of-plane flexural mode (184 Hz), (b) the 1st torsional mode (458 Hz). (c)-(d) 3D contour plots illustrating distribution of air pressure forces in the gap for the corresponding structural mode shapes.*

Figure 2 illustrates the first two vibration modes: a) the 1st out-of-plane flexural mode, b) the 1st torsional mode. This analysis also provided results on distribution of air pressure forces in the gap when the structure is vibrating in its flexural and torsional resonant modes. Pressure mode shapes in figure 2(c,d) reveal obvious coupling between structural displacements of the structure and pressure distribution in the gap. For example, in the 1st torsional mode (figure 2(b)), the upward motion of the left side of the proof mass corresponds to a concave profile in the respective region of pressure mode shape (figure 2(d)), which indicates the reduction of pressure in this part of the gap (i.e. decompression effect). And, in contrast, the downward motion of right side corresponds to a convex pressure profile – zone of increased pressure with respect to atmospheric (i.e. compression effect).

B. Harmonic and Transient Analysis

Dynamic simulations were carried out in order to evaluate the influence of squeeze-film damping on vibrational behavior and voltage output of the PMPG. Zero structural damping was used for the numerical experiments. The model was subjected to sinusoidal kinematic excitation by applying vertical acceleration through body load equal to $F_z = a\rho$ in each subdomain, where $a = Ng$ (N = 0.1 or 0.5, g = 9.81 m/s^2) and ρ is density of the corresponding material (Si or PZT-5A).

Firstly, frequency response analysis was conducted with the parametric solver that was applied in order to sweep over the frequency range of 0 – 250 Hz. Thereby a series of amplitude-frequency characteristics and voltage responses were computed with different values of air-film thickness h_0 (figure 3) and initial ambient pressure p_0 (figure 4) since these parameters decide the magnitude of the induced squeeze-film damping. Frequency response curves provided in figure 3 demonstrate that when the PMPG operates under conditions of

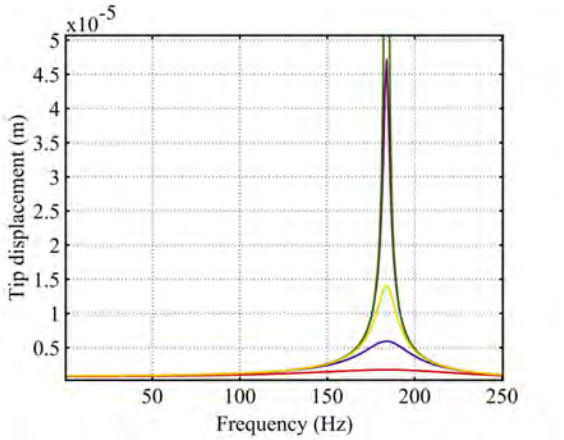

Figure 3: *Amplitude-frequency characteristics of end point of the cantilever structure, obtained in the vicinity of the fundamental frequency of the PMPG in the presence of squeeze-film damping for a constant ambient pressure (p_0 = 100 kPa) at different air-film thickness h_0: 50 μm, 75 μm, 100 μm, 150 μm (curves from bottom to top). The topmost curve (green) is a frequency response with damping excluded (a = 0.1g).*

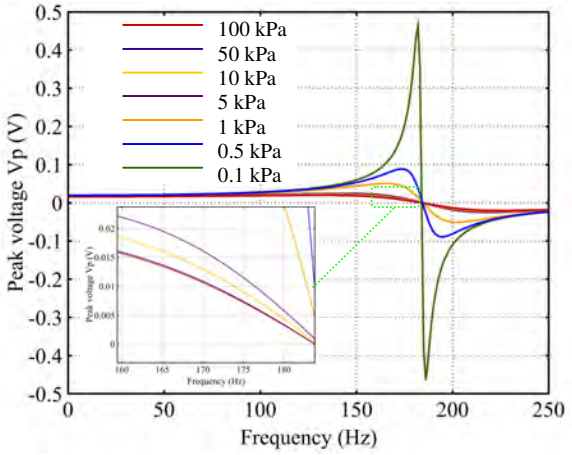

Figure 4: *Voltage response obtained in the vicinity of the fundamental frequency of the PMPG in the presence of squeeze-film damping for a constant air-film thickness (h_0 = 50 μm) at different levels of ambient pressure p_0: 100 Pa, 500 Pa, 1 kPa, 5 kPa, 10 kPa, 50 kPa, 100 kPa (a=0.1g).*

atmospheric pressure, air-film thickness of less than 100 μm leads to a significant reduction of vibration amplitude, which implies a high level of air damping. The resonance peak is suppressed for h_0 less than approximately 25 μm. Peak voltage (open circuit) variation with frequency in figure 4 shows that in the considered case (h_0 = 50 μm), ambient pressures of more than 1 kPa severely attenuates the motion of the cantilever structure, which results in considerable drop in generated voltage. The juxtaposition of voltage curves in the inset of figure 4 reveals that the magnitude of exerted squeeze-film damping force is nearly the same for ambient pressures that are in the range of 10 – 100 kPa. Computations reveal that if the PMPG has to operate under h_0 of less than 50 μm, the working environment should be rarefied to pressures not exceeding 10 Pa in order to avoid excessive levels of air damping (significant increase in voltage output is observed when p_0 is

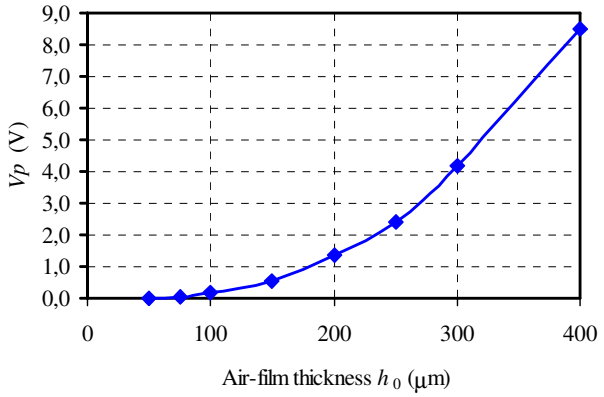

Figure 5: *Peak voltage vs. air-film thickness for a constant ambient pressure p_0 = 100 kPa obtained from the frequency response analysis (a = 0.1g).*

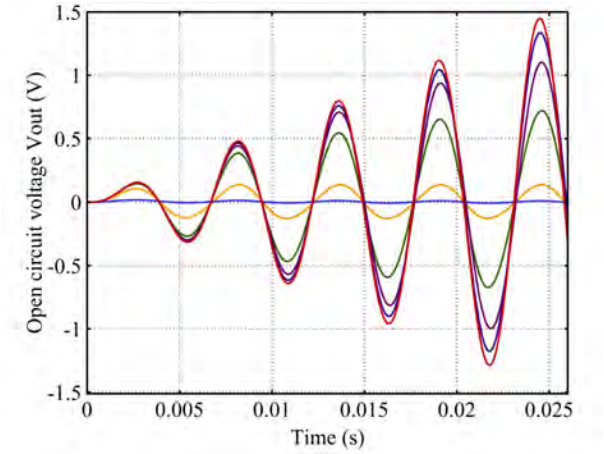

Figure 6: *Temporal variation of generated open circuit voltage during harmonic base excitation with acceleration of a = 0.5g and frequency of 184 Hz for p_0 = 100 kPa and with different air-film thickness h_0: 10 μm, 25 μm, 50 μm, 75 μm, 100 μm (curves from bottom to top in positive y-axis direction). The topmost curve (red) is a voltage response with damping excluded.*

reduced from 100 Pa to 10 Pa). In addition, figure 5 illustrates that influence of air damping when operating at atmospheric pressure is also appreciable for larger air gaps of several hundred micrometers.

Detrimental effect of squeeze-film damping on generated voltage is also obvious from results of transient analysis (figure 6), which was carried out by applying sinusoidal kinematic excitation at frequency of 184 Hz, which corresponds to the fundamental frequency of the converter. One can observe that under atmospheric pressure air gaps of less than 100 μm significantly reduce open circuit voltage, which is in agreement with findings of the harmonic analysis.

III - Conclusion

A multiphysics finite element model of a PMPG was built that takes into account mechanic, piezoelectric and fluidic domains. The latter is represented by air-film between bottom face of the proof mass and fixed ground surface. Nonlinear compressible isothermal Reynolds equation was used to evaluate counter-reactive pressure force that is generated by squeezed air-film during operation of the device. Results of dynamic simulations indicate that the magnitude of air damping is strongly dependent on the ambient pressure and air-film thickness: particular combination of values of these parameters leads to quality factor that is less than unity. Numerical analysis revealed that significant air damping may be induced under atmospheric pressure leading to substantial reduction of voltage output, particularly for air gaps below 100 μm. At gaps below 50 μm (at atmospheric pressure), the generated open circuit voltage is negligible as the exerted air pressure force is so high that it suppresses the resonance. In this case only reduction of ambient pressure below ca. 10 Pa may restore power generation capability of the PMPG. These results demonstrate that during design of the device its configuration has to be tailored so as to minimize detrimental influence of the squeeze-film damping.

Acknowledgments

This research was performed under postdoctoral fellowship, which is funded by EU Structural Funds project “Postdoctoral Fellowship Implementation in Lithuania”.

References

[1] S. Roundy, P.K. Wright and J. Rabaey, *Energy Scavenging for Wireless Sensor Networks with Special Focus on Vibrations*, Kluwer Academic Publishers, 2004.

[2] R.J.M. Vullers, R. van Schaijk, I. Doms, C. Van Hoof, R. Mertens, "Micropower energy harvesting," *Solid-State Electron.*, vol. 53, pp. 684-693, 2009.

[3] K.A. Cook-Chennault, N. Thambi, A.M. Sastry, "Powering MEMS portable devices - a review of non-regenerative and regenerative power supply systems with special emphasis on piezoelectric energy harvesting systems," *Smart Mater. Struct.*, vol. 17, 2008.

[4] A. Khaligh, P. Zeng, C. Zheng, "Kinetic Energy Harvesting Using Piezoelectric and Electromagnetic Technologies–State of the Art," *IEEE Trans. Ind. Electron.*, vol. 53(3), pp. 850-860, 2010.

[5] D. Zhu, M.J. Tudor, S.P. Beeby, "Strategies for increasing the operating frequency range of vibration energy harvesters: a review," *Meas. Sci. Technol.*, vol. 21, 2010.

[6] R.M. Lin, W.J. Wang, “Structural Dynamics of Microsystems - Current State of Research and Future Directions,” *Mech. Syst. Sig. Process.*, vol. 20, pp. 1015-1043, 2006.

[7] K.S. Breuer, “Chapter 9. Lubrication in MEMS,” in *The MEMS Handbook,* M. Gad-el-Hak, ed. CRC Press, 2002.

[8] T. Veijola, H. Kuisma, and J. Lahdenperä, “The influence of gas-surface interaction on gas film damping in a silicon accelerometer,” *Sens. Actuators, A*, vol. A66, pp. 83-92, 1998.

FULLY INTEGRATED MICROSYSTEM USING MICROFLUIDIC DEVICES TO TUNE OR RECONFIGURE RF CIRCUITS.

S. Pinon[1,2], D.L. Diedhiou[3,4], , A-M Gue[1,2], N. Fabre[1,2], G. Prigent[2], V. Conedera[1,2], E. Rius[3,4], C. Quendo[3,4], B. Potelon[3,4], J-F. Favennec[3,4], and A. Boukabache[1,2]

[1]*CNRS ; LAAS ; 7 avenue du colonel Roche, F-31077 Toulouse, France*
[2]*Université de Toulouse ; UPS, INSA, INP, ISAE ; LAAS ; F-31077 Toulouse, France*
[3]*Université Européenne de Bretagne, France*
[4]*Université de Brest ; CNRS, UMR 3192 Lab-TICC, 6 avenue Le Gorgeu, CS 93837, 29238 Brest cedex3*

***Abstract* — This paper presents preliminary devices and results of tunable microwave microsystem associating RF circuits and microfluidic components. Dielectric fluids are used to disrupt the permittivity of a microstrip structure and thus change its operating frequency. In this approach, stop-band metallic stubs are placed on top of SU8 structured substrate. Without changing the shape of RF function, its frequency shift is more than 20% when deionized water is flowing in fluidic channels.**

Keywords : microsystem, RF, microfluidic, SU8, tunable filter, microwave.

I - Introduction

The next generation of communication systems requires more and more use of reconfigurable devices for multiband operating mode. This perspective avoids the multiplication of devices and keeps a small footprint. Several techniques has been used to tune filters : MEMS (Micro Electro Mechanical Systems) [1] [2], PIN diodes [3] or varactor [4] etc...

Our approach consists to integrate a microfluidic channels close to a transmission line. The effective permittivity seen by the electromagnetic wave is different depending on whether the channel is full or empty. This combination leads to very innovative devices. Only few studies deal with both technologies, microfluidic and microwaves, in the same time.[5],[6].

The benefits expected from a fluidic control are a low noise figure (passive component), a command buried, and the ability to adjust the working frequency of devices or cavities (resonators).

In this paper, we present the first realizations of microfluidic tunable notch filters. This is a microstrip quarter wavelength stub on a SU8 substrate fabricated by using the lamination of a dry SU8 film. In parallel, simulations have been conducted in order to predict the behavior of projected structures. The preliminary electrical characterizations show that the measurements are consistent with simulations.

II – Conception and realization

A. Choice of RF design

The two main technologies of planar filters are microstrip and coplanar waveguide. Since the tuning will be done through the introduction of a fluid inside the substrate, the main criterion is the concentration of electromagnetic field in it. As it is shwon in Figure 1, the most favorable configuration is the microstrip technology (a) which allows a maximum electric field line inside the substrate. We have therefore adopted this layout to realize our devices.

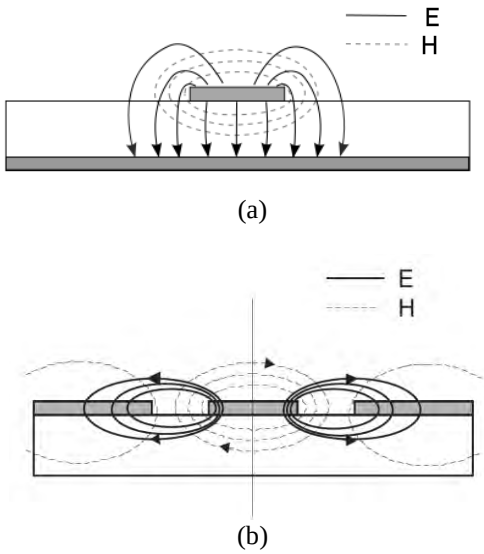

Figure 1. *Electromagnetic field in microstrips (a) and in coplanar lines (b).*

B. Choice of microfluidic technology

The realization of microfluidic channels can be done by using different methods: engraving, casting, stamping, dry film postponed ... All these techniques involve the use of specific materials, from which some, such silicon or glass, are inconsistent with 3D applications. The final objective of this work is to realize 3D microfluidic filters; it appears clearly that the polymer technology is more relevant.

Among all the existing resins (PDMS, PMMA, PET, PEEK...), the one with prominent properties is the SU8, an epoxy photoresist developed by IBM for UV-LIGA applications [7]. It allows the fabrication of high-aspect-ratio microstructures, typically from 1 µm up to 1.5 mm, by using a single coating [8]. It also presents excellent chemical resistance, good mechanical properties and high transparency. Also, photolithography allows its use in a conventional microtechnology process.

In our laboratory, it has been developed a technology to realize 3D microfluidic structures [9]. This technique uses simple tools and is based on not wafer bonder but on lamination techniques which are more flexible processes.

This technology was therefore chosen. Knowing that SU-8 has a large dielectric loss, tan (δ) of 0.02, we decided to scoop out the resin locally and replace the bulk material with a structure as shown on Figure 2. This structure has the interesting feature of having only 33% of hard material.

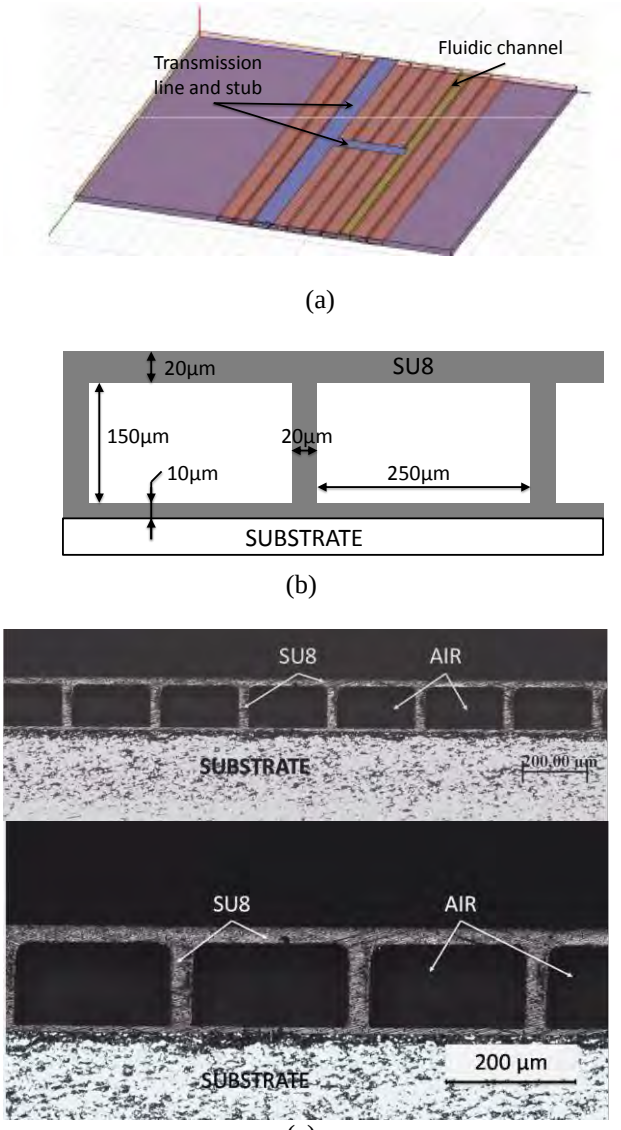

Figure 2. *Schema and details of complete microsystem. (a) schema of microsystem, (b) plan in section of structured substrate and (c) Photo in section of realized substrate (c).*

C. Realization of device

The technological process used for realizing complete microsystem consists to associate two complementary parts: microfluidic channels and RF circuits.

- As a first step, 200 nm of aluminum was deposited by sputtering on top of a 1.1 mm 4" silicon wafer. This layer is the ground plane.
- In order to protect this ground plane from liquids a layer of resin must be deposited. Therefore 10 µm thickness SU-8 3005 was spin-coated : The soft bake was performed at 95 ◦C for 7 min to evaporate the solvent. The resist was subsequently exposed to UV light in order to induce SU-8 cross-linking. The exposure dose was of 90 mJ cm−2. The post-exposure bake was performed at 95 ◦C for 2 min in order to complete the polymerization process and to obtain a hard material. Finally, the layer was developed in a bath of propylene glycol methyl ether acetate (PGMEA) for 5 min and rinsed in isopropanol (IPA).
- Then, 150 µm thickness SU-8 3050 was spin-coated on the previous layer: The soft bake was performed at 95 ◦C for 60 min. The UV-exposure dose was of 460 mJ cm−2. The post-exposure bake was performed at 95 ◦C for 2 min. Finally, the layer was developed in a bath of PGMEA for 15 min and rinsed in isopropanol. This layer structures the wall of channels.
- The next step is more critical, it is the fabrication of SU-8 dry film to close channels by using the lamination technique. On a second wafer, a 50 µm thick adhesive was laminated (manual laminator Shipley 350HR). Then a stack PET/adhesive/PET (50/25/75 µm thick AR-Clear® -8796 from AdhesivesResearch) was laminated on top of the adhesive sheet. 20 µm thickness SU-8 3025 was spin-coated on PET, the time of the soft bake was voluntarily increased compared to 'standard process' in order to evaporate most solvent and harden the layer. The SU-8/PET stack was then peeled from the substrate. The resist was then exposed to UV with 170 mJ cm−2. The post-exposure bake was performed at 95 ◦C for 2 min. Finally, the layer was developed in a bath of PGMEA for 5 min, rinsed successively with isopropanol (IPA) and with water in order to limit heat shock during evaporation of IPA.
- Afterwards, 1µm of aluminum was deposited by sputtering in order to realize transmission line and electrical vias.
- Positive resin was deposited manually by spraying to protect vias. The soft bake was performed at 80°C for 5 min. The exposure dose was of 500 mJ cm−2. The resin is developed in alkaline developer MF-CD 26.
- Finally aluminum was wet etched and the positive resin was dissolved.

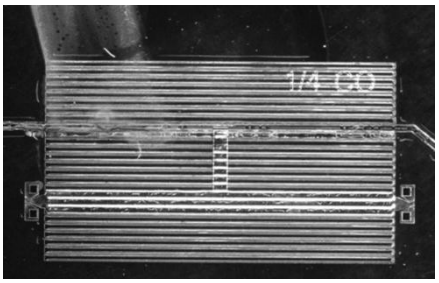

Figure 3. *Top view of realized device.*

D. Choice of liquid

The liquid that will realize the tuning must have a large dielectric constant. More the contrast with air is significant more the ability of tuning is high. Elements that have the largest permittivity are polar elements. Their dielectric polarization depends primarily on the ability of their dipoles to orient in the direction of the applied electric field. But around several gigahertz frequencies rotations of the molecule cannot follow the excitation field. The result is a collapse of the permittivity; and the liquid behaves as a non-polar element. When the dipoles are in phase opposition with the electric field there is a pick of dielectric losses.

On the contrary non-polar elements have low losses but also low permittivity (typically around 5), so a tuning capability lower.

For first measurements deionized water was used, it is a polar element; its pick of losses is around 20 GHz. But dielectric constant (real part on Figure 3) stay upper than 10 until 50 GHz.

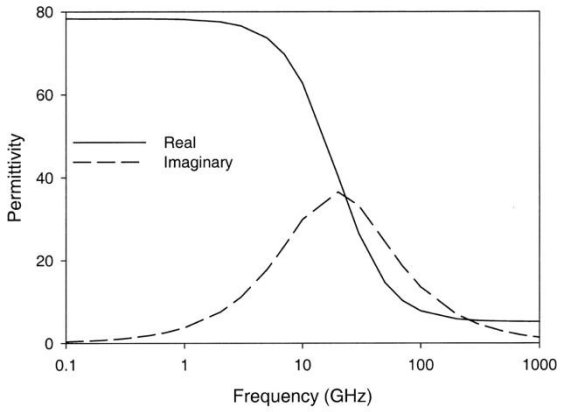

Figure 3. *Dielectric spectra plot for water at 25°C.*

III – Results and discussions

The S-parameters were measured from 10 GHz to 40 GHz with an Agilent 8510 network analyzer and cascade Microtech GSG probes thanks to a CPW – microstrip transition. The filing of channels with deionized water has been carried out with a syringe towards molded PDMS plots for the fluidic connection. We obtained a shift of 20%, figure 4 (b), between the empty channel and the channel filed with deionized water.

Moreover it is consistent with simulation made with HFSS, even if dispersion of water permittivity has not been considered. The implemented dielectric constant was fixed at 80 and the losses was fixed at tan(δ) = 0.1.

The difference of 5dB of losses which there are on all the range on measurements is due to the transition part.

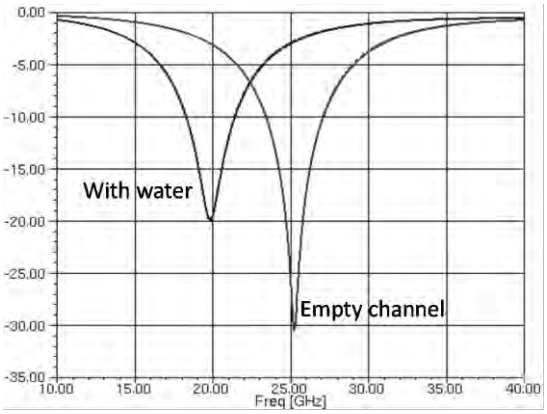

(a)

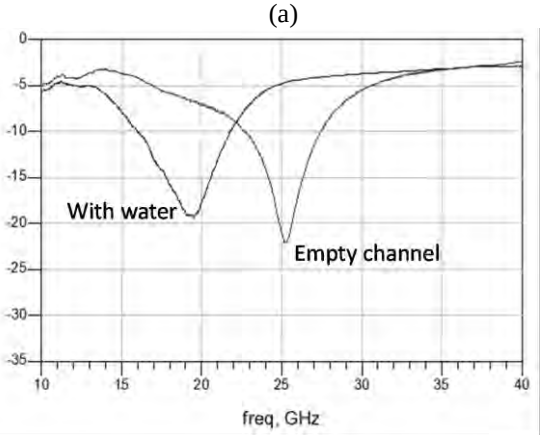

(b)

Figure 4. *S-parameter of transmission (S21) of the filter without water and with deionized water at 25°C (a) by simulation (b) by measurement.*

IV - Conclusion

A microfluidic 25GHz tunable stop band device has been designed, simulated and realized by using a fully compatible microelectronic process. The structural material used both for the fluidic part and the RF circuit part is the SU8 photoresist. Physical characterizations and RF measures performed on complete microsystem show that the structure is functional both microfluific and microwave aspects.

The EM waves convoyed by the transmission lines are influenced by the fluid circulating in channels underneath the end of stub placed on the top of microsysteme. The presence of water (or other fluids in the future) shifts significantly the S parameters: when the microfluidic channel is filled with deionized water, the response of filter is shifted for more than 20%.

References

[1] E. Fourn et al., « MEMS switchable interdigital coplanar filter », *Microwave Theory and Techniques, IEEE Transactions on*, vol. 51, n°. 1, p. 320-324, 2003.

[2] C. L. Goldsmith, A. Malczewski, Z. J. Yao, S. Chen, J. Ehmke, et D. H. Hinzel, « RF MEMS variable capacitors for tunable filters », *International Journal of RF and Microwave Computer-Aided Engineering*, vol. 9, n°. 4, p. 362–374, 1999.

[3] F. Mahe et al., « Electronically Switchable Dual-Band Microstrip Interdigital Bandpass Filter For Multistandard Communication Applications », in *Microwave Conference, 2000. 30th European*, 2000, p. 1-4.

[4] B. Kapilevich, « A varactor-tunable filter with constant bandwidth and loss compensation », *Microwave Journal*, vol. 50, n°. 4, p. 106, 2007.

[5] D. T. McCormick, Z. Li, et N. Tien, « Dielectric fluid immersed MEMS tunable capacitors », in *2003 IEEE MTT-S International Microwave Symposium Digest*, 2003, vol. 1.

[6] I. El Gmati et al., « Liquid RF MEMS variable inductor », *Procedia Engineering*, vol. 5, p. 1380-1383, 2010.

[7] K. Y. Lee, « Micromachining applications of a high resolution ultrathick photoresist », *Journal of Vacuum Science & Technology B: Microelectronics and Nanometer Structures*, vol. 13, n°. 6, p. 3012, 1995.

[8] C.-H. Lin, G.-B. Lee, B.-W. Chang, et G.-L. Chang, « A new fabrication process for ultra-thick microfluidic microstructures utilizing SU-8 photoresist », *Journal of Micromechanics and Microengineering*, vol. 12, n°. 5, p. 590-597, 2002.

[9] P. Abgrall, C. Lattes, V. Conédéra, X. Dollat, S. Colin, et A. M. Gué, « A novel fabrication method of flexible and monolithic 3D microfluidic structures using lamination of SU-8 films », *Journal of Micromechanics and Microengineering*, vol. 16, p. 113, 2006.

MINIATURIZATION OF A MICRO CORIOLIS MASS FLOW SENSOR WITH LORENTZ ACTUATION

J. Groenesteijn[1], T.S.J. Lammerink[1], J.C. Lötters[1,2], J. Haneveld[1,2], R.J. Wiegerink[1]

[1]*MESA+ Institute for Nanotechnology, University of Twente, The Netherlands*
[2]*Bronkhorst High-Tech BV, Ruurlo, The Netherlands*

***Abstract* — In this paper we present a significant reduction in size of a micromachined Coriolis mass flow sensor without sacrificing resolution or range. The sensor has a flow range from 10 mg/h up to more than 1000 mg/h, which is equivalent to 10 ul/h to 1 ml/h water. The reduction is achieved by using a more localized magnetic field for the actuation of the sensor.**

***Keywords:* micro Coriolis mass flow sensor, Lorentz actuation, miniaturization**

I – Introduction

Coriolis mass flow sensors are capable of measuring large flow rates, but their resolution is limited due to the extremely small Coriolis forces. The sensor we presented in [1, 2] has a very thin tube wall of only 1 µm made using the surface channel technology presented in [3]. This significantly improved the resolution compared to earlier devices[4, 5]. However, bulky external magnets were required for actuation of the tube. In order to decrease the sensor's footprint and to allow easier integration into other systems we show that these magnets can be replaced by miniature magnets without sacrificing the resolution of the sensor.

II – Coriolis Mass Flow Sensor

A. Coriolis mass flow sensing

A Coriolis flow sensor consists of a vibrating tube. A fluid that flows through the tube results in a small Coriolis force which can be detected. Figure 1 shows a schematic drawing of a Coriolis sensor based on a rectangular tube shape. The tube is actuated in a torsional mode, indicated by $\vec{\omega}_{\mathrm{am}}$, by Lorentz force. The mass flow $\vec{\Phi}_{\mathrm{m}}$ through the tube results in a Coriolis force $\vec{F}_{\mathrm{C}}$ given by equation (1). The Coriolis force induces an out-of-plane mode (swing mode) with an amplitude proportional to the mass flow. The amplitude of the swing mode can be detected capacitively using the method presented in [2].

$$\vec{F}_{\mathrm{C}} = -2L_x(\vec{\omega}_{\mathrm{am}} \times \vec{\Phi}_{\mathrm{m}}) \qquad (1)$$

Figure 2 shows a photo of the old design with large magnets next to the chip. A schematic representation of the sensor structure is shown in Figure 3. The fluid inlets are shown to the left on the chip. The square Coriolis tube is shown in the middle and the fluid outlets are shown at the right. The miniature permanent magnets with a volume of only 1 mm^3 are placed right outside the Coriolis tube. For comparison, the position of the large magnets that were previously used is shown. The electrodes at the bottom are used for the actuation of the tube and provide a high-frequency carrier signal for the capacitive readout. The electrodes at the top are used for the capacitive readout signals.

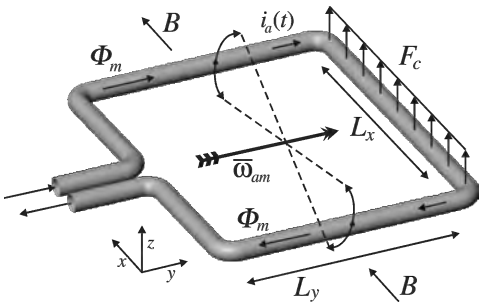

Figure 1: *Schematic of a Coriolis flow sensor*

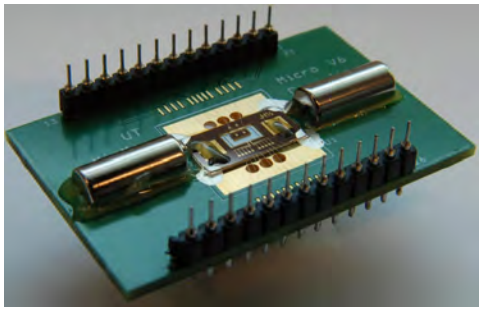

Figure 2: *Photo of the chip mounted on a PCB with the large permanent magnets mounted next to it.*

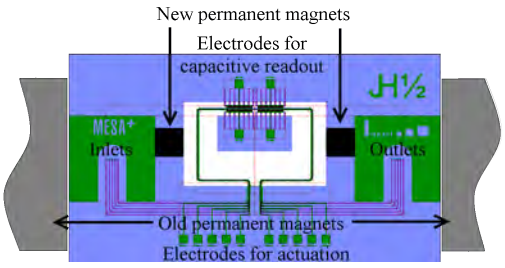

Figure 3: *Structure of the micro Coriolis Mass Flow Sensor*

B. Lorentz actuation

The sensor tube is actuated by Lorentz forces acting on the two tube segments with length L_y. The Lorentz force on each of these segments is given by equation (2).

In this equation $\vec{F}_L$ is the Lorentz force, $\vec{i}_a$ is a vector representing the AC-signal through the wire, $\vec{B}$ is the magnetic field vector and L_y is the length of the part of the wire that aligns with the y axis. The magnetic field is caused by two permanent magnets. Previously, this were large magnets next to the chip. These have been replaced by miniature magnets on the chip right next to the tube.

$$\vec{F}_L(t) = L_y(\vec{i}_a(t) \times \vec{B}) \quad (2)$$

By applying an AC-signal through a wire on top of the tube, the tube will vibrate in the torsional mode. The amplitude of the vibration is directly proportional to the actuation current and the magnitude of the magnetic field.

III – Fabrication process

The Coriolis sensor consists of a silicon nitride micro channel that is freely-suspended over an etched cavity in the silicon substrate. A brief summary of the fabrication process outlined in Figure 4 is given below. A more detailed description can be found in [6].

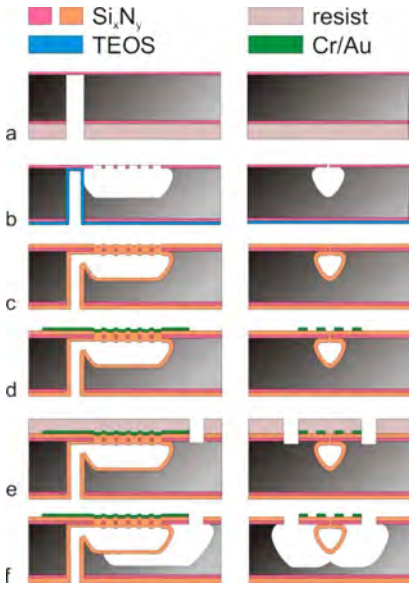

Figure 4: *Outline of the fabrication process to make the micro Coriolis mass flow sensor. Left column: cross-section along the length of the tube. Right Column: cross-section perpendicular to the sensor tube.*

Starting with a highly doped <100> p++ wafer, a 500 nm thick low stress LPCVD silicon-rich silicon nitride (Si_xN_y) layer is deposited. Then the fluid inlet/outlet holes are etched from the backside of the wafer using the Si_xN_y layer at the top side as etch stop (Figure 4a). Next, a 1 µm thick TEOS (tetraethyl orthosilicate) oxide layer is deposited and removed from the front side of the wafer. Then a 50 nm layer of chromium is sputtered on the front side of the substrate. This chromium layer is patterned using a mask containing arrays of 5×2 µm holes, spaced 3 µm apart. This pattern forms the centerline of the final channel. The pattern is then transferred into the nitride layer by reactive ion etching and subsequently the channels are etched in the silicon using isotropic plasma etching (Figure 4b). The TEOS layer and chromium mask are then removed and another Si_xN_y layer is grown with a thickness of 1.8 µm to form the channel walls and seals the etch holes in the first nitride layer (Figure 4c). A 10 nm layer of chromium and 200 nm layer of gold are sputtered (chromium serving as the adhesion layer for gold) and patterned to create the metal electrodes for actuation and readout (Figure 4d). Next, the release windows are opened by reactive ion etching of the Si_xN_y layer (Figure 4e) and the structure is released by isotropic etching of silicon (Figure 4f)).

Figure 5 shows a SEM photo of a realized Coriolis mass flow sensor. A chip with the new miniature magnets of 1 mm^3 is shown in Figure 6. The chip is mounted on the same PCB that was also used for the large magnets.

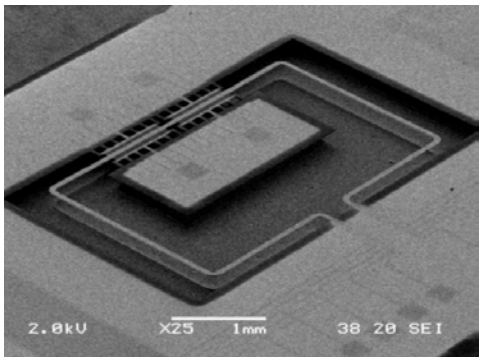

Figure 5: *SEM photo of the realized Coriolis mass flow sensor.*

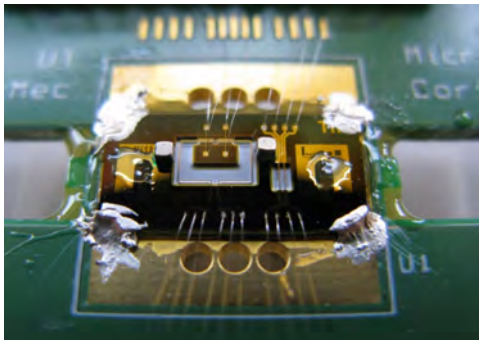

Figure 6: *Photo of the chip mounted on the same PCB with the miniature permanent magnets mounted on the chip. The shown chip has combined a Coriolis Mass Flow Sensor and a Thermal Flow Sensor on one chip which is presented in [7].*

IV – Simulation and measurements

There are several differences with respect to the magnetic fields between the large and miniature magnets. First, the distance between the magnets and the tube is different. Due to the size, the large magnets had to be placed next to the chip at a distance of 8 mm from the tube. The miniature magnets can be placed on the chip right next to the tube at a distance of less then 1 mm. The

second major difference is the uniformity of the field. The large magnets have a larger magnetized area which results in a field between them that is nearly uniform over the complete chip. The miniature magnets have a more localized field which will be less uniform over the complete length of L_y.

Four different methods have been used to compare the performance of the Coriolis mass flow sensor with miniature magnets and with the large magnets. The magnetic field is simulated using Comsol Multiphysics. The magnetic field of the separate magnets is measured using a Gaussmeter. Third, the quality of actuation is measured by comparing the amplitude of the tube vibration at the same AC actuation signal and last, the performance of the sensors are tested by measuring a volume flow of water of 1 µl/h up to 1 ml/h.

A. Simulations

Using Comsol Multiphysics 3.5a, models are made containing the permanent magnets and the gold wire on top of the tube. Separate models are made for the large magnets and the miniature magnets. Figures 7 and 8 show the simulated magnetic field of both models. An image of the mask of the chip is semi-transparently shown on top of the figures as a reference for the size and location of the magnets. As specified by the manufacturer of the real magnets (Supermagnete.de), the magnetization of the magnets was set to the same value. The x-component of the magnetic flux density is integrated over L_y to find the total magnetic field strength that can be used for Lorentz actuation. The simulation results show that the field caused by the large magnets is 1.93 times larger than the field caused by the miniature magnets.

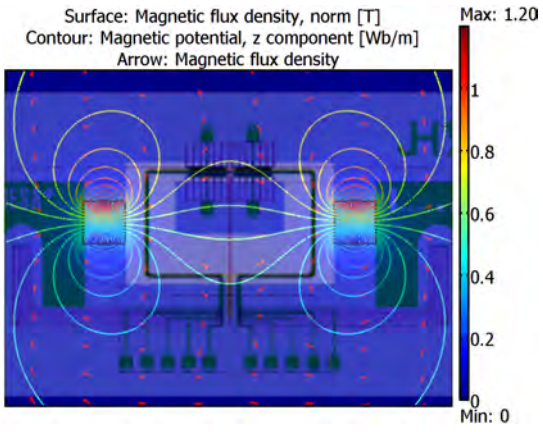

Figure 7: *Simulation result showing the magnetic field of the miniature magnets*

B. Magnetic field measurements

Using a LakeShore 455 DSP Gaussmeter, the magnetic field of several of the large and miniature magnets is measured. The magnetic field on the chip is caused by two magnets. So to find the total field at the part of the tube denoted with L_y in Figure 1, the field from the magnet closest to it has to be added to the field of the magnet on the other side of the tube. The width of the tube is 4 mm, which means that the magnet furthest away is 4 mm further away then the closest magnet. For the large magnets, this means a distance of 8 mm and of 12 mm. For the miniature magnets, this means a distance of 1 mm and 5 mm. At 8 mm, the field of the large magnets is between 25 mT and 28 mT. At 12 mm, this is 11 mT to 13 mT. At 1mm the field of the miniature magnets is 18 mT to 22 mT, at 5 mm, the field is reduced to 0.5 mT to 1 mT. Together, this gives a ratio between the fields of 1.57 to 2.22. The field measured at 0 mm from the magnets is 470 mT to 480 mT for the large magnets and 50 mT to 55 mT for the miniature magnets.

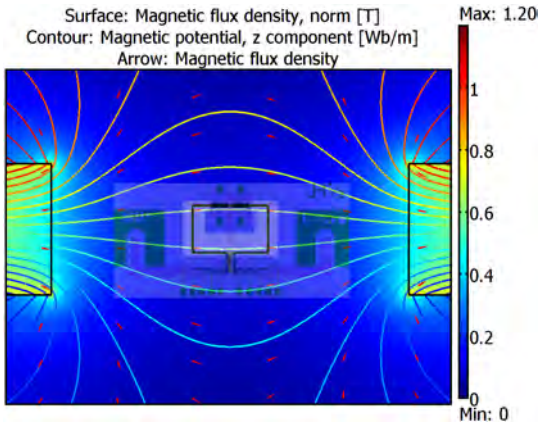

Figure 8: *Simulation result showing the magnetic field of the large magnets*

A second way to measure the magnetic field is by measuring the amplitude of the vibration of the tube. The amplitude is proportional to the Lorentz force acting on the tube, which in turn is proportional to the magnetic field. To estimate the Lorentz force acting on the tube, the tube is brought into resonance by an AC-signal through the wire over the tube. To compare the performance of the different magnets, the amplitude of the current through the wire is kept constant. The amplitude of the vibration of the tube is then directly proportional to the magnetic field strength. Using this method it was found that the magnetic field of the large magnets is a factor 1.56 to 1.82 larger than that of the miniature magnets.

C. Mass flow measurements

To compare the quality of the mass flow measurement using the different magnets, the setup shown in Figure 9 is used. A syringe pump is used to apply a constant volume flow of demineralized, degassed water which is measured using the Coriolis sensor. The measurement is been repeated for different volume flows between 1 µl/h and 1 ml/h. Figure 10 shows the measurement results. The results of the measurements that were done using large magnets are shown with squares while the measurement results of the miniature magnets are shown

with circles. The black line shows the applied flow.

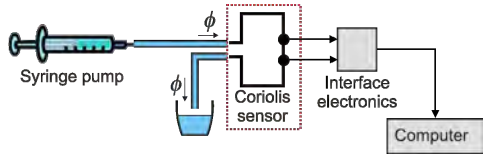

Figure 9: *Measurement setup for the mass flow measurements.*

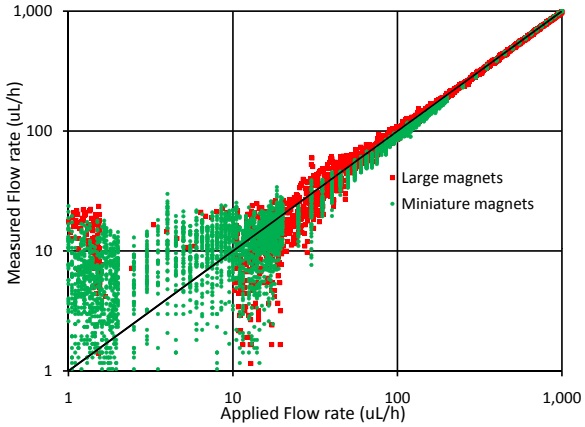

Figure 10: *Mass flow measurements using a volume flow of 1 µl/h up to 1 ml/h of water.*

V – Summary and Discussion

To investigate the influence of the different magnets, the magnetic field is simulated using Comsol Multiphysics and measured in two different ways. Furthermore, the sensors are used for mass flow measurements.

Using the actuation current as a measure for the magnetic field at the tube, a ratio between the large and miniature magnets of 1.56 to 1.83 was found. The simulations in Comsol show a ratio between field strength of 1.93. Using a Gaussmeter, the magnetic field due to the large magnets right at the end of the magnet was found to be 9 times larger than that of the miniature magnets. However, because they are much further away from the tube, the difference at the tube is much lower: a ratio between the magnetic field at the tubes between 1.57 and 2.22. Both the Comsol simulations as the current measurements give results within this range. The variation can be caused by the difference between magnetization of individual magnets.

The electronics that control the sensor adjust the actuation current in such a way that the amplitude of the vibration reaches a certain magnitude. As a result, the mass flow measurements show comparable results for both types of magnets.

VI – Conclusion

To minimize the size of a micro Coriolis mass flow sensor and the effect of the Lorentz actuation outside the chip, the magnets used for Lorentz actuation have been replaced by miniature magnets. These magnets can, because of their size, be placed right next to the tube instead of next to the chip. As a result, the required area of the chip, including the magnets, is reduced by a factor 3. The influence of the miniature magnets is investigated using simulations and measurements. The simulations and measurements gave matching results and even though the magnetic field available for Lorentz actuation has decreased, the performance of the mass flow sensor did not deteriorate. The magnetic field just outside the required sensor area due to the magnets has been reduced to less then 1 mT compared to over 400 mT with the large magnets.

The presented miniaturization has been achieved by using the same chip design for both types of magnets. Further miniaturization can be achieved by making an optimized chip design to accommodate the miniature magnets, for instance inside the rectangular loop of the sensor tube. The PCB used to mount the chip and magnets can also be significantly reduced in size now that the space required for the large magnets is no longer needed.

Acknowledgements

This research was financed by the Dutch MicroNed, PIDON High Tech Factory, Kenniswerkers and NanoNextNL programs. The authors would like to thank the industrial partners in these projects for many fruitful discussions.

References

[1] Haneveld, J., Lammerink, T. S. J., Dijkstra, M. A., Droogendijk, H., de Boer, M. J., and Wiegerink, R. J. (2008) *MEMS 2008* pp. 920–923.

[2] Haneveld, J., Lammerink, T. S. J., de Boer, M. J., and Wiegerink, R. J. (2009) *MEMS 2009* pp. 463–466.

[3] Dijkstra, M., de Boer, M. J., Berenschot, J. W., Lammerink, T. S. J., Wiegerink, R. J., and Elwenspoek, M. (2007) *J. Micromech. and Microeng.* **17(10)**, 1971–1977.

[4] Enoksson, P., Stemme, G., and Stemme, E. (1997) *J. MEMS* **6(2)**, 119 –125.

[5] Sparks, D., Smith, R., Cripe, J., Schneider, R., and Najafi, N. (2003) *Proc. IEEE Sensors Conference* **2(1)**, 337–339.

[6] Haneveld, J., Lammerink, T. S. J., de Boer, M. J., Sanders, R. G. P., Mehendale, A., Lötters, J. C., Dijkstra, M. A., and Wiegerink, R. J. (2010) *J. Micromech. and Microeng.* **20(12)**, 125001.

[7] Lammerink, T., Lötters, J., Wiegerink, R., Groenesteijn, J., and Haneveld, J. (2011) *To be presented at Transducers 2011*.

FABRICATION OF POLYMERIC MICRO STRUCTURES BY CONTROLLED DROP ON DEMAND INKJET PRINTING

L.Jacot-Descombes, M.R.Gullo, V.J.Cadarso and J.Brugger

Microsystems Laboratory, École Polytechnique Fédérale de Lausanne (EPFL) 1015, Lausanne, Switzerland

***Abstract* — Well controlled spherical microstructures could enable several novel MEMS devices. However, micro machining of spherical shapes has proven to be difficult with conventional planar microfabrication processes [1]. This paper presents a method allowing to fabricate controlled micro spherical structures. Drops of approximately 30 picoliters of polymeric solution were accurately inkjet printed on rounded platforms. The deposited volume is confined by rim of these platforms, thus allowing a fine control of the spherical cap edge angle as well as the volume and the radius of curvature. The process proposed allowed to fabricate large arrays of micro spherical shapes, with a controlled edge angle between 25° and 110°. Several arrays of 30 by 30 micro hemispheres with an edge angle of 90° have been successfully fabricated with a yield above 98%.**

Keywords: **SU-8-based epoxy ink, drop-on-demand inkjet printing, micro drop confinement, micro spherical cap arrays, micro lens arrays, radius of curvature controlled.**

I - Introduction

The controlled micro machining of spherically shaped MEMS has shown to be challenging. Especially in the case of micro lens arrays, it is crucial to precisely control the radius of curvature in order to achieve an equal focal length for each lens in the array [1]. Several methods have been proposed for micro lens fabrication, such as LIGA (Lithographie, Galvanoformung, Abformung) process, photoresists reflow, micro-intrusion process or isotropic etching process [2]. However most techiques suffer from a lack of flexibility and control.

During the past decade, inkjet printing has been widely used in micro fabrication due to its ability to print various polymeric materials, liquids containing nano particles, metals, nucleic acids and proteins [3]. Inkjet printing has already been used to fabricate sol-gel based micro lens arrays [4]. However, from the best of our knowledge, a precise control of lens shape and dimension using a confinement effect has not been described in the literature. Furthermore SU-8 would provide interesting properties in terms of chemical and mechanical stability, low Young's modulus and optical transparency [5].

In this paper we present a novel inkjet technique by which it is possible to micro machine sol-gel based spherical shape arrays with a precise control on the radius of curvature by surface chemistry and local confinement. This generic fabrication method can furthermore find applications either for a variety of MEMS that require a specific micro spherical shape or for the fabrication of SU-8 based microlens arrays.

II - Theoretical background

In order to achieve a high precision with inkjet based micro fabrication techniques, it is crucial to control the generation of the micro drops and the interaction of the printed material with the substrate.

A. Microdrop generation

Precise inkjet printing requires a stable micro drop generation. The two main parameters that influence the drop generation are the viscosity and the surface tension of the material to be printed [6]. Using the Weber number, the Reynolds number, and the parameter Z (1/Ohnsorge number) [7], the inkjettability of liquids can be characterized [8]. Generally a dynamic viscosity bellow 40 mPa·s and a surface tension in the range of 10^{-3} to 10^{-1} N·m^{-1} are required.

B. Drop to substrate interaction

The shape of a liquid drop on a solid flat substrate depends mainly on the interface tensions and the gravity. The capillary length of the liquid determines the weight of these two interactions. The capillary length, λ, is given by (1), where γ is the surface tension, ρ is the mass density and g is the gravity:

$$\lambda = \sqrt{\frac{\gamma}{\rho g}} \qquad (1)$$

The shape of a drop with a diameter D is strongly influenced by the gravity, if D >> λ and by surface tension if D << λ [9].

In the case of a micro drop, with D much smaller than λ, the drop shape is mainly conditionned by the surface tensions. The link between the surface tension and the contact angle θ, is given by the Young's equation (2), where γ_{SL}, γ_{LV}, and γ_{SV} are the interfacial tensions between the solid and the liquid, the liquid and the surrounding gas, and the solid and the surrounding gas respectively.

$$\gamma_{SG} = \gamma_{SL} + \gamma_{LG}\cos\theta \qquad (2)$$

The contact angle can therefore be tuned by changing the surface energies, i.e. by a chemical surface treatment.

Another possibility to control the drop shape is the use of a topographical confinement. In case of a drop confined on a platform, see Figure 1, the drop edge angle ν is given by (3), where ϕ is the angle between the top and side wall of the platform.

Figure 1: *Scheme of a drop confined on a platform with lateral dimension below the capillary length.*

$$\nu = \theta + \pi - \phi \tag{3}$$

In the specific case of a platform with vertical side walls, the maximal value of ν is given by (4).

$$\nu = \theta + \pi/2 \tag{4}$$

The volume of a drop confined by a platform, thus having a spherical cap shape, is given by (5). The formula has been adapted from [9], where D is the spherical cap diameter; ν the edge angle and R the radius of the inkjetted micro drop in flight.

$$V_{S.Cap}(\nu, D, R) = \left(\frac{\pi}{3}\right)\left(\frac{D}{2}\right)^3 \frac{\pi R^3}{3} \frac{(2+\cos\nu)(1-\cos\nu)^2}{(\sin\nu)^3} \tag{5}$$

Confining micro drops on platforms gives the possibility to precisely control their edge angles thus their radius of curvature by varying their volume. The volume is given by the number and size of inkjetted drops on the platforms.

III - Experimental Details

The fabrication of the spherical shape array for instance a micro lens array is a two step process: (I) Fabrication of a substrate containing an array of confinement platforms, (II) inkjet printing the SU-8 based solution on the platforms.

A. Pre-patterned substrate fabrication

The fabrication process is shown in Figure 2. The platforms were fabricated starting from a standard Si wafer Figure 2A. After an adhesion priming with hexame-thyldisilazane a 5 µm thick negative tone photoresist (nLOF) was spin-coated on the wafer, Figure 2B. The photoresist was patterned by masked UV exposure (80 mJ/cm2) and spray-spin developed, see Figure 2C and Figure 2D. The remaining photo resist was used as a mask for the deep reactive ion etching (DRIE) of 25 µm [10], Figure 2E. After the etching, the remaining resist was striped in SVC-14 remover and the surface was cleaned in an O_2 plasma, Figure 2F. Finally the surface energy was adjusted for the inkjet step by deposition of a silane monolayer (Trichloro (1H, 1H, 2H, 2H-perfluorooctyl)silane), Figure 3.

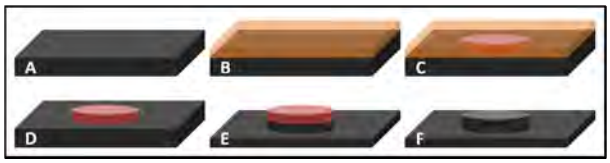

Figure 2: *Side view schemes of the fabrication process for Si platforms: (A) Si wafer; (B) A 5 µm layer of a negative tone photoresist spin-coating; (C) Masked UV exposure and (D) development; (E) Deep Reactive Ion Etching; (F) Mask stripping in remover bath, surface cleaning with O_2 plasma and silane monolyer (Trichloro (1H, 1H, 2H, 2H-perfluorooctyl)silane) deposition.*

As it can be observed in Figure 3, silanizing the silicon substrate increases the contact angle of SU-8.

Figure 3: *Advancing contact angle of the SU-8 based solution on (A) bare and (B) silanized Si. The contact angles are 20° and 70°, respectivelly, showing that the silane layer increases the contact angle.*

We fabricated Si platforms with 100 µm and 200 µm diameters. Figure 4 shows the scanning electron micrographs (SEM) of the fabricated platform arrays with 100 µm diameter. The scalloping effect due to the DRIE is also clearly visible.

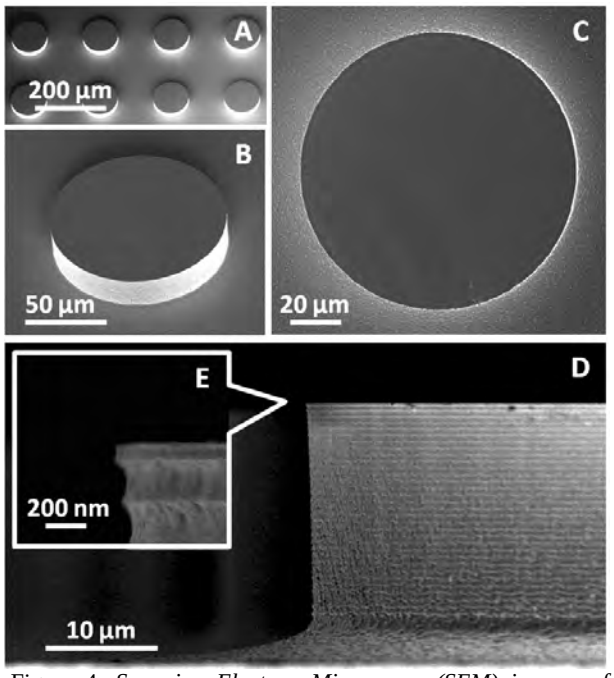

Figure 4: *Scanning Electron Microscope (SEM) images of 100 µm diameter Si platforms. (A) Tilted view of a part of the array; (B) Zoom on one platform; (C) Top view showing the perfect circle; (D) Side view, showing the verticallity of the walls; (E) Zoom on the edge of the platforms showing the scalopping effect of the DRIE Bosh process.*

B. Inkjet printing setup

Figure 5 shows a schematic of the inkjed setup. It consists of an inkjet nozzle head and a top view camera for alignment. The substrates are mounted on a computer controlled and motorized XY stage. The printing controller and the stages are synchronized through a Labview program.

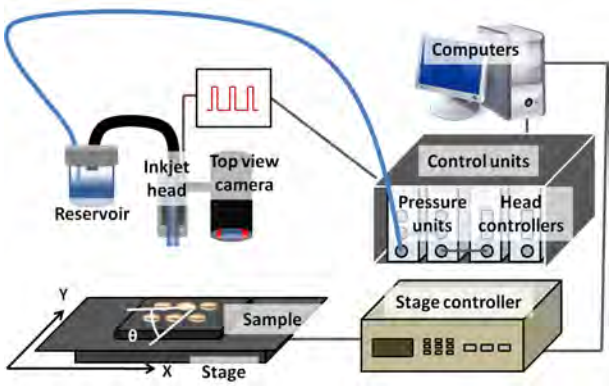

Figure 5: *Scheme of the Inkjet printing setup. The sample is mounted on the stage which is connected to the stage controller; monitored by a computer. The reservoir pressure, pushing the solution into the inkjet head is monitored by a pressure controller in the control units, which also involve the actuator of the printing head piezo element for the drop generation. The top view camera allowing the alignment of the inkjet head with the substate is also shown.*

C. Drop deposition on platforms

Since the SU-8 solution contains solvents that evaporate, it is necessary to deposit the drops layer by layer in order to control the spherical cap volume and avoid overflow. We start by depositing a first array of 5 drops on top of each Si platform, wait that the solvents evaporate, inkjet print a second array, and repeat this process until we reach the desired number of drops. The platform filling process is schematized in Figure 6. For few inkjetted drops, the liquid does not reach the platform edge and is thus not confined by the Si platform and its contact angle is defined only by the surface energies. Once enough drops have been deposited and, the platform edge is reached, the edge angle can grow from θ until θ + π/2. Above a certain number of inkjet printed drops, depending on the contact angle, the solution overflows.

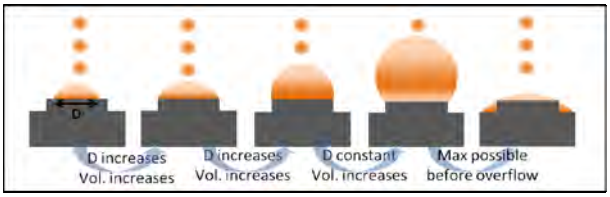

Figure 6: *Scheme representing the filling of the platform by inkjet printing. With few deposited drops, the platform is not filled and the conatct angle is given by the surface energy. Once the drops cover the full platform the edge angle increases until its maximum value (θ + π/2 for vertical platform walls). Adding more drops results in an overflow.*

VI - Results and Discussion

A. Control of the spherical cap edge angle

For a precise control of the spherical shape, it is necessary to determine the number of drops that needs to be deposited. From equation (5), we can express the number of drops, N_d, equation (6), to be inkjetted for a specific radius of curvature, given by the edge angle. This depends on the platform diameter, the in-flight drop radius, R, and the proportion of solution that evaporates, represented by the factor E_V. This factor is defined as the initial volume / final volume.

$$N_d(\nu, D, R) = E_V \left(\frac{3}{4\pi R^3}\right)\frac{\pi}{3}\left(\frac{D}{2}\right)^3 \frac{(2+\cos\nu)(1-\cos\nu)^2}{(\sin\nu)^3} \qquad (6)$$

Figure 7 shows the theoretical evolution (red curve) and the experimental data (blue markers) of the deposited drop number on 100 µm and 200 µm platforms needed to reach a specific edge angle. The green area represents the systematic error in the theoretical evolution, which has been calculated, based on the measured in flight drop diameter suffering from an imprecision of ± 2 µm. The evaporation factor, E_V, was measured as 3.136. Images of platforms with different inkjet printed drop numbers and small arrays are also shown in Figure 7 for both platform diameters. A good agreement between the theoretical expectation and the experimental results is observed.

This evolution allows us to fabricate micro spherical cap shapes of a photo-curable SU-8 based polymeric material by inkjet printing with a controlled edge angle ranging from 25° to 110° and from 60° to 95° on platforms of 100 µm and 200 µm, respectively.

B. Hemisphere array fabrication by inkjet printing

With an appropriate number of inkjetted drops, it has been possible to produce arrays of SU-8 hemispheres (edge angle of 90°) on top of Si pedestals. Figure 8 shows a SEM image of a 30 by 30 SU-8 hemisphere array. This was obtained by depositing 35 SU-8 solution drops on each Si platform. In this array of 900 hemispheres only few suffered of misalignment and have overflowed, leading to a fabrication yield over 98%.

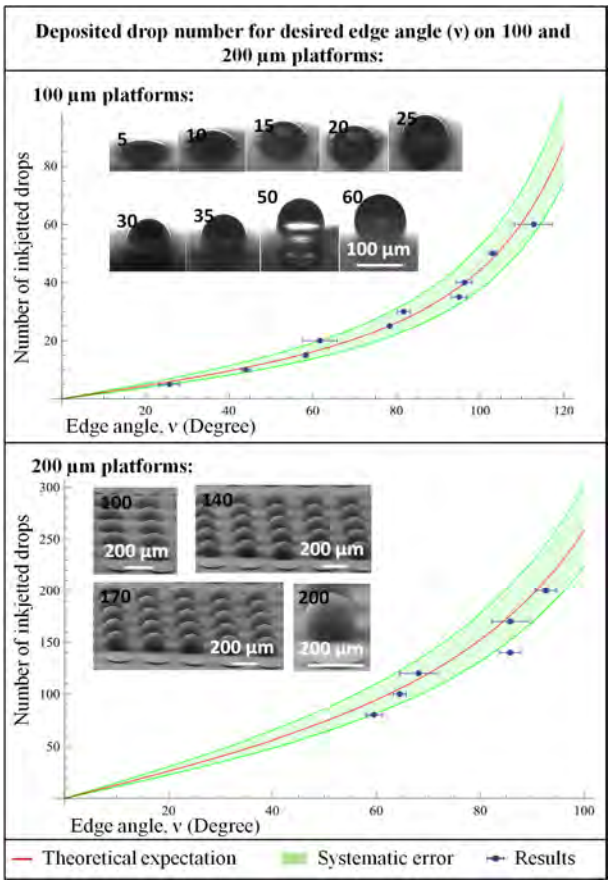

Figure 7: *Number of drops vs expected edge angle (Degree) of SU-8 based epoxy deposited on a top of silanized Si platforms of 100 µm and 200 µm in diameter. Experimental results are shown in blue and theoretical expectation by the red curve for a in flight inkjetted drop size of 36 ± 1 µm for the 100 µm and of 40 ± 1µm for the 200 µm platforms. The green area shows the systematic error, due to the in flight drop diameter measurement.*

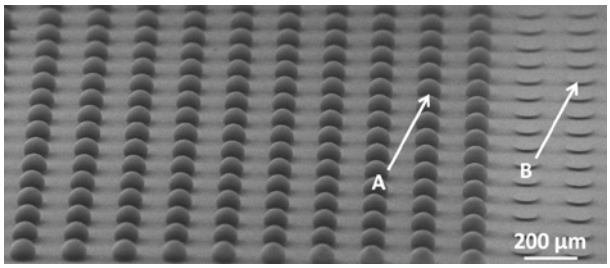

Figure 8: *SEM image (tilted view) showing part of a 30 by 30 array of SU-8 hemispheres (edge angle of 90°) sitting on 100 µm silanized Si platforms. (A) shows a hemisphere and (B) a platform.*

V - Conclusion

In this work we demonstrated the ability to obtain SU-8 epoxy based micro spherical caps with controlled edge angles between 25º and 110° and between 60º and 90° on top of 100 µm and 200 µm platforms, respectively. Using inkjet printing technology, we deposited a precisely controlled number of drops on Si platforms to achieve a confinement effect. This effect has been studied theoretically, showing a good agreement with the experimental results. This allows determining the number of drops needed to reach a specific edge angle. Furthermore, we demonstrated the ability to produce large arrays of precise micro hemispheres on pre-patterned substrates with a yield above 98%. This result presents the proposed method as an interesting candidate for the future development of micro-optical elements, such as lenses and micro-mirrors with well controlled radius of curvature.

Acknowledgements

We would like to express our gratitude to Micro Resist Technology GmbH who provided the epoxy ink solution in the framework of the FP7 Marie-Curie Project “Acapoly”. We also thank Nano-Tera.ch and the project “SELFSYS” who funded the work presented here. We finally express our sincere gratitude to the Center of Micro-Nanotechnology (CMi) of EPFL for the help during the microfabrication.

References

[1] Z. Xuefeng and J. Hongrui, "Polydimethylsiloxane Microlens Arrays Fabricated Through Liquid-Phase Photopolymerization and Molding," *Microelectromechanical Systems, Journal of*, vol. 17, pp. 1210-1217, 2008.

[2] S.-K. Lee, *et al.*, "A simple method for microlens fabrication by the modified LIGA process," *Journal of Micromechanics and Microengineering*, vol. 12, pp. 334-340, 2002.

[3] P. Calvert, "Inkjet Printing for Materials and Devices," *Chemistry of Materials*, vol. 13, pp. 3299-3305, 2001.

[4] A. Voigt, *et al.*, "New inks for the direct drop-on-demand fabrication of polymer lenses," *Microelectronic Engineering*, vol. In Press,

[5] V. Fakhfouri, *et al.*, "Inkjet printing of SU-8 for polymer-based MEMS a case study for microlenses," *Proceedings of the 21st IEEE International Conference on Micro Electro Mechanical Systems*, pp. 407-410, 2008.

[6] V. Fakhfouri, *et al.*, "Drop-On-Demand Inkjet Printing of SU-8 Polymer," *Micro and Nanosystems*, vol. 1, pp. 63-67, 2009.

[7] J. E. Fromm, "Numerical calculation of the fluid dynamics of drop-on-demand jets," *IBM J. Res. Dev.*, vol. 28, pp. 322-333, 1984.

[8] B. Derby, "Inkjet Printing of Functional and Structural Materials: Fluid Property Requirements, Feature Stability, and Resolution," *Annual Review of Materials Research*, vol. 40, pp. 395-414, 2010.

[9] D. Quere, "Non-sticking drops," *Reports on Progress in Physics*, vol. 68, pp. 2495-2532, Nov 2005.

[10] S. A. McAuley, *et al.*, "Silicon micromachining using a high-density plasma source," *Journal of Physics D: Applied Physics*, vol. 34, pp. 2769-2774, 2001.

QUADRATURE ERROR CANCELLATION IN HIGH ORDER ΣΔ MODLATOR CLOSED LOOP INTERFACES FOR MICRO-GYROSCOPES

P. Salimi[1] and M. Kraft[1]

[1]*University of Southampton, Electronics and computer science, Southampton, UK*

***Abstract* — In this paper a novel approach for cancellation of quadrature error for a micro-gyroscope embedded in a high order closed loop electromechanical sigma-delta ΣΔ modulator is proposed. Vibratory micro-machined gyroscopes utilize the Coriolis force to detect the rotation rate. Embedding the sensor in an electromechanical ΣΔ modulator results in increased linearity, dynamic range, bandwidth and immunity to fabrication variations. However, in the case of vibratory gyroscopes, a mechanical coupling exists due to fabrication imperfections: this mechanical effect is known as quadrature error. Existence of this effect results in limiting the dynamic range of the gyroscope. In this work, a novel interface is proposed that considerably attenuates the quadrature error while retaining the advantages of an electromechanical ΣΔ modulator interface for micro-gyroscopes.**

Keywords : Electromechanical sigma-delta, Micro-gyroscope, MEMS, Quadrature error

I - Introduction

Micro-fabrication technology has opened new horizons for a large variety of applications in different sectors of science and commerce, in particular inh sensing. One type of sensor in particular which has drawn a lot of interests is the micro gyroscope. These sensors are usually used to monitor the angular velocity of an object (e.g. airplane, car, missile, etc.) and help to keep the balance of it while travelling [1,2]. Also, this type of sensors are used for different aspects of controlling a car such as roll-over and skidding prevention, and find increasing application in consumer electronics [3]. However, their performance still lags behind macroscopic gyroscopes by several orders of magnitude.

Most micro-gyroscopes use a proof-mass compliantly suspended in two degrees of freedom (2D) to measure the angular rate of an angular motion by exploiting the Coriolis force effect. This couples energy from a driven mode into a secondary sense mode. The sense mode motion causes a capacitive change which is converted to a voltage change through a suitable readout circuit. One of the important limiting factors in further improving the performance of micro-gyroscopes is the quadrature error, which originates from a misalignment of the drive axis to the ideal hence results in unwanted mechanical coupling into the sense axis. This work proposes a new quadrature cancellation scheme relying on a closed loop, force feedback control system.

The sense mode of the micro-machined gyroscope sensing element is embedded in a band-pass 6th order electromechanical ΣΔ modulator (EMΣΔM). Such interfaces have been reported before for micro-gyroscopes[4,5]: By embedding the sense mode of the micro-gyroscope sensor in a closed loop force feedback system the dynamic range, bandwidth, and tolerance against fabrication imperfection of the sensor are increased; furthermore it produces a direct digital output signal suitable for signal processing. However, the closed loop control systems presented to date can not suppress quadrature error. The main objective of this work is to retain the advantages of the closed loop ΣΔ modulator architecture and attenuate the quadrature error by using a dual channel ΣΔ modulator architecture; one channel operating on the Coriolis signal, the other on the unwanted quadrature signal. In this paper a system level comparison is presented between the quadrature error output component of the novel system and a previously proposed 6th order electromechanical band-pass ΣΔ modulator [4].

II – Band-pass EMΣΔM without Quadrature Cancellation

Micro-gyroscopes can be modeled to first order as shown in fig.1.

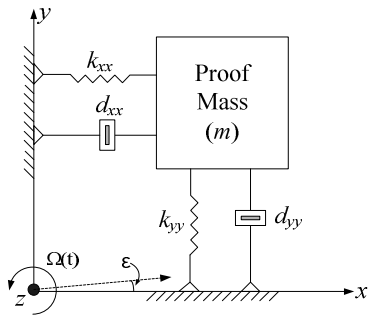

Figure 1: *Systematic lumped model of a vibratory gyroscope. k_{xx},d_{xx} and k_{yy},b_{yy} are spring constants and damping factors for drive mode and sense mode respectively and m represents the mass of the proof mass* [6].*The doted line represents the misalied oscilation direction of the drive mode with $\mathcal{E}$ degree divertion from ideal X-axis.*

As shown in the mechanical lumped model of a micro-gyroscope in fig. 1, the proof mass is driven by a regulated force (i.e. electrostatic force) along the drive mode axis at the resonance frequency (ω_d). In the absence of any rotational motion about the Z axis, ideally the movement along the sense mode axis is zero. In the presence of an angular motion about the Z axis the proof mass starts to oscillate along the sense mode at the

natural resonant frequency of the drive mode. The amplitude of oscillation in the sense mode is proportional to the angular movement rate [7]. In this work a micro-gyroscope is used with the specification shown in table 1 [8].

Table 1: *Specifications of the micro gyroscope*

Sense mode proof mass weight (m)	1.986e-6Kg
Drive mode quality factor (Q_d)	216
Sense mode quality factor (Q_s)	100
Drive mode resonance frequency (ω_d)	3987Hz
Sense mode resonance frequency (ω_s)	4080Hz

The architecture of the closed loop system without quadrature suppression is a 6th order band-pass EMΣΔM for the sense mode of the gyroscope. The system presented in [4] was adapted to the gyroscope sensing element parameters used in this work. A Simulink model of the control system is shown in fig. 2.

The control system capacitively measures the displacement of the proof mass of the micro-gyroscope in the sense mode. A compensator is required to provide phase lead for overall system stability. An electronic filter part follows, mainly comprising two electronic resonators, and some minor feedback loops. A sample and hold and a 1-bit quantiser is used to produce a bit-stream at the output signal; this is also used to control the feedback electrostatic force to counteract the Coriolis force and maintain the proof mass close to its rest position. The dynamics of the sensing element and the electronic filter shapes the quantization noise away from the signal band which is around the drive mode resonance frequency. The output of this system is a pulse density modulated bit stream with a sampling frequency of f_s=2OSRf_{bw} where OSR is the oversampling ratio and f_{bw} is the bandwidth of the input angular rate. The advantage of a band-pass sigma delta modulator over a low-pass sigma delta modulator is that the band-pass architecture works with a significantly lower sampling rate, therefore reducing the circuit implementation requirements.

The power spectral density (PSD) of the output bit stream is shown in fig. 3 for an input angular rate signal of 300º/s amplitude and 50Hz frequency. After optimizing the feedback coefficients (kf1-kf4 in fig. 2) and feedback voltage for the electrostatic feedback force, a SNR (signal to noise ratio) of more than 93dB was achieved in simulation. The PSD of fig. 3 shows very good quantization noise shaping around the resonance frequency of the micro-gyroscope.

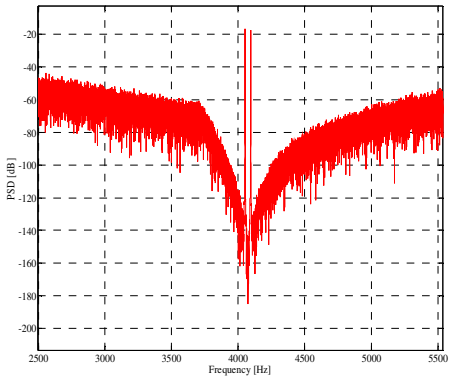

Figure 3: *Power spectral density of the output bit-stream of the 6th order band-pass EMΣΔM control system for an input signal of 300°/s amplitude and 50Hz frequency using the model of fig. 2.*

Further simulations using the system level model indicate a dynamic range of 1200º/s and a noise floor of 1.8 °/h/√Hz.

So far, the system model disregarded quadrature error; if at the input of the model a quadrature error is assumed in addition to the angular rate, the spectrum changes drastically. Assuming a quadrature error with magnitude equivalence of 238°/s a frequency component in the PSD appears at the drive mode frequency as shown in fig. 5. The magnitude of the quadrature error is realistic and it was taken from [8] but for avoiding overloading the interface it was reduced by 10%.

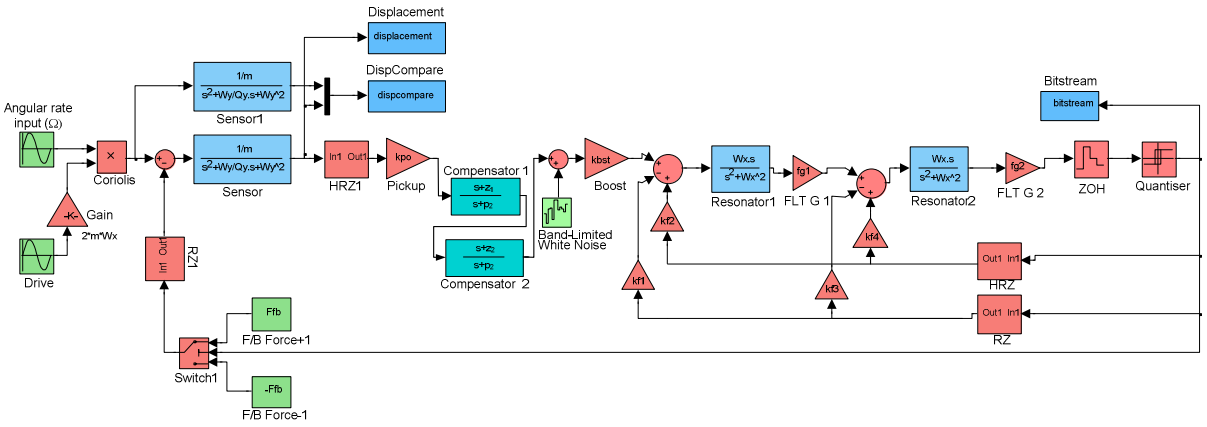

Figure 2: *Simulink model of the 6th order band-pass electromechanical ΣΔ modulator embedding the sense mode of a micro-gyroscope. This model also contains an open-loop sensing element for purpose of comparing the proof mass displacement in both closed-loop and open loop mode.*

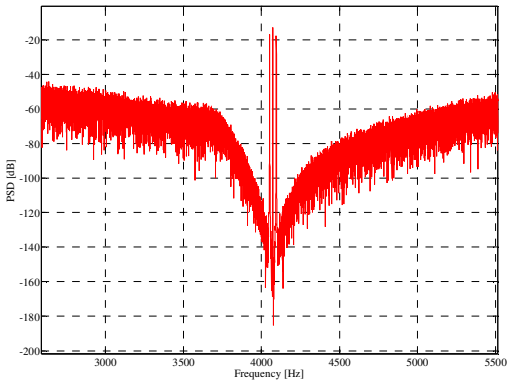

Figure 4: *Power spectral density of a bit stream output of the 6th order electromechanical ΣΔ modulator (fig.2) with quadrature error assumed at the input.*

As it shown in fig. 4, providing quadrature error compensation is required.

III – New Quadrature Error Compensation Method

In designing the new interface two facts were taken in account. The input forces resulting from quadrature error and angular rate signal are in quadrature as illustrated by following equations [9]:

$$F_{Coriolis} = 2 \times m \times \Omega \times \omega_d \times A \times \sin(\omega_d t) \quad (1)$$

$$F_{Quadrature} = \varepsilon \times A \times \omega_d^2 \times m \times \cos(\omega_d t) \quad (2)$$

Where m is the proof mass, Ω is the input angular rate, ω_d is the drive mode resonance frequency, A is the oscillation amplitude of the drive mode and ε is the degree of diversion of the drive axis comb fingers from ideal drive axis (as shown in fig.1). To separate these two signals, the process of quadrature amplitude modulation and demodulation is adopted from the communication systems field [10] resulting in an angular rate signal Ω_{AR} and a signal due to quadrature error Ω_{QE}. These two signals are then processed in two separate channels, effectively forming a complex electromechanical bandpass sigma-delta modulator. This concept is well known in the telecommunications area [11] but proposed here for the first time for a force-feedback control system of a micro-sensor. Since the fundamental principle of EMΣΔM is that any displacement of the proof mass is nulled out by the feedback system. The quadrature error compensation signal must be combined with the main feedback system.

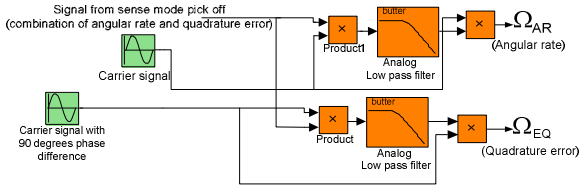

Figure 5: *Quadrature amplitude demodulation and modulation for separating information signal and quadrature error and then taking the two signals back to the drive resonant frequency band.*

As it is shown in fig. 5 the output of the pick off block is demodulated and then each component (angular rate and quadrature error signal) are modulated with the same carrier signal (at the drive frequency) to move the signal to the carrier signal frequency band. After that, the two output signals are fed to two are electronic filters with the same architecture as described in section II. The filter coefficients were optimized separately for the two channels. In both channels a sampled quantiser is used to generate a pulse density modulated bit stream; then both bit-streams are fed to a multiplexer that switches between them at four times of the sampling frequency; i.e. F_m=4F_s. Where F_m is the multiplexer switching frequency and F_s the sampling frequency of the two quantisers in fig. 6. The digital output signal of the multiplexer determines which feedback electrode is

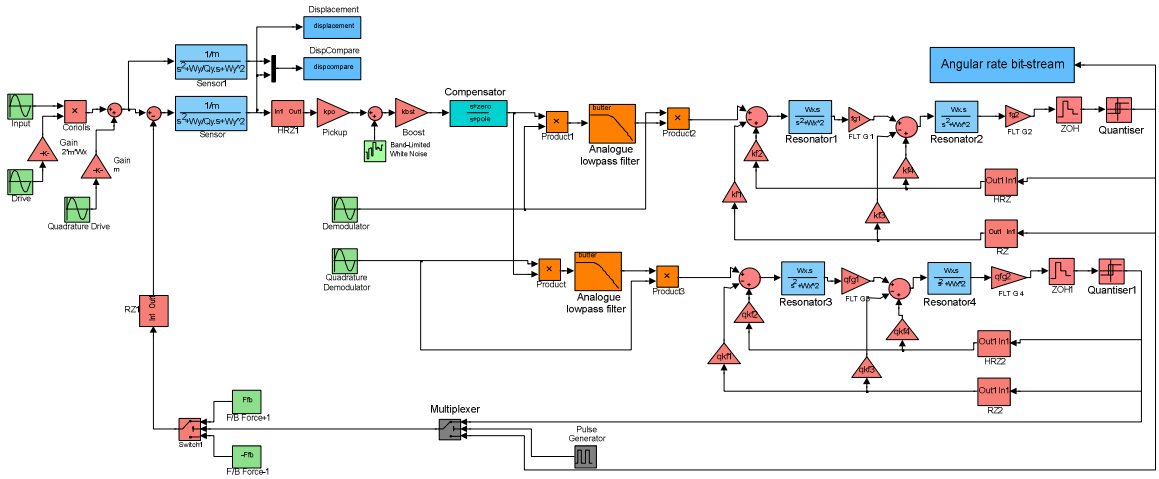

Figure 6: *Simulink model of the sense mode of a micro-gyroscope embedded in the novel 6th order electromechanical ΣΔ modulator with quadrature error compensation mechanism.*

energised generating an electrostatic feedback force nulling out both for the Coriolis force and the force due to quadrature error. Here, a constant feedback voltage of 10V was assumed.

There are two output bit-streams generated by the control system. The bit-stream generated by the channel for the angular rate signal (see fig. 6) constitutes the output signal of the gyroscope. For an angular input of 300 °/s and a quadrature error (equivalence magnitude of 265 °/s) an attenuation of approximately 75dB of the quadrature error was achieved. This is illustrated in the PSD shown in fig. 7.

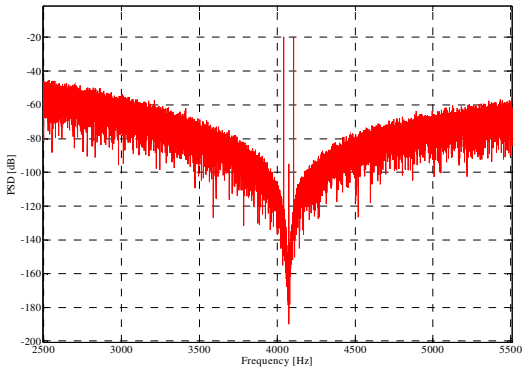

Figure 7: *Power spectral density of output bit-stream with the same input signal and quadrature error signal as in Section II. In comparison to fig. 5 an attenuation of 75 dB of the quadrature error was achieved by the novel control interface.*

IV - Conclusions

In this work, the performance of a 6th order bandpass EMΣΔM based on an architecture originally proposed in [4] and a new 6th order EMΣΔM with quadrature compensation under the same condition was investigated at the system level. Realistic values for quadrature error magnitude and input angular rate levels were assumed for both systems. The simulation results indicate that the control system with quadrature cancellation retains the advantages of the EMΣΔM and at the same time is capable of attenuating significantly the quadrature error.

References

[1] Farrokh Ayazi, Khalil Najafi and Navid Yazdi , "Micromachined Inertial Sensors," *Proceeding of IEEE*, vol. 86, no. 8, August 1998.

[2] Kai Liu, Weiping Zhang, Wenyuan Chen, Kai Li, Fuyan Dai, Feng Cui, Xiaosheng Wu, Gaoyin Ma and Qijun Xiao , "The Development of Micro-Gyroscope Technology," *Journal of Micromechanics and Microengineering*, vol. 19, no. 11, October 2009.

[3] Stephen J. Posser , "Automotive Sensors: Past, Present and Future," *Journal of Physics: Conference Series*, vol. 76, no. 1, 2007.

[4] Yufeng Dong, Michael Kraft and William Redman-White , "High Order Bandpass Sigma Delta Interfaces for Vibratory Gyroscopes," *IEEE Sensors Journal*, vol. 7, no. 1, 2005.

[5] Chinwuba D. Ezekwe and Bernhard E. Boser , "A Mode-Matching Sigma Delta Closed-Loop Vibratory Gyroscope Readout Interface With a 0.004 deg/s/sqrt(Hz) Noise Floor Over a 50 Hz Band," *IEEE Journal of Solid State Circuits*, vol. 43, no. 12, pp. 3039-3048, December 2008.

[6] Riccardo Antonello, Roberto Oboe, Lucia Prandi, Carlo Caminada, Fabio Biganzoli , "Open Loop Compensation of Quadrature Error in MEMS Vibrating Gyroscopes," in *Industrial Electronics, 2009. IECON '09. 35th Annual Conference of IEEE*, Porto, 2009, pp. 4034 - 4039.

[7] Huikai Xie and Gary K. Fedder , "Integrated Microelectromechanical Gyroscope," *Journal of Aerospace Engineering*, pp. 65-75, 2003.

[8] Haitao Ding, Xuesong Liu, Longtao Lin, Xiaozhu Chi, Jian Cui, M. Kraft, Zhenchuan Yang, Guizhen Yan , "A High-Resolution Silicon-On-Glass Axis Gyroscope Operating at Atmospheric Pressure," *IEEE Sensors Journal*, vol. 10, no. 6, pp. 1066 - 1074, June 2010.

[9] William A. Clark, Roger T. Howe, Horowitz Roberto , "Surface Micromachined Z-Axis Vibratory Rate Gyroscope," in *Technical Digest Solid-State Sensor and Actuator Workshop*, Hilton Head Island, SC, USA, 1996, pp. 283-287.

[10] Harold P. E. Stern, Samy A. Mahmoud, Lee E. Stern , *Communication Systems: Analysis and Design*.: Pearson Prentice Hall, 2004.

[11] Frank Henkel, Ulrich Langmann, André Hanke, Stefan Heinen and Elmar Wagner , "A 1-MHz Bandwidth Second-Order Continuous-Time Quadrature Bandpass Sigma–Delta Modulator for Low-IF Radio Receivers," *IEEE Journal of Solid-State Circuits*, vol. 37, no. 12, pp. 1628-1635, December 2002.

[12] Bo Yang, Bailing Zhou, Shourong Wang, Libin Huang, Yong Yin , "A quadrature error and offset error suppression circuitry for Silicon Micro-Gyroscope," in *Nano/Micro Engineered and Molecular Systems, 2008. NEMS 2008. 3rd IEEE International Conference*, Sanya, Jan 2008, pp. 422-426.

DESIGN AND SIMULATION OF A NOVEL DECOUPLED MICROGYROSCOPE

X. Yan[1], L. J. Che[1, 2] and X. Y. Chen[1, 2]

[1]*Xiamen University; Pen-Tung Sah Micro-Nano Technology Research Center; Xiamen, China*
[2] *Vestfold University College, Faculty of Science and Engineering, Horten, Norway*

***Abstract* — This paper present a novel decoupled microgyroscope. The new design consists of drive frame, sense frame, movable sense electrode, springs and isolation connection. The mode coupling error in partially decoupled gyroscope and novel decoupled microgyroscope are modeled analytically. The FEM simulation performed in ANSYS software to estimate the displacement between fingers from proof mass and movable sense electrodes. The cross-talk displacement ratio ηDtS in FDS is 0.19% at the frequency of 5932 Hz. The results show that the design minimizes cross-axis coupling errors.**

***Keywords : Microgyroscope, mode coupling error,* Simulation**

I - Introduction

The one of the limitations of microgyroscope is the mechanical coupling between drive mode and sense mode owing to poor microfabrication tolerances and its intrinsic connection between the shuffles and sense frame. Without perfectly alignment with principle drive axis, a spurious sense displacement introduced in the drive mode results in an acceleration term called quadrature error. The quadrature error is as small as the coriolis acceleration even the misalignment of the oscillation direction to principle drive axis is about a fact of 0.27 ppm [1]. In ideal microgyroscope, the drive and sense mode are matched perfectly and it will produce a phase shift of 180 degree between drive displacement and sense displacement. The mass oscillates along a straight line at an angle defined by the Coriolis acceleration. But in more general case, the oscillation pattern of mass is an ellipse [2, 3, 4]. Modeling of mode coupling error was also made by many research groups [5, 6, 7]. The modeling work mainly focused on single mass system. The imperfection of process, such as deep reactive ion etching shown in figure 1, is the one of the fact of introducing the coupling error [8].

The mode coupling error can be reduced by some methods, such as electrostatic quadrature error nulling [1, 9] and decoupled structure design, which decomposed the motion between drive mode and sense mode [10]. To achieve the decoupled structure, Frame structure and several 1 DOF springs are usually needed. However, the electrostatic quadrature error nulling method is rarely used in cancellation the mode coupling error on the proof mass due to the complex inner suspended proof mass structure.

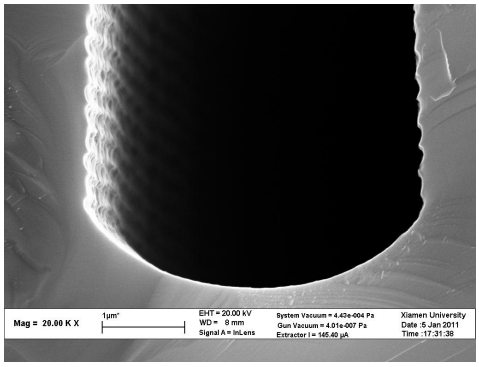

Figure 1*: Imperfection of microfabrication in the deep reactive ion etching process*

This paper presents a novel design of partially decoupled microgyroscope. the relative motion between proofmass and the sense electrode by suspending the sense electrode with drive frame. The trench isolation technology is introduced in the design. The detail is shown in section II. Modeling of cross-axis coupling in conventional partially decoupled gyroscope and in novel design was made. The design was simuled by FEM simulation and Matlab was also used for illustrate the modeling of mode coupling error.

II – Design and Modeling

A. Design and Work Principle

The schematic top view of the design is shown in figure 1. The design consists of drive frame, proof mass, springs, isolation connection, and movable sense electrode (shown in Figure 2). The sense electrodes are connected with the drive frame directly but electrically isolated from the drive frame by silicon dioxide. The movable sense electrodes move with the drive frame synchronously. The three types of springs Kx, Ky and Ksx decouple the motion between drive frame and proof mass in drive direction and keep high stiffness in sense direction. The fold-flexure suspension is widely used in suspended structures for its large stiffness ratio. Proof mass is almost at rest in drive direction when the microgyroscope is working on the drive mode. In the presence of an angular rotation, the proof mass will vibrate in sense direction (Y-axis) and the Coriolis displacement can be sensed by the relative motion between movable sense electrodes and proof mass. The signal will pass along the spring and the sense electrode anchor to the readout circuit.

The dynamic equation for the system is expressed as

$$\begin{cases} m_d\ddot{x} + b_1\dot{x} + k_1 x = F_0 \sin\omega t \\ m_s\ddot{y} + b_2\dot{y} + k_2 y = -2m_2\dot{x}\Omega \end{cases} \quad (1)$$

where m_d, m_s, b_1, b_2 correspondingly are the mass and the damping coefficient in drive mode and sense mode. F_0, ω are excitation force and its natural frequency. Ω is the external rotation rate.

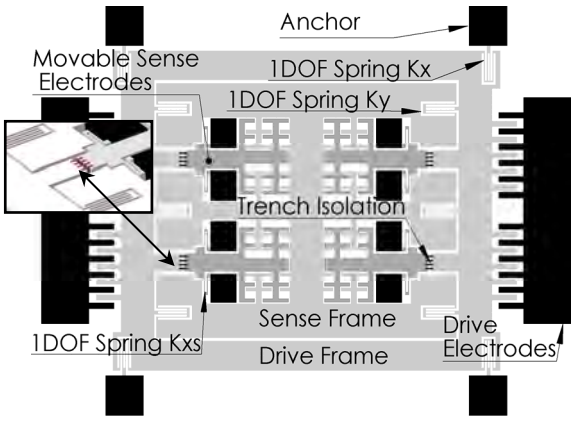

Figure 2:*Schematic top view of the decoupled microgyroscope*

Generally, the sense electrodes are fixed on the substrate in most of the decoupled microgyroscope. The drive frame, proof mass and movable sense electrodes suspend on the substrate shown in figure 3. The electrostatic force can tune the coupling error by applying DC voltage on the sense electrode. The sense finger gap is designed of 3 μm so the proof mass could rotate with an angle of 0.1° relative to the drive frame.

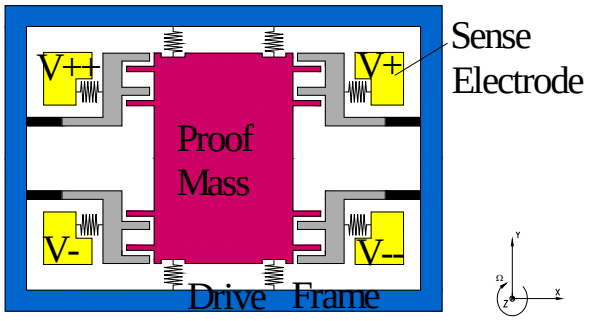

Figure 3:*electrostatic coupling error cancellation of the design*

B. Modeling of Mode coupling error

The decoupled design decomposed the motions of two modes. But poor microfabrications result in the mode coupling error which could cause drive frame vibrates along the *x* axis and with an angle α to principle axis in X direction shown in figure 4. In general case of partially decoupled microgyroscope (figure 4a) and the design (figure 4b), the oscillation directions of proof mass are misaligned for a angle β. When the drive frame shuffles along the *x*-axis, a force due to drive oscillation is applied on the proof mass. The force has a decomposition force along the proof mass oscillation direction *y1*-axis. Considering the drive frame as a reference frame, the proof mass can be modeling as harmonic spring oscillator. The drive frame is a frame

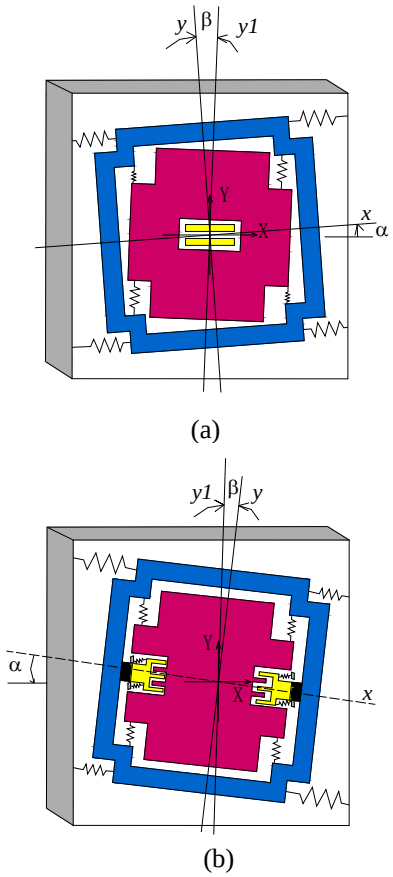

Figure 4: *imperfections cause the mis-alignment error between the motion directions and principles.a) Conventional partially decoupled microgyroscope; b)the design*

of non-inertial reference. In non-inertial reference, the fictitious force is needed to be considered. In this case, the fictitious force along the *y1*-axis is $m_2\ddot{x}$, the direction is opposite to the direction of drive-frame's acceleration. In the design, the movable electrodes move with drive frame simultaneously, so the first anisoelasticity error α can be neglected. Without external rotation rate, the dynamic equation is,

$$\begin{cases} (m_1 + m_2\cos^2\beta)\ddot{x} + b_1\dot{x} + k_1 x = F_0\sin\omega t - k_2 y_1\sin\beta \\ m_2\ddot{y}_1 + b_2\dot{y}_1 + k_2 y_1 = m_2\ddot{x}\sin\beta \end{cases} \quad (2)$$

when the external rotation is introduced, the dynamic equation become to,

$$\begin{cases} (m_1 + m_2\cos^2\beta)\ddot{x} + (b_1 - m_2\sin 2\beta)\dot{x} + k_1 x = F_0\sin\omega t - k_2 y_1\sin\beta \\ m_2\ddot{y}_1 + b_2\dot{y}_1 + k_2 y_1 = m_2\ddot{x}\sin\beta - 2m_2\Omega\dot{x}\cos\beta \end{cases} \quad (3)$$

where m_1, m_2, b_1, b_2 correspondingly are the mass and the damping coefficient in drive mode and sense mode. F_0, ω are excitation force and its natural frequency. Ω is the external rotation rate. The coupled term in equation (2) is $m_2\ddot{x}\sin\beta$ and $k_2 y_1\sin\beta$. The ratio of coupling term to coriolis is,

$$m_2\ddot{x}\sin\beta / 2m_2\Omega\dot{x}\cos\beta \approx \beta\omega / 2\Omega \quad (4)$$

Assuming β, ω, Ω are 0.001, 40000, 1, respectively, the ratio is about 20.

C. Process for the Isolation trench

The key connection between drive frame and movable sense electrode is the isolation trench. We etched the trench by DRIE, and performed the wet oxidation

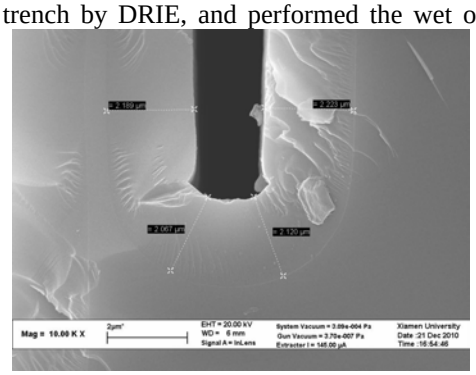

Figure 5*: SEM picture of the cross section in isolation trench.*

for 11 hours. The picture of test sample shows the thickness of oxide layers is above 2 μm in figure 5. Considering the time consuming and process error, such as misalignment in photolithography, undercutting in DRIE, ,deep narrow trench line with width of 1.8 μm can be oxided completely.

III - Simulation and Discussion

A. Mode analysis and Harmonic analysis

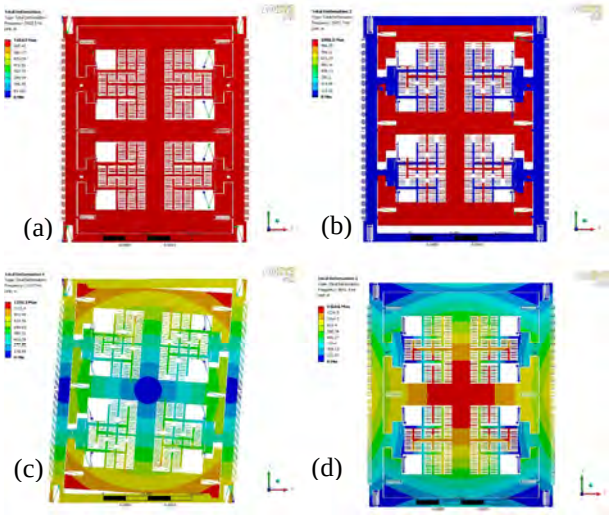

Figure 6 : *Resonant mode shapes with undeformed shape, a) the drive mode; b) the sense mode; c) the third mode; d) the forth mode;*

The dimension of the design is 4.2×4.2×0.05 mm^3, the total mass is about 1.88e-6 kg. The natural frequency of drive mode is 5932 Hz and 5970 Hz for sense mode with 0.7% mismatch. The resonant mode shapes is shown in Figure 6. The natural frequency of third mode is 9541Hz. ANSYS™ has also been used to obtain the displacement response to the natural frequencies and to simulate the effect of two direction force load by harmonic analysis. In our simulation, the parameters we used are listed as the following, the Young's Modulus is 165 GPa, the density is 2330 kg/m^3, the damping ratio is 0.0001, the thickness of structure layer is 50 μm, and the force load is 1 μN along the X-axis. We define a ratio η_{DtS} to characterize mode coupling error. The ratio (η_{DtS}) of drive mode to sense mode decoupling $\eta_{DtS}=A_{S\text{-}Y}/A_{D\text{-}X}$, where $A_{D\text{-}X}$ is the displacement of drive frame in X-axis in the drive mode and $A_{S\text{-}Y}$ is displacement of sense frame in Y-axis in the same time. The η_{DtS} was obtained as 430~750 ppm by harmonic analysis.

B. Simulation of Mode coupling error

The Simulink was used to simulate the mode coupling error. Assuming the drive mode and sense mode are perfectly matched, and then the angle β was introduced to define the anisoelasticity error.

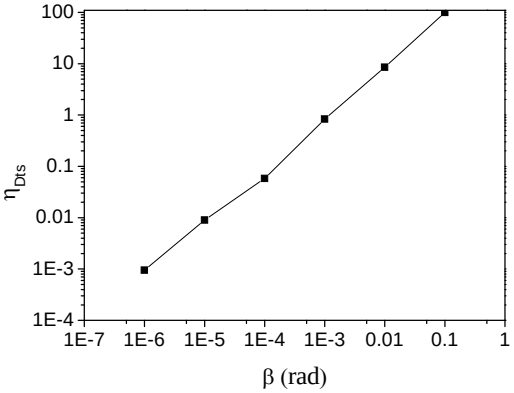

Figure 7*: Responding of η_{DtS} to β*

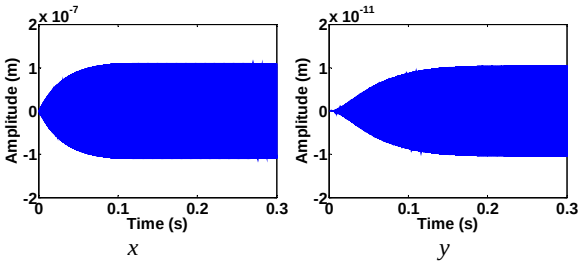

Figure 8*: Amplitude vs time of the mode coupling error responding, (β=1e-7)*

the responding of η_{DtS} to β is shown in Figure 7. When changing the β from 1e-6 to 1e-1 by a step of 10, the η_{DtS} increase sharply after β of 1e-3 and the η_{DtS} is above 1. That means the displacement of sense mode is close to the displacement. When the β is lower than 1e-4, the anisoelasticity error can be neglected due to drive amplitude almost unchanging with β. The amplitudes in drive mode and sense mode are shown in Figure 8. The mode coupling excites the sense mode to oscillate when β is 1e-7 rad. Generally, the span of the proof mass is about 3 μm due to its small sensing gap. For the relative tuning angle of 0.1° (~0.001 rad), the electrostatic coupling error cancellation in the novel design can be used to minimize the mode coupling error effect.

IV - Conclusion

The novel partially decouple microgyroscope is present. the new design consist of drive frame, proof mass, springs, isolation connection, and movable sense electrode. The movable sense electrodes connect drive frame and proof mass. The suspension structure can be tuned by electrostatic force to lower the mode coupling effect. The modeling of mode coupling error was made based on the Newton's second law. Due to necessity of the isolation trench, the oxidation process was also performed. The ANSYS and Simulink have been used to perform the modal analysis, harmonic analysis and the mode coupling error. According to the results, the mode coupling error influence the output dramatically even the angle β is small as 1e-3 rad. For The relative tuning angle is 0.1° (~0.001 rad), the electrostatic coupling error cancellation in the novel design can be use to minimize the mode coupling error effect.

References

[1] W.A. Clark, , Howe R. T., and R. Horowitz, *Digest of Solid-State Sensors and Actuator Workshop*, pp 283-287, 1996

[2] Y. Mochida, M. Tamura, K. Ohwada, *Micro Electro Mechanical Systems, 1999. MEMS '99. Twelfth IEEE International Conference on* , pp.618-623, 17-21 Jan 1999

[3] A. Shkel, R. T. Howe, and R. Horowitz, Int. Conf. Modeling Simulation of Microsystems, Puerto Rico, pp 605-608, April , 1999

[4] Cenk Acar, Ph.D. Thesis, University of California Irvine, 2004

[5] Y. Y. Bao, Liang, C. L. Yung, E. H. Francis, *Analog Integrated Circuits and Signal Processing*, vol. 29, pp 85-94, 2001

[6] I. Sitaraman, Z. Yong and M. Tamal, *Modeling and Simulation of Microsystems*, pp. 632–635, 1999.

[7] Y. Ansel, Ph. Lerch, Ph. Renaud, Mode coupling error aspects in a vibrating gyroscope, *Sensors and Actuators A*, vol. 62, pp 576-581, 1997

[8] A. Shkel, R. T. Howe, R. Horowitz, In: *International conference on modeling and simulation of microsystems*, pp 605–608 , 1999

[9] E. Tatar, S. E. Alper, T. Akin, *Micro Electro Mechanical Systems (MEMS), 2011 IEEE 24th International Conference on* , pp.569-572, January 23-27 2011

[10] W. Geiger, W. U. Butt, A. Gaiβer, J. Frech, M. Braxmaier, T. Link, A. Kohne, P. Nommensen, H. Sandmaier, W. Lang and H. Sandmaier, *Sensors and Actuators A*, Vol 95, pp. 239-249, 2002

DISK-BASED PROTEIN NANOARRAY USING DIP-PEN NANOLITHOGRAPHY

Hui-Hsin Lu[1], Chia-Jen Yeh[1], Yu-Hui Lin[1], Chii-Wann Lin[1,2,3*], Joseph Zyss[4]

[1] *Institute of Biomedical Engineering, National Taiwan University, Taiwan*
[2] *Department of Electrical Engineering, National Taiwan University, Taiwan*
[3] *Institute of Applied Mechanics, National Taiwan University, Taiwan*
[4] *Institut d'Alembert, Ecole Normale Supérieure de Cachan, Cachan, France*
**Corresponding author: Prof. Chii-Wann Lin, cwlinx@ntu.edu.tw*

***Abstract* —We reported the first development of a CD-based bioassay device by dip-pen nanolithography (DPN) for expanding the screening density of biomolecuar array toward higher CD storage capacity in this study. The array made of hydrogel mixed with 60 nm gold nanoparticles were deposited on the various gold coated substrates to compare the effects of localized surface plasmon resonance (LSPR) caused by gold nanopartices and gold coated CD track patterns, which has potential to enhance the signals of biomolecular interaction in the nanoarray. Our results show that the pitches of array is adjustable and precise to match the pitch of CD tracks patterns, and the hydrogel array with gold nanoparticles has strong LSPR effect to develop a CD-based bioassay device with high throughput.**

Keywords : **Hydrogel, Nanoarray, CD-based bioassay, Dip-pen nanolithography, Gold nanoparticles**

I - Introduction

Optical disks provide several advantages for bioassay other than their traditional uses for the storage the digital information. The driving force for a compact disc read-only memory (CD-ROM) drive to read the information stored in the disk is also used to provide the centrifugal force or the flow of solution for the biomolecular interaction. Hence, many CD-based microfluidic chips have been invented for the biomolecular detection and also applied it for the disease diagnosis in the practical applications. [1-2] The size of such optical disk-based bioassay devices is smaller than these equipments in biochemical laboratory or clinical laboratory, and the cost to fabricate these chips is also low due to adopting the disposable materials.[3-4]

The track patterns with pits in the optical disks are the location to store the digital information for the computer files. Moreover, the device used to couple the surface plasmon resonance (SPR) could be prism-based and grating-based. [5-6] Thus, the track patterns in the optical disk are able to be a coupler adopted to SPR detection. Bipin K. Singh *et al.* proposed a SPR sensor array based on the grating substrate on CD by coating with gold film and applied it to detect the biomolecular interactions. [7] Although SPR provides the high sensitivity for the biomolecular detection, the dot sizes in these sensor arrays are about a few hundred micrometers. The track patterns in their studies are only for coupling the incident light, and the size of whole system, including optical system, is too large for the applications of point of care. Yunchao Li *et al.* proposed a digital signal readout protocol for screening disk-based bioassays with a standard optical drives of ordinary desktop/notebook computers. The detection site for biomolecules was on the polycarbonant layer, and the metal nanoparticles were deposited for enlarging the interacting signals of biomolecular binding.[8] Their result has potential for rapid, low-cost, and high-throughput biomedical diagnostics, but the size of sensing site is at the millimeter scale. Here, we propose to deposit the array with the nanometer size for matching the pitch of the track patterns on CD by dip-pen nanolithography (DPN). DPN provides high spatial registration and mask-free to rapidly make array for biomilecular interaction.[9] Herein, the hydrogel arrays made by DPN were deposited directly on CD and were imaged by the optical microscopy. For the biomolecular detection with low concentration and small volume in these arrays, the gold nanoparticles and latex beads doped with fluorescence dye mixed individually in the hydrogel were deposited on the various the gold surface, and then the absorption curves of these specimens were collected to explore the effect caused by localized surface plasmon resonance (LSPR).

II - Experimental Details

The hydrogel were composed by the solid phase of Poly(ethylene glycol) dimethacrylate (Mn=1000) (Polysciences Inc., U.S.A) and the liquid phase of Poly(ethylene glycol) dimethacrylate (Mn=550) (Sigma-Aldrich Co, U.S.A). The mixed ratio in volume is 2: 1. The mixed solution was treated by a vortex genius for 5 minutes and then by the ultra-sonic processor for 30 minutes. The 30 nm latex beads doped with fluorescein (Sigma-Aldrich Co., U.S.A.), and 60 nm gold nanoparticles (Colloidal Nanogold, BBI International, U.K.) were added in this mixed solution, respectively, with a ratio of 4:1. Before starting the experiment of making array patterns, the 5% (volume ratio) photo-initiator was added in this mixture.

The glass substrates are the common glass slides with a size of 1 by 3 inch^2. The CD was purchased from local company (RiTEK Co.) in Taiwan. The CD's polycarbonate layer was removed at first, and then a small piece of reflection layer and dye layer was tore by a tweezers with sharp tips and then fixed on the gloss

slide by a twin adhesive tape. The gold film with a thickness of 50 nm was deposited on the surfaces of glass slides and CD by an electron beam evaporator (FulinTec Engineering Co，Taiwan).

A few micro-liters of mixture were put in the inkwell (NanoInk, U.S.A) with a micropipette. The type M probe with 12 pens (NanoInk, U.S.A) was mounted in DPN machine (NanoInk Inc., U.S.A) and was used to dip the solution in inkwell before patterning. The dwell time that is the time when probe contacts with surface of substrate is ranged from 0.1 s to 1 s per dot. After patterning, the specimen was treated by an ultra-violet light (Compact UV lamp 254/365 nm, Entela Co., Taiwan) for 90 minutes. The array patterns were imaged by an optical microscopy (Zeiss Corp., Germany) embedded with a spectroscopy (HORIBA Jobin Yvon, U.S.A).

III - Results and Discussion

The hydrogel array was patterned by the type M probe with 12 probes, and the pitches of arrays were 4.5 μm and 3 μm. After treating by ultra-violet light, the hydrogel dots became hardened. Figure 1 is shown the optical images of dot array with a dwell time of 0.5 s per dot and with a pitch of 4.5 μm (Figure 1 (a)) and 3 μm (Figure 1 (b)) imaged by the dark-field microscopy with a white light source, so the background of dots is black, and only the light scattered by dots would be collected. Due to the hydrophilic property of hydrogel, the surface wettability of substrates produces the influence for the formation of dot in the array. The shape of hydrogel dot becomes round as the surface is hydrophobic. The substrate in Figure 1 is made by gold film with a contact angle of 67∘, so the shape of dot is not regular. Another reason to cause the irregular pattern shapes is the used probe. The working principle of patterning by DPN is operated without feedback and is to deposit the pattern directly by forcing the probe contacted to surface of substrate. The repeatable usage would make the probe disintegrated. Hence, the there are two or three points in the dot shown in Figure 1. Moreover, the pitch is decided by the software that is used to design the patterns of hydrpgel, and thus, the pitches of array in the results of Figure 1 have a small difference compared with the scale bar in the optical image.

For patterning the hydrogel dot array on CD surface, the direction of track patterns on the disk should be adjusted to correspond to the orientation where the DPN start to pattern. As shown in Figure 2 (a), no track patterns are observed using a 10X objective lens, so the orientation of CD substrate was fixed position under a 100X objective lens. The result of patterning the hydrogel array with a pitch of 10.5 μm on the CD surface is shown in Figure 2 (b). Note that the pitch of CD track patterns is about 1.5 μm. The patterns on the gold coated CD surface are smaller than its in the Figure 2 (b). This result indicates that the dot array made of

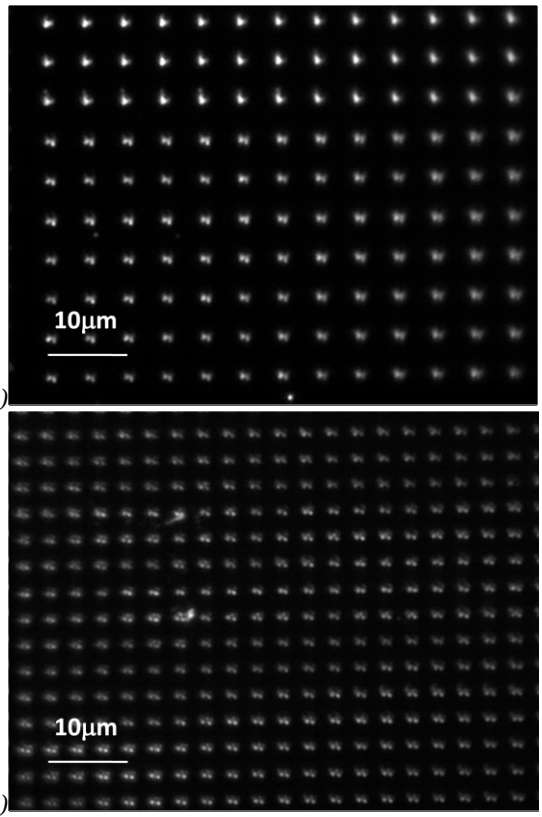

(a)

(b)

Figure 1 Optical images of hydrogel array with pitches of 4.5 μm (a) and 3 μm (b) by the dark-field microscopy with an objective lens of 100X.

hydrogel is well-aligned using DPN. The shapes and sizes of dot are able to be fine-tuned by changing the surface wettability and dwell time, respectively, to match the CD's track patterns. The final aim of our study is to deposit the dots on the pits' locations on the tracks, and thus, in this way this CD-based bioassay made by DPN has a potential for a plenty of sites that is as large as CD's capacity for bioassay. By the way, it is also possible to apply to other type of optical disks.

The hydrogel mixed with 60 nm gold nanoparticles was patterned on the gold surface of glass slides. In Figure 3 (a), the pitch is about 3 μm. Figure 3 (b) is the result of nanoarray mixed with 30 nm latex beads. White light was used to illuminate these two specimens in dark-field microscopy, and the same acquisition time of 0.1 s for both two images in Figure 3. The intensity of latex beads is brighter than it of gold nanoparticles, because the latex beads have been doped with fluorescein. Both of gold nanoparticles and latex beads have been treated by the amine and carboxylate modification that could be applied for the protein assay by a covalent bonding.

The absorption spectra of the above specimens were collected to show the interaction caused by localized surface plasmon resonance (LSPR) between gold nanoparticle and gold coated track patterns of CD surface. In Figure 4, the solid line is the absorption curve of gold coated CD surface, and the broad band ranged from 450 nm to 550 nm is caused by the surface

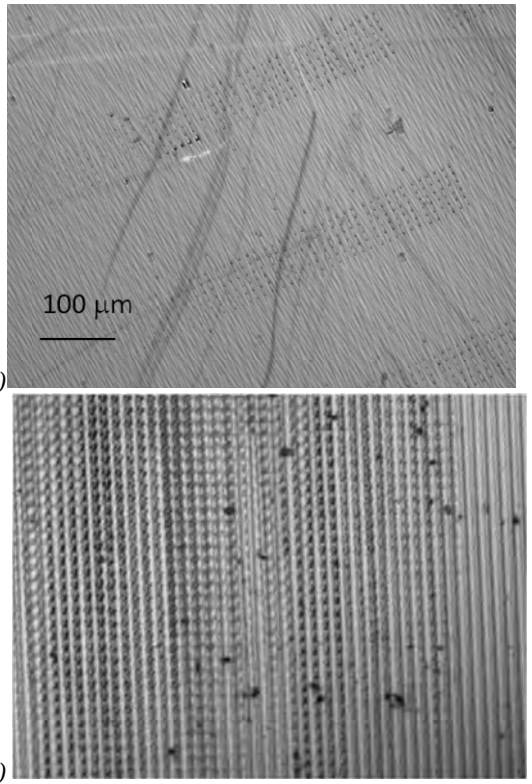

(a)

(b)

Figure 2 The dark-field images of hydrogel array, dwell time of 1s per dot, on the CD surface by 10X objective lens (a) and 100X objective lens.

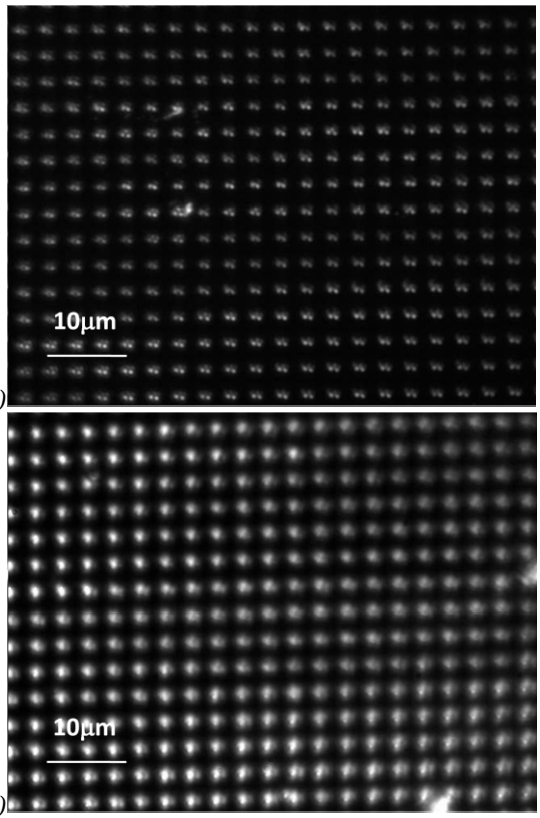

(a)

(b)

Figure 3 Dark-field images of hydrpgel array mixed with (a) 60 nm gold nanoparticles and (b) 30 nm latex bead.

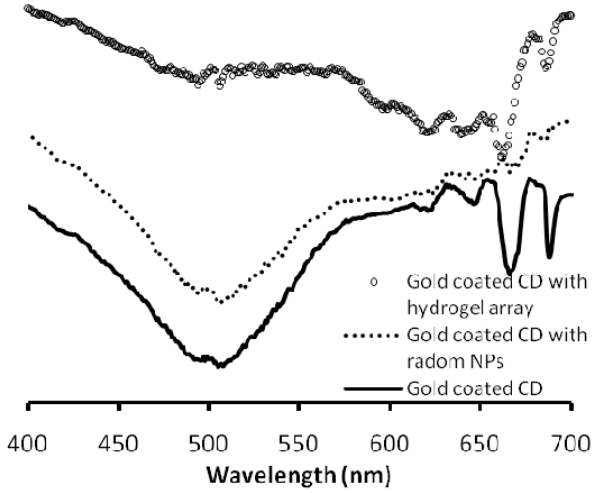

Figure4 absorption spectra of gold coated CD surface (solid line) and gold coated CD surface with random distribution of gold nanoparticles (dash line). The circle line is spectral subtraction from the hydrogel array mixed the gold nanoparticles on the gold coated glass surface and gold coated CD surface.

plasmon resonance (SPR) of gold film. The same phenomenon also appears in the absorption curve, dash line, of gold coated CD surface with the random distribution of 60 nm gold nanoparticles. Then three peaks at 628 nm, 650 nm and 677 nm and two deeps at 664 nm and 688 nm in solid line represent the SPR effect. However, the three peaks and two deeps are not apparent as randomly distributing the gold nanoparticles on this gold coated CD disk, which may cause by canceling the vectors of electrical fileds between the gold nanopartices and gold coated track patterns. The circle line is the result of subtraction of spectra from the specimens that are the hydrogel array mixed the gold nanoparticles on the gold coated glass surface, in Figure 2 (b), and gold coated CD surface, Figure 3 (a). Hence, the broad peak in the range from 450 nm to 550 nm is removed due to the spectral subtraction. The peaks and deeps from 600 nm to 700 nm are apparent due to the gold coated track patterns on CD, and thus, there are obvious three peaks, 627 nm, 649 nm and 678 nm, and two deeps, 660 nm and 685 nm, in the circle line. The main reason to have peaks and deeps in the circle line is from the gold coated CD track patterns, but compared to solid line, the locations of these peaks and deeps in wavelength are a little shifting, and their intensities are not identical, which means that the LSPR produced from gold nanoarticles in hydrogel array affects the behavior of LSPR of gold coated CD track patterns. Moreover, compared to the dash line with the circle line in the range from 600 nm and 700 nm, the gold nanoparticles deposited by DPN represent the stronger LSPR effect than them randomly distributed on gold coated CD surface.

IV - Conclusion

In this study, we demonstrate the deposition of the hydrogel array on the CD surface by DPN. The results

show that the array is precisely deposited on the CD tracks and matched the pitch of track well. The amine-modification gold nanoparticles and latex beads doped with fluorescein were mixed with the hydrogel and were deposited on the gold coated glass and CD surface, which shows the potential to apply it for advanced biomolecular detection. Additionally, the spectral results demonstrate that the hydrogel array contained with gold nanoparticles on the gold coated CD has stronger effect of localized surface plasmon resonance than the gold nanoparticles randomly distributed on the same substrates. Based on these results, the CD-based bioassay with hydrogel array made by DPN could be applied on the large amount of examination than before, which is possible to approach the storage capacity of CD. The readout method of our CD based bioassay device will integrated with the current commercial compact CD drive in the future.

Acknowledgments

The authors would like to thank the National Science Council of the Republic of China, Taiwan, for financially supporting this research under Contract No. NSC 99-2221-E-002 -117 -MY3. Nanoink Co. is appreciated for the technical support.

References

[1] D. D. Nolte, *Review of Scientific Instrument*s, vol. 80, p. 101101, 2009.
[2] J. J. La Clair and M. D. Burkart, *Organic & Biomolecular Chemistry*, vol. 1, pp. 3244-3249, 2003.
[3] A. Rothert, et al., *Analytical Biochemistry*, vol. 342, p. 11, 2005.
[4] M. Pallapa, et al., *Sensors and Actuators B: Chemical*, vol. 148, pp. 620-623, 2010.
[5] J. Homola, et al., *Sensors and Actuators B: Chemical*, vol. 54, pp. 16-24, 1999.
[6] J. Homola, et al., *Sensors and Actuators B: Chemical*, vol. 54, pp. 3-15, 1999.
[7] B. K. Singh and A. C. Hillier, *Analytical Chemistry*, vol. 78, pp. 2009-2018, 2006.
[8] Y. Li, et al., *Analytical Chemistry*, vol. 80, pp. 8216-8223, 2008.
[9] P. L. Stiles, *Nat Meth*, vol. 7, 2010.

DESIGN OF A RESONANT TRIAXIAL NANOPROBE FULLY INTEGRATED IN A SILICON SUBSTRATE

B. Goj[1], M. Hoffmann[1]

[1]*Ilmenau University of Technology; IMN MacroNano®; D-98693 Ilmenau, Germany*

***Abstract* — We present the design of a resonant triaxial nanoprobe. The complete integration of three axes, the resonant motion in three axes, and the almost equal x-, y- and z-stiffness are the main features of the system.**

***Keywords :* triaxial nanoprobe, CMM – coordinate measurement machine, resonant capacitive probe**

I – Introduction

The probing system is the crucial part of coordinate measurement machines (CMM). Its task is to measure the geometrical parameters of an object (e. g. topology, roughness). Therefore, it is necessary to scan points of a workpiece (in contact or non-contact mode) with a sensing device. [1]

This paper is focused on triaxial tactile probing systems which basically consist of a tip ball, a stylus, a passive suspension, as well as sensors and actuators (Fig. 1).

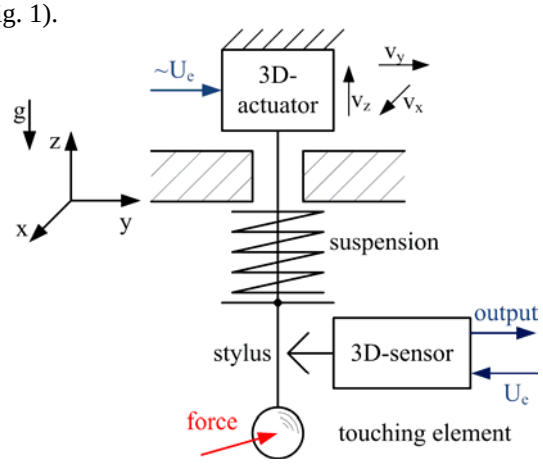

Figure 1: *Parts of tactile probing systems*

Resonant scanning is favourable in order to avoid sticking effects between the tip ball and the workpiece. Nevertheless, most probing systems work in non-resonant mode. Disadvantages of a static system are low measurement accuracies and higher measurement times because of the static contact regime, [1-4].

The connection between stylus and passive suspension is challenging during the design process of a probe. Common systems (see Table 1 for state-of-the-art systems) need a coupling between stylus and suspension. This leads to an undefined position of the tip ball and thereby to lower measurement accuracy.

The aspired system obviates the disadvantages of commonly used probing systems. It features three oscillations (perpendicular to each other) to avoid sticking effects. Electrostatic actuators and a passive suspension are utilized to generate resonant movements with a frequency in the kilohertz range. Position sensing is realized by capacitive sensors. That simplifies the fabrication.

The components of the triaxial nanoprobe are designed for integration in a shared silicon substrate. Thus, there is neither coupling between stylus and tip ball what increases the measurement accuracy of the system, nor assembly of the different axes is required.

Table 1: *Commonly available triaxial probing systems*

	Balldiameter in µm	**Stiffness in N/m**	**Frequency in kHz**
Fan 2010 [2]	100	11 - 119 (z)	-
Dai 2009 [3]	300	6,8 - 175 (z)	-
XPRESS [4]	50 - 500	10 - 50 (z)	-
Woody 2003 [5]	4000	10.000	10-50 (2 axes)
SBL 2010 [6]	50 - 70	167	1 (z - axis)
Femtotools [7]	-	-	2 (z - axis)
Ogura 2002 [8]	700	-	0,01 (2 axes)
Nanoprobe (IMN)	10 - 100	5 - 20	1 - 3 (3 axes)

II – Design of the triaxial nanoprobe

The principle of the triaxial nanoprobe is shown in Fig. 2. The system is guided by a spring arrangement which has three different stiffnesses in three Cartesian directions. Thus, it is possible to oscillate the mass with different resonant frequencies for x-, y-, and z-direction. This allows an independent measurement of the three oscillations by electronic filtering. The oscillations are unsymmetrically damped if the tip ball resides near the workpiece. Thereby, the modulation of the three oscillations depends on the contact point between the workpiece and the tip ball. If the contact point is in coincidence with the y-axis, moszly the oscillation in y-direction is damped and the frequency is decreased. [1, 5]

The actuators in y- and z-direction are interdigital capacitors. A plate capacitor is utilized in x-direction. The independent motion of the three actuators is realized with an adapted design of the electrode fingers. On the one hand, the fingers have steps so that a motion in y-direction does not change the capacitance of the z-direction (Fig. 2). On the other hand, the moved fingers have a smaller height than the fixed fingers. After a voltage U_x is applied and the electrodes are in the middle position, movement in x-direction has small influence on the capacitances of the y- and z-direction (cf. Fig. 2).

The position of the nanoprobe is sensed by three sensor evaluation boards HT 133 (GEMAC GmbH,

Germany). Three additional flexible measurement capacitances and three fixed reference capacitances are necessary to sense the position of the nanoprobe. The motion of the actuators is independent from the sensor voltages because the frequency of the pulsed signal is much higher than the mechanical frequencies of the nanoprobe (cf. section 3c).

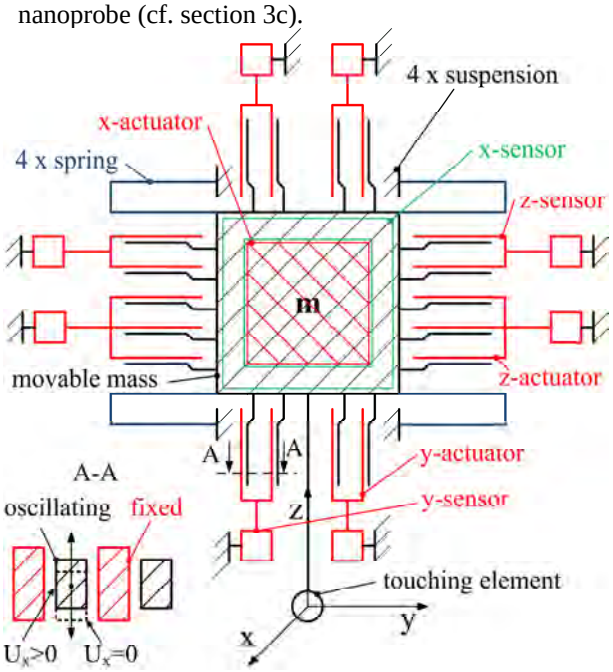

Figure 2: *Principle design of the nanoprobe*

A Silicon-On-Insulator substrate (SOI substrate) is utilized to fabricate the triaxial nanoprobe. The structuring of the device layer is designed for a deep reactive ion etching (DRIE) process that allows high aspect ratios. The structuring of the backside can be done utilizing wet etching (KOH) or dry etching (DRIE).

The fully integrated fabrication of the nanoprobe in one SOI substrate is an innovative approach. The fabrication of the spherical touching element in silicon is a challenge. Some approaches are described in literature, but not for silicon. [9-10]

III - Dimensioning of the triaxial nanoprobe

The design of the triaxial nanoprobe includes different calculations und simulations:

1. Simulation of different springs
2. Design of the actuators
3. Design of the sensors

The dimensioning of the nanoprobe is described in the following sections. Important boundary conditions for the dimensioning are given in Table 2.

Table 2: *Boundary conditions for the nanoprobe*

Condition	Value
Environment	air
Pressure	1 bar
Temperature	20°C, constant
Substrate	SOI

A. Simulation of different miniaturized springs

A variety of springs can be applied in micro systems, [11]. However, only arrangements as illustrated in Figure 3 are investigated for the nanoprobe. Membranes or cantilevers are not investigated because they have in general two soft stiffness directions and one hard stiffness direction. This is disadvantageous for the sensitivity of the nanoprobe.

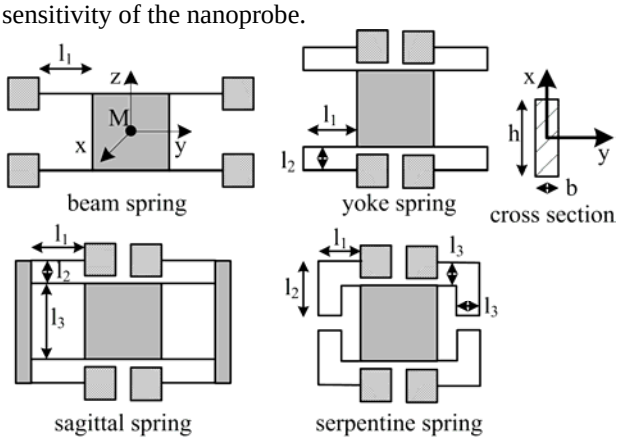

Figure 3: *Investigated 4-spring arrangements*

The goal of the mechanical simulation in ANSYS is to find a spring arrangement which has slightly different stiffnesses in the Cartesian coordinate directions. Thus, different resonance frequencies occur and a separate evaluation of the oscillations is possible. The stiffness has to be in the same range of magnitude (5 to 20 N/m) for all three axes to gain a nearly equal sensitivity in each spatial direction.

The solutions based on ANSYS simulations are shown in Table 3. The force was applied in the centre of gravity M of the mass. The height h of the springs was set to 100 µm and the width b to 10 µm (Fig. 3).

Table 3: *Best solutions for different springs*

Spring	C_x N/m	C_y N/m	C_z N/m	l_1 mm	l_2 mm	l_3 mm
Beam	8000	5,1	2700	2,2	-	-
Yoke	15,8	10,9	5,0	1,73	0,80	-
Sagittal	1706	5,0	396,4	2,0	0,5	2,0
Serpentine	19,8	4,9	9,9	1,29	1,65	0,13

An arrangement of serpentine springs is the favoured passive suspension for the nanoprobe (cf. Table 3). On the one hand, the dimensions of the spring are small in comparison to the other springs. On the other hand, the stiffness's are in the same range of magnitude. The relative difference between the stiffness of z- and y-direction is four.

B. Dimensioning of the actuators

The nanoprobe was separated to three subsystems for the dimensioning process. This simplification is possible because the Cartesian directions are independent from each other. [12]

The electro-mechanical circuit of one separated actuator is shown in Figure 4. The system (Equation 1-3)

cannot be solved directly because it is a nonlinear differential equation system of second order. [13, 14]

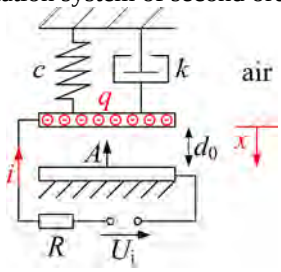

Figure 4: *Electro-mechanical circuit of one actuator*

$$\dot{q} = \dot{x_1} = \frac{1}{R}\left(U_\mathrm{i} - \frac{x_1\,(d_0 - x_2)}{\varepsilon \cdot A}\right) \tag{1}$$

$$\dot{x} = \dot{x_2} = x_3 \tag{2}$$

$$\ddot{x} = \dot{x_3} = \frac{1}{m}\left(\frac{x_1^2}{2 \cdot \varepsilon \cdot \mathrm{A}} - c \cdot x_2 - k \cdot x_3\right) \tag{3}$$

With Taylor's theorem and the Jacobian matrix a linearized differential-equation-system is generated which is valid for small oscillations around an operating point. [14]

$$\begin{pmatrix} \mathrm{d}\,\dot{x_1} \\ \mathrm{d}\,\dot{x_2} \\ \mathrm{d}\,\dot{x_3} \end{pmatrix} = \left.\begin{pmatrix} \frac{d_0 - x_2}{R\,\varepsilon\,A} & \frac{-x_1}{R\,\varepsilon\,A} & 0 \\ 0 & 0 & 1 \\ \frac{x_1}{m\,\varepsilon\,A} & \frac{-c}{m} & \frac{-k}{m} \end{pmatrix}\right|_{\substack{\vec{x_0} \\ \vec{u_0}}} \begin{pmatrix} \mathrm{d}\,x_1 \\ \mathrm{d}\,x_2 \\ \mathrm{d}\,x_3 \end{pmatrix} + \left.\begin{pmatrix} \frac{1}{R} \\ 0 \\ 0 \end{pmatrix}\right|_{\substack{\vec{x_0} \\ \vec{u_0}}} \mathrm{d}\,U_\mathrm{i} \tag{4}$$

The electrostatic force is calculated using Equation 5.

$$F_e = \frac{A \cdot \varepsilon}{2 \cdot d^2} \cdot U_\mathrm{i}^2 \tag{5}$$

A voltage supply $U_\mathrm{i} = U_0 + U_0 \sin(\omega t)$ is assumed to get a sinusoidal waveform of the actuator motion. This generates a motion with the same frequency ω as the AC voltage which is advantageous for measurement tasks, [13]. The insertion of U_i into (5) and some trigonometric transformations lead to Equation (6).

$$F_\mathrm{e} = \frac{A\varepsilon}{2d^2} U_0^2 \left(\frac{3}{2} + 2\sin(\omega t) - \frac{1}{2}\cos(2\omega t)\right) = F_0 + F_1 + F_2 \tag{6}$$

The force F_0 generates an offset for the actuator position due to the constant component of U_i. F_1 and F_2 generate two harmonic oscillations. If the system is running near the resonant frequency ($\omega = \omega_r$) the sinus oscillation due to F_1 is much larger than cosine oscillation due to F_2. Thus, the waveform of the actuator motion is nearly sinusoidal because the influence of the force F_2 can be neglected. [13]

The following different damping effects are considered in the calculation: slide film damping on the bottom and the top side, side wall damping and air drag force damping.

The mathematically description of the damping effects is not presented here. However, the utilized equations to calculate the damping constant can be extracted from [13].

Table 4 gives a short overview of the calculation, including input and output parameters.

Table 4: *Results of actuator dimensioning*

	x-axis	**y-axis**	**z-axis**
Voltage U_0	1,8 V	1,3 V	1,9 V
Voltage U_1	26,3 V	1,3 V	1,9 V
mass m	$9{,}4\cdot10^{-4}$ g	$9{,}4\cdot10^{-4}$ g	$9{,}4\cdot10^{-4}$ g
stiffness c	9,9 N/m	4,9 N/m	20,0 N/m
damping k	$4{,}3\cdot10^{-4}$ kg·s	$7{,}4\cdot10^{-6}$ kg·s	$7{,}7\cdot10^{-6}$ kg·s
distance d_0	20 µm	20 µm	20 µm
Capacitance C	1,7 pF	1,2 pF	1,2 pF
Frequency ω	3251 Hz	2304 Hz	4608 Hz
Offset X_0	6 µm	10 nm	5 nm
Amplitude X	6 µm	6 µm	6 µm

The magnitude of the oscillation is limited to one third of the plate distance d_0 in order to avoid pull-in. A higher magnitude could be achieved if an additional capacitor is utilized to avoid the pull-in effect [12].

A Matlab SIMULINK simulation was additionally applied to investigate the influence of parasitic capacitances between the electrode fingers. The gap between one pair of electrode fingers is three times d_0.

Fig. 5 shows that the parasitic capacitance damps the oscillation of the actuators. The sinusoidal waveform and the frequency are obtained.

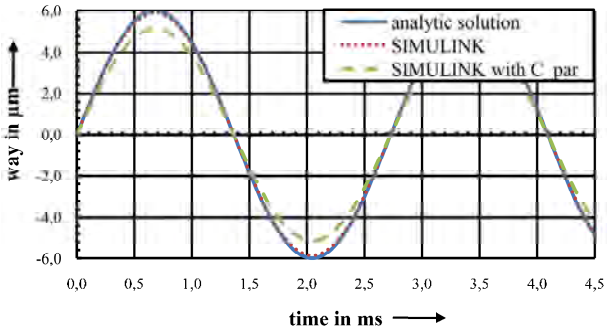

Figure 5: *Comparison of the analytic calculation and the simulation of the y-actuator motion*

Table 5: *Properties of the evaluation board HT 133*

Property	**Value**
Supply voltage	5 V, DC, 500 kHz (pulsed)
Power consumption	7,5 mW
Sensor capacitance	< 30 pF
Resolution	0,2 fF
Output signal	Digital, 11bit + sign

C. Sensing of the actuator position

The capacitances are measured utilizing three evaluation boards HT 133 (GEMAC GmbH, Germany). This electronic device measures differential capacitances in a range of 0,32 pF to 4 pF. Other properties are shown in Table 5. The position of the nanoprobe is sensed by three capacitors (C = 0,32 pF). Three refer-

ence capacitors (C_r = 0,32 pF) are needed in addition to build up a differential system as required by the board HT 133.

The influence of the sensor force on the actuator motion is very low because of the high pulse frequency and the low sensor capacitance. The forces of the z-actuator are shown in Fig. 6. The parasitic force damps the oscillation as mentioned in section B. The sensor add an oscillation with low magnitude and high frequency (f_{sensor} >> f_R) to the actuator force but the mass cannot follow the sensor frequency.

The output voltages of the sensors are shown in Fig. 7.

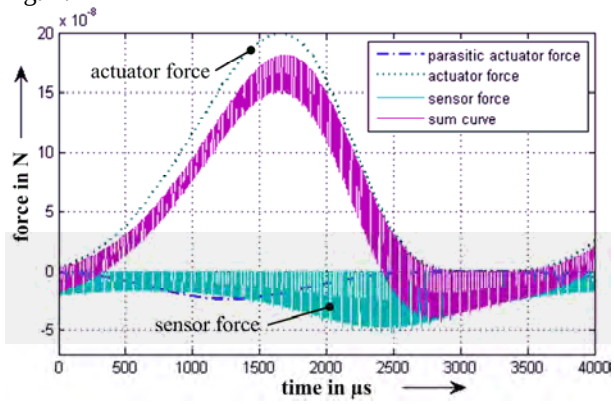

Figure 6: *Balance of forces for the y-actuator (Based on Matlab SIMULINK model comparable to [14])*

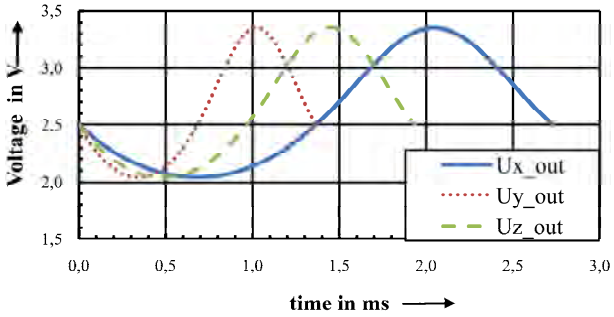

Figure 7: *Output voltages of the sensor capacitors*

IV - Conclusion

The future trends in the design of tactile probing systems are higher manufacturing precision, a higher grade of miniaturization (e. g. to measure MEMS), and a faster measurement speed, [1]. The design of a tactile triaxial nanoprobe is presented which achieves the requirements to future probing systems.

The fully integrated design in a silicon substrate avoids coupling elements and increases the manufacturing accuracy as well as the silicon micromachining process itself.

The good scalable design of the nanoprobe is another advantage. Common systems cannot utilize touching elements with small diameters because of sticking effects (van-der-Waals forces). The nanoprobe obviates that problem because of the resonant measurement mode, [4].

The measurement speed is also increased utilizing a resonant touching regime. A scanning mode is possible (in non-contact measurements) which is more economical because of low measurement times.

In further works, different 1D and 2D probes will be tested to prepare the fabrication of the triaxial nanoprobe. The independent motion of the three axes has to be demonstrated as well as the independent damping of the resonant oscillations near a workpiece.

Acknowledgement

The presented works were funded by the German Research Foundation (DFG) under contract SFB 622.

References

[1] Weckenmann, A. et al: Probing Systems In Dimensional Metrology. In: Annals of the 54th CIRP General Assembly, p. 657-684, February 2004

[2] Fan, K.-C. et al.: A scanning contact probe for a micro-coordinate measuring machine (CMM). IOP Publishing - Meas. Sci. Technol. 21, 2010

[3] Dai, G. et al.: A high precision micronano CMM using piezoresistive tactile probes. IOP Publishing: Meas. Sci. Technol. 20, 2009

[4] XPRESS B. V.: Gannen XM- Ultra Precision tactile scanning. [Online]. Available (12th April 2011): http://www.xpresspe.com/probe_xm1.htm

[5] Woody, S. C.; Smith, S. T.: Resonance-based vector touch sensors. Elsevier: Precision Engineering 27, p. 221-233, 2003

[6] Stoyanov, S. et al.: Modelling and Prototyping the Conceptual Design of 3D CMM Micro-Probe, IEEE: 2nd Electronics System integration Technology Conference, Greenwich (UK), 2008

[7] Femtotools GmbH: FT-S540 Force Sensing Probe. [Online]. Available (12th April 2011): http://www.femtotools.com/index.php?id=31

[8] Ogura, I.; Okazaki, Y.: Development of micro probe for micro-CMM. In: ASPE Proceedings, October 20 - 25, 2002

[9] Fan, K.-C. et al.: Fabrication optimization of a micro-spherical fiber probe with the Taguchi method. IOP Publishing – Journal of Micromechanics and Microengineering 18, 2008

[10] Sheu, D.-Y.: Micro-spherical probes machining by EDM. IOP Publishing: Journal of Micromechanics and Microengineering 15, p. 195-189, 2005

[11] Gerlach, G.; Dötzel, W.: Introduction to microsystem technology - A guide for students. West Sussex (UK): John Wiley and Sons Ltd., 2008

[12] Hahn, H. G.: Technische Mechanik fester Körper. München: Hanser Verlag, 1992

[13] Bao, M. H.: Micro Mechanical Transducers. Elsevier: Handbook Of Sensors And Actuators 8, Amsterdam, 2000

[14] Senturia, S. D.: Microsystem Design. Boston: Kluwer Academic Publishers, 2001

CHARACTERIZATION OF METALLIC WAFER LEVEL BONDING FOR HERMETIC APPLICATIONS

Ani Duan, Kaiying Wang, Knut Aasmundtveit, and Nils Hoivik

HiVe - Vestfold University College, Department of Micro and Nano Systems Technology (IMST, Norway)
Postbox 2243, N-3103 Tønsberg, Norway
Email: Ani.Duan@hive.no

***Abstract*—To avoid contamination and ensure stable and reliable performance for MEMS (micro electro mechanical systems) devices, they may require to be operated in a vacuum environment. Wafer level hermetic bonding is one of the main requirements for successful micro-packaging. However, the hermetic package for some devices is required to guarantee that the atmosphere inside the cavity remains stable during the lifetime of the device. How can one test whether such a package is hermetic? The purpose of this paper is to review and present how traditional hermeticity test done when applied to typical MEMS cavity volumes. The optical leak test structure have been designed and fabricated for estimate the leak rate of ultra-low cavity through observation of a deformed membrane using interferometer equipment. This hermetic test method has been successfully performed on wafers bonded using anodic bonding, glass frit and the result and provides a starting point for further investigation into wafer level metallic bonding.**

Keywords: **MEMS, wafer level packaging, hermetic testing, metallic bonding.**

I - Introduction

Most MEMS devices contain movable and fragile parts whose operating responses are sensitive to variations of ambient conditions such as contamination, moisture, changes in gas content or pressure. For the packaging of such a MEMS device, it should be hermetic in order to preserve these environmental conditions. Hermeticity testing is commonly done using the MIL-STD-883 test method [1]. Pushed by advances in micromachining, package volumes are decreasing and current leak detection methods are no longer sensitive enough. It was shown both experimentally and theoretically [2] that MIL-STD-883 standards are not always suitable for microsystem packages.

This paper discusses this problem and lists possible solution to test the hermeticity of MEMS packages of wafer level metallic bonding. The benefits and drawbacks of the commonly used hermeticity test methods are described in section II. In summary of section II, the comparison on sensitivity of hermetic testing methods is shown. Following the review, the designed and fabricated test structure using optical leaking test method and estimate leaking rate of anodic wafer level bonding result and glass frit wafer level bonding result are shown in section III. Furthermore, a new simple hermetic test structure is designed to estimate the wafer level metallic bonding such using Au-Sn or Cu-Sn metallic sealing.

II – The common hermeticity test methods

There are a great many methods used for the hermetic testing. Firstly the sensitivity and resulting issues of volume range for each method in reference is shown in table 1. Then the concept, limitations and sensitivity dependences of the most common methods are discussed respectively.

Table 1: *Leak testing methods and their lowest detectable leak rates*

Testing method	Sensitivity ($atm.cm^3.s^{-1}$)	Volume (mm^3)	Ref.
Gross leak testing	10^{-4}	≥10	[3]
He-leak testing	10^{-9}	≥3	[4]
Q-factor testing	10^{-11}		[4]
Membrane deflection	10^{-12}	≤3	[5]
Through hole testing	$5x10^{-12}$-10^{-11}		[4]
Thermal conductance	10^{-15}	≤3	[4]
Micro-Pirani gauge	10^{-15}	≤3	[6]

1. Gross bubble and Helium fine leak testing

Gross bubble and Helium fine leak testing are the most commonly used test methods in the MEMS industry based on standards MIL-STD-883. The gross bubble test process is described by visually inspecting for streams of bubbles from a defect while a MEMS device is gently pressurized and submerged under water. Test pressure is gradually increased until this defect begins to show a constant stream of bubbles. But the sealed cavity of most MEMS devices is smaller than 3 mm^3, as shown in table 1, the sensitivity of this method is not fit for the hermetic testing of micro devices.

The Helium fine leak testing is the detection of a tracer gas, Helium, using a mass spectrometer. The packages under test are bombed in a helium chamber at high pressure for a given time then quickly transferred to the detector. The lowest leaking rate is dependent on the cavity volume, bombing time, pressure and the sensitivity of detector used, and a estimation was given out from Millar [7] which is using equation (1). Normally the sensitivity of the He leak detector is around $0.4\times10^{-9}atm.cm^3/s$. This estimation does not take into account the different leak rates associated with different gasses and assumes that the package is contained in air at atmospheric pressure.

$$L \cong (\Delta P \cdot V)/t \quad (1)$$

Where L is the leak rate in atm.cm^3/s, ΔP is the change of pressure inside the cavity in atm, V is the volume of the cavity in cm^3 and t is time in seconds.

2. Q-factor testing

This method is widely used in MEMS industry. It allows monitoring the long-term stability of hermeticity. The sealed package atmosphere is consisted to measure the Q-factor of packaged free standing MEMS. The change in the Q-factor over time gives an indication of the leak rate of the sealed cavities. But this method is limited to devices containing freestanding structures. Calibration of the Q-factor response to changing pressure is also required before packaging.

3. Through hole testing

Through hole testing is an alternative method for hermeticity testing using the gross or fine leak tests. A hole in the bottom of samples is used for the connection with Helium leak detector. When Helium sprayed on tested device, the leaked gas will detected by detector. Adhesion and hermeticity between the detector and the device are ensured by an O-ring coated with vacuum grease. The drawback of this method is destructive, instantaneous and no indication on the long-term stability.

4. Thermal conductance testing

The thermal conductance properties of MEMS can be used to check the pressure inside a cavity. The thermal leak is proportional to the pressure. The minimum pressure limit and hence the minimum leak rate detectable is given by the thermal conductance of the device itself. It is possible to fabricate a freestanding structure inside MESM cavity to allow hermeticity monitoring electrically.

5. Micro-Pirani gauge

A resistive meander is electrically heated and the resistance change due to heat transfer from the hot meander to the cold substrate is measured. This resistance change is indicative of the ambient pressure surrounding the meander. Micro-Pirani gauge is capable of measuring pressure in the range of 10^{-7} to 1 atm, where heat transfer via convection is dominant. The structure is connected in a Wheatstone bridge configuration to ensure temperature stability within the structure. The voltage required to supply the necessary current to stabilise the bridge is monitored. It is very sensitivity using this method to estimate the leakage of package very difficult to apply into the cavity.

III- Optical testing method

A method evaluates the hermeticity of a package by monitoring the pressure-driven deflection of package cap using optical interferometer equipment [5, 8]. This is the most simple, non-destructive hermeticity testing method in the MEMS system. After bonding in vacuum chamber, the hermetically sealed cavity was exposed to atmospheric pressure. Because of the difference in pressure between the inside and outside of the package, the thin membrane will deflect if properly sealed. The schematically is shown in figure 1. The optical non-contact interferometer is used to measure the deflection of package surface. Using this method, the stability of any hermetic package can be examined by monitoring the time dependent of surface deflection. If the package contains a fine leak, the deflection will reduce over time until the pressure inside and outside the cavity is equal.

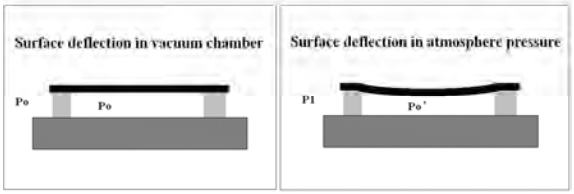

Figure 1: *The principle of optical leak test. P_0 equals pressure in cavity set by bonding process parameter and P_1 is atmosphere pressure*.

1. Design and fabrication of optical test structures

This hermetic test method has been successfully performed on 3 different wafer level bonding results, wafer level anodic bonding [9], wafer level glass frit bonding [10], wafer level metallic bonding [11]. It was also applied on the hermeticity test of BOL device based on metallic bonding. The designed bonding structure is shown in figure 2.

The anodic wafer level bonding is based on a fabricated SOI wafer and a glass wafer in figure 2(a). The anodic bonding was carried out with parameters 400°C, 1000N bonding force, 1000 mbar pressure in bonding chamber and 600V bonding voltage in steps. The wafer level bonding is carried out using EVG 501 wafer bonder. In figure 2(b), the glass frit wafer level bonding was carried out on a fabricated SOI wafer and a silicon substrate wafer with screen printed glass frit sealing. The glass frit bond is formed at 430°C using 0.01mbar bonding pressure. For the test structure in figure 2(c), two metallized silicon wafers with thickness equal to 100µm and 400µm are used to create a package. Electroplated metallic materials could be Au-Sn or Cu-Sn. The structure of multi-layer we used is shown in figure 3. The cavity presented in figure 2(c) is formed by bonding the two wafers together with sealing ring materials face to face. Wafer level bonding was carried out at 260°C for 30 min with 4000N force per 4-inch wafer, with corresponds to a bonding pressure of 10 MPa. This metallic wafer level bonding also used for the hermeticity test of BOL device.

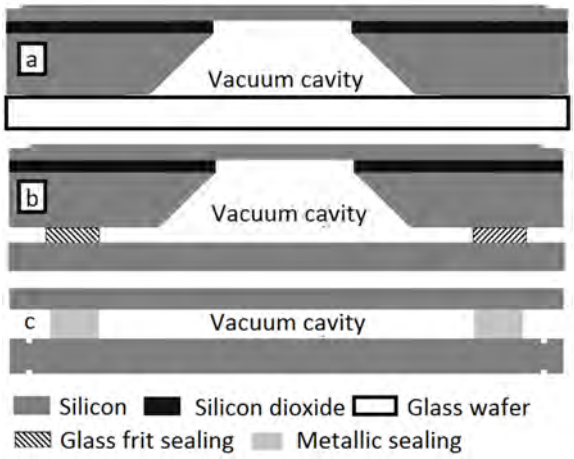

Figure 2: *The schematic of single bonded cavity. (a) Testing structure for anodic wafer level bonding,(b) Testing structure for glass frit wafer level bonding and (c) Testing structure for metallic wafer level bonding.*

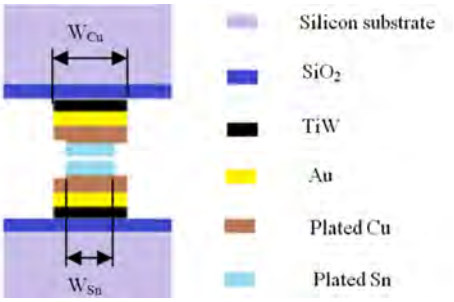

Figure 3: *The schematic of multi-layer for sealing.*

2. *Hermeticity testing result*

After the structures were fabricated, the hermeticity of sealed cavity was inspected using optical method. Figure 4 shows the top view and bottom view of the sealed cavity by wafer level anodic bonding. Figure 5 shows the interferometer scan of membrane deflection of wafer level glass frit bonding result. Image on left shows the deflected membrane and the plot on right shows the measurement result of membrane deflection. The result of wafer level metallic bonding is characterized using interferometer. The top view interferometer image from thin wafer is shown in figure 6. Figure 7 shows the time dependence of membrane deflection from sealed Cu-Sn sealing ring. The measurement is carried over a period of 43 days. No measurable change in the deformation indicates that the integrity of the bond frame is intact.

3. *Discussion of optical leaking test*

The deflection of membrane and wafer is clearly observed which indicates the package is sealed. The leaking rate of wafer level bonding using optical method could be estimated by the deformation of wafer deflection. The calculated leaking rate has reported in our paper [9]. The leak rate detection by the interferometer is based on physical volume of the gas in the cavity. From the increase of pressure inside the package, the leak rate can be calculated from equation (2) from the reference [3].

$$L = \ln\left(\frac{\Delta p(t_1)}{\Delta p(t_2)}\right)\frac{Vp_0}{t_{2-}t_1}\sqrt{\frac{M_1}{M_0}} \qquad (2)$$

Where, L is the equivalent leak rate in [atm cm^3/s]. Δp is the pressure difference between outside and inside cavity in [Pa]. t_1 and t_2 are measuring time. V is the enclosed volume of the package in [cm^3]. p_0 is the atmospheric pressure in atmospheres absolute. $M1$ is the molecular mass of air inside the enclosed package in [g]. $M0$ is the molecular mass of air outside the enclosed package. Thus, the pressure difference Δp between the inside and outside the package is obtained from the membrane deflection δ. The relationship is shown in equation

$$\Delta p(t_1) = \frac{\delta(t_1)Ed^3}{aX^4} \qquad (3)$$

Where, E is the young's modulus of silicon in [Pa]. d is membrane thickness in [μm]. a is the shape constant, equal to 0.0138 when the membrane shape is square. X is the membrane length in [μm]. Here the variation changed the membrane deflection might include the following items: atmosphere pressure, environment temperature, and the measurement error from facility. To increase the data accuracy, the membrane deflection is measured n times.

Advantage of non-destructive, simplest method in traditional hermeticity test, monitoring the long-term stability and can be used on wafer level directly after sealing the MEMS devices makes the optical leaking test very popular in MEMS systems. But this method still has the limitation of hermeticity estimation. The package cap should be flexible enough to show deflection. It is well known that silicon has an excellent elasticity modular. This makes the possible silicon to be the package cap in the small cavity hermeticity testing. Each package has varying cap area, thickness and volume of cavity. This may affect the sensitivity of sealed package. This could be calibrated by the calibration curve for every package.

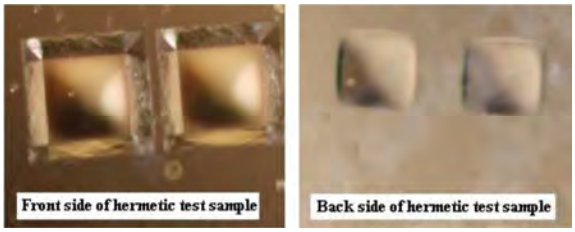

Figure 4: *Photographs of the wafer level anodic bonding.*

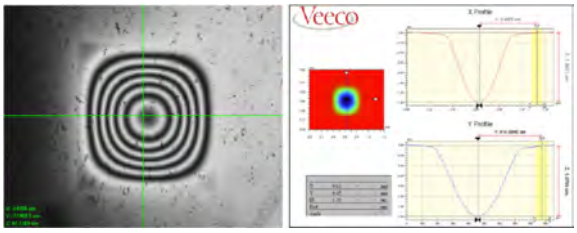

Figure 5: *Interferometer scan of wafer deflection of wafer level glass frit bonding result.*

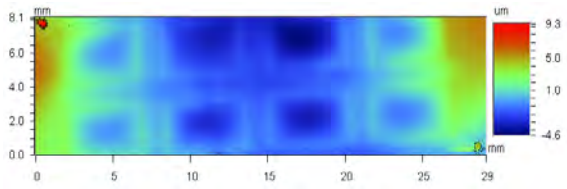

Figure 6: *Top view interferometer image of metallic wafer level bonding result.*

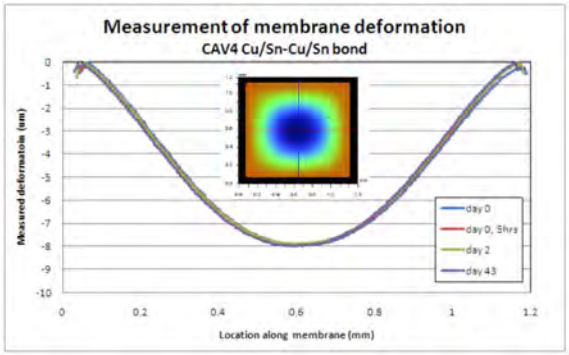

Figure 7: *Time duration of membrane deformation from sealed Cu-Sn sealing ring.*

IV - Conclusion

The optical method is suitable for hermeticity leaking test of metallic wafer level bonding for the observed long time stability of membrane deflection. In the future work, we expect a successful design and manufacture of hermetic sealing on a micro sensor based on the metallic wafer level bonding. The further investigation will focused on the leaking rate determination and characterization of metallic wafer level bonding result. High density wafer level achieve is based on minimize of sealing width. So the sealing ring is designed from 80μm to 250μm.

V. Acknowledgments

This work is partially funded by the RCN BIA project No. 174320, '3DHMNS-3D heterogeneous micro nano systems' and the authors wish to thank Zekija Ramic, Guttorm Salomonsen, and Ragnar Dahl Johansen for lab assistance and fruitful discussions.

References

[1] "Test method standard microcircuits," in *MIL-STD-883*, ed: USA defence, Feb 28. 2006.

[2] A. P. Malshe and Tao, "Theoretical investigation on hermeiticity testing of MEMS packages based on MIL-STD-883E," *Microsystems reliability* 2005.

[3] H. Greenhouse, "Hermeticity of electronic packages," *William Andrew Publishing*, 2000.

[4] D. Wolf, "Hermeticity testing and failure analysis of MEMS packages," in *14th IPFA* Bangalore india, 2007, pp. 147-154.

[5] C. Ferrandon, "Hermetic wafer-level packaging development for RF MEMS switch," 2010.

[6] S. Millar, "In situ test structures for ultra low leak detection," *Proceeding of ESTC* 2010.

[7] S. Millar, "MEMS ultra low leak detection methods: a review," pp. 339-344, 2009.

[8] G. Elger, *et al.*, "Optical leak detection for wafer level hermeticity testing," *Electronics Manufacturing technology symposium*, 2004.

[9] A. Duan, *et al.*, "Characterization of wafer-level bonded hermetic packages using optical leak detection," *Proceedings of SPIE, the international society for optical engineering*, vol. 7381, pp. 73811Y-73811Y-9, 2009.

[10] B. W. Ani Duan, Knut Aasmundtveit, Kristin Imenes and Nils Hoivik, "Characterization of Screen Printed Glass Frit Seals for High Density Wafer Level Bonding," in *IMAPS Nordic Annual Conference* Tonsberg, Norway, 2009, pp. 78-82.

[11] K. Wang, *et al.*, "A simple method for evaluationg hermeticity of wafer-level metallic bonding," *Proceeding of the MSW*, 2010.

Finite Element Modeling of One Port Surface Acoustic Wave Resonator

T.T.K. Tran[1], Ø. Johansen[2] and A. Johannessen[1]
[1]*Vestfold University College; Institute for Microsystems Technology , Norway*
[2]*Norspace AS, Norway*

***Abstract* — In this paper, we present the simulation of a one port Surface Acoustic Wave (SAW) resonator by finite element modeling. Different kinds of materials are used to investigate the characteristic wave mode and resonance frequency. Simulations performed for the Rayleigh SAW mode on YZ-$LiNbO_3$, the Leaky SAW (LSAW) on 36^oYX-$LiTaO_3$ and the Longitudinal Leaky SAW (LLSAW) on YZ-$LiNbO_3$, demonstrated that finite element modeling using COMSOL Multiphysics gave an accurate prediction of device behavior compared to prior art.**

Keywords : **Surface Acoustic Wave Resonator, Finite Element Modeling, $LiTaO_3$ and $LiNbO_3$.**

I - Introduction

SAW devices play an important role in modern communication systems due to their outstanding filter characteristics, their excellent reproducibility and their high performance [1]. SAW devices are not only used for signal processing such as filter, resonator or delay lines[2] but also used for sensor applications [3]. Lithium Niobate ($LiNbO_3$), Quartz and Lithium Tantalate ($LiTaO_3$) are the most used piezoelectric materials for SAW devices. $LiNbO_3$ and $LiTaO_3$ materials are most applicable for low loss devices because of their large wave velocity (v) large electromechanical coupling factor (K^2) and small propagation loss (α) [4].
In this paper, the wave velocity and the propagating wave mode on YZ-$LiNbO_3$ and 36^oYX-$LiTaO_3$ materials are investigated. The frequency response is simulated for one port resonator devices which have a single IDT generating and receiving the SAW and two grating reflectors which reflect the SAW and generate a standing wave [5].

II - Simulation procedure

A. Model Description

The IDT structure in SAW resonator consists of periodically arranged electrodes on top of a piezoelectric substrate. The mode shape of the whole resonator is described by modeling a period of the resonator structure, thus one period of the electrode is sufficient to model the SAW resonator [6]. The base cell used for the simulations is shown in Figure 1. The advantage of analyzing just one period of IDT structure is the reduction in the size of the numerical model. Furthermore, the aperture of the electrodes is much larger than the electrode gap and the lateral effect therefore can be neglected [7]. Hence, it is possible to reduce the general 3-D model to 2-D model simulation.

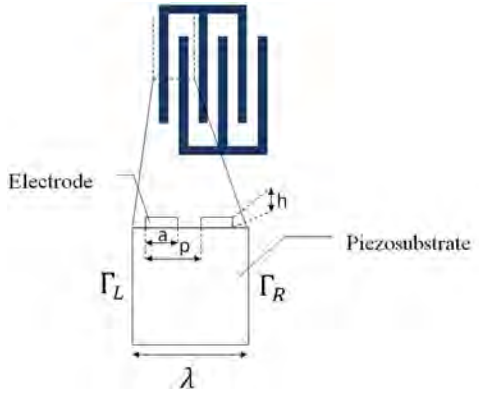

Figure 1: *Geometry employed as a periodic cell in the simulation*

B. Geometry settings

The simulation structure consists of 2 electrodes on top of a piezoelectric materials substrate as shown in Figure 1. The simulation is performed using Aluminum electrodes. The electrodes have the width a and the height h. The distance p between successive electrodes, determines the elastic wavelength λ which is given by:

$$\lambda = 2p \tag{1}$$

The resonance frequency f can be determined by [8]:

$$f = \frac{v}{\lambda} \tag{2}$$

where v is the acoustic wave velocity.
All the geometry values used in the simulation are shown in Table 1.

Table 1: *Dimensions of IDT structure and substrate used for simulation*

Geometry number	**I**	**II**	**III**
Periodicity of electrodes p (μm)	2	1	2
Width of electrode a (μm)	1	0.7	1.2
Electrode height h (μm)	0.20	0.20	0.32
Substrate thickness h_s (μm)	6	6	4

For the frequency response simulation, the summation of the individual mutual admittances between active electrodes gives directly the admittance of the device [9]. The complex admittance of the structure representing the response of one port SAW resonator can be determined from the charge collected at the electrode [7]. The input admittance can be computed from the following relation [7]:

$$Y = j\frac{wQ}{V} \tag{3}$$

where Y is the complex admittance, j is the imaginary number, Q is the charge on the entire electrode, w is the angular frequency and V is the driving voltage.

C. Boundary settings

The application of boundary conditions is important to ensure the realistic representation of the simulated model. To simulate surface acoustic wave propagation, a stress-free boundary condition is assigned to the top surface of the piezoelectric layer. The bottom surface of the substrate is fixed in its position. IDT is periodic in nature alternatively consisting of positive and negative potential and therefore a polarization voltage is applied to the Aluminum electrodes. The electrostatic charges underneath the electrodes are the sources of excitation of the acoustic waves [10]. The periodic boundary conditions, in the left Γ_L and the right Γ_R boundaries (Figure 1) are applied. The periodic conditions define a constraint that makes two quantities equal on two side walls. When the boundary is periodic, the inflow through one of the boundaries equals the outflow through the other. Thus, the leftmost and the rightmost boundaries and vertices share the state variables displacement u, velocity v and also electrical potential V when appropriate.

III - Rayleigh SAW on YZ-$LiNbO_3$

The YZ-$LiNbO_3$ substrate indicates that the crystal Z-axis is the propagation direction of the surface wave, and the Y-axis is normal to the surface. Piezoelectric generated surface waves are launched in a direction normal to the electrodes when an electrical signal is applied to the input transducer [11]. The intensity energy of SAW is mostly confined within 1λ thickness of the substrate [12]. The depth of YZ-$LiNbO_3$ in this model is chosen to be 1.5λ from the surface. The geometry I is used for the modeling and all the values are shown in the Table 1. The material properties used for $LiNbO_3$ have been obtained from [13] and material properties for Aluminum have been taken from material data of COMSOL.

The wave mode propagating in the YZ-$LiNbO_3$ is the Rayleigh SAW wave mode [14]. At first, no mechanical loading needs to be considered. Although the case of no mechanical loading does not exist in reality, it is highly useful to find the wave velocity on a free surface piezoelectric substrate material and to investigate the displacement profile of Rayleigh wave mode. For this model, the width and the thickness of electrodes are assumed to be zero and therefore the mechanical loading generated by the mass of electrodes can be ignored. The point source is used to apply the driving voltage to the surface of the piezoelectric substrate. The eigenfrequency analysis as a simulation approach is then applied for calculation of the wave velocity.

Figure 2 shows the eigenfrequency of the Rayleigh wave on YZ-$LiNbO_3$. The resonance frequency of this model f_r is 873.186 MHz. Thus, the wave velocity of free surface YZ-$LiNbO_3$ calculated from the equation (2) is v=3492 m/s. This value is approximate to the velocity of propagation of Rayleigh SAW on the free surface of YZ-$LiNbO_3$ v=3488 m/s, reported by Drafts [15]. The error between two values is about 0.1%. This is probably due to the difference of the used material constants.

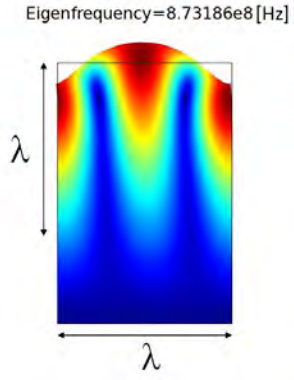

Figure 2: *Eigenfrequency of Rayleigh wave on YZ-$LiNbO_3$*

The deformation field due to the Rayleigh wave propagating along the z-axis on a free surface can also be seen in Figure 2. This deformation field is identical to the Rayleigh wave mode shape as illustrated by Lerch *et al.* [16]. Evidently, Rayleigh wave has its most acoustic energy confined within one wavelength of the surface as described above.

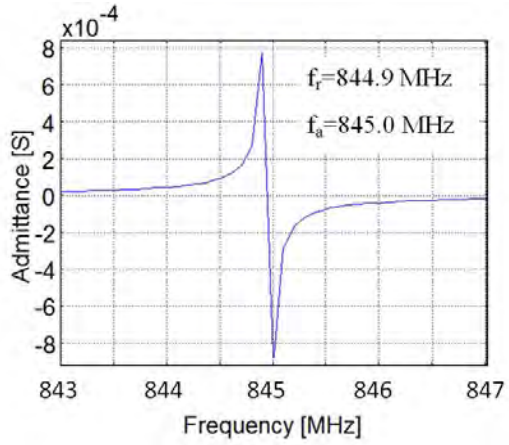

Figure 3: *Frequency response of an IDT structure on YZ-$LiNbO_3$*

The operating frequency of the SAW resonators is mainly determined by the period of the IDT structure. However, the electrode dimensions such as the width and the height are also extremely important parameters for frequency response analysis. They determine the mass of the electrodes on top of the substrate which slows down the velocity of SAW. Figure 3 shows the frequency response of an IDT structure (Geometry I Table 1) on YZ-$LiNbO_3$. The resonance frequency of this IDT model f_r is 844.9 MHz and the antiresonance frequency f_a is 845.0 MHz. From the resonance frequency, the velocity of Rayleigh wave under IDT

structure is 3379.6 m/s. It can be seen that the wave velocity reduces from 3492.0 m/s of a free surface of piezoelectric substrate to 3379.6 m/s of an IDT structure. This difference can be explained by the mass loading effect which changes the wave velocity due to the change of the energy trapping under the electrode [17].

Figure 4 shows the displacement field of the structure at resonance and anti-resonance frequencies respectively and these mode shapes are the same with the reported Rayleigh mode shape in [6]. These mode shapes have also been referred to as symmetric and antisymmetric SAW modes, depending on the symmetry of the electric potential about the center of electrodes.

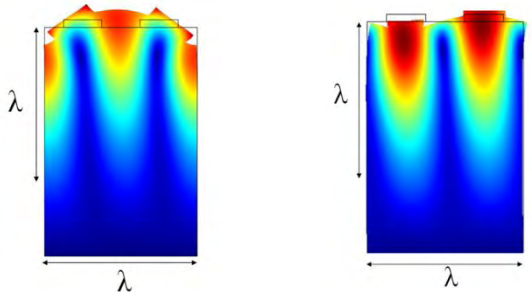

Figure 4: *Displacement mode shape of the symmetric (a) and antisymmetric (b) Rayleigh mode*

IV - Leaky SAW (LSAW) on 36^oYX-$LiTaO_3$

In the 36^oYX-$LiTaO_3$, the wave propagates in the X-axis direction and Y-axis is normal to the plane. However, the coordinate system is rotated in the YZ plane by an angle θ of 36^o. LSAW wave mode is a combination of both surface and bulk acoustic wave modes. The energy of Rayleigh SAW mode is leaked into the bulk acoustic wave (BAW) mode propagation and therefore its amplitude on the surface decays exponentially. Therefore, this type of wave mode is called the leaky surface acoustic mode (LSAW) [4].

In this section, the frequency response simulation for 36^oYX-$LiTaO_3$ is investigated. The geometry II is used in this model (Table 1). The substrate thickness in this model is chosen to be 3 wavelengths. The material properties for $LiTaO_3$ are taken from reference [13] and has been transformed into Euler angles (0,36,0) using transformation equations from the reference [13].

The frequency response of LSAW on 36^oYX-$LiTaO_3$ is shown in Figure 5. The resonance frequency is at 1902.6 MHz. The displacement field is shown in Figure 6. This field is completely consistent to the results presented by Westafer *et al.* [18]. It can be seen that the displacement of particles is not just confined on the top surface of the substrate but there is also the propagation of bulk wave components through the thickness of the substrate.

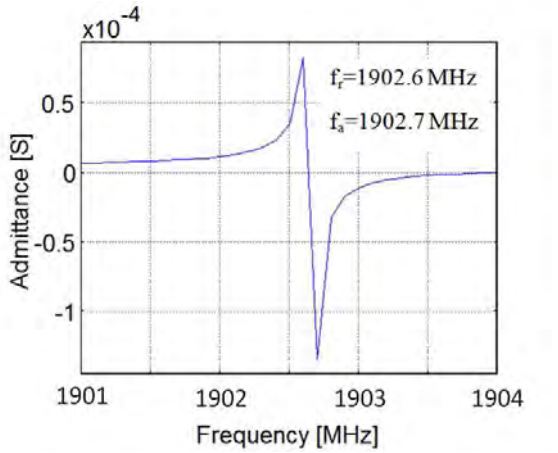

Figure 5: *Frequency response of LSAW on* 36^o*YX-*$LiTaO_3$

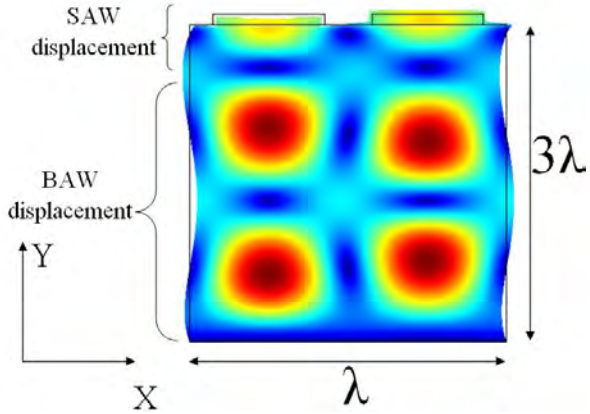

Figure 6: *Displacement field of LSAW on* $LiTaO_3$ *with different aspect ratio in X and Y directions*

V - Longitudinal Leaky SAW (LLSAW) for high frequency resonator on YZ-$LiNbO_3$

The research approaches to increase the operation frequency of SAW devices. In principle, the higher operation frequency of SAW devices can be obtained either by decreasing the SAW wavelength or by increasing the wave velocity. It is a challenge to obtain a SAW device with center frequency above 2 GHz using standard optical lithography. The resolution of optical lithography process limits the smallest period of electrode of the interdigital transducer (IDT) structure. As a result, the wave modes with the high velocity need to be evaluated in order to increase the operation frequency of SAW devices. The LLSAW is promising for a high velocity acoustic wave mode. The LLSAW propagating in periodic system of Al electrodes on YZ-$LiNbO_3$ surface have velocities above 6100 m/s [19] which is about 1.7 times that of Rayleigh SAW.

In this section, the frequency response of LLSAW on YZ-$LiNbO_3$ under IDT structure is investigated. This can be seen from literature in both calculation and simulation that the relative Al electrode height h/λ which provides the minimum attenuation at resonance is 8% for a metallization ratio of a/p=0.6 [20]. It can be seen from literature in both calculation and simulation that the relative Al electrode height h/λ which provides the minimum attenuation at resonance is 8% for a

metallization ratio of a/p=0.6 [20]. The geometry III in Table 1 is used for this simulation model. All the material properties for $LiNbO_3$ and Aluminum are taken from the COMSOL Multiphysics materials data.

The frequency response of LLSAW simulation on YZ-$LiNbO_3$ is shown in Figure 7. The resonance frequency of LLSAW is f_r=1533 MHz. The wave velocity of LLSAW is calculated to be 6132 m/s. This value is close to the reported wave velocity of 6100m/s for LLSAW in YZ-$LiNbO_3$ [19].

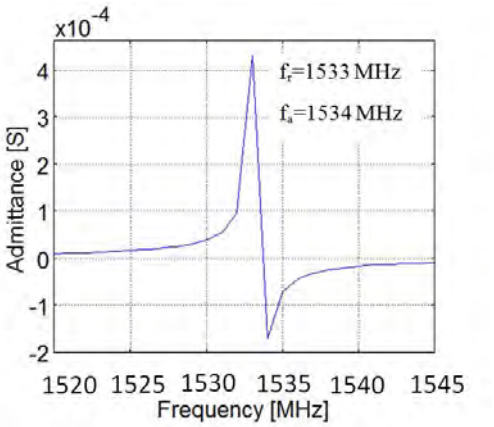

Figure 7: *Frequency response of LLSAW on YZ-$LiNbO_3$*

The simulation of the displacement profile of LLSAW is shown in Figure 8 which is similar to LLSAW displacement field presented in the reference [21].

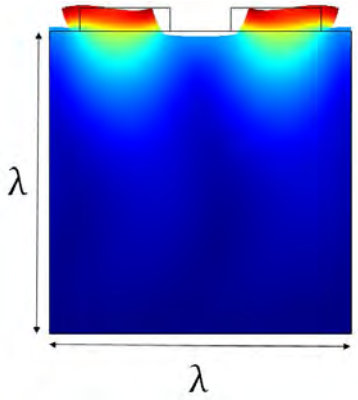

Figure 8: *Displacement profile of LLSAW*

IV - Conclusion

In this paper, the Rayleigh SAW mode and the LLSAW mode on YZ-$LiNbO_3$ is discussed. The simulation of Rayleigh wave velocity on a free surface of YZ-$LiNbO_3$ is performed within 0.1% error. The reduction of the wave velocity on a metallised surface of YZ-$LiNbO_3$ due to the mass loading effect is also investigated. The frequency response and displacement profile of LSAW on 36^oYX-$LiTaO_3$ is presented. Finally, the simulated wave velocity of LLSAW 6132 m/s is achieved which is close to the reported value of 6100 m/s [19].

References

[1] H. Meier and P. Russer, in *Ultrasonics Symposium, 1993. Proceedings., IEEE 1993*, 1993, pp. 201-204 vol.1.

[2] A. Springer *et al.*,*Microwave Theory and Techniques, IEEE Transactions on*, vol. 47. 2312-2316.

[3] Z. Zheng *et al.*, in *Solid-State and Integrated-Circuit Technology, 2001. Proceedings. 6th International Conference on*, 2001, pp. 781-784 vol.2.

[4] K. Y. Hashimoto *et al.*, in *Ultrasonics Symposium, 1997. Proceedings., 1997 IEEE*, 1997, pp. 245-254 vol.1.

[5] C. K.Campbell,vol. ISBN 0-12-157340-0.

[6] Y. Yook-Kong, in *Ultrasonics Symposium, 2001 IEEE*, 2001, pp. 781-790 vol.1.

[7] M. Hofer *et al.*, in *Ultrasonics Symposium, 2002. Proceedings. 2002 IEEE*, 2002, pp. 53-56 vol.1.

[8] F. Sidek *et al.*, in *Research and Development (SCOReD), 2010 IEEE Student Conference on*, 2010, pp. 343-347.

[9] P. Ventura *et al.*, in *Ultrasonics Symposium, 1998. Proceedings., 1998 IEEE*, 1998, pp. 175-186 vol.1.

[10] A. F. Molisch and F. J. Seifert,*Microwave Theory and Techniques, IEEE Transactions on*, vol. 42. 1494-1498.

[11] G. Xu,*Smart Materials and Structures*, vol. 9. 973-980.

[12] Y. L. Rao and G. Zhang,*Excerpt from the Proceedings of the COMSOL Users Conference 2006 Boston,*

[13] B. A. Auld,*ISBN 0-471-03700-1*, vol. 1.

[14] A. Zarka, *et al.*, in *Frequency Control Symposium, 1994. 48th., Proceedings of the 1994 IEEE International*, 1994, pp. 315-322.

[15] B. Drafts,*Microwave Theory and Techniques, IEEE Transactions on*, vol. 49. 795-802.

[16] R. Lerch, in *Circuits and Systems, 1988., IEEE International Symposium on*, 1988, pp. 1399-1403 vol.2.

[17] M. N. Hamidon *et al.*,*Proceedings of the World Congress on Engineering 2009 Vol I,*

[18] R. S. Westafer *et al.s,COMSOL Conference 2009 Boston,*

[19] J. V. Knuuttila *et al.*, in *Ultrasonics, 2003 IEEE Symposium on*, 2003, pp. 617-620 Vol.1.

[20] T. Makkonen *et al.*, in *Ultrasonics Symposium, 2002. Proceedings. 2002 IEEE*, 2002, pp. 317-320 vol.1.

[21] O. Holmgren *et al.*,*Applied Physics Letters*, vol. 86. 024101-024101-3.

A MEMS 0-LEVEL PACKAGING TECHNOLOGY BASED ON CuSn/Cu CHIP CAPPING BONDING

L. Bogaerts[1], A. Phommahaxay[1], X. Rottenberg[1], Y. Naito[2], J. De Coster[1], O. Varela Pedreira[1], N. Van Hoovels[1], V. Cherman[1], P. Helin[1], K. Onishi[2] and H.A.C. Tilmans[1]

[1]*imec, Leuven, Belgium*
[2]*Panasonic, Advanced Devices Development Center, Osaka, Japan*

***Abstract* —This paper presents a 0-level "chip capping" packaging technology for (RF-)MEMS implementing horizontal buried feedthroughs and CuSn/Cu metal bonding. The packages display a high bond strength and from monitoring the MEMS inside they appear to be hermetic (air tight).**

***Keywords :* 0-level MEMS package, chip capping, CuSn/Cu bonding, hermeticity**

I - Introduction

MEMS devices, unlike ICs, contain movable fragile parts that must be packaged in a clean and stable environment. The package or encapsulation should not only offer protection to the MEMS during operation but also during fabrication. Difficulties in the wafer handling (e.g., dicing of a wafer with free standing MEMS is not evident) and cost considerations have initiated the development of wafer-level or 0-level packaging technologies [1]. Zero-level packaging creates an on-wafer, device-scale, enclosure around (or sealed cavity for) the MEMS, serving as a first protective interface. Two general approaches exist for the 0-level packaging, designated as "thin-film capping" and "chip/die capping" [1,2]. For the latter, it is common practice to bond a (recessed) capping chip or die onto the MEMS device wafer as schematically shown in Figure 1. Chip capping is either done as a Die-to-Die (D2D), Die-to-Wafer (D2W) or Wafer-to-Wafer (W2W) capping. In packaging MEMS, hermetic sealing is often required to ensure the long-term stability of the MEMS and to increase the reliability and the lifetime. Metals are the preferred materials to be used for the bond as these provide strong bonds and the best seals, with a low permeation rate for gases and moisture [1,2,3]. Solder-based bonds and seals make available a relatively low temperature (<300°C) option that helps in preserving the integrity of the MEMS. In RF-MEMS device packaging in particular, the package itself should have minimal impact on the RF performance. In an ideal package the RF characteristics before and after 0-level packaging should be the same.

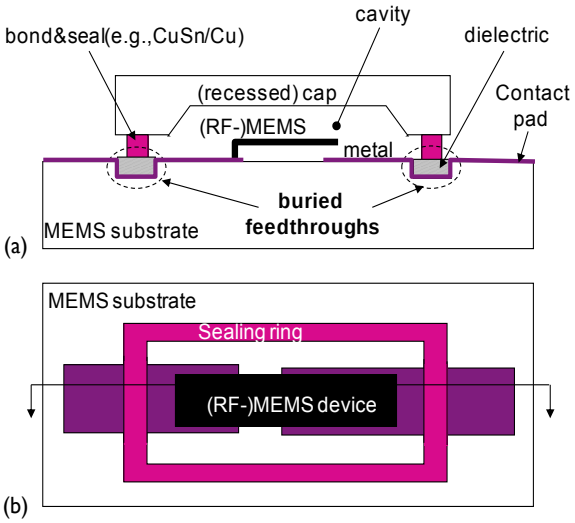

Figure 1: Schematic illustration of the 0-level "chip capping" implementing a buried (RF) feedthroughs. (a) Cross-sectional view. (b) Top view.

This paper describes the use of CuSn/Cu as bonding material in the 0-level "chip capping" packaging [3] for an in-house developed RF-MEMS switching device. Both the preceding processing of the capping wafer as well as the BEOL-processing of the MEMS device will be discussed in detail.

II - Technology and Processing

Metals (as opposed to polymers) provide a hermetic seal, which is crucial for attaining reliable operation of the MEMS inside. The build-up is such that both the cap wafer and the device wafer are equipped with a CuSn or Cu (sealing and bonding) ring. The thicknesses and relative ratios of the Cu and Sn layers are adjusted such that after the bonding process is completed, all of the Sn is converted into a Cu_xSn_y intermetallic compound (IMC). Cu mating layers of 5µm thick on the MEMS wafer and a corresponding Sn layer of 3-5µm on the cap wafer give rather optimal formation of the IMCs [3, 4].

The processes discussed in this paper use 200mm Si wafers, both for the (RF-) MEMS component and for the capping chip. Front-end of line processing has been finished in imec's P-line. Figure 2 depicts the status of the MEMS device wafer before back-end processing (top) and before the 0-level chip capping assembly (bottom). Key back-end processes are oxide and (optional) SiC etching, choice of the seed layer, Cu clean-

ing and electroplating and final vHF-release etch of the MEMS.

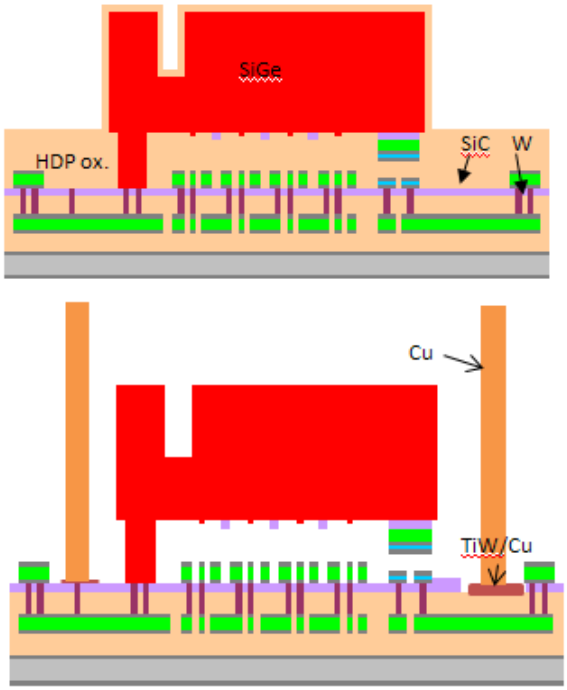

Figure 2: Cross-sectional build-up showing the situation before back-end processing (top) and after back-end processing (i.e., before 0-level assembly) (bottom).

The first critical step is the etching of the thick HDP oxide (Figure 3) which should stop on the SiC layer and should have a high selectivity towards SiC and the W (of the plugs).

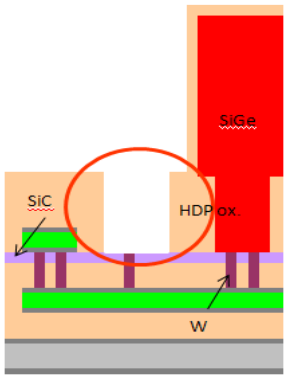

Figure 3: Etching of high density plasma (HDP) oxide

These requirements force us to implement a dry oxide etch process so as to avoid penetration along the W-plugs when using wet etching in buffered HF as shown in Figure 4. Buffer HF offers the advantage of a much higher selectivity towards SiC and W compared to the dry etch process. The oxide etch uniformity and the high topography of the device can be show stoppers in the dry etch recipe.

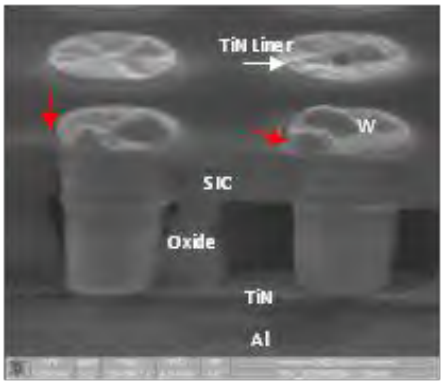

Figure 4: Penetration along W in bHF

Furthermore, the SiC layer has been optimized by removal of the He densification or by single layer deposition. Indeed, delamination of the sealing ring was observed after assembly due to the combination of high stress in Cu and insufficient adhesion strength within the SiC layer. Alternative is the local removal of the SiC by dry etch.

The choice of seed layer is very crucial with regard to further processing. For the standard Ti/Cu seedlayer, the interface is attacked at >1µm/min by vHF as pointed out in Figure 5. The release of a full MEMS wafer will take ~90min.

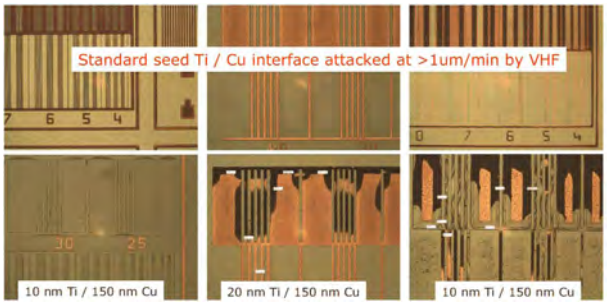

Figure 5: Results after 60min vHF: Ti/Cu interface is attacked

Alternative seed layers that have been investigated are TiN/Cu, TaN/Cu and TiW/Cu (30nm/150nm). TiN/Cu is also not compatible with vHF. TaN/Cu is a good candidate for seedlayer since no attack is observed when exposed to vHF. However an extra litho step is needed to protect the plated Cu-ring during the TaN etch. TaN is removed by a fluorine based plasma. Figure 6 illustrates the attack of exposed Cu in a F-based plasma.

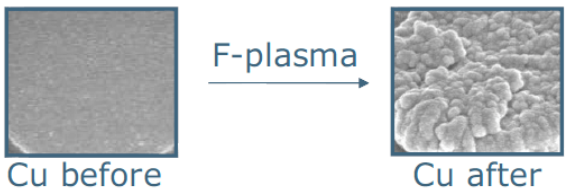

Figure 6: Attack of Cu in fluorine-based plasma

Besides the extra litho and resist strip step, the dry etch of TaN consumes a lot of the SiC layer. Since no delamination occurs of the TiW/Cu seed layer, TiW/Cu

is chosen as the preferred seed layer when vHF is used during the further processing. TiW is removed by wet etching in H_2O_2 and no SiC has been consumed. The oxidation of the Cu during TiW seed etch can be removed by a MS6020 clean. MS6020 is a commercially available citric acid based chemical. Figure 7 shows Cu after TiW seed etch (A.) and after CuOx removal in MS6020 (B.), clearly illustrating the effectiveness of the treatment.

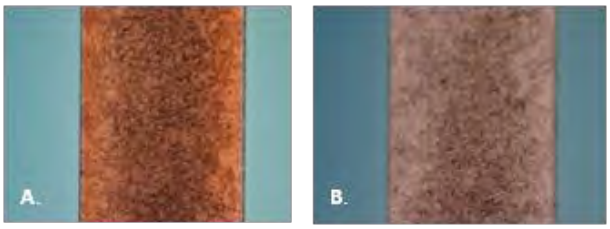

Figure 7: Cu after TiW seed etch (A.) and after MS6020 clean (B.)

The shape of the plated Cu ring can be tuned by playing with the current. Increasing the current will result in a dome shaped ring but will also increase the number of defects. Ideally, the ring surface should be flat to offer a uniform formation of IMC during the following assembly with a cap chip with a CuSn metallization. With a hollow Cu surface, IMCs are only formed at the edge of the ring, resulting in assemblies with low shear strength. Figure 8 shows a non-ideal hollow shape (A.) and the ideal flat shape (B.)

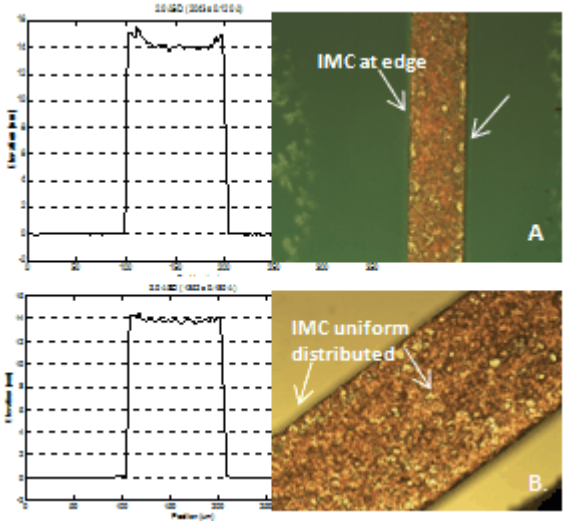

Figure 8: Influence of Cu plating shape on IMC distribution: the graphs show the shape of the Cu ring after plating, the pictures show the surface after assembly and shear testing.

During assembly, one has to accommodate for the released SiGe armature (~ 12µm thick). On the MEMS side, a Cu ring is electroplated to a thickness of 5µm or 15µm, depending of the CuSn thickness of the matching cap wafer, which is 5µm or 10µm Cu and 5µm Sn. On some cap wafers, a recess (see Figure 1) was foreseen to reduce the Cu thickness and stress build-up in the assembly. The Cu and CuSn ring width was kept constant at 90µm. Figure 9 shows a schematic cross sectional view of the MEMS-CAP combinations prior to making the bond.

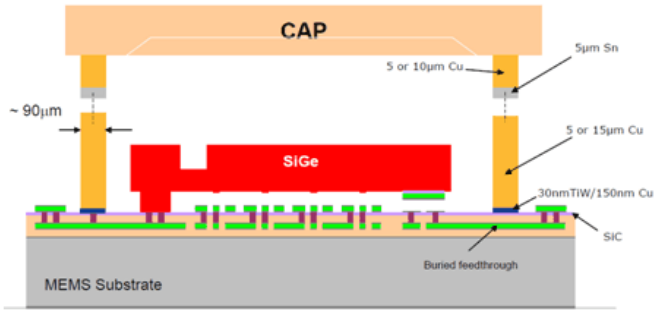

Figure 9: Schematic cross section of assembly parts

The processing of the cap wafer has been done on both Si as well as on pryex wafers. The formation of the recess is done by DRIE. As no vHF is involved, Ti/Cu can be used as the seed layer for the Cu and Sn plating (Figure 10).

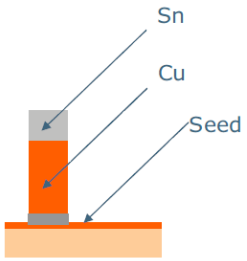

Figure 10: Schematic cross section of metal ring build-up on the capping wafer.

Special attention has to be payed to the use of the Cu seedlayer etchant. Standard etch solutions like $(NH_4)_2S_2O_8$ show modified or strong reactions in the presence of Sn. As depicted in Figure 11, Sn is randomly attacked and Cu residues are visible. By increasing the pH, by adding NH_4OH, Cu is completely cleared and only few attacked Sn spots can be seen (Figure 12).

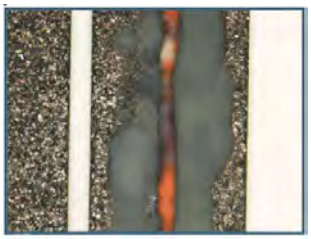

Figure 11: random attack on Sn in $(NH_4)_2S_2O_8$

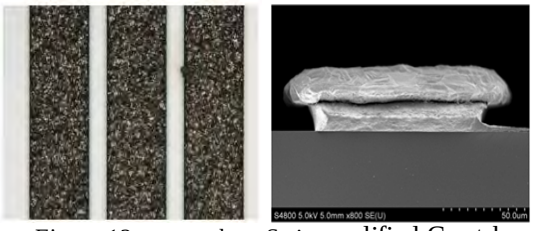

Figure 12: no attack on Sn in modified Cu etchant

D2D or D2W assembly is executed on a flip-chip bonder (FC150 from Süss Microtec). The typical bonding profile consists of two parts. Firstly, a relative-

ly high bonding force in the range of 11MPa is used at a temperature of 175ºC. Scrubbing is implemented during this first part for removal of oxidation. Secondly, no pressure is applied at the peak temperature of 250ºC at which the solder (Sn) is melted and the reflow takes place. This reflow can be done directly on the flip-chip bonder in air or in a reflow oven at vacuum. The latter will result in assemblies with higher shear strength. For any metal bonding, a key requirement is to remove (or prevent) any oxide formation on the bonding surfaces. Here the CuSn surface (of the cap side) is given a pretreatment in a MS6020 solution, just before assembly. For obvious reasons can the Cu on MEMS side only be treated before the MEMS release etch. Figure 13 shows an assembly with a pyrex cap. The MEMS (circular shape) is clearly visible through the pyrex cap. Figure 14 shows a D2W assembly using a Si cap.

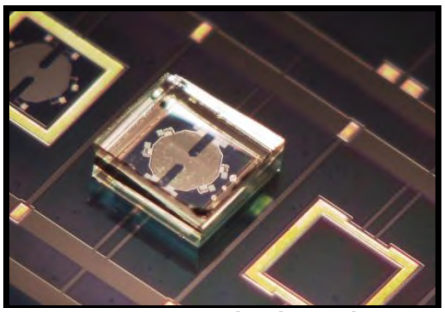

Figure 13: CuSn/Cu D2W bonding with pyrex cap

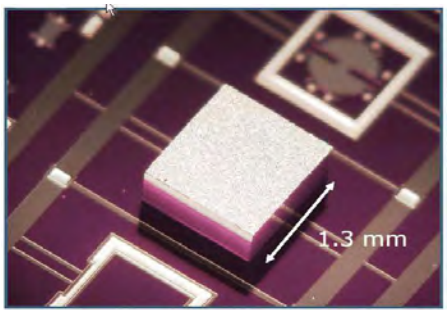

Figure 14: CuSn/Cu D2W bonding with Si cap

III – Package characterization

Shear strength:

The shear strength of a CuSn/Cu sealed package is measured on a shear tester (type CONDOR from XYZ-TECH), by shearing off the capping chip. As explained above, assemblies have been made in a 2-steps process, consisting of a pre-bonding and a reflow at high temperature. Assemblies with a reflow step in air show an average shear strength of 15.4MPa while the shear strength increases to an average of 25.7MPa if the reflow is performed in a vacuum oven. The shear stress of both processes satisfy the MIL-STD-883, which specifies that for areas smaller than 4mm^2 (and larger than 0.3mm^2) the shear stress must exceed 6MPa.

Hermeticity:

Long-term tests have been performed on pyrex- as well as Si-based assemblies to further confirm and assess their hermeticity. For this, samples are placed in 10^{-3} mbar N_2-dominated atmosphere and measured every 30 minutes for 2 days. Pyrex-capped devices were excited using a piezo-shaker and monitored optically through the transparent cap using a laser Doppler vibrometer. No resonance appeared during the 2 days long measurement campaign on some samples (Figure 15). However, after package removal, a resonance peak appeared close to the 14kHz nominal resonance frequency, demonstrating the hermeticity of the package pre-removal.

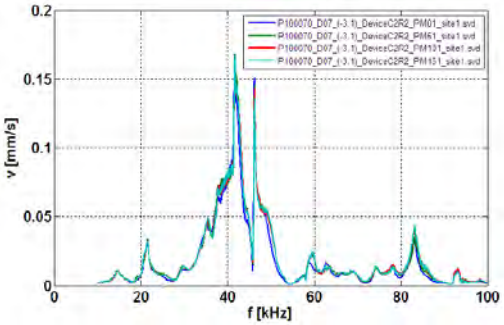

Figure 15: Optically measured frequency response of a pyrex-capped device as a function of the surrounding pressure (spikes around 40kHz are parasitic shaker resonances)

In contrast, Si-capped devices were tested electrically as Si is not transparent for wavelengths in the visible portion of the electromagnetic spectrum. Figure 16 shows first the frequency response of the packaged device. No resonance is apparent. This is attributed to the large damping of the device due to the internal pressure of the package, not impacted by the surrounding low pressure. The functionality of the packaged device was confirmed by the measurement of a functional capacitance-voltage characteristic. Further Figure 16 shows the frequency response of the same device after Si-cap removal. The resonance is clearly visible. All these measurements tend to confirm the hermeticity of the package under test.

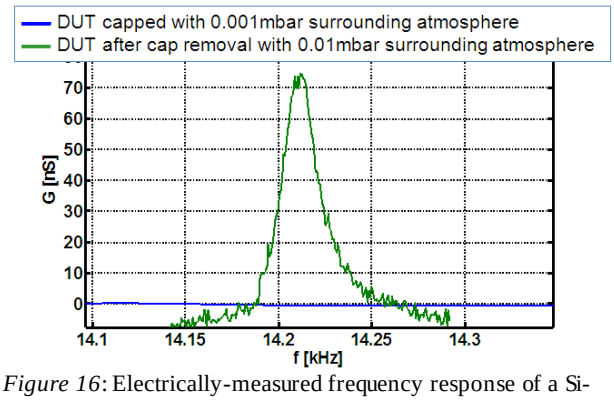

Figure 16: Electrically-measured frequency response of a Si-capped device packaged and after package removal

IV - Conclusion

A 0-level D2D (Die to Die) or D2W (Die to Wafer) packaging process for a RF-MEMS switching device has been developed using CuSn/Cu bonding. A 2-step bonding process with a pre-bonding at 175 ºC and a reflow at 250 ºC results in assemblies with high shear strength. Pre-cleaning of the Cu or CuSn on the MEMS and cap before assembly and scrubbing during assembly play a important role in the success of the package. From monitoring the MEMS inside they appear to be hermetic (air tight).

Key processes in the back-end of line processing of the device are oxide (and SiC) etching, choice of the seed layer, Cu cleaning and electroplating and final vHF-release of the MEMS.

References

[1] H.A.C. Tilmans, A. Jourdain, P. De Moor, "Packaging", Chapter 9 in "Advanced RF MEMS", S. Lucyszyn (ed.), Cambridge Press, 2010.

[2] K. Najafi, "Micropackaging technologies for integrated Microsystems: Applications to MEMS and MOEMS", proc. of SPIE, vol. 4979, 2003, pp. 1-19.

[3] N.P. Pham et al., *Proc. EPTC 2010,* "Metal-bonded, hermetic 0-level packaging for MEMS", *Proc 12th Electronics Packaging Technology Conf. (EPTC2010)*, Singapore, Dec. 2010, pp. 1-6..

[4] R. Labie, *"Mechanical and physical behaviour of intermetallics in leadfree flip chip interconnects"* Ph. D dissertation, K.U. Leuven (Belgium), 2007.

SMART TEXTILES - ENCAPSULATION OF SENSORS

Thanh-Nam Tran[1], Andreas Larsson[2], Erik Andreassen[2], Knut E. Aasmundtveit[1], Trine M. Seeberg[2]

[1]*Vestfold University College, Horten, Norway*
[2]*SINTEF ICT, Oslo, Norway*

***Abstract* — In the recent years, wearable devices have attracted substantial attention from researchers and industrial manufacturers. The use of smart textiles can give a high evolution of the interaction of human individuals with electronic devices. However, the technology faces challenges regarding packaging of electronic components on textiles as high durability, flexibility and washability are demands. This study investigates the adhesion between encapsulants of electronics and various textiles in order to improve the reliability of integration of sensors into textiles. For textiles with low adhesion properties a pretreatment process, chemical primer and oxygen plasma treatment, was applied to improve the adhesion. The methods used for evaluating the adhesion were a 180^0 peel test and washing tests. Learning from this study, the authors succeeded to integrate a humidity and temperature sensor onto a textile.**

***Keywords*: smart textiles, peel test, plasma treatment.**

I - Introduction

Nowadays, clothing is not simply a fashion concept but represent also a possible platform for development of new innovative applications. The technical drive is to integrate sensors and electronics into textiles by using the fabrics as the circuit board providing bus structures and interconnection between modules [1]. Usage, comfort and other obvious advantages of clothes must however be maintained despite a possible integration of electronics. Smart clothing aims to improve awareness of user situations, monitor sport activities and health conditions. The opportunities within the field have attracted high attention from scientists and industrial manufacturer recently due to the development of mobile technologies and the needs to improve the interaction of human individuals and electronic devices. Applications closer to fashion, leisure and entertainment are entering the market. However, technology still faces challenges regarding packaging of electronic components into textiles with high reliability, durability, flexibility and washability.

For electronic textiles, the daily application can be evaluated as a harsh environment. In working conditions, textiles are being draped, crumpled and stretched, etc. Especially, during washing, even more stress is applied while the fabric is wet and hot [2]. Therefore, the encapsulation for protection of the electronics and interconnection is an important issue. Limited research has been done in this area so far. In the encapsulation process, the adhesion between encapsulants and textiles is an important issue for high reliability of integration of electronic components into textiles.

This study investigates the adhesion of various encapsulation materials on textiles and the encapsulation process is varied in order to be able to integrate sensors in textiles. The adhesion has been evaluated according to a 180^0 peel test and washing tests. For challenging textiles such as waterproof textile, a pretreatment process using primer and oxygen plasma is applied to increase the adhesion.

II - Experimental Procedure

A. Material selection for encapsulation

This study investigates two materials representing two main material groups: silicone and epoxy. The two materials were chosen based on the requirements for textile application. The silicone MED-6015 (Nusil) is commonly used in medical applications [3] and has some excellent properties that satisfy most of the requirements: easy to remove from the mold after curing, bio-compatible and stretchable. The epoxy 353ND (Epo-TEK) is stiff, bio-compatible and commonly used in semiconductor, hybrid, optical fiber and medical applications. The applicability of these materials for a variety of textiles such as cotton, nylon, wool and waterproof textile was evaluated during manufacturing of test samples and subsequent testing of these. Cotton, nylon and wool were manufactured by weaving of fibers in a matrix type structure so that encapsulation materials easily penetrate into the fibers. On the other hand, waterproof textile is coated by polyvinyl chloride (PVC) since this hydrophobic polymer repels water.

During the encapsulation process, although a mold release agent (Mikon 305 - Microjoining) was used, it was very difficult to remove the epoxy sample 353ND out of the mold while this was straight forward for silicone. Therefore, only MED-6015 was chosen as the encapsulation material in the remaining of the presented study.

Table 1: *Material specifications (from datasheet)*

	Nusil MED-6015	EpoTEK 353ND
Appearance	Optically clear	Black
Mixed viscosity (mPas)	5000 – 7000	3000 - 5000
Press cure (min/150^0C)	15	60
Working time (h)	4	3
Tensile stress (MPa)	8.6	>35
Elongation at break (%)	100	0
Bio-compatibility	Yes	Yes

B. Textile pretreatment

Two common ways to pre-treat textiles are chemical treatment by primer and physical treatment by oxygen plasma. In this study the efficiency of primer and the combination of plasma treatment and primer to increase the adhesion between silicone MED-6015 and waterproof textile was investigated.

A primer was used in the first pretreatment procedure as a coupling agent between silicone and waterproof textile. MED-163(Nusil) is a general purpose primer which is suitable for bonding to the most demanding substrates, especially iridite coated materials. Before encapsulating silicone onto the waterproof textile, a thin film of this primer was coated onto the surface of textile and cured for 1 hour at room temperature/ 25% relative humidity.

In the second pretreatment procedure, oxygen plasma treatment and primer coating was combined to increase the number of chemical bonds between silicone and waterproof fibers. Low temperature plasma technology is well established in different industrial applications and is now being introduced in textile industry as well [4]. The purpose of plasma treatment is oxidizing the surface of textile and generating hydroxyl radicals. A piece of waterproof textile (200 x 50 x 0.5 mm) was placed inside a tubular reactor of plasma MARCH PLASMOD instrument for treatment. The gas used was oxygen (>99%). The pressure inside the plasma chamber was kept at 0.2 torr for plasma treatment time of 5 and 10 minutes. The plasma treated specimen was coated by primer subsequently following the above described drying procedure.

Table 2: *Primer specification (from datasheet)*

	MED-163 Nusil
Viscosity (mPas)	1
Components	- Naphtha (75%) - Platinum complexes (10%) - 7-Octenyl-trimethoxy silane (5%) - Beta-(3,4-Epoxyclcohexyl)-ethyltrimethoxysilane (5%) - Tetrabutyltitanate (5%)

C. Peel test

In this work, the 180^0 peel test was applied to investigate the adhesion between encapsulation materials and textiles. The peel resistance represented for the adhesion strength is defined by the measured peel force divided by the width of the peel front [5]. Since silicone is quite soft, a specific design was required for the peel test. Therefore, a testing device was designed to play the role of the mold for the encapsulation process as well as the clamp of silicone for the peel test. The contact area of silicone was 30 x 10 mm while the thickness of the silicone was 8 mm.

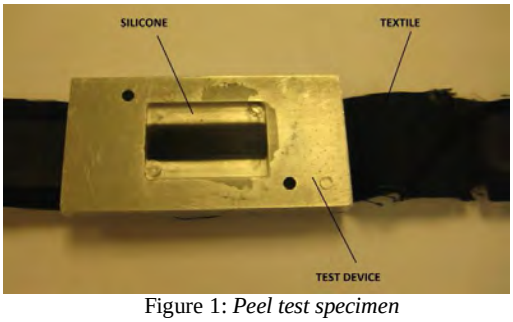

Figure 1: *Peel test specimen*

The 180^0 peel test was induced by an axial stretch loader (LR50K, Lloyd Instruments Ltd, Fareham, UK) with a 500 N loadcell (NLC 500N, Lloyd Instruments Ltd, Fareham, UK) to measure the peel force. The testing speed was 10mm/min.

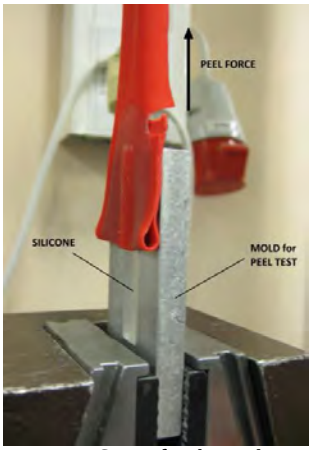

Figure 2: *Set up for the peel test*

D. Wash cycling test

The reliability of integrating sensors into textiles by silicon (MED-6015) was tested by a wash cycling test. The samples for each kind of textiles were stitched into a fabric as shown in figure 3. The wash cycling test followed normal washing conditions for cotton (60^0C, 1400 rpm) using a standard detergent. After 20 wash cycles, the adhesion and deformation of silicone on various textiles was monitored. Based on the peel resistance and the wash cycling test results, the adhesion between encapsulation materials and textiles can be considered as either suitable or not.

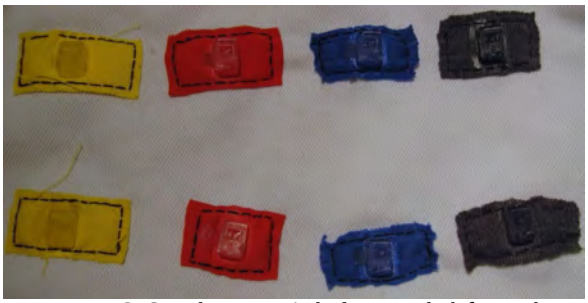
Figure 3: *Samples were stitched onto a cloth for wash cycling test*

III - Results and Discussion

A. Peel test

Delamination of silicone from the tested kinds of textiles was observable after the peel test. Figure 4 shows a typical peel test results, in which the maximum peel force was measured at the place where the delamination first appeared. After being torn, the peel force decreased significantly due to the easy crack propagation in the bulk silicone. Therefore, the peel resistance was calculated based on the maximum peel force rather than average peel force.

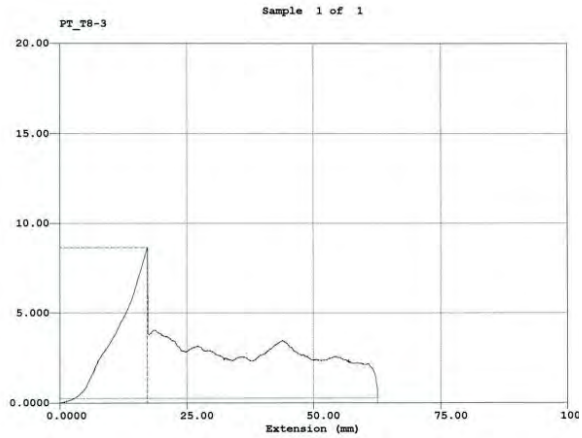

Figure 4: *Peel force (N) vs. extension (mm) curve for cotton sample*

Table 3: *Average peel resistance (N/mm) of silicone for different kinds of textile*

Textile	Garment	MED-6015	MED-6015 + Primer
COTTON	Wenaas –Inner coating Jacket	0.52 ± 0.22	0.42 ± 0.08
NYLON	Swix VM 2011 cross country suit	0.31 ± 0.15	0.24 ± 0.002
WOOL	Janus under-wear	High (Silicone was torn before delamination)	High (Silicone was torn before delamination)
WATER-PROOF	Wenaas -Outer coating Jacket	0.17 ± 0.03	0.57 ± 0.36

Table 3 gives the average peel resistance for 3 samples and indicates that the presence of primer did not affect the adhesion of silicone to cotton, nylon or wool where the physical bond probably dominated. Meanwhile, primer improved significantly the adhesion of silicone to waterproof textile, possibly creating chemical bond with the PVC film on the surface of this textile. Lanjun et al. [6] explained the bonding mechanism between epoxy functional group of silane coupling agents and PVC. The large scatter in peel resistance could be due to the cleaning of the substrate, the application of the primer, humidity or other factors slightly varying for the test. Another reason could be a slight misalignment between the pull axis and the testing device which would causes the certain change of the width of the peel front. The wider peel front, the higher peel force is measured.

B. Textile pretreatment

After the pretreatment using the combination of oxygen plasma treatment and primer, the peel test was applied to evaluate the adhesion.

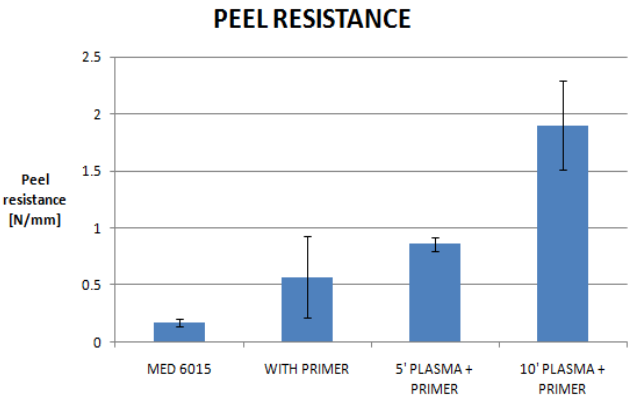

Figure 5: *Average peel resistance of silicone on waterproof textile after different pretreatment procedures.*

Figure 5 gives the average peel resistance for 3 samples of each kind and indicates that the pretreatment using the combination of oxygen plasma and primer improved significantly the adhesion of silicone to waterproof textile. The explanation might be that the oxygen plasma process has oxidized the textile surface (shown in figure 6) and created hydroxyl radicals. These radicals will react with the reactive silanols in the primer to create strong chemical bonds. This would result in a high peel resistance. The longer the time of the plasma treatment, the higher peel force was observed. Figure 7 explains the bonding mechanism between silane coupling agents in primer with the hydroxyl radicals on textile surface.

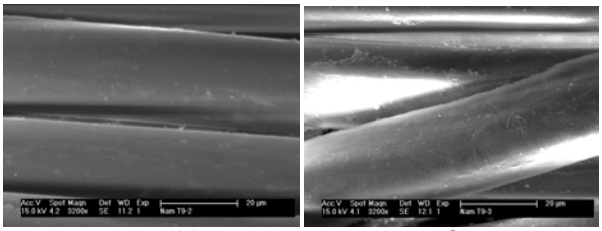

(a) (b)

Figure 6: *SEM image of the difference of textile surface before (a) and after (b) oxygen plasma treatment.*

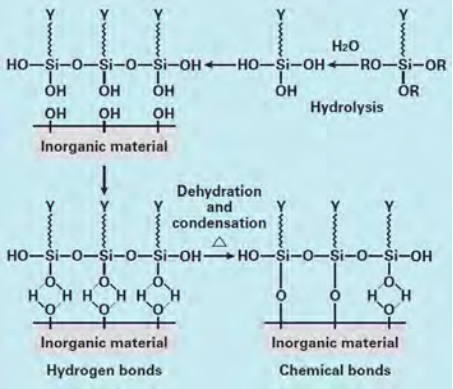

Figure 7: *Bonding mechanism of silence coupling agents and hydroxyl radicals* [7]

C. Wash cycling test

After 20 wash cycles of 2 samples of each kind, no deformations or cracks in the bulk silicone were observed. Most of the samples passed the wash cycling test in terms of adhesion. The only exceptions were the waterproof textile samples with and without primer, but this was also as predicted due to the non-penetration of silicone into textile fibers. However, the pretreatment using the combination of oxygen plasma treatment and primer gave satisfactory results even for silicone on waterproof textile. Therefore, the silicone MED-6015 proved that it is a reliable encapsulation material for integration of electronics and sensors onto textiles.

IV - Application: Packaging on sensor onto textile

The MED-6015 silicone was applied as encapsulation for a humidity and temperature sensor from Sensirion (SHT21) to study the feasibility as an encapsulant material for electronics in smart textiles. A suitable mold was fabricated and the encapsulation was done using vacuum molding (to be published). The packaged sensor, see Fig. 8, worked after encapsulation and shows that the MED-6015 is a feasible option for encapsulation of electronics in smart textile.

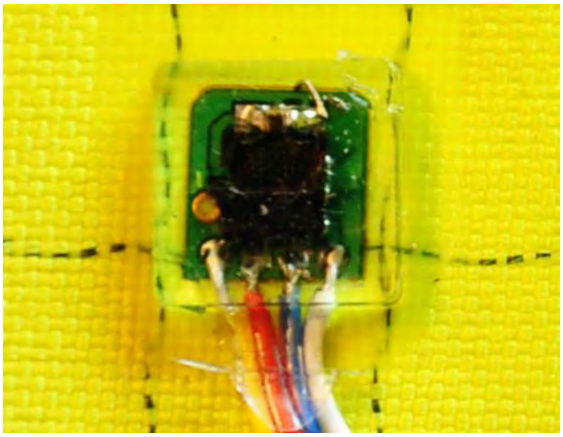

Figure 8: *A successful encapsulated sensor*

V - Conclusion

For encapsulation of electronics components onto textile, the silicone MED-6015 was demonstrated to be a highly attractive solution for an encapsulant. Its applicability was tested successfully by manufacturing of test samples and subsequent testing such as peel test and wash cycling test. Even with challenging substrates such as waterproof textiles, a satisfactory adhesion was obtained by applying a combination of oxygen plasma and primer as a pretreatment. Finally, successful integration of a humidity and temperature sensor onto textile using MED-6015 as the encapsulant was shown.

Acknowledgment This work was supported by the Research Council of Norway and the partners of the Coldwear project 188002/I40 (http://www.sintef.no/Coldwear). We especially thank Swix, Wenaas and Janus for providing textile samples.

References

1. Reichl, H., C. Kallmayer, and T. Linz, *Electronic Textiles*, in *True Visions*, E. Aarts and J. Encarnação, Editors. 2006, Springer Berlin Heidelberg. p. 115-132.
2. Linz, T., *Embroidered Interconnections and Encapsulation for Electronics in Textiles for Wearable Electronics Applications.* Advances in Science and Technology, 2008. 60: p. 85.
3. Imenes, K., et al., *Assembly and packaging of a three-axis micro accelerometer used for detection of heart infarction.* Biomedical Microdevices, 2007. 9(6): p. 951-957.
4. Höcker, H., *Plasma treatment of textile fibers.* Pure and Applied Chemistry, 2002. 74(3): p. 423-427.
5. Linz, T., M. von Krshiwoblozki, and H. Walter. *Novel Packaging Technology for Body Sensor Networks Based on Adhesive Bonding A Low Cost, Mass Producible and High Reliability Solution.* in *Body Sensor Networks (BSN), 2010 International Conference on.* 2010.
6. Lanjun Li, B.H., Xian Chen, *Epoxylsilane crosslinking of rigid poly(vinyl chloride).* Journal of Applied Polymer Science, 2007. 106(6): p. 3610-3616.
7. B.Arkles, Chem. Tech, 1977. 765.

SLID BONDING FOR WAFER-LEVEL INTEGRATION AND PACKAGING

N. Hoivik, K. Aasmundtveit and K. Wang

HiVe – Vestfold University College, Department of Micro and Nano Systems Technology (IMST), Norway

***Abstract* — In this paper we present and discuss the application of solid-liquid interdiffusion (SLID) bonding for wafer-level encapsulation and packaging. Binary metallic systems Au-Sn and Cu-Sn are presented and analyzed. For Au-Sn, the degration temperature of the bond was examined by applying shear force while heating bonded samples. No direct bond delamination was observed for temperatures up to 350–400 °C, which is 100 °C higher than the melting temperature of the eutectic Au–Sn bonds (80 wt% Au, melting at 278 °C). For Cu-Sn, using a 1.5 μm thick Sn layer as oxidation barrier for 5.0 μm thick Cu bond frames, the surface does not require pre-cleaning or use of any flux agent prior to, or during bonding. With a tailored temperature and pressure bonding profile, the amount of Sn squeeze-out is reduced. Both for Cu-Sn bonds performed with new and aged electroplated films the measured shear strength is above 20 MPa. Further temperature cycling of bonded dies does not result in any reduction in bonding yield or shear strength.**

Keywords : **Cu-Sn, Au-Sn, wafer-level bonding, hermeticity**

I - Introduction

Solid-Liquid Interdiffusion (SLID) bonding is a bonding technique based on intermetallic formation that has received high interest in the industrial and scientific community. SLID bonding has several appealing properties, such as: [1]

- High temperature stability
- Moderate processing temperature in an isothermal process
- Allowing repeated processing without bond melting – e.g. for stacking purposes
- Allowing fine pitch interconnects
- Thermodynamically stable bonds
- Corrosion-resistant bonds
- Well suited for wafer bonding
- May use low-cost metallization
- Flux-free processes are possible

The SLID process makes use of a binary metal system, one metal having a high melting point (M_H), and the other having a low melting point (M_L). The melting points will be designated T_H and T_L, respectively, in the following. Typically these metals will be deposited as multi layers, as shown in the inset in Figure 1, e.g. by electroplating. A metal system for SLID shall exhibit thermodynamically stable intermetallic compounds (IMC) with high melting points, as shown in the schematic phase diagram in Figure 1.

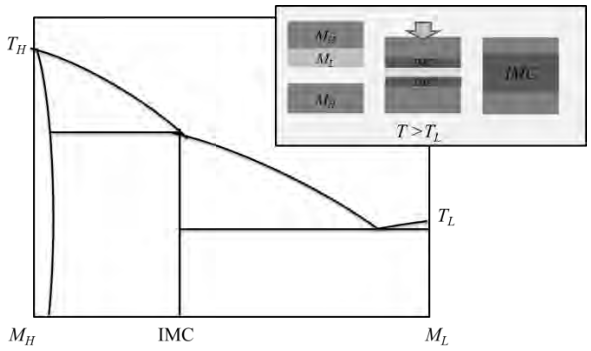

Figure 1: Schematic phase diagram, showing a binary metal system with high and low melting point, respectively, and with IMC with high melting point. Inset: Sketch of typical layer structure for SLID bonding, and the bonding process.

Bonding is performed by processing at a temperature somewhat above T_L. M_L melts, and the two metals interdiffuse. In particular, the solid M_H diffuses into the liquid M_L, reacting to solid IMC. Thus, the bond solidifies at the constant bonding temperature. Note that the interdiffusion process takes place already at lower temperature, although slowly. The kinetics of the diffusion process is highly accelerated above T_L. In an ideal SLID bonding, the process will consume all the M_L material, ensuring that the final bond consists only of IMC and M_H, both being of high-temperature stable materials, ensuring thermodynamic stability. It is important to ensure that the metal system is designed such that there is a surplus of M_H in the system, for several reasons:

- To ensure all M_L is converted to IMC (taking process variations and uncertainties into account)
- To prevent diffusing M_L to reach the under-bump-metallization (UBM), potentially creating undesired IMCs and/ or giving rise to delamination.
- Ensuring a remaining layer of metallic M_H, normally being more ductile than the (often) brittle IMC, for stress handling.

SLID bonding has been investigated by several groups. As a consequence, different terminologies exist. The bonding process is also referred to as Transient Liquid Phase (TLP) bonding [2, 3], Isothermal Solidification (IS) [4], or off-eutectic bonding [5].

The SLID process shows several similarities with a soldering process: The existence of a liquid metallic phase during the process, and the formation of IMC as the actual bonding material. The same metals are commonly used for both processes: Most solders are Sn-based, with small amounts of alloying metals (such as

Cu and/or Ag), and Cu is a commonly used pad material. Similarly, Cu–Sn is the most common metal system for SLID, as discussed below. Processing temperatures are also similar. Despite the similarities, SLID and soldering are fundamentally different processes, each with distinct and unique properties. Table 1 lists the properties of two SLID bonding metal candidates. Whereas soldering is a reversible process, where the solder melts and solidifies at the same temperature; SLID bonding is irreversible, resulting in an IMC bond that melts only at temperatures far above the process temperature.

Table 1: Properties of metal candidates used in SLID bonding.

M_H	M_L	T_H [°C]	T_L [°C]	Target IMC	Stability of IMC [°C]
Au	Sn	1064	232	Au_5Sn	190: Solid-state PT 519: Melting
Cu	Sn	1085	232	Cu_3Sn	676: Solid-state PT ~700: Melting

PT: Phase transition

One of the key requirements for successful SLID bonding is to remove, or convert, the oxides which are formed on the bonding surface. Both Cu and Sn oxidize at room temperature in atmosphere, but with different rates, and Cu oxidizes faster than Sn. Au is a noble material and chemically inert in atmosphere. Thin SnO layer can be tolerated and incorporated into the molten Sn during bonding. Therefore, the most critical process is to remove copper oxides on the metallic Cu surface prior to, and during bonding, which can be accomplished by i) bonding in hydrogen environment, ii) exposing Cu to formic acid vapor – reduction of Cu oxide back to Cu or iii) use of an acid (HCl) to etch – removal of Cu oxide.

These, and other methods described in [6], have also been attempted to convert SnO to Sn, with the formic acid vapor having a good effect to reduce the stable oxides [7]. However, these methods would be prohibited from use of wafers which contain released and fragile MEMS devices, in addition to getter materials. We have therefore developed a method to avoid all these issues, by either capping Sn with a thin layer of Au, or capping the Cu with thicker layer of Sn in a so-called symmetric bonding scheme. In the latter case, the Sn layers are sufficiently thick to both prohibit oxidation of the Cu surface and to form a pure Sn/Sn intimate interface when the wafers are brought into contact. This minimizes oxidation and makes flux-less bonding possible [8-10].

II - Experimental Approach

Metallic Cu–Sn is by far the most studied SLID system. Both metals are low-cost and readily available. The materials have extensive heritage in the microsystem/microelectronic sector, as Sn is the basis of all soldering and Cu is a commonly used substrate and chip pad metallization.

Cu–Sn SLID initially form two distinct phases: η-Cu_6Sn_5 and ε-Cu_3Sn. At a bonding temperature above the melting point of Sn (232 °C), molten Sn dissolves Cu and the IMC η–phase (Cu_6Sn_5) is formed. This phase actually forms even at room temperature; however the reaction is greatly accelerated when raising the temperature above the Sn melting point. Since there is excess Cu in the system, the η-phase (Cu_6Sn_5) will furthermore react with Cu to form the second IMC ε -phase (Cu_3Sn). Both phases will grow in thickness as long as there is liquid Sn (and solid Cu) available. When all liquid Sn is consumed, the bond has solidified isothermally to a Cu/IMC/Cu structure, as shown in Figure . The IMC formation process will terminate upon complete transformation of all IMCs to the stable Cu_3Sn ε-phase.

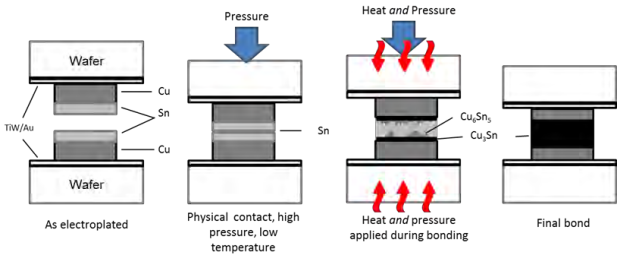

Figure 2:Illustration of Cu-Sn SLID bonding, where electroplated Cu (5 μm) and Sn (1.5 μm) are patterned on respective wafers and brought into contact to form the final intermetallic composition Cu_3Sn sandwiched between Cu.

Cu-Sn test vehicles were fabricated by electroplating Cu on oxidized Si wafers with sputtered TiW/Au or Ti/Au adhesion and seedlayers. The thickness of the adhesion layer was 100 nm and the Au seedlayer 500 nm. For all experiments, photoresist AZ4562 was used to define the bond frames. Ar+O_2 plasma treatment was carried out before the electroplating process to ensure a clean seed layer surface. The Cu and Sn features were electroplated using a commercial Cu- and Sn sulphate-based solution at room temperature, with a current density of 10 mA/cm^2. Pulse-reverse current was applied to ensure proper uniformity across the wafer. The targeted Cu thickness was 5 μm and 1.5 μm for Sn.

A bonding profile which takes advantage of the ductile Sn layers to conform to each other, given any non-uniformity across the wafer, compared to the significantly harder Cu surface was applied. The reason behind this approach is that the interdiffusion process between Cu and Sn would occur with a slow temperature ramp past the melting point of Sn. Combining this with reducing the bond force at 240 °C, a little above T_m for Sn (232 °C) to account for any thermal gradients between the wafers, the reduction in bonding pressure can reduce squeeze-out of any molten Sn.

Figure 3 shows a schematic of such a bonding profile where a high temperature ramp rate to 150 °C (7 °C/min), is followed by a low temperature ramp rate (3 °C/min) until reaching melting temperature of Sn and the final soak temperature. This was done as to reduce the amount of Sn left at the interface when reaching 240 °C, and allow for the diffusion process to occur in the

bond line early in the process. The wafers were brought into contact with a bond force of 7 kN (20 MPa) after the temperature had reached 150 °C. Following making contact, the force was either reduced to 1 kN (3 MPa) at a temperature right above the melting point of Sn (240 °C), or maintained high throughout the soak time.

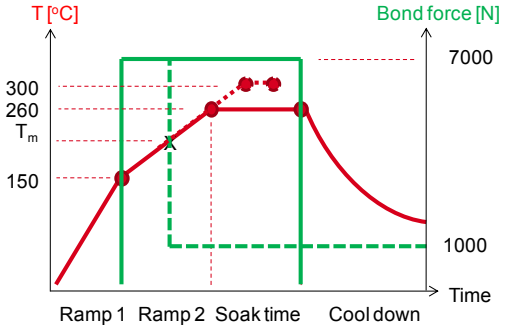

Figure 3: Schematic illustration of the bonding profile. The bonding force is applied at 150 °C and either kept constant (7 kN) throughout or reduced at a temperature near the melting point of Sn (240 °C) and kept at a lower value (1 kN).

Au–Sn is another SLID system that is of particular interest. Although being more costly than Cu–Sn, the use of Au has particularly two important features: Due to the inertness of Au, flux-free processes are more easily implemented in this system. Furthermore, a SLID bond consisting of Au/IMC/Au layers may take advantage of the ductility of Au for stress handling.

The Au-Sn intermetallic compound formation process is more complicated than for Cu-Sn. All of the IMCs have a higher melting point than pure Sn, and the δ and ζ/ ζ' phases have melting points higher than the eutectic composition (419.3 °C and up to 519 °C, respectively). For applications where the bond is to resist higher temperatures, either during later processing or during applications, a bond made of one of these IMCs may be appropriate. For a system where there is surplus of pure gold after formation of the IMC bond line, a bond made of the δ-phase may be susceptible to be converted into a eutectic or near-eutectic structure over time, due to Au–Sn interdiffusion, thus lowering the melting point. However, a bond made of the ζ/ ζ' phase, in the vicinity of surplus Au, is not expected to convert into lower-melting phases over time.

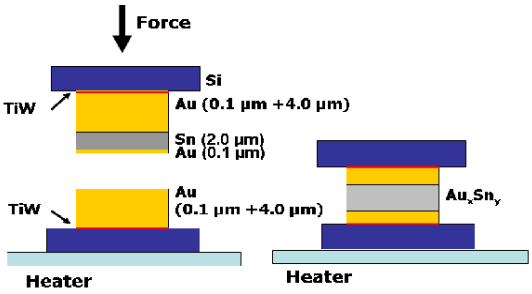

Figure 4: Schematic illustration of layer structure of samples for bonding. a): Layers as plated. b): Expected structure after bonding.

Pairs of samples, consisting of one Au-layered chip and one Au/Sn/Au-layered chip were fabricated and bonded, as shown in Figure 4. All metals were electroplated on wafers (as previously described). Gold electroplating was performed in gold cyanide solution at a temperature range of 60–65 °C, with a current density 5.4 mA/cm^2.

For all Au-Sn samples, a bonding temperature of 350 °C was selected. This is a realistic temperature for getter activation, a required process for obtaining low pressure in a vacuum cavity. Using such a bonding temperature, there may not be need for an additional process step for getter activation. The bonding was carried out in two steps. First, a flip chip bonder (MAT-6400), was used for pick and place at room temperature in air (applying a force of 30 N for 30 seconds), then the positioned sample pair was bonded, using a hotplate in a vacuum chamber. Samples were bonded using different bonding times (2 min, 10 min, 20 min, 30 min). The bonding temperature profiles are shown in figure 5. Several samples (3 pairs) were bonded for each choice of bonding time. This allows testing of high-temperature shear strength, and microscopic investigations of cross-sections of samples bonded under identical conditions.

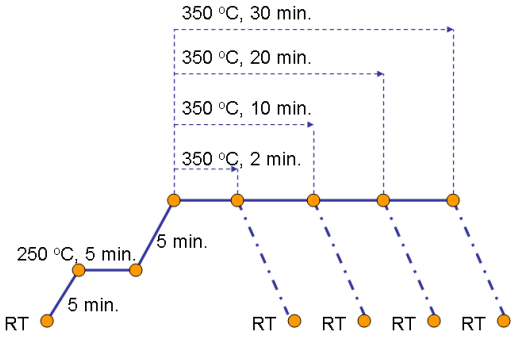

Figure 5:Temperature profile for Au-Sn SLID bonding.

III - Results and Discussion

A. Bond Line Analysis

From the bonding experiments performed, it was observed that a continuous high contact force in general leads to a higher bonding yield. In contrast to what has been presented in earlier studies using a low, even zero bonding force, there appears to be only small amounts of squeezed out Sn – even with a high pressure of 20 MPa applied. No large areas of pure Sn outside the bond frames could be observed, and any excess typically measured about 10-15 µm. It is believed that this is a result of the wafer bonding surfaces being brought into contact at a low temperature (150 °C) and kept in contact while the temperature is increased at a low rate (3 °C/min) past the melting point of Sn. Thus, the interdiffusion process will be near symmetrical and lead to a good IMC formation in the bond line, as shown in Figure 6.

Figure 7 shows an optical micrograph of a cross-section of a Au-Sn sample bonded for 2 minutes at 350 °C. The bond line is seen to be uniform. A yellow/ golden phase is found in the vicinity of the Si surfaces, and a uniform, greyish phase makes up the bonding

layer. All cross-sectioned samples show a similar phase structure, independent of the bonding time at 350 °C

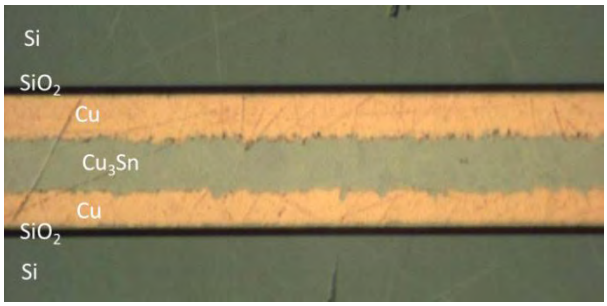

Figure 6: Cross section images of a Cu-Sn bond line. All available Sn has been converted to Cu_3Sn, as verified by SEM-EDX analysis.

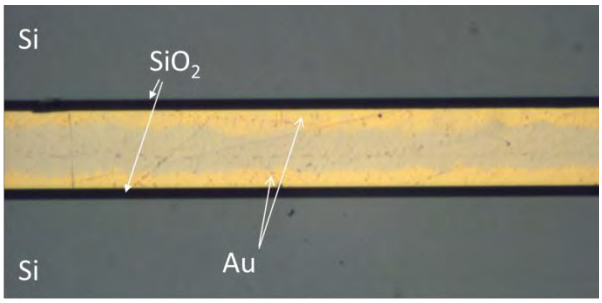

Figure 7: Optical micrograph of cross-sectioned bonded sample (bonding at 350 °C for 2 min [11]), where the bond line was identified as $Au/Au_5Sn/Au$

C. Characterization and Testing

Compared to eutectic soldering, interconnects with pure intermetallic will be stronger, but also more brittle. For both Au-Sn and Cu-Sn samples, the bond strength was determined from die shear testing, and typical results >20MPa were achieved. This is comparable with high strength results from other bonding technologies making both metal systems suitable for interconnect and packaging applications.

For Cu-Sn samples, thermal cycling (1000 cycles, -40 °C/+150 °C) did not reveal any significant impact on the shear strength, nor change in intermetallic composition or degradation of the bond frames. Furthermore, annealing experiments up to 350 °C for 30 minutes was carried out in order to simulate the getter activation process. From cross-sectional analysis no major phase transitions (aside from conversion of $Cu_6Sn_5 \rightarrow Cu_3Sn$) was observed in the bond line [8].

To verify the temperature stability of the bonded Au-Sn samples, the resistance to shear force at elevated temperatures was investigated. Results show that the actual bond is stable up to 375 °C or higher, being around 100 °C higher than the eutectic point. Varying the bonding time (in the range 2–30 minutes) does not have significant effect on the result. The bonding structure is expected to be stable over time, and not to change composition due to interdiffusion of Au and Sn.

IV – Summary

Solid-Liquid Interdiffusion (SLID) bonding is a bonding technique based on intermetallic formation that has received high interest in the industrial and scientific community due to the high temperature stability and possibility for repeated processing without the bonds melting. Cu–Sn is by far the most studied SLID system. Both metals are low-cost and readily available. The materials have extensive heritage in the microsystem/ microelectronic sector, as Sn is the basis of all soldering and Cu is a commonly used substrate and chip pad metallization in addition to BEOL and TSV interconnections. Au–Sn SLID bonding has also been demonstrated, and is of particular interest for CTE mismatched systems and since a flux-less process is easily implemented. Flux-less symmetric Cu-Sn bonding makes it very suitable for protection and packaging of sensitive MEMS and similar devices.

Compared to eutectic soldering, SLID interconnects with pure intermetallic will be stronger, but also more brittle. Reliability investigations such as shear strength at and after high temperature storage in addition to temperature cycling have been – and continue to be research topics. The electrical performance and mechanical strength both for interconnects and bond frames demonstrate very high yield and excellent performance.

References

[1] A. Munding, *et al.*, "Cu/Sn solid-liquid interdiffusion bonding," in *Wafer –level 3D ICs process technology*, ed: Springer Science 2008.

[2] Y. Iino, "Partial transient liquid-phase metals layer technique of ceramic-metal bonding," *Journal of Materials Science Letters*, vol. 10, pp. 104-106, 1991.

[3] D. S. Duvall, *et al.*, "TLP Bonding: A New Method for Joining Heat Resisant Alloys," *Welding Journal* vol. 53, pp. 203–214, 1974.

[4] R. L. Schmid-Fetzer, R.Y. & others (ed.), "Fundamentals of Bonding by Isothermal Solidification for High Temperature Semiconductor Applications," in *1996 TMS Annual Meeting, Physical Chemistry of High Temperature Composites and Intermetallics II: Joining*, Anaheim, California, 1996.

[5] R. W. Johnson, *et al.*, "Power device packaging technologies for extreme environments," *IEEE Transactions on Electronics Packaging Manufacturing*, vol. 30, pp. 182-193, Jul 2007.

[6] C. C. Lee, *et al.*, "Advanced Bonding/Joining Techniques," in *Materials for Advanced Packaging*, D. L. a. C. P. Wong, Ed., ed: Springer US. , 2009.

[7] A. Munding, "Interconnect Technology for hree-Dimensional Chip Integration," Dr.-Ing., Fakultät für Ingenieurwissenschaften und Informatik, Universität Ulm, 2007.

[8] N. Hoivik, *et al.*, "Fluxless wafer-level Cu-Sn bonding for micro- and nanosystems packaging," in *Electronic System-Integration Technology Conference (ESTC), 2010 3rd*, 2010, pp. 1-5.

[9] K. Wang, *et al.*, "Surface evolution and bonding properties of electroplated Au/Sn/Au," in *Electronics System-Integration Technology Conference, 2008. ESTC 2008. 2nd*, 2008, pp. 1131-1134.

[10] A. Lapadatu, *et al.*, "Cu-Sn Wafer Level Bonding for Vacuum Encapsulation of Microbolometer Focal Plane Arrays," *ECS Transactions*, vol. 33, pp. 73-82, 2010.

[11] K. E. Aasmundtveit, *et al.*, "Au-Sn SLID bonding: Fluxless bonding with high temperature stability to above 350C," in *Microelectronics and Packaging Conference, 2009. EMPC 2009. European*, 2009, pp. 1-6.

HIGH SPEED THERMAL INFRARED EMITTERS COMBINING NANOAMORPHOUS CARBON THIN FILM TECHNOLOGY AND BULK SILICON MICROMACHINING

P. Ohlckers[1,2], T. Skotheim[2], A. Kropachev[2] and B. Potapov[3]

[1]*Vestfold University College, 1384 Borre, Norway*
[2]*INTEX, Tucson, AZ, USA*
[3]*MIRL, Moscow, Russia*

***Abstract* — Combining Bulk Silicon Micromachining (BSM) with NanoAmorphous Carbon (NAC) thin film technology can be favourably used to make high performance MicroElectroMechanicalSystems (MEMS) devices. Intex is using this unique combination of technologies to design and manufacture a family of high performance infrared emitters with the most distinctive features being high speed with a modulation depth of more than 100 Hz, broadband IR emission from 1 to 14 micrometer, with around 10% power efficiency, and a lifetime beyond 100,000 hours. Rated input power is 950mW. This year (2011), two new versions will been launched, one with 25 % higher output IR radiation for demanding application, and a low power version with smaller chip size for low cost applications. Use in non-dispersive infrared gas sensors is the most important application.**

Keywords: **Nanoamorphous carbon, infrared emitter, gas sensors**

I Introduction: Thermal IR Emitters for Non Dispersive Gas Sensors

We define here "Infrared emitters" (IR emitters) as microdevices designed and manufactured using micro- and nanotechnologies (MNT) to enable specific attractive features such as small size, high radiation efficiency, high switching speed, high reliability and low cost. IR emitters are mostly thermal broadband emitters giving heat radiation to a large degree following Planck's law as greybody emitters, where the term greybody means that the emissivity deviates from the ideal blackbody emitters exactly following Planck's law. The most common application for microdevice IR emitters is in Non-Dispersive InfraRed (NDIR) gas sensors [1] using the infrared gas absorption principle. Non-dispersive simply means that dispersion of different wavelengths of the radiation is not used in the sensing principle, in contrast to dispersive techniques like spectrometers.

Most microdevice thermal IR emitters are MicroElectroMechanical System (MEMS) devices using bulk silicon micromachining (BSM) to define a thin membrane or a beam structure with low thermal mass as a carrier structure for a resistive film that is current heated to emit greybody infrared radiation. The resistive film can be made of different materials, with polysilicon, doped nanoamorphous carbon and metal as examples of thin film materials used.

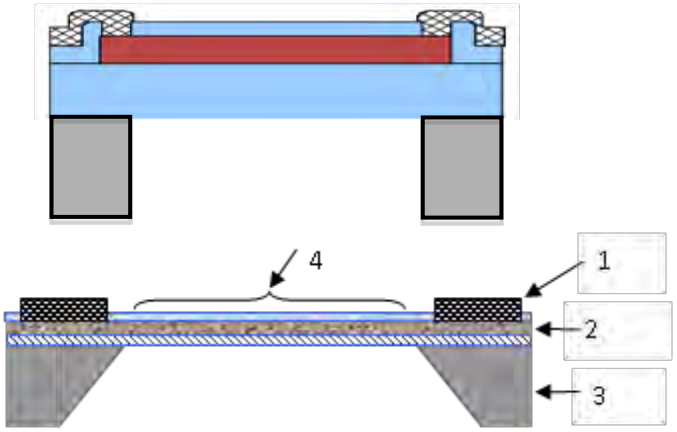

Figure 1 *Top figure shows cross section view of the principle design of a microdevice infrared emitter with a micromachined multilayer membrane film structure. At bottom figure a cross section view of a practical design using anisotropic silicon micromachining; the Intex INTX 17-0900: 1) Bonding pads; 2) NAC multilayer membrane, 3) Silicon support, 4) Active emitter area. Chip size is 3.8mmx3.8mm with chip thickness of 380 micrometer.*

A principal configuration is shown in Figure 1 where we can see a micromachined membrane with dielectric thin film layers covering both sides of the heater film structure. The dielectric films have both the function to give environmental protection and the function to set a proper stress level in the membrane or beam structure. In addition, the dielectric films may be designed to improve radiation emissivity at specific wavelengths by manipulating transmission, with constructive interference in the forward direction and destructive interference in the backward direction. In addition, emissivity can be improved by a surface film giving emissivity closer to blackbody radiation.

The carrier structure needs to have low thermal mass to achieve high switching speed and high emission efficiency, while having sufficient mechanical strength to survive the typical pulsed powering between off mode at low temperature and on mode at high temperature. Off-mode temperature would typically be 50 centigrade – at or close to the silicon frame temperature, which would be ambient temperature with the addition of a modest over temperature due to heat pick up from

emitting membrane, mostly acquired by conduction and convection from the heating resistor. On-mode temperature in the membrane or beam structure will be given by the on-mode saturation temperature balance as a balance between high emission output and sufficient lifetime for the used materials. Typical in-mode saturation temperatures will be in the range from 600 to 800°C.

The silicon micromachining is today mostly being done by anisotropic wet etching, giving the typical sloped cavity sidewalls at 54.7 degrees inclination, as for the Intex emitter chips shown in Figure 1. Mostly, such micromachining is done using TetraMethyl Ammonium Hydroxide and Water (TMAH) but sometimes also with potassium hydroxide (KOH) and water.

This is expected to gradually change to Deep Reactive Ion Etching (DRIE) [2], a dry etching process giving vertical sidewalls with an aspect ratio typically around 20:1, meaning a deviation from ninety degrees of less than 1 micron for each 20 micron depth, as shown in Figure 1. The main advantage will be smaller chip footprint because of the vertical etch pit sidewalls, while main disadvantage is higher processing cost, which will decrease as the DRIE technology becomes a more mature industrial process.

Also, surface micromachining could in principle be used by etching out a beam structure supported at both ends containing a thin film resistive element, e.g. polysilicon. However, no commercial emitters of such configuration are to our knowledge available – maybe because of the challenges to passivate the resistive thin film structures.

II Intex Silicon Micromachined IR Emitters Using Nanoamorphous Carbon as Resistive Heating Element

The IR emitter INTX 17-0900 from Intex is a microdevice thermal IR emitter using bulk silicon micromachining to achieve a carrier structure with low thermal mass for the resistive element generating the infrared radiation [3] These emitters are using a proprietary nanoamorphous thin film technology to make the resistive heating element on these thermal emitters.

Nanoamorphous carbon (NAC) is a diamond-like-carbon (DLC) material that has the following major material characteristics that are important when used as resistive thin film material in IR Emitters:

- Extraordinary Yield Strength of up towards 30 times better than stainless steel and up to 5 times *better than silicon.*
- High thermal conductivity.
- Superior chemical and corrosion resistance
- Processing of DLC films compatible with most silicon processes up to 500 °C ((short pulsing to ~800°C).
- The NAC thin films can be made by different Physical Vapour Deposition and Chemical Deposition Methods, or combined methods.
- Combination of silicon MEMS with NAC thin films can be used to make devices combining the versatility of silicon processing with the unique features of NAC thin film

In addition other important features are:

- Extraordinary stiffness with Young Modulus of Elasticity of around 8 times stiffer than silicon and around 7 times stiffer than steel.
- Indentation hardness and wear resistance approaching diamond, the best among any other materials.

The emitters are packaged in TO5 metal can transistor headers as shown in Figure 2 with an open header cap. The cap can alternatively be sealed in nitrogen with an infrared filter window like calcium fluoride, sapphire, silicon etc., depending upon the spectral properties wanted for the cap window.

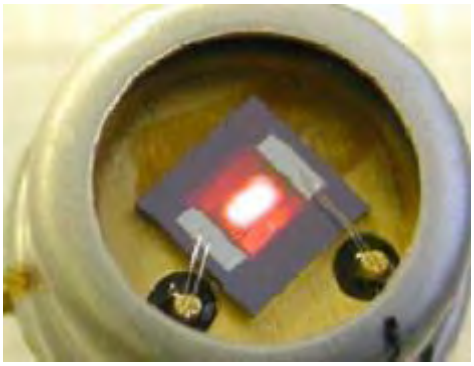

Figure 2: *Picture of the Intex INTX 17-0900 infrared emitter. It is packaged in a metal can transistor header. The picture is taken during operation, showing the visible part of radiation from the emitting membrane.*

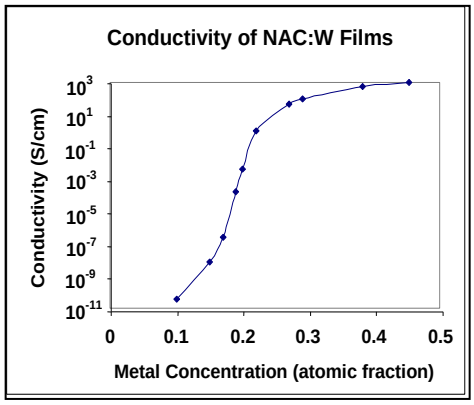

Figure 3: *Conductivity of the NAC film as a function of the atomic fraction of tungsten as the metal additive cosputtered during the NAC deposition process.*

The conductivity of the NAC film can be controlled by the atomic fraction of a metal as the resistive additive, as shown in Figure 3 with tungsten (W) as the metal additive.

INTEX has two new versions in development to be launched in 2011, one branded INTX 22-1000 with 25 % higher output IR radiation for demanding application, and a low power version INTX 08-0300 with smaller

chip size for low cost applications. Use in non-dispersive infrared gas sensors is the most important application.

III - Results and Discussion

The INTX 17-0900 emitters radiate like a greybody thermal infrared emitter, as shown in Figure 4 for different power levels from 657 to 851 mW. It can be observed that these emitters shine with high emissivity in the important wavelength band from 2 to 5 micrometer, where many gases with C-H bonds and C-O bonds have strong absorption lines making this band useful for sensing gases with such bonds, like methane and carbon dioxide. The measurements were made by Intex using FT-IR spectrometer Nicolet 6700 with Detector DTGS KBr. All these power levels are below the rated power level of 950 mW, which would give 750°C peak temperature in the centre of the membrane area. However, the emissivity at the band from 8 to 9.5 micrometer is less impressive, although still very high. To increase the emission in the long wavelength region, Intex is developing a high-emissivity coating (e ~0.95). This is important for applications like ethanol sensing, where there is a strong absorption line at 9.49 micrometer. The source can pulse at frequencies up to 100Hz at ~50% modulation depth. High frequency pulsed sources are important for achieving good signal-to-noise ratios (high sensitivity) in IR gas sensors. Recent specifications of the INTX 17-0900 (earlier MIRL17-900) are listed in Table 1.

Parameter	Typical
Spectral Output Range	1.0 - 20 µm
Emitter Surface Area	1.7x1.7 mm²
Hot Resistance	50 Ω
Drive Voltage (pulsed, bi-polar or DC)	6.9 V
Drive Current	140 mA
Working Temperature	750 °C
Modulation Frequency	0 - 100 Hz
Maximum Frequency at 50% Modulation	100 Hz
Power Consumption	950 mW
Integrated Power Emission (Emission Efficiency)	100 mW
Warm-up Time	<30 msec
Decay time	<5 msec
Lifetime	>100,000 hours at 500°C

Table 1*: Specifications of the Intex INTX 17-0900 emitter. Data apply @ 10 Hz and 50% duty cycle.*

The difference between cold and hot resistance is within 5%.

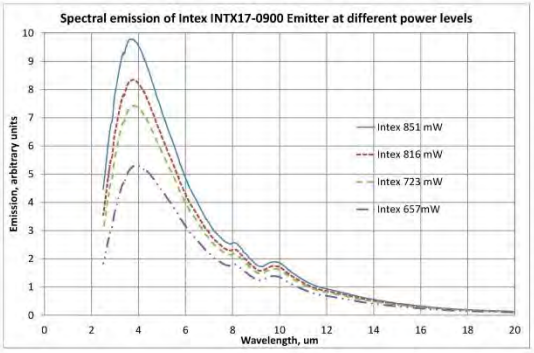

Figure 4: *Spectral emission of INTX 17-0900 (earlier Intex MIRL17-900) at different power levels, with higher power giving higher emission and peak values at shorter wavelengths.*

Intex will in year 2011 introduce two new emitters:

a. A high power version, INTX 22-1000, with 1050 mW input power and 25% higher infrared radiation output than the existing Intex INTX 17-0900, focused towards applications needing higher IR radiation intensity. The higher power rating is mainly achieved by increasing the IR emitting membrane from 1.7mmx1.7mm to 2.2mm x 2.2mm.

b. A low cost version, INTX 08-0300 with 300 mW input power for applications where low cost, small size and low power operation are most important features.

INTX 22-1000 has been qualified and is now in production. Spectral emission tests of the new high power Intex emitter INTX 22-1000, compared with the existing INTX 17-0900 emitter is shown in Figure 5 The tests are done with the same test setup as described for INTX 17-0900 in the previous chapter.

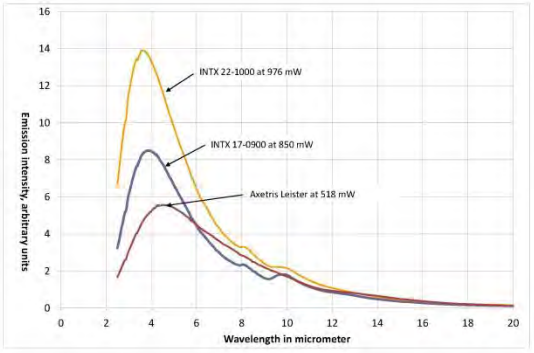

Figure 5: *Spectral emissions versus wavelength of Intex INTX 17-0900 and the new Intex high power emitter INTX-22-1000 at comparable power levels, showing that the new INTX 22-1000 outshines the present emitter with > 25% higher emission.*

The Intex emitters have particularly high output in the band from 2 to 5 micrometer, where for instance methane and carbon dioxide have strong absorption lines, at 3.4 and 4.3 micrometers, respectively.

Prototypes of the INTX 08-0300 has also successfully been processed, and test results will be published in the near future.

Switching speed, which we prefer to characterise as modulation depth, is an important feature in many applications, allowing for higher signal to noise ratio in NDIR gas sensors, or allowing for lower duty cycle, therebyreducing power consumption. In Fig. 6, taken from [6] it is shown that the INTX 17-0900 can be modulated up to 100 Hz – to our knowledge the fastest thermal IR emitter in the market.

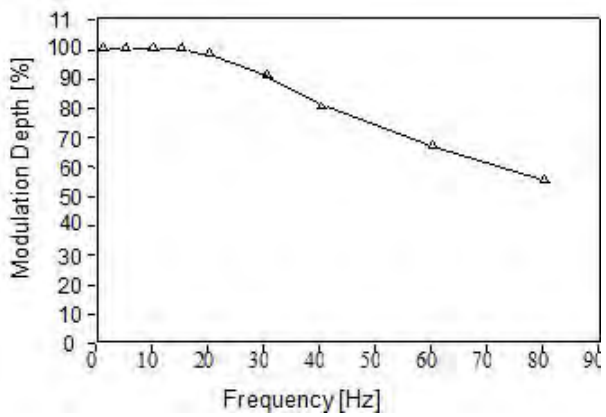

At present, we are using anisotropic bulk micromachining to define the membrane, as shown in Fig.1 at bottom. However, we expect membrane definition by using Deep Reactive Ion Etching (DRIE), as shown at top of Fig. 1, will soon be cost effective when added batch processing costs are balanced out by allowing smaller chip size with more chips per wafer, and reduced packaging cost with smaller chip footprint needed. We have already made demonstrator samples showing that such DRIE processing is compatible with the other process steps when manufacturing NAC based thermal emitters.

This is a part of our running R&D work, with a balanced focus on performance improvements and cost reductions – a needed approach to stay competitive and open up new applications.

IV - Conclusions

Intex is successfully manufacturing microdevice IR emitters for NDIR gas sensor applications with high IR intensity and high speed as highlighted features,. 2011 has seen the launch of a new emitter INTX 22-1000 with 25% improved radiation intensity, and a low power version INTX 08-0300 with smaller size and lower cost will follow. Future work will focus on performance improvements, in particular implementing a high emissivity coating for the long wavelength region and more cost effective manufacturing enabling wider market acceptance. Chip size optimisation by replacing anisotropic bulk silicon micromachining with deep reactive ion etching for the low thermal mass carrier membrane is a promising concept for future improvements.

References

[1] U. Zaghloul, A. Abelarni, F. Coccetti, G. Papaioannou, R. Plana and P. Pons, *MRS Fall Meeting*, Boston, December 1-5, 2008.

[2] 1.Luft, K.F., Schaefer, W., and Wiegleb, G. 50 Jahre NDIR-Gasanalyse, Odenbourge Verlag. in Technisches Messen 60. 1993. Bremen, Germany.

[3]. Laermer, F.S., DE), Schilp, Andrea (Schwa/ bisch Gmu/ nd, DE), Method of anisotropically etching silicon. 1996, Robert Bosch GmbH (Stuttgart, DE): United States.

[4] Per Ohlckers, Alain. M. Ferber, Vitaly K. Dmitriev and Grigory Kirpilenko: "A Photoacoustic Gas Sensing Silicon Microsystem" Proceedings of Transducers'01, pp. 780-783, Munich, Germany, June 2001.

[5] Dorfman, V.F., Diamond-like nanocomposites (DLN). Thin Solid Films, 1992. 212(1-2): p. 267-273.

[6] Ohlckers, P., et al. Advantages and Limitations of Diamond-Like Carbon as a MEMS Thin Film Material. in 2008 NSTI Nanotechnology Conference and Trade Show - Nanotech 2008. 2008. Boston: NSTI.

AN ELECTROSTATIC ENERGY HARVESTER WITH END-STOP EFFECTS

C. P. Le and E. Halvorsen

Department of Micro and Nano Systems Technology, Vestfold University College, Norway

***Abstract* — This paper presents characterization and modeling of an in-plane overlap varying electrostatic energy harvester with end-stops to limit proof mass motion under large amplitude acceleration. A model of the impact force between the proof mass and the end-stops is analyzed from their contact geometry and material properties. Performance prediction of the model is validated by excellent agreement between simulation and measurement results. In wideband excitation, we also found that the response bandwidth can be enhanced with the end-stop effects for sufficiently high acceleration power spectral density (PSD).**

***Keywords :* energy harvesting, electrostatic transduction, impacts, Hertz's contact**

I - Introduction

Electrostatic energy harvesting from a vibrating environment is currently considered as a promising alternative to replace batteries in sensor applications [1-3]. The output power is obtained by conversion from mechanical to electrical energy using a capacitive transducer driven by the motion of a proof mass. One challenge in the design of the energy harvester is to obtain substantial output power over a range of accelerations. For increasing acceleration, the proof mass displacement increases resulting in a corresponding output-power increase. In practice, the proof mass displacement can be limited under high acceleration due to the restricted device dimensions. Also, proof mass motion must be limited by design to avoid beam fracture at large amplitude displacement. This is accomplished by design of mechanical end-stops.

The proof mass hits the end-stops for a sufficient acceleration level. The impact force causes the device to behave nonlinearly, resulting in the jump phenomenon and other nonlinear phenomena. The impacts must be modeled to predict the performance at high accelerations. A linear impact force model with very large, in some cases somewhat arbitrarily chosen, spring stiffness has been considered by several authors [4-7].

We investigate the influence of a practical impact model represented by a parallel-connected spring and damper as in previous work, but obtain the stiffness value analytically from analysis of Hertz's contact problem [8-9]. The damping coefficient is fit to the jump phenomenon observed in the measurements. The impact force model is then incorporated into the mechanical domain of the electrostatic energy harvester model.

II – Analysis and modeling

A. Device structure description

An overlap varying capacitance structure is used for the capacitive transduction under environmental vibration. A design of such an electrostatic energy harvester is shown in Figure 1. In this design, the proof mass is suspended in four linear springs with folded shape. The harvester is operated by an external bias voltage connected to pads deposited on the anchors and the output power is simply obtained by connection of the fixed electrodes to external loads.

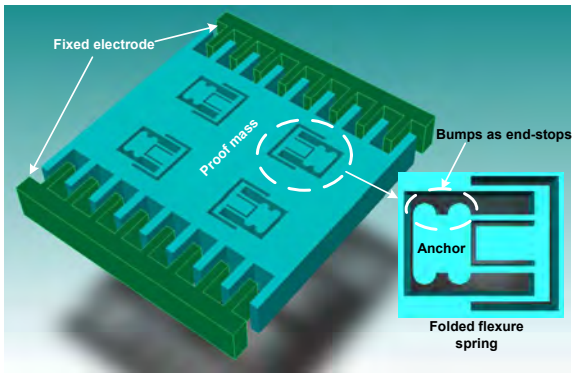

Figure 1. *An electrostatic energy harvester design with capacitive transduction and use of anchors as stoppers*

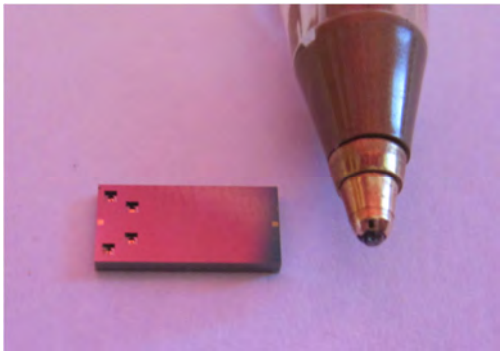

Figure 2. *Picture of device fabricated in Tronics MPW services using 60µm SOI high aspect ratio micromachining with die dimension of 4x8mm*^{2}

In this design, the bumps on the anchors function as end-stops. The bumps have cylindrical geometry with radius R=30µm and thickness t=60µm. The capacitive transducer has a length of the capacitor fingers l=25µm, a width of the capacitor fingers w=4µm, a gap between electrodes g_0=3.2µm and an initial capacitor finger overlap x_0=10µm. The maximum displacement of the proof mass is x_{max}=7µm. Figure 2 shows a picture of the device which is fabricated in Tronics MPW services

using 60μm SOI high aspect ratio micromachining. The die dimension is 4x8mm^2. The number of fingers is N_f= 438. All device structure parameters are listed in Table 1.

Table 1: *Device structure parameters*

Parameters	Value
Die dimensions	8mmx4mm
Device thickness, t	60 µm
Length of capacitor fingers, l_f	25µm
Width of capacitor fingers, w_f	4µm
Gap between capacitor, g_0	3.2µm
Number of capacitor fingers on each electrode, N_f	438
Initial capacitor finger overlap, x_0	10µm
Maximum proof mass displacement, x_{max}	7µm
Bump radius, R	30µm

B. Impact force

The end-stops confine the proof mass motion to the range $-x_{max} \le x \le x_{max}$. The end-stop force F_{im} for displacement amplitudes beyond these limits can be modeled as a parallel connected spring-damper system, given by

$$F_{im} = k_{im}\delta + b_{im}\dot{\delta} \qquad \text{for } |x| > x_{\max} \qquad (1)$$

where k_{im} is the end-stop stiffness, b_{im} is damping coefficient and δ the relative displacement between the proof mass and the end-stops during impact

$$\delta = |x| - x_{\max} \qquad (2)$$

This impact is considered as a Hertzian line contact between a surface and a half cylinder with a radius of R and a length of t as shown in Figure 3. The contacting bodies are made from the same elastic material with Young's modulus E and Poison's ration υ. In order to determine k_{im}, we use static analysis.

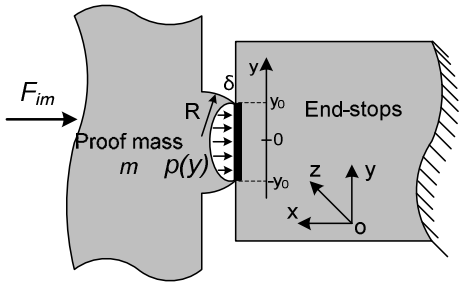

Figure 3. *Deformed body analysis of Hertz's contact between the proof mass and the end-stops for determination of the impact force*

At high acceleration, the impact between the proof mass and the end-stops cause deformation of the two bodies. The contact area is rectangular with dimension of $2y_0t$. This is a result from a pressure force $p(y)$ created by the impact force F_{im}. This pressure force is expressed by [8-9]

$$p(y) = \frac{2F_{im}}{\pi y_0 t}\sqrt{1-\frac{y^2}{y_0^2}} \qquad (3)$$

where,

$$y_0 = \sqrt{\frac{8\lambda R F_{im}}{t}} \text{ and } \lambda = \frac{1-\upsilon^2}{\pi E}$$

The relative displacement δ between the proof mass and the end-stops is simplified as being uniform in the entire contact area and $t >> y_0$. Thus, the relative displacement δ can be straightforwardly calculated by

$$\delta = \left[1 + \ln\frac{t^3}{2\lambda R F_i}\right]\frac{2\lambda}{t}F_{im} \qquad (4)$$

The relative displacement δ is small compared to the proof mass displacement x. Furthermore, the impact force is generally non-linear for increasing the relative displacement δ. The damping constant in (1) is determined by a fit to match the simulations to the observed frequency of the jump phenomenon in the measured device frequency response.

C. Device model

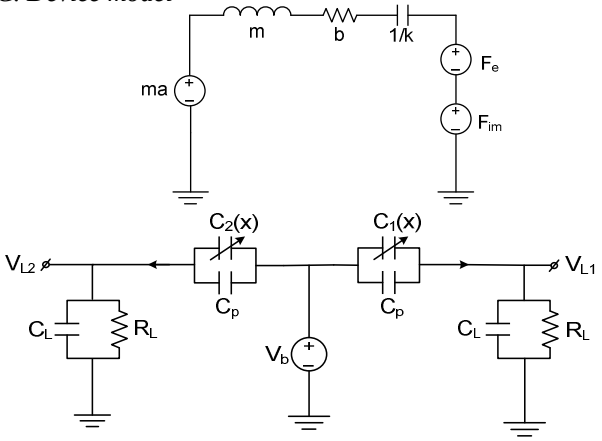

Figure 4. *Energy harvester model in mechanical and electrical domains with impact force between the proof mass and the end-stops*

A complete model of the capacitive transducer is shown in Figure 4. The mechanical and electrical domains are captured by following equations

$$m\ddot{x} + b\dot{x} + kx + F_e + F_{im} = ma \qquad (5)$$

$$V_b = -\frac{q_{1/2}}{C_{1/2}(x) + C_p} + V_{L1/L2} \qquad (6)$$

where q_1 and q_2 are the charges on the transduction 1 and 2 respectively. The electrostatic force is represented by

$$F_e = \frac{1}{2}q_1^2\frac{\delta}{\delta x}\left(\frac{1}{C_1(x)+C_p}\right) + \frac{1}{2}q_2^2\frac{\delta}{\delta x}\left(\frac{1}{C_2(x)+C_p}\right) \qquad (7)$$

and

$$C_{1/2}(x) = C_0\left(1 \pm \frac{x}{x_0}\right) = 2N_f\varepsilon_0\frac{x_0 t}{g_0}\left(1 \pm \frac{x}{x_0}\right) \quad (8)$$

A parasitic capacitance C_p in parallel with the variable capacitance is also included in the model. All parameters of the model are listed in Table 2.

Table 2: *Model parameters of the capacitive transducer*

Parameters	Value
Inertial proof mass, m	2.8mg
Spring stiffness, k	166.5N/m
Damping coefficient, b	3.75e-3Ns/m
Initial variable capacitance, C_0	1.6pF
Parasitic capacitance, C_p	17.3pF
Load resistance, R_L	4.9MΩ
Load parasitic capacitance, C_L	4.0pF

III – Results and Discussion

A. Narrow-band excitation

Figure 5 shows the device frequency response in simulations and measurements at a bias voltage V_b=30V. For an acceleration a_{rms}=4.1g, the proof mass displacement is excited to a small amplitude. Therefore, there is no impact between the proof mass and the end-stops, and no clear signatures of nonlinear behavior as observed. There is agreement between the simulation and the experimental results, giving a resonance frequency f_0=1220Hz.

With an increase of the acceleration to a_{rms}=5.5g, the excitation level is sufficient to drive the proof mass into the end-stops. In the up-sweep frequency response, the output voltage increases with increasing frequency up to f=1135Hz. At this point, the proof mass hits the end-stops, causing a kink in the output voltage and a moderate further increase. The output voltage jumps down at a frequency f=1425Hz. This can be understood as an effective increase of stiffness when the proof mass impacts the end-stops. The harvester behaves nonlinearly, resulting in the jump phenomenon.

The relative displacement between the proof mass and the end-stops during impact is small. It is possible to approximate the non-linear relation between the impact force and the displacement by a linear fit over the relevant range of displacements. For a range of δ from 0-0.5µm, a linear fit to (4) leads to a constant impacting stiffness k_{im} approximated by

$$k_{im} \approx 0.116\frac{\pi E t}{2\left(1-\upsilon^2\right)} \quad (9)$$

As observed in Figure 5, both linear and nonlinear end-stop models properly capture the stopper under high acceleration. The results of simulations and measurements are approximately regardless of the stiffen model. Hence, we have shown that a linear model is adequate and that the stiffness can be predicted.

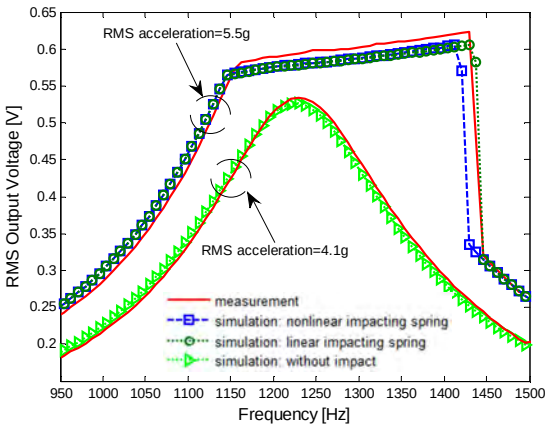

Figure 5. *Up-sweep frequency response of RMS output voltage at bias voltage V_b*=30V

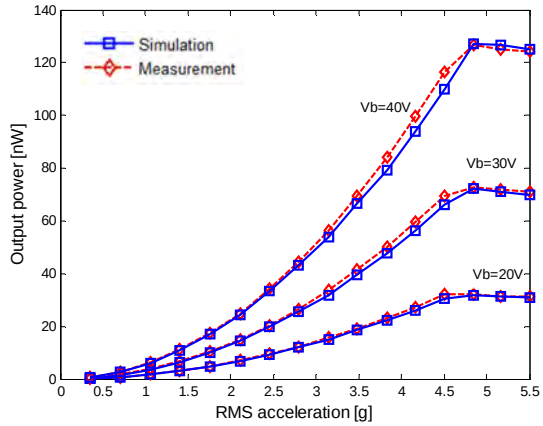

Figure 6. *Output power with end-stop effects for increasing acceleration amplitude for different bias voltages*

Figure 6 shows variations of output power with increase of the rms acceleration for different bias voltages V_b. For higher bias voltage V_b, the greater output power is obtained. Both the simulation and measurement results exhibit impact at the acceleration of a_{rms}=4.5g. At this excitation level, the end-stops confine the proof mass motion at the maximum displacement x_{max}, leading to saturated output power or voltage. Furthermore, the proof mass impacts the end-stops at the same acceleration level for various bias voltages V_b=20, 30 and 40V. This means that the mechanical damping is still dominant in comparison with the electrical damping for this range of the bias voltage V_b.

B. Wide-band excitation

Performance of the energy harvester under wide-band excitation was also characterized. The transducer model with inclusion of parasitic capacitance gives a good agreement between the measurements and the simulations. Higher output power is achieved for larger power spectral densities (PSDs) of the acceleration as shown in Figure 7 for a bias voltage V_b=30V. The acceleration PSD levels are small enough that the device performs in the linear regime. The bandwidths of the

responses are consequently equal for the different acceleration PSDs in this range.

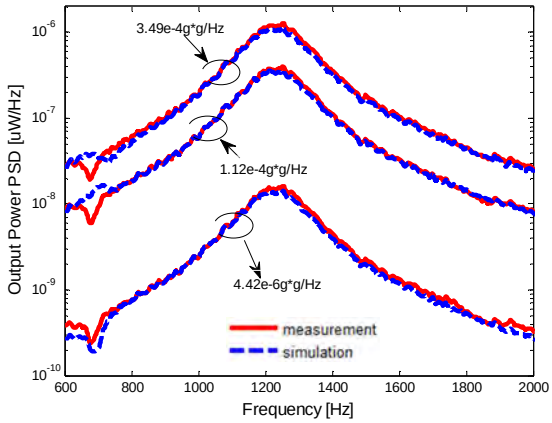

Figure 7. *Output PSDs for various acceleration PSDs at* V_b=30V

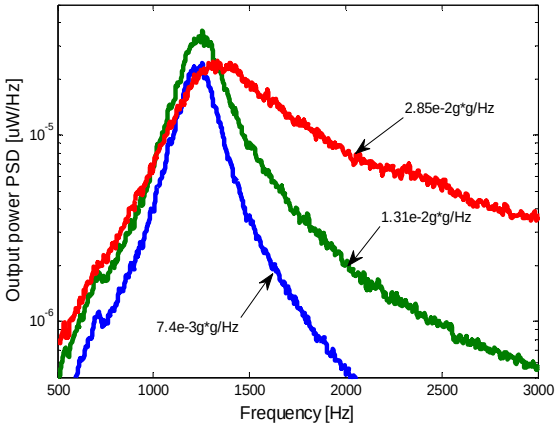

Figure 8. *Simulation results of bandwidth increase due to end-stops for sufficiently high acceleration PSDs at* V_b =30V

At high acceleration PSD, the output spectrum is only evaluated from the simulation model due to experimentally limited vibration level. Further increase of the acceleration PSD results in frequent impacts between the proof mass and end-stops and the harvester behaves nonlinearly. The bandwidth now increases with increasing acceleration PSD. Therefore, the device bandwidth can be improved with the stopper effects under wide-band excitation as shown in Figure 8. For example, the 3dB-bandwidth is enlarged from 380Hz to 600Hz for increasing the acceleration PSD from 7.40x10^{-3} [g^2/Hz] to 2.85x10^{-3} [g^2/Hz]. The experimental results under large acceleration level of the wide-band excitation will be further investigated in future work.

IV – Conclusion

An electrostatic energy harvesting device was characterized and modeled taking into account stopper effects under large amplitude displacement excitation. The impact force between the proof mass and the end-stops was analyzed using Hertz's line contact model. The device model with a nonlinear impact force efficiently captured the device behavior giving agreement between the simulation and measurement results. A stopper model with linear stiffness fit to the nonlinear stiffness model over a limited range performed equally well. For wide-band excitation, the bandwidth improvement is a positive effect of the end-stops for large accelerations.

References

[1] P. D. Mitcheson, E. M. Yeatmen, G. Kondala Rao, A. S. Holmes, T. C. Green, "Energy harvesting from human and machine motion for wireless electronic devices", *Proceeding of the IEEE*, Vol.96, pp.1457-1486, Sep 2008.

[2] S. Roundy, P. K. Wright, J. Rabaey, "A study of low level vibrations as a power source for wireless sensor nodes", *Computer Communications*, Vol. 26, pp. 1131-1144, Oct. 2003.

[3] S.Roundy, P. K. Wright, and J. M. Rabeay, "Energy scavenging for wireless sensor networks",1st ed. Boston, MA: Kluwer Academic, 2003.

[4] L. G. W. Tvedt, L.-C. J. Blystad and E. Halvorsen, **"**Simulation of an electrostatic energy harvester at large amplitude narrow and wide band vibration", *in Proc.Symp.Des.,Test.,Integr.Packag.DTIP2009*, Nice, France, Apr. 9-11, 2008, pp.296-301.

[5] M. S. M. Soliman, E. M. Abdel-Rahman, E. F. El-Saadany and R. R. Mansour, "A wideband vibration-based energy harvester", *J. Miromech. Microeng.*, vol. 18, no. 11, pp. 115 021, Nov. 2008.

[6] D. Hoffmann, B. Folkmer and Y. Manoli, "Fabrica tion, characterization and modeling of electrostatic miro-generators", *J. Miromech. Miroeng.*, vol. 19, no. 9, pp. 094 001, Sep. 2009.

[7] K. R. Gandu, P. D. Mitcheson, and T. C. Green, **"**Simulation toolkit for energy scavenging inertial micro power generators", *POWERMEMS2007*, Freiburg, Germany, Nov. 28-29, 2007, pp.137-140.

[8] K. L. Johnson, "*Contact mechanics*", *Cam. Uni. Press*, 9th *edit*.(2003), ISBN 0-521-34796-3.

[9] E. J. Hearn, "Mechanics of materials II: The mechanics of elastic and plastic deformation of solids and structural materials", *Butterworth Heinemann Press*, 3th *edit*.(1997), ISBN 0-7506-3266-6.

PREVENTION OF SIDEWALL REDEPOSITION OF ETCHED BYPRODUCTS IN DRY AU ETCH PROCESS

A. Aydemir[1], T. Akin[1, 2]

[1]*Middle East Technical University, MEMS Research and Application Center, Ankara, Turkey*
[2]*Middle East Technical University, Dept. of Electrical and Electronics Eng., Ankara, Turkey*

***Abstract* — In this paper we present a new technique of etching thin Au film in a dual frequency inductively coupled plasma (ICP) system on Si substrate to prevent redeposition of etched Au particles over the sidewall of the masking material called as veils. First, the effect of lithography step was investigated. Then the effect of etch chemistry and the process parameters on the redeposition of etched Au particles on the sidewall of the masking material have been investigated. After minimizing the effect, by depositing a thin Ti film over the masking material acting as a hard mask, redeposition effect has been examined. The results showed us that depositing a thin Ti film over the masking material prevents the redeposition of etched Au particles. Based on the results of this study, we propose a new technique that eliminates the redeposition of etched Au particles on the sidewall of the masking material in dry Au etch process.**

Keywords : **Au Etch, ICP, Veils, Plasma Etch, Veils**

I - Introduction

Several materials can be used as a metallization layer in the fabrication of MEMS devices. Choice of the material is determined by considering the performance requirement of the device including electrical resistivity, adhesion characteristics, deposition conditions of the film, and selectivity issues. Au offers several notable performance features like having a low resistivity, high chemical stability, high melting point, and low surface work function which gives good ohmic contact with other metals [1]. Therefore it has been extensively used as a metallization layer in the fabrication of MEMS devices.

Thin film patterning methods fall into two categories; dry and wet etch chemistries. Dry etch chemistry becomes more important when you are concerned with the feature resolution. So the most important advantage of etching Au in plasma environment is having less undercut compared to wet etch processes. Different masking materials including photoresist and hard masks using chlorine and fluorine containing etch chemistries have been reported for etching Au in plasma environment. However, even etching Au in an ICP system operating at low pressure with ease control of bias voltage, redeposition of etch Au particles cannot be completely eliminated by optimizing the process parameters [2, 3].

Having tapered profile for the masking material, photoresist, may eliminate this problem by enhancing the removal of the deposited Au particles on the sidewall of the masking material by resputtering it with the incoming ions. However, making profile angle of the photoresist negative becomes difficult when the feature size gets smaller.

It has also been reported that using hardmask will also eliminate the redeposition effect with a well optimized etch process parameters [4]. However it is not always possible to use hard mask as an etch mask especially when you are concerned with the selectivity of the etch stop layer with the masking material while removing the masking material after etching is completed.

The main objective of this work is to present for the first time a technique that eliminates the redeposition of etched Au particles on the sidewall of the masking material in dry Au etch process using photoresist as an etch mask even for nano scaled feature sizes. First, the effect of the masking material, photoresist, and its profile angle on redeposition rate using our standard etch recipe were investigated. Then process parameters were optimized to minimize the redeposition effect. Finally, we have investigated the redeposition of the etch Au particles on the sidewall of the masking material by depositing a thin Ti film over the masking material that will act as a hard mask.

II - Experimental Details

For the investigation of the redeposition effect, 0.2μm stress free SiN film deposited 6” Si wafers were used as a substrate. SiN film was deposited at 300^{o}C using a dual frequency, 13.56MHz and 380kHz, PECVD system. Then 10nm Cr layer was deposited as an adhesion layer before depositing 200nm Au layer in a sputtering system. Plasma etching of Au thin film was performed using an ICP etching system with a dual frequency RF generator. Figure 1 shows the schematic diagram of an ICP chamber. Finally visual inspections were done in SEM.

First, the profile angle of three different photoresists, Shipley S1805, S1813, and ULTRA-i 123 08, spun at 4000rpm were investigated after hardbaking at 115^{o}C for 20 minutes in an oven. Redeposition rate after etching Au in an ICP system using the standard etch recipe was investigated with these three different photoresists in SEM.

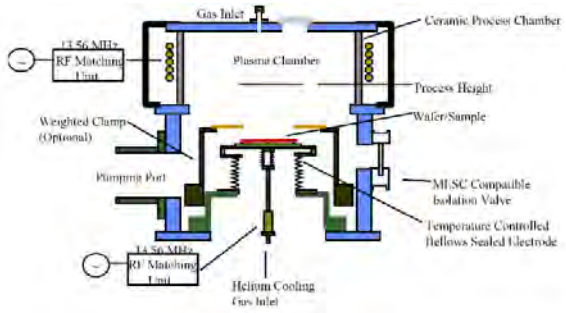

Figure 1: *Schematic diagram of an ICP chamber [5].*

Secondly, effect of the etch chemistry and the process parameters on the redeposition rate were investigated using a dual frequency ICP etch system. Standard etch recipe process parameters that was used as the starting point for the optimization of the etch process is listed in Table 1.

Specifically, effect of the HBr/Ar and Cl_2/Ar gas mixtures with a constant gas flow rates were investigated in SEM as the etch chemistries using the gas flow rates constant. After determining the etch chemistry, effect of the coil RF and platen RF powers on the redeposition rate were investigated. For the coil RF power 3 different set values were applied, 600W, 800W, and 1000W and for the platen RF power 50W, 150W, and 250W set values were applied. Redeposition rates after each etch process were investigated in SEM.

Table 1: *Standard Au etch process parameters*

	Set values
HBr	15 sccm
Ar	5 sccm
Pressure	2 mTorr
RF Coil Power	800 W
RF Platen Power	150 W
Temperature	20^{c}C

Even after achieving the optimum process parameters, there was still redeposition effect on the sidewall of the photoresist for submicron size structures. Because using hardmask, SiO_2, was not applicable in our process considering the selectivity of the SiO_2 film with the SiN etch stop layer, we have developed a new technique for the prevention of the redeposition effect of the etch Au particles on the sidewall of the photoresist by depositing a thin Ti film over the patterned photoresist that will act as an hardmask on the sidewall of the photoresist for submicron size structures in which profile angle of the photoresist is almost vertical. 7nm thick Ti film was deposited in a sputtering system over the patterned photoresist before etching process is done.

After etching is completed lateral component of the deposited Ti film was completely etched away and the vertical component of the Ti film on the sidewall of the small structures was removed by dissolving the photoresist in EKC265 polymer removal. Then 30 minutes O_2 plasma was also applied to remove the remaining contamination.

III - Results and Discussion

A. Effect of Masking Material Profile Angle

The effect of profile angle of photoresist on the redeposition rate of etch Au particles on the sidewall of the photoresist has been studied by using three different photoresists, Shipley S1805, S1813, and ULTRA-i 123 08 by spinning at 4000 rpm and hardbaking at 115^{o}C for 20 minutes in an oven.

Figure 2 shows the cross sectional SEM images of the plasma etching done Au thin films using different photoresists. Highest redeposition rates were observed on the ULTRA-i 123 08 type photoresist in which profile angle was 70.07^o, and lowest rates are observed on the S1805 type photoresist in which profile angle was 56.57^o.

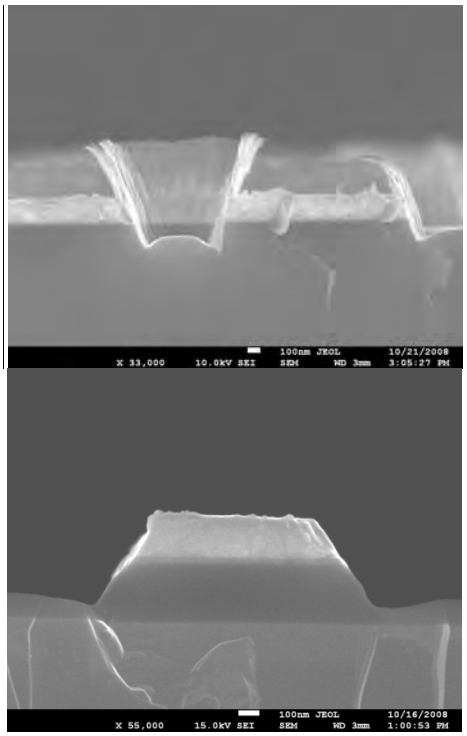

Figure 2: *Cross sectional SEM images of the plasma etching done Au thin films with using different photoresists. Top: with Ultra-I 123 08, Bottom: with S1805.*

B. Effect of Process Parameters

Etch chemistry has been investigated by using HBr/Ar and Cl_2/Ar gas mixtures and setting the process parameters as given in standard Au etch recipe. Decrease in Au redeposition rate on the sidewall of the photoresist has been observed with Cl_2/Ar etch chemistry. For the rest of the processes Cl_2/Ar chemistry has been used.

The effect of coil and platen RF powers have been investigated by applying different RF powers on the redeposition rate of etch Au particles on the sidewall of the photoresist.

First, by keeping the platen power and process time constant, 150W and 75 seconds, three etch runs were done by setting the coil RF power to 600W, 800W, and 1000W.

No significant effect on the redeposition rate on the sidewall has been observed with a change in the coil RF power. Only change in the etch rate and the etch uniformity were affected by changing the coil RF power.

Second, the effect of the platen RF power has been investigated by applying different RF powers and keeping the coil RF power and the process time constant, 600W and 75 seconds. Three etch runs were done by setting the platen coil power to 50W, 150W, and 250W.

As the platen RF power set value decreases, an increase in the redeposition rate of etch Au particles on the sidewall of the photoresist and a decrease in the Au etch rate have been observed. On the other hand, photoresist etch rate also increases with the increased platen power. Optimum results were achieved by setting the platen RF power to 250W. SEM images of the plasma etching done samples are shown in figure 3.

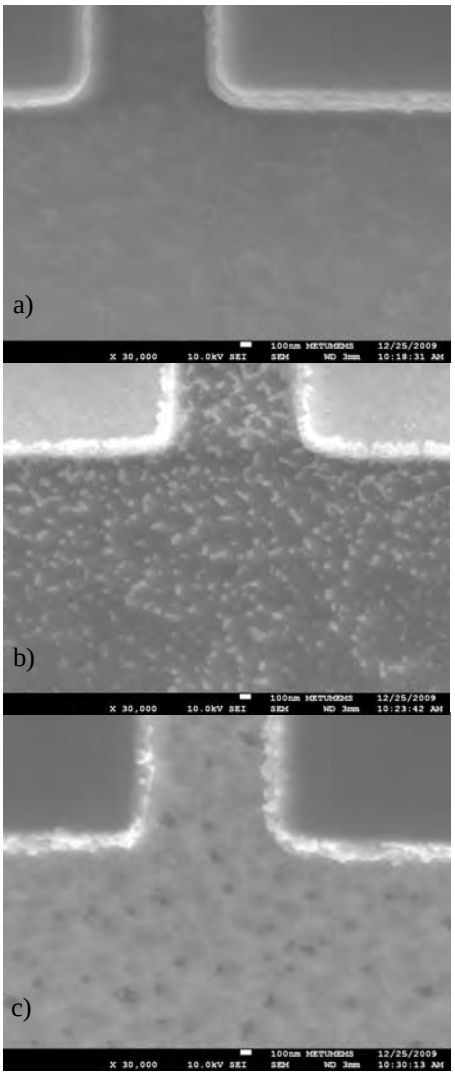

Figure 3: *SEM images of the etched Au thin films with different platen RF powers .a) 250W, b) 150W, c) 100W.*

After determining the last process parameter, Au etch recipe that is optimized to reduce the Au redeposition effect on the sidewall of the photoresist have been updated as given in table 2.

Table 1: *Updated Au etch process parameters*

	Set values
Cl_2	15 sccm
Ar	5 sccm
Pressure	2 mTorr
RF Coil Power	600 W
RF Platen Power	250 W
Temperature	20^{c}C

C. Effect of Deposited Thin Ti Film

Even after optimizing the lithography step and plasma etch process parameters, there were still redeposition of etch Au particles on the sidewall of the photoresist for submicron size structures.

In order to prevent this redeposition effect we have introduced a new technique by depositing 7nm thick Ti film over the patterned photoresist that will act as an hardmask to prevent the redeposition of etched Au particles for submicron size structures in which profile angle of the photoresist is almost vertical. For this Au etch run, optimized lithography step and ICP etch process parameters were used. SEM images after depositing 7nm Ti layer on the patterned structures are shown in figure 4.

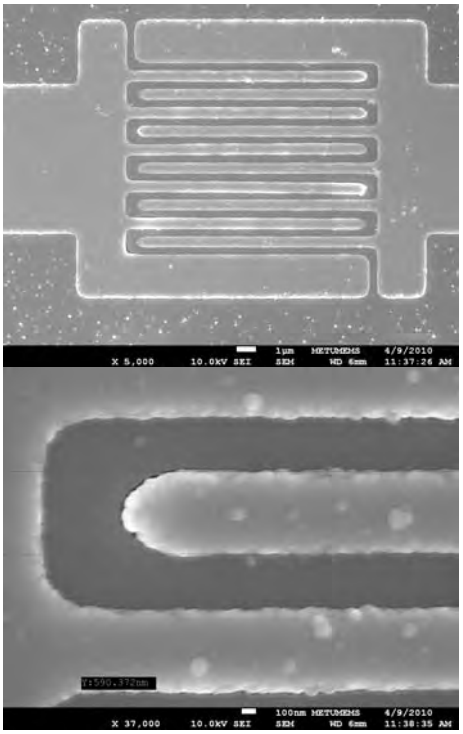

Figure 4: *SEM images of Ti deposited structures after lithography step.*

After 75 seconds etch process, photoresist was removed in EKC265 polymer removal and 30 minutes O_2 plasma run was also done to clean the remaining contamination. SEM images after cleaning the wafer were taken as shown in figure 5 for submicron size structures.

Depositing a thin layer of Ti over the patterned photoresist completely eliminates the redeposition of etched Au particles over the sidewalls of the photoresist for submicron structures.

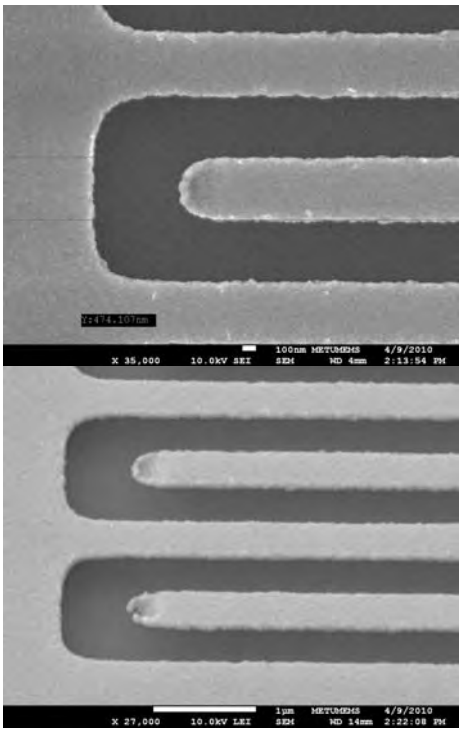

Figure 5: *SEM images of plasma etch done 0.5µm wide structures.*

IV - Conclusion

A new Au etch technique in plasma environment has been introduced to prevent the redeposition of etched Au particles on the sidewalls of the masking material, photoresist. Redeposition rate of etched Au particles has also been investigated for two important parameters; the profile angle of masking materials and the ICP process parameters. Redeposition rate is related to the thickness of the photoresist and the maximum profile angle that can be achieved after hardbaking step. ICP process parameters have also been investigated in order to reduce the redeposition rate after optimizing the lithography step. Both effects of coil and platen RF powers on the redeposition rate have been investigated. According to results, an update has been made on the etch recipe. Although the improvements made by optimizing the lithography and process parameters were eliminating the redeposition effect for structures having dimensions in the order of micrometer level, redeposition effect still existed for the structures with a submicron dimension. The reason is that, it becomes difficult to give a negative profile angle as the size of the structure becomes smaller. This problem can be eliminated by the technique that has been introduced by depositing a thin Ti layer over the patterned photoresist which will act as a hardmask and prevent the redeposition of the etch Au particles.

References

[1] H. Ohtake, S. Samukawa, H. Oikawa and Y. Nashimoto, *Jpn. J. Appl. Phys.* 37, 2311, 1998.

[2] H. S. Kim, M. D. Dawson and G. Y. Yeom, *J. Korean Phys. Soc.* 40, 567, 2002.

[3] J. K. Jung and W. J. Lee, *Jpn. J. Appl. Phys.* 40, 1408, 2001.

[4] P. Werbaneth, Z. Hasan, P. Rajora, M. Rousey-Seidel, Tegal Corporation.

[5] A.M. Hynes, H. Ashraf, J.K. Bhardwaj, J. Hopkins, I. Johnston, J.N. Shepherd, *Sensors and Actuators* 74, pp. 13-17, 1999.

SENSING APPLICATION OF NANOCELLULOSE MODIFIED WITH DOUBLE-WALLED CARBON NANOTUBE AND GRAPHITE NANOPOWDER

F. Toomadj[1,2], S. Farjana[1,2], A. Sanz-Velasco[2], O. Naboka[2], P. Lundgren[2], K. Rodriguez[3], G. Toriz [1], P. Gatenholm[1], and P. Enoksson[2]

[1]*Wallenberg Wood Science Center and Department of Chemical and Biological Engineering, Biopolymer Technology, Chalmers University of Technology, Göteborg, Sweden*
[2]*Wallenberg Wood Science Center and Department of Microtechnology and Nanoscience – MC2, BioNano Systems Laboratory, Chalmers University of Technology, Göteborg, Sweden*
[3]*Department of Materials Science and Engineering, Virginia Tech, Blacksburg, USA*

***Abstract* — Electrically conductive nanocellulose films were prepared by immersion in dispersions of double walled carbon nanotubes or graphitized nanopowder. These solutions were prepared by using the surfactant cetyltrimethylammonium bromide (CTAB) under heating and stirring which were followed by a short time sonication. Electrospun cellulose and bacterial cellulose were used as a backbone of these films. Controllable modification of cellulose with conductive agents was performed by treatment with their dispersions for 24 – 72 hours.**

Electrical conductivities of the resulting films are from 0.009 S cm^{-1} to 0.395 S cm^{-1} which is higher or comparable to previously reported results.

Some methods have been employed to study the electrical conductivity behavior of samples. The electrical conductance of the films displays a high sensitivity to strain when tensile stress is applied.

***Keywords :* sensor, conductive cellulose, double walled carbon nanotube**

I - Introduction

Strain sensors based on nanostructured materials represent a new class of microelectronic devices which have gained a great interest due to their low power consumption, high sensitivity, selectivity and prompt response [1]. Conventional strain and pressure sensors are characterized by rigidity and fragility which significantly restrict their application area. Flexible large-area sensors can be produced by inserting nanoparticles with appropriate thermal and electrical properties into a suitable polymer matrix [2].

The outstanding properties of carbon nanotubes e. g. with regards to electrical conductivity and piezoresistivity make them one of the best candidates to use as building blocks of sensors [3]. To process CNTs, well dispersed and stable CNT solutions are required but due to the strong van der Waals forces between carbon nanotubes, they form bundles which are difficult to dissolve in water or other organic solvents. Commonly to improve dispersability of CNT in water surfactants need to be used [4,5].

Cellulose is one of the most widely used natural materials [6]. Owing to its biocompatibility, easy modification and low price, nanocellulose is a very appealing substrate for the development of carbon nanotube based sensors. Due to its good mechanical properties, high porosity, and biocompatibility, bacterial cellulose has recently attracted a great deal of attention for academic and industrial point of view [7]. Electrospinning is the fast and simple process for forming submicron scale structures through the action of electrostatic forces in which cellulose could be arranged in nonwoven fibrous materials with well controlled morphology such as fiber diameter, and surface area [8,9].

The goal of the present work is to prepare nanocellulose materials with controlled electrical conductivity by incorporation of double walled carbon nanotubes (DWCNT) or graphite nanoparticles (GNP) into the nanostructured cellulose and to investigate their strain sensing properties.

II - Experimental Details

Bacterial cellulose (BC) and electrospun cellulose (EC) were used to obtain conductive films. The EC was obtained by electrospining of a cellulose acetate solution (17% wt) in acetone and dimethylacetamide (2:1 volume ratio). The cellulose regeneration process was carried out by deacetylation with NaOH in ethanol (0.05 mol/l) for 24 hours. Bacterial cellulose was produced with Gluconacetobacter xylinum. DWCNT modified with carboxyl groups (+90% purity, Nanocyl S A, Belgium) and graphitized carbon nanopowder purchased from Sigma-Aldrich (<500 nm particle size (DLS), >99.95% trace metal basis) were used as a conductive agent for impregnation of cellulose.

Cellulose swelling was performed by treatment of cellulose pellicles in NaOH solution (0,5 mol/l) for 1 hour at 70 °C under stirring. Before modifying with DWCNT or GNP, cellulose pellicles were washed until a pH of 7 was reached. The washing process was done with rinsing and soaking in de-ionized water and checking the pH until reaching a pH of 7.0 This process was done at room temperature.

DWCNT and GNP water dispersions were prepared in the presence of cetyltrimethylammonium bromide

(CTAB). DWCNT or GNP was mixed with half of final volume and was heated (90 °C, 1 hour). After, the solution was sonicated (20 minutes) and CTAB was added to the solution (1:1 CTAB to DWCNT (GNP) weight ratio). Water/DWCNT (GNP)/CTAB mixtures were heated (90 °C, 1 hour) and sonicated for 20 minutes. Prepared dispersions were centrifuged for 20 minutes (3500 rpm, room temperature) in order to remove undispersed carbon. For modification of cellulose samples DWCNT (GNP) dispersions differing by volume and concentrations were used which were 15ml of 1mg/ml, 15ml of 2mg/ml and 30ml of 2mg/ml.

Cellulose pellicles (3×3 cm) were immersed in DWCNT or GNP dispersions for 24 - 72 h. After treatment with conductive agent dispersion, the nanocellulose pellicles were washed by deionized water and they were subsequently dried in a fumehood between Teflon plates. The thicknesses of the dried conductive films were 25 – 65 µm. The drying process was continued until a constant weight of the samples was reached.

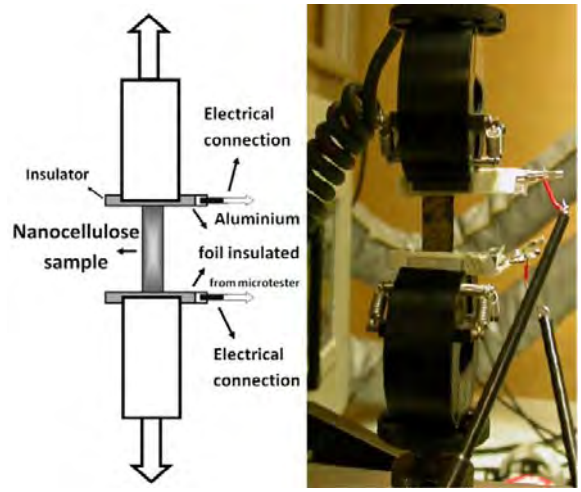

Figure 1. Experimental setup for tensile testing. The direction of the applied force and the direction of the electrical resistance measurement are parallel.

The surface morphology of samples was observed by using scanning electron microscopy (SEM) performed with Leo Ultra 55 FEG SEM. The electrical conductivity measurements were performed by using a four-point probe system (CMT-SR2000N, AIT, Korea). To characterize the electromechanical properties of the modified cellulose an Instron Material Testing Instrument (Series 5500) was used and digital multimeter (Agilent 34401A) has registered the variation of resistance. Constant tensile stress was applied to measure the resistivity of the modified cellulose (figure 1). The sizes of the samples were 30 mm in length and 10 mm in width.

III - Results and Discussion

Both EC and BC have fibrous structure .EC consists of fibers of 0.3 – 0.6 µm in diameter (fiure 2 A), Diameter of BC pellicles is 40-80 nm (figure 2A). Due to the differences in the thickness of the fibers and the structure of the scaffold the same modification procedure leads to different level of DWCNT (GNP) penetration to BC and EC.

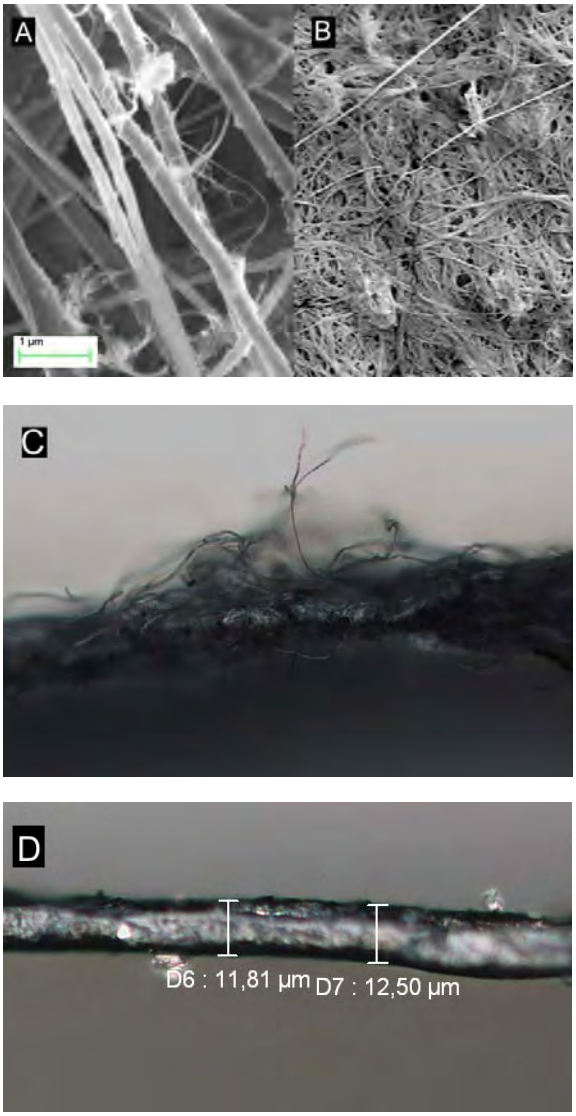

Figure 2. SEM images of electrospun cellulose (A) and bacterial cellulose (B) which have been modified with DWCNT.

Optical microscope images of DWCNT modified electrospun cellulose (C) and bacterial cellulose (D).

Because of the rather closed porous structure and small pores (figure 2 B), the modifying agents cannot penetrate to the BC. As a result, thin asymmetric layers of modifying agent were formed on both sides of the cellulose material (figure 2 D).

The thicker fibers of electrospun cellulose form an open matrix with larger pore size. As a consequence the

DWCNT modify all surface of the EC fibers. This is clearly observed in the SEM picture and in the optical microscope image (figure 2A, 2C)

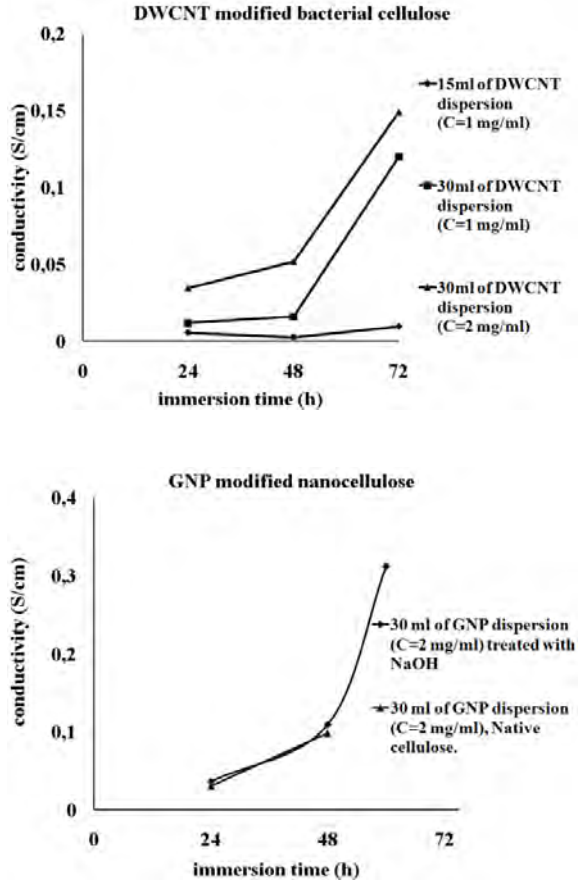

Figure 3. Conductivity of bacterial cellulose modified with DWCNT as a function of immersion time (top plot) and conductivity of bacterial cellulose modified with GNP (native and treated with NaOH) as a function of immersion time (bottom plot).

A. Conductivity as a function of immersion time and dispersion concentration

We measured the electrical conductivity of the modified nanocellulose when varying the immersion time, the concentration, and the volume of DWCNT dispersions.

Different conductivities were obtained for different cellulose pellicles which were modified under different conditions. The best results were found approximately 3.95×10^{-1} S cm^{-1} for BC/DWCNT, 0.334×10^{-1} S cm^{-1} for BC/GNP film and 8.2×10^{-3} for EC/DWCNT film.

Generally, the electrical conductivity of the modified cellulose and the distribution of DWCNT in its volume appear to be affected by the volume and concentration of dispersions and by the immersion time (figure 3). In the case of nanocellulose pellicles modified with the 15 ml of DWCNT or GNP dispersions of the 1mg/ml concentration increasing the immersion time did not show any significant effect on the conductivity of the resulting material. However, by increasing the concentration of the solutions, the immersion time starts to play a significant role.

A swelling process was applied for BC to open their matrix during immersion. Conductivity results shows that there is no significant difference between cellulose which has been treated by NaOH and cellulose which was not subjected to the swelling process (figure 3, bottom plot).

The conductivities of the nanocellulose materials prepared in our work from electrospun and bacterial celluloses are higher than or comparable to previously reported results [10].

B. Variation of resistance as a function of strain

Figure 4 shows the relatively large fractional increase in resistance with the fractional extension obtained by the application of tensile force for two samples of DWCNT modified nanocellulose. The nanocellulose pellicle which is modified with a higher concentration of DWCNT showed more sensitivity to an increase in the strain.

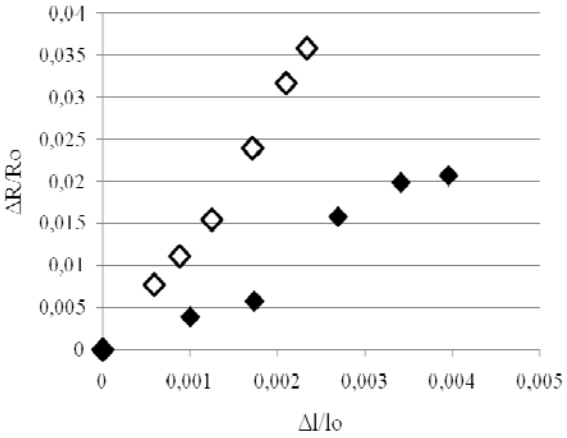

Figure 4, Fractional increase in resistance (ΔR/Ro) as a function of the fractional extension (Δl/lo) of a strain gauge for two different samples of bacterial cellulose. Bacterial cellulose which is modified in 30ml of DWCNT dispersion with 1 mg/ml concentration (filled markers) and bacterial cellulose which is modified in 30 ml of DWCNT dispersion solution with 2 mg/ml solution (open markers).

IV – conclusion

DWCNTs and GNPs-incorporated bacterial and DWCNTs-incorporated electrospun celluloses were prepared by immersing cellulose films in DWCNT and graphitized carbon nanopowder water dispersions. The morphology of the resulting electrical conductive cellulose material has been studied by optical microscope and SEM and the electrical properties were monitored under strain. The electrical conductivity of the cellulose was found to be approximately 3.95×10^{-1} S

cm^{-1} for bacterial cellulose/DWCNT, 0.334×10^{-1} S cm^{-1} for bacterial cellulose/GNP film and 8.2×10^{-3} for electrospun cellulose/DWCNT film.

It was found that electrical conductivity of resulted Bacterial cellulose/DWCNT depends on fractional extension obtained from applied force which make it good candidate for sensing application.

References

[1] W. D. Zhang and W. H. Zhang. ―Carbon Nanotubes as Active Components for Gas Sensors, Journal of Sensors, Vol. 2009: 160698, 2009.

[2] M. Knite, V. Tuporeina, A. Fuith, J. Zavickis, V. Teteris. ―Polyisoprene—multi-wall carbon nanotube composites for sensing strain, Material science engineering, Vol. C27, pp. 1125–1128, 2007.

[3] K.J. Loh, J.P. Lynch, B.S. Shim and N.A. Kotov, ―Tailoring Piezoresistive Sensitivity of Multilayer Carbon Nanotube Composite Strain Sensors, Journal of Intelligent Material Systems and structures, Vol. 19, pp. 747-768, 2008.

[4] Qiaohuan Cheng, Sourabhi Debnath, Elizabeth Gregan, and Hugh J. Byrne. Ultrasound-Assisted SWNTs Dispersion: Effects of Sonication Parameters and Solvent Properties, J. Phys. Chem, 114, pp. 8821–8827, 2010.

[5] Hwang, J. Y. Nish, A. Doig, J. Douven, S.Chen, C. W. Chen, L. C. Nicholas, R. J. Polymer structure and solvent effects on the selective dispersion of single-walled carbon nanotube. J. Am. Chem. Soc, 130,pp. 3543–3553, 2008.

[6] P.J. Wakelyn, A.D. French, N.R. Bertoniere, D.P. Thibodeaux and B.A. Triplett, Cotton fiber chemistry and technology, CRC Press, Taylor & Francis Group, Boca Raton, 2007.

[7] W. Czaja, A. Krystynowicz, S. Bielecki and R.M. Brown Jr., Microbial cellulose – the natural power to heal wounds, Biomaterials 27, pp. 145–151, 2006.

[8] Kulpinski, P., Cellulose nanofibers prepared by the N-methylmorpholine-N-oxide method. Journal of Applied Polymer Science,Vol. 98, pp. 1855-1859, 2005.

[9] Kim, C.-W., Preparation of submicron-scale, electrospun cellulose fibers via direct dissolution Journal of Polymer Science Part B: Polymer Physics, Vol. **43**, pp. 1673-1683, 2005.

[10] S.H. Yoon, H.-J. Jin, M.-C. Kook and Y. R. Pyun. ―Electrically Conductive Bacterial Cellulose by Incorporation of Carbon Nanotubes, Biomacromolecules, Vol. 7, pp. 1280–1284, 2006.

.

MODELING OF A SCALABLE COUPLED RESONATOR ARRAY FOR MICROSHUTTER APPLICATIONS

D. Agten[1], K. Brinkfeldt[2], M. Wieser[3], S. Barabash[3] and P. Enoksson[1]

[1]*Department of Microtechnology and Nanoscience, Chalmers University of Technology, 412 96 Gothenburg, Sweden*
[2]*Swerea IVF, 431 22 Mlndal, Sweden*
[3]*Swedish Institute of Space Physics, 981 28 Kiruna, Sweden*

***Abstract* — In this paper we present the results from the finite element analysis of a scalable coupled resonator array for ultrafast microshutter applications. This new design concept builds on the design of a previous microshutter array, but couples the shutters to each other to allow them to move in a coupled antiphase resonance mode. Simulations for array scalability show that the resonance frequency does not change significantly when adding rows or columns to the array. The desired resonance mode stays present during scaling. Analyzing the sensitivity to changing dimensions results in slightly different amplitudes but no change in phase difference between adjacent shutters at the resonance frequency.**

***Keywords:* Shutter, Array, Resonance, Coupling, MEMS**

I – Introduction

MEMS shutters exist in many varieties and for many applications. Different actuation systems can be used, such as electrostatics [1], thermal expansion [2], residual stress [3], resonance [4] or a combination of electrostatics and magnets [5]. These different actuation mechanisms lead to different shutter speeds, ranging from 3 μs [3] to 2 ms [6]. Shutters with these speeds can then be used in applications such as displays [7], cameras [6] or even telescopes [5]. For some applications however, faster devices with shutter speeds between 10 and 100 ns can be required. One example of such an application is a particular type of time-of-flight (TOF) mass spectrometer.

In TOF mass spectrometers the mass of a particle is determined by measuring its time-of-flight over a known distance. With this data of time and distance, the velocity of the particle can be calculated. This velocity then leads to the energy or mass of the particle by using the formula for kinetic energy (the mass or energy has to be known from other measurements). To measure the flight time of the particle, the device makes use of a start section and a stop section. In conventional mass spectrometers, the start section is a thin carbon foil that lets the particles through, releasing secondary electrons in response (see figure 1). However, when low-energy particles need to be measured, this approach poses a problem: large errors are introduced in the measurement as the particle loses part of its energy through the interaction with the carbon foil.

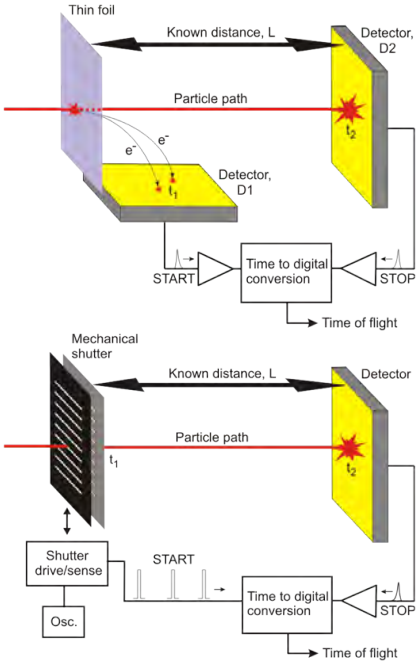

Figure 1: *Conventional (top) and shutter-based (bottom) TOF systems. Top: The start section is formed by a carbon foil. It releases secondary electrons when it interacts with the particles. Bottom: The start section is formed by a mechanical (micro)shutter. The opening time of the shutter relates to the start signal [8].*

A possible solution to this problem is to use mechanical (micro)shutters for the start section. The start signal is in this case derived from the opening time of the shutters. Since there is no interaction between the shutters and the particles, the latter do not lose energy and the measurement will give more accurate results (see figure 1).

This particular solution was implemented by [8] for the PRIMA instrument, an ion detector that is part of the PRISMA mission. PRISMA is a technology mission consisting of two satellites that are used to demonstrate several sensor technologies and navigation strategies for rendezvous and formation flying in space. A MEMS shutter array was fabricated in which the shutters are driven in resonance using piezoelectric actuation. The design consists of a plate suspended over a substrate, with both the substrate and the plate having slits of 90 μm long and 1 μm wide. The plate is made to resonate in the horizontal plane, thereby aligning the slits during short periods of time and allowing the particles to pass through (see figure 2). The dimensions of the plate and the slits were decided upon based on the requirements

for the PRIMA instrument and its operating conditions in space. The shutters are placed into an array in order to increase the transparency of the TOF mass spectrometer. One problem of this design however, is its sensitivity to small changes in the resonance frequencies of the individual shutters. This can occur due to small changes in the dimensions of the shutters (an inherent aspect of the fabrication process). With slightly different resonance frequencies, the individual shutters are not opened and closed at the same time, leading to inaccurate TOF results.

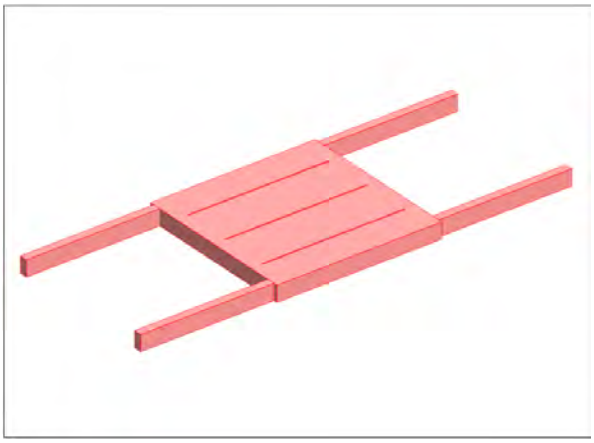

Figure 2: *Single shutter as designed by [8].*

In this paper we present a solution to this problem by coupling the shutters to each other and making use of a coupled antiphase resonance mode. This antiphase mode makes the zero-crossings of the shutters synchronized, thereby synchronizing the opening times as well. We describe the design and simulations performed for this new design concept.

II – Design specifications

The newly designed (micro)shutter array largely builds on the design by [8]. The dimensions of the shutter plate are kept the same, 105 μm by 105 μm. Also the beams connecting the shutters to their frames have the same dimensions, 85 μm long and 5 μm wide. The separation between these two beams however, is decreased from 80 μm to 22.5 μm. When the beams are closer together, the structure is less stiff, allowing the desired coupled antiphase resonance mode to occur. The frames themselves again have the same dimensions as before: 105 μm by 60 μm. In order to allow adjacent shutters to move in antiphase, the frames are loosely coupled to the substrate. This coupling is achieved using a centered underetched pillar of silicondioxide, 10 μm in diameter and 1.5 μm high. The antiphase motion is then passed along to the other shutters with a beam that coupls the frames together. This beam is 120 μm long and 10 μm wide. Except for the pillars, all structures are 13 μm thick and are to be made out of silicon. A top view of this design can be seen in figure 3.

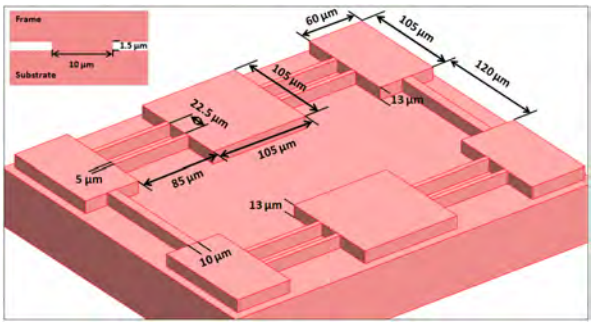

Figure 3: *Design of the coupled resonator array with an indication of the dimensions. The underetched pillars are shown in the inset.*

This particular design was decided upon after considering several different concepts and variations and simulating them in the finite element analysis program COMSOL 3.5. This program was also used to explore different aspects of the final design, such as its scalability and its sensitivity to changing dimensions. Also a stress analysis was performed with the same program. The results of these simulations are presented in the next section, followed by a discussion pointing out the important features of the design.

III – Results and Discussion

A. Scalability of the shutter array

The first step in analyzing the new design concept was to investigate the effects of scaling on the resonance frequency of the array. A single shutter as designed previously has a resonance frequency of $3.068 \cdot 10^5$ Hz [8]. This resonance frequency guarantees that the shutter reaches the specified opening times necessary for correct measurements with the TOF mass spectrometer. The resonance frequency of the new shutter array should thus not deviate too much from this value. Eigenfrequency simulations in COMSOL 3.5 started with a 2x2 array of coupled shutters. The resulting coupled antiphase resonance mode can be seen in figure 4. Since the results of this simulation were satisfactory, the array was expanded by adding rows and columns to it. Also arrays with just one row or just one column were investigated. The resonance frequencies of all these arrays were calculated and are shown in figure 5.

As can be seen in figure 5, the resonance frequency ranges from $3.309059 \cdot 10^5$ Hz for the 1x5 array to $3.333141 \cdot 10^5$ Hz for the 5x1 array. This represents a difference of only 0.73 % between the minimum and maximum values of the resonance frequency. Adding a row to the array increases the resonance frequency while adding a column decreases the resonance frequency. Even though the resonance frequency changes slightly, the desired coupled antiphase resonance mode stays present for all array sizes, up to the 6x6 array with a total of 36 shutters. The coupled resonator array thus scales very favorably with regards to resonance frequency, allowing very large arrays

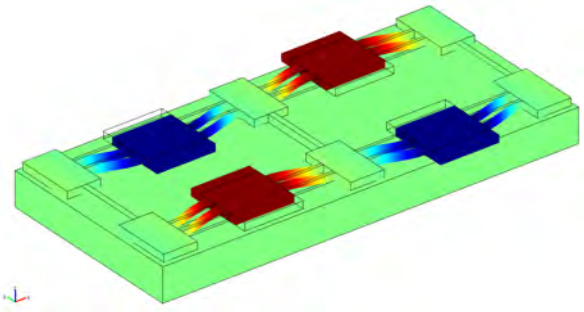

Figure 4: *First resonance mode of a 2x2 array of coupled shutters, showing the desired antiphase behaviour. The colours indicate the displacement in the y-direction.*

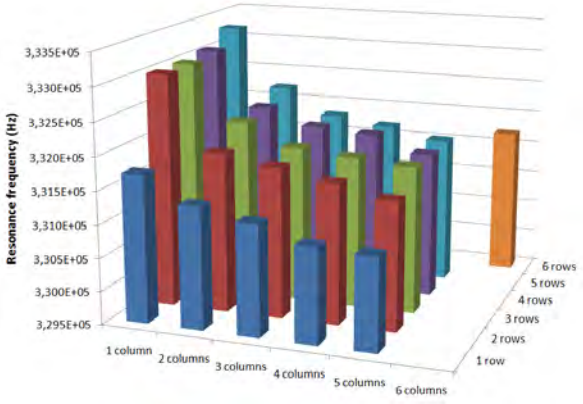

Figure 5: *Comparison of the resonance frequencies of shutter arrays of different sizes.*

to be implemented without any change in behaviour. This is advantageous for the TOF mass spectrometer application, but it can also be useful for other systems, such as tunable resonators for filter applications. The resonance frequency can then be finely tuned by adding or subtracting a row or a column from the array.

B. Stress & sensitivity analysis

It is imperative that the shutters do not fail while they are resonating. The shutters can fail when the stress in the material reaches the Ultimate Tensile Strength (UTS), which has a value of 7 GPa for silicon. COMSOL 3.5 can calculate the von Mises stress in the material when a fixed displacement is applied to the shutters. The maximum displacement of a shutter is 21 μm since the slit closest to the edge of the shutter plate lies at this distance from the edge. For displacements larger than this value the shutter plate no longer covers the slits below it, allowing the particles to pass through for a longer period of time. This displacement of 21 μm is thus applied to the shutters and the calculated von Mises stress is compared with the UTS (this is the von Mises stress criterion). The results for shutter arrays of different sizes can be seen in figure 6. The maximum von Mises stress does not reach the UTS of silicon for any array, ensuring that the shutters will not fail during resonance.

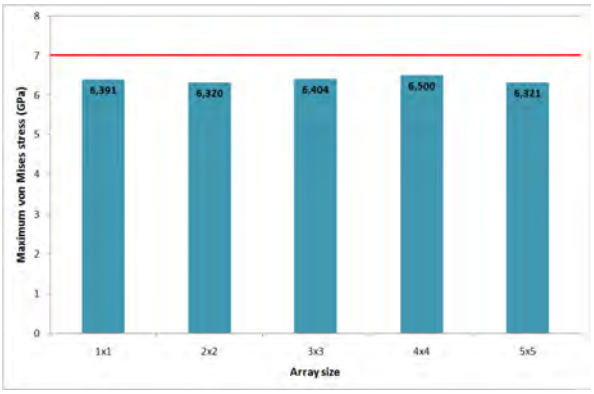

Figure 6: *Maximum von Mises stress for different shutter array sizes. The red line indicates the Ultimate Tensile Strength (UTS) of silicon.*

Since the previous design from [8] was very sensitive to small changes in the dimensions of the shutter elements, this feature also had to be investigated for the new design. The first step was to determine which parts of the shutters had the largest influence on the resonance frequency of the array. Therefore different parts of a 2x2 shutter array were changed by 10 % and the resonance frequency was recalculated.

It turned out that changing the width of the spring beams (the beams connecting the shutter plates to the frames) had the most significant effect on the resonance frequency of the array, so for further sensitivity analysis this dimension was used. To start with, the widths of all the spring beams of a 2x2 array were changed with percentages between -10 % and 10 %. The changes in resonance frequency compared to the resonance frequency of the unmodified array were noted and compared with the same results from the previous design [9]. The new design is less sensitive to changes in the spring beam width (e.g. for a -10 % change in spring beam width, the resonance frequency decreases by 14.6 % for the previous design, while it drops with only 12 % for the new design). On top of that, the coupled antiphase resonance mode does not change or disappear.

This analysis method gives some ideas about the sensitivity of the design towards dimensional changes, but during fabrication it is more probable that there is a gradient in the spring beam width. For example, when the etching process is not uniform, one side of the array will have thinner spring beams than the other side, with a gradual change in between. Therefore, also a gradient sensitivity analysis was performed on the shutter arrays. In figure 7 the resulting frequency response is shown for a 3x3 array.

Just like for an unmodified array, adjacent shutters show a peak in amplitude (with different magnitude however) at the resonance frequency. The phase behaviour is also the same as for the shutters without a gradual change in spring beam width: the shutters move in antiphase (180° phase difference) and have zero added phase difference at the resonance frequency.

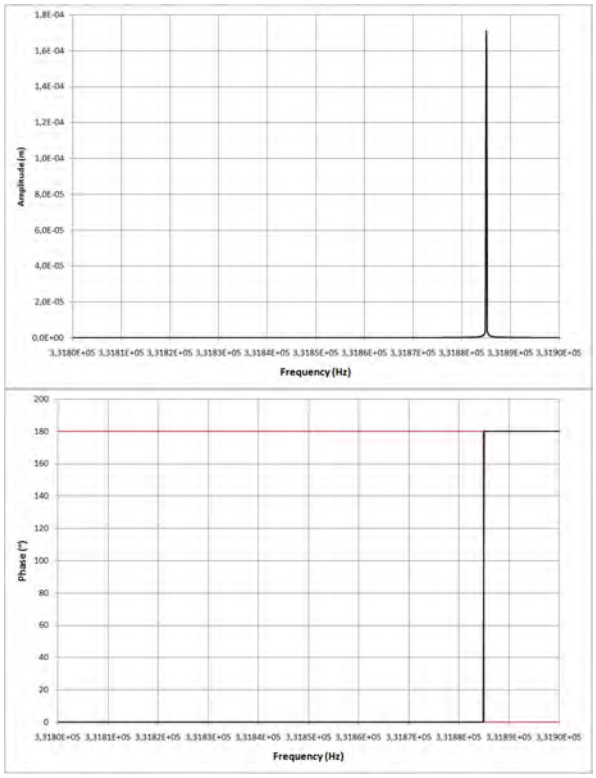

Figure 7: *Frequency response of 3 adjacent shutters of a 3x3 array where the adjacent shutters in a row have spring beam widths of 5.005 µm, 5 µm and 4.995 µm respectively. The resonance frequency is* $3.31885 \cdot 10^5$ *Hz.*

The difference in amplitude between adjacent shutters results in a speed difference between them, which leads to different opening times for these shutters.

IV – Conclusion

A new design concept for a (micro)shutter array has been modeled and investigated with finite element simulations using COMSOL 3.5. The shutters are coupled to each other and the frames of the shutters are underetched to allow a coupled antiphase resonance mode to occur. This particular resonance mode aims to solve the timing issues of a previous design.

The scalability of the array was investigated by adding rows and columns to it and calculating the resonance frequency. The resonance frequency does not change significantly and the desired coupled antiphase resonance mode stays present.

A stress analysis was performed and for all investigated array sizes the maximum von Mises stress does not exceed the Ultimate Tensile Strength of silicon.

Sensitivity analyses were performed by (gradually) changing the width of the spring beams connecting a shutter plate to its frames. The resulting frequency response for adjacent shutters shows peaks with different amplitude and zero added phase difference at the resonance frequency. The different amplitudes lead to different shutter opening times.

References

[1] T. Takahashi, M. Mita, H. Fujita, and H. Toshiyoshi. In *Optical MEMS and Their Applications Conference, 2005. IEEE/LEOS International Conference on*, pages 119–120, August 2005.

[2] D. Langley, L. Starman, R. A. Coutu, Jr., and S. Rogers. In D. L. Dickensheets, H. Schenk, and W. Piyawattanametha, editors, *MOEMS and Miniaturized Systems VIII*, volume 7208, page 720809, 2009.

[3] D. Langley, S. Rogers, and L. Starman. In D. P. Casasent and S. Rogers, editors, *Adaptive Coded Aperture Imaging and Non-Imaging Sensors II*, volume 7096, page 70960G, 2008.

[4] S. Orsini, A. M. di Lellis, A. Milillo, E. de Angelis, A. Mura, S. Selci, I. Dandouras, P. Cerulli-Irelli, R. Leoni, V. Mangano, S. Massetti, F. Mattioli, R. Orfei, C. Austin, J.-L. Medale, N. Vertolli, and D. di Giulio. In M. Hirahara, Y. Miyoshi, N. Terada, T. Mukai, and I. Shinohara, editors, *American Institute of Physics Conference Series*, volume 1144 of *American Institute of Physics Conference Series*, pages 91–101, June 2009.

[5] D. B. Mott, S. Aslam, K. A. Blumenstock, R. K. Fettig, D. Franz, A. S. Kutyrev, M.J. Li, C. J. Monroy, S. H. Moseley, and D. S. Schwinger. In M. E. Motamedi and R. Goring, editors, *MOEMS and Miniaturized Systems II*, volume 4561, pages 163–170, 2001.

[6] C.-H. Kim, K.-D. Jung, and W. Kim. In *22nd IEEE International Conference on Micro Electro Mechanical Systems (MEMS 2009)*, pages 156–159, January 2009.

[7] K.-H. Lee, J.H. Chang, and J.-B. Yoon. *Journal of Micromechanics and Microengineering*, 20(7):075030, 2010.

[8] K. Brinkfeldt, P. Enoksson, M. Wieser, S. Barabash, and M. Emanuelsson. In *24th IEEE International Conference on Micro Electro Mechanical Systems (MEMS 2011)*, pages 597–600, January 2011.

[9] B. Front. Master's thesis, Chalmers University of Technology, 2008.

HOLED MEMS RESONATORS WITH HIGH ASPECT RATIO AND FREQUENCY COMPENSATED

Y. Civet[1], F. Casset[2], J.F. Carpentier[3], B. Icard[2], J. Bustos[3], F. Leverd[3], D. Mercier[2] and S. Basrour[1]

[1]*TIMA (CNRS-Grenoble INP-UJF) – UMR 5159, 46Av. Félix Viallet, 38031 Grenoble, France*
[2]*CEA-Leti, MINATEC Campus, 38054 Grenoble, France*
[3]*ST Microelectronics, 850 rue Jean Monnet, 38926 Crolles, France*

***Abstract* — In this paper, we present the design and manufacturing of frequency compensated Micro-Electro-Mechanical (MEM) resonators, which fulfilled industry requirements combining high accuracy and collective correction. Both clamped-clamped beam and bulk mode resonators with holes compensation are treated. First electrical measurements of holed beam resonators are discussed.**

***Keywords :* MEMS, Resonator, Frequency shift, SOI technology**

I - Introduction

For High-frequency time-reference oscillator applications, MEM resonators are one of the alternatives offering CMOS compatibilities, low polarization voltage, multifrequency applications and low cost. State-of-the-art (Tab. 1) shows the great performances of MEMS in terms of resonant frequencies and quality factors, making them competitive with Quartz devices.

Table 1*: State-of-the-Art of MEMS resonators*

State-of-the-art	f(MHz)	Q	f.Q (10^{12})	V_{DC} (V)
[1]	13.1	130 000	1.7	75
[2]	61.2	48 000	2.94	12
[3]	5.59	112 000	0.626	3
[4]	100	60 000	6	5
[5]	104.92	101 550	10.6	10

However, components dimensions (proportional to the frequency as shown in Equation (1)) variations due to microfabrication are a major issue for industrial prospects. Indeed, frequency, currently obtained, is typically shifted in the worst case from +/-1500ppm to the mean-value. To date, few methods have been implemented and show interesting results (Tab. 2). Although promising, none of them combine high accuracy and collective correction.

In this study, we present a novel approach, expected to fulfill industry requirements. It consists in changing the resonant frequency by depositing at the wafer level a material into compensation holes smartly located on the resonator in order to control finely the resonant frequency accuracy. An analytical model has been developed for flexural modes in order to understand the influence of compensation holes and compared with finite element analysis (FEA) under CoventorWare®.

Table 2*: State-of-the-art of MEMS resonators frequency compensation*

State-of-the-art	Methods	Performances	
		Max. Variations	*Resolution*
[6]	Selective deposition	1,96%	-
[7]	Laser trimming	4%	2,6ppm
[8]	Au Diffusion	0,24%	20ppm
[9]	PLL	-	1ppm

We will first present the analytical modeling of MEM resonators and identify principal parameters. In the second hand, we will present manufacturing steps allowing demonstrators realization. Before conclusions, we will deal with first electrical measurements of clamped-clamped (CC) beam resonators.

II – MEMS resonators analytical modeling

As mentioned in Table 1, several kinds of resonators have been studied for decade. The oldest one and well-known is the CC beam for which the resonant frequency follows the generic formula:

$$f_b = \frac{6.481}{2\pi}\frac{W}{L^2}\sqrt{\frac{E}{\rho}} \quad (1)$$

whose different parameters are listed in Table 3. Flexural beam resonators present lower Q factor but have a higher tunability versus bias voltage.

Table 3*: Parameters and values*

Symbol	Parameter	Values
W	width	-
L	Beam length	-
E	Young modulus	1,69GPa
ρ	Mass density	2330kg.m^{-3}
R	Disk radius	-
L	Plate length	-
k	Frequency constant	1,002
υ	Poisson ratio	0,29
Y_{2D}	Effective Young's modulus	169GPa

We also reported bulk mode resonators (Disk and plate), presenting higher Q factor whose resonant frequencies can be written as :

$$f_{Disk} = \frac{k}{2\pi R}\sqrt{\frac{E}{\rho(1-\upsilon^2)}} \quad (2)$$

$$f_{Plate} = \frac{1}{2L}\sqrt{\frac{Y_{2D}}{\rho}} \quad (3)$$

where different parameters are mentioned in Table 3.

In the case of a beam resonator with holes distribution, the microbeam is assumed to be composed of several cross-section segments (including holes or not) which are serially connected. The resonant frequency of such a microbridge is simply a summation of the single-profile distributed stiffness and mass properties of the individual segments k_e and m_e.

$$k_e = E\left\{S_{1b}^{(k)} + S_{2b}^{(k)} + I\left[\int_0^{a_m}\left(\frac{d^2v_b(x)}{dx^2}\right)^2 dx + \int_{a_m+2r+(m-1)p}^{L}\left(\frac{d^2v_b(x)}{dx^2}\right)^2 dx\right]\right\}$$

where

$$\begin{cases} S_{1b}^{(k)} = r\sum_{j=1}^{m}\int_0^{\pi} I(\phi)\left[\frac{d^2v_{bj}(\phi)}{dx^2}\right]^2 \sin(\phi)d\phi \\ S_{2b}^{(k)} = I\sum_{j=2}^{m}\int_{a_m+2r+(j-2)p}^{a_m+(j-1)p}\left[\frac{d^2v_b(x)}{dx^2}\right]^2 dx \end{cases}$$

and

$$m_e = \rho t\left\{S_{1b}^{(m)} + S_{2b}^{(m)} + w\left[\int_0^{a_m} v_b(x)^2 dx + \int_{a_m+2r+(m-1)p}^{L} v_b(x)^2 dx\right]\right\}$$

In this equation, $S_{1b}^{(m)}$ and $S_{2b}^{(m)}$ can be calculated following the expressions below

$$\begin{cases} S_{1b}^{(m)} = r\sum_{j=1}^{m}\int_0^{\pi} w(\phi)v_{bj}(\phi)^2 \sin(\phi)d\phi \\ S_{2b}^{(m)} = w\sum_{j=2}^{m}\int_{a_m+2r+(j-2)p}^{a_m+(j-1)p} v_b(x)^2 dx \end{cases}$$

r, *m*, *n*, *a* and *p* represent the hole radius, holes number along the length, holes number along the width, the distance from the first hole to the beam edge and the pitch between 2 consecutive holes (Fig. 1).

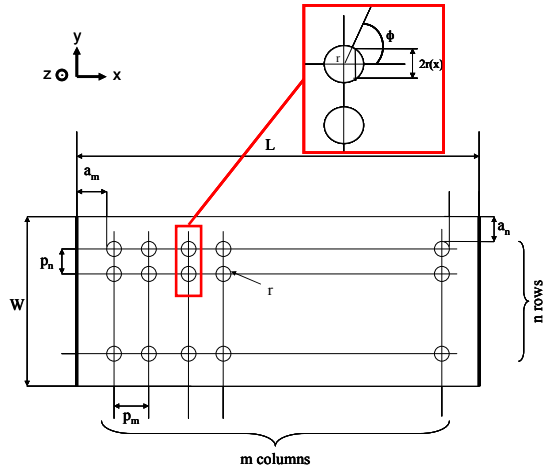

Figure 1: *Scheme of the CC beam used for the analytical model, hole detail from the microbeam*

We have used these formulae to plot the resonator bending frequency variation as a function of the hole radius and position, linked to the stress distribution of bended flexural CC beam (Fig. 2). We note that increasing the hole radius in cases "A" and "M" decreases the resonant frequency.

Thanks to an array of holes, we have increased the developed surface. Thus, we reduce the required compensation material thickness to obtain the needed material volume. FEM simulations confirm our analytical model (Tab. 4) which has been used to design our various structures.

Then, we proposed to fill the holes after an initial frequency measurement (allowing to fix the compensation material needed to meet our specification). In the case of 99 holes located in "M" (r=141nm), our model reports a correction up to 0.4% (using a silicon compensation material thickness of 50nm) and also a decrease of 350ppm (10nm), making this compensation method compatible for industrial perspectives.

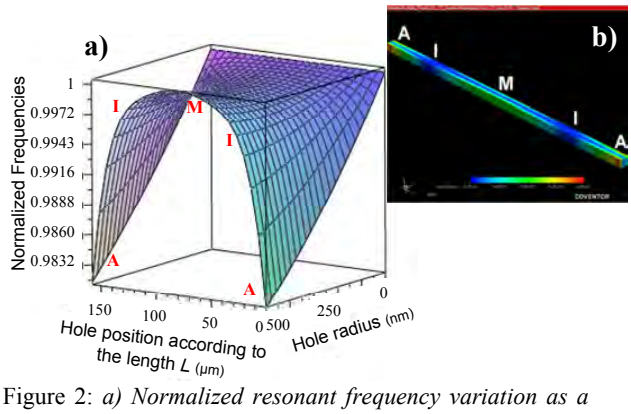

Figure 2: *a) Normalized resonant frequency variation as a function of the hole radius (r) of one hole and the position of the latter (Analytical mode: f_i=714kHz), b) stress of a microbeam*

Table 4*: Frequencies comparison for CC beam, 2x5 holes array (Analytical & FEM), f_i = 714kHz*

Type	Frequencies (MHz)		Delta %
	Analytical	*FEM*	
Without hole	714.883	714.492	-0.19
Intermediate "I"	712.115	715.139	0.42
Anchors "A"	703.414	714.141	1.50
Middle "M"	721.759	716.000	-0.80

II – Technological realization

Demonstrators with impressive aspect ratio (~35) and deep submicron resonator to electrode gaps have been built. CC beam and bulk mode plate devices are realized on 12 inches SOI wafers.

First, top silicon is implanted. We performed a mono-crystalline epitaxy of Silicon to get a 1.4µm thick active layer. A SiO_2 layer (200nm), which is used as a hard mask for Si etching, is deposed onto the wafers. E-beam lithography is used onto the latter to define resonators, electrodes and capacitive resonator to electrodes gaps. The hard mask and the silicon layer are then etched in a single step process (Fig. 3 & 4). One can see 39nm-wide, 1.4µm-deep gaps, corresponding to an high aspect ratio of 35. To our knowledge, this value of the aspect ratio respect to the narrow gap is at the moment the highest ever obtained using DRIE process in MEMS technology (Tab. 5).

After depositing Cr/Au metal layer by lift-off step, the resonators are released thanks to vapor-HF etching step. Fig. 3 & Fig. 4 show respectively SEM view of Bulk mode and CC beam resonator.

Table 5: *State-of-the-Art of Si etching*

State-of-the-Art	Gap(nm)	Height(µm)	Height / gap²
Tiang [10]	140	5.6	28
Durand [11]	70	1.09	22
Our work	40	1.4	87

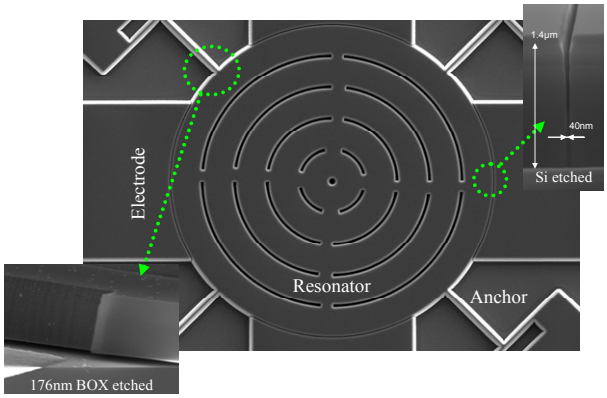

Figure 3*: SEM view of bulk mode disk resonator*

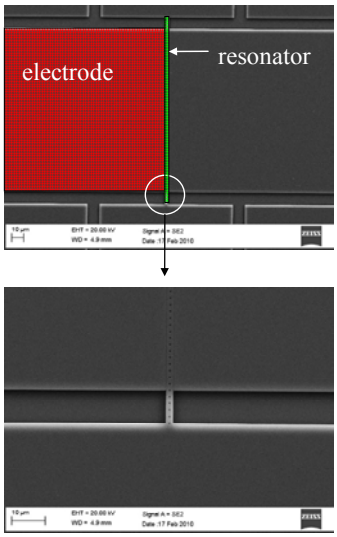

Figure 4*: SEM view of CC beam resonator*

III - Results and Discussion

Electrical characterizations of CC beam resonators have been performed using a Lock-In Amplifier (LIA). A bias voltage V_{DC} is applied on the beam resonator and an *AC* signal is provided to the first electrode. We measure the transmitted signal through the second electrode.

Fig. 5 shows the output signal for different V_{DC} in the case of a beam with 2x5 holes distributed in the middle of the beam (*L=159µm, W=2µm, t=1,4µm, r=141nm*).

The fundamental resonance frequency was measured at 715kHz for V_{DC} = 5V. This is in good agreement with analytical model and FE simulations that respectively give 715,916kHz and 716kHz. A motional resistance of 81kΩ was extracted from measurements. A low quality factor of 950 under vacuum was extracted from the measured response considering the FWHM. It can be explained by the particular design of compensation holes, non-optimized for Q aspect but for frequency compensation aspect. We note a shift downward of the

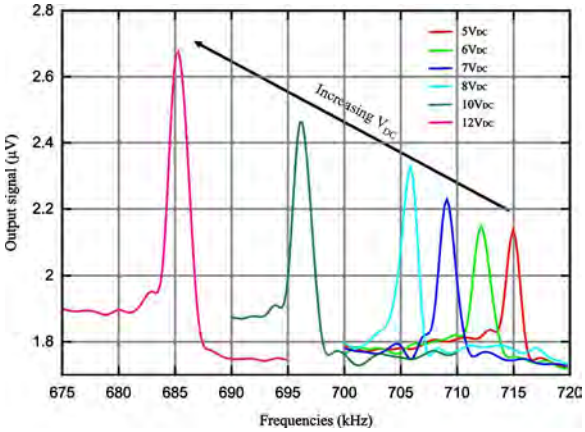

Figure 5*: Frequency response measured on a clamped-clamped beam resonator as a function of V_{DC}*

resonance frequency while increasing the polarization voltage. This is because V_{DC} acts as a negative stiffness. Moreover, the resonant frequency shifts linearly with V_{DC}^2 as shown in Fig 6.

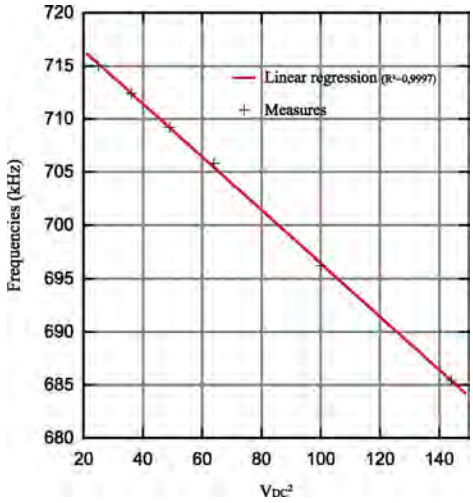

Figure 6*: Frequency response as a function of V_{DC}^2*

IV - Conclusion

We developed an analytical model taking into account the presence of holes onto CC beam resonators, required for sizing resonant structures precisely frequency addressed. The correction on these structures permitted by the presence of holes was modelled. Thus, it was shown that a frequency adjustment from -350ppm to 4000ppm of its initial value is possible in the case of an epitaxy approach for a holed array structure. The sensitivity of this compensation method, in link with the retained technology, must be estimated. We confronted our model to FE simulations which gave good agreement between the two methods. Finally, we measured first prototypes of CC beam resonators. Correction and further measurements are under development.

Acknowledgement

This research was supported by NANO 2012 program from the French government and has been performed with the help of the "Plateforme Technologique Amont" (PTA) de Grenoble, with the financial support of the "Nanosciences aux limites de la Nanoélectronique" Fundation. The authors wish to thank Pierre Cemeli from SOITEC.

References

[1] V. Kaajakari et al, 'Square-Extensional Mode Single-Crystal Silicon Micromechanical Resonator for Low-Phase Noise Oscillator Applications', IEEE Electron Devices Letter, vol 25 (4), pp 173-175, 2004.

[2] Y-W. Lin et al, 'Series-resonant VHF micromechanical resonator reference oscillators', IEE Journal of Solid-State Circuits, vol 39 (12), pp 2477-2491, 2004.

[3] G. Ho et al, 'Micromechanical Ibars: tunable high- resonators for temperature-compensated reference oscillators', Microelectromechanical Systems, Journal of, vol. 19 (3), pp 503-515, 2010.

[4] E. Ollier et al, 'IC integration-compatible single crystal silicon 100MHz MEMS resonator with 60nm air-gap and sub 5V polarization voltage', in the Proc. of the MEMSWAVE 2010 conference, 2010.

[5] A. Samarao et al, 'Passive tcf compensation in high q silicon micromechanical resonators', IEEE Micro Electro Mechanical Systems (MEMS), pp 116-119, 2010.

[6] J. Daphne et al, 'Characterization of selective polysilicon deposition for MEMS resonator tuning', Journal of microelectromechanical system, vol 12, pp 193-200, 2003.

[7] W-T. Hsu et al, 'Frequency trimming for MEMS resonator oscillators', IEE International Frequency Control Symposium, pp 1088–1091, 2007.

[8] A. Samarao et al, 'Post-fabrication electrical trimming of silicon bulk acoustic resonators using joule heating', IEEE Micro Electro Mechanical Systems (MEMS), pp 892-895, 2009.

[9] J. Salvia et al, 'Phase lock loop based temperature compensation for MEMS oscillators', IEEE Micro Electro Mechanical Systems (MEMS), pp 661-664, 2009.

[10] W-C. Tian et al, 'Comparison of Cl2 and F-based dry etching for high aspect ratio Si microstructures etched with an inductively coupled source', J. Vac. Sci. Technol., vol 18, pp 1890-1896, 2000.

[11] C. Durand et al, 'In-plane silicon-on-nothing nanometer-scale resonant suspended gate mosfet for in-ic integration perspectives', Electron Device Letters, IEEE, vol 29 (5), pp 494-496, 2008.

IMPLANTABLE MICROCOILS DEDICATED TO MAGNETIC RESONANCE IMAGING : EFFECTS OF THE PACKAGING ON ITS CHARACTERISTICS

M. Couty[1], A. Rubin[1, 2], J.-C. Ginefri[3], L. Darrasse[3], M. Woytasik[1], F. Lethimmonier[2], F.Boumezbeur[2], M. Tatoulian[4] and E. Dufour-Gergam[1]

[1]*Univ. Paris-Sud, Laboratoire IEF, UMR-8622 CNRS, F-91405 Orsay, France*
[2]*IB2M, Neurospin, CEA Saclay, Bât. 145, F-91191 Gif-sur-Yvette, France*
[3]*IR4M, UMR-8081 CNRS/Université Paris-Sud 11, Bât. 220, F-91405 Orsay, France*
[4]*LGPPTS, ENSCP, EA3492, F-75005 Paris, France*

***Abstract* — In this paper, we present implantable microcoils dedicated to Magnetic Resonance Imaging (MRI) at 7Tesla of the rat brain for the diagnosis and the monitoring of neurodegenerative diseases and tumors. The coils are fabricated on flexible polymer substrate by copper micro-molding process combined with specific plasma treatments. The coils are then coated with PDMS for the biocompatibility aspects and also to prevent the dielectric coupling with biological tissues which present a high permittivity value (responsible of resonance frequency shift and *Q*-factor degradation). Effects of the PDMS thickness on the characteristics of the coil were investigated in air and in saline agar phantoms for two types of coil geometry in a frequency range from 300 to 400MHz. A first *in vivo* image is also presented.**

***Keywords :* Flexible microcoil, MRI, PDMS, implantation**

I - Introduction

In this paper, we present the design and fabrication of implantable RF microcoils in order to develop a diagnosis and monitoring tool for tumors and neurodegenerative diseases, such as Alzheimer's one, in medical research models on small rodents. These coils are dedicated to implantation into the rat brain for MRI. It requires high Signal to Noise Ratio (SNR) and spatial resolution to obtain images with high quality at the microscopic scale.

Several authors have shown the great interest of implantable RF microcoils for local imaging with high SNR [1-3]. These coils have only a small field-of-view but are suitable when the area of interest is specifically localized ─ implanted in the center of this area. The design must satisfy the following specifications: easy fabrication and minimal invasiveness for implantation e.g. flexible wireless coils.

If the configuration of macroscopic MRI coils is transposed to microscopic scale, miniaturization is quickly limited (about the centimeter) by the use of discrete components, e.g. capacitors and inductances. Transmission lines design ─ described in section II.A. [4] ─ is an appropriate solution to avoid this limitation, and is compatible with easy and low-cost fabrication processes on flexible substrates using microtechnologies [3, 5]. The design has also the advantage to provide auto-resonant structure without any wire connections, which is very suitable for implantation.

Implantation of this kind of devices requires a specific packaging to ensure biocompatibility and to limit the loading effect generated by dielectric coupling between the coil and the biological tissues (permittivity about 80). This coupling induces a shift of the resonance frequency F_0 and reduces the performances of the coil e.g. *Q*-factor and SNR [1, 5]. Yung et al. demonstrated that this loading effect is very important particularly on the Q-factor value which can be reduced by a factor 2 [2]. This impact is difficult to predict with conventional analytical models.

Silicone elastomers [1, 2] or parylene [6] are often used as biocompatible coatings. Parylene is a very attractive material but is often limited to submicronic thicknesses. In our case, the metallic lines are several micrometers thick. Among silicone elastomers, we chose PolyDiMethylSiloxane (PDMS) which is widely considered as biocompatible for short term ─ days ─ implantation [7]. Its preparation and deposition need no specific expensive equipment and an accurate control of thickness can be achieved through rotation speed for spin-coating, and curing conditions (temperature, time). It is also a dielectric material with a low permittivity and loss tangent ($\varepsilon = 2.65$ and $\tan\delta = 1.10^{-3}$ at 100kHz).

Ideally, performances of the coil should be the same, or closest as possible, both in unloaded (in air) and loaded environment (in biological tissues or phantom) to optimize the imaging parameters and set-up *ex vivo*. Our approach is to reach this condition through PDMS packaging. Before the imaging step, the influence of he PDMS thickness on the characteristics of the coil ─ F_0 and *Q*-factor ─ must be perfectly controlled in the range from 300 to 400MHz (corresponding to 7Tesla magnetic field, available for our experiments).

II – Material and Methods

A. Multi-turn Transmission Line Resonator design

Multi-turn Transmission Line Resonator (MTLR) consists in conductor e.g. copper lines ─ concentric split-rings connected in series ─ deposited on both sides of a dielectric substrate e.g. polymer (Figure 1) allowing a continuous distribution of the capacitive effect along the transmission lines. The substrate is 125µm thick FEP Teflon® film (provided by MICEL) with a permittivity ε of 2.15 and a low loss tangent $\tan\delta$ of 3.10^{-4} at 1MHz.

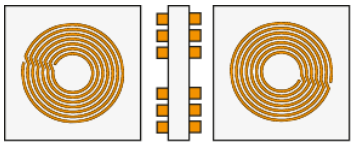

Figure 1*: Multi-turn Transmission Lines Resonator.*

For a 7Tesla MRI system, the ^{1}H Larmor frequency is 299MHz. To estimate the shift due to the PDMS coating in air and in a saline phantom (modeling dielectric characteristics of biological tissues), we chose to developed two types of coil geometry, called A and B, corresponding to resonance frequencies from 300 to 400MHz, in air and without packaging. This wide range has been chosen because a decrease of F_0 with the elastomer coating is expected (as the PDMS permittivity is greater than those of the air). Geometrics parameters of the coils given in Table 1 were defined using an analytical model dedicated to this application. The diameter of the coils is from 5 to 6mm. Expected values of the Q-factor in these conditions are about 120.

Table 1: *Geometric parameters of the coils.*

Type of geometry	*A*	*B*
Number of turns N	6	7
Width of the winding w (µm)	88	118
Gap between two windings s (µm)	40	110

Both A and B-types have been chosen because their dimensions are not critical for microfabrication and to investigate the effect of the inter-turn capacitance. 14 coils are available for each substrate.

B. Fabrication process

Then, coils were fabricated by copper micromolding process described in [3]. The fabrication steps are summarized in Figure 2. Both sides of the substrate are structured with bottom side alignment.

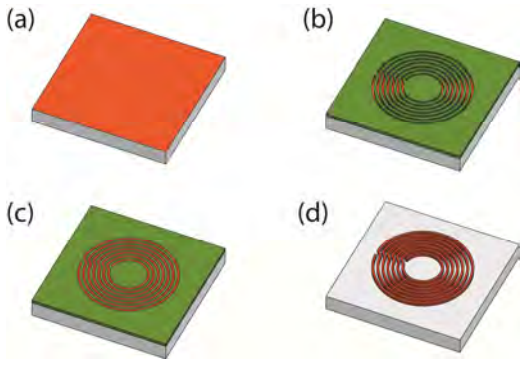

Figure 2*: Steps of copper micromolding process : (a) sputtering of Ti./Cu (10/100nm) seed layer, (b) patterning AZ4562 photoresist (20µm) mold by UV photolithography, (c) copper electroplating (10µm), (d) photoresist removal and wet etching of seed layer.*

A critical point of this structure is the first metallization step. As the fluorinated polymer substrate presents well-known hydrophobic properties [8], we developed a specific N_2/H_2:25/75 plasma treatment to improve the metal adhesion on Teflon [9].

C. Packaging of the coil with PDMS

After the fabrication of the coils, we propose to cover the surface with PDMS as packaging material. The polymer mixture is prepared using the commercial kit Sylgard® 184 (Dow Corning Corporation) with a weight ratio between pre-polymer and cross-linker of 10:1 and then deposited by spin-coating at 3000rpm during 90s, and cured in oven at 95°C for 30min. In these conditions, thickness measured is 23±1µm. This thickness value has been chosen to ensure the total covering of the thick copper lines to ensure the biocompatibility (no contact between tissues and metallic material). Steps are repeated for each side of the coil. The adhesion of PDMS at the top of the device is also a problem, thus the coils were previously treated with a He/O_2 plasma [10].

A such coil coated with PDMS layer was cryo-fractured for SEM observation. (Figure 3) It shows a good filing of the gap between two turns and a planar surface.

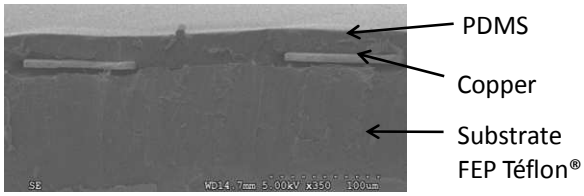

Figure 3*: SEM view of a cross section of PDMS deposit for a B-type coil..*

To limit the cross effect between neighboring coils, the substrate is then cut to obtain single antenna which will be individually characterized. To investigate the impact of the thickness of the dielectric material on the characteristics of the coil, the measurements of F_0 and *Q*-factor are systematically done after one thickness increment of 20µm. The size of the sample (less than 1cm²) is too small to obtain uniform deposition of the polymer film by spin-coating. That is why we prepared some PDMS films (20µm thick) on a separate FEP Teflon® substrate. No plasma treatment is done on its surface. So, the PDMS adhesion is very poor and the dielectric films can be easily released and reported on the coils surface. Between two increments, a surface activation by O_2 plasma is needed.

D. Electromagnetic characterization

F_0 and *Q*-factor are measured using the single-loop probe method [11] and a E5061A network analyzer (Agilent Technologies). The magnetic coupling between the coil and the single loop must be sufficiently weak so that the performances of the coil are not affected by the presence of the probe and are neither dependent on the input nor on the distance between the probe and the coil. This condition is achieved when the reflection coefficient at the single loop terminal is less than -40dB.

Saline agar phantoms are prepared with 5% agarose gel in NaCl 0,45% Cooper® solution. Permittivity is

about 80 and electrical conductivity about 0.7S/m, close to the electrical properties of biological tissues in the rat brain. Measurements are performed in air and in agar phantom to evaluate the influence of a conducting environment on the performances of the coil.

E. Magnetic Resonance Imaging

A coil with thick PDMS packaging is implanted between the rat brain lobes. Signal transmission is done using inductive coupling between the implanted-coil and a figure-of-eight pick-up loop connected to the MRI unit preamplifier. Imaging is performed at 7Tesla with a standard 3D FLASH acquisition sequence with in-plane resolution of 150x150µm² and a slice thickness of 1mm. The entire data set is composed of 18 images corresponding to an explored volume of 2.9x1.4x1.8cm^3 that covers the entire rat brain. The total acquisition time is 3min04s.

III – Results and Discussion

The study is led on 3 groups of 2 or 3 exactly identical coils for A and B-types. Good reproducibility is observed for each group.

A. Influence of the PDMS thickness on unloaded F_0 and Q-factor

Figure 4 shows the variation of unloaded F_0 with the PDMS thickness for A and B-types coils. As expected, F_0 decreases with the PDMS thickness. This effect is more important for the first increments. This is due to the decrease of the magnetic field intensity with the distance from the coil [5, 12-13]. For a threshold value of thickness e.g. 250µm, the electric field seems to be totally confined and the F_0 evolution becomes negligible.

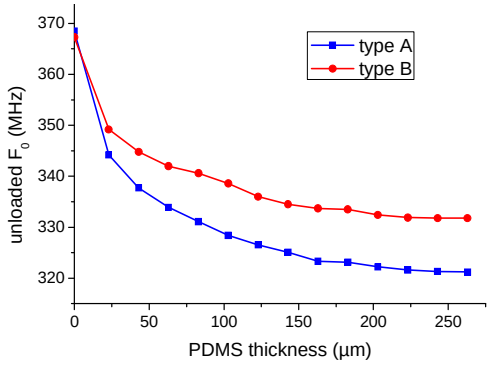

Figure 4: *Variation of unloaded F_0 with PDMS thickness for A and B-types coils.*

From the first layer of dielectric, the impact of the PDMS between windings is more important for A-type than B-type, 13 to 9% respectively. Gap between two turns for A-type is smaller than B-type thus the impact of the dielectric on the inter-turn capacitance must be higher [14]. This inter-turn capacitance value determines also the final value of F_0 which is lower for A-type.

Figure 5 shows the variation of unloaded *Q*-factor with PDMS thickness. Values without any packaging are respectively about 98 and 115, quasi similar for A and B-types, which corresponds to the expected values. Both types show a small linear decrease (around 10%) as it could be expected from the variation of F_0. *Q*-factors are still excellent with a PDMS thickness of 280µm— respectively 87 and 99 for A and B-types.

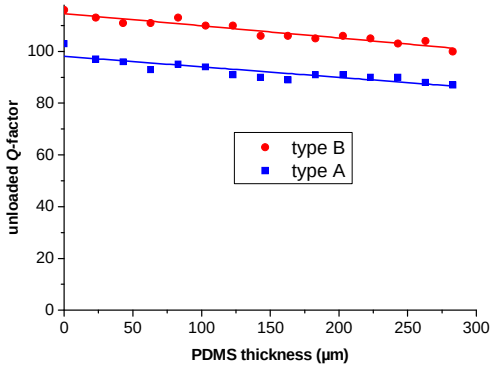

Figure 5: *Variation of unloaded Q-factor with PDMS thickness for A and B-types coils.*

B. Influence of the PDMS thickness on loaded F_0 and Q-factor

Characterization in air (unloaded environment) and in saline agar phantoms (loaded environment) have been done for other A and B-types coils.

Figure 6 shows the typical variation of F_0 with the PDMS thickness in loaded and unloaded environment obtained with both A and B-types. In the case of highly conducting environment with a high dielectric permittivity, the value of F_0 increases with the PDMS thickness. For the minimal thickness (23µm), F_0 is drastically shifted down compared to the unloaded environment (divided by factor 2). As for measurements in the air, the impact of the thickness is more significant for the first PDMS layers. The difference between the two curves decreases with the coupling effect limited by the PDMS thickness. Both curves converge on the same value of F_0, e.g. 300MHz, for approximately the same thickness around 270µm. For higher values of the thickness, F_0 is dependent neither on PDMS thickness nor on the environment conductivity.

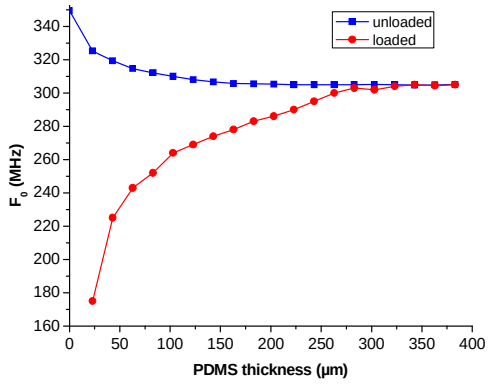

Figure 6: *Variation of loaded and unloaded F_0 with PDMS thickness for A-type coil.*

A PDMS thickness higher than 270µm for the packaging of the coil is totally in agreement with the frequency specification for MRI at 7Tesla.

Figure 7 shows the variation of *Q*-factor with the PDMS thickness in loaded and unloaded environment. With only 23µm of PDMS, the *Q*-factor value in loaded environment is drastically reduced (by a factor 10 compared with the unloaded one). But it increases very quickly with the PDMS thickness until the same value than in the air for thicknesses higher than 350µm. In this case, the *Q*-factor is around 80 and totally suitable to obtain high quality images.

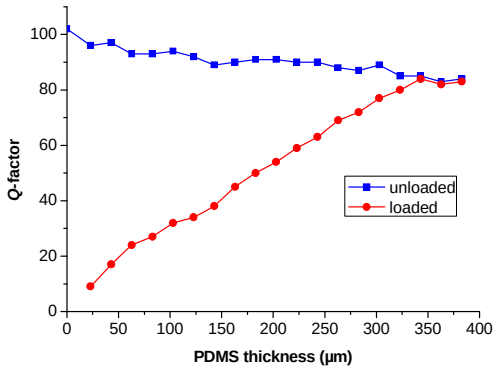

Figure 7: *Variation of loaded and unloaded Q-factor with PDMS thickness for A-type coil.*

C. In vivo imaging

After the characterization *ex vivo* of the coils, we optimized the MRI conditions in order to prepare the first experiment in the rat brain. A 5.6mm in diameter B-type coil with a thick PDMS packaging and adequate characteristics for 7Tesla MRI (F_0 = 299MHz and *Q*-factor = 75 with PDMS in air) is implanted between the lobes of the rat brain. Images are acquired *in vivo* using the parameters described in section II.E. Figure 9 presents the image of the center of the brain. The average SNR close to the implanted coil is about 120. This result is very satisfying and totally validates our approach.

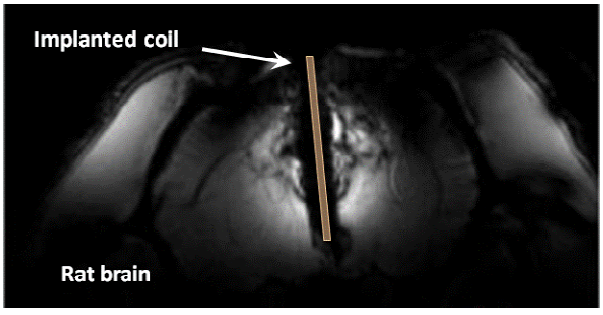

Figure 9: *In vivo image of the rat brain at 7Tesla using an implanted coil with a thick PDMS packaging.*

IV – Conclusion

We showed in this study that PDMS is a suitable material for packaging of implantable microcoils. Optimization of the packaging (PDMS thickness) have been done in air and in saline agar phantoms. This optimization in the phantom gel has allowed to obtain pertinent F_0 and *Q*-factor values, totally compatible with MRI conditions. At 7Tesla, the achievement of an *in vivo* image of the rat brain with a SNR of 120 validates this approach. Through the knowledge of the maximal F_0 shift *ex vivo* with the PDMS packaging, it is now possible to predict the required value of F_0 without any packaging in air (after fabrication) to reach a given frequency identical in air, in agar phantoms and thus in such a conducting environment e.g. *in vivo*. The necessary thicknesses are in these conditions about 300 to 350µm. These high values increase the distance between the coil and the tissute and thus reduce the detected sample volume (lower filing factor). Moreover, it increases the the rigidity of the coil, which is undesirable for the surgical act and may induce congestion in the brain during long term implantation. A solution could be the use of a material with higher permittivity than PDMS one.

References

[1] M. Bilgen, *J. Neurosci. Methods*, vol. 159, pp. 93-97, 2007.

[2] A. C. Yung, P. Kozlowski, *Magn. Reson. Imaging*, vol. 25, pp. 1215-1221, 2007.

[3] M. Woytasik, J.-C. Ginefri, J.-S. Raynaud, M. Poirier-Quinot, E. Dufour-Gergam, J.-P. Grandchamp, L. Darrasse, P. Robert, J.-P. Gilles, E. Martincic, O. Girard, *Microsyst. Technol.*, vol. 13, pp. 1575-1580, 2007.

[4] S. Serfaty, N. Haziza, L. Darrasse, and S. Kan, *Magnet. Reson. Med.*, vol. 38, pp. 185-191, 1997.

[5] X. Zhang, K. Ugurbil, W. Chen, *Magnet. Reson. Med.*, vol. 46, pp. 443-450, 2001.

[6] D. Ellersiek, H. Fassbender, P. Bruners, J. G. Pfeiffer, T. Penzkofer, A. H. Mahnken, T. Schmitz-Rode, W. Mokwa, U. Schnakenberg, *Sensor Actuat. B-Chem.*, vol. 144, pp. 432-436, 2010.

[7] A. Mata, A. J. Fleischman, S. Roy, *Biomed. Microdevices*, vol. 7, pp. 281-293, 2005.

[8] D. M. Brewis, R. H. Dahm, *Adhesion to Fluoropolymers*, vol. 16, pp. 17-23, 2003.

[9] C. Sarra-Bournet, G. Ayotte, S. Turgeon, F. Massines, G. Laroche, *Langmuir*, vol. 25, pp. 9432-9440, 2009.

[10] Q. Chen, *J. Electrostat.*, vol. 59, pp. 3-13, 2003.

[11] J.-C. Ginefri, E. Durand, L. Darrasse, *Rev. Sci. Instrum.*, vol. 70, pp. 4730-4731, 1999.

[12] N. Baxan, H. Rabeson, G. Pasquet, J.-F. Châteaux, A. Briguet, P. Morin, D. Graveron-Demilly, L. Fakri-Bouchet, *C. R. Chimie*, vol. 11, pp. 448-456, 2008.

[13] S. Eroglu, B. Gimi, B. Roman, G. Friedman, R. L. Magin, *Concept. Magnetic Res.*, vol. 17B, pp. 1-10, 2003.

[14] C. Massin, G. Boero, F. Vincent, J. Abenhaim, P.-A. Besse, R. S. Popovic, *Sensor Actuat. A-Phys.*, vol. 97, pp. 280-288, 2002.

OPTIMIZED PIEZOELECTRIC ENERGY EXTRACTION METHOD FOR PRESSURE ENERGY HARVESTING

M. Deterre[1, 2], E. Lefeuvre[1, 2], E. Dufour-Gergam[1, 2]

[1]*Univ Paris- Sud, Laboratoire IEF, UMR 8622, Orsay F-91405, France*
[2]*CNRS, Orsay F-91405, France*

***Abstract* — This paper presents an energy harvesting method to power autonomous systems and more particularly active implantable medical devices. A piezoelectric diaphragm is placed in a fluidic environment with pressure variations (blood for instance). We propose an optimized extraction method of the piezoelectrically generated charge through the application of a controlled voltage. An analytical model and experimental results are presented. In the considered regime, the extracted energy is proportional to the amplitude of the applied voltage and is several times greater than the energy extracted using the classical method.**

***Keywords:* Energy harvesting, energy scavenging, pressure energy, piezoelectric generation, charge extraction**

I - Introduction

Recent developments in microfabrication and biotechnology are increasingly enabling the development of a variety of miniaturized implantable systems. These systems can be applied to health monitoring, diagnostics or localized treatments. In most cases, these devices need an energy source to power their active elements. Traditionally, implants are powered with batteries but a new promising approach for advanced miniaturization consists in developing components harvesting energy from the surrounding environment. As the human body produces a substantial amount of energy that can take different forms such as dissipated heat, inertia, muscle contraction, joint movement or heel strike [1], numerous microsystems have been recently developed to harvest part of it [2]. More specifically, Goto *et al.* [3] have already proven the feasibility of using an energy harvesting system taken from a SEIKO watch to power a mongrel dog's pacemaker, even though the extracted energy was still insufficient.

The vast majority of up-to-date energy harvesters is based on inertial power generation [4] as vibrations are widespread in our environment and inherently transferred through packaging. Best performances are found in resonant systems excited at specific known, stable and high frequencies. But in body environment, frequencies of organ generated vibrations are very low (below a few tens of Hertz) and unsteady which is not ideal for inertial energy harvesting systems.

II – Harvesting pressure energy piezoelectrically

In this work we propose to study energy harvesting for implants from pressure variations in blood environment. During cardiac cycles, blood pressure actually varies with an amplitude of about 20 mmHg in the right ventricle, 100 mmHg in the left ventricle, and 40 mmHg in the arterial system as can be measured by routine medical exams. In each case, the frequency of the variation is given by the heart rate (between 1 and 3 Hz depending on the patient activity and morphology). Energy can be generated when this pressure is deflecting a flexible element coupled to a transducer such as a piezoelectric diaphragm. Clark and Mo [5] have studied the mechanical deflection and dimensions optimization of a piezoelectric layer (depicted in Figure 1) fixed on a diaphragm subjected to such pressure variations. After an analysis of the different electrical and mechanical variables of the system when the diaphragm is deflected, they present numerical simulations yielding the optimal piezoelectric layer radius. However, they do not discuss in this work a method to extract the theoretically calculated available energy.

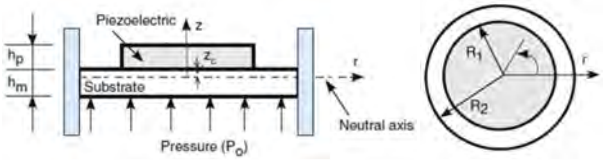

Figure 1: *Diaphragm consisting in a substrate and a piezoelectric layer [5].*

The blood pressure excitation frequency is very small compared to reasonably achievable resonant frequencies for such systems (in the order of a few hundreds of Hertz). Hence, the following analysis assumes a quasi-static excitation where inertial forces are negligible. This differs significantly from usual piezoelectric energy harvesters presented in the literature where resonance effects are predominant [6, 7]. As these effects largely amplify the harvested power, they are an integral part of energy extraction optimization methods as presented for instance in [8, 9, 10].

III – Analytical model

The linearized equations governing the behavior of a piezoelectric energy harvester can be written under quasi-static approximation as:

$$\begin{cases} F = kx + \alpha V \\ Q = \alpha x - C_0 V \end{cases} \quad (1)$$

where F represents the force applied on the diaphragm by the pressure, k the diaphragm stiffness, x its displacement, α the electromechanical coupling, Q the extracted charge, V the voltage across the piezoelectric element, and C_0 its capacitance. When the displacement is canceled from the equations, the extracted charge can be expressed as:

$$Q = \alpha/k\, F - \left(\alpha^2/k + C_0\right)V \,. \qquad (2)$$

When a force F_0 is applied, we deduct from this equation that the open-circuit voltage $V_{o.c.}$ and short-circuit generated charge $Q_{c.c.}$ are equal to:

$$Q_{c.c.} = \alpha F_0/k \quad \text{and} \quad V_{o.c.} = \frac{F_0}{\alpha + kC_0/\alpha} \,. \qquad (3)$$

A. Classical AC energy extraction method.

First we consider the simple case where a resistive load R is connected directly on the piezoelectric element, as depicted in Figure 2.

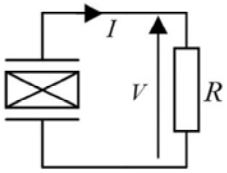

Figure 2: *Classical AC energy extraction method.*

This approach is realistic and can be appropriate only in the specific case of an excitation at very stable and known amplitude and frequency. For a harmonic load F at an angular frequency ω and an amplitude F_0, the complex current I and the power through the load P can be expressed as:

$$I = \frac{j\omega F_0\, \alpha/k}{1 + \left(\alpha^2/k + C_0\right)Rj\omega} \qquad (5)$$

$$P = \frac{1}{2}\left(\frac{\alpha}{k}F_0\right)^2 \frac{R\omega^2}{1 + \left(\alpha^2/k + C_0\right)^2 R^2\omega^2} \,. \qquad (6)$$

Hence for an optimal load $R_{opt}=((\alpha^2/k+C_0)\omega)^{-1}$, the power P is maximized and is equal to:

$$P_{\max} = \frac{1}{4}\left(\frac{\alpha}{k}F_0\right)^2 \frac{\omega}{\alpha^2/k + C_0} \,. \qquad (7)$$

For one cycle and using (3), this corresponds to an extracted energy $W_{classical\ AC}$ of:

$$W_{classical\ AC} = \frac{\pi}{2}\frac{\alpha^2 {F_0}^2}{k\alpha^2 + C_0k^2} = \frac{\pi}{2}Q_{c.c.}V_{o.c.} \,. \qquad (8)$$

B. Classical DC energy extraction method.

A more realistic approach that commonly addresses most of the applications requiring a DC power supply consists in connecting the piezoelectric element to a rectifier circuit followed by a filtering capacitor, as illustrated in Figure 3.

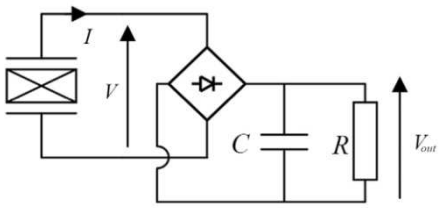

Figure 3: *Classical DC energy extraction method.*

In this case, the output power V_{out} is held constant to the desired value as the filtering capacitor C is chosen to have a time constant RC large compared to the excitation periods. The applied force F does not need to be harmonic this time but is considered periodic (with a period T) and ranging from a value of $-F_0$ to $+F_0$, as blood pressure can be modeled.

For this circuit, the typical waveform of the voltage V across the piezoelectric element when the applied force varies is drawn in Figure 4. When V is lower than the output voltage V_{out}, the piezoelectric element is in open-circuit configuration, no current is generated and V increases proportionally with F (2). When the absolute value of V reaches the rectified voltage V_{out}, its value is held constant and the generated current I rises, effectively recharging the capacitor. As the force starts to decrease, V falls back in open-circuit configuration.

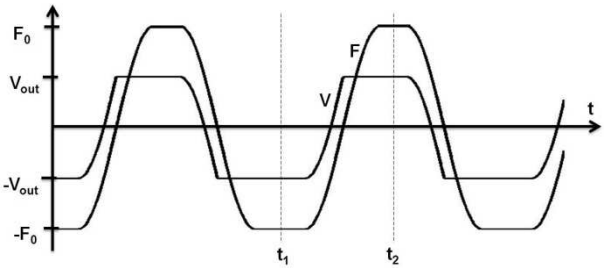

Figure 4: *Piezoelectric voltage for a periodic applied force.*

For half an excitation period T (between t_1 and t_2 in the plot from Figure 4), which corresponds to a full period for the components following the rectifier, the charge extracted from the piezo has been fully transferred to the load R as no net charge has been accumulated in the capacitor. Expressing this charge as the integral of the different currents yields:

$$\int_{t_1}^{t_2} I dt = \int_{t_1}^{t_2} \frac{V_{out}}{R} dt = \frac{V_{out}T}{2R} \qquad (9)$$

and using (2) we also have:

$$\int_{t_1}^{t_2} I dt = 2F_0\, \alpha/k - 2\left(\alpha^2/k + C_0\right)V_{out} \,. \qquad (10)$$

The combination of the latter two equations yields an expression of the output voltage as a function of the amplitude of the excitation force:

$$V_{out} = \frac{\alpha F_0}{\alpha^2 + kC_0 + kT/4R} \qquad (11)$$

This gives the mean power through the load $P=V_{out}^2/R$ which is maximized for an optimal value of the load R_{opt} as follows:

$$R_{opt} = \frac{T}{4\left(\alpha^2/k + C_0\right)} \quad (12)$$

$$P_{\max} = \frac{\alpha^2 F_0^{\,2}}{kT\left(\alpha^2 + kC_0\right)}. \quad (13)$$

The energy extracted per cycle is then:

$$W_{classical\ DC} = \frac{\alpha^2 F_0^{\,2}}{k\alpha^2 + k^2 C_0} = Q_{c.c.}V_{o.c.}. \quad (14)$$

C. Forced voltage energy extraction method.

From (1) and (2) we can also elaborate a charge extraction method based on the forced application of a tension V across the piezoelectric element, similarly to the Ericsson type conversion cycle presented in [8]. V is chosen to have a square profile with an amplitude V_0 in phase with the direction of variation of the force on the diaphragm (see profiles at the top of Figure 5). When the pressure varies on the diaphragm, the piezoelectrically generated charge Q will be extracted under a voltage V_0 without affecting the current I (from (2)). Hence, within the validity limits of this model, the harvested power $V_0 I$ is proportional to the amplitude of the applied voltage.

By drawing the energetic cycle Q-V of this conversion (Figure 6), the extracted energy per cycle $W_{forced\ V.}$ can be written as:

$$W_{forced\ V} = 4\frac{\alpha}{k}F_0 V_0 = 4Q_{c.c.}V_0. \quad (15)$$

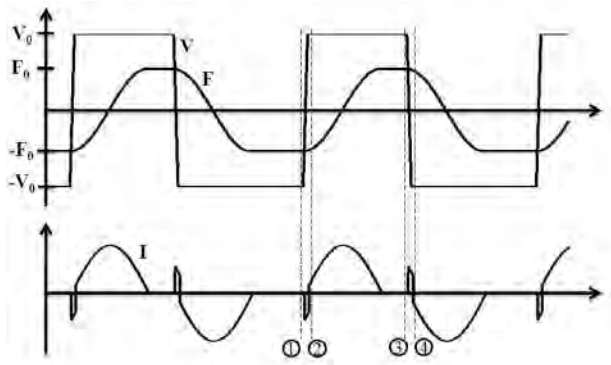

Figure 5: *Voltage and current profiles for the square wave forced voltage energy extraction method.*

These expressions confirm the linear behavior of the extracted energy in function of V_0. Hence, there is no theoretical limit on the extracted energy as long as we applied a voltage large enough. One simply needs to apply a voltage V_0 greater than one fourth of the natural open-circuit voltage $V_{o.c.}$ to achieve better performances than the classical DC power extraction method, assuming same control electronics efficiencies for both systems. In reality, the piezoelectric element will suffer from increasing resistive losses as V_0 gets larger and eventually will not tolerate the growing electric field.

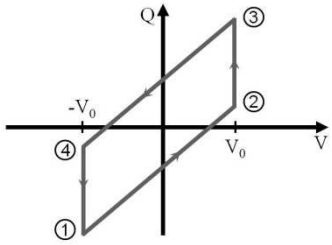

Figure 6: *Energetic cycle of the forced voltage energy extraction method.*

One of the potential circuits to achieve this type of energy extraction is to use a PWM (Pulse Width Modulation) inverter as depicted in Figure 7. Similarly to the classical DC case, the output voltage is constant and regulated as required by most of the energy harvesting applications including implants. As the output voltage V_0 might be too large to directly act as the power source, a DC-DC step-down converter can be added before the load.

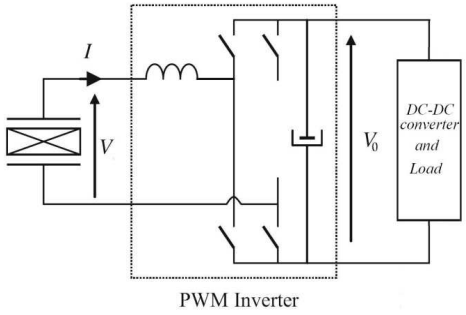

Figure 7: *PWM Inverter implementation of the square wave forced voltage charge extraction method.*

As the PWM inverter solution might not be the most efficient, other electronics circuits can be envisaged to achieve this charge extraction method.

IV – Experimental results

A. Model validation

A 4.5 cm diameter diaphragm with a 2.5 cm diameter piezoelectric layer arranged according to the schematic from Figure 1 has been experimentally subjected to a varying pressure. To simulate blood pressure variation, a pressure with an amplitude ranging from 0 to 50 mmHg (0 to 6600 Pa) and a frequency of 1 Hz was applied. The system parameters have been preliminary determined, mostly by measuring the voltage $V_{o.c.}$ generated when the piezoelectric element is in open circuit and the extracted charge $Q_{c.c.}$ when it is short-circuited.

To validate the model proposed in the previous section, the extracted energy per cycle has been measured for different values of the amplitude of the applied constant voltage V_0 and for different values of the pressure variation. These measures have been plotted in Figure 8 and clearly show the predicted linear behavior of the extracted energy in function of V_0. Additionally,

the slopes of theses plots can be linked to the model parameters using equation (15). For instance, $\alpha F_0/k$ ($=Q_{c.c.}$) has been measured for P=30 mmHg at 970 nC. A linear regression of the extracted energy for this pressure value yields an approximate slope of 210 nJ/V which matches the theoretical equation (15) with a precision of less than 15%.

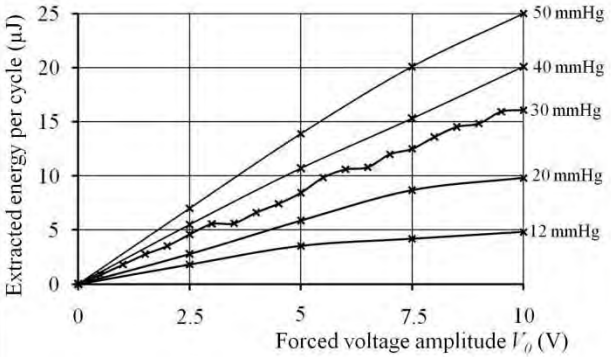

Figure 8: *Measured energy extracted per cycle as a function of the applied voltage V_0 for different pressure amplitudes.*

From the measurements of $Q_{c.c}$ and $V_{o.c.}$, we also calculated the energy extractable by the classical DC method using (14) for different values of the applied pressure. In Figure 9 these calculated energies are compared to the values of the extracted energy using the proposed forced voltage method. This shows that an amount of energy higher by a factor 3 to 4 for V_0=10 V can be extracted using the proposed method.

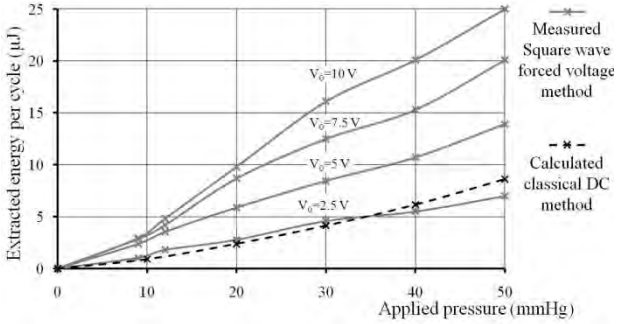

Figure 9: *Extracted energy per cycle from the square wave forced voltage method compared to the classical DC method.*

B. Limits of the proposed method

The proposed model is based on the linearized equations of the piezoelectric element behavior as written in (1). Non-linear effects start to appear as values of displacement, voltage or force become high. For instance, the linearized model (kx) for the diaphragm elastic resistance breaks up as the displacement is in the order of the diaphragm thickness. Moreover, the voltage V applied on the piezoelectric element affects the stiffness. Micro-indentation measurements have been carried out for several voltages applied on the piezoelectric layer to quantify this effect (Figure 10). Additionally, resistive losses and material depolarization must be taken into account when the voltage rises. A more comprehensive model taking those effects into account is currently in development.

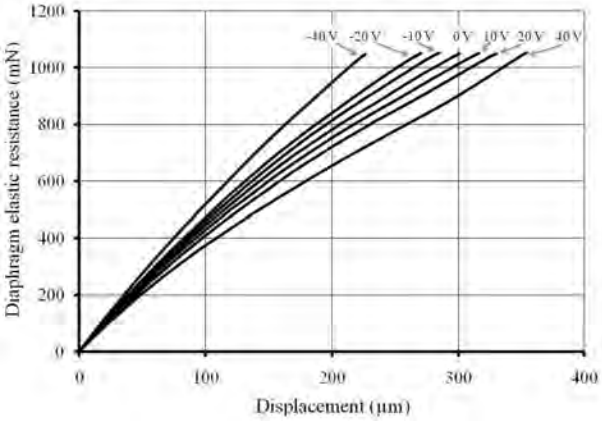

Figure 10: *Diaphragm elastic resistance dependence on the voltage applied to the piezoelectric layer.*

V - Conclusion

Blood pressure variations generate periodic and regular mechanical forces that can be harvested and converted into electrical energy when in contact with a piezoelectric diaphragm. This energy harvesting technique could be used to power active medical implants in blood environment. We proposed in this study a method to efficiently extract electrical energy from the piezoelectric diaphragm by applying a square wave controlled voltage. A theoretical model and experimental measurements have shown the linear dependency of the extracted energy to the amplitude of the applied voltage and for a latter value of 10 V energy harvesting performances were enhanced by a factor 3 to 4 compared to the classical method.

References

[1] T. Starner and J. A. Paradiso , *Low Power Electronics Design*, CRC Press, Summer 2004

[2] E. Romero, R. O. Warrington and M. R. Neuman, *Physiol. Meas. 30* (2009) R35–R62

[3] H. Goto, T. Sugiera, Y. Harada and T. Kazui, *Med. Biol. Eng. Comput.*, 1999, 37 377–80.

[4] S.Roundy *J. Intell. Mater. Syst. Struct.* 2005 16 809

[5] W. Clark and C. Mo*, Energy Harvesting Technologies 2009,* Part V, 405-430

[6] S. Anton and H. Sodano, *Smart Mater. Struct. 16* (2007) R1–R21

[7] D.-A. Wang, N.-Z. Liu, *Sens. Actuators A: Phys. (2011),* In Press

[8] E. Lefeuvre, G. Sebald, D. Guyomar, M. Lallart, C. Richard, *J Electroceram* (2009) 22:171–179

[9] E. Lefeuvre , A. Badel, C. Richard, L. Petit, D. Guyomar, *Sensors and Actuators A* 126 (2006)

[10] D. Guyomar, A. Badel, E. Lefeuvre, C. Richard, *IEEE Trans.Ultrason. Ferroelectr. Freq. Control.* 52, 584 (2005)

ROBUST SOLDER-ARMOURED MEMS FOR HIGH-SHOCK APPLICATIONS

A. Delahunty and W.T. Pike

Optical and Semiconductor Devices Group, Electrical and Electronic Engineering, Imperial College London.

***Abstract* —We explore a novel concept for the shock protection of MEMS suspensions: protective armouring of silicon bumpers with solder. The solder is incorporated into the suspension so as to provide solder-solder contact at the extremes of the suspension travel. Upon impact the more ductile solder deforms and absorbs the kinetic energy of the collision thereby protecting the brittle silicon. A model suspension system has been designed and fabricated using deep reactive-ion etching (DRIE) and reflowed solder. The suspensions have been tested using drop rig with no failures up to a shock level of 350g.**

***Keywords:* MEMS, Shock protection, Impact.**

I - Introduction

As budgets for space exploration continue to be cut MicroElectricalMechanical Systems (MEMS) offer an attractive alternative to conventional technology. Due to their extremely low mass and volume, and with costs of up to $10,000 to place 1kg in low orbit, using MEMS can result in significant monetary savings without a loss in functionality. Other benefits include their low power consumption and tight integration with electronics which makes them very suitable for use in nano and pico-satellites which have far shorter development times than their larger counterparts [1-3].

However, if MEMS are to be used in space applications they need to be able to withstand significant shock and vibration levels during the launch phase as well as during entry, descent and landing. Furthermore, if they are included on board penetrator missions the level of shock which they need to survive significantly increases again– up to 10,000g, enough force to bury them 2 - 5m under a planet's surface [3, 4]. Because MEMS are fabricated from brittle silicon this presents a considerable challenge for any MEMS device that contains moveable mechanical components, such as suspensions and shock protection is imperative.

There are two directions one can take when shock hardening MEMS, external protection or permitting the collision and accommodating the energy release. External protection measures include mechanical latching [5], electrostatic clamping [6] and electromagnetic clamping [7] of the movable parts of the device. Electrostatic and electromagnetic clamping both require an external power source during the shock event, often difficult to achieve. They also, along with mechanical latching methods only provide limited clamping forces. Hopf *et al* [4] demonstrated an effective external passive shock isolator where the structures are encapsulated in a waxy solid that subliminates in vacuum conditions to release the suspension; however, issues regarding how the MEMS are exposed to the vacuum upon landing and where the wax resolidifies would need to be addressed in any mission scenario. Where collisions are permitted and accommodated, the traditional method of shock hardening devices in order to minimise fracture is to optimise the dimensions of the structure in question so that the stresses do not exceed the fracture strength [8]. However, device performance including sensitivity will suffer as a result of this protection and such an approach is only applicable to cases where the shock requirement is known. Yoon *et al* [9] investigated non-linear springs and soft coatings as methods of shock protecting MEMS, but the former affects the Q-factor of the entire system and the latter is not compatible with DRIE. Younis *et al* [10] explored using squeeze-film damping as a method of mitigating the effects of shock, but as space is a vacuum squeeze-film damping is not an option. Yoon *et al* [11] present a method of shock protection which uses a microgranular bed to protect micromachined electronic devices for use in high-g military applications, but the micro glass beads prevent movement and thus cannot be used with moving structures. Hard shock stops have been investigated [9] but were found to be limited in their protection as they themselves can generate secondary sources of shock; and fluid-damping shock isolators which dissipate energy through heat and acoustic energy were found to be too bulky for use in MEMS.

II - Experimental Details

A model suspension system was designed for experimental purposes, see figure 1 below. It consists of a single folded cantilever beam either side of a proof mass, with central bumpers that prevent the suspension from being crushed and destroyed by limiting the travel of the proof mass when a force is applied.

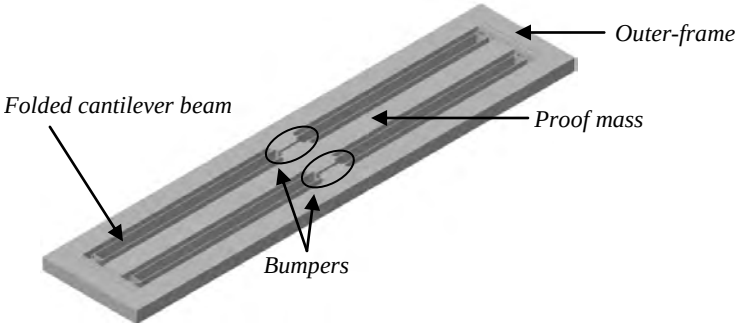

Figure 1: *Model suspension system.*

However, while these bumpers protect the springs of the suspension, they themselves are fabricated from

silicon and thus are also extrememly susceptible to fracture upon impact.

Our proposal for shock protection is to armour the silicon bumpers with a material that has a lower coefficient of restitution than silicon and therefore has the potential to absorb the kinetic energy of a collison. Coating the bumpers in a thin film of a soft metal [9] is not compatible with our fabrication methods. Instead we propose re-flowing solder on finished devices - creating solder buffers which extend beyond the silicon bumper edges.

Surface Evolver [12], an interactive program that can model liquid surfaces shaped by surface tension and other energies, was used to investigate various solder-pad geometries that might provide the optimum geometry for a shock-resistant solder buffer on reflow of solder balls placed on the pads. The design objectives were: production of a solder cushion which extends beyond the silicon; maximisation of the contact area between the solder and pad to minimise the shear at this interface; minimisation of the height of contact to reduce the overturning moment acting at the interface.

The optimum pair of buffers corresponded to a tongue and groove geometry: the groove was produced using a u-shaped solder pad (figure 2), while a filleted-rectangle pad with a narrower tip provided the tongue. A solder cushion is easily achieved with the groove buffer as the solder webs over the gap, see figure 2 below.

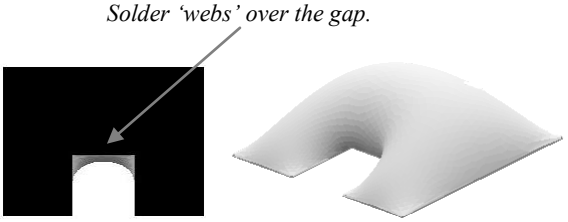

Figure 2: *Surface Evolver simulations of the groove geometry.*

The tongue, however, is slightly more complicated. It needs to feed into the opening, but if a rectangular pad alone were to be used, the majority of the solder would extrude over the longer side of the pad and as a result the tip of the tongue which collides with the base of the groove would be without any solder protection. Our solution to this problem is to make use of the capping die which forms part of the packaging for the final device. This die, 500µm in thickness, is separated from the frame by a gap of 40µm. By designing the solder pad so that it extends beyond the frame and cap and ensuring that the area of the pad is too small to accommodate the volume of the solder within the 40µm height, a geometry can be created whereby the excess solder flows into the free area and creates a bulbous tongue that provides an ample cushion. This cushion also receives support from the cap and solder body behind it, see figures 3b and c. The capping die was fabricated from silicon and strips were used to represent the portion of the capping die attached to the frame, see figure 3a.

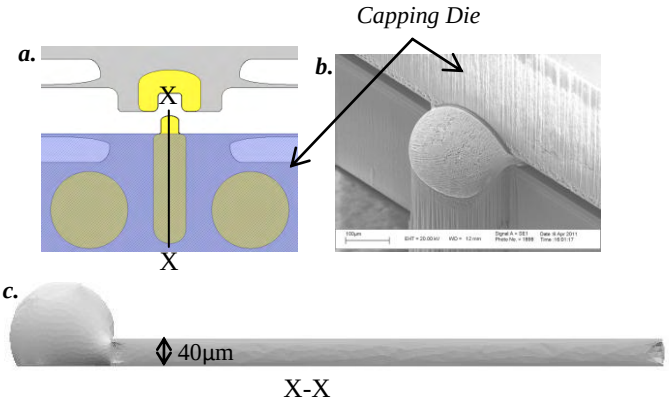

Figure 3: T*ongue-Buffer – a) Mask design, b) SEM Image of the fabricated device, c) Surface Evolver simulation.*

The merit of this geometry can be appreciated if it is compared to a simple ball-shaped buffer, see figure 4a. Upon impact the ball-buffer experiences an overturning moment at the interface which is equal to the force times the impact height. It will also experience significant shear stresses *Б* at the interface which are equal to the shear force divided by the area of the solder pad. However with the tongue-buffer, the capping die provides an opposing reaction force to the impacting force (see figure 4b) and the shear stresses become insignificant because they are distributed between the multiple solder pads which connect the suspension die to the capping die. The SEM image in figure 4c demonstrates how the ball-buffer de-adheres and ruptures the silicon base upon impact.

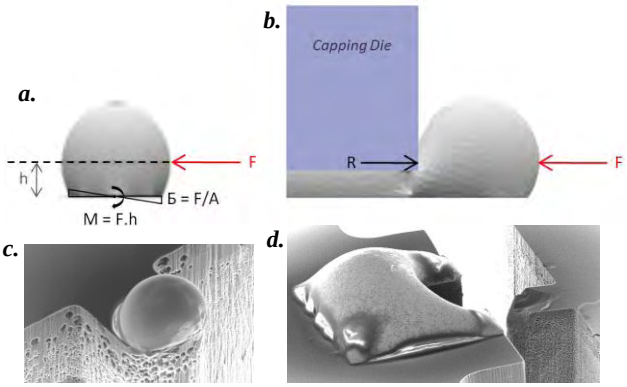

Figure 4: *a) Resultant forces on the Ball-Buffer, b) Resultant forces on the Tongue-buffer, c) Ball-buffer prior to impact, d) Ball-buffer post impact.*

A 20 x 20mm die which contains four independent suspensions per die was designed. The advantage of this is two fold; it allows more devices to be tested in a single go and it also provides a means for direct comparison. It also allows the merits of varying buffer geometries to be compared. There are three different die designs in total; they investigate changes in *1)* the impact height above the wafer surface, *2)* the groove width and *3)* the effect of gold metallization. Figure 5 shows the mask design for Die 1.

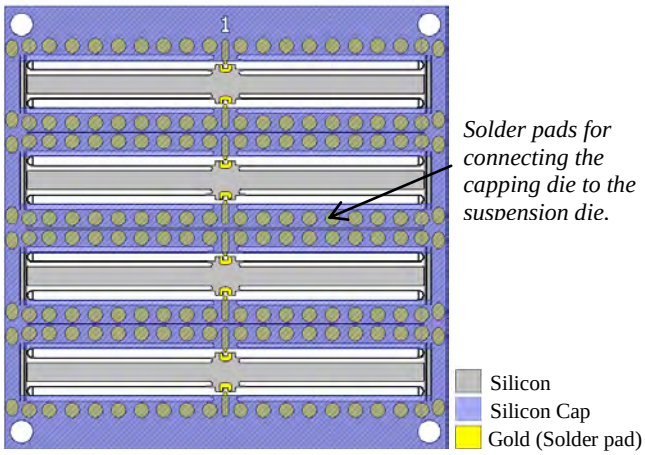

Figure 5: *Mask Design for 20 x20mm die with four model suspensions.*

To aid alignment during reflow 1mm diameter steel pins were fitted into the openings at each of the four corners of the device die and capping die. See figure 6.

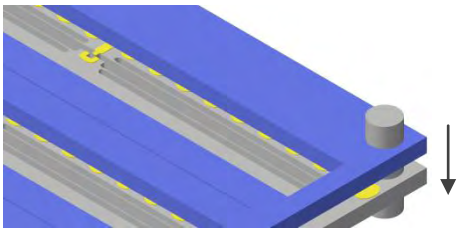

Figure 6: *Steel pins used for reflow alignment.*

Figures 7a, b and c show SEM images of the final fabricated devices.

a.

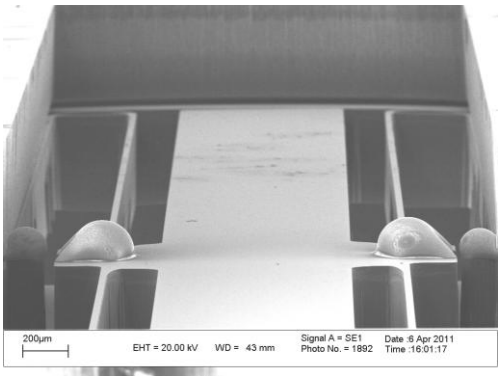

b.

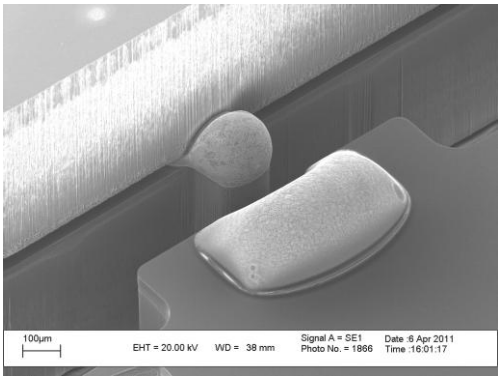

c.

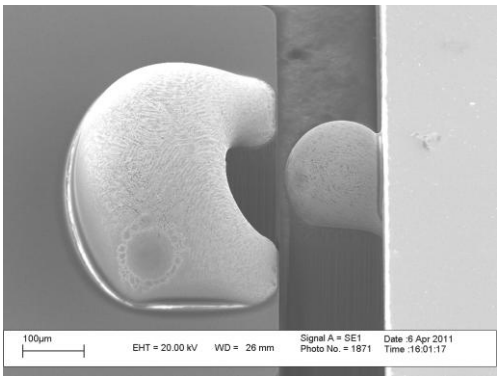

Figure 7: *SEM Images of the solder buffers.*

III - Results and Discussion

A. Results and analysis

Using a drop testing rig the three different die designs were subjected to shocks up to 350g. The solder armour was successful in protecting the silicon suspensions from fracture during each shock event while their un-armoured counterparts shattered each time. It was not possible to compare the merits of the varying buffer geometries – all successfully protected their suspensions. The impact contact region on the groove buffer was evident in post-shock imaging (see figure 8) as a smoothed area.

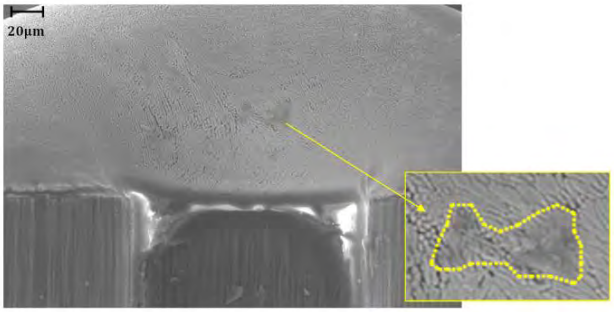

Figure 8: *Groove-Buffer post collision.*

Modelling the impact as a Hertzian contact between two elastic half bodies, the radius of the area of contact *a* can be calculated from equation 1 [13]. As there are two principal radii of curvature for each buffer the resulting area of deformation will in elliptical and *a* needs to be calculated separately in both principal directions.

$$a = \left[\frac{3F}{4}\left(\frac{(1-\vartheta_1^2)}{E_1} + \frac{(1-\vartheta_2^2)}{E_2}\right)\left(\frac{R_1 R_2}{R_1+R_2}\right)\right]^{\frac{1}{3}} \quad \{1\}$$

Where: F = force, ϑ_1, ϑ_2= Poisson's Ratios, E_1, E_2 = Young's Modulii and R_1, R_2 are the radii of the two curved bodies.

The actual contact area was estimated to be approximately 200µm² with a total width of approximately 20µm (see figure 8) while the theoretical prediction was

an elliptical area with a width of 30µm and height of 18 µm. The theoretical value is larger because the theory is based on two elastic bodies pressed against each other under purely static conditions, while in this case there is plastic deformation.

B. Future work

For soft materials impacting at high velocities it is more accurate to take into account both the plastic deformation and the relevant strain rates [14]. The area of plastic deformation incurred upon impact can be predicted by idealising the curved surfaces as two spheres and assuming that there are three different periods of the contact interval – Stage 1: the elastic interval which follows the force-deformation law (equation 2) and which ends as the yield stress and the maximum relative compression of the two bodies, α is reached (equation 3), stage 2: which considers a continuous pressure moving out from the centre of impact and stage 3: a restitution which begins as the relative velocity between the two bodies reaches zero and involves the restoration of the accumulated strain energy.

$$F = k_2 a^{\frac{3}{2}} \qquad \{2\}$$

$$\textit{Where:} \qquad k_2 = \frac{4}{3}\frac{E}{1-\vartheta^2}\sqrt{R}$$

$$\alpha = R\left[\frac{\pi p_0(1-\vartheta^2)}{2E}\right] \qquad \{3\}$$

Where: a = radius of the circular area of contact, p_0= yield stress, R = radius of the sphere.

Using these assumptions the radius of the area of permanent plastic deformation *r* can be calculated from equation 4:

$$r^2 = \left[\left\{\frac{p_0\pi^2R(1-\vartheta^2)^2}{6E^2}\right\}^2 + \frac{m}{p_0\pi R}\left(\frac{1}{4}u_0^2 - \frac{4}{5}\frac{k_2}{m}\alpha^{\frac{5}{2}}\right)\right]^{\frac{1}{2}} - \frac{p_0\pi^2R^2(1-\vartheta^2)^2}{6E^2} \qquad \{4\}$$

m = mass of one sphere, u_0 = initial velocity. [14]

The newly fabricated devices seen in figures 7a-c will be tested until failure on a new high-shock drop testing rig. The devices will be mounted in a holder which is attached to a single rail of height 2m and a high-shock piezoelectric accelerometer will be used to measure the deceleration experienced by the devices. Work on this rig is currently in progress. This new testing equipment will allow us to test the solder buffers until failure and will also permit us to analyse the merits of the varying solder buffer geometries.

V – Conclusion

Initial testing has proven that armouring silicon with solder in order to replace a brittle silicon-on-silicon impact with a ductile solder-on-solder impact can be an effective method of shock protection for MEMS. When tested at shock levels up to 350g the armour successfully protected the silicon suspension from fracture. The area of deformation predicted using Hertzian contact stresses also proved to be consistent with the actual deformation observed and theory which accounts for plastic deformation and its associated strain energies has been identified for use on future higher shock experiments.

Acknowledgements

The author's would like to thank Dr. Werner Karl and Robert Hergert for all their kind help.

References

[1] H. Shea. In *Photonics West 2006:* Reliability, Packaging, *Testing, and Characterization of MEMS/MOEMS V*. San Jose, CA, USA, 2006.

[2] H. Shea. In *Photonics West, MOEMS and Miniaturized Systems VIII*. San Jose, CA, USA, 2009.

[3] B. Stark. *MEMS Reliability Assurance Guidelines for Space Applications*, Jet Propulsion Laboratory: Pasadena, California, 1999.

[4] T. Hopf, S. Kumar, W.J. Karl and W.T.Pike. *Advances in Space Research*, 45(3): p. 460-467, 2009.

[5] R. Buser. *Sensors and actuators. B, Chemical*, 21(1): p. 323, 2009.

[6] F.T. Hartley. In *SPIE Conference on Electronics and Structures for MEMS*. Qld, Australia, 1999.

[7] K. Ikuta, S. Aritomi, and T. Kabashima. In *Micro Electro Mechanical Systems, MEMS '92, Proceedings. An Investigation of Micro Structures, Sensors, Actuators, Machines and Robot. IEEE*. 1992.

[8] D.M. Tanner, J.A Walraven, K.Helgesen, L.W. Irwin, F. Brown, N.F. Smith and N. Masters. In *Reliability Physics Symposium, 2000. Proceedings. 38th Annual 2000 IEEE International*. 2000.

[9] S.W. Yoon, N. Yazdi, N.C. Perkins and K. Najafi. *Sensors and Actuators A: Physical*, 130-131: p. 166-175, 2006.

[10] M.I. Younis, D. Jordy, and J.M. Pitarresi, *Journal of Microelectromechanical Systems*, 16(3): p. 628-638, 2007.

[11] S.H. Yoon, J. E. Roh and K.L Kim. *Journal of physics. D, Applied physics*. 42(3): p. 035501, 2009.

[12] K. Brakke. *Surface Evolver Susquehanna University*. 2008.

[13] K.L. Johnson, *Contact Mechanics*, 1999.

[14] W. Goldsmith, *The Theory and Physical Behaviour of Colliding Solids*. 1960.

MICROMACHINED RIDGE GAP WAVEGUIDE FOR SUB MILLIMETER AND MILLIMETER WAVE APPLICATIONS

S. Rahiminejad[1], A. U. Zaman[2], E. Pucci[2], H. Raza[2], V. Vassilev[1], S. Haasl[3], P. Lundgren[1], P.-S. Kildal[2] and P. Enoksson[1]

[1]*Chalmers University of Technology; Department of Microtechnology and Nanoscience, SE-412 96 Gothenburg, Sweden*
[2]*Chalmers University of Technology, Department of Signals and Systems, 41296 Gothenburg, Sweden*
[3]*Royal Institute of Technology, Stockholm, Sweden*

***Abstract* — High-frequency waveguide technology has become a field of great interest lately. In this paper we present a ridge gap waveguide with two** 90 *degree* **bends and a ridge gap waveguide resonator, both fabricated with MEMS technology. It is the first time the ridge gap waveguides have been fabricated for millimeter waves. The ridge gap waveguides is realized of two conducting plates, one of them with a texture, and can provide low transmission losses without any requirements to alignment between the two plates, and with neither conductive joints nor sidewalls. The Ridge gap waveguide makes use of a ”bed of nails” structure which acts as a magnetic conductor and creates a cut-off for parallel plate modes between the two plates. Thereby, wave propagation is confined to the electric conducting ridge, without making use of electrically conducting sidewalls. MEMS technology can provide precision machining which makes it possible to go up in higher frequency bands than with conventional machining. The purpose of this paper is to describe the the fabrication process of the surface textured with pins and ridge.**

Keywords: **GHz, High-frequency, MEMS, RF, Waveguide**

I – Introduction

Sub millimeter and millimeter waveguide technology is an expanding new field. Conventionally solid rectangular waveguides and coaxial transmission lines are use due to their low losses at high frequencies. However they experience some practical problems when integrated in a high-frequency system. Other waveguides have been introduced but often requires electrically conductive sidewalls and good alignment. Even though some structures do not require solid walls they are still in need for electrical contact between separately manufactured pieces. Recently, a ridge gap waveguide has been introduced [1], constructed, manufactured by milling, and verified to work between 10 and 20 GHz [2]. The fabrication method by milling is impossible when dimensions are decreased to achieve higher frequencies, and in particular above 100 GHz. On the other hand, MEMS technology can offer precision machining and open up a new frontier of high frequency microwave components. In this paper, we present for the first time a ridge gap waveguide and a ridge gap resonator for the range of 210-340 GHz fabricated with MEMS technology.

Ridge gap waveguides use metamaterial to confine the electromagnetic wave without using solid or conductive walls. At the operation frequency the metamaterial will act as an Artificial Magnetically Conducting (AMC) surface. Thereby, it creates together an overlying parallel electric conducting surface a cutofffor parallel-plate modes. By surrounding the conducting ridge with the AMC surface, the electromagnetic wave will follow the ridge and is forbidden to propagate in any other direction due to the parallel-plate cutoff. The ridge gap waveguide has the benefit of low losses at the same time as being easier to manufacture, and allowing more freedom in assembly, alignment and fabrication than other lowloss waveguide technologies.

II – Structure & Design

Here in this work a ridge gap waveguide (figure 1) and an ridge gap resonator (figure 2) has been

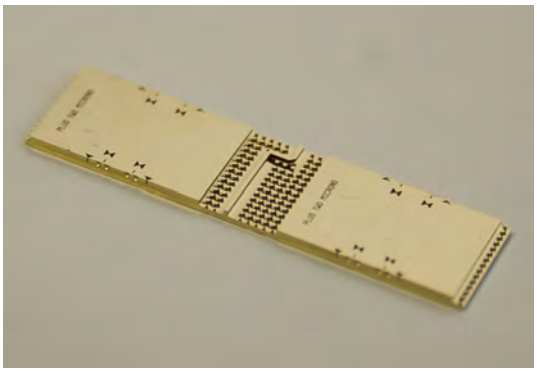

Figure 1: *The waveguide chip*

fabricated using MEMS technology. By having a electric conducting surface parallel to an AMC surface with a distance smaller than one fourth of the wavelength, the wave is prohibited from propagating between these two surfaces [3]. In this structure a conductive ridge is embedded in the AMC surface allowing the electromagnetic wave to propagate between the ridge and the smooth electric conductor above. The AMC is obtained by a structure known as ”bed of nails” [4]. Here the ”bed of nails” structure

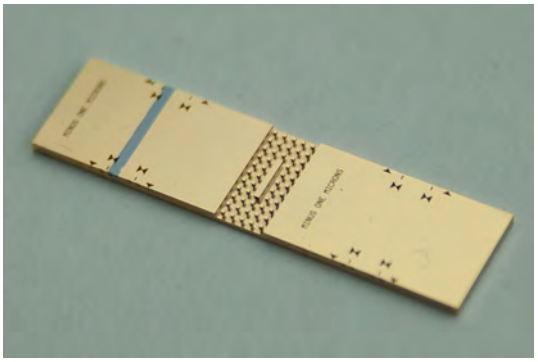

Figure 2: *The resonator chip*

is constructed with micromachined pillars. The pillar height is around 277 μm, the active area of the ridge gap waveguide chip is 5.290 $mm \times 3.5$ mm and for the ridge gap resonator it is 4.95 $mm \times 2.28$ mm. The electrically conducting lid over the ridge gap waveguide has a height of 55 μm above the ridge and the lid over the resonator is placed 167μm above.

The ridge gap waveguide has a ridge with two 90° bends which show that the electromagnetic wave follows the ridge. To obtain a signal a rectangular waveguide situated in a measuring flange needs to be attached. A surrounding copper package, figure 3, is milled to support the chip when the measuring flange is connected to it. The copper package has besides support two more purposes. 1) It provides the smooth electric conducting lid above the ridge as seen in enlarged area of figure 3 with the AMC surface at a fix distance from it. 2) It has a transition interface structure for the electromagnetic wave to transfer from the ridge gap waveguide to the rectangular waveguide in the measuring flange. The transition is done with a staircase structure, milled into the copper package connected to the ridge figure 4.

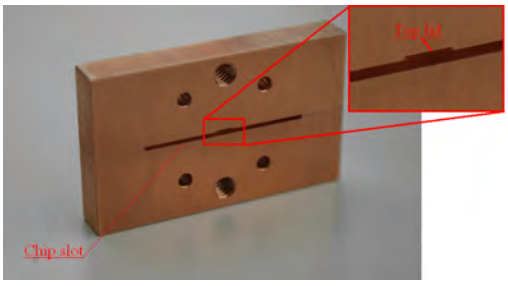

Figure 3: *The copper support package. The enlargement show the milled area which will act as a conducting lid over the chip.*

The resonator consists only of a single ridge surrounded with the ”Bed of nails” structure from every direction. The resonator is weakly coupled to

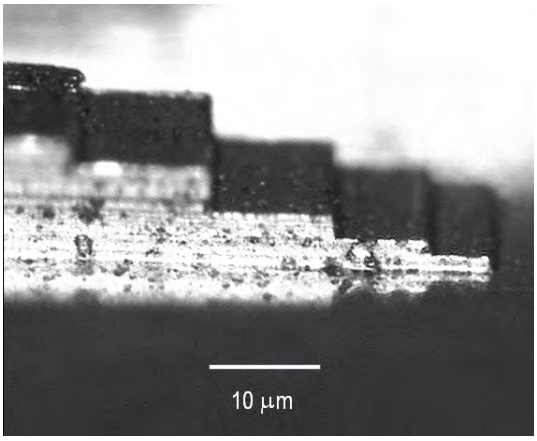

Figure 4: *The transition structure from the ridge waveguide to the rectangular waveguide*

the measuring flange and therefore there is no need for a transition interface structure. The rectangular waveguide is simply connected to the short side of the resonator and there are fewer requirements for a perfect connection.

III – Fabrication Process

The process for fabricating the waveguide and the resonator is shown in the schematic process plan in figure 5. Both devices have the same pillar height and therefore the same processplan is used. A more detailed description will follow.

A 0.5 μm thick aluminum layer was sputtered on a silicon wafer to act as a hard mask during etching. Aluminum was used and not silicon dioxide because it gives a better lateral resolution than an oxide hard mask when etching. The etch selectivity for Al/Si is higher than for SiO_2/Si. Since Aluminum is used as a hard mask, a thin photoresist is sufficient when etching. In contrast when using oxide with the given equipment, a thick resist layer would have been needed to compensate for the reduced selectivity.

To achieve vertical walls, deep reactive ion etching was used. Similar work has been done in [5]. Here the etch rate was up to 3 $\mu m/min$. The height of the pillars were aimed to be in the range of 277 μm to achieve the operation frequencies of 210-340GHz. When etched slower black silicon was observed in the trenches.

The aluminum and the remaining photoresist is stripped of the wafer. Thereafter the wafer was diced into strips to ease the electroplating of gold. Gold is used to make the surface conducting and needs to be 5-6 times thicker than the skin depth at 270 GHz which results in a requirement of an approximately 1 μm thick gold layer. First a 50 nm layer was sputtered as a seed layer on all sides to achieve electrical contact

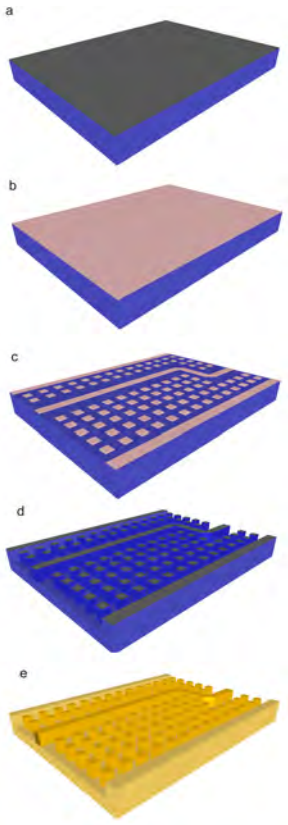

Figure 5: *Process plan for both the waveguide and the resonator. a) A* 0.5μ*m layer of Al is sputtered, b) a thin photoresist layer is spun on top, c) the photoresist is developed and the exposed Al is etched, d) Deep reactive ion etching is used to etch the pillars and the Al and remaining resist is stripped, e)* 1 μ*m gold is sputtered and electroplated*

to the package. The line of unplated surface visible in figure 2 is a consequence of the clamp used when electroplating. Electroplating is used to give a better step coverage and a more even distribution compared to if the entire layer was only sputtered. The strips are also sputtered and electroplated on the sides to achieve electrical contact with the copper package.

IV – Measurement specification

Measurements will be done using three basic components [6] i) a performance network analyzer (Agilent E836x system), ii) a millimeter wave test set controller (Agilent N526x), iii) a waveguide module. Here the module is the flange WR03 used for the range 220-325 GHz 6.

V – Results & Conclusions

Simulations for the ridge gap waveguide including the rectangular waveguide transition shown in figure 7 show how the electric field is propagating over the ridge gap waveguide at different frequency points. The simulation takes into consideration of the rectangular waveguide transition point. The propagation is

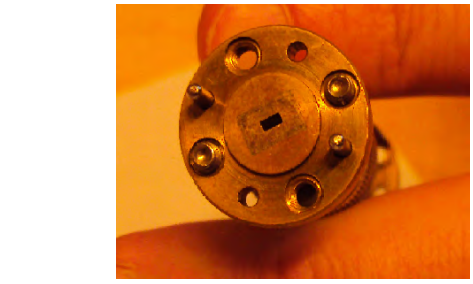

Figure 6: *The measuring flange with the inner rectangular waveguide of the dimension* 0.846×0.432 *mm*

concentrated along the ridge and it is restrained in all other directions by the pins surface within the operation frequency range, between 210 GHz and 340 GHz. Outside the frequency range, the electromagnetic field starts to spread all around the structure, as shown from the color plots (figure 7) at 180 GHz and 350 GHz.

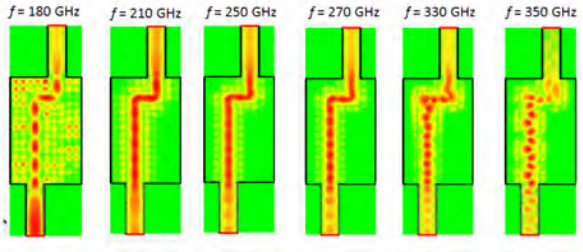

Figure 7: *Figure 7 shows 2D color plots of the simulated absolute value of E-field for the ridge gap waveguide at each frequency point, including rectangular waveguide transitions.*

The same simulations are done for the ridge gap resonator. Figure 8 shows the simulated electric field over the resonator. The third order mode is propagating over the ridge gap along the ridge, and the pins surface stops the field propagation in all other directions inside the cavity.

The simulated transmission and reflection coefficients, S2 respectively S1 , for the ridge gap waveguide including rectangular waveguide transitions can be shown in figure 9. The return loss is below -15 dB between 240 GHz and 340 GHz for the straight ridge case. The oral presentation will also show the measured S-parameters.

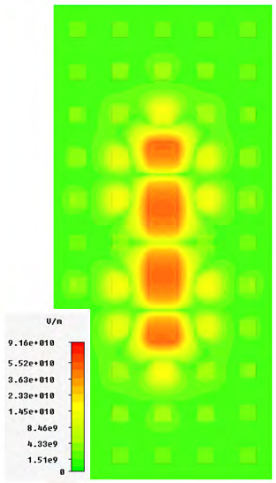

Figure 8: *This Figure shows 2D color plot of the simulated absolute value of the electric field for the open circuit ridge gap waveguide resonator.*

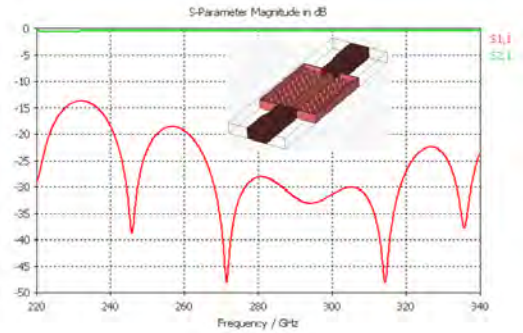

Figure 9: *The simulated reflection- (S2) and the transmission- (S1) coefficient for the straight ridge gap waveguide case*

References

[1] P.-S. Kildal, E. Alfonso, A. Valero-Nogueira, and E. Rajo-Iglesias. Local metamaterial-based waveguides in gaps between parallel metal plates. *IEEE Antennas and Wireless Propagation letters (AWPL)*, Vol. 8:pp. 84–87, 2009.

[2] P.-S. Kildal, A. Uz Zaman, E. Rajo-Iglesias, E. Alfonso, and A. Valero-Nogueira. Design and experimental verification of ridge gap waveguides in bed of nails for parallel plate mode suppression. *IET Microwaves, Antennas & Propagation*, Vol. 5(No 3):pp. 262–270, March 2011.

[3] M. Silveirinha, C. A. Fernandes, and J. R. Costa. *Electromagnetic characterization of textured surfaces formed by metallic pins*. *IEEE Transactions on Antennas and Propagation*, Vol. 56(No. 2):pp. 405–415, Februari 2008.

[4] E. Rajo-Iglesias and P.-S. Kildal. *Numerical studies of bandwidth of parallel plate cut-off realized by bed of nails, corrugations and mushroom-type EBG for use in gap waveguides*. *IET Microwaves, Antennas & Propagation*, Vol. 5(No. 3):pp. 282–289, March 2011.

[5] D. Karln, L.-G. Huss, J. Swedin, C. Rusu, and P. Enoksson. *A Micromachined 94 GHz Dielectric Resonator Antenna for Focal Plane Applications*. *IMS2007*.

[6] Agilent. PNA Microwave Network Analyzers. In *Application Note 1408-15,Banded Millimeter-Wave Measurements with the PNA*.

OPTIMIZED ELECTRODE CONFIGURATION FOR LINEAR CAPACITIVE PRESSURE SENSOR BASED ON SOI-TECHNOLOGY

Robert Waldingbrett, Ulrik Hanke, Nils Høivik

HiVe-Vestfold University College, Institute of Micro- and Nano- Systems Technology (IMST) Raveien 197, 3384 Borre, Norway

***Abstract* — Silicon micromachined capacitive pressure sensors are relatively cost-effective and are excellent candidates for wireless applications because of their low power consumption. However, their high inherent non-linearity requires the compensation of the output signal by a microcontroller. This article describes various electrode shapes decreasing the non-linearity, combining them in different low-parasitic-capacitance sensor layouts. The sensor is based on SOI technology enabling a convenient packaging without introducing a high parasitic capacitance. The behaviour of different electrode-shapes is studied using a circular silicon membrane. The different solutions have been modelled in SolidWorks® and analysed in COMSOL Multiphysics®. The different sensor-structures perform 1.28% - 0.76% of non-linearity and 179.7-146.6Hz/kPa sensitivity in the pressure range of 600kPa.**

***Keywords:* Linearized capacitive pressure sensor, shaped electrode design, SLID-bonding, SOI technology, COMSOL 3D modelling.**

I. – Introduction

Several studies have been carried out on the non-linearity of capacitive pressure transducers during the last decade. This sensor presents interesting features for applications in the wireless domain. It has very low power consumption, high temperature stability and may directly be integrated in resonant devices without signal processing in contrast with piezoresistive pressure sensors. This study aims for a relatively low-cost design with inherent linear output response.

The different sensor layouts presented in this work are based on SOI technology. Their improved linearity is due to the optimized fix-electrode shape and the low parasitic capacitance. Several studies [1, 2] propose electrode-shaping to improve the linearity. Among the different electrode shapes the optimal electrode design has to be found. The device layer of the SOI wafer provides with a stress free, highly uniform membrane. The handle wafer is isolated by the buried oxide (BOX) enabling to use it as a substrate for packaging. It is also demonstrated that the parasitic capacitance has the highest contribution to the non-linearity, because of the small geometry and device capacitance in a microsensor. SLID (Solid to Liquid Inter-Diffusion)-bonding [3] is an inexpensive process adaptable to batch-fabrication in order to make a reference pressure cavity or stacking wafers together. It is also a highly reliable process providing excellent hermeticity. These considerations have led to adopting this bonding technique in the capacitive sensor design. The bonding interface has a relatively small area introducing low stress in the sensor structure due to thermal expansion. Since the bonding results in a high-melting-temperature intermetallic compound it is also suitable for high temperature applications.

II. – Transducer design and electrode-shaping functions

A. Structure and microfabrication

Figure 1 shows the cross-section of the sensor based on the SOI wafer, which is bonded to the silicon wafer including the shaped fix-electrode.

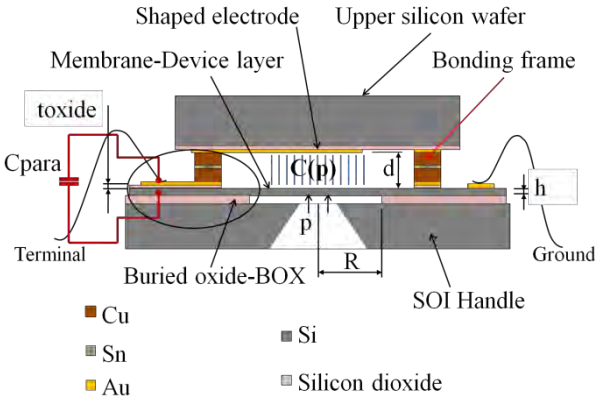

Figure 1: *Cross-section of the sensor using SLID-bonding[3]. The bonding-frame has the largest contribution to the parasitic capacitance.*

The handle is back-etched using wet-etching for opening an etch-hole. Then the membrane is released using hydrofluoric acid. On the device layer as well as on the upper silicon wafer Ti adhesion layer and Au seed-layers are sputtered for the subsequent copper-tin electroplating process. The gold electrode is shaped by gold etching. After electroplating the SOI wafer is stacked to the silicon wafer using wafer-level SLID bonding.

B. Electrode-shaping functions

The analysis of the deflection function to derive the adequate electrode-shaping function is associated to a circular membrane because of its radial symmetry. Considering pure bending for the small-deflection scheme the function depending on the pressure and the radial coordinate is from [4] on page 102:

$$w(r,p) = \frac{p\,R^4}{64\,D}\left(1-\frac{r^2}{R^2}\right)^2 \quad (1)$$

R is the radius of the membrane, r defines the position across the membrane according to the radial coor-

dinates, p is the ambient pressure and D is the flexural rigidity of the membrane written as:

$$D = \frac{E\,h^3}{12(1-\nu^2)} \quad (2)$$

E is the Young's modulus of silicon and ν is the Poisson ratio. The thickness of the membrane is defined by the thickness of the device layer.

For signal conditioning the sensor is connected in an astable multivibrator, which output frequency is:

$$f_{(p)} = \frac{1}{\ln(2)(R_A+2R_B)(C_{(p)}+C_{para})} \quad (3)$$

The resistors R_A and R_B in the voltage divider are connected as shown in the circuit diagram in figure 2. The capacitor C_T corresponds to $C_{(p)} + C_{para}$.

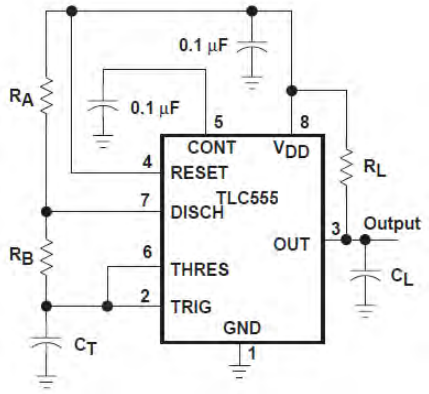

Figure 2: *Circuit diagram of the readout circuit[5].*

The capacitance for the whole membrane-area is:

$$C(p) = \epsilon_0 \int_0^{2\pi} \int_0^R \frac{r}{d-w(r,p)}\,dr\,d\theta \quad (4)$$

Evaluating the double integral we get:

$$C(p) = \frac{8\pi\sqrt{D}\,\epsilon_0\,ArcTanh\left(\sqrt{\frac{pR^4}{64D\,d}}\right)}{\sqrt{p\,d}} \quad (5)$$

Since the output frequency is inverse proportional to the sensor capacitance the conversion of (4) is proposed to the following form:

$$C(p) = \frac{1}{p}\epsilon_0 \int_0^{2\pi} \int_0^R \frac{r}{\frac{d}{p}-\frac{R^4}{64\,D}\left(1-\frac{r^2}{R^2}\right)^2}\,dr\,d\theta \quad (6)$$

Ideally the term $\int_0^R \frac{r}{\frac{d}{p}-\frac{R^4}{64\,D}\left(1-\frac{r^2}{R^2}\right)^2}\,dr$ would be independent on the pressure resulting in linear output dependence. It suggests a gap d as small as possible to cancel the dependence on p of the integrand. To maintain a predefined non-linearity as a function of $\tilde{w} = \frac{w_{max}}{d}$ it also implies a high D because the maximal deflection is inverse proportional to D and given by $w_{max} = \frac{P_{max}R^4}{64\,D}$. The function $\frac{d}{p}-\frac{R^4}{64\,D}\left(1-\frac{r^2}{R^2}\right)^2$ is a multivariable function. This means that either the term varying according to p or to r might be considered. Thereby it is not possible obtain complete suppression of each term contributing to the non-linearity.

In this work we suggest to improve the linearity minimizing the non-linear term according to p in (6). Since the term varying with p has a higher contribution to the non-linearity, minimizing this term must achieve a higher linearity than the compensation of the non-linear term with respect to r. In order to minimize the variation of the integrand in (6) with respect to p, the polar function of the optimized electrode shape has to fulfil the following condition:

$$\frac{\partial}{\partial\theta}\left(r(\theta)\right) = c_1\,\frac{\partial}{\partial p}\left(\frac{d}{p}-\frac{R^4}{64\,D}\left(1-\frac{r^2}{R^2}\right)^2\right) \quad (7)$$

This gives for the electrode shaping function:

$$r(\theta) = -c_1\theta d\,\frac{1}{p^2} \quad (8)$$

The function cannot vary according to p, however the same trend is given if $r(\theta)$ varies with r itself. Also including the parameter d in c_1 leads to:

$$r(\theta) = -c_1\theta\,\frac{1}{r^2} \quad (9)$$

Using the relationship $r = \cos(\theta)r(\theta)$ the final form of the electrode-shaping function is:

$$r(\theta) = -\sqrt[3]{c_1\theta sec^2\theta} \quad (10)$$

Solving (10) for the boundary condition $r(2\pi) = R$ and introducing an optimization constant c_2 we get:

$$r(\theta) = -c_2\left(\frac{R^3}{2\pi}\theta sec^2\theta\right)^{\frac{1}{3}} \quad (11)$$

This electrode-shaping function for different values of the constant c_2 and R=500µm is shown in figure 3.

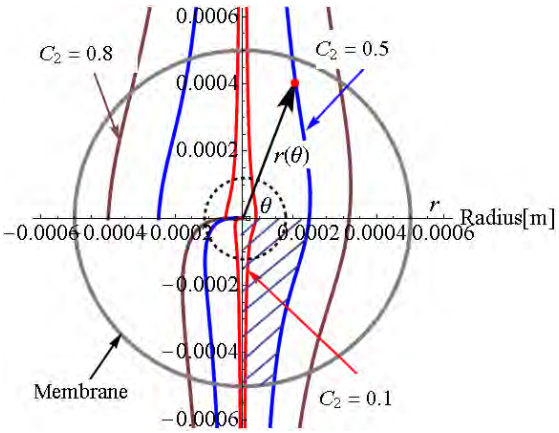

Figure 3: *Electrode-shaping by* $r(\theta) = -c_2\left(\frac{R^3}{2\pi}\theta sec^2\theta\right)^{\frac{1}{3}}$.

As the above function have singularities at $n\frac{\pi}{2}$ $(n = 1,3..)$. This means that there is no closed form solution for the electrode shaping function $r(\theta)$ for any value of c_2. Decreasing c_2 to reduce the non-linearity leads to the singularity of suppressing the electrode. Hence, a trial function of (11) is used for $\frac{\pi}{2} < \theta < \pi$ setting $c_2 = 0.5$. The shaded area in figure 3 has been distributed along the membrane using the coordinate system as an axis of symmetry, giving the electrode design shown in figure 4.

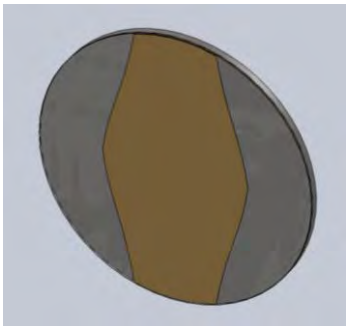

Figure 4: *Electrode design* $r(\theta) = -0.5\left(\frac{R^3}{2\pi}\theta sec^2\theta\right)^{\frac{1}{3}}$.

Because of the small electrode area the idea, the same electrode shape rotated by $\frac{\pi}{2}$ has been inserted. Since it is complicated to give an analytic solution for the capacitance using (11), the electrode-shaping function is approximated by polar function of a circle $r(\theta) = R_1\left(cos(\theta) + sin(\theta) - \sqrt{sin(2\theta)}\right)$. For the angle θ=$\left(0, \frac{\pi}{2}\right)$ the electrode shape for the first quadrant of the coordinate system is obtained. R_1 is set to 600 µm to avoid feature-sizes smaller than the critical dimension. This function observes the same trend for the variation of the electrode area as (11). This yields for an electrode design having a concave-square shape shown in figure 5.

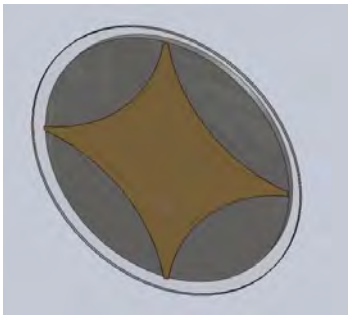

Figure 5: *Concave-square shaped electrode design.*

The results for the non-linearity and sensitivity using the concave-square electrode has been compared to the electrode design proposed in [1]. In this experimental work a spiral shaped electrode design is used and its polar function is given by $\theta(r) = \frac{2\pi}{R^4}(R^2 - r^2)^2$. This function yields to the electrode shape shown in figure 6.

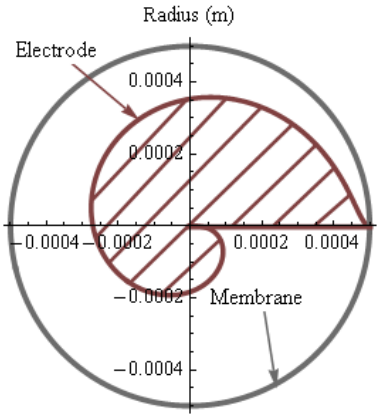

Figure 6: *Spiral shaped electrode design proposed in [1].*

Simulations have been done to demonstrate the non-linearity and the sensitivity improvement with the above electrode shapes, comparing them to the traditional circular electrode configuration.

III. – Simulation results

A. *Models without parasitic capacitance*

As a first approach, simulations of different electrode structures have been carried out using a simple membrane-free space-electrode model neglecting the effect of parasitic capacitance. The simulation result for the output frequency response is shown in figure 7. Among the three electrode shapes proposed the concave-square-shaped provides with the lowest non-linearity as seen in figure 8. In addition, this design also has a higher initial capacitance due to its larger area comparing to the spiral shaped electrode design. It is an important feature reducing the effect of the parasitic capacitance. It can be concluded that electrode shaping results in a gain in both sensitivity and non-linearity according to the shaping-function.

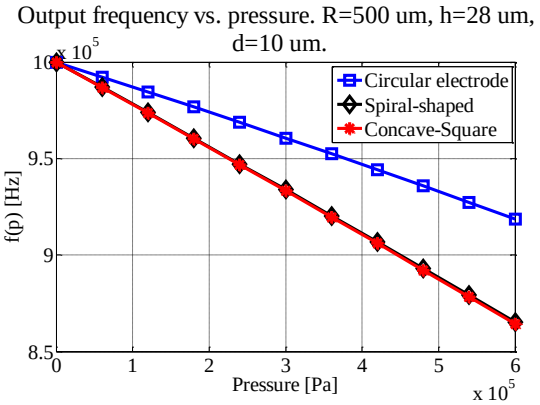

Figure 7: *Comparison of the output response for the different electrode shapes. The shaped electrodes have higher sensitivity than the traditional circular configuration.*

Furthermore, it is also demonstrated that improved non-linearity is not only due to the fact that decreasing electrode area (i.e. capacitance) results in lower non-linearity.

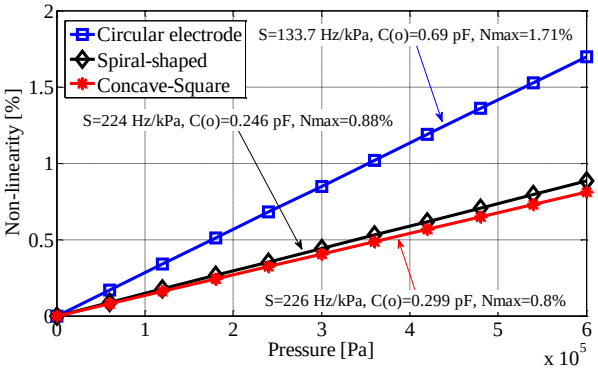

Figure 8: *Non-linearity improvement due to electrode-shaping. The best performance has been obtained with the concave-square electrode for the sensitivity, capacitance and maximum non-linearity.*

B. *Models reducing the effect of parasitic capacitance*

Parasitic capacitance degrades the non-linearity and sensitivity of the transducer significantly. Because of the low device capacitance the reduction of the parasitic capacitance is the most important concern in the design of the microsensor.

The model in figure 9 shows a design without biasing the bonding-frame. The device layer is separated by etching to isolate the biased membrane from the ground plane. Thus, the cavity made by SLID-bonding is not hermetically sealed. Hence, the pressure die has to be placed in a hermetical package. This design controls the

parasitic capacitance to a very low level. However, it also needs additional microfabrication processes to etch the device layer as well as to be mounted in a hermetical package, which is expensive.

This prompts to develop the next sensor design shown in figure 10. For hermetical sealing and to provide the sensor with a reference pressure cavity, the handle wafer is bonded to a glass wafer using anodic bonding. Therefore, the membrane is inverse bended compared with the previous structure. The upper silicon wafer including the electrode is fixed to the SOI device layer using CuSn SLID-bonded interconnects. These interconnects are shown in the wire frame of the COMSOL model and can be seen in figure 11.

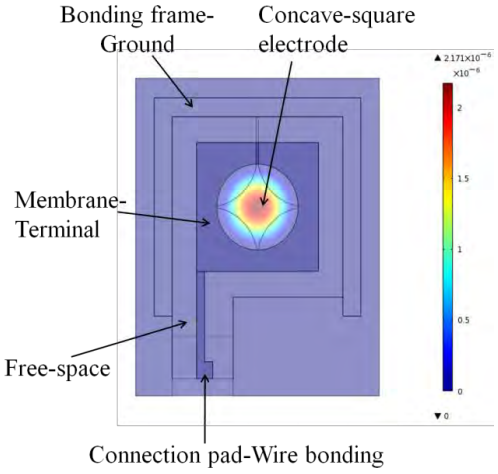

Figure 9: *Low-parasitic capacitance design including concave-square-shaped electrode, displacement field at p=600kPa.*

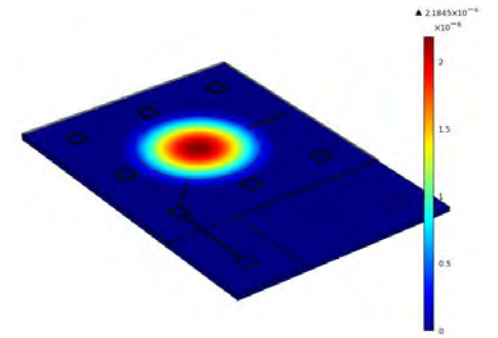

Figure 10: *Design with circular electrode and reference pressure cavity made by anodic-bonding, displacement field p=600kPa.*

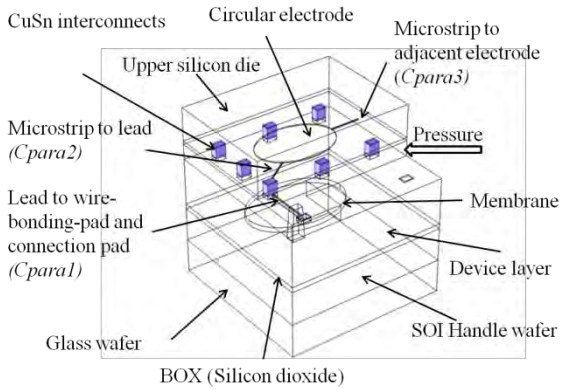

Figure 11: *Model of the stacked structure: The SOI handle wafer is bonded to a glass wafer and the device layer is bonded to the silicon wafer including the shaped electrode.*

This structure enables arraying several pressure dies to increase the ratio of the electrode-capacitance to the parasitic capacitance and improving the linearity as well as the sensitivity. In order to analyse an array-structure, a two-model simulation has been carried out. One of the two models has lead and wire-bonding pad, which has the highest contribution to the parasitic capacitance. The second model only includes a microstrip for connecting the electrodes together. This enables to have a result for an arbitrary number of sensors composing an array, using the pressure as a global variable.

IV. – Conclusion

The design of the transducers proposed in this study has been developed towards a simpler layout and microfabrication process. The capacitance of the sensor at p=0 should further be increased for using a shaped electrode design due to its reduced area. The increasing capacitance can be obtained reducing the gap between the electrodes. This leads to further challenges in the reduction of the height of SLID-bonded interconnects. The three-dimensional simulation is efficient for getting a realistic image of the sensor behaviour and is especially useful in measuring the magnitude of the parasitic capacitance. The simulation of the effect of imperfections of manufacturing, for instance the effect of the non-perfectly circular membrane is planned as future research.

References

[1] D. Crescini, V. Ferrari, D. Marioli, and A. Taroni, "A thick-film capacitive pressure sensor with improved linearity due to electrode-shaping and frequency conversion," *Measurement Science & Technology*, vol. 8, pp. 71-77, Jan 1997.

[2] H. Kim, Y.-G. Jeong, and K. Chun, "Improvement of the linearity of a capacitive pressure sensor using an interdigitated electrode structure," *Sensors and Actuators A: Physical*, vol. 62, pp. 586-590, 1997.

[3] N. Hoivik, W. Kaiying, K. Aasmundtveit, G. Salomonsen, A. Lapadatu, G. Kittilsland, and B. Stark, "Fluxless wafer-level Cu-Sn bonding for micro- and nanosystems packaging," in *Electronic System-Integration Technology Conference (ESTC), 2010 3rd*, 2010, pp. 1-5.

[4] M. Bao, "Analysis and Design Principles of MEMS Devices," in *Analysis and Design Principles of MEMS Devices*, ed Amsterdam: Elsevier Science, 2005, pp. 1-312.

[5] http://focus.ti.com/lit/ds/symlink/tlc555.pdf.

ADVANCEMENTS IN BIOMIMETIC HAIR FLOW-SENSOR ARRAYS

A.M.K. Dagamseh, T.S.J. Lammerink, R.J. Wiegerink and G.J.M. Krijnen

University of Twente, MESA+ Research Institute, Transducers Science and Technology, P.O. Box 217 7500AE, Enschede, The Netherlands

***Abstract* — In this paper we present the latest developments in the design, fabrication and application of single and arrays of biomimetic hair flow-sensors towards high-resolution air-flow imaging. Redesigning the electrode system of the hair sensor (using SOI wafer technology) has led to improve the detection limit down to 1 mm/s air-flow amplitude using 3 kHz measurement bandwidth. SOI technology facilitates the fabrication of wafer-scale arrays, which can be interrogated individually using a smart array interfacing scheme e.g Frequency Division Multiplexing (FDM). The combination of high-sensitive hair sensors and FDM opens possibilities for high spatial-resolution air-flow measurements. A chip-scale single hairs array is used to demonstrate flow-pattern measurements by reconstructing the field of a dipole projected at its position. The separation distance between array elements is determined using the reconstructed dipole field.**

Keywords : **Biomimetic hair, FDM, spatio-temporal flow pattern**

I - Introduction

Biomimetics is a growing field that examines principles and solutions for challenging environmental interaction problems as derived from biological examples. The added values aimed at in using bio-inspired sensor designs are mainly to surpass the performance and robustness of traditionally engineered sensory systems. This attains e.g. improvements in sensitivity, detection limit, operational capabilities, reliability, size, robustness, costs and ease of use of such sensory system. Additionally, the availability of such biomimetic sensory systems helps scientists to understand nature. Imitating the principles from eyes to spike based cameras, from whiskers of rodents to sensors for collision avoidance, from biological neurons to artificial neural networks, from sonar systems in bats to acoustic detectors and from cricket or fish hair-sensors to artificial hair flow-sensors are examples of biomimetic sensors and sensory systems. The last example forms the core of the study presented here.

The sensing hairs of crickets and the cilia-based lateral-line system of fish are examples of array-based sensory systems used to detect flows in air and water, respectively. A large mechano-sensory hair-array resides on the cerci of crickets, at the rear of their abdomen, forming the sensing part of a cricket's escape mechanism for example during spider-attacks [1]. Typically, air movement due to approaching predators causes crickets to turn rapidly away from the stimulus. The large number of hairs, their mechanical properties and directivity result in a smart sensory system. This system enables the cricket to detect, localize and distinguish between various predators using the detected hydrodynamic air-flow signatures [1].

II - Artificial hair flow-sensor

Recently, the mechano-sensory hairs of crickets have been a common research topic for both biologists and engineers [2]. Biologists try to understand nature by investigating their hypotheses using man-made hairs while engineers try to design high-performance sensory systems based on their knowledge of the biological systems.

Inspired by crickets and using MEMS technological advances, we developed artificial hair flow-sensors mimicking the hair-sensors of crickets [3,4]. Our hair flow-sensors were fabricated using a surface micro-machining technology to form a suspended silicon nitride membrane with ~ 1 mm long SU-8 hair on top. The detection principle is based on differentially measuring capacitance changes between two electrodes deposited on top of the membrane with a common underlying electrode i.e. the silicon substrate. Due to the viscous drag torque acting on the hair, the membrane tilts and in consequence to that the capacitors, on both halves of the sensor, change equally but oppositely. Two out-of-phase alternating voltage sources (carrier signals at ~ 1 MHz) are used to detect capacitance changes and convert these to voltage signals by modulation of the carrier amplitude (AM signal). Subsequently a synchronous demodulation technique is used to recover the original (baseband) air-flow signal. Figure 1 shows our artificial hair sensor and its source of inspiration.

A. Hair sensor detection limit

Sensor interfacing is a crucial factor affecting the detection-limit. Parasitic capacitances, inherent to the use of capacitors, pose limitations in attaining highly-sensitive flow sensors. We look at improvement of the detection-limit by reducing the parasitic effects using Silicon-on-Insulator (SOI) wafer technology. This technology enables us to measure small capacitance changes and, hence, to fabricate sensitive hair sensors. This allows to drastically reduce the number of hairs per device (previously up to 124 sensors in parallel) to ultimately a single-hair sensor. Figure 2 illustrates the fabrication scheme of the current hair-sensor design using SOI technology.

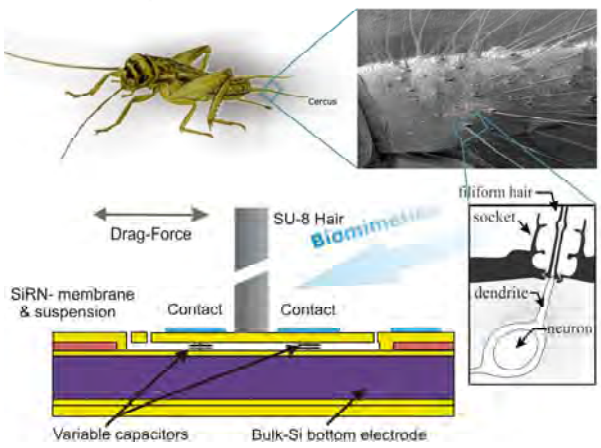

Figure 1: *Schematic representation of flow sensors inspired by crickets. (SEM close-up of a cricket's cercus, courtesy of Prof. J. Casas, Institut de Recherche sur la Biologie de l'Insecte, Tours, France).*

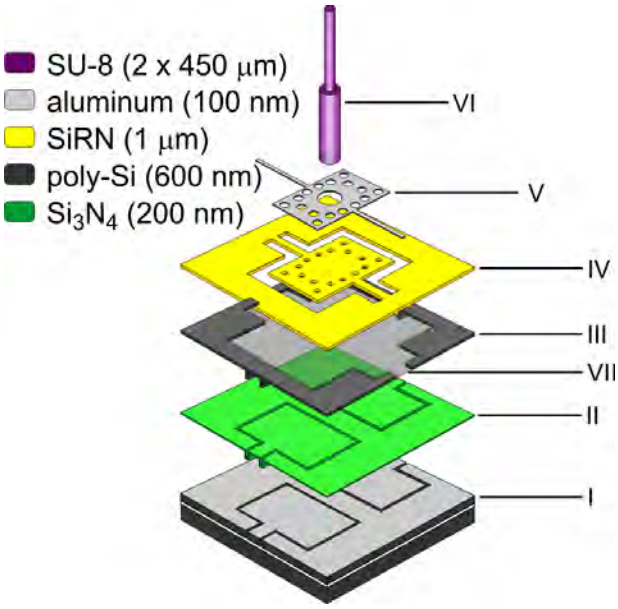

Figure 2: *Schematic representation of hair sensor: (I) RIE of the isolation trenches in the device layer of the SOI wafer; (II) LPCVD of an insulating Si_3N_4 layer; (III) LPCVD of sacrificial poly-Si and RIE of the insulation trenches in poly-Si; (IV) LPCVD of a silicon-rich nitride (SiRN) layer and RIE of membrane/torsion beam structures; (V) Sputtering of Al and wet etching of the top electrode; (VI) Two-step SU-8 processing of the hair; (VII) Sacrificial layer etching with XeF_2.*

To investigate the improvements due to the adapted hair sensor design, the threshold limits of the single-hair sensor (current design using SOI) and the hair sensor array (previous design with the substrate as common electrode) are measured and compared. The detection limit is defined as the air-flow amplitude at which the sensor output voltage has a signal-to-noise ratio (SNR) equal to one. The results show that the detection limit of the single-hair sensor is improved by 52 % (down to 1 mm/s air-flow amplitude as measured with a bandwidth of 3 kHz) compared to the previous hair-sensor. Figure 3 shows an example of the output voltage of both hair sensors as function of air-flow amplitude oscillating at 250 Hz [5].

B. Interfacing hair sensor arrays

Flow-sensor arrays, using sensitive hair sensors, have the potential to measure flow patterns rather than just 'single-point' flow measurements. However, smart interfacing mechanisms are needed to interrogate individual hair elements. Frequency Division Multiplexing (FDM) is a possible mechanism for interrogating each element in the array simultaneously while maintaining continuous interfacing and signal to noise ratio at a much reduced number of interconnects.

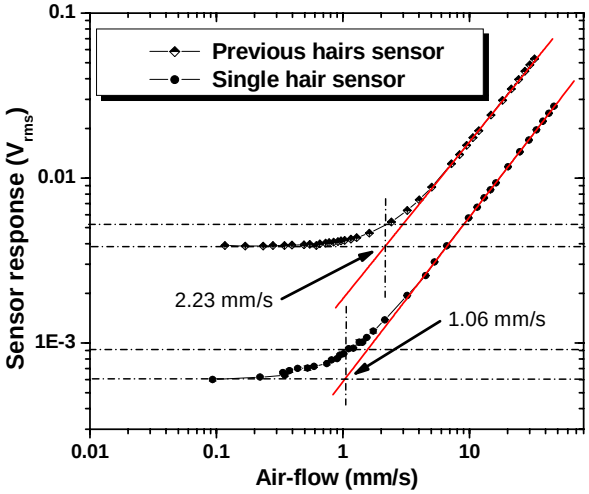

Figure 3: *Output voltage of previous hair sensor and new single-hair sensor as function of flow velocity amplitude at 250 Hz plotted together with the noise levels and the asymptotic lines (in red) to determine the threshold flow amplitude.*

Using FDM, different carrier frequencies are provided along each of the columns of the array for probing the hair sensors. The carrier signals are modulated by the sensors and along the rows the different carrier frequencies, which are mutually shifted in the frequency spectrum, are summed. Per row the stream of these amplitude-modulated signals is fed out of the array chip into a single charge amplifier, hence using a much reduced number of interconnects. Figure 4 shows the basic principle of the FDM array-interfacing scheme.

Figure 5 shows the frequency spectrum of the signals at the output of two charge amplifiers representing the four AM FDM channels from two rows. The results show that we are able to simultaneously retrieve the individual flow signals, as detected by different hair sensors at their position, off-chip. By multiplying the stream signal of each row with the same frequency as used at the columns side (i.e. synchronous demodulation), the information of the individual sensors is retrieved providing simultaneous real-time flow measurements from multiple hairs.

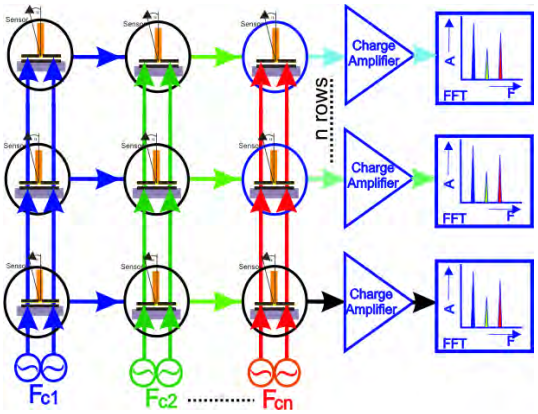

Figure 4: *Principle of FDM addressing technique as applied to our hair sensor array.*

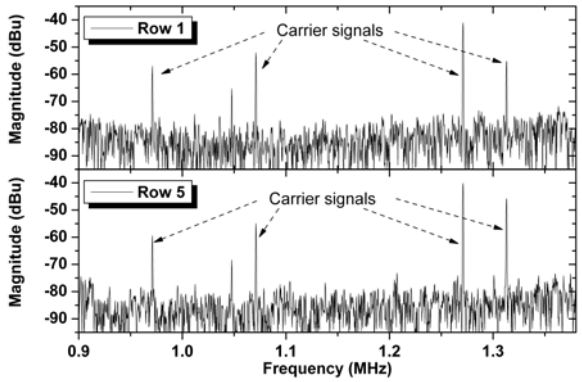

Figure 5: *FFT spectrum of AM signals from two rows at the output of the charge amplifiers while employing FDM.*

C. Flow pattern recognition

By obtaining signals from individual array elements, it is possible to form a real-time image of the air-flow and deduce extra information. The lateral-line system in fish is an example of arrays system used to localize preys by means of flow pattern recognition. Biologists try to understand fish techniques in source localisation by investigating different hypotheses [6,7]. One of these hypotheses is based on reconstructing the flow field generated by a moving dipole source and determining the characteristic points of the flow field. Since the characteristics of dipole sources are well-known from the literature [8], a vibrating sphere generating a dipole velocity field can be conveniently used to analyze object – sensor-array interactions. In an ideal fluid, a sphere vibrating parallel (//) to a linear array line generates a flow velocity in the direction of the *x-axis* (see Figure 6) with amplitudes [6,7]:

$$V_{x,//}(x) = s\,\omega a^3 \frac{(2x^2 - D^2)}{(x^2 + D^2)^{5/2}}$$

where ω is the angular vibration frequency, a is sphere radius, s is sphere displacement amplitude and D is the distance between the centre of the sphere and sensor reference line. The distance D is reflected in the characteristics of the velocity fields [6,7]: for $V_{x,//}$ the distance between the two zeros equals $\sqrt{2}D$. Figure 6 shows simulated dipole velocity field as projected on the *x-axis*.

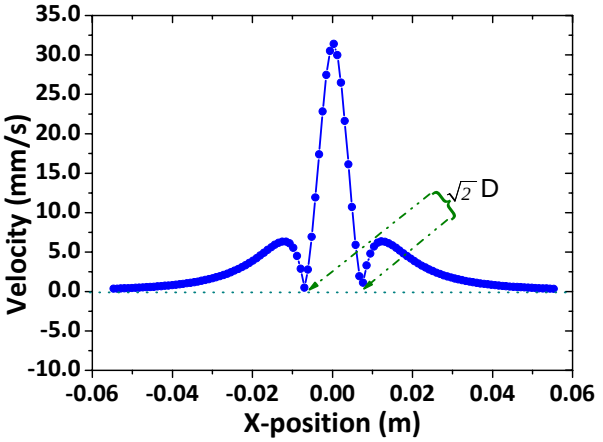

Figure 6: *Simulated velocity amplitude Vx as function of sensor position along the x-axis. The position of the dipole source is encoded in the distance between dipole characteristics.*

Figure 7 shows photograph for the measurement setup used in this study. As demonstration for successful reconstruction of flow fields by the hair-sensor array the dipole fields were measured along different rows and the relative positions of the dipole source to the array elements were determined. Figure 8 represents the dipole field measured simultaneously by each hair-sensor by means of a virtual lateral line system (shifting the dipole source in discrete steps to construct a lateral line system).

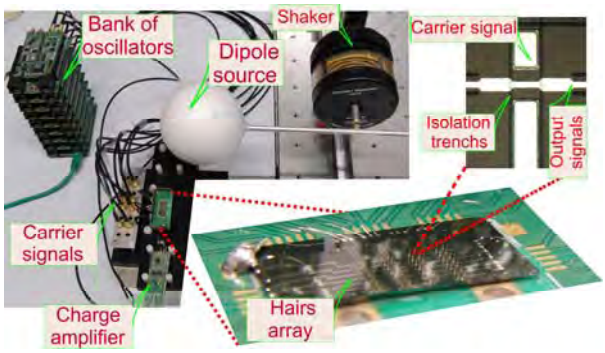

Figure 7: *Photograph of the measurement setup and sensor arrays. Isolation trenches are also shown.*

In these results the peak position represents the sensor output voltage when the dipole is positioned at its minimum distance to the sensor. The shift in peak position (2 mm) represents the column separation distance between sensors and perfectly matches the physical design distance. This proofs that each hair element faithfully reflects the dipole field, at its position, while employing the FDM technique.

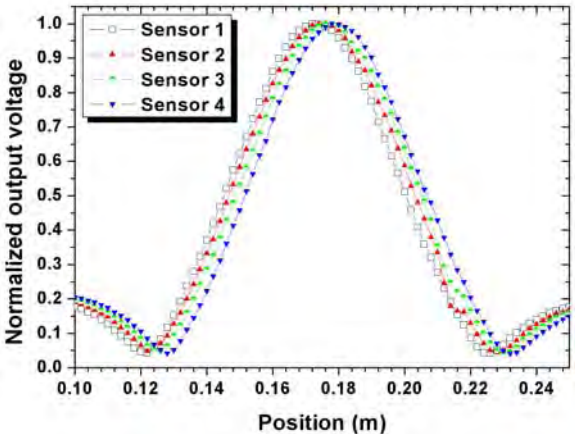

Figure 8: *Normalized flow field measurements simultaneously detected by 4 hairs in one row. The separation between peaks matches with the hair separation (2 mm).*

III - Conclusions

In conclusion, this contribution details the developments of biomimetic hair flow-sensor arrays. The improvement in the detection limit of our artificial hair flow-sensor results from the proper sensor electrodes design by means of reducing the parasitic capacitances. Taking advantage of deep isolation trenches to define electrode areas, SOI technology opens possibilities to fabricate wafer-scale arrays made of single-hair sensors. By obtaining signals from multiple sensors simultaneously (using FDM), it is possible to form real-time images of air-flow patterns. These arrays, by virtue of array signal processing techniques, will be beneficial for sensing and controlling functions of e.g. vehicles by imaging the surrounding environment even in total darkness.

References

[1] T, Shimozawa, T, Kumagai and Y. Baba, “Structural scaling and functional design of the cercal wind-receptor hairs of cricket”, *Journal of Comparative Physiology*, A183, pp. 171-186, 1998.

[2] (a) J. Casas, T. Steinmann and G. Krijnen, “Why do insects have such a high density of flow-sensing hairs? Insights from the hydromechanics of biomimetic MEMS sensors”, *Journal of the Royal Society Interface*, 7, pp. 1487-1495, 2010. (b) G.J.M. Krijnen, T.S.J. Lammerink, R.J. Wiegerink, and J. Casas, “Cricket inspired flow-sensor arrays” *In: IEEE Sensors*, USA., pp. 539-546, 2007.

[3] M. Dijkstra, J.J. Van Baar, R.J. Wiegerink, T.S.J. Lammerink, J.H. De Boer and G.J.M. Krijnen, ”Artificial sensory hairs based on the flow sensitive receptors hairs of crickets”, *Journal of Microelectronics and Microengineering*, 15, pp. S132-138, 2005.

[4] C.M. Bruinink et.al., ”Advancement in technology and design of biomimetic flow-sensor arrays”, *In Proceedings of the IEEE MEMS*, Italy, pp. 152-155, 2009.

[5] A.M.K. Dagamseh, C.M. Bruinink, R.J. Wiegerink, T.S.J. Lammerink, H. Droogendijk and G.J.M. Krijnen, “Developments in biomimetic hair flow-sensor towards high resolution sensitive arrays”, in progress.

[6] J-MP Franosch, A.B. Sichert, M.D. Suttner and J.L. Van Hemmen, ”Estimating position and velocity of a submerged moving object by the clawed frog Xenopus and by fish—A cybernetic approach”, *Biological Cybernetics* ; 93, pp. 231-238, 2005.

[7] A.M.K. Dagamseh, T.S.J. Lammerink, M. Kolster, C.M. Bruinink, R.J. Wiegerink and G.J.M. Krijnen, ”Dipole-source localization using biomimetic flow-sensor arrays positioned as lateral-line system”, *Sensors and actuators: A*, 162, pp. 355-360, 2010.

[8] H. Lamb, Hydrodynamics, 6th edn. Cambridge University Press, Cambridge, (1932).

ANISOTROPIC CONDUCTIVE FILM FOR FLIP-CHIP INTERCONNECTION OF A HIGH I/O SILICON BASED FINGER PRINT SENSOR

A. Larsson[1], F. Oldervoll[1], T. A. T. Seip[1], H.-V. Nguyen[2], H. Kristiansen[3], Ø. Sløgedal[4]

[1]*SINTEF ICT, Forskningsveien 1, N-0314 Oslo, Norway*
[2]*HiVe – Vestfold University College, Raveien 197, N-3184 Borre, Norway*
[3]*Conpart AS, Dragonveien 54, N-2013 Skjetten, Norway*
[4]*IDEX ASA, Rolfsbuktveien 17, N-1346 Fornebu, Norway*

***Abstract* — Anisotropic conductive film (ACF) has been used for flip chip interconnection of a silicon based MEMS finger print sensor to a signal processing ASIC. The assembled sensor device was subjected to a short term high temperature profile with peak temperature 260 °C simulating subsequent reflow soldering of the device, and to thermal shock cycling from -40 to +85 °C. The reliability of interconnects during ageing was investigated by monitoring changes in electrical resistance of single interconnects and interconnect daisy chains. The electrical resistance increased after exposure to the high temperature soldering profile, but no failures were observed even after 10 repetitions. Thermal shock cycling showed an increase in electrical resistance and no failures. A relatively large resistance increase was found for some interconnection points.**

***Keywords:* Anisotropic conductive adhesive, flip-chip, fine-pitch, reliability**

I - Introduction

Anisotropic conductive film (ACF) has during the last decade emerged as an alternative to soldering for interconnection of devices to various substrates such as glass, PCB and flex. ACF offers advantages like fine pitch capability and improved mechanical and thermal properties [1]-[3]. Solder interconnects struggles with pitches below 200 µm whereas ACF has been demonstrated down to 70 µm for display applications [4].

ACF consist of an adhesive film matrix filled with mono-disperse conductive particles. The particles can be solid metal spheres or metal coated polymer spheres (MPS). Electrical connections is achieved when the spheres are trapped between interconnect bumps on substrate and device, see Figure 1.

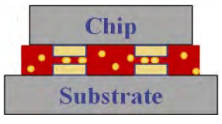

Figure 1. *ACF interconnection of chip to substrate.*

This paper reports the use of ACF for flip-chip interconnection of a silicon based MEMS finger print sensor to a signal processing silicon ASIC. The device has more than 250 I/O's, and fine pitch is required to minimize the size of the assembled device and reduce the device cost. The device is intended for handheld devices and must withstand rough environments including large temperature variations, mechanical shock and humidity exposure. The assembled device will be soldered to a PCB, see Figure 2, and thus it is important that the ACF interconnection is compatible with subsequent reflow soldering. In the present work assembled sensor devices have been subjected to short term high temperature exposure simulating subsequent reflow soldering. Devices have also been subjected to thermal shock cycling from -40 to +85 °C. The device reliability during ageing has been investigated by monitoring changes in electrical resistance and by cross-sectioning and microscopy analysis of the interconnections.

Figure 2. *The assembled finger print sensor from IDEX ASA, ASIC on top. The larger solder balls are for subsequent interconnection to PCB. Outer dimensions: ASIC (5.5 x 3.1 mm), sensor (10.1 x 4.4 mm)*

II - Experimental Details

Sample description

Silicon test dies with similar outer dimensions and pad distribution as the actual fingerprint sensor and ASIC were designed for interconnect testing. The dies were populated with 80 µm diameter electroless Ni/Au bumps with a 200 µm pitch. Two different types of test samples were produced. The two types were identical except in the number of interconnection bumps on the MEMS and ASIC chips. The *reduced* and the *identical* versions had 73 and 286 bumps respectively. The reduced version had two daisy chains along its long side borders (named D1 and D2) and the identical had two additional chains extending to the central parts under the ASIC (D3 and D4). Both versions had six structures for 4-point resistance measurements distributed at each corner and on the two short sides (referred to 41 to 46).

Assembly process

The ACF used in this study was a 20 µm thick single layer ACF. The conductive particles in the ACF are Ø5 µm Ni/Au coated polymer spheres fabricated by Conpart. The assembly process involves two main steps: pre-bonding and final bonding. Bond parameters including bond temperature, time and pressure were selected based on a previous study of Nguyen *et al.* [5].

A MAT-6400 flip-chip bonder at HiVe was used to assemble the reduced version of MEMS sensor to ASIC

substrate. For the identical version, a relatively larger bond force is required due to significantly higher number of interconnects, compared to the reduced version. The force limit of the MAT-6400 flip-chip bonder is 4 kg, which is not sufficient for the assembly of the identical version. Therefore, the bonding process of the identical version was conducted using Toray FC1000 flip-chip bonder at Tampere University of Technology, which can provide a bond force corresponding to more than 20 kg. The assembly processes of the reduced version and the identical version of the sensor were slightly different due to the differences in the availability of the equipments. Table 1 summarizes the assembly processes of the MEMS sensor to ASIC device. A photo of an assembled sample is shown in Figure 3.

Figure 3. MEMS finger print sensor dummy assembled onto a dummy ASIC.

Reflow compatibility test

To simulate the compatibility of the MPS filled ACF technology with industrial reflow processes, a total of 19 samples were subjected to a typical reflow process. A Madell Technology AE-RF330-R reflow oven were used for the reflow tests. The profile used were 160 °C – 220 °C – 260 °C and the speed set to 500. The oven does not have heating from below the belt.

Reduced – Two sets of reduced samples were tested. Six samples were subject to a single reflow process. Three samples were exposed to two sequential runs through the reflow oven. Two of the three samples were placed on a carrier where holes were made to expose them to more direct cooling. This was done since some devices may be stacked onto a PCB with a hole in it to make room for the device, exposing them directly to the environment on the other side of the PCB. The last sample was kept as a reference.

Identical – Ten samples were subjected to ten sequential runs through the reflow oven to investigate the degradation properties when exposed to longer times at high temperatures, above T_g ($T_g \approx 140$ °C of the film epoxy). This corresponds to an exposure of more than 30 min at 100 °C or more and more than 13min above 200 °C.

Thermal shock cycling

Identical – Ten samples were prepared for thermal shock cycling (TSC). A Heraus HT 7012 S2 was used to expose the test samples to TSC. The test profile was calibrated to cycle between -40 °C and +85 °C with a dwell time of 5 min, see Figure 4. Since the test chamber consist of a two chamber solution with a lift system enabling a fast transition from hot to cold and back, it was possible to generate a tough ramp rate during testing. The fast temperature transition for the samples puts them under large local thermal gradients, or thermal shock. I.e. the thermo-mechanical stress is high within the components compared to when exposed to more regular thermal cycling (TC) with slower transitions. TSC is believed to age the test samples faster than with TC.

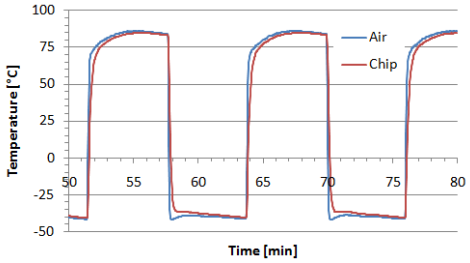

Figure 4. *Thermal shock cycling profile. A temperature change of 90% of the maximum* $\Delta T = |T_{max} - T_{min}|$ *was reached in less than one minute.*

Electrical resistance measurement

The electrical resistance of the single interconnects was measured with a Keithley 3706 system switch/multimeter using a custom-made Wentworth Laboratories 4-point probe card and LabVIEW 8.2. In a 4-point measurement separate pairs of current-carrying and voltage-sensing electrodes are used. This voltage and current separation minimizes the resistance contribution of the wiring and contact resistances, giving very accurate local measurements.

Table 1: Assembly process of reduced and identical versions of the MEMS finger print sensor to ASIC device

Bond steps	Reduced version	Identical version
Pre-bonding	▪ ACF is laminated on MEMS chip. ▪ Bond pressure: 1.5 MPa (Estimated force per area of ACF) ▪ Bond temperature: 80 °C ▪ Bond time: 5 s	▪ ACF is laminated on ASIC substrate. ▪ Bond pressure: 1.5 MPa (Estimated force per area of ACF) ▪ Bond temperature: 80 °C ▪ Bond time: 11 s
Final bonding	▪ Bond pressure: 90-110 MPa (force per area of bump) ▪ Bond temperature: 180 °C (Heat comes only from bottom stage where ASIC substrate is placed.) ▪ Bond time: 30 s	▪ Bond pressure: 100 MPa (force per area of bump) ▪ Bond temperature: 180 °C (Heat comes from both pick-up tool on top via MEMS chip and bottom stage via ASIC substrate) ▪ Bond time: 30 s ▪ Cooling time after 30 s of bond time: 10 s with external cooling air while keeping bond force

Visual inspection

To inspect the quality of bond and interconnect, cross-sections were performed on both the reduced and the identical samples. Each cross-section was prepared with polishing. The finest polishing step was with ¼-µm sized particles.

General remarks

A total number of 144 plus 318 (reduced and identical samples resp.) individual interconnect resistance measurements distributed on six different locations around the periphery of 29 samples were performed. Corresponding daisy chain measurements were performed in addition.

III - Results and Discussion

Assembly process

Reduced – The assembled samples showed a non-uniform interconnect resistance at different locations around the periphery of the chips. The typical average interconnect resistance ranged from 40 to 225 mΩ, depending on location, c.f. Figure 5. This was found to be a result of a co-planarity issue between the ASIC and the MEMS sensor during assembly. The minimum individual interconnect resistance measured was 16.5 mΩ. Figure 6 show a cross-section of a reduced sample showing MPS deformed into their desired shape. MPS compressed to stand off height of about ⅔ to ½ of its uncompressed diameter is expected to be a feasible compromise between contact resistance and flexibility.

Identical – The identical samples showed similar co-planarity issues as the reduced samples did. The measured resistance typically ranged from 7.5 to 82.5 mΩ, with an individual minimum measurement of 3.6 mΩ. The cross-section, cf. Figure 7, show that the MPS were highly deformed beyond their optimum shape. Some MPS were observed to have collapsed and fractured, exposing the internal polymer core. This could explain the difference in measured interconnection resistance between the reduced and the identical samples. I.e. a more compressed interconnect produce more deformed MPS, hence creating a larger contact area between MPS and bump surfaces. It also shortens the distance between the bumps, both reducing the resistance. The main drawback is fractured MPS which increase the resistance. Nguyen *et al.* [5] showed that highly deformed MPS also may give random and unpredictable results. A highly deformed MPS is also believed to be less reliable than an optimally deformed one, since its flexible properties are inhibited.

Reflow compatibility

Reduced – The six samples run through the single reflow process showed a decreased interconnect resistance after the exposure, see Figure 8. This is believed to be a result of additional curing of the epoxy in the ACF when exposed to the high temperature. That would lead to additional shrinkage of the ACF, hence increasing the contact pressure i.e. reducing the contact resistance between the MPS and the interconnection pads.

The three samples exposed to two reflow processes also showed similar improvement in the resistance measurements, cf. Figure 9. No apparent difference in the interconnect or daisy chain resistance was found for the two samples mounted above holes in the carrier when compared to the one that was not exposed to the additional cooling. The variation was found to be noticeable typically stretching up to around 30% deviation from the average measurement. The divergence decreased some after exposure to the reflow process. This is again believed to be due to curing of the epoxy.

Identical – The interconnect resistance significantly increased after ten reflow processes, cf. Figure 10. Figure 11 show that also the daisy chains showed a resistance increase after the test. Note that the resistance increase, or interconnect degradation, is much clearer for the interconnect measurements than for the daisy chain ones. Thus, indicating the importance of actually measure the degradation properties at interconnect itself instead of using daisy chains. It shall be noted that the divergence is higher for the identical samples than for the reduced. This is believed to be due to the highly compressed MPS, as described in the *Assembly* section.

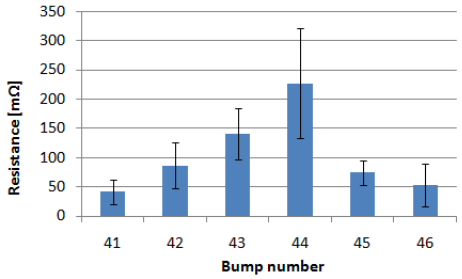

Figure 5. The average interconnect resistances for each interconnect location (all nine reduced samples).

Figure 6. Cross-section of a reduced sample showing the shape of compressed MPS in-between two pads.

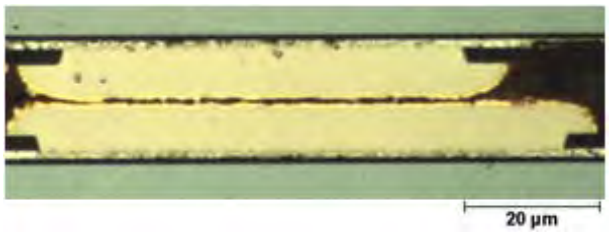

Figure 7. Cross-section of an identical sample showing highly deformed MPS in-between two pads.

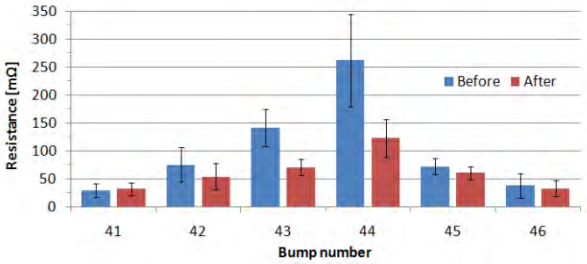

Figure 8. *Average interconnect resistance before and after exposure to a single reflow process for six reduced samples.*

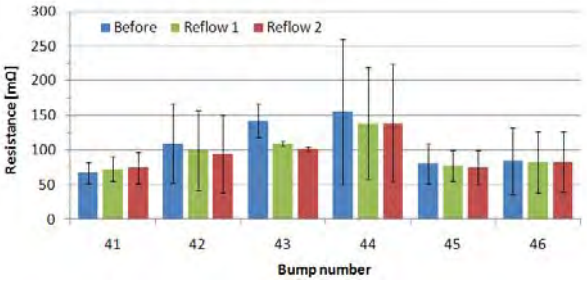

Figure 9. *Average interconnect resistance before and after exposure to two reflow processes for three reduced samples.*

Thermal shock cycling (TSC)

Identical – The results from the TSC tests shows, a trend with increasing electrical resistance as the samples were exposed more cycles, see Figure 12. It also shows an increase in the divergence. Interconnect 42 was excluded from the results due to a malfunctioning probe card, i.e. non reliable measurements. Two data points were excluded from the statistics for point 46 due to an unexpectedly large increase in resistance for the 1000 cycle measurements. These are believed originate from the randomly behavior described in the *Assembly process* results section.

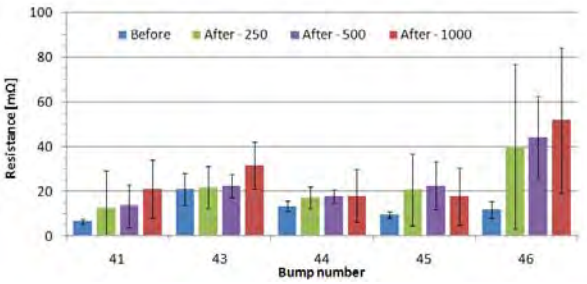

Figure 12. *Average interconnect resistance before and after exposure to 250, 500 and 1000 TSC for ten identical samples.*

IV - Conclusion

The electrical resistance measurements show resistances ranging from a few to hundreds of mΩ, depending on the quality of the assembly process. An industrial and optimized process is expected to give resistances in range of tens of mΩ. This is well within the feasible range (up to 250mΩ) of the intended use in the fingerprint sensor described in the introduction.

Considering the number of measurements, it's remarkable how consistent and reliable the MPS filled

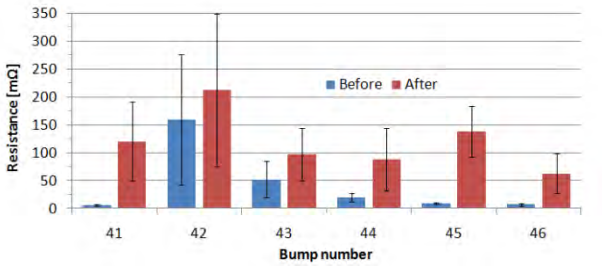

Figure 10. *Average interconnect resistance before and after exposure to ten reflow processes for ten identical samples.*

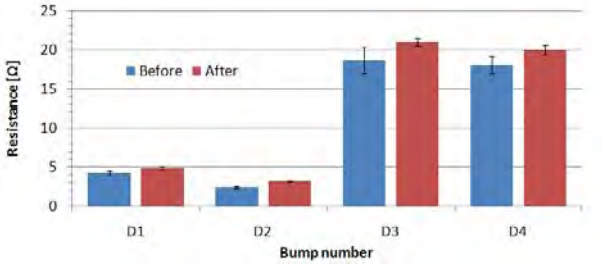

Figure 11. *Average daisy chain resistance before and after exposure to ten reflow processes for ten identical samples.*

ACF are when exposed to thermal stress, even when the MPS was a bit too deformed for the identical samples.

Future and ongoing work to be published includes thermal ageing and humidity/thermal ageing and MPS shape response tests.

Acknowledgement

The present study was performed in the ReMi project funded by the Research Council of Norway through BIA project number: 187971. The authors would like to acknowledge Knut Aasmundtveit at HiVe-Vestfold University College and Laura Frisk at Tampere University of Technology for their contribution to the work.

References

[1] M. J. Yim and K. W. Paik, "Recent advances on anisotropic conductive adhesives (ACAs) for flat panel displays and semiconductor packaging applications", *International Journal of Adhesion and Adhesives*, vol. 26, pp. 304 – 313, 2006.

[2] Y. C. Lin and J. Zhong, "A review of the influencing factors on anisotropic conductive adhesives joining technology in electrical applications", *Journal of Material Science*, vol. 43, pp. 3072 – 3093, 2008

[3] S. Lu and W. Chen, "Reliability and Flexibility of Ultra-Thin Chip-on-Flex (UTCOF) Interconnects With Anisotropic Conductive Adhesive (ACA) Joints, *IEEE Transactions on Advanced Packaging*, Vol. 33, No. 3, pp. 702 – 712, 2010

[4] M. J. Yim, J. Hwang, K. W. Paik, "Anisotropic conductive films (ACFs) for ultra-fine pitch Chip-On-Glass (COG) applications, *International Journal of Adhesion and Adhesives*, Vol. 27, pp. 77 – 84, 2007

[5] H.-V. Nguyen, *et al.*, "Effect of Pitch Factor on Reliability of Interconnects Using Anisotropic Conductive Films: An Initial Study," in *The IMAPS Nordic Annual Conference 2009*, Tønsberg, Norway, 2009, pp. 63-68.

DESIGN, SIMULATION AND FABRICATION OF OPTICAL FILTERS FOR NARROW BAND IMAGING IN ENDOSCOPIC CAPSULES

M. F. Silva, D. S. Ferreira, J. F. Ribeiro, L. M. Goncalves,
J. P. Carmo, C. A. Silva, G. Minas, J. H. Correia

University of Minho, Dept. Industrial Electronics, Campus Azurem, 4800-058 Guimaraes, Portugal

***Abstract* — This paper presents the design, simulation and fabrication of two optical filters that could be integrated in endoscopic capsules (EC) to perform narrow band imaging (NBI) analysis. The thin-film optical filters were designed for two specific spectral regions (blue, centered at 415 nm, and green, centered at 540 nm) and will be placed on top of current EC white light emitting diodes (LEDs). The filters are composed by 7 thin-film layers of titanium dioxide (TiO_2) and silicon dioxide (SiO_2) and will be deposited using RF-sputtering technique. The integration of NBI functions in EC represents an important clinical and technological advance, since it will improve the EC diagnostic functions, e.g. enhanced visibility of capillaries and veins for the diagnosis of dysplasia, as a complement to the current capsule vision based in white light.**

***Keywords :* Optical filters, Endoscopic capsule, Narrow band imaging.**

I - Introduction

The developments in endoscopic capsules (EC) have been grown in the past years since these devices are able to perform diagnosis in a less invasive way, when compared with traditional exams, such as gastroscopy and colonoscopy. Also, using EC it is possible to access new areas of the gastrointestinal (GI) tract that were previously accessed only by surgery, such as some parts of the small intestine. Unlike conventional endoscopy, no drugs are administered to the patient and air insufflation is not necessary. Cessation of anticoagulant therapy is unnecessary, in contrast to conventional endoscopy during which scope trauma, perforation of the bowel or biopsies can cause excessive bleeding that might require surgery. Moreover, it doesn't require the continuous presence of a physician, and it is disposable, which minimizes the risk of infection [1-3]. However, its diagnosis depends mainly on white-light images taken during its travel through the GI tract, and even in a high-resolution image, some lesions are still missed.

Nowadays, the diagnostic capability of standard endoscopy is improved by using narrow band imaging (NBI). This technique uses spectral characteristics of endoscopic light to enhance the mucosa, including vascular structures, in greater details without dyes [4]. The use of NBI has been proven to enhance the diagnosis of: inflammatory disorders of the GI mucosa [4]; dysplasia in patients with Barrett's esophagus and ulcerative colitis [5-6]; colorectal cancer [7]; polyps [8]; among others. In these studies, NBI was integrated in conventional endoscopes using band-pass filters that narrow white-light to wavelengths around 415 nm (blue region of the spectrum) and 540 nm (green spectral region).

This paper proposes the development of a NBI system to be incorporated in an EC. Such a system would have a huge clinical utility, since it would take not only advantage of all the benefits associated with the use of an EC, but also it would add important diagnostic functions to current capsule white-light imaging functions.

In Figure 1 it is presented the EC with the NBI system. This is based on thin-film optical filters that will be placed on top of 2 of the 4 capsule white LEDs (light-emitting diodes) to select the two specific spectral bands: blue and green. The blue light penetrates the mucosa only superficiality and is mainly absorbed by hemoglobin, enhancing surface and capillary details. The green light penetrates more deeply in the tissue, displaying sub-epithelial vessels. When the two images are combined, an extremely high contrast image of the tissue surface is shown. This way, combining the capsule endoscopy and the NBI technique a more accurate diagnostic can be obtained.

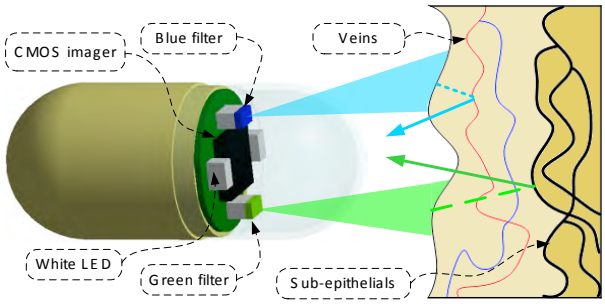

Figure 1: *EC with an integrated NBI system.*

II – Optical filters design

Thin-film optical filters are designed for the selection of two particular spectral bands that will be used for tissue illumination: one band centered at 415 nm (blue filter) and another band centered at 540 nm (green filter). This light filtering system is based on Fabry-Perot thin-film resonators, which consist of two parallel mirrors separated by a resonance cavity (Figure 2). The thickness of the resonance cavity, or the distance between the mirrors, determines the specific central wavelength that is transmitted, i.e., each filter can be easily tuned to a different central wavelength by adjusting only the thickness of one layer.

The filter structure is a multilayer composed by 7 layers: the top 3 layers correspond to the first mirror, whereas the bottom 3 layers correspond to the second mirror (see Figure 2). The mirrors are composed by dielectric materials with high and low-refractive indexes (titanium dioxide, TiO_2, and silicon dioxide, SiO_2, respectively) which provide good optical performance characteristics (high reflectivity and low absorption losses) [9-10]. These optical filters should be designed to yield a band-pass around the specific central wavelength, with FWHM (Full-Width-Half-Maximum) less than 25 nm.

The mirrors thicknesses are the same for both filters: 38 nm for the TiO_2 layers and 82 nm for the SiO_2 layers. This procedure enables the simultaneously fabrication of both filters, minimizing the global deposition time. The resonance cavity thickness is equal to 122 and 208 nm for the blue and green filter, respectively.

The use of these filters takes advantage of the currently available capsule white LEDs thus avoiding the integration of new light-sources on the EC.

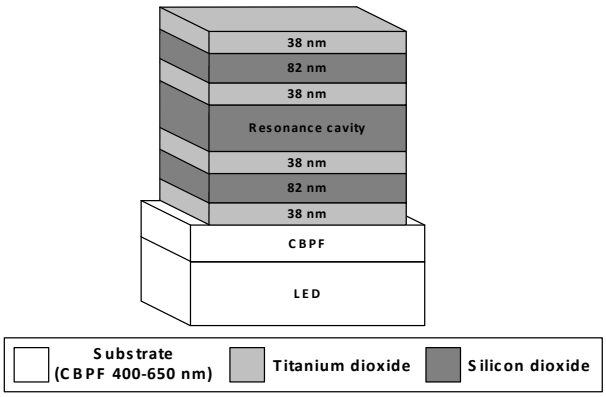

Figure 2: *Structure of the Fabry-perot optical filter on the commercial optical band-pass filter (CBPF).*

II – Simulation results

The structure of both filters was optimized and simulated using the optics software TFCalc™ 3.5.

In Figure 3 and Figure 4 it is presented the simulated transmittance for the two designed Fabry-Perot optical filters, together with the spectral transmittance of a commercial band-pass filter (CBPF) [11] on top of which the filters are deposited. In Figure 3 and Figure 4 it is shown that each filter is sensitive to its specific spectral band, with FWHM < 25 nm, and a ratio of maximum transmittance to background noise greater than 90/20 (enough for this application in terms of optical characteristics).

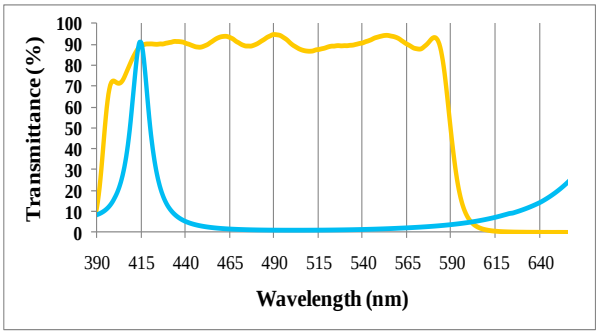

Figure 3: *Simulated spectral transmittance of the blue Fabry-Perot optical filters, together with the spectral transmittance of a CBPF between 400-650 nm.*

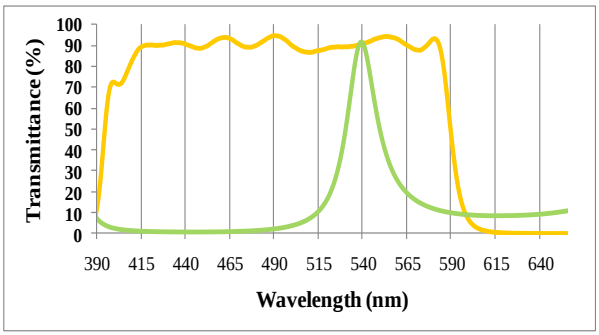

Figure 4: *Simulated spectral transmittance of the green Fabry-Perot optical filters, together with the spectral transmittance of a CBPF between 400-650 nm.*

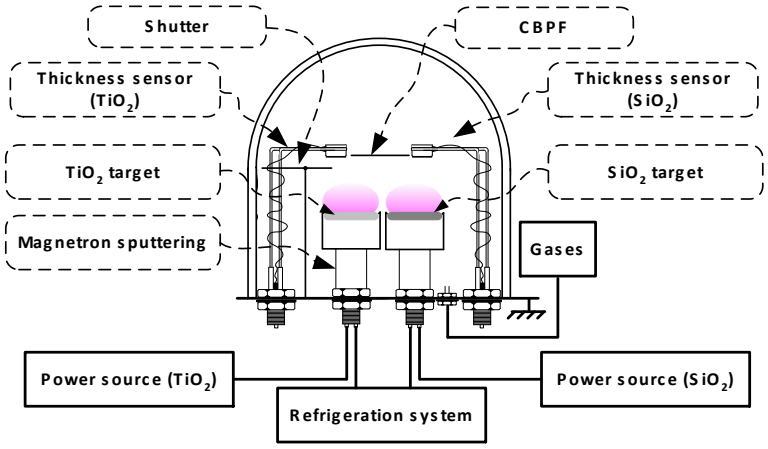

Figure 5*: Deposition scheme for the fabrication of the two optical filters using a twin RF-sputtering system.*

III – Optical filters fabrication

The deposition scheme to fabricate the optical filters is shown in Figure 5. Each layer of TiO_2 and SiO_2 is deposited by using a twin RF-sputtering system. With this deposition scheme the seven layers of the optical filters are deposited in the same vacuum process, which provides a better adhesion between the different thin-film layers, and obviates the oxidation of the thin-films. Moreover, the fabrication process is maskless.

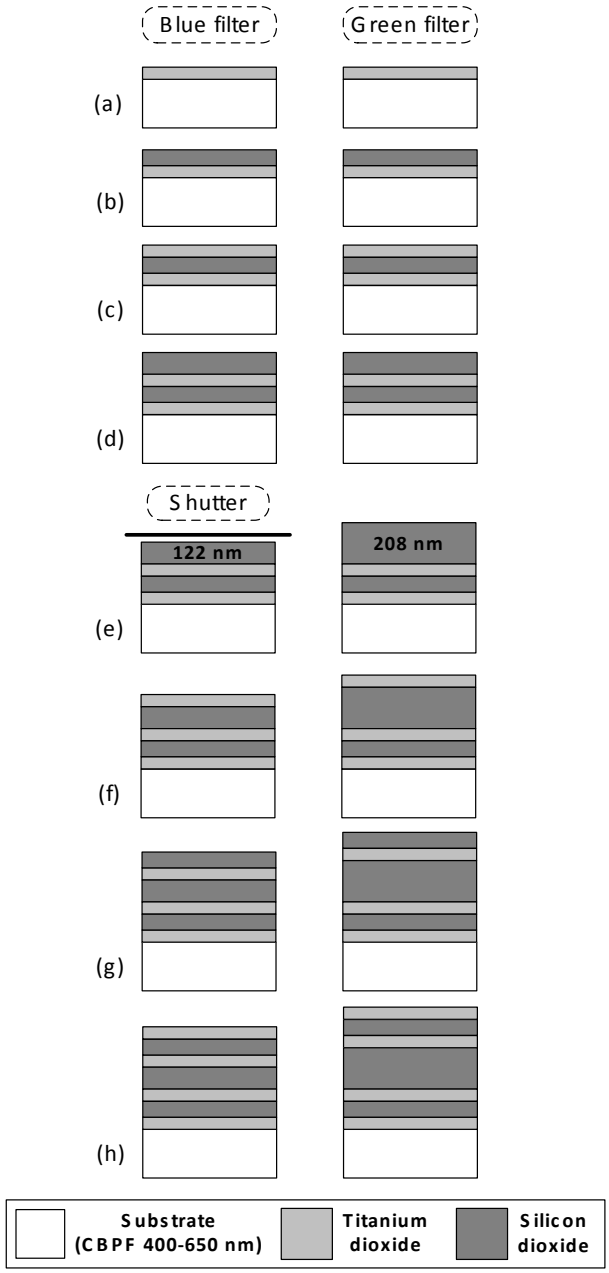

Figure 6: *Fabrication steps of the optical filters.*

As a substrate for the optical filters deposition, it will be used a CBPF, with a band between 400 nm and 650 nm, in order to avoid the transmission of wavelengths far outside the visible range. The fabrication steps for both filters are shown in Figure 6.

In Figure 6(a) a thin-film of TiO_2 is first deposited with the thickness of 38 nm. In step (b) it is deposited the SiO_2 thin-film, with the thickness equal to 82 nm. The second layer of 38 nm thick TiO_2 is deposited in step (c).

In step (d) the middle layer is deposited, to form the resonance cavity, until a thickness of 122 nm. As previously demonstrated, the blue filter requires a resonance cavity thickness of 122 nm while the green filter requires a thickness of 208 nm. In step (e) a shutter is activated to stop the deposition of the resonance cavity layer for the blue filter, while the resonance cavity layer of the green filter is continuously deposited until it reaches 208 nm. The steps (a), (b) and (c) are repeated on steps (f), (g) and (h). The total thickness of the blue filter is 438 nm and the green filter is 524 nm.

IV – Conclusions

In this work it is described the integration of NBI function in ECs. For the NBI system, two different thin-film optical filters are designed. Its fabrication process is also described using a twin RF-sputtering technique with 2 magnetrons. The targeted fabrication process enables a good adhesion of the thin-film layers and avoids the oxidation between the different layers. The NBI function in EC will improve the diagnosis capability of current available ECs. NBI uses two discrete bands of light: one blue at 415 nm and one green at 540 nm. Narrow band blue light displays superficial capillary network, while green light displays sub-epithelial vessels and when combined offer an extremely high-contrast image of the tissue surface.

Acknowledgements

This work was supported by ADI with the reference NFCE-FCOMP-01-0202-FEDER-005358.

Debora Ferreira was supported by the Portuguese Foundation for Science and Technology under the MIT|Portugal Program (SFRH/BD/38978/ 2007).

References

[1] G. Iddan, G. Meron, A. Glukhovshy, "Wireless capsule endoscopy", *Nature*, Vol. 405, pp. 417, 2000.

[2] W. Qureshi, "Current and future applications of the capsule camera", *Nature Rev. Drug Disc.*, Vol. 3, pp. 447-480, 2004.

[3] D. Fleischer, "Capsule Imaging", *Clinical Gastroenterology and Hepatology*, Vol. 3, pp. S30-S32, 2005.

[4] K. Kuznetsov, R. Lambert, J. F. Rey, "Narrow-band imaging: potential and limitations", *Endoscopy*, Vol. 38, pp. 76-81, 2006.

[5] H. C. Wolfsen, *et al.*, "Prospective, controlled tandem endoscopy study of narrow band imaging for dysplasia detection in Barrett's esophagus", *Imaging and Advanced Technology*, Vol. 135, pp. 24-31, 2008.

[6] T. Matsumodo, *et al.*, "Magnifying colonoscopy with narrow band imaging system for the diagnosis of dysplasia in ulcerative colitis: a pilot study", *Gastrointestinal Endoscopy*, Vol. 66, pp. 957-965.

[7] J. E. East, *et al.*, "Narrow band imaging for colonoscopic surveillance in hereditary non-polyposis colorectal cancer", *GUT*, Vol. 57, pp. 65-70, 2007.

[8] A. Rastogi, et al., "Narrow-band imaging colonoscopy-a pilot feasibility study for the detection of polyps and correction of surface patterns with polyp histologic diagnosis", *Gastrointestinal Endoscopy*, Vol. 67, pp. 280-286, 2008.

[9] G. Minas, R. F. Wolffenbuttel, J. H. Correia, "A lab-on-a-chip for spectrophotometric analysis of biological fluids," *Lab Chip*, Vol. 5, pp. 1303-1309, 2005.

[10] G. Minas, R. F. Wolffenbuttel, J. H. Correia, "An array of highly selective Fabry–Perot optical channels for biological fluid analysis by optical absorption using a white light source for illumination," *Journal of Optics A: Pure and Applied Optics*, Vol. 8, pp. 272-278, 2006.

[11] SCHOTT AG. Available online at: http://www.schott.com.

THIN-FILM SOLID-STATE RECHARGEABLE LITHIUM BATTERY

J. F. Ribeiro[1], M. F. Silva[1], L. M. Goncalves[1], J.P. Carmo[1], J. H. Correia[1],
M. M. Silva[2], F. Cerqueira[3], P. Alpuim[3], J.-E. Bourée[4]

[1]*University of Minho, Algoritmi Centre, Guimarães, Portugal*
[2]*University of Minho, Chemistry Centre, Braga, Portugal*
[3]*University of Minho, Physics Centre, Braga, Portugal*
[4]*Lab. de Physique des Interfaces et des Couches Minces, CNRS UMR 7647, E. Polytechnique, France*

***Abstract* — This paper describes the optimization and the materials technology required for fabricating thin-film solid-state rechargeable lithium batteries. The following materials were selected, deposited and optimized: a glassy lithium-phosphorus oxynitride electrolyte (LiPON) between a lithium (Li) anode and crystalline lithium-cobalt dioxide cathode ($LiCoO_2$), deposited by RF-sputtering. Ti/Pt layers, deposited by evaporation (using the e-beam technique) were used in contacts and a silicon nitride thin film (Si_3N_4), deposited by Hot-wire CVD protects the battery. This technology allows batteries with a potential of 4.5 V, typical capacities of 50 µA.cm^{-2} and charge discharge rates up to 4C.**

***Keywords :* Solid-state, thin-film battery, materials technology, lithium, energy-harvesting, microsystems**

I – Introduction

It's undeniable the fact that batteries are systems with the highest number of applications known up to know. Since the invention of the first pile by Volta on 1800, batteries are used in applications that range from vehicles to the most modern cell phones, toys/gadgets and biomedical devices. Despite the developments made by the microelectronic industry, the battery technology didn't accompany these breakthroughs [1]. The increased demand of stand-alone microsystems in critical energy applications, such as radio-frequency identification tags, integrated circuit smart cards [2], data acquiring systems on extreme industrial harsh environments, oil drilled sinks and wireless sensor networks, led to the investigation and development of solid-state rechargeable batteries [3]. In energy harvesting systems, thin-film batteries of solid-state materials are suitable power sources to fill the time gaps, when the external power source is not available, thus assuring that microsystems are still powered and active. This is of special concern when the target applications are in the biomedical field or for long cycle operations without requiring human activity [4, 5].

Two forms of film batteries have been developed so far: the polymer based lithium batteries and the film lithium batteries. The polymer batteries (that are already common in the market) have high capacity and stability but low charge/discharge rates, mainly due to temperature limits. Solid-state film batteries show faster charge rates and very high cycle life, compared with classical liquid electrolyte batteries, withstanding several thousands of cycles with no pronounced fading. The integration of batteries with solid-state circuits requires the use of solid-state anode, cathode and electrolyte. These batteries are intrinsically safe since all materials are solid and no leaking or explosion could occur. Moreover, this technology allows the fabrication of batteries that are not damaged during the soldering process of microchips. Film battery chemistry is being developed at ORNL (Oak Ridge National Laboratories) [4] with a solid electrolyte between the anode and cathode. These batteries have a potential of 4.5 V, typical capacities below 100 µAcm^{-2} and charge times of 2C to 5C. As illustrated in Figure 1, the film batteries present the highest volumetric energy density (800 Whl^{-1}) and gravimetric energy density (350 Whg^{-1}) and charge-discharge rates up to 5C (only exceeded by super-capacitors) [6, 7]. However, due to the process of deposition of thin-films, the thickness is limited to few micrometers, resulting in a small capacity. The market of film batteries is in the trial stage and it's predictable to reach 10 billion units by 2012.

This paper presents the fabrication process and characterization details of all materials used in a thin-film lithium rechargeable battery for integration with stand-alone microsystems.

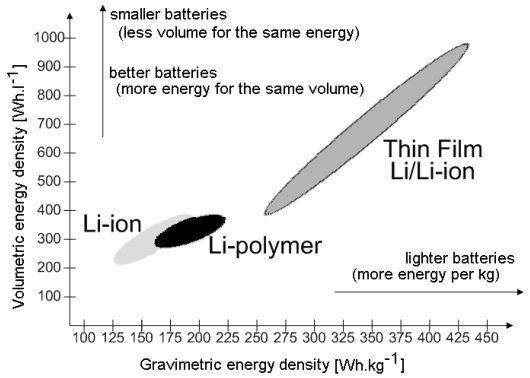

Fig 1: *Size and capacity with different battery technologies.*

II – Materials Selection

The integration of batteries with solid-state circuits requires the use of solid-state anode, cathode and electrolyte. The Figure 2 shows an artwork of a film battery fabricated by successive layers deposition on top of a silicon compatible substrate (among the glass, the [100] undoped double-side polished silicon wafer was used for thin-films depositions). The first layer are the battery contacts, and platinum was chosen for allowing a good distribution of electrons trough the cathode surface without reacting with it. The cathode is a lithium cobalt dioxide ($LiCoO_2$) thin-film; the electrolyte is a glassy lithium-phosphorus oxynitride electrolyte (LiPON) thin-film and anode is a lithium (Li) thin-film. The

protection layer is a silicon nitride (Si_3N_4) thin-film [8]. This protective layer avoids the reaction of lithium with air.

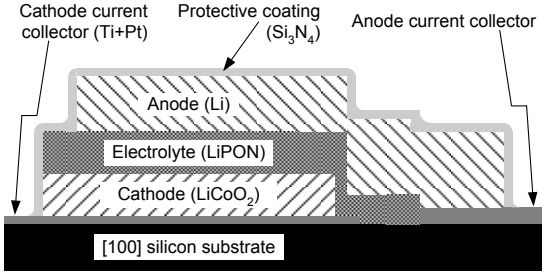

Fig 2: *Artwork of a thin-film battery.*

The operation of lithium batteries is based on reversible insertion and removal of lithium ions to and from their positive and negative electrodes [9]. Metals that are compounds of lithium (Li) and presents a layered structure, especially the ones containing 3D transition metals such as nickel (Ni), manganese (Mn), vanadium (V) and cobalt (Co). The lithium oxides containing these materials are excellent candidates as active compounds for use as high capacity cathode materials due to their high energy density, a long life cycle, a very good safety, constant discharging properties and a wide range of operation temperatures [10], without compromising the structural stability [11]. Compared with other materials such as the $LiMn_2O_4$ and $LiNiO_2$, the $LiCoO_2$ is easy to fabricate and has a relatively high charge storage capacity (140 $mAhg^{-1}$).

Thin-film solid electrolytes are required to have high ionic conductivity, a negligible electronic conductivity and be stable in contact with the anode and cathode electrodes [7] that will allow for a high current capacity and low self-discharge current, respectively. As suggested by Hamon et al [12], the LiPON films with an amorphous structure are the most suitable candidates for obtaining films with high ionic conductivity when compared with crystalline structures. LiPON films present an exceptional electrochemical stability, an electronic resistivity greater than 10^{12} Ωm and ionic conductivity in of 10^{-6} Scm^{-1} range. Films of LiPON can obtained by RF sputtering of a lithium phosphate (Li_3PO_4) target in an argon (Ar)/nitrogen (N_2) plasma. Behind electronic properties, LiPON have low stress (typically, less than 100 MPa) and a good stability in air atmosphere [13].

The transition metal oxides were used as anode materials in previous works [14, 15], as it is the case of the tin dioxide (SnO_2). However, this compound presents a serious problem related with an irreversible reaction during the first battery charge, resulting in small clusters of tin metal (Sn) with lithium oxide (Li_2O). An anode material with higher degree of reversibility results in a battery with higher specific capacity. For this reason, the lithium (Li) metal was selected for the anode material, but also because it exhibits the highest capacity and discharge rate despite the fast oxidation in contact with the air. A way to overcome the last drawback is covering the battery with a protective layer of silicon nitride (Si_3N_4)**.** Multilayers of SiNx thin films are used to achieve higher protection against moisture and avoid reaction with air. Each layer has a low-frequency Ar-plasma treatment for surface compaction.

II - Fabrication Details

On top a silicon wafer where a thin layer of dioxide was grown by thermal oxidation, the current collector (contact) of platinum (100 nm) was deposited by e−beam. A titanium (Ti) layer with a thickness of 30 nm was previously deposited to improve the adhesion of the platinum to the substrate.

The 1 µm thick $LiCoO_2$ cathode was deposited by RF magnetron sputtering technique using a RF power source 13.56 MHz at 150 W, a pressure of 0.2 Pa in a 30 sccm flow of argon (Ar) and 10 sccm flow of oxygen (O_2). A deposition rate from 3.5 $Ås^{-1}$ to 4.5 $Ås^{-1}$ was obtained. This process is still the most effective way to provide the required crystalline structure of $LiCoO_2$ films. The best annealing temperature was found experimentally using a different temperatures (from 500 ºC to 800 ºC), during 30 minute, in vacuum.

The electrolyte (LiPON) was deposited by RF magnetron sputtering technique with 1 µm thickness. A Li_3PO_4 target was used in a 20 sccm reactive Ar/N_2 plasma. The depositions were done with controlled: the pressure inside the deposition chamber (from 0.03 Pa to 1 Pa) and controlled power in the RF source (13.56 MHz) of the sputtering system (150W to 200W), with a deposition rate from 0.4 $Ås^{-1}$ to 2.5 $Ås^{-1}$.

The lithium anode was deposited by thermal evaporation, in a large molybdenium boat (3 cm^3). A base pressure of 10^{-6} mbar and a deposition rate of 30 $Ås^{-1}$ were measured.

A thin layer of Si_3N_4 is deposited just after lithium (without open the chamber). This layer (100 nm) is deposited by RF magnetron sputtering technique at 300 W, a pressure of 0.2 Pa in a 20 sccm flow of N_2. This layer offers the necessary air protection to transfer the battery to the Hot-wire chemical vapor deposition (HWCVD) chamber, where the silicon nitride capping multilayer is deposited. These were obtained by using a sequence of HWCVD deposition of the SiNx followed by a low-frequency (100 kHz) Ar-plasma treatment for surface compaction. The final thickness of the structure was 120 nm, composed of 4×30 nm. The HWCVD deposition of SiN_x was performed at 25 mTorr from silane and ammonia gaseous mixtures using two hydrogen dilutions, namely 88% and 90%. The Ta current filament was 16 A, corresponding to a filament temperature of 2000 ºC. The Ar treatment was performed at 230 mTorr using a pulsed source for a short time. The sequence of SiNx deposition and Ar treatment was performed without breaking the vacuum, by moving the sample between two twin chambers connected by a gate valve. For each hydrogen dilution, two samples were deposited under a different NH_3 to SiH_4 flow rate ratio, R, namely R = 2 and R = 3, so fabrication receipt could be tuned.

IV –Results and Discussion

A. $LiCoO_2$ cathode

The Figure 3 shows the X−ray diffraction (XRD) spectrum of the $LiCoO_2$ films for three annealing temperatures (600 ºC, 650 ºC and 700 ºC). The joint analysis between the difractograms of the Figure 3 and the peak positions of planes [003], [101], [104], [018] and

[110] confirms the predominance of crystalline $LiCoO_2$ in the composition of the selected samples (diffraction patterns 016-0427 [16] were used in crystallographic analysis).

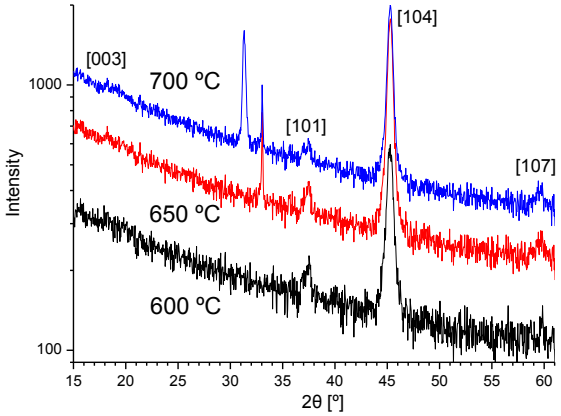

Fig 3: *XRD spectrogram of three $LiCoO_2$ films annealed at different temperatures (600 ºC, 650 ºC and 700 ºC).*

In the Figure 3 it is also possible to observe the evolution of $LiCoO_2$ peaks in XRD pattern with the increase in the annealing temperature. The annealing temperature increase resulted in a polycrystalline structure with strong orientation in the [104], [018] and [110] planes and fewer at [003] and [101] planes as it was presented before [17]. This structure improves the ion diffusing, thus increasing ionic conductivity and ion insertion and extraction. However, a phase transition occurs at 650 ºC, as depicted in Figure 4. The in-plane resistivity was measured using the Van der Pauw technique, for $LiCoO_2$ samples annealed at different temperatures (see the Figure 4).

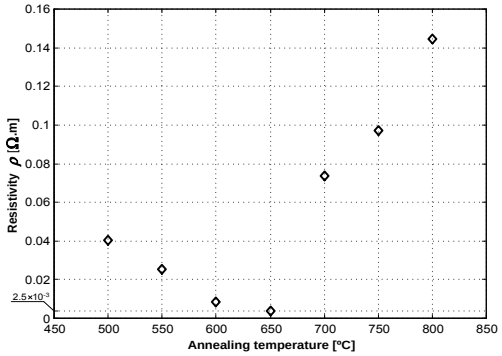

Fig 4: *Resistivity of $LiCoO_2$ samples, as function of annealing temperature.*

A decrease of resistivity was found with an increase of annealing temperature. The minimum resistivity value of 2.5×10^{-3} Ωm was measured (at room temperature) in sample annealed at 650 ºC. However, for annealing temperature above 650 ºC, the resistivity rapidly increases with annealing temperature. This behavior was also reported before [17].

B. LiPON electrolyte

The ionic conductivity of LIPON was measured on the best samples with the procedure described [12]. A sinusoidal voltage with amplitude of 25 mV (peak to peak) was used to measure the impedance of the sample at several values of frequency (from 0.5 Hz to 65 kHz). The inset in Figure 5 shows the LiPON thin-film with top and bottom contacts of platinum (Pt) for measuring the ionic conductivity. Both real (Z') and imaginary (Z'') parts of the impedance were respectively projected in x−axis and y−axis, in order to obtain a two dimensional Nyquist plot.

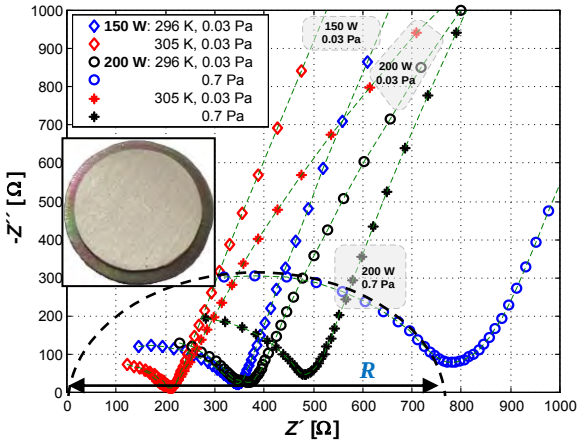

Fig 5: *Typical Nyquist plots of LIPON samples.*

Nyquist plots (measured at temperatures of 296 K and 305 K) are presented in Figure 5, for samples deposited at N_2 pressures of 0.03 Pa and 0.7 Pa, with RF sputtering power of 150 W and 200 W. The diameter of each semi−circle indicates the resistance of the electrolyte (R), whose values were obtained with the help of Autolab software.

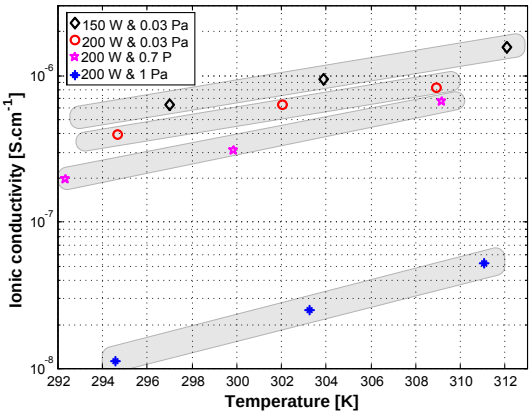

Figure 6: *Ionic conductivity of LIPON thin-films.*

Considering the area (A) and the thickness (d) of the electrolyte, the ionic conductivity, σ [Scm^{-1}], of LiPON is given by σ =d/(A*R) where and R [Ω] is the resistance from Nyquist diagram. The best ionic conductivity archived was between 10^{-7} $S.cm^{-1}$ and 10^{-6} $S.cm^{-1}$. The Figure 6 shows the ionic conductivity of LiPON films deposited at N_2 pressures from 0.03 Pa to 1 Pa and with RF power of magnetron sputtering from 150 W to 200 W, measured in temperature range of 292 K to 312 K. The highest ionic conductivity of LIPON (10^{-6} Scm^{-1} at 304 K) was measured in the sample deposited at N_2 pressure of 0.03 Pa and a RF power of 150W. It was observed the decreases of ionic conductivity with increase of power or pressure.

C. Li anode

The Li resistivity was measured during the deposition using a four point setup and values around 10 μΩm were measured for 3 μm thick film. After the deposition, the resistivity of Li was measured at room temperature and atmospheric pressure without any protective layer in order

to evaluate the oxidation of Li. These results show that a protective layer is essential to keep the battery functional.

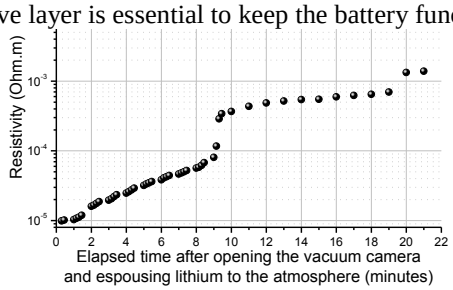

Fig 7: *Evolution of lithium resistivity in contact with air*.

D. Silicon nitride capping layer

Multilayers of SiNx thin-films, having refractive index of 2 (at 650 nm), were obtained. The final thickness of the structure was 120 nm, composed of 4×30 nm. All the samples are highly transparent in the visible/NIR range reaching more than 85% of transmission at 650 nm. The spectral refractive index was obtained from the transmission spectra in the visible and near infrared range (from 250 to 2500 nm) [18]. The multilayers will be electrically characterized by measuring the disruption field and the transport mechanism in the dielectric, under low and high applied electric field, in metal-insulator-metal (MIM) patterned structures defined lithographically. The quality of the multilayer as a device encapsulation barrier will be tested by measuring the water vapor transmission rate using the calcium test. The best samples will then be grown on top of the battery and the lifetime of the battery will be compared with that of batteries without encapsulation.

E. Battery

A battery, including all described materials, was fabricated using shadow masks to pattern different regions. Figure 8 shows a SEM image of the battery.

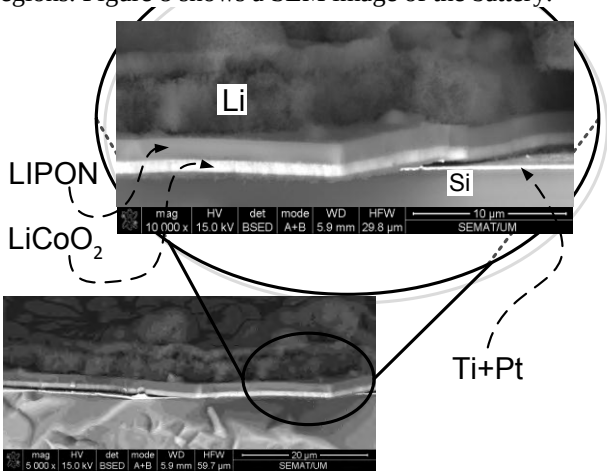

Fig 8: *Cross-sectional SEM image of the thin-film battery.*

IV - Conclusions

This paper presented the materials technology of rechargeable solid-state film lithium batteries for integration in stand-alone harvesting microsystems.

The RF magnetron sputtering, the e-beam evaporation and Hot-wire CVD were the techniques used for depositing the successive layers of the battery. The elements of the film battery are a $LiCoO_2$ cathode, a LiPON amorphous electrolyte and a Li anode. The contacts are made of platinum and battery is protected with a Si_3N_4 layer. The best $LiCoO_2$ films, annealed at 650ºC showed a resistivity of 0.25 Ωm. The best LiPON films have an ionic conductivity of 10^{-6} Scm^{-1} (at 304 K), obtained from a deposition at 20 sccm of N_2 with a pressure of 0.03 Pa and with an applied power of 150 W. The Li anode was deposited by thermal evaporation and presents a low resistivity (10 μΩm). However, a rapid oxidation of Li occurs in contact with atmosphere, so a protective layer must be deposited at the same run. These materials have as good properties as standard large sized batteries and are suitable for the fabrication of solid-state lithium film batteries.

Acknowledgements

This work was financial supported by FCT funds, by project PTDC/EEA-ELC/114713/2009.

References

[1] M. Armand, and J. M. Tarascon, “Building better batteries”, Nature, Vol. 451, pp. 652 657, 7 February 2008.
[2] H. Nishide, and K. Oyaizu, “Toward flexible batteries”, Science, Vol. 319, pp. 737 738, 8 February 2008.
[3] J. P. Carmo, L. M. Gonçalves, and J. H. Correia, “Thermoelectric microconverter for energy harvesting systems”, IEEE Transactions on Industrial Electronics, Vol. 57, No. 3, pp. 861 867, March 2010.
[4] N. J. Dudney, and B. J. Neudecker, "Solid state thin films lithium battery systems", Solid State & Materials Science, Vol. 4, pp. 479 482, 1999.
[5] B. Kang, and G. Ceder, “Battery materials for ultrafast charging and discharging”, Nature, Vol. 458, p. 190, 2009.
[6] N. J. Dudney, “Solid-state thin-film rechargeable batteries”, Materials Science and Engineering – B, Vol. 116, pp. 245 249, 2005.
[7] A. Patil, *et al.*, “Issue and challenges facing rechargeable thin film lithium batteries”, Materials research bulletin, Vol. 43, pp. 1913 1942, 2008.
[8] P. Alpuim, *et al.*, “Deposition of silicon nitride thin films by hot-wire CVD at 100 °C and 250 °C”, Thin Solid Films, Vol. 517, pp. 3503 3506, 2009.
[9] B. L. Ellis, K. T. Lee, and L. F. Nazar, “Positive electrode materials for Li-ion and Li-batteries”, Chemistry of Materials, Vol. 22, No. 3, pp. 691 714, 2010.
[10] L. Predoana, *et al.*, “Electrochemical properties of the $LiCoO_2$ powder obtained by sol gel method”, J. of the European Ceramic Society, Vol. 27, pp. 1137 1142, 2007.
[11] L. Predoana, *et al.*, “Advanced Techniques for $LiCoO_2$ Preparation and Testing”, in Proc. International Workshop Advanced Techniques for Energy Sources Investigation and Testing, Sofia, Bulgaria, September 2004.
[12] Y. Hamon, *et al.*, “Influence of sputtering conditions on ionic conductivity of LiPON thin films”, Solid State Ionics, Vol. 177, pp. 257 261, 2006.
[13] S. Oukassi, *et al.*, “Above IC micro power generators for RF MEMS”, in Proc. Symposium on Design Test Integration and Packaging of MEMS/MOEMS (DTIP of MEMS & MOEMS), Stresa, Italy, pp. 1 4, April 2006.
[14] J. P. Carmo, *et al.*, "Integrated thin-film rechargeable battery in a thermoelectric scavenging microsystem", in Proc. Powereng 2009, Lisbon, Portugal, pp. 359 363, 2009.
[15] J. P. Carmo, *et al.*, "Sputtered SnO2 for application in thin-film solid state microbatteries", in Proc. Materiais 2009, Lisbon, Portugal, April 2009.
[16] Powder Diffraction File, Joint Committee on Powder Diffraction Standards, ASTM, Philadelphia, PA, 1967.
[17] J. B. Bates, *et al.*, “Thin film lithium and lithium ion batteries”, Solid State Ionics, Vol. 135, pp. 33 45, 2000.
[18] D. A. Minkov, J. Phys. D: Appl. Phys. 22, 199 (1989).

ULTRASONIC ASSISTED ROOM TEMPERATURE SN-SN AND CU-CU BONDING

H.N.P. Cu, H.-V. Nguyen, N. Hoivik, K.E Aasmundtveit

HiVe - Vestfold University College, Department of Micro and Nano Systems Technology - IMST, Postbox 2243, N-3103 Tønsberg, Norway

***Abstract* — In this paper we present metal-to-metal bonding method performed at room temperature, that is suitable for temperature-sensitive materials. It is demonstrated that two samples with electroplated Cu or Sn interconnects can be reliably bonded together using thermo-sonic bonding. The ultrasonic energy is used to mechanically deform the material and enhance the inter-diffusion between the two bonding surfaces. The effect of bonding parameters, e.g. bonding force and ultrasonic power, on joint quality has been investigated. The electrical resistance and mechanical strength of the joints have been characterized. The bonded interfaces were inspected using SEM characterization on cross-sectioned samples. The maximum shear strength measured is around 28MPa for Sn-to-Sn interconnects, using a bonding pressure of 73MPa. The maximum shear strength of Cu-Cu bonded interconnects is 116MPa using a bonding pressure of 340MPa. Measured resistance is of 30mΩ for Sn-Sn and 27mΩ for Cu-Cu bonded interconnects.**

I – Introduction

For interconnection technology, metal-to-metal bonding is advantageous because mechanical and electrical interconnection can be created simultaneously. However, this kind of method needs to be performed at elevated temperature which is a serious problem for particular materials, for example piezoelectric crystals onto silicon wafers [1]; or for some electronic device such as CdZnTe detector[2]. Also, residual stress due to thermal expansion mismatch of dissimilar materials is avoided by room temperature bonding. Therefore, the demand of a bonding method at room temperature is of great interest. To realize a low-temperature bonding technology Surface Activated Bonding (SAB) has been developed[3]. The main principle is that two surfaces are activated in vacuum or low pressure chamber to minimize the oxidation and contamination layer, and then brought together under a certain pressure to cause the intimate contact of bare metal surface at room temperature. The bond is generated by inter-diffusion at the interface. SAB flip chip method using atom beam and plasma irradiation has been presented in [4] demonstrating Au micro bump could achieve good interconnection with Au pad. Kim *et al.* [5]reported Cu-Cu direct bonding at room temperature obtained between two wafers surface-activated by low energy Ar ion beam irradiation. In contrast, this study presents a die attach method at room temperature in ambient atmosphere using ultrasonic energy without surface treatment. The purpose of using ultrasonic energy is to break up any oxidation and contamination layer, and to supply the friction heat at the bonding interface to enhance inter-diffusion. The metals investigated in this bonding method are Sn-to-Sn and Cu-to-Cu.

The thermo-sonic bonding mechanism is not entirely understood [6], however the theories have converged to explaining the effect of the ultrasonic energy as follows. Firstly, applied pressure causes plastic deformation of surface asperities and reducing interfacial voids. Then, the ultrasonic power is introduced; the contamination and oxide layer will be broken or removed by the ultrasonic induced vibration at interface. The underlying clean metal surfaces are brought into contact under a pressure. Ultrasonic energy also causes friction heating which enhances the inter-diffusion. Finally, inter-atomic forces will come into effect and atomic bonding will occur[7].

II - Experimental Details

A. Metal-bump test sample preparation

The samples are produced from 100mm silicon wafer with silicon dioxide as the isolating layer. The wafer is metalized by sputtering 200nm-thick Ti/W as adhesion layer and a 300nm-thick Au as seed layer. The fabrication steps are illustrated in figure below.

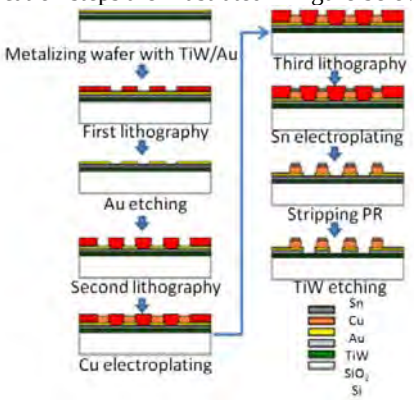

Figure 1*: Test sample fabrication processes.*

The gold layer is patterned with squares (160x160 μm^2) as the plating base for bump structures while TiW is kept as conductor layer serving for electroplating. Irregular geometries, for example trace lines, alignment marks, pads, dicing lines are also created on the gold layer, so that these features are not electroplated. The plating mask only includes the interconnect array with identical opening 120x120μm^2 for copper electroplating. Using such optimized mask, we can achieve the best uniformity for the bump height [8]. The 5µm-thick Cu and 2µm-thick Sn deposition is performed using pulse-reverse electroplating in Cu and Sn sulfate based

electrolytes, respectively. The uniformity of the bump height is measured by ratio (max-min)/min. The variation is about 8% for a total bump height of 7µm. After electroplating, the TiW layer is removed using H_2O_2 , leaving only the isolating layer SiO_2 to measure electrical resistance after bonding. A final electroplated metal bump is shown in Figure 2 with TiW/Au/Cu/Sn. For Cu-Cu bonding, the bumps will have TiW/Au/Cu layers.

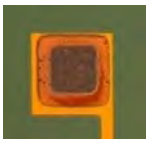

Figure 2: *Photograph of electroplated interconnect. The Sn area is smaller than Cu to avoid Sn squeezing-out during bonding.*

After completing the bump fabrication process, the wafers are diced into individual chip as showed in Figure 3.

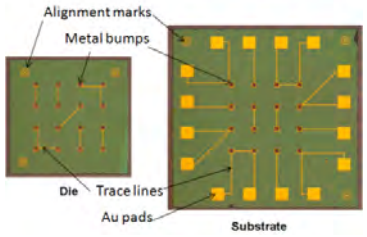

Figure 3: *Photographs of die and substrate prepared for bonding. The dimension of die is 4x4 mm^2 and substrates is 6x6 mm^2. Au trace lines and Au pad is for electrical measurement.*

B. Test sample bonding

The thermo-sonic bonding is carried out using MAT 6400 semi-automatic flip chip bonder. The die attach method is applied for the Cu/Sn-Cu/Sn and Cu-Cu bonding, with the mating parts held together in five seconds under a predefined pressure, following by one second of applied ultrasonic energy, and the bonding is completed after four more seconds of compressing. The ultrasonic power is applied to the backside of the chip, transferred to the chip through the bonding force and the use of vacuum suction. The bonding profile at room temperature is illustrated in figure below.

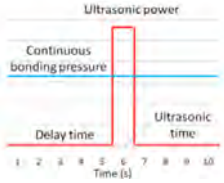

Figure 4: *Illustration of the bonding profile used. The bonding force is applied and kept constant throughout bonding time while ultrasonic power is applied for one second after a specified delay time.*

In this study, the bonding time is kept constant at 10 seconds and bonding temperature is 20°C. The effects of bonding force and ultrasonic power will be investigated mainly on Sn-Sn joints. The bonding force ranges from 100g to 1200g, equivalent to 30MPa-120MPa. The ultrasonic power varies between 4W and 24W. The conditions for Cu-Cu bonding is higher since Cu is harder than Sn, with bonding force of 2000g, approximately 340MPa, and ultrasonic power of 20W.

C. Die shear strength measurement

Assembled samples were subjected to mechanical die shear test using DELVOTEC 5600 Die shear tester. The parameters for die shear test were a shear height of 60µm and shear speed of 100µm/s. Visual inspection was performed on samples after the destructive die shear test to analyze the fracture surface, and to measure the bond area. Die shear strength was then determined based on the maximum measured die shear force and the measured contact area.

D. Interconnection resistance measurement

Four-probe station and Dual-channel Source-Meter Instrument 2602A are utilized to measure the interconnection resistance. The measurement is set up as show in Figure 5. The applied current is 10mA, deemed to be safe enough for Au trace lines. The resistance of a single bump is induced directly from the measured voltage and input current from the four-point measurement.

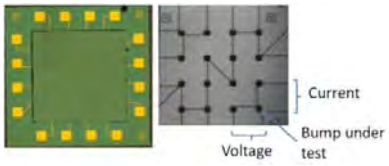

Figure 5:*Photographs of the test sample after bonding (left), and infrared- picture (right) of the same bonded sample. Current source is applied on two pads and voltmeter measures on other two ones.*

E. Cross section

After bonding, the samples are prepared by using molding, grinding, and polishing with 3µm and 1µm diamond powder. The cross section is inspected by microscopy and SEM to investigate the bond interface.

III - Results and discussion

A. Cross section analysis

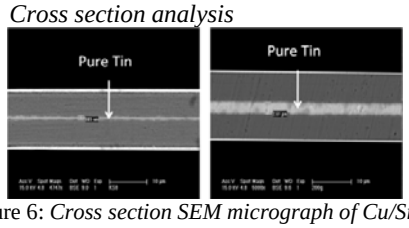

Figure 6: *Cross section SEM micrograph of Cu/Sn-Cu/Sn bonds. Thickness of pure Sn at the bond line is 2.6µm in the left image and nearly 1µm on the right.*

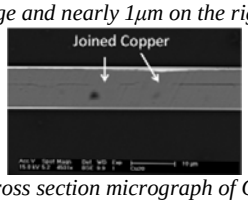

Figure 7: *Cross section micrograph of Cu-Cu bond*

Table 1: *Bonding condition for different samples.*

	Cu/Sn	Cu/Sn	Cu-Cu
Sn thickness on each side	4µm	2µm	0µm
Bonding force	200g	400g	2000g
Ultrasonic power	8W	12W	20W
Bonding temperature	20°C	20°C	20°C

Figure 6 and Figure **7** shows SEM cross section of Cu/Sn-Cu/Sn and Cu-Cu bonds. The bright line of Sn at the middle in Figure 6 and joined Cu in Figure 7 demonstrated that materials from both sides is bonded together to form the joined solid at bonding interface. The bonding parameters for samples in Figure 6 and Figure **7** are summarized in Table 1.

B. Die shear test result

The die shear strength and bonding yield increases significantly from about 6 MPa to about 20 MPa with prolonged bonding time from 2 to 10 seconds. Therefore the bonding time is kept constant at 10 seconds during characterizing to ensure highest possible yield.

Figure 8 presents die shear test results with bonding force ranging from 100g to 1200g and ultrasonic power varying from 4W to 24W. The samples used in this investigation have Cu/Sn bumps with 2µm-thick Sn layer. Correponding to each bonding force value, the ultrasonic power is varied. Outside this range, insufficient ultrasonic energy gives no bond, whereas excessive energy causes failed bonding. The second failure is because the specimens are not strongly fixed in place and can be improved by increasing bonding force.

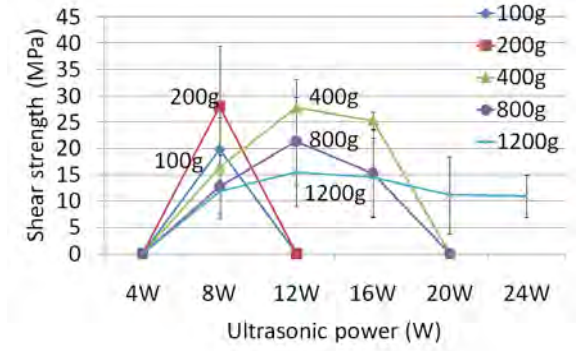

Figure 8: *Die shear strength versus ultrasonic power when applying different bonding force. Samples of Cu/Sn bumps with 2µm-thick Sn layer*

From the experiments, performing a higher bonding force allows for a higher level of ultrasonic power. However, for a bonding force of 1200g, the die shear strength is stable and lower compared to die shear strength at other power levels. One possible explanation is that a high bonding force constrains the vibration of chip when ultrasonic is applied.. Therefore, the effect of ultrasonic energy is limited, resulting in lower die shear strength than other bonding force. In this study, force of 200g and power of 8W, equivalent to 73MPa, yields the best bonding condition, with average shear strength of 27MPa. This is comparable to the shear strength of pure Sn, reported to be in the range 11-31MPa [9]. The observation of fracture surface after die shear test shows that most failures occur at the original interface (Sn is visible on both surfaces), thus the shear strength of specimens is comparable to shear strength of pure Sn. This implies that the bonds show the maximum achievable shear strength. For Cu-Cu bonds, the maximum shear strength of the tested specimens is 116MPa, in the order of pure Cu strength 174MPa [10].

C. Electrical resistance

Figure 9 illustrates the correlation between die shear strength and resistance of interconnection with pure Sn thickness. For the Cu/Sn-Cu/Sn bonded samples, the interconnection resistance is higher compared to those of Cu-Cu joint. The results are in accordance a report of Tonegawa *et al.* [11], which stated that sheet resistance of CuSn alloy is higher than that of pure Cu. The die shear strength of Cu-Cu joint is in the order of pure Cu strength while that of Cu-Sn-Cu interconnection is comparable with pure Sn, regardless of the thickness of Sn layer.

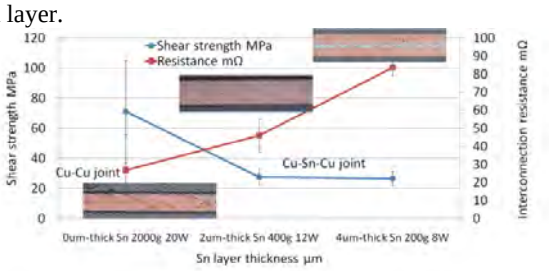

Figure 9:Die *shear strength and interconnection resistance of Cu-Cu joint compared to Cu-Sn-Cu joint. Sn thickness measures 2µm and 4µm on both sides. After bonding, the Sn thickness is reduced to about 1µm and 2.6µm, which also depends on bonding force.*

D. Comparison with other publications

Table 2 and 3 compare the specific results to similarly demonstrated results. The interconnection resistance of Cu-Sn-Cu in this study is comparable to that of solder joints in [12]. The difference in resistance measurement systems and bumps geometry also leads to distinction.

Table 2: *Comparison of bump structures, bonding processes, mechanical strength, and electrical resistance with related works for Cu-Sn-Cu bonding.*

	SLID [13]	This study	Solder joints[12]
Bonding method	Solid-liquid Inter-diffusion	Thermo-sonic	Thermo-compression
Bump structure	Cu/Sn-Cu	Cu/Sn-Cu/Sn	Cu/Sn/Ag-Cu/Sn/Ag
Bump diameter	7µm	120µm	100µm
Bump height	4µm Cu, 2.5µm Sn	5µm Cu, 2µm Sn	5µm Cu, 1µm Sn, 0.1µm Ag
Bonding pressure	102MPa	73MPa	20-80MPa
Bonding temperature	275°C	20°C	200°C
Bonding time	3 minutes	10seconds	30 seconds
Ultrasound	No	8W	No
Shear strength	42-114MPa	20-40MPa	12-17MPa
Resistance per interconnect	Estimated 10-27mΩ	Measured 25-33mΩ	9-12mΩ

Table 3: *Comparison different works for Cu-Cu bonding*

	Metal-metal bonding[13]	This study
Bonding method	Thermo-compression	Thermo-sonic
Bump structure	Cu-Cu	Cu-Cu
Base diameter	7μm	120μm
Bump height	4μm Cu	5μm Cu
Bonding pressure	340MPa	~340MPa
Bond temperature	300°C	20°C
Bonding time	15 minutes	10 seconds
Ultrasonic power	No	20W
Shear strength	>114MPa	40-116MPa
Resistance per interconnect	Estimated 15mΩ	Measured 27mΩ

IV - Conclusion

The study demonstrates a fluxless, room-temperature die metal-metal bonding method suitable for 3D-Integration of MEMS. It is demonstrated that samples with electroplated Cu or Sn bumps interconnects can be reliably bonded together using thermo-sonic bonding at room temperature, in ambient atmosphere. The die shear strength of interconnection is equivalent to previously demonstrated work, as well as bulk material values. Electrical resistance is comparable to conventional solder joints. Sn-Sn interconnections exhibited the die shear strength in the range of 20-40MPa, with contact resistance of 25-33mΩ. Cu-Cu interconnects give the maximum die shear strength of 116MPa and contact resistance of 27mΩ. This study opens a direct bonding method suitable for MEMS structures that may not tolerate high temperatures, such as polymer and piezoelectric material, or for direct bonding to organic substrates.

Acknowledgements

The authors gratefully thank Guttorm Salomonsen, Zekija Ramic, Ragnar D. Johansen, Tormod Vinsand, Thomas Martinsen at Departmentof Micro and Nano Systems Technology (IMST) for their support in experimental work.

References

[1] H. Takagi, R. Maeda, N. Hosoda, and T. Suga, "Room-temperature bonding of lithium niobate and silicon wafers by argon-beam surface activation," *Applied Physics Letters*, vol. 74, pp. 2387-2389, 1999.

[2] X. Lin, C. Jian, L. Lei, Z. Lan, and W. Shuidi, "Polymer Flip Chip Bumping and Its Application for CdZnTe Detectors," in *Electronic Packaging Technology, 2006. ICEPT '06. 7th International Conference on*, 2006, pp. 1-5.

[3] A. Shigetou, T. Itoh, M. Matsuo, N. Hayasaka, K. Okumura, and T. Suga, "Bumpless interconnect through ultrafine Cu electrodes by means of surface-activated bonding (SAB) method," *Advanced Packaging, IEEE Transactions on*, vol. 29, pp. 218-226, 2006.

[4] X. Zhonghua and T. Suga, "Surface activated bonding - high density packaging solution for advanced microelectronic system," in *Electronic Packaging Technology, 2005 6th International Conference on*, 2005, pp. 398-403.

[5] T. H. Kim, M. M. R. Howlader, T. Itoh, and T. Suga, "Room temperature Cu-Cu direct bonding using surface activated bonding method," *Journal of Vacuum Science & Technology A: Vacuum, Surfaces, and Films*, vol. 21, pp. 449-453, 2003.

[6] Z. Kun, J. Lei, D. Ji'an, and Z. Jianhua, "Effects of thermosonic bonding parameters on flip chip LEDs," in *High Density Microsystem Design and Packaging and Component Failure Analysis, 2006. HDP'06. Conference on*, 2006, pp. 101-107.

[7] J. Qi, N. C. Hung, M. Li, and D. Liu, "Effects of process parameters on bondability in ultrasonic ball bonding," *Scripta Materialia*, vol. 54, pp. 293-297, 2006.

[8] H. Liu., E. M. Husa., Z. Ramic., A. Munding., K. Aasmundtveit., and N. Hoivik., "Uniformity Requirements for Electroplated Cu-Sn Interconnects Used in Heterogeneous 3-D MEMS/ASIC Stacks," *IMAPS Nordic, September 14-16, 2008, Helsingør, Ddenmark,*, 2008.

[9] J. Maveety, P. Liu, J. Vijayen, F. Hua, and E. Sanchez, "Effect of cooling rate on microstructure and shear strength of pure Sn, Sn-0.7Cu, Sn-3.5Ag, and Sn-37Pb solders," *Journal of Electronic Materials*, vol. 33, pp. 1355-1362, 2004.

[10] J.-H. Li, "Joint zone evolution in infrared brazed titanium-aluminum(6)-vanadium(4) with copper thin film," Ph.D. Ph.D., Materials science, University of Cincinnati, Cincinnati, Ohio, 2005.

[11] T. Tonegawa, M. Hiroi, K. Motoyama, K. Fujii, and H. Miyamoto, "Suppression of bimodal stress-induced voiding using high-diffusive dopant from Cu-alloy seed layer," in *Interconnect Technology Conference, 2003. Proceedings of the IEEE 2003 International*, 2003, pp. 216-218.

[12] S.-H. Lee, H.-R. Roh, Z. Chen, and Y.-H. Kim, "Contact resistance and shear strength of the solder joints formed using Cu bumps capped with Sn or Ag/Sn layer," *Journal of Electronic Materials*, vol. 34, pp. 1446-1454, 2005.

[13] A. Huffman., J. Lannon., M. Lueck., C. Gregory., and D. Temple., "Fabrication and characterization of metal-to-metal interconnect structures for 3-D integration," *Journal of Instrumentation JINST* vol. 4, 2009.

DIRECT INTEGRATION OF CARBON NANOTUBES IN SI MICROSTRUTURES

Knut E. Aasmundtveit, Bao Q. Ta, Nils Hoivik and Einar Halvorsen
Department of Micro and Nano Systems Technology (IMST) – Vestfold University College (HiVe), P.O. Box 2243, N-3130 Tonsberg, Norway

***Abstract* — In this paper we present a low-cost, room-temperature process for integrating carbon nanotubes on Si microsystems. The process uses localized resistive heating by controlling current through suspended microbridges, to provide local temperatures high enough for CVD growth of carbon nanotubes. Locally grown carbon nanotubes make electrical connections through guidance by electric fields, thus eventually making circuits.**

The process is scalable to a wafer level batch process, and is controlled electrically, thus enabling automated control.

Direct integration of carbon nanotubes in microstructures has great promise for nano-functional devices, such as ultra-sensitive chemical sensors.

Keywords : **Carbon nanotubes, micro-nano system integration, nanomaterials, nano system devices**

I - Introduction

A. Carbon nanotubes

Carbon nanotubes (CNTs) have been the *de facto* symbol of nanotechnology ever since their discovery in soot of arc discharge in 1991by Ijima [1]. CNTs are one of the stable allotropes of carbon. 3-dimensional carbon structures include diamond and graphite; graphene is the 2D-structure; CNTs are 1D carbon structures, whereas fullerenes such as C_{60} may be regarded as the 0D carbon structure. CNTs have a highly one-dimensional nature, with diameters in the nm-range and lengths in the µm-to-mm range. Conceptually, a CNT can be regarded as a single graphene sheet rolled up to a cylinder, its *chirality* given by the symmetry along the cylinder periphery. The molecular structure of a CNT is sketched in figure 1.

Figure 1: *Sketch of single-walled carbon nanotube in different orientations, and the conceptual image of a CNT as a rolled-up graphene sheet.*

CNTs exist as single-walled (SWCNT) and multi-walled (MWCNT), the latter consisting of concentrically arranged nanotubes. CNTs have gained massive interested because of its unique properties, such as:

- Extraordinary mechanical properties: The highest known tensile strength and Young's modulus of any material (besides graphene)
- Excellent thermal conductivity
- Electrical properties depending on chirality: metallic or semiconducting
- High current density capacity

The 1D nature of CNTs make them ideally suited as model systems for low-dimensional physics. Technologically, they are interesting for a variety of reasons:

- As additive in composites for improving mechanical properties
- As thermal interface materials (TIM)
- As active material in nanoelectronics and nano-electromechanical systems (NEMS)

The latter use is the focus of this paper, where the miniaturized nature of CNTs, its high surface-to-volume ratio, its electrical properties and its extreme aspect ratios make CNTs a prime candidate for transistors (as CMOS miniaturizing approach a quantum mechanical limit), for ultra-sensitive sensors, and for field ionization devices, to mention a few examples.

CNTs are commonly produced by

- Arc discharge
- Chemical Vapour Deposition (CVD), using a carbon-containing gas
- Laser ablation

Common to these techniques is that the synthesis temperature of CNTs is high: in the order 800 ^{o}C – 1000 ^{o}C

B. CNT-microsystem integration

For proper use of the nanomaterial functionality of CNTs as active material, their integration with microsystems is essential, as the microsystem can act as the bridge connecting the nanomaterial to the macroscopic world. A complete, integrated system should contain MEMS-, CMOS- and CNT-functionality, preferably all integrated on the same die. However, the high synthesis temperature is a major obstacle to CNT-microsystem integration. Processed MEMS/ CMOS devices should not be exposed to temperatures above ~300 ^{o}C in the post-processing. (Somewhat higher temperatures, up to ~400 ^{o}C, may be acceptable if the exposure is very limited in time.)

One way to address this issue is to synthesize CNTs separately, with subsequent assembly to a microsystem. This has indeed been demonstrated, using manual transfer of CNTs by micro-manipulators, and welding the terminals of the CNT to MEMS structures by electron-beam-induced deposition (EBID) in a SEM [2]. This is indeed a technique highly relevant in a research laboratory, where the aim is either to measure individual CNT properties or to demonstrate the working principle of an integrated nano-microsystem device. However, it is not scalable to an industrial process, because of the serial process occupying high-cost equipment. Other examples of CNT-microsystem integration include CNT wafer-scale growth on a 4'' quartz wafer and a process to transfer CNTs into Si wafer. The transfer process is done by evaporating 100 nm Au on top of the grown CNTs and using a special tape to transfer the Au layer, including CNTs, from the quartz wafer to the Si wafer to fabricate CNT-FETs by photolithography technique [3].

For a process to be acceptable for the industrialization of CNT-microsystem integration, some of the requirements are:

- Low cost (CNT integration should not be the dominating system cost)
- Batch fabrication possibility
- Low process temperature (CMOS-compatible – below 300 ^{o}C)
- Localized CNT positions (for integrating active functionality)

If such a process can be implemented, it would enable post-processing of CMOS/ MEMS integrated wafers, to add the nano-functionality CNT will give, thus rendering a truly integrated micro-nano-system at a wafer-level, low-cost process.

This paper describes the efforts towards such a process, where a CVD process based on localized heating is selected. This approach has been addressed by several groups: [4][6][7][8]

II - Experimental Details

A. Main Concept

The main concept of CNT-Si microsystem integration by localized heating was first introduced by Christensen et al [4], and the further work includes work in our own research group[8][9].

A model microsystem is designed with suspended bridges, using micromachining processes including release of a sacrificial layer such as oxide. The suspended microbridges may consist of single-crystal Si (in a SOI process), or polysilicon (in a process including poly-Si deposition). Catalyst, such as Fe or Ni, is deposited on the bridges. By applying and controlling a current through one microbridge, this is locally heated to reach temperatures sufficient for CVD growth of carbon nanotubes, while the anchor of the structure itself is kept at ambient temperature. Thermal transport through other channels than conduction through the Si microbridge must be minimized to obtain such a temperature distribution, hence the importance of suspended bridges for avoiding thermal conduction to the substrate. A typical implementation of a growth structure, and the electrical arrangement, is sketched in figure 2, showing a pair of microbridges. One is locally heated to serve as the growth structure. An electric field is established between the two microbridges, to guide the growth direction of CNTs. Figure 3 shows a SEM image of such a growth structure, including wire bonds for electrical connection.

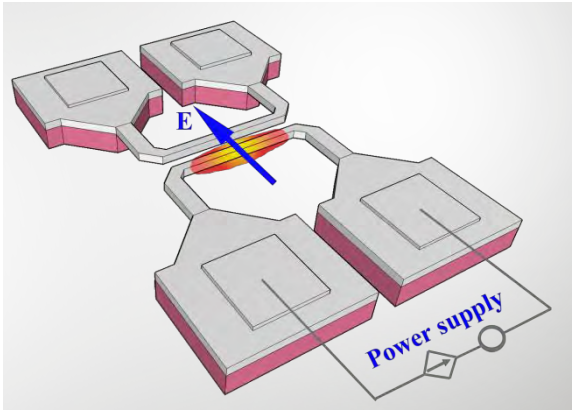

Figure 2*: Illustration of the CNT synthesis structure and electrical arrangement*

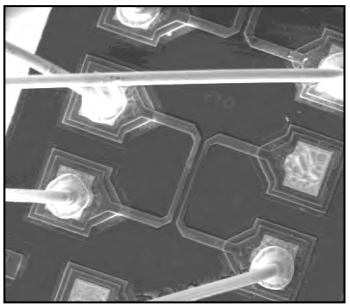

Figure 3*: SEM image of a typical microbridge growth structure, with wire bonds as electrical connections.*

The growth structure is designed with dimensions to obtain the desired temperature distribution with a reasonable current. Figure 4 shows the simulated temperature distribution of a design, and figure 5 shows a microscope image of a current-carrying, heated microbridge.

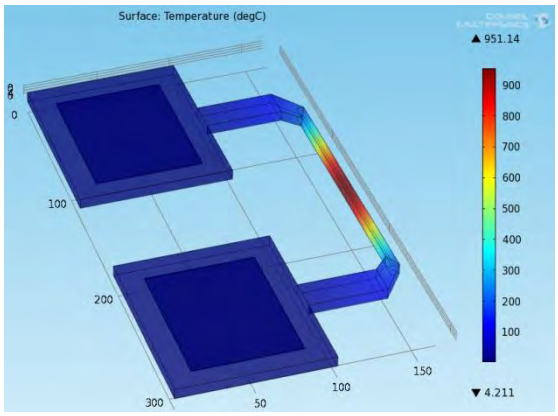

Figure 4: *Simulated temperature distribution in a microbridge*

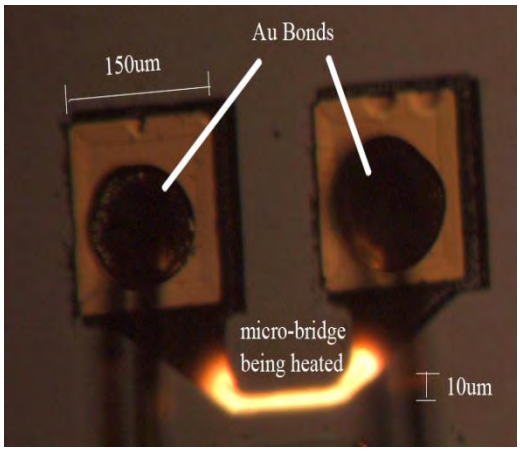

Figure 5: *Image of a heated micro-bridge, showing the localized heating*

Growth of CNTs occurs when the structure is locally heated in an environment of carbon-containing gas such as acetylene (C_2H_2) or methane (CH_4).

B. Present experiment

The microstructure used in the present experiment consists of two suspended polysilicon microbridges of 5 µm width, 160 µm length, 3.5 µm suspension, and 15 µm separation. A double thin layer of 3 nm thick Fe and 2 nm thick Ni, is evaporated to serve as the catalyst. No patterning of the catalyst was needed, since the selection of areas for CNT growth is performed by the localized resistive heating. The synthesis is accomplished using resistive heating on the growth structure while a local electric field is established between the two bridges to guide the growth direction of CNTs [1-2]. The synthesis is conducted in a room temperature chamber with a pressure of 0.4 bar, acetylene (C_2H_2) gas of 30 ccm (cubic centimeter per minute) after the growth structure is heated to the desired temperature (850-950^{o}C). The temperature is monitored by measuring the resistance of the microbridge. Doped Si shows a highly temperature-sensitive resistivity, with a positive temperature coefficient of resistivity (TCR) at moderate temperatures, and a negative TCR at higher temperatures when intrinsic conductivity becomes dominating. The temperature-to-resistance relation is calibrated through the use of temperature-sensitive indicating paint.

When CNTs grown connect the two microbridges, it can be detected electrically, either by monitoring the electrical potential of the second microbridge, or by monitoring the current across the microbridges.

III - Results and Discussion

Individual CNT connections was detected by monitoring the current across the two bridges as a function of synthesis time, as shown in figure 6.

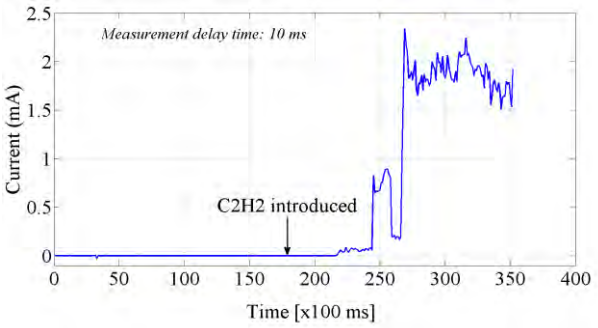

Figure 6: *Current across bridges vs synthesis time. Each jump signifies a CNT connection established.*

Figure 7 shows a scanning electron microscopy (SEM) image of locally synthesized CNTs, some connecting the two microbridges. CNTs grown appear straight and connect two microbridges over a gap of 15 µm.

SEM inspection shows that the synthesized CNTs have a good uniformity, high aspect ratios up to 1000:1 (length/diameter), and an apparantly narrow distribution of the diameters, with many in the range of 15-18 nm.

Current *I* – voltage *V* measurement is taken between the two microbridges. The I-V curve in figure 8 shows a fairly ohmic behavior, and an overall resistance of 400 kΩ. The present result is comparable with the previous results from [4][5] (from 400 kΩ up to 6 MΩ).

The measured resistance consists both of the intrinsic resistance of the carbon nanotube, and of the contact resistance at the CNT-Si interface. The current data is insufficient to quantitatively determine those values individually. Analytic estimation of the order of magnitude of these values shows that the contact resistance may dominate in the total resistance. Many techniques to reduce the contact resistance have been studied. H. Chiamori et al. demonstrated a simple and fast annealing technique for locally synthesized CNTs that can decrease the contact resistance from 20% to over 80% [5].

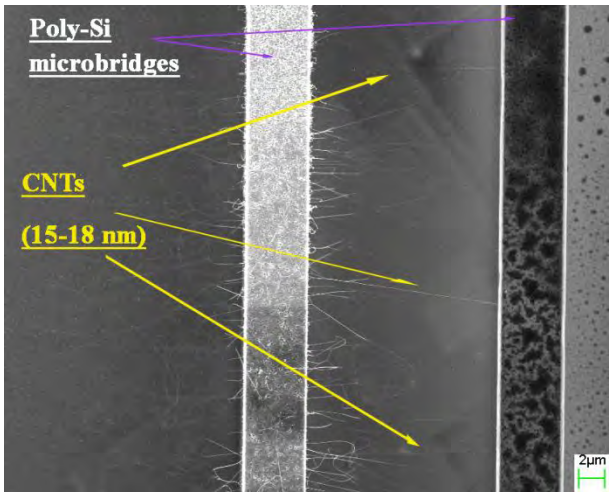

Figure 7: *A close-up SEM image of locally synthesized CNTs, where some connect two polysilicon microstructures*

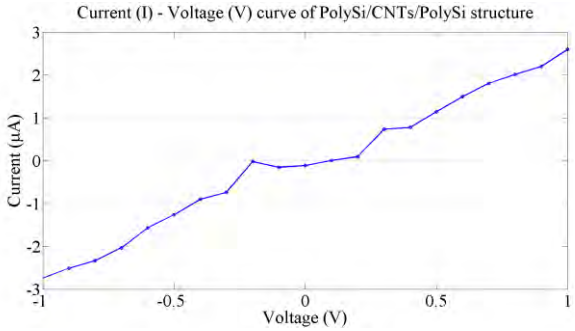

Figure 8: *I-V curve of a bridging CNT, measured between two microbridges, at room temperature.*

IV - Conclusion

The process shown for direct integration of CNTs in Si microsystems is demonstrated to obtain nanotubes that can close the circuit between to defined microstructures. For a suitable microsystem design, the process is therefore capable of producing functional nano-devices in a single process step.

The process is CMOS-compatible and low cost. A crucial process parameter is the local temperature, governed by the current flowing in the microbridge. Since the temperature can be measured through a resistance measurement, it can easily be controlled automatically. Since individual CNT connections can be measured electrically, an automated process may be set up to produce the desired number of CNT connections. This ensures that the process can be scaled to an effective, easily controlled, wafer-level batch process.

Potentially, the process may be used as a last process step for integrated CMOS + MEMS wafers, producing truly integrated micro-nano systems.

Acknowledgements

The authors are grateful to Egil Erichsen and Bodil Holst, University of Bergen, for SEM imaging of samples.

References

[1] S. Iijima, "Helical microtubules of graphitic carbon". *Nature* **354** (6348): 56–58, (1991).

[2] J. J. Brown et al., *"Microsystem for nanofiber electromechanical measurements,"* Sensors and Actuators A-Physical, Vol. 155, pp. 1-7, (2009)

[3] N. Patil et al., *"Wafer-Scale Growth and Transfer of Aligned Single-Walled Carbon Nanotubes,"* IEEE Transactions on Nanotechnology, vol. 8, no. 4, July 2009

[4] D. Christensen, O. Englander, J. Kim, and L. Lin, *"Room Temperature Local Synthesis of Carbon Nanotubes,"* IEEE-Nano 2003, Technical Digest, San Francisco, August 2003, pp.581-584

[5] H. Chiamori, X. Wu, X. Guo, B. Q. Ta, and L. Lin, *"Annealing nano-to-micro contacts for improved contact resistance,"* NEMS Conference 2010, Xiamen, China.

[6] Alain Jungen et al., *"Localized and CMOS Compatible Growth of Carbon Nanotubes on a 3x3 m^2 Microheater Spot,"* TRANSDUCERS'05, The 13th International Conference on Solid-State Sensors, Actuators and Microsystcms, Seoul, Korea, June 5-9, 2005.

[7] D. S. Engstrom *et al.*, *"Vertically aligned CNT growth on a microfabricated silicon heater with integrated temperature control—determination of the activation energy from a continuous thermal gradient,"* J. Micromech. Microeng. 21 (2011) 015004 (7pp)

[8] B. Q. Ta, *"Carbon Nanotubes: Local Synthesis and Characterization"*, Master Thesis, Institute of Micro- and Nano-Systems Technology, Vestfold University College.

[9] B. Q. Ta, N. Hoivik, E. Halvorsen, K. E. Aasmundtveit, *"Electrical Control of Synthesis Conditions for Locally Grown CNTs on Polysilicon Microstructure"*, IEEE NANO 2011, August 15-18, Portland, Oregon, USA

GAAS RESONANT BIOSENSOR: THEORETICAL RESULTS, MICRO-FABRICATION AND TESTS

A. Bienaime, C. Elie-Caille and T. Leblois

Institut FEMTO-ST, Dpt MN2S, F-25044 Besançon, France

***Abstract* — In this paper we present new results on a lateral field excited gallium arsenide membrane used as active surface for detection of biological analytes in liquid media. This mode of excitation is an alternative to thickness field excitation which is more appropriate for measurements in liquid media. The theoretical results were obtained using an analytical method based on Christoffel-Beckman formalism. The size of the structure elements was designed using finite element method software to increase performances, particularly the sensitivity. The micromachining of the resonant structure was performed by wet etching that is a batch process. The chemical attack of GaAs in acidic solution is also anisotropic even if the anisotropy ratio is smaller than for silicon. Hence, it is possible to adopt the micromachining process for the realization of the membrane structure. Finally, the sensor was packaged to be investigated in air and in liquid media. Electric responses of the sensor are given.**

***Keywords :* GaAs micromachining, lateral field excited acoustic wave sensor, resonant membrane**

I - Introduction

Piezoelectric devices are very attractive for biosensor applications due to their high sensitivity and time stability [1-4]. Several materials are used but up to now quartz crystal remains the reference material for bulk acoustic wave or surface acoustic wave resonators for sensors applications [3-6]. Indeed, reproducible high quality crystal can be found easily. The microfabrication of quartz microresonators is well known but cantilevers, disks and membranes with small sizes are not easily obtained with a low cost and reproducible process. The wet etching is often used to fabricate resonators in Z or AT cuts [7]. But, this method becomes uneasy in the case of non conventional orientations of structures [8, 9]. An other way to obtain resonant devices consists of thin film deposition (AlN or ZnO) on silicon wafer. The response of the microelectromechanical system is highly dependent on the morphological film properties [10, 11] and requires the adjustment of the deposition technology. Moreover, the use of thin films deposited on silicon surface makes the regeneration of the surface difficult after measurements in liquid media. So, the choice of a massive piezoelectric crystal is preferred. Semi-insulator gallium arsenide crystal constitutes a good example of material that combines piezoelectric properties and advanced MEMS technology [12-16]. Moreover, some authors investigated the possibility to bio-functionalize GaAs surfaces with thiolates or silane molecules [17, 18]. GaAs can also be considered as a promising material for resonant bio-sensors. The main objective from this work is to present for the first time a detailed investigation on the GaAs micromachined membrane performances in liquid media. Due to the measurements in liquid media the piezoelectric membrane was driven by lateral field excitation (LFE). This mode of excitation for bulk acoustic waves presents besides some other advantages such as a higher Q value and a better sensitivity of detection in solution. The investigation is presented here in three parts:

(i) The first part is devoted to the design of the resonant structure, the determination of the orientations of both substrate and electric field. The study was performed using an analytical model based on Christoffel-Beckmann formalism and a numerical simulation.

(ii) The second part deals with the microfabrication process and the characterization of the structure shapes.

(iii) Finally, different electrical measurements of the packaged device which were carried out are analyzed.

II – GaAs lateral field excited sensor

A. Analytical formulation

The main objective of this sensor is to have a good sensitivity to detect molecules of interest in biological fluids. This implies that the biosensor must work in liquid medium and that the excited electrodes must be out of the active surface. Figure 1 shows the design of the structure.

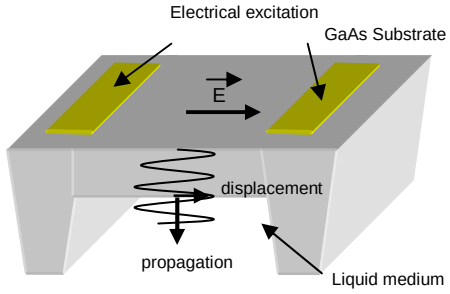

Figure 1: *Structure of the lateral field GaAs excited sensor.*

The LFE and TFE (thickness field excitation) electromechanical coupling coefficients of the acoustic modes of vibration noted a (quasi extensional), b (fast quasi shear mode) and c (slow quasi shear wave) were calculated using Christoffel-Bechmann method [19]. The calculation on GaAs was done using the elastic,

piezoelectric and dielectric tensors. In a general case of orientation, the eigenvalues equation is solved:

$$\left|\Gamma^{*}_{jk} - c^{*}\delta_{jk}\right| = 0 \qquad (1)$$

where Γ^{*} is the full stiffened Christoffel matrix. It determines three piezoelectrically stiffened eigenstiffnesses, c^{*}_{m}, yielding the acoustic wave phase velocities $v_m = \sqrt{\frac{c^{*}_m}{\rho}}$, and corresponding eigenvectors $\gamma^{(m)}$, specifying the directions of particle displacement for each mode m with respect to the crystallographic axes. Important quantities associated with the vibrational modes are the values of the piezoelectric coupling factors k_m.

The LFE piezoelectric coupling factors are given by eq.2:

$$k_m(LFE) = \left|\gamma_n^{(m)}\, e_{inp}\, \alpha_{1i}\, \alpha_{2p}\right| / \sqrt{\varepsilon_{ip}\, \alpha_{1i}\, \alpha_{1p}\, c^{*}_m} \qquad (2)$$

where α_{1j} and α_{2j} are the elements of the first and second row of the rotation matrix.

The calculated results show that, in the (100) plane, the LFE is promising. The LFE coupling factors for the a, b and c modes in the (100) GaAs are given in Figure 2.

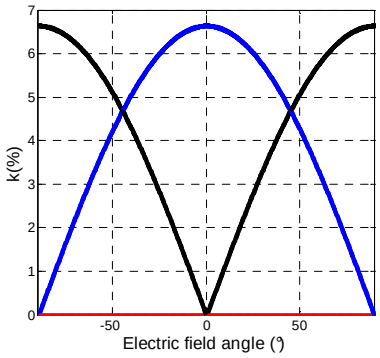

Figure 2: *Electromechanical coupling coefficients as a function of electric field angle (ψ) for the (100) cut. The three modes of vibration are given in red lines (quasi-longitudinal mode), blue lines (fast quasi-shear mode) and black lines (slow quasi-shear mode). ψ=0 indicates the <100> direction.*

These plots are symmetric about Ψ=0° (<100 direction>) which reflects an underlying crystallographic symmetry of the (100) plane with respect to this direction. It is clear that the b and c modes can be excited with a maximum value of k=6.66%. The orientation of field Ψ=0° indicates that the gap generated by the two electrodes should be normal to the <001> orientation. In this case, only the b mode is excited at the resonant frequency f_R given by eq.3 and no coupling occurs between the different modes of vibration.

$$f_R = \frac{n}{2e}\sqrt{\frac{c^{*}_m}{\rho}}\left(1 - \frac{8\,k_m{}^2}{n^2\,\pi^2}\right)^{1/2} \qquad (3)$$

where e and n are the thickness of the membrane and the positive odd number respectively.

B. Simulation

To finalize the design of the structure, the size of electrodes and the gap between electrodes must be investigated. This study was conducted using the finite element model software called COMSOL®. The membrane was excited via semi-circled electrodes of 1.4 mm diameter and a gap distance g that constitutes a variable parameter. The mass contribution of electrodes is not included. The electric potential is defined asymmetrically by a sinusoidal voltage (+/- 1V) at one electrode while keeping the other electrode grounded. First, the intensity of electric field components was investigated to verify that the given electrode structure can generate an electric field consisting of a primarily lateral component. The calculation results demonstrated that in the area between the gap (100 µm<g<1200 µm) the field is aligned parallel to the surface while just beneath the electrodes the field is aligned primarily normal to the surface.

The gap value was determined performing calculation of the displacement as a function of the gap g. Figure 3 shows the results and gives the optimal value g=100µm in the considered range.

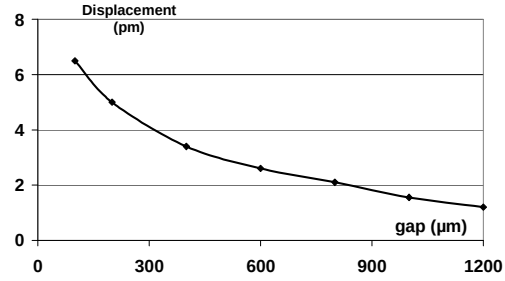

Figure 3: *Displacement (pm) versus gap (µm)*

Finally, the resonance frequency as computed from the analytical method and as evaluated by the simulator were compared; the relative deviation doesn't exceed a discrepancy of 0.3%

III- Experimental Details

Based on the design obtained with numerical and analytical calculations, we present the microfabrication process. It is based on photolithography and wet chemical micromachining technologies. Wet etching is motivated by the mass process and low cost properties.

Six steps are necessary to fabricate the membrane as shown in the flow chart given in Figure 4. The six steps consist in:

- Step 1: a cleaning process and the photoresist induction.
- Step 2: the lift-off process and the chromium-gold deposition for electrode fabrication.
- Step 3: the thinning of one face in the 7 H_3PO_4: 5 H_2O_2: 8 H_2O solution whereas the other face is protected using a chuck.

- Step 4: the thickness control which overcomes the difficulty due to the reproducibility problem of the chemical etching process for a long etching duration. It consists of a small hole whose depth, perfectly controlled, was equal to the final required membrane thickness.
- Step 5: the micromachining of the membrane in the 1 H_3PO_4: 9 H_2O_2: 1 H_2O solution. The opposite face is covered by a chuck to avoid etching and to protect electrodes. The wet etching bath composition as well as parameters such as temperature, stirring, concentration, were investigated to define the best operating conditions. The characteristics we have to take care concern the etching rates, the anisotropy ratio and the surface roughness of the membrane [20-22]. As an example, the GaAs etch rates as a function of temperature in the anisotropic 1 H_3PO_4: 9 H_2O_2: 1 H_2O solution are shown in Figure 5. To control the membrane thickness, we performed the etching at the constant temperature T=0°C.
- Step 6: the stripping of the photoresist.

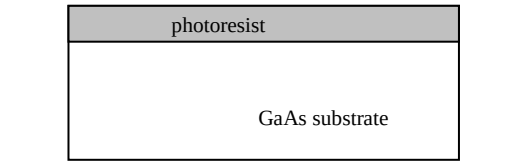

Step 1: photoresist deposition

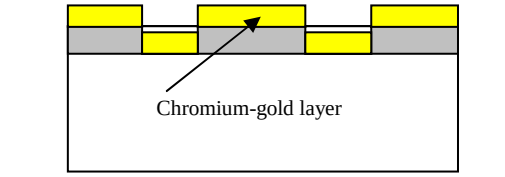

Step 2: lift-off and chromium-gold

Step 3: Thinning by chemical etching. The top side is protected by a chuck. Etching bath is 7 H_3PO_4 : 5 H_2O_2 : 8 H_2O

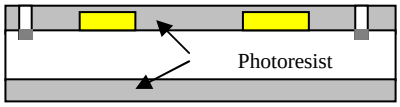

Step 4: Anisotropic wet etching of the thickness control (50µm) in H_3PO_4 : 9 H_2O_2 : 1 H_2O solution

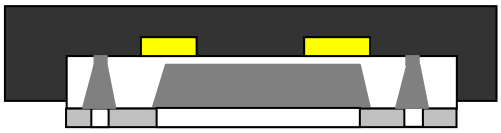

Step 5: Anisotropic wet etching of the membrane. The top side is protected by a chuck. Etching bath is H_3PO_4 : 9 H_2O_2 : 1 H_2O

Step 6 : Stripping of photoresist

Figure 4*: Flow-Chart.*

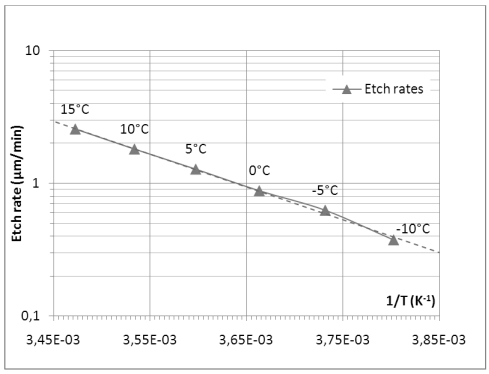

Figure 5: *(100) GaAs etch rates in 1 H_3PO_4 : 9 H_2O_2 : 1 H_2O at several temperatures T.*

IV - Results and Discussion

The micromachined membrane is then characterized using optical and atomic force microscopies. Figure 6 gives the optical images of the micromachined membrane and the semi-circled electrodes at the opposite face. The expected thickness of the membrane was 30 µm. The membrane is 150 µm depths and its surface area is 3x4 mm^2.

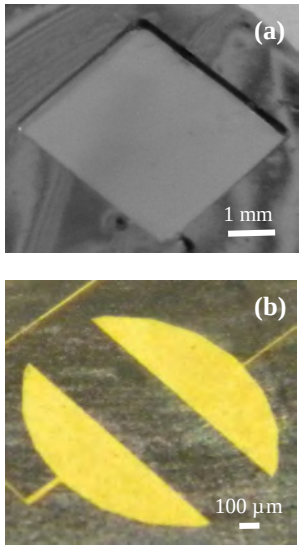

Figure 6*: Optical images of the device: (a) Top view of the micromachined membrane and (b)the electrodes coating*

The device is then packaged as seen in figure 7. The first set of experiments considers the LFE sensor in air. The measured impedance spectrum of the laterally excited GaAs membrane is shown in figure 8. The experimental impedance results show that the resonance frequency is within the expected range. A difference in the membrane thickness causes the deviation of the resonance frequency as seen in table 1.

Figure 7: GaAs device packaged for electrical measurements

The quality factor Q is equal to 2277 which gives a frequency quality factor product slightly higher than 1.1 $10^{(11)}$ which is a rather good result. Nevertheless, the electric noise around the resonance frequency is too high needing an isolation by placing a additional electrode surrounded the existing electrodes.

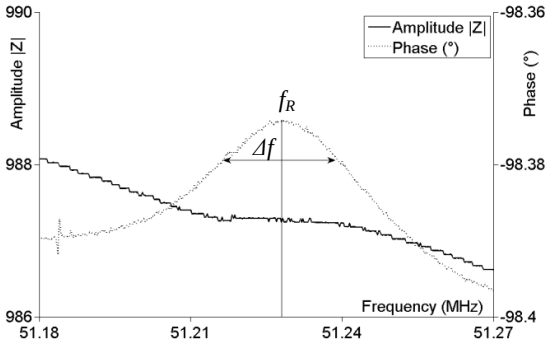

Figure 8*: Impedance measurements as a function of frequency.*

Table 1: *Comparison between theoretical and experimental results*

Parameters	Theory	experiments
Thickness e (µm)	30	32.53
Resonant frequency f_R (MHz)	55.55	51.228
Static capacitance C_0 (pF)	1.1	3.13
Static resistance R_0 (MΩ)	>200	160
Quality factor Q		2277
Product $Q.f_R$		0.114 $10^{(12)}$

V – Conclusion

A lateral excited GaAs membrane has been investigated using fundamental relations in piezoelectric theory. Finite element modeling was performed to control and optimize the electric field in the membrane. The microfabrication of the device has been proved. The electrical results show that one can expect the stress component and the resonance frequency (51.23 MHz) generated by the electrical field in <100> direction. The experimental and theoretical results are in adequation. The signal-to-noise ratio must be improved by a encapsulation of the device before testing its sensitivity to fluid parameters.

References

[1] L. Nicu, M. Guirardel, F. Chambosse, P. Rougerie, S. Hinh, E. Trevisiol, J.M. François, J.P. Majoral, A.M. Caminade, E. Cattan, C. Bergaud, *Sensors and Actuators B,* vol. 110**,** pp. 125-136, 2005.

[2] D. Maraldo, R. Mutharasan, *Sensors and Actuators B*, vol. 143**,** pp. 731-739, 2010.

[3] Y. Hu, A. French, J.K. Radecsky, M. Pereira da Cunha, P. Millard, J.F. Vetelino, *IEEE Trans. On Ultrasonics, Ferroelectrics, and Frequency Control*, vol. 51 n°11, pp. 1373-1380, 2004.

[4] S.J. Martin, G.C. Frye, K.O. Wessendorf, *Sensors and Actuators A* vol.44**,** pp. 209-218, 1994.

[5] B.P. Stehrer, H. Gruber, R. Schwödiauer, I.M. Graz, S. Bauer, *Eurosensors XXIII, Procedia Chemistry*, vol.1, pp.1507-1510, 2009.

[6] J. Zhang, S.O'Shea, *Sensors and Actuators* B, vol. 94**,** pp. 65-72, 2003.

[7] J. Soderkvist, *Sensors and Actuators A*, vol. 43**,** pp.65-71, 1994.

[8] C.R. Tellier, T. Leblois, *IEEE Trans. on Ultrasonics, Ferroelectrics, and Frequency Control*, vol. 47 n°5, pp. 1204-1216, 2000.

[9] T. Leblois, C.R. Tellier, *Sensors and Actuators A*, vol. 99**,** pp. 256-269, 2002.

[10] K. Kano, K. Arakawa, Y. Takeuchi, M. Akiyama, N. Ueno, N. Kawahara, *Sensors and Actuators A*, vol. 130-131, pp. 397-402, 2006.

[11] G. Wingqvist, J. Bjurström, L. Liljeholm, V. Yantchev, I. katardjiev, *Sensors and actuators B*, vol. 123, pp. 466-473, 2007.

[12] C.R. Tellier, G. Huve, T. Leblois, *Sensors and Actuators A*, vol. 127, pp. 179-, 2006.

[13] F. Fricke, *Journal of Applied Physics*, vol. 70, pp.1914-1918, 1991.

[14] H. Ukita, Y. Uenishi, H. Tanaka, *Science*, vol. 260, pp.786-789, 1993.

[15] K. Hjort, J. Söderkvist, J.A. Schweitz, *Journal of Micromechanics and Microengineering*, vol. 4, pp.1-13, 1994.

[16] S. Iida, K. Ito, *Journal of Electrochemical Society: Solid State Science*, vol. 118, pp. 768-771, 1971.

[17] D. Wieliczka, X. Ding, J. Dubowski, *Journal of Vacuum Science and Technology A*, vol. 24(5), pp. 1756-1759, 2006.

[18] H. Budz, R. LaPierre, *Journal of Vacuum Science and Technology A*, vol. 26(6), pp.1425-1431, 2008.

[19] A. Ballato, *IEEE/EIA International Frequency Control Symposium and Exhibition*, pp. 340-342, 2000.

[20] A. Bienaime, C. Elie-Caille, T. Leblois, *Journal of Nanoscience and Nanotechnology*, accepted, 2011.

[21] Y. Mori, N. Watanabee, *Journal of the Electrochemical Society*, vol. 147 (1), pp 1510-1514, 1978.

[22] C. Tellier, G. Huve, T. Leblois, *Sensors and Actuators A*, vol. 99, pp 256-269, 2002.

DESIGN AND MODELING OF A MEMS-BASED MICRO STIRLING ENGINE

Kerwin Khu, Liudi Jiang, and Tom Markvart

University of Southampton, School of Engineering Sciences, Southampton SO17 1BJ, United Kingdom

***Abstract* — Micro Stirling engines can be potentially useful for a number of applications such as micro scale power generation. A novel micro Stirling engine design is presented here for the first time, consisting of conventional MEMS components that could potentially be microfabricated. A linear dynamic model of the engine is derived to ensure a stable operation of the design. Finite element simulation is carried out to evaluate the MEMS components and hence the overall performance of the engine.**

***Keywords:* Micro engine, Stirling engine, Stability, Diaphragm, Membrane**

I – Introduction

Miniaturization of conventional engine designs leads to a class of devices known as micro engines, which have a number of potential benefits[1] and thus have attracted much research attention. However, previous micro engine efforts have run into difficulties in implementation. This in part due to detrimental frictional forces between the moving parts which is particularly significant at the microscale, limiting the overall efficiency of these micro engines, as well as significantly affecting reliability[2]. In addition, the requirement of complicated microfabrication processes such as multi-stack wafer bonding has also hindered the implementation of these microengines. On the other hand, MEMS components such as cantilevers and membranes that do not involve frictional or sliding contact have been operated to millions of cycles and are relatively simple to fabricate. Hence, a micro engine design utilizing these MEMS components could be promising for microfabrication as well as performance.

Stirling engines attract interest for their high efficiency, relatively simple architecture, and compatibility with renewable energy sources. Applications include power generation, cooling and refrigeration, locomotion and actuation, and thermal energy harvesting. However, there are few studies on MEMS Stirling engines which eliminate the use of sliding components. Micro Stirling engines with membranes in place of pistons and gas springs in place of kinematic cranks have previously been reported[3][4]; however, it is not clear how operational stability of these designs will be implemented.

In this paper, we report a new micro Stirling engine design using MEMS-based components including a diaphragm, a displacer suspended by cantilever beam springs, and a flexible coupling wall enclosed in a sealed cavity. This design takes inspiration from the Harwell thermomechanical generator (TMG)[5], which is a free casing type Stirling engine that features mechanical simplicity and very reliable operation. In particular, coupling walls are for the first time included in a micro Stirling engine design to enhance the stability of the engine. A linear dynamic model has been developed to ensure all the dimensions chosen will lead to stable dynamic operation. Finite element modeling has also been conducted to assess the potential performance of the design.

II – New Micro Stirling Engine Design

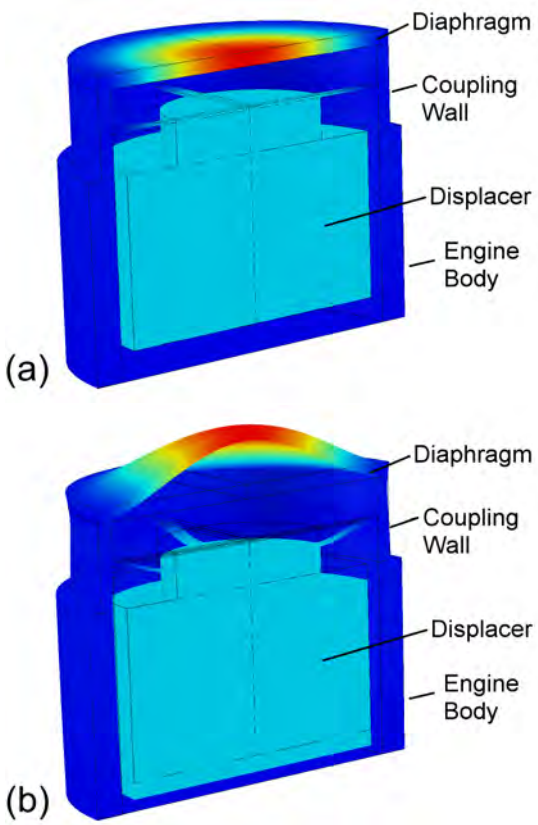

Figure 1: *(a) Cross section of micro Stirling engine (b) Micro Stirling engine when diaphragm is expanded*

The design of the novel micro Stirling is shown in a cross-sectional view in Figure 1. This is essentially a sealed cavity containing working fluid (e.g. air). Heat enters the engine through the bottom part of the engine and leaves the engine through the diaphragm at the top. The diaphragm also acts as the power piston. The flexible side wall at the top portion of the engine acts as a spring to couple displacer motion to diaphragm motion. The space between the displacer and the cavity

wall acts as a regenerator. In Figure 1(a), most of the working fluid is at the bottom part of the engine where it is exposed to heat input, causing the pressure of the working fluid to rise. This causes the top diaphragm to deflect outwards as shown in Figure 1(b). This motion of the diaphragm causes the flexible coupling wall to deflect inwards, resulting in the displacer deflecting downwards. The motion of the displacer forces the working fluid to the top part of the engine, where it is cooled through the diaphragm at the top, resulting in a decrease in pressure. This causes the engine to revert back to the original position. This is conceptually similar to the TMG design[5], but with the mechanical spring of the TMG replaced by a flexible coupling wall to improve ease of fabrication.

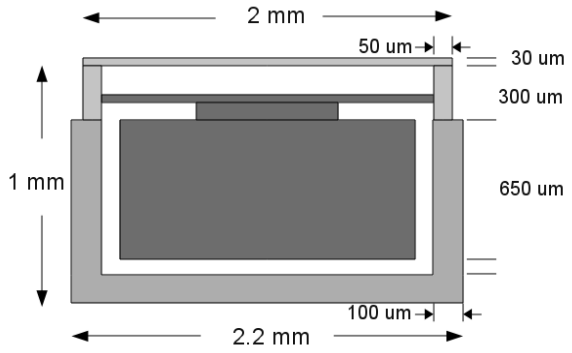

Figure 2: *Dimensions for the micro Stirling engine, shown in cross section*

In order to evaluate the potential performance of the design, we consider SU-8 for the main structural material of the engine which is built on a common silicon substrate. SU-8 is chosen for its compatibility with high aspect ratio structures as well as its low thermal conductivity (0.2 W/m-K), reducing heat leakage through the engine. To simplify the potential fabrication processes, we assume that a polymer layer (such as a thin adhesive tape) can be taped over the main engine chamber to seal the cavity, as well as serving as the diaphragm of the engine. Unpressurized air is assumed as the working fluid as it can be readily achieved during the fabrication process. Nonetheless, the main consideration in the design process is ensuring stable dynamic operation. In Stirling engines of this type, the correct choice of masses, gas springs, and other components, is necessary to ensure stable reciprocating motion[6]. In the case of the micro Stirling engine, Figure 2 shows the proposed dimensions for the design based on the linear stability study and component simulation which is presented in the following sections.

III – Linear Stability Theory

The micro Stirling engine can be modelled as a mass-damper-spring system to analyze its dynamic motion as illustrated in Figure 3. Linear dynamic analysis of the motion of free piston Stirling engines was proposed by Benvenuto and de Monte[7]. Some of the assumptions of this type of analysis are that displacements are small allowing linear approximation and that heat flow is isothermal, i.e. constant temperature is maintained throughout each chamber.

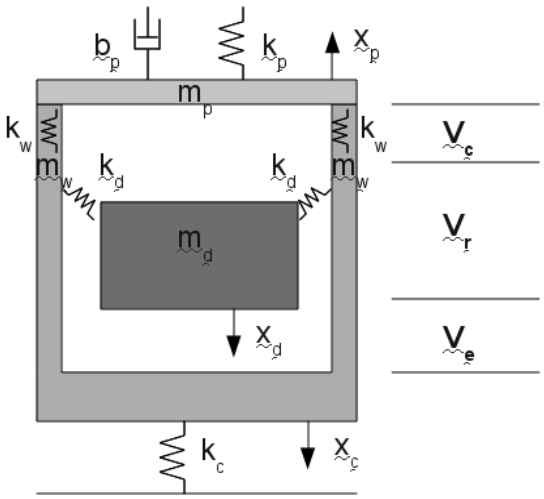

Figure 3: *Mechanical model of micro Stirling engine as lumped element mass-damper-spring system.*

The motion of the piston and the displacer in a free piston Stirling engine determines its performance. The equations of motion of the diaphragm and the displacer are obtained from the mechanical model of Figure 3, as follows:

$$m_p\ddot{x}_p = (p - p_{\text{atm}})A_p - k_p x_p - b_p\dot{x}_p - k_w x_d$$

$$m_d\ddot{x}_d = -k_d x_d - b_d\dot{x}_d$$

The pressure term p is then linearized so that the equations of motion can be written in this form:

$$\ddot{x}_p + S_{pp}x_p + S_{pd}x_d + D_{pp}\dot{x}_p + D_{pd}\dot{x}_d = 0$$

$$\ddot{x}_d + S_{dp}x_p + S_{dd}x_d + D_{dp}\dot{x}_p + D_{dd}\dot{x}_d = 0$$

Where the expressions for the linearized S and D parameters are obtained by matching coefficients, as shown in Table 1.

The criteria for stability is based on the roots of the following characteristic polynomial[7][6]. Applying the stability condition to the designed micro Stirling engine as shown in Figure 1, we find that the S_{dp} term can be isolated and thus the stability condition can be written in this form:

$$S_{dp} = \frac{1}{S_{pd}}\left(S_{pp}S_{dd} - \frac{\beta\gamma}{\alpha} + \frac{\gamma^2}{\alpha^2}\right) \qquad (1)$$

Table 1: *Expressions for the micro Stirling engine parameters*

S_{pp}	$\frac{k_p}{m_p} + \frac{\frac{1}{3}A_p^2 mr}{S_0^2 T_k}$
S_{pd}	$-\left(\frac{1}{T_k} - \frac{1}{T_h}\right)\frac{A_p A_d mr}{S_0^2}$
S_{dp}	$\frac{k_w}{m_d}$
S_{dd}	$\frac{k_d}{m_d}$
D_{pp}	$\frac{b_p}{m_p}$
D_{pd}	0
D_{dp}	0
D_{dd}	$\frac{b_p}{m_d}$

Where $\alpha = D_{dd} + D_{pp}$, $\beta = S_{dd} + D_{pp}D_{dd} + S_{pp}$, and $\gamma = D_{pp}S_{dd} + D_{dd}S_{pp}$.

Thus, to ensure stability, the parameter S_{dp} needs only to be chosen such that the equation (1) above is satisfied. The parameter S_{dp} is determined by the spring constant k_w of the coupling wall, which in turn is dependent only on the geometric (length, thickness) and material properties of the coupling wall. Thus, stable operation of the micro Stirling engine can be obtained solely from the control of coupling wall design. The appropriate parameters for the coupling wall in this work are as shown in Figure 2.

IV – Stirling Engine Modeling and Results

For dynamic analysis of the engine performance, the values for the parameters k_p, k_w, and k_d should be obtained. For this membrane-based micro Stirling engine, the flexible components act as nonlinear springs whose behaviors are determined by the mechanical load as well as the physical geometry. In order to fit the framework of linear dynamic analysis, we linearize these components into simple spring constants for the expected operating conditions of the engine.

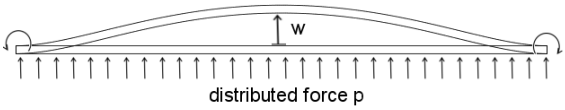

Figure 4: *Distributed force from gas pressure acting on diaphragm*

There is an analytical expression for the maximum deflection of a circular diaphragm under constant pressure[8], where the deflection is a function of the applied pressure, as well as the diameter, Young's modulus and moment of inertia of the diaphragm, as shown in Figure 4. The value for the diaphragm spring constant $k_p = 1956.5$ is obtained for the proposed design shown in Figure 2.

The flexible couple wall which is essentially a vertical bending beam acting as a spring. Ideally, the coupling wall should bend inwards when driven by the diaphragm's bending moment. At the same time,

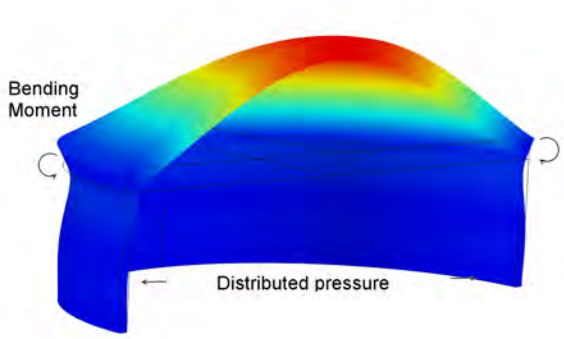

Figure 5: *Bending of diaphragm creates moment in coupling wall*

the coupling wall must be rigid enough such that the working gas pressure will not bend the coupling wall outwards. For the operation mode of the coupling wall, as shown in Figure 5, the applied force comes from the bending moment due to the diaphragm's deformation. In addition, pressure is being applied by the working fluid on the interior of the coupling wall. To obtain the equivalent linear spring constant k_w of this complex condition, finite element simulation of the structure using the commercial package COMSOL is used to obtain a table of corresponding force and deflection values.

Table 2: *Applied force and resulting deflection in the coupling wall component*

Force (mN)	Deflection (μm)
5	0.17
10	0.34
20	0.67
50	1.67
100	3.33

The spring constant k_w can be calculated from each pair of data points by dividing the applied force by the resulting deflection. These values are averaged to obtain $k_w = 29798$ for the proposed design shown in Figure 2.

The displacer is suspended on four cantilever arms, and the bending of the arms results in vertical motion for the displacer. As shown in Figure 6, the displacer arms buckle from the bending of the coupling wall, causing the displacer to move downwards. Finite element simulation is also used for the displacer motion analysis, the results of which are shown in Table 3.

Again, averaging the spring constant values obtained from this table gives an estimate for the displacer spring constant $k_d = 3703.7$ for the proposed design.

By inputing these spring constant values into equation (1), the linearized parameters can now be calculated as shown in Table 4. Using these values, the motion of the diaphragm and displacer can be calculated. For the design in Figure 2, the maximum deflection of the diaphragm is 200 μm, while the maximum deflection

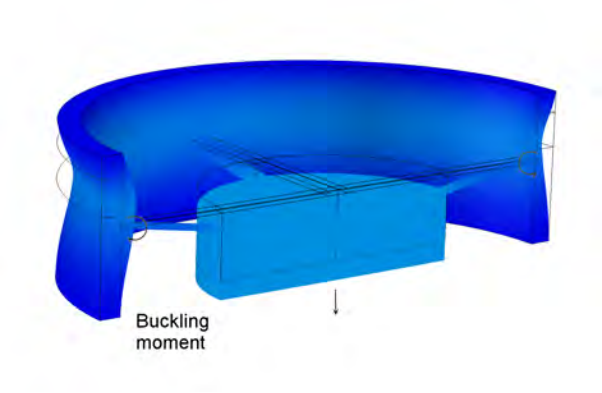

Figure 6: *Coupling wall transmits force and bending moment to displacer*

Table 3: *Applied force and resulting deflection in the displacer component*

Force (mN)	Deflection (μm)
5	1.36
10	2.71
20	5.40
50	13.4
100	26.7

of the displacer is 50 μm. The engine exhibits stable dynamic operation at a speed of 19.2 kHz. Pressure varies from 97 kPa to 113 kPa while volume varies from 0.39 mm^3 to 0.48 mm^3.

Performance improvement could come from use of a lower density working fluid, higher charge pressure, or higher operating temperature. The design could also be further optimized by reducing the amount of dead space inside the engine chamber. Note though that the current approach only involves mechanical design of the micro Stirling engine. Thermodynamic considerations such as heating and cooling rate would greatly influence the actual operating speed.

V – Conclusion

A novel micro Stirling engine design is presented in this paper which is compatible to conventional MEMS fabrication process as well as having potentially very reliable operation. Linearized dynamic modeling has been utilized for the stability analysis. In particular, a new coupling wall feature is included in the design which is directly linked to the dynamic stability of the engine. More importantly, since the coupling wall can be designed such that it is independent from the rest of the system, it enables easy control of the design to ensure stable operation. In addition, the dynamic motion of the key microengine components such the diaphragm, coupling wall, and displacer are analyzed, and the potential performance of the designed micro Stirling engine is obtained. Experimental verification of the design components and their implementation through MEMS microfabrication processes will be the main focus of future work.

Table 4: *Values for the micro Stirling engine parameters*

S_{pp}	$1.85 \cdot 10^{10}$
S_{pd}	$-9.2 \cdot 10^{9}$
S_{dp}	$7.41 \cdot 10^{9}$
S_{dd}	$7.87 \cdot 10^{8}$
D_{pp}	15000
D_{pd}	0
D_{dp}	0
D_{dd}	50000

VI – Acknowledgements

The authors would like to thank Fabien Formosa for many illuminating discussions.

References

[1] Stuart Jacobson and Alan Epstein. An informal survey of power MEMS. In *Proc. International Symposium on Micro-Mechanical Engineering*, December 2003.

[2] Derek Dunn-Rankin, Elisangela Martins Leal, and David C. Walther. Personal power systems. *Progress in Energy and Combustion Science*, 31(5-6):422–465, 2005.

[3] Lyn Bowman and Jariath McEntee. *Microminiature Stirling Cycle Cryocoolers and Engines*. US Patent No. 5,749,226, 1995.

[4] Fabien Formosa. Nonlinear dynamics analysis of a membrane stirling engine: Starting and stable operation. *Journal of Sound and Vibration*, 326(3-5):794–808, October 2009.

[5] E H Cooke-Yarborough. Stirling-cycle thermomechanical power sources for remote or inaccessible communications sites. In *Telephone Energy Conference, 1978. INTELEC '78. International*, pages 71–78, Oct. 1978.

[6] E. D. Rogdakis, N. A. Bormpilas, and I. K. Koniakos. A thermodynamic study for the optimization of stable operation of free piston stirling engines. *Energy Conversion and Management*, 45(4):575–593, March 2004.

[7] G. Benvenuto, F. De Monte, and F. Farina. Dynamic behaviour prediction of free-piston stirling engines. In *Energy Conversion Engineering Conference, 1990. IECEC-90. Proceedings of the 25th Intersociety*, volume 5, pages 346–351, Aug. 1990.

[8] J. N. Reddy. *Theory and analysis of elastic plates and shells*. CRC Press, 2007.

FACILE FABRICATION OF SELF-ORGANIZED, FREE-STANDING TITANIUM DIOXIDE NANOTUBE MEMBRANES

Guohua Liu, Nils Hoivik, Kaiying Wang and Henrik Jakobsen

Department of Micro and Nano Systems Technology, Vestfold University College - Hive, Horten, Norway

***Abstract* — in this paper, a series of experiments have been carried out to understand the formation mechanism and to increase control over the morphology of free-standing TiO_2 nanotube membranes. It was found that immobilized TiO_2 nanotube arrays with ordered structure were prepared under anodization with low voltage (≤60V). High anodization voltage (>80V) can directly induce detachable nanotube membranes, but the surface of membrane is covered by many disordered nanowire. A facile two-step anodization has been developed to solve this problem. By taking advantage of conventional anodization of Ti, followed by a thermal treatment and an additional low voltage anodization step, crystallized free-standing membrane with ordered TiO_2 nanotube arrays has been synthesized. The resulting membrane is mechanically robust and can be obtained over a large area. The ability to fabricate this free-standing TiO_2 nanotube membrane is an essential step towards the exploitation of extended applications.**

Keywords : **TiO_2 nanotube, free-standing, membranes, anodization**

I - Introduction

TiO_2 nanotube (TNT) arrays have attracted a growing interest in recent years because of their remarkably enhanced photoelectric properties and technological importance for various applications, including photovoltaic [1], catalysis [2], gas sensors [3], nano-template [4] and conversion of CO_2 into small organic molecules [5]. Among various synthesis methods demonstrated, electrochemical anodization is an excellent approach to fabricate TNT arrays due to its simplicity, low cost and the ease of controlling nanotube morphology [6]. However, the nature of as-prepared TNT membranes adhered on opaque Ti foil restricts their feasibility for further applications. As an example application in solar cell, the opaque Ti substrate precludes the use of front illumination, which severely limits the cells efficiency because the light intensity is attenuated by the Pt electrode and the iodine electrolyte [1, 7]. Free-standing TNT membranes have shown better performance than the nanotube layer on a Ti foil due to the absence of a blocking layer [1]. The advantages of free-standing nanotube membranes lie on their optimized microstructure, direct electrons transfer, stability to mechanical vibrations, and it also can be directly used or attached onto other substrates.

Several procedures have been investigated for the synthesis of free-standing TNT membranes, including ultrasonic splitting [3], solvent evaporation [8], chemically assisted delamination [9] and selective dissolution of the metallic substrate [2]. The method to decrease or increase the voltage [7] at the end of anodization process has also been developed. However, applications of these free-standing membranes in devices were greatly hampered by their amorphous crystalline. To get crystallized TNT arrays, the free-standing membrane should be further annealed at high temperature, but this process causes the membranes normally curling up and even fracturing into small pieces. Other attempts including selective dissolution of the amorphous layer between the desired crystalline TNT array and the Ti substrate were also proposed [3]. Nevertheless, fabrication of large-area and crystallized free-standing TNT arrays is still remains a challenge. Herein, a series of experiments have been carried out to prepare free-standing TiO_2 nanotube membranes in this study.

II - Experimental Details

Before anodization, Ti foils are cut into the required size and shape (15mm×32mm×0.3mm, 99.8% purity), degreased in acetone for 10 min, followed by an isopropyl alcohol rinse and ultrasonically cleaned in distilled water. Then after drying it in air for about 1h, the Ti foil's backside are protected by a scotch tape and put into a polyflon cell with a rectangular area of 4 cm^2 exposed to the electrolyte.

The conventional anodization was performed in a two-electrode configuration connected to a DC power supply with Ti foil as the working electrode and Pt foil as the counter electrode, under constant potential at room temperature approximately 20^oC. The distance between two electrodes is 3.5cm. A magnetic stirring apparatus (60 rpm) was used to make sure that the reaction occurred in a uniform electrolyte. An ethylene glycol composition of 0.5wt% ammonium fluoride (NH_4F) and 3vol% water was employed as electrolyte.

An effective two-step anodization with handy experimental procedures is developed for fabrication of free standing crystalline TNT membranes, as in figure 1. The process starts with the preparation of high aspect-ratio TNT arrays on Ti foil first (figure 1a), and then the membrane was ultrasonically washed in ethanol solution to remove the electrolytes, followed by annealing at high temperature to crystallize the membrane (figure 1b). Subsequently, the as-annealed film was anodized again in the same stock electrolyte with a bias of voltage (figure 1c). After the secondary anodization and rinsed in ethanol, the crystallized TNT arrays on the first layer was easily separated from the substrate (figure 1d).

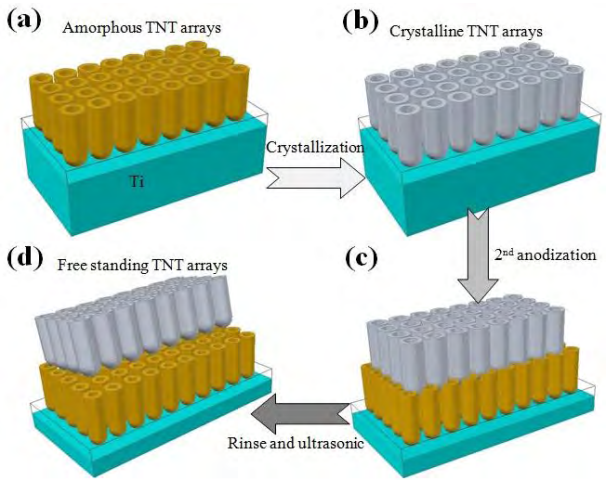

Figure 1: *Schematic illustration of the fabrication process of the crystallized free-standing TNT membranes*

III - Results and Discussion

A. TNT arrays prepared by conventional anodization

In conventional anodization, we carried out a voltage-dependent investigation on the morphology evolution of the TNT membranes. Figure 2 presents typical SEM images of the obtained TNT membrane. The samples in figure 2a~c are anodized under 40V, 60V, 100V for 6h respectively. Then it was rinsed by pure alcohol and mild ultrasonic in ethanol followed by drying in air. The insets are digital images and the top-view SEM image for nano-oxides at 100V. The digital images clearly show that the color of anodized Ti changes from gray at 40V to dark at 60V. This uniform colored nanotube membranes adhere firmly to the substrate. The SEM images indicate that their surface morphology constituted by highly ordered TNT arrays. The diameter of the TNT increased from 65nm to 120nm corresponding to 40 and 60V. Further increasing the anodized voltage to 100V, the sample surface will be deposited by lots of white oxides, and the nanotube layer also easily detached from substrate, as indicated by the inset image in figure 2c. It clearly illustrate that lots of nanograss cluster on the sample surface. This comparably dense, disordered layer presents after long anodization times is in literature mostly referred to as nanowire [10]. Although after repeated ultrasonic agitation, nanowire can be removed and a clear surface morphology appeared as in figure 2c. But the disordered TNT will be present on the surface.

B. Amorphous free-standing TNT membranes

To clarify the separation mechanism of the amorphous free-standing TNT membranes, typical SEM images of free-standing TNT arrays anodized at 80V were shown in figure 3. Figure 3b presents the top-view image of the TNT membrane. It shows that lots of nanowires cluster on the surface which resulting from bundling of nanotubes and microcracks in oriented TiO_2

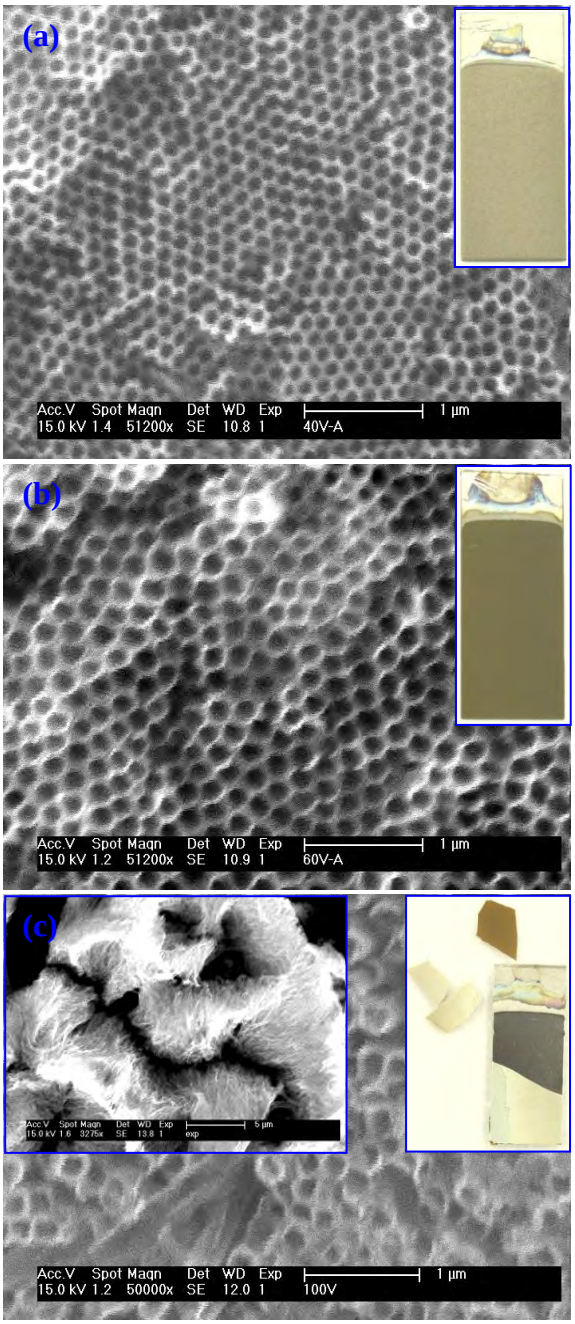

Figure 2: *Typical SEM top-view and optical images of TiO_2 nanotube arrays obtained by conventional anodization at (a) 40V, (b) 60V, (c) 100V for 6h.*

arrays. This architectural disorder is caused by the nanotube lateral deflection resulting from the action of capillary forces between adjacent nanotubes during evaporative drying of the wetted films [10]. Figure 3c display the cross section image of the tube, the tubes were of average length of 310 µm and straight with a diameter of 160nm. Figure 3d shows the surface morphology of the bottom of TNTs array. A barrier layer existed between the TNTs and the Ti substrate, and which result in the closed bottom. The outer diameter of the tube is ~200nm. In the barrier layer, the ions migrated through the oxide film and upon arrival at the oxide-metal interface forms a sacrificial soluble oxyfluoride layer. This thin layer forms because various

anions (F^-, O^{2-}, OH^-) and metal cations M^{n+} combine in many different ways at the interface. The prior study has indicated that the relatively fast migration of fluoride ions as compared to other ions (such as O^{2-}) account for the poor adhesion between the metal oxide membrane and the underlying substrate [11]. The presence of trace amounts of element is observed from the energy-dispersive X-ray spectroscopy analysis (EDX). The characteristic peaks in the spectrum are composed of Ti, F and O ignoring some undetectable light elements and background signals. Strong K_α and K_β signals from Ti were seen at 4.51 and 4.93 keV, respectively. The L_α peak from Ti is at 0.452 keV and the K_α peak from O is at 0.523 keV. The quantitative analysis results in figure 3a reveals that the weight ratio of each element on the sample, indicating a large occupation of oxides on the membrane surface then that of the patterned substrate.

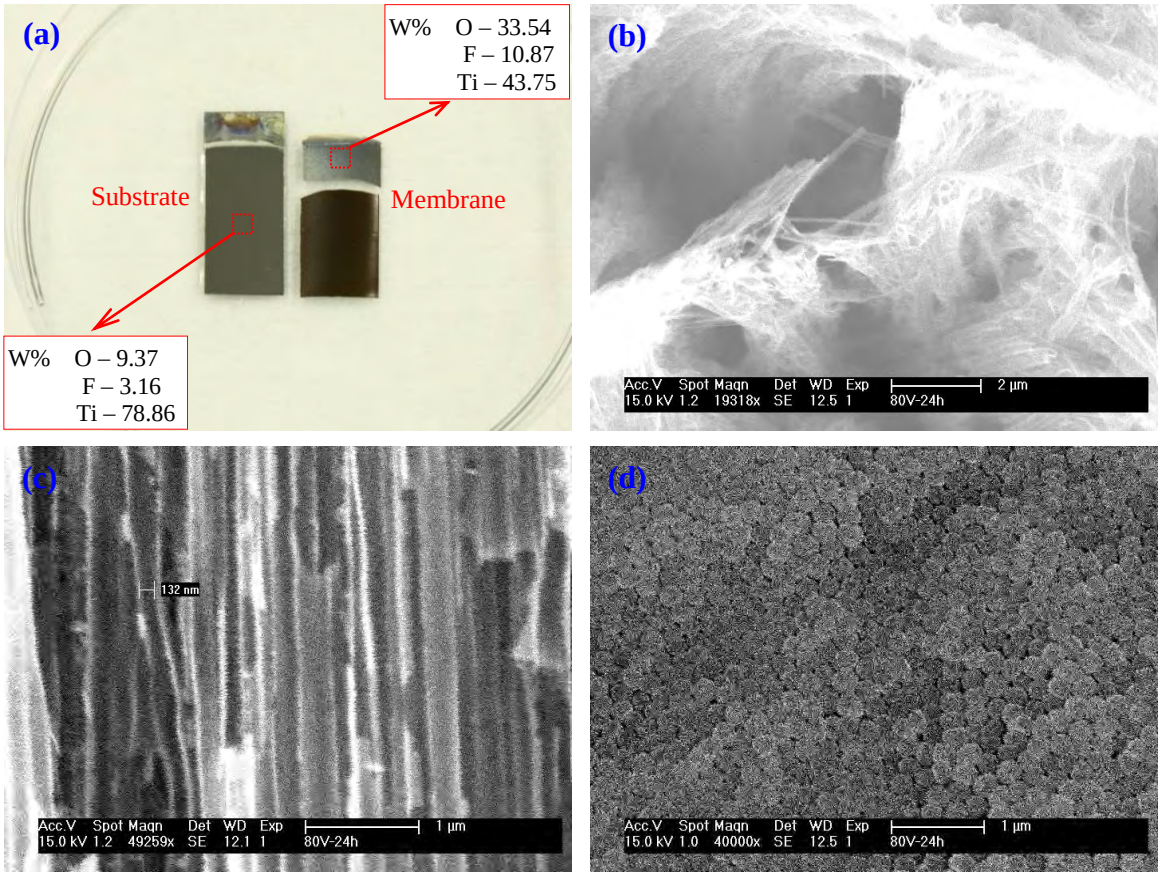

Figure 3: *Photograph and SEM images of the amorphous free-standing TNT membranes, the sample was anodization at 80V for 24h then rinsed by ethanol (a) photograph, (b) top view, (c) cross section morphologies,(d) bottom view.*

C. Crystallized free-standing TNT membranes obtained by two step anodization

Typical SEM images of crystallized free-standing TNT arrays obtained by two-step anodization are shown in figure 4. Figure 4b shows the SEM top-view images of the membrane. It indicates that the TiO_2 nanotube arrays remain compact and no destructive changes are observed after they are peeled from the Ti substrate. The average inner diameter of the nanotube is about 140 nm with a wall thickness of 25 nm. Based on measurement on the cross-section of the TNT membrane (figure 4c), the tube length is found to be ~15µm. That can be explained that the oxide dissolution occurs after repeated anodization, so the thickness of the membrane is greatly reduced. The bottom view of the free-standing TiO_2 nanotube membrane (figure 4d) shows that the arrays were preserved and the bottom of tube thermal treated at 500 ℃ is closed. The thin non-ordered compact oxide layer is present at the bottom of crystallized layer. A new layer was formed during the second step under the barrier layer. After separation of the crystallized membrane, the trace amounts of element on the membrane surface and the substrate are analysis by EDX (insets in figure 4a). The quantitative results illustrates that the weight ratio of O and Ti element on the top surface and on the patterned substrate is quite similar, indicating that the crystallized membrane and the under layer are all composed by TNT arrays. The large weight ratio of F on the substrate is due to the residue barrier remained on the top surface of amorphous layer 2. This can be explained that after thermal treatment, anatase crystals formed on the top layer which shows high resistance to chemical etching. While the lower tube layer formed by 2nd anodization presents an amorphous structure. Therefore, the crystallized TiO_2 membrane on top layer can be easily peeled off by taking the advantage of the different material properties between the layers.

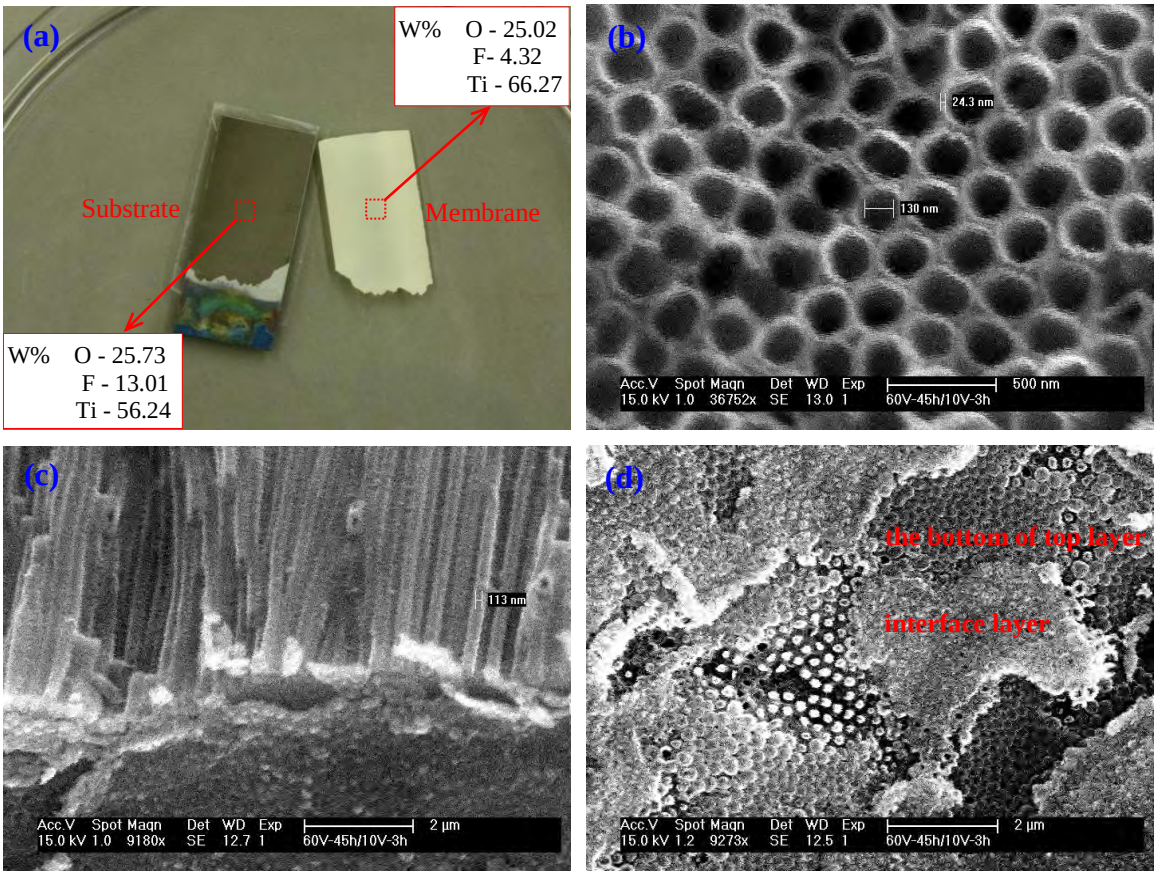

Figure 4: *Photograph and SEM images of the free-standing TNT membranes, the sample was first anodized at 60V for 45h, then annealing at 500^{o}C for 3 hours before further anodization at 10V for 3hours (a) photograph, (b) top view, (c) cross section morphologies, (d) bottom view.*

IV - Conclusion

In conclusion, we have experimentally demonstrated that under anodization at low voltage (≤60V), only immobilized TiO_2 nanotube arrays was prepared. Although the amorphous free-standing TiO_2 nanotube membrane can be synthesized under high anodization voltage (>80V), but the morphology of membrane is deposited by disorder nanowire. And also the membrane is easily breakup into small pieces. A facile and reliable two-step anodization method has been developed. In this process, highly ordered TNT arrays can be obtained under optimized electrochemical condition in first step, then after a thermal treatment and followed by a further step of low voltage anodization. A free-standing crystallized TNT membrane with ordered nanotube arrays could be separated from the substrate by taking advantage of different mechanical stability between the layers. The prepared membranes feature high-quality surfaces and this method would be generally applicable for the synthesis of various metal oxide membranes.

Acknowledgment

We are grateful to Zekija Ramic and Ragnar D. Johansen for help of the experimental set up, Tormod Vinsand and Knut Aasmundtveit for help with SEM.

References

[1] B.X. Lei, J.Y. Liao, R. Zhang, J. Wang, C.Y. Su, D.B. Kuang, *J. Phys. Chem. C.* 114, pp.15228-15233, 2010.

[2] S.P. Albu, A. Ghicov, J.M. Macak, R. Hahn, P. Schmuki, *Nano Lett.* 7(5), pp.1286-1289, 2007.

[3] Q.W. Chen, D.S. Xu, Z.Y. Wu, Z.F. Liu, *Nanotechnology.* 19, 365708 (5pp), 2008.

[4] D. Fang, K.L. Huang, S.Q. Liu, Z.P. Luo, X.X. Qing, Q.G. Zhang, *J. Alloys Compd.* 498, pp.37-41, 2010.

[5] O.K. Varghese, M. Paulose, T.J. LaTempa, C. A. Grimes, *Nano Lett.* 9(2), pp.731-737, 2009.

[6] Y. Shin, S. Lee, *Nanotechnology.* 20, 105301 (5pp), 2009.

[7] D.A. Wang, L.F. Liu, *Chem. Mater.* 22, pp.6656-6664, 2010.

[8] J. Wang, Z.Q. Lin, *Chem. Mater.* 20, pp.1257-1261, 2008.

[9] D.A. Wang, B.Yu, C.W. Wang, F. Zhou, W.M. Liu, *Adv. Mater.* 21, pp.1964-1967, 2009.

[10] K. Zhu, T.B. Vinzant, N.R. Neale, A.J. Frank, *Nano Lett.* 7(12), pp.3739-3746, 2007.

[11] S. Singh, M. Festin, W.R.T. Barden, L. Xi, J.T. Francis, P. Kruse, *ACS Nano.* 2(11), pp. 2363-2373, 2008.

STATIC BUCKLING OF TOP-DOWN FABRICATED SILICON NANOWIRES

P.E. Allain, X. Le Roux, A. Bosseboeuf, F. Parrain

[1]*Univ. Paris Sud, Institut d'Electronique Fondamentale, UMR CNRS 8622, 91405 ORSAY Cedex, France*

***Abstract* — Single crystal Silicon nanowires with a width down to 20 nm and a length to width (L/w) aspect ratio up to 150 were fabricated by surface micromachining of thin SOI wafers. It is demonstrated that such top-down fabricated clamped-clamped nanowires are laterally buckled when L/w is larger than 36. This is attributed to an unexpected high compressive residual stress estimated to be in the 270-335 MPa range from a simple post-buckling model. Origin of this stress is investigated by considering several axial stress generation mechanisms in the Si nanowires such as thermomechanical stresses, surface layers and dies deformation stresses induced by patterning or die attachment.**

***Keywords:* nanowires, silicon, SOI wafers, mechanical stress, buckling**

I - Introduction

From a fundamental point of view, silicon nanolines and nanowires are attractive low dimensional structures for the investigation of size effects on electrical or thermal transport in silicon nanostructures and on their electrical or optical properties [1]. Their high potential for sensing applications was also demonstrated for mechanical, chemical and bio sensors and for electronic devices [1-4]

Control of the mechanical residual stress in nanolines or released nanowires is requested as stress can induce large deformations and/or variations of their properties. Elastic properties and/or fracture strength of Si nanowires were measured by several authors (see for example [5, 6]) but only few experimental works have been published on stress measurements and modeling in these nanostructures: buckling of Si nanowires grown by Vapor Liquid Solid (VLS) was investigated by S.R. Ryu et al. for transferred nanowires on elastomers [7] and by C.-H. Hsin et al. for nanowires loaded by a manipulation probe [8]. In this work, buckling of top-down fabricated nanowires induced by internal compressive stress is investigated, to our knowledge, for the first time. This phenomenon was observed in a reproducible way on two different types of thin Silicon on Insulator (SOI) wafers. The experimental results are analyzed from analytical models or from FEM simulations of various possible stress generation mechanisms such thermomechanical stresses, surface layers and die bending induced stresses.

II - Experimental Details

Single crystal silicon nanowires with various widths in the 20 nm to 150 nm range and lengths in the 2 µm to 3.5µm range were fabricated by surface micromachining of 2x2cm^2 thin SOI dies by the following processes.

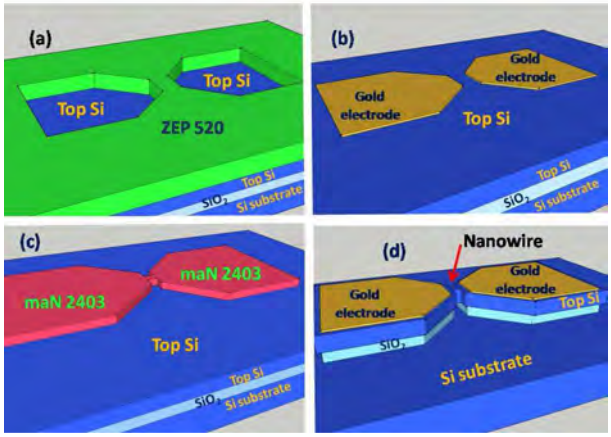

Figure 1*: Silicon nanowire device fabrication steps*

For the first run (batch 1), dies were cut into a 100 mm in diameter SOI wafer purchased from SOITEC Company. This wafer has a 1 µm thick buried oxide and a 340 nm thick top Si layer (substrate thickness: 525 µm) with a Boron doping level of $7.5x10^{14}$ cm^{-3}. The top layer was thinned to 220 nm by successive dry thermal oxidation and BHF chemical etching steps. This set of devices includes Au electrodes patterned by lift-off for further electrical measurements. First a positive resist (ZEP 520) was spin coated at 1000 rpm onto the top Si layer. For each device this resist was patterned over a field of 500X500 µm^2 with a Raith 150 electron-beam lithography system (Figure 1a). An e-beam energy of 20 keV, a writing dose of 70 µC/cm² and a step size of 20 nm, were used for this lithography step. A 20 nm layer of Chromium and a 150 nm layer of Gold were then deposited by e-beam evaporation and patterned by lift-off (Figure 1b). Si nanolines along the <100> direction were then patterned by e-beam lithography over a smaller writing field of 50x50 µm² by using a maN 2403 negative photoresist spin-coated at 3000 rpm (Figure 1c). This resist was e-beam written at 20 keV with a step size of 8 nm (dose: 145 µC/cm²). The resist was then developed in a MIF 726 bath for 30 sec. The unprotected top silicon layer was then etched at 5 °C by reactive ion etching in a SF_6/O_2 plasma. For the used generator power (30 Watts), the measured electrical potential was 265 Volts. SEM observations have shown that the nanolines patterns were straight whatever their size. The nanowires were then released by HF vapor etching of the buried silicon oxide (Figure 1d). A high resolution SEM picture of a 100 nm wide nanowire device fabricated by this process is shown in Figure 2. As detailed below, nanowires with high aspect ratio were found laterally buckled.

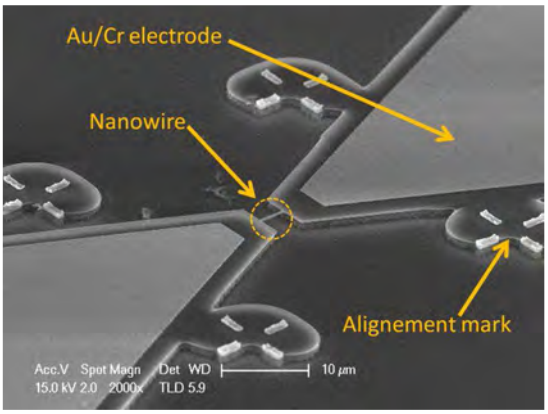

Figure 2*: SEM-FEG image of a Si nanowire device with alignment marks and contact electrodes.*

The second batch of nanowire devices was made from a 725 µm/400 nm/160 nm, 200 mm in diameter SOI wafer also purchased from SOITEC Company. The top Si layer had a similar dopant concentration (Boron concentration: $5x10^{-14}$ cm^{-3}) as in the SOI wafer used for the first batch. For this second batch, the Au/Cr metallization step was skipped to avoid its eventual influence on nanowire buckling. The electron-beam lithography step of nanolines was performed with the same negative resist but with a spin coating speed of 5000 rpm and a writing step size of 2 nm. All other parameters of the nanowire fabrication process were the same as for the first batch. Again, all high aspect ratio Si nanowires fabricated in this second batch were found in-plane buckled after fabrication.

III - Results and Discussion

After a closer look of SEM images, we noticed that all released Si nanowires having a length to width aspect ratio of above 36 were laterally buckled.
This is illustrated in the SEM pictures of Figure 4 for a set of 3.5 µm long nanowires with different widths.
The shapes of most buckled beams were found to be in very good agreement with the first buckling mode shape of a prismatic beam.

This is demonstrated in Figure 3 where the measured longitudinal profile of a 2 µm long, 42 nm wide and 160 nm thick nanowire is compared to the textbook theoretical buckling mode shape given by:

$$\frac{\delta(x)}{\delta_{max}} = \frac{1}{2}(1 - Cos\frac{2\pi x}{L}) \qquad (1)$$

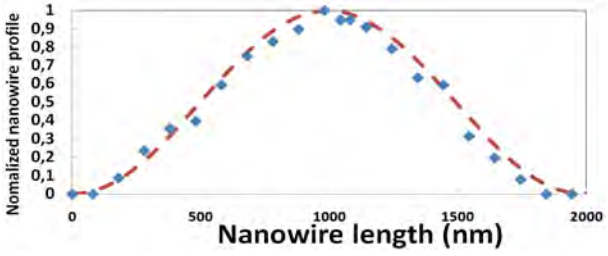

Figure 3: *Comparison of measured normalized deflections (dots) and theoretical first buckling mode shape (dashed line) of a 42 nm wide Si nanowire.*

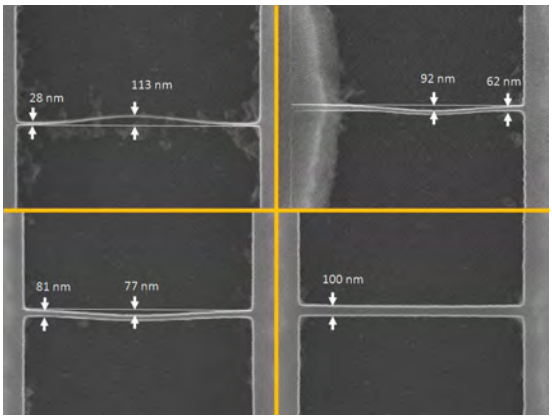

Figure 4: *SEM pictures of Si nanowires (batch 1) with different widths. L=3.5* µm*, Thickness t=220 nm.*

Where δ is the lateral deflection, δ_{max} its maximum value at the nanowire center and L is the nanowire length. In the following sections, we apply a simple post-buckling model to estimate the required compressive stress for Si nanowire buckling and then we analyze various mechanisms which can induce stress in the Si nanowires during fabrication or observation.

A. Post-buckling analysis

Straightforward linear buckling analysis predicts that the critical stress over which a nanowire with a rectangular cross section w×t (t>w) buckles, is given by:

$$|\sigma_c| = \frac{E\pi^2}{3}\left(\frac{w}{L}\right)^2 \qquad (2)$$

Where L, w, t and E are respectively the length, the thickness, the width and the longitudinal Young's modulus of the nanowire.

By adapting to our case the simple non linear post-buckling model of W. Fang et al. [9], it can be shown that the maximum normalized central deflection δ_{max} /L in the post-buckling regime ($|\sigma|>|\sigma_c|$) is given by:

$$\frac{\delta_{max}}{L} = \frac{2}{\pi\sqrt{E}}\sqrt{|\sigma| - \frac{E\pi}{3}\left(\frac{w}{L}\right)^2} \qquad (3)$$

Where σ (σ<0) is the compressive initial stress in the nanowire before buckling.

This model was applied to a set of Si nanowires with different lengths and widths fabricated in batch 1 and 2. Some of the narrowest nanowires (<25 nm) were defective and an absence of stiction on the substrate could not be warranted for other ones having very large aspect ratio (>150). These nanowires were discarded for the analysis.

Figure 5 shows experimental values of the normalized maximum deflection as function of inverse aspect ratio w/L and the critical stress together with theoretical post-buckling curves for different stress amounts. This analysis demonstrates that the compressive stress required to explain the experimental results is in the 270-335 MPa range.

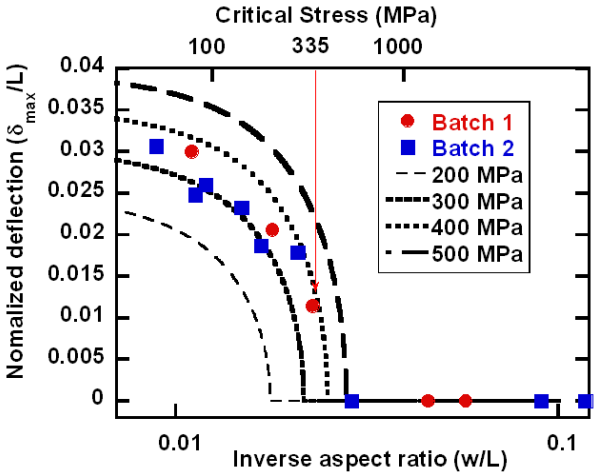

Figure 5: *Buckling induced maximum deflection of different nanowires versus their inverse aspect ratio (width over length). Top axis: Critical stress. Dashed lines: theoretical curves for E=130GPa, σ=200 to 500 MPa (see text)*

Values were found higher for batch 1 (SOI wafer with 1 µm buried oxide) than for batch 2 (0.4 µm buried oxide). In both cases, these values are unexpectedly very high. However they are slightly underestimated by this model which does not take into account lateral SiO_2 underetching at the clamped ends of the Si nanowires. Underestimated values of the buckling stress can be calculated by considering that the lateral underetching blocks relax part of the compressive stress. The new critical stresses values are accordingly imperceptibly higher by a factor of 1.002 for a 1 µm-deep underetching (the width of this extra silicon has been taken to be 5 µm). The extra silicon is indeed very stiff because of its geometry. This fact has been confirmed by FEM analysis and by a simple model that uses Hooke's law.

B. Discussion

As mentioned in part I, buckling of VLS grown Si nanowires was already observed but it was induced by loading or by its transfer on flexible substrates. To our knowledge, stress-induced static buckling of top-down fabricated Si nanowire was not yet reported. Lateral buckling of SiO_2 nanowires was already observed and used to realize a bistable device by B. Charlot et al. [10] but in that case a high compressive residual stress in SiO_2 is expected. This not the case for Si nanowires fabricated from a thin SOI wafer in which, according to the SOI wafers manufacturer, the residual stress in the top Si layer should be low.

In the following we analyze various stress generation mechanisms in order to attempt to clarify the origin of the axial compressive stress responsible for nanowire buckling.

1) Stress generation during SOI wafer fabrication

Several processing steps can generate stress during the SOI wafer fabrication: SiO_2 growth, wafer direct bonding, and thinning/polishing of the top Si layer. Parameters are proprietary of SOITEC Company but the SOI wafer fabrication clearly involves high temperature steps for SiO_2 growth and wafer bonding. After thermal oxidation, the SiO_2 layer is expected to be in compressive stress with a stress value of a few hundred MPa. Some thermomechanical stress can remain after bonding in the top Si layer if it is performed at a lower temperature than SiO_2 growth

The resulting thermomechanical stress distribution was estimated by using the model elaborated by X.C. Zhang et al [11]. This model provides the thermomechanical stresses in a multilayer system after a temperature variation. Both the thermally induced strain and the resulting bending strain are taken into account. By using the layer and substrate thicknesses, the Young moduli and the thermal expansion coefficients as inputs of this model, it can be shown that the resulting stress in the top Si layer cannot exceed a few 0.1 MPa even for a temperature difference of 500°C between the SiO_2 growth and the wafer bonding steps. In addition, if we make the reasonable assumption that the wafer bonding temperature is lower than the thermal oxide growth temperature; a tensile stress is predicted in the top silicon layer. Moreover stress relaxation might occur at high temperature by viscous flow of the oxide. Lapping, polishing and thinning during SOI wafer fabrication could generate compressive stress into the top Si layer but we did not observed die curvature by optical profilometry. This is in agreement with findings of SOITEC Company who claimed that the top Si layer of their SOI wafer should have a very low stress. It is therefore clear that the high compressive stress on the top layer should not arise from SOI wafer fabrication.

2) Surface layers

Various surface layers may be generated on the Si nanowires during and after processing: An amorphized silicon surface layer may be produced during RIE etching of silicon [12]. It is known that Si amorphization induces a high compressive stress (up to -100 MPa) [13]. In our case only nanowire sidewalls exposed to the plasma might be amorphized. From the electrical potential observed during RIE etching (265 V), we can estimate that the thickness of this damage layer should be much lower than 10 nm. A native silicon oxide grows in air all around the Si nanowires after their HF vapor release. This native oxide of silicon, grown at room temperature, is estimated to be in the 0 to 1.5-2.5 nm range according to air exposure time and previous cleaning procedure [12]. Stress in this typically carbon contaminated hydroxide film is difficult to estimate but the extrapolated value at zero thickness of the average compressive stress of SiO_2 films was found to be -400 MPa at all temperatures [13]. This value can then be taken as the maximum stress value in the native oxide. Finite elements simulations were performed to estimate the axial stress that could be generated in the nanowires by these surface layers. Figure 6 (top) shows that even in the worst case of the narrowest simulated nanowire (width 10 nm, length 3 µm) the generated axial com-

pressive stress in this Si nanowire does not exceed -35 MPa for a 2 nm thick SiO_2 film having a -100 MPa compressive residual stress. Values of the same order of magnitude were obtained in the case of an amorphized layer on the sidewalls of nanowires (Figure 6 bottom): for a 10 nm thick amorphized layer around the worst case 30 nm wide nanowire, the stress value is around -67 MPa if the amorphized silicon has a -100 MPa residual compressive stress. The generated axial stress being proportional to the film residual stress it is clear that surface layers can only very partly explain the high compressive stress responsible for the buckling of nanowires.

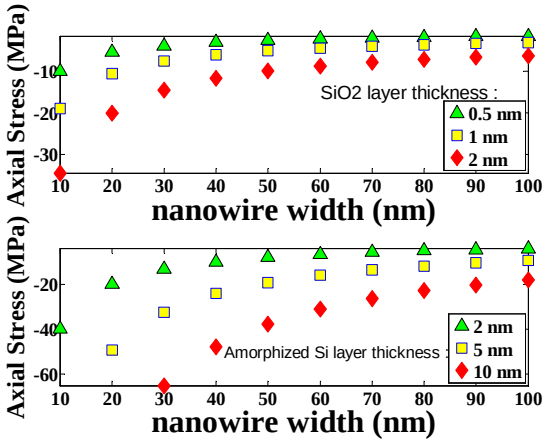

Figure 6: *Axial compressive stress in nanowire induced by SiO_2 layer (top) and amorphized Si layer (bottom). Both layers have a residual stress of -100 MPa; computed for 3.5 µm long, 160 nm high nanowires.*

3) Die bending

A surface stress might be generated in the top Si layer if the dies becomes more concave (or less convex) during fabrication or testing. During fabrication, most of the top Si layer and buried oxide are removed. As the buried oxide is expected to be in compressive stress, such a die curvature variation might occur. Likewise, if the die has a convex shape after fabrication, an axial compressive stress on the nanowires could be generated during die clamping required for SEM observations. 3D surface profiles of bare and processed dies were measured with a Fogale nanotech interferometric optical profiler to check these assumptions. In all cases die bows lower than about 30 nm were measured for areas of 1.2 mm in diameter so stress generation by die bending is not a major cause of buckling of the Si nanowires.

IV - Conclusion

It was demonstrated that an unexpected high compressive stress may be generated in silicon nanowires fabricated by surface machining of SOI wafers. Origin of this stress could not yet be identified, however the effect of thermomechanical stresses during SOI wafer fabrication, of surface layers and of die bending during fabrication and testing could be eliminated as major contributions of this stress. Thorough post-buckling FEM analyses are in progress to extract a more accurate value of the maximum deflection. Occurrence of a large stress in silicon nanowires fabricated by the top-down approach must obviously be considered for future investigations of transport phenomena in these devices and of their properties as well as for their applications in sensors.

Acknowledgments

This work was supported by the French national Agency of Research (ANR) as a part of the “ARIANE” project (ANR-08-NANO-046)

References

[1] P. Yang, *Dalton Trans*. pp. 4387-4391, 2008.
[2] L. J. Chen, *J. Mater. Chem*., 17, pp. 4639-4643, 2007
[3] W. Lu and C. M. Lieber, *J. Phys. D.:Appl. Phys*., 39, pp.R387-R406, 2006
[4] F. Demami, L. Ni, R. Rogel, A.C. Salaun and L. Pichon, *Procedia Engineering,*, 5, pp.351-354,2010
[5] Y.-S. Sohn, J. Park, G. Yoon, J. Song, S.-W. Jee, J.-H. Lee, S. Na, T. Kwon, K. Eom. *Nanoscale res. Lett*. 5, pp. 211-216, 2010.
[6] Y. Zhu, F. Xu, Q. Qin, W.Y. Fung and W. Lu, *Nano letters*, 9, pp.3934-3939, 2009.
[7] S.Y. Ryu, J. Xiao, W.I. Park, K.S. Son, Y.Y. Huang, U. paik and H. A. Rogers, *Nanoletters* 9(9), pp. 3214-3219, 2009.
[8] C.-H. Hsin, W. Mai, Y. Gu, Y. Gao, C.-T. Huang, Y. Liu, L.-J. Chan and Z.-L. Wang, *Advanced materials*, 20, pp. 3919-3923, 2008.
[9] W. Fang and J. Wickert. *J. Micromechanics Microeng*. 4 pp. 116-122, 1994
[10] B. Charlot, W. Sun, K. Yamashita, H. Fujita and H. Toshiyoshi, *J. Micromech. Microeng.*, 18, pp.045005-045012, 2008
[11] X.C. Zhang, B.S. Xu, H. D. Wang, Y.X. Wu, Thin Solid Films, 488 (1-2), pp 274-282, 2005
[12] M. Nemiroff, M. Stuber, R. Troutt, D. gerber, S. Mittal, *J. Appl. Phys.*, 62(9), pp3677-3681, 1987.
[13] C.A. Volkert, *J. Appl. Phys*., 70(7), pp. 3521-3527, 1991.
[14] V. Subramanian, P.K. Bhattacharya and A.A. Memon. Int. J. Electronics, 78(3), pp.519-525, 1995 ou R.J. Archer, *J. Electrochem. Soc.*, 104, pp.619-622, 1957.
[15] E. Kobeda and E.A. Irene, J. Vac. Sci. Technol. B, 6, pp.574, 1988.

EFFECT OF ELECTRIC FIELDS GENERATED BY MICROACTUATORS ON THE IMAGING IN ELECTRON MICROSCOPY

R. Vermeer, L.A. Woldering and L. Abelmann

Transducers Science and Technology group, MESA+ Institute for Nanotechnology, University of Twente, Enschede, The Netherlands

***Abstract* — In this paper we are investigating the potential to employ small devices in crucial areas with limited volumes in electron microscopes. We present the analysis of the electric fields that are present in an electrostatically actuated micro electro mechanical systems (MEMS) device. The electric fields are modeled using finite elements methods (FEM). Preliminary results are shown from scanning electron microscope (SEM) measurements of an electrostatically actuated two degrees of freedom (2DOF) nanometer precision table. From the FEM results the influence of the electric fields on an electron beam traversing the devices can be calculated. This influence is calculated to be a trajectory displacement in the order of tens of nanometers for typical acceleration voltages. SEM measurements show significant vibrations in the images of non-movable parts of the devices when applying actuation voltages to the devices. This shows an effect of actuation on the detected electrons while imaging. Deflections up to 2.2 µm have been observed for a voltage of 80 V_{pp}. This deflection cannot be fully attributed to deflections of the incoming beam. Therefore we include in a qualitative analysis the trajectory of emitted secondary electrons that are detected.**

Keywords : MEMS, electron microscopy, electrostatic actuation, FEM

I - Introduction

We are investigating the potential to employ small devices in crucial areas with limited volumes in electron microscopes. For instance, we want to investigate if it is possible to position small apertures in the electron beam column.

To this end, micro electro mechanical systems (MEMS) devices could be used. For nanometer precise actuation in the plane of imaging, we use a two Degrees of Freedom (2DOF) manipulator with electrostatic comb drive actuation. [1]

It is clear however, that electrostatic actuation can potentially complicate the imaging of the electron microscope. Electric fields from the electrostatic actuator may influence the trajectory of the incoming beam or the amount and trajectory of secondary electrons that can be detected.

Therefore we decided to thoroughly investigate the influence of electrostatic actuation on the imaging of electron microscopes. Finite element modeling (FEM) has been used to calculate the relevant electric fields at and in the vicinity of our complex geometries and to calculate the effect on the electrons while they traverse the device. Furthermore we show preliminary results that indicate the effect of electrostatic actuation during Scanning Electron Microscopy (SEM) imaging.

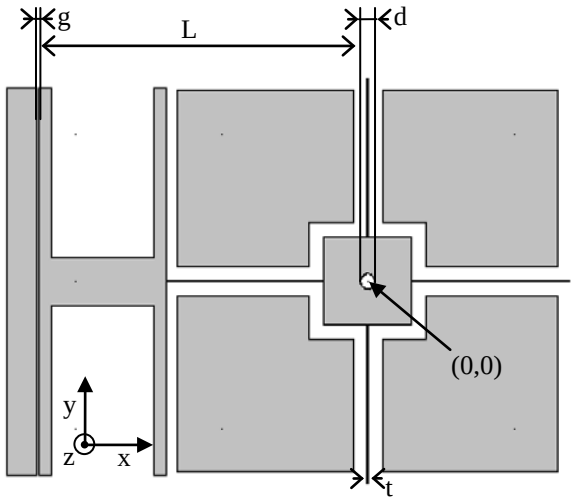

Figure 1: *Illustration of the geometry used for the FEM calculations. It consists of a table with an aperture, see arrow, and suspending beams. On the left the electrostatic parallel plate actuator is shown. The voltage is applied to the left part of the parallel plate actuator.*

SEM is used for imaging the MEMS devices and to visualize the actuation of the table. Another benefit of using SEM is that the effect of the actuation on the imaging can be visualized more easily at lower magnification, certainly because secondary electrons have a relative low energy. [2] Since low energy electrons are slow, they will be longer exposed to the electric field and thus be more deflected. We use their deflections to test our models.

II - Finite Element Modeling

The modeled geometry consists of a scanning table with an aperture in the center, see Figure 1. The table is suspended by four flexible beams. Electrostatic actuation of the table is performed by comb drives at the ends of the suspending beams. To simplify the geometry, only one simplified parallel plate actuator is considered. Table 1 shows typical length scales of this model. The point (0,0,0) is the center of the aperture, see the arrow.

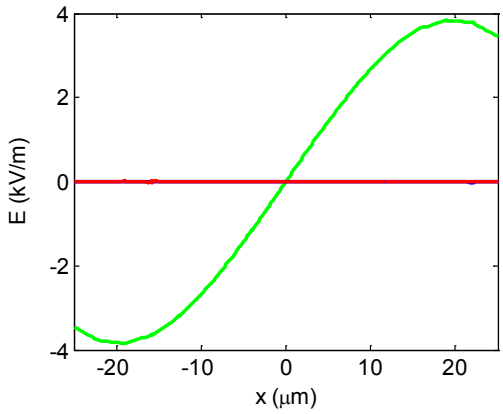

Figure 2: *The electric field in the aperture. The y-component E_y (blue) and z- component E_z (red) of the electric field are zero and thus overlap, the x-component E_x of the electric field is shown in green.*

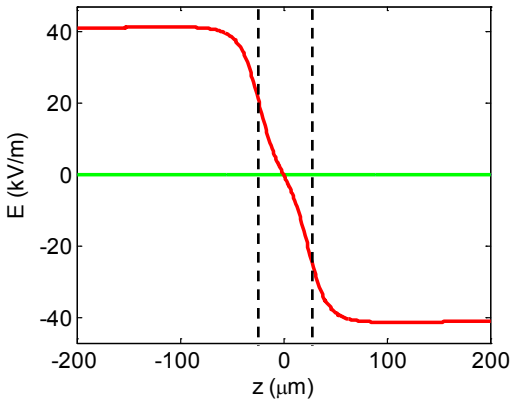

Figure 3: *The electric field in the aperture along the z-direction. E_x and E_y, shown in green, are both zero. The electric field in the z-direction E_z is shown in red. The device thickness is shown between the dotted lines.*

Table 1: typical length scales of the modeled geometry

Description	*Name*	*Value*
Gap between parallel plates	*g*	3 μm
Diameter of aperture	*d*	50 μm
Length from gap to aperture	*L*	1140 μm
Height (z-direction) of device	*h*	50 μm
Thickness of beams	*t*	3 μm

In the model the electric fields have been calculated for a constant voltage on the actuator of 100 V. This voltage is the maximum actuation voltage for the device. The electric field in the aperture is investigated. Figure 2 shows the electric fields in the middle of the aperture in the x-direction. This figure shows that the y-component E_y and z-component E_z are zero, which is as expected from symmetry considerations. The x-component E_x is negative for x<0 and positive for x>0, which means incoming electrons from an electron beam will be subject to a force towards the middle of the aperture. The same argument applies to the y-axis through the center of the aperture. On that axis the x-component E_x and z-component E_z of the electric field are zero and the y-component E_y is the same as the x-component in Figure 2. This means that a distribution of emitted secondary electrons coming from the device will be spread out in the x- and y-direction.

The z-axis (x=y=0) shows a different behavior, see Figure 3. Here, the x-component E_x and y–component E_y are zero, which can be explained from symmetry. The z-component E_z of the electric field is positive for z<0 and negative for z>0. This means that electrons from an electron beam will first encounter a decelerating force until z=0 is reached. Subsequently, the electron will be accelerated again. Thus, when actuation voltages are applied an electron beam will reach the surface of a device later than when no actuation voltages are applied. Similarly, a time difference can be expected for the secondary electrons detected in SEM imaging. As the energy of primary electrons from the electron beam differs significantly compared to the energy of secondary electrons, this effect will be much stronger for secondary electrons. Therefore, they will be detected later when actuation voltages are applied.

These simulations give clear qualitative insights of the influence of actuation voltages while imaging with electron microscope. The results indicate that the electric fields generated by the actuator should not be ignored.

III - Experimental Details

Preliminary SEM imaging has been performed on slightly different devices than modeled, see Figure 4. These devices and their fabrication have been earlier described in [3]. The geometry differs, but similar electric fields are expected. The device consists of a movable table suspended by four flexible beams. On two opposite sides of the table a comb drive structure is fabricated to actuate the table.

For imaging a FEI Quanta 450 SEM has been used, at a high vacuum of 10^{-3}~10^{-5} Pa. Acceleration voltages of 5 kV to 25 kV are used, at working distances of 10 to 20 mm. Detection of secondary electrons is done using an Everhart-Thornley Detector at 250 V bias. The SEM chamber has been modified to facilitate electrical connections to actuate the devices using a home-built custom sample holder.

The moving table and substrate of the device are grounded. An AC voltage is applied to the fixed part of the comb drive to actuate the table. The voltage is applied using an Agilent 33120a waveform generator and is amplified ten times using an ESyLAB LM3325 8 channel HV Amplifier with an ESyLAB LM3322 HV Power Supply. For actuation a sine wave is used with typical peak to peak voltages of up to 80 V_{pp}. Frequencies were set of 1 to 10 Hz, depending on the chosen scanning speed of the SEM. While actuating the device, the suspended table and several fixed parts are imaged by SEM.

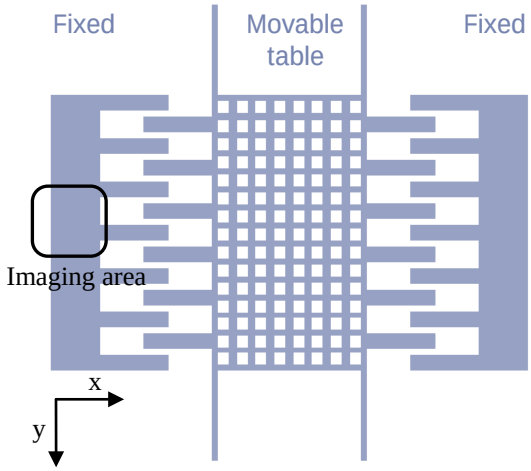

Figure 4: *Schematic view of the devices used for measurements. A movable table is suspended by four flexible beams. On the left and right are two comb drive structures, which are fixed to the substrate. The device is actuated by applying a voltage to the left comb drive structure of the device. The imaging area of Figure 5 is indicated also.*

IV - Results and Discussion

When imaging fixed parts of the actuated device in the SEM, multiple effects are observed, see Figure 5. The applied voltage results in contrast differences in the SEM image, and a vibration is observed in the image. This vibration is not the result of actuation as the object that is imaged is fixed to the substrate. Therefore, the vibrations must result from an effect on the detected electrons.

The contrast difference is caused by the voltage applied to the object. For instance, when applying a negative voltage to the object, more secondary electrons are detected, which results in a brighter area in the image.

Figure 6 shows the gray level averaged in the x-direction between the red lines, versus the y-direction. The fit in Figure 6 is a fit of the intensity of the detected electrons, based on the inverse distribution function that is shown in Eq. 1.

$$I(y) = \text{offset} + \frac{\text{scaling}}{\exp\left(k_1 - k_2 V(y)\right) + 1} \qquad (1)$$

with $V(y)$ the applied voltage according to Eq. 2

$$V(y) = \frac{V_{pp}}{2} \sin\left(b\, y + \phi\right) \qquad (2)$$

In the formulas, *offset* and *scaling* depend on imaging settings, $k_1 = D_L^0 / D_T$ is the relative detectability, depending on the signal-to-noise ratio and SEM settings. D_L^0 is the detection level at $V = 0$, and D_T is the detection threshold. $k_2 = a / D_T$ is the relative sensitivity of the detection to V_{pp}. a is the detection sensitivity

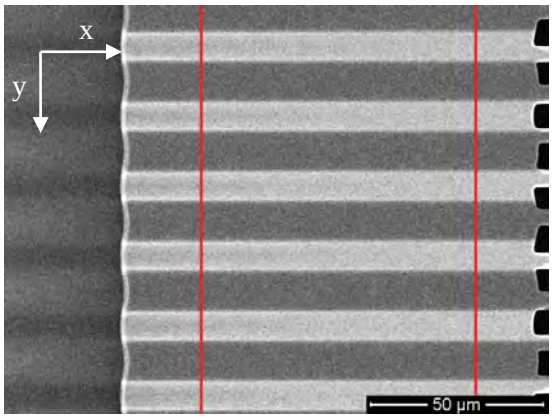

Figure 5: *SEM image of the fixed part of a comb drive, which is actuated with a 3 Hz 81 V_{pp} sine wave. The scale bar equals 50 µm.*

to V_{pp}, with V_{pp} is the applied peak to peak voltage, b is the period of the sine in the image, which is calculated from the frequency of the sine wave and the scanning speed of the SEM. ϕ is the phase of the actuation with respect to imaging, which is arbitrary. This model fits the data excellently. The main focus in further research will be on the detection sensitivity a. This parameter is expected to be influenced by several physical phenomena, such as the Fermi level of the electrons in the device and the time-of-flight of the detected secondary electrons.

To further investigate the vibrations in Figure 5, the voltage dependence of the amplitude of the vibrations has been studied. In addition the vibrations have been measured at 3 different locations in the x-direction, with the y-coordinate remaining constant. The first location is shown in Figure 5 and is 0.16 mm away from the comb fingers, the second and third location are 1.3 and 2.3 mm away from the comb fingers, on an electrically grounded part of the device. In these locations, substantial vibrations are observed.

The amplitude of the vibrations has been measured for a range of 0 to 80 V_{pp} in steps of 10 V, at distances of 0.16 mm, 1.3mm and 2.3mm from the place of actuation, see Figure 7. The amplitude has a linear relation with the applied voltage. The measured amplitudes drop with distance from the place where actuation takes place, as is expected.

If we assume that vibrations in the image are accounted only to vibrations in the electron beam that are caused by the applied voltage, our calculations indicate a deflection of less than 100 nm for 5kV acceleration voltage and 100V actuation. This deflection would be significantly lower with a lower actuation voltage, like the maximum peak to peak voltage of 80 V_{pp} that is used in our experiment. Therefore our observations cannot be purely accounted to vibrations in the electron beam.

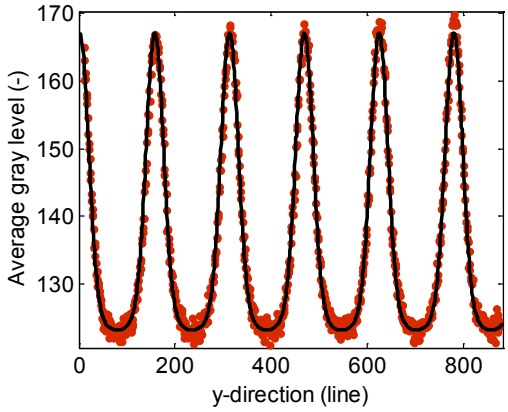

Figure 6: *Averaged gray level intensity versus the y-coordinate, shown in red, displays a periodic behavior with the same period as the applied AC voltage. The black line is a fit to the data with a goodness of fit* R^2*=0.994.*

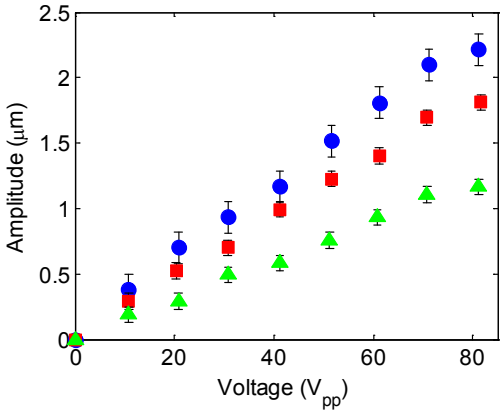

Figure 7: *Measured amplitude of the observed vibrations versus actuation voltage. Amplitudes were measured at distances from the actuator of 0.16 mm (blue circle), 1.3 mm (red square) and 2.3 mm (green triangle).*

The vibrations could also be caused by disturbances to the detected secondary electrons. The energy of the primary electrons from the electron beam is equal to several keV's, depending on the acceleration voltage used. However, secondary electrons have an energy which is in the order of a few or tens eVs. Therefore, the influence of external electric fields on the secondary electrons and their detection is expected to be significantly larger.

The exact mechanism behind this is different from the disturbance of the electron beam that is caused by the applied voltage. The detector detects intensity only, and not the location of the emitted secondary electrons. Vibrations of the secondary electrons are therefore not detected. The location where the detected secondary electrons come from is related to the position of the electron beam and to the detection lag, *i.e.*, the time between the electron beam hitting the object and the time when the emitted secondary electrons from that area are detected. The key to explain why the vibrations that are observed in the SEM images occur, might be in this detection lag. If the electric fields that are caused by the applied voltages cause a deceleration or acceleration of the secondary electrons, the synchronization between the location where the secondary electrons came from and when they were detected might be influenced such that vibrations are observed.

V - Conclusion

We have shown FEM simulations of electric fields in an electrostatically actuated MEMS device. We have calculated the electric field in positions, for instance an aperture, far from the actuator. A quantitative exploration of the influence of the electric fields on incoming electrons has been given. Our analysis shows that an incoming electron beam will be narrowed and decelerated before it arrives at the surface. The next step will be to calculate electron space-time trajectories of electrons from an electron beam.

SEM images of MEMS structures to which an AC voltage is applied show an alternating contrast. This periodic contrast is due to the electrons intensity being influenced by the actuation voltage. We fitted the measured data for the intensity fluctuations to a model which assumes that the intensity variation is caused by modification of the energy barrier for secondary electrons leaving the silicon Even though the model fits our data very well, the physical nature of the intensity variation is not quite well understood.

SEM measurements of fixed parts on the actuator also show clearly visible vibrations with amplitudes of more than 1 μm up to distances of 2.3 mm from the source of the electric fields. These vibrations cause deformed SEM images. Calculations and qualitative analyses have shown that the vibrations cannot be purely related to deflections of the incident electron beam of the SEM, caused by the applied actuation voltage. A detailed analysis of the causes of the vibration is our main focus to continue this research.

References

[1] E. Sarajlic et al., in *Transducers '05*, vol. 2, pp. 1404-1405, 2005

[2] H. Seiler, *Journal of Applied Physics*, vol. 54 (11), pp. R1-R18, 1983

[3] J. Engelen et al., in *MME2010 Abstracts: 21st Micromechanics and Micro systems Europe Workshop*, pp. 193-196, 2010

MEMS PROBE DESIGN FOR THE TESTING OF ORGANIC FIELD EFFECT TRANSISTORS

M.C. Rosamond and D. Wood

School of Engineering and Computing Sciences, Durham University, South Road, Durham, DH1 3LE, UK

***Abstract* — This paper reports on a novel probe card for the testing of organic electronic devices, with an organic field effect transistor (OFET) used as the test vehicle. Careful attention has been given to the design and fabrication of probe tips that can test devices with the minimum of damage to the soft and fragile materials commonly used in organic electronics. The design has been shown to be simple and adaptable, the fabrication was successful and the testing confirms the electrical performance of the probe and the minimal device damage. The scaling up of the technology to make more complicated probes with a greater number of tips is quite straightforward, and the probe is a potential major competitor against more established technologies in the plastic electronics market.**

***Keywords:* Probe card, organic FET, plastic electronics, contact damage, testing**

I - Introduction

Probe cards in the integrated circuit (IC) industry form the temporary electrical connections between devices and test equipment in order to perform wafer level testing. The probes themselves are in the form of a metallic needle-like structure, and the test points on the device are metallic squares known as contact or bond pads.

An orthodox type of probe card, using an epoxy bonded tungsten needle, was first designed in the 1960's. The refinement of this design to address the needs of successive International Technology Roadmap for Semiconductors (ITRS) requirements, such as bandwidth, pin count, fine pitch, tip co-planarity, etc., has been a story of continual improvement. But the basic problems of cost, speed of manufacture and fragility remain, which has led to considerable activity in MEMS to produce alternative structures. Some of these designs have been released on to the commercial market; example technologies include those from Advantest and FormFactor, based respectively on metal tracks backed by a silicon skeleton [1], or microsprings using electroplated gold wire [2].

In addition to the commercial probes, there are many technologies still at the research stage that use MEMS to make silicon and/or metal cantilever-type arrays for probe cards, e.g. [3, 4]. We have previously published a manufacturing technology that not only produces nickel probe structures in the form of cantilevers for bond pads, but also is versatile enough to produce hoops or springs for solder ball based electronics [5]. A further development of this technology improved the robustness of the probes by incorporating a PDMS polymer layer beneath the cantilevers themselves [6].

The emerging and rapidly expanding field of plastic electronics has not received much attention from the probe card manufacturers, since the drivers for innovation are still mainly from the silicon industry. This is because many of the more obvious aspects of plastic electronics, such as relaxed pad pitches and low number of bond pad I/O's, can be easily accommodated by established epoxy probe card or MEMS-based technology.

However, plastic electronics does generate some unique demands on probe cards, in particular the need for a low contact force. In plastic electronics, the active layer is a soft organic material, and in the future the industry is likely to also require both the isolating dielectrics and the interconnects to also be organic-based. The increasing emergence of this industry will then provide the necessary impetus for a greater consideration of contact force in wafer level testing of plastic electronics.

This paper describes a probe designed for the particular purpose of testing thin film organic field effect transistors (OFETs). The design and fabrication of the probe are very different from our previous work, and indeed those of others. The design concept was to build a probe that could be used to test a single OFET at a time. The OFETs that were to be used were fabricated externally and had the following general structure:

- patterned titanium/gold films formed the source and drain electrodes on a glass substrate,
- a thin (10-100 nm) active organic layer was spin coated on top of the source and drain electrodes,
- a 500-600 nm dielectric layer was then deposited,
- the gate electrode was formed by evaporating through an aligned shadow mask.

This OFET device then represents a structure that is all organic apart from the thin metal interconnects. As such, the requirement to form contacts to thin metal films on top of soft dielectric layers provides an ideal opportunity to assess how any device probe can operate with current plastic electronic devices.

To contact to the source and drain connections it was necessary for the probes to penetrate the organic and dielectric layers. Conversely, to contact the gate electrode it was necessary to apply a low force so as not to punch through the organic and dielectric layers. This made for a unique set of challenges when designing a monolithic probe card for an OFET. Further challenges are likely to be found in other OFET design variations.

II - Experimental Details

A. Probe Design

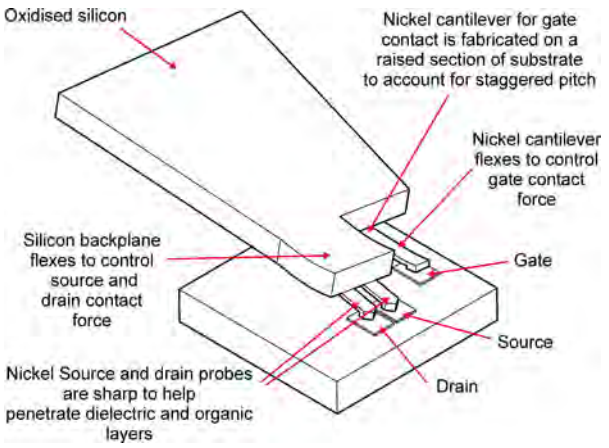

Figure 1: Key features of the probe design.

The important aspects of the probe design are shown and annotated in Figure 1. The design consisted of a structured silicon chip held at an angle (~7°) to the OFET substrate. Attached to the underneath of the silicon were nickel probes. The probes for the source and drain were short cantilevers. These were sufficiently stiff that under an applied load it was the silicon substrate and not the cantilevers that flexed. The gate electrode was a long cantilever, which deflected under the load caused by contact to the gate bond pad. The deflection of the gate probe, and so the contact force, can then be controlled by the geometry of this cantilever independent of the source and drain probes.

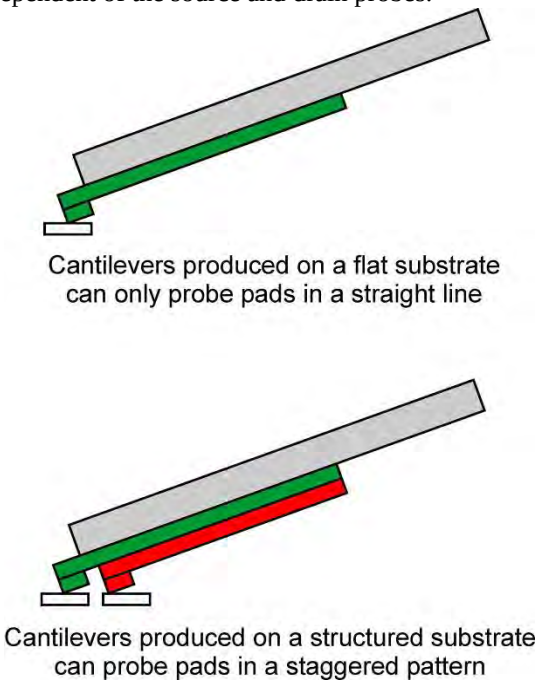

Figure 2: *The principle of probing staggered contact pads.*

The design of the OFET under test meant that the gate electrode was staggered with respect to the source and drain electrodes. To account for this offset the gate cantilever had to be fabricated on a raised section of substrate. This was achieved by structuring the silicon substrate to create two levels before the cantilevers were deposited. This concept is shown in Figure 2.

B. Probe Fabrication

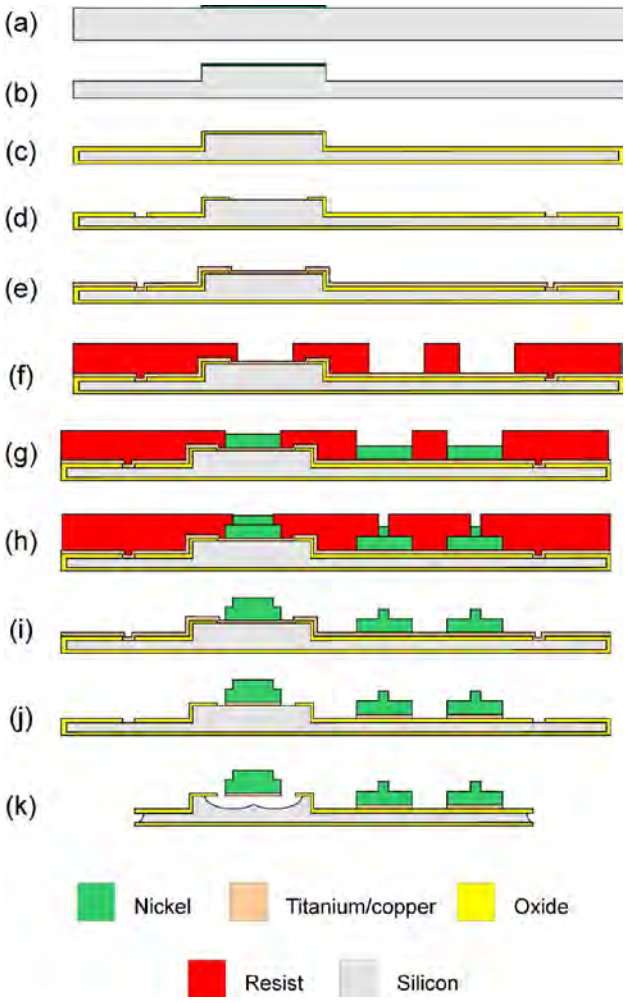

Figure 3: *OFET probe fabrication.*

The fabrication process sequence is shown in Figure 3. P-type silicon of 10-30 Ωcm resistivity was chosen as the substrate material. A thin layer of nickel was evaporated and patterned as the first stage of the fabrication process (a). This metal was used as a mask against a subsequent SF_6 based reactive ion etch (RIE) of the substrate to a depth of 50 µm (b). The titanium was then removed by wet etching. The wafer was oxidised to a depth of 2 µm (c), the oxide patterned (d) and a seed layer metallisation of titanium and copper was sputter deposited (e). Further patterning (f) was required with thick photoresist (AZ9260, 55 µm) to define the area for nickel electroplating to a thickness of 35 µm (g). These last two processes were repeated (this time the electroplated nickel was 10 µm thick) to help define the shape

of the probe tips (h). All the thick photoresist was then stripped (i) and the exposed copper and titanium seed layers removed, again by wet etching (j). The gate probe was then released by a vapour phase XeF_2 process (k). Finally, the probe was sprayed with high pressure nitrogen to shatter the unwanted suspended oxide layers that are a result of the undercutting during step (k).

III - Results and Discussion

A. Fabricated Probes

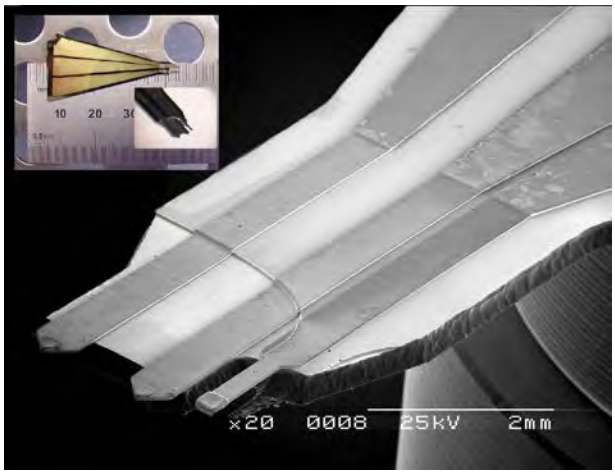

Figure 4: *Typical OFET probe.*

The realisation of the probe design is shown by a typical OFET probe fabricated using the above process, as in Figure 4. The source and drain contacts are the larger ones on the fixed part of the probe. The smaller, cantilever structure at the front of the image is the flexible gate probe. Note that, as can be seen in the inset picture of Figure 4, the probe shown had a 100 nm gold layer evaporated on top of the nickel in places. This is not shown in the fabrication sequence but was to ensure a good quality electrical connection could be made to the probe.

B. Leakage Current

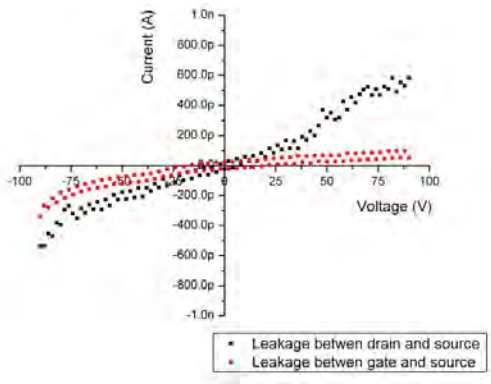

Figure 5: *Leakage current between probes.*

Good electrical isolation between adjacent probes is an essential feature of any probe card, and MEMS designs in particular have to be aware of this issue because of the use of a silicon substrate. The problem is made more important still by the nature of organic FETs: in general, they have much higher operating voltages (both drain and gate) than semiconductor based devices.

The leakage current between adjacent probes was measured using a HP4145B parameter analyser. One probe was grounded while a voltage was applied to the other. The voltage was swept from -90 V to 90 V in 2 V steps. The current passing between the probes is shown in Figure 5. As can be seen, the isolation between adjacent probes was excellent, with leakage currents less than 1 nA at 90 V.

C. Wafer Level Device Testing

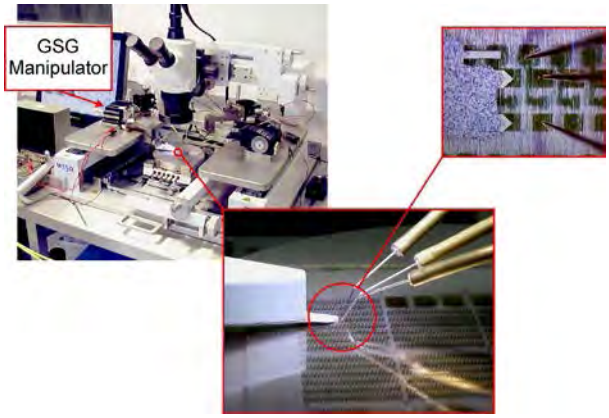

Figure 6: *OFET probe mounted to a standard GSG manipulator and pictured alongside orthodox tri-axial tungsten probes.*

The fabricated probe was mounted onto a specially machined plastic adapter, which allowed it to connect to a standard ground-signal-ground (GSG) probe manipulator (Cascade Microtech Inc.). This allowed control of x-y-z positioning as well as y-z tilt correction. Electrical connections were made by gluing wires to the gold coated nickel tracks (Figure 4, inset) using silver paste. Through these wires the probes were connected to the parameter analyser. Photos showing the final assembly as mounted in a probe station and a visual comparison to orthodox tri-axial tungsten probes can be seen in Figure 6. The benefits of a design that incorporates all probe tips in one monolithic structure, e.g. compactness, ease of alignment and control of contact force, can be readily seen by the close-up comparisons between our all-in-one probe and separate, tri-axial assemblies.

Standard source-drain *I-V* sweeps were performed for a series of gate voltages. An example of the measurements obtained can be seen in Figure 7, where the V_{ds} limit of 15 V confirms the need for concern over isolation and leakage currents within any monolithic probe assembly. Such results indicated that the probes functioned as expected, and they compared well with similar results taken by the OFET supplier.

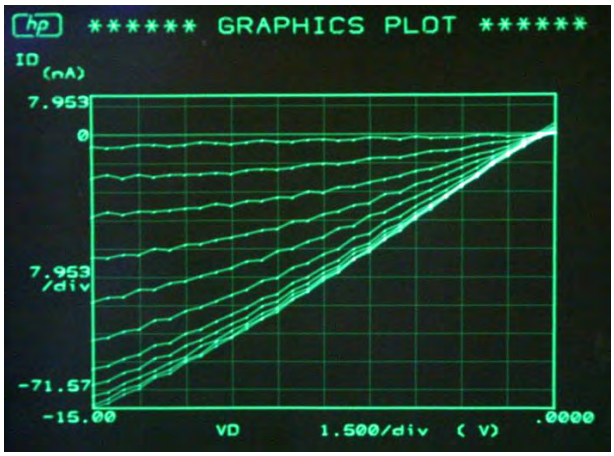

Figure 7: *Example I_{DS}-V_{DS} plot for varying V_{GS} on an OFET using the probe.*

D. OFET Damage Minimisation

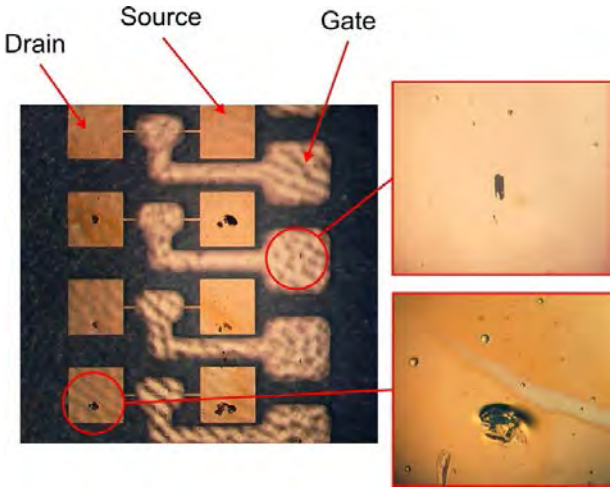

Figure 8: *Scrub marks on tested OFETs.*

Images of the scrub marks can be seen in Figure 8, where the damage caused by the gate probe is much less than that from the source or drain probes. However the gate probe still applies sufficient force to scrape some of the gold from the dielectric. We are working on the geometry of the cantilever to further minimise the force applied by the gate probe.

IV - Conclusion

A simple process has been described that allows the fabrication of robust probes that can be mounted on a traditional GSG manipulator. By varying the length of the nickel cantilevers, the probe force can be adjusted such that different probes apply different forces for the same level of overdrive. By structuring the silicon substrate before forming the nickel probes it was possible to align the cantilevers with staggered pad arrangements. Results for leakage current, OFET *I-V* curves and evidence for physical damage to the device under test were very promising, and further development of the probe may lead to this type of design being adapted by the plastic electronics industry.

References

[1] K. Lee, B. Aldaz, Y. Zhou, D. Yu, G. Hohenwarter and T. Golnas, *IEEE Southwest Test Workshop*, San Diego, S01_02_Aldaz, 2003.

[2] S. Spiesshoefer, L. Shaper, K. Maner, E. Porter, F. Barlow, M. Glover, W. Marsh, G. Bates and M. Lucas, *52nd IEEE Electronic Components and Technology Conference*, San Diego, pp. 1106-1109, 2002.

[3] T. Nazumu, Y. Tashiro and S. Inoue, *J Micromechanics and Microengineering* vol. 17, pp. 154-162, 2007.

[4] K-Y. Lee, J-T. Huang, H-J. Hsu, C-K. Chen, T-C. Tsai, *5th IEEE Conference on Microsystems Packaging Assembly and Technology (IMPACT)*, Taipei, DOI 10.1109/IMPACT.2010.5699512, 2010.

[5] M. Rosamond and D. Wood, *Microelectronic Engineering*, vol. 84, pp. 1207-1210, 2007.

[6] M. Rosamond, A.J. Gallant and D. Wood, *Proc Eurosensors XXIII*, Lausanne, September 6-9, 2009, *Procedia Chemistry* vol. 1, pp. 792-795, 2009.

CHARACTERISATION OF CHEMICAL MECHANICAL POLISHING PROCESS FOR POLYIMIDE MEMS SACRIFICIAL LAYER

John Love[1], Martin Hill[1], Conor O'Mahony[2] and Alan Blake[2]

[1]*Adaptive Wireless Systems Group, Cork Institute of Technology, Bishopstown, Cork, Ireland*
[2]*Tyndall National Institute, University College Cork, Ireland*

***Abstract* – The operation and reliability of MEMS devices can be significantly enhanced if stress concentration due to contours in the MEMS structural layer are minimised. In this paper a CMP process to planarize a polyimide sacrificial layer for the fabrication of dual-gap MEMS tuneable capacitors is presented. The requirement for the CMP process and the successful planarization of the structural layer using interferometry is demonstrated. During this inspection scratches were observed on the MEMS device surface. The measured scratch depth was approximately 30nm. Pull-in voltage tests confirm the elastic operation of the devices and results are presented for both parallel plate and two-gap capacitor devices.**

***Keywords:* MEMS, CMP, parallel plate, two gap, tuneable capacitor, fixed-fixed beam.**

I – Introduction

RF-MEMS is evolving as an exciting technology for providing improved solutions in the development of RF wireless applications due to its proven superior performance over existing solid state technology [1-4]. MEMS tuneable capacitors operate by varying the gap between two metal plates using electrostatic actuation. Devices of this type, often referred to as tuneable electrostatic parallel plate capacitors, are unstable due to the electrostatic pull-in effect which limits the tuning range that can be achieved to 50% [1-2].

One method used to extend the tuning range, known as the two gap design, uses different gap heights for sensing and actuation electrodes as shown in Figure 1. In this design the centre electrode which forms a tuneable capacitor with the moveable beam is raised above the actuation electrodes by the formation of an oxide table prior to metal deposition. Previous publications on implementing this operating principle reported tuning ranges of 56% to 600% [5-7].

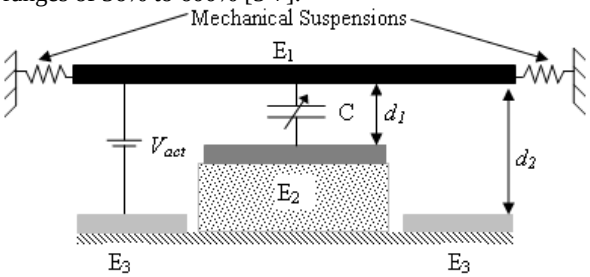

Figure 1: *Side profile of a two gap capacitor showing the gap height (d_2) for the actuation voltage (V_{act}) and the gap height (d_1) for the tuned capacitance (C).*

In the proposed fabrication process using a polyimide sacrificial layer where significant step changes in underlying topography are replicated in the MEMS structure as the polyimide deposition is conformal. This results in the top moveable component replicating the underlying topography resulting in unsatisfactory device operation and poor reliability due to stress concentration at beam contours. This problem is illustrated in Figure 2 for a planar MEMS tuneable capacitor over a coplanar waveguide. Troughs in the MEMS metal are indicated over the waveguide slots.

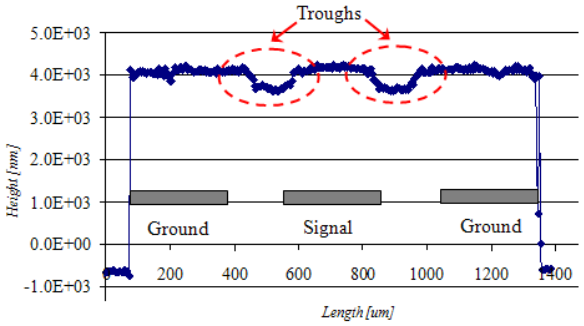

Figure 2: *Side profile of a co-planar waveguide with a deformed top plate.*

This paper presented a CMP (Chemical Mechanical Polishing) process [8] to be added to the standard process flow at Tyndall National Institute to planarize the polyimide sacrificial layer. The effectiveness of the process is verified for planarization of a two gap tuneable and electrostatic actuation of test devices from the process confirms that surface imperfections resulting from the CMP process do not have a significant adverse effect on device operation.

II - Device Fabrication

The standard process, without CMP, begins with a 1.2µm thick layer of thermal dioxide grown on the wafer and etched to form the oxide table for the centre electrode as shown in part (a) in Figure 3. A 0.5µm layer of aluminium was then sputtered and patterned to form pads and tracks followed by a 0.1µm layer of PECVD silicon dioxide was deposited over the aluminium. A 2µm sacrificial layer of polyimide was spun and cured on top of the silicon dioxide, conforming to the contours of the previous layers on the wafer. The sacrificial layer was then etched to define the beam anchors. A 1µm thick film of aluminium was cold sputtered and patterned to form the MEMS device structural layer. Finally the sacrificial layer was removed by an oxygen plasma etch. The

resulting top moveable beam is not planarized and has a large step up in its centre.

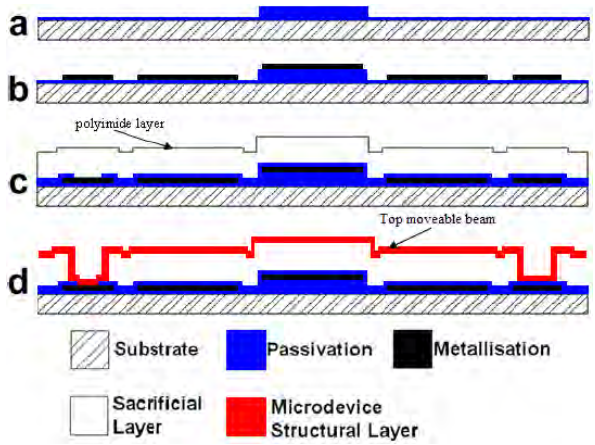

Figure 3: *Fabrication flow schematic: (a) deposition of silicon dioxide and formation of the centre step up; (b) patterning and etching of tracks and pads; (c) deposition of a second passivation layer and sacrificial layer; (d) formation of the top moveable beam and etching of the sacrificial layer.*

A. With CMP

The addition of the CMP process planarizes the polyimide layer as displayed in part (c) in Figure 4. The CMP was carried out using a Logitech CDP51 system. The polishing-pad used was an industry-standard Rohm & Haas IC-1000™ pad and the polishing-slurry was a colloidal alumina slurry, Eminess Technologies Inc Ultra-Sol™ A12. The specified mean particle-size for the colloidal alumina slurry was 240 nm. The CMP polishing parameters were set-up for a high removal-rate of the polyimide, in particular the down-force on the wafer-carrier was 5 PSI (as compared to 3 PSI for more standard applications); the higher down-force increased the tendency for scratches on the surface of the polished layer. After polishing, the wafers were immediately transferred to a post-CMP cleaning system, the Nanomaster SWC-4000, where a combination of Megasonic spray-cleaning with de-ionized water and PVA brush-cleaning in de-ionized water was used to remove slurry residue from the wafers.

After the CMP step is completed the same steps as in the standard process to form the top moveable beam are performed.

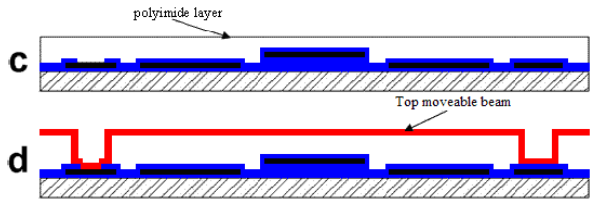

Figure 4: *Fabrication flow schematic: (c) deposition of a second passivation layer and sacrificial layer, the CMP process planarizes the top surface of the polyimide; (d) formation of the top moveable beam and etching of the sacrificial layer.*

The CMP slurry leaves scratches in the top surface of the polyimide because it is soft, and these scratches are replicated in the top moveable beam as shown in Figure 5.

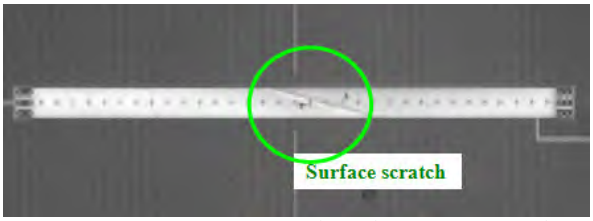

Figure 5: *A scratch on the top surface of a 528μm x 30μm fixed-fixed tuneable capacitor.*

III – Process Verification

The planarization benefits of the CMP process were verified with interferometer measurements of fixed-fixed beams and two gap tuneable capacitors. Electrostatic pull-in measurements of fixed-fixed beams with widths of 30μm and 50μm and lengths from 228 to 528μm are used to characterise the residual stress and elasticity of the fabricated device.

A. Zygo Measurements

The deflection due to applied voltage of fixed-fixed beam, such as that shown in Figure 6, was measured using a Zygo white light interferometer and a Keithley 237 power supply. The measurements confirmed that the top surface was planarized and that surface scratches were present as demonstrated in Figure 6. As can be seen, there is difference in the shape of the scratch at 25V compared to the rest of the voltage points. This is due to the scratch protruding downwards from underneath the moveable beam and when it collapses on the bottom pad it pushes the surrounding top beam metal upwards.

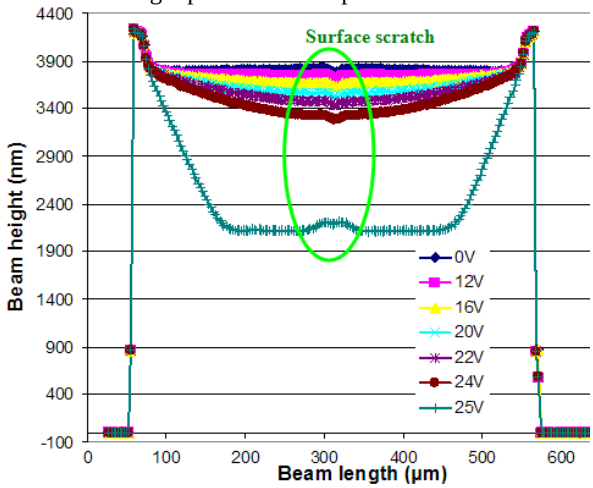

Figure 6: *A side view a 528μm x 30μm fixed-fixed tuneable capacitor demonstrating a planarized top surface also a scratch in the top surface is highlighted.*

The scratch in Figure 6 was measured and found to be 30nm in depth. The average scratch depth was approximately 25nm.

B. Pull-in Voltage

The pull-in voltages of fixed-fixed beams were obtained using Capacitance – Voltage tests. The test setup consisting of a Keithley 237 voltage supply, a HP4275A LCR meter, a HP16048D test cable and probe station surrounded by blacked out Faraday cage.

The results of these tests for three fixed-fixed devices from two die with widths of 30µm and 50µm and lengths varying from 228µm to 528µm are shown in Figure 7. These graphs demonstrate that the performance of the devices is repeatable across the wafer.

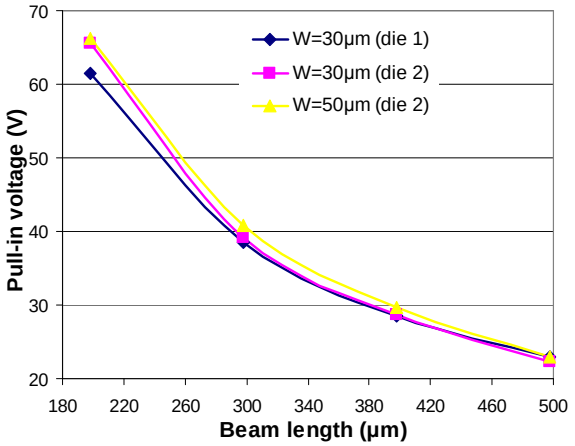

Figure 7: *Capacitance – voltage pull-in graphs for the fixed-fixed tuneable capacitors from different die with widths (W) of 30µm and 50µm and lengths varying from 228 to 528µm.*

The V_{pi} of a fixed-fixed beam is related to the dimensions and parameters of the structure and is represented mathematically by equation (1) [9]

$$V_{pi} = \sqrt{c_1 \frac{Et^3 d^3}{{}_0 L^4} + c_2 \frac{d^3 t_{\ 0}}{{}_0 L^2}} \qquad (1)$$

Where: V_{pi}: Pull-in voltage, c_1: Constant derived from the bending energy of the beam, c_2: Constant derived from the stretching energy of the beam, E: Elastic modulus, $_o$: Permittivity of free space, d: Initial gap spacing, L: Beam length, t: Beam thickness and $_o$: Initial (un-deflected) tensile residual stress. The constants c_1 and c_2 have to be evaluated for each type of structure as they depend on the dimensions and characteristics of the structure.

The pull-in voltages of these devices were compared using equation (1) in the form of:

$$V_{pi}{}^2 L^4 = L^2 \frac{c_2 d^3 t_{\ 0}}{0} + \frac{c_1 E t^3 d^3}{0} \qquad (2)$$

As V_{pi} and L are the only parameters of the structure that vary and the rest of the parameters are constants, when $V_{pi}{}^2 L^4$ is plotted against L^2 it should produce a straight line if all the devices are operating correctly. A plot of the four fixed-fixed devices (W=30µm) is shown in Figure 8.

A least squares linear fit was applied to this graph and was used to derive a formula for a straight line and it is also displayed in Figure 8. The slope of this straight line was used to calculate and the offset was used to calculate E. The values for c_1 and c_2 used in the calculations were obtained from [10]. The results found that E was 36.5GPa and was 63MPa. As stress dominates the beam stiffness the elastic modulus value cannot be quantified with any confidence.

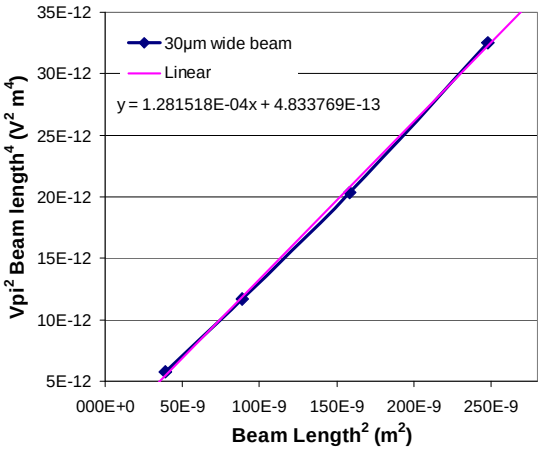

Figure 8: *A graph of Vpi^2L^4 as function of L^2 for different length fixed-fixed beams also plotted is a straight line of the function and the formula of the straight line.*

IV – Two Gap Tuneable Capacitor

The CMP process allowed the two gap tuneable capacitor in Figure 9 to be fabricated. This SEM side view demonstrates a planarized top beam with a visibly smaller tuned capacitor gap height compare with the drive capacitor gap height.

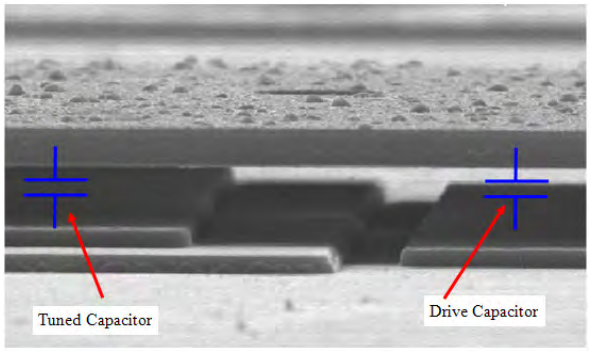

Figure 9: *SEM of the two gap tuneable capacitor and the planarized top moveable beam*

The step-height of the polyimide layer over the patterned metal structures beneath was measured on the wafers before and after polishing using a KLA-Tencor P-15 stylus profilometer. Before polishing, a step-height of polyimide was measured as 500 nm (equivalent to the thickness of the underlying metal layer). After CMP, the

same structures were measured again and the step-height was measured ~ 50 nm indicating good planarization of the polyimide layer had been achieved.

The profile of a two gap tuneable capacitor fabricated in the CMP process with different actuation voltages is shown in Figure 10. With zero voltage it is observed that the moveable top beam is planarized even though the height difference between the Tuned Capacitor and Drive Capacitor is 940nm. As previously stated, there are scratches visible on the top surface of the device but again their presence does not affect the actuation of the device.

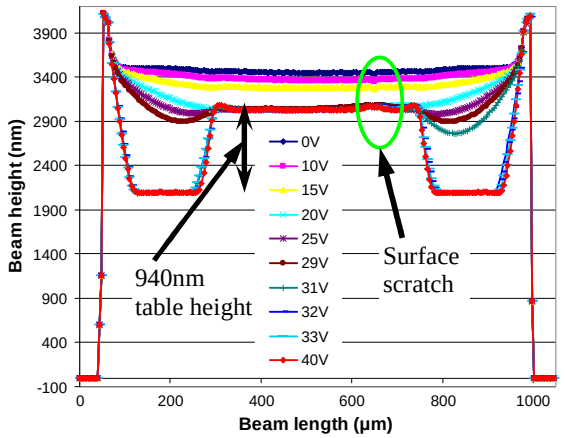

Figure 10: *Side profile of a two gap tuneable capacitor with a CMP induced planarized top surface. The step height and the position of surface scratch are highlighted.*

V - Conclusions

A Chemical Mechanical Polishing, (CMP) process for a polyimide MEMS sacrificial layer has been presented. Interferometer measurements show that the top surfaces of fixe-fixed beams and two gap capacitor devices were level and uniform. Scratches are visible on the structural layer top surfaces and have a measured average depth of 25nm. Electrostatic actuation of fixed-fixed beams using C-V measurements for different device lengths shows that the device performance was repeatable. Analysis of the measured pull-in voltages is as theoretically predicted and was used to estimates the structure residual stress at 63.1MPa. The planar beam in the two-gap capacitor demonstrates the ability of the CMP process to planarize the sacrificial layer over underlying topography with steps heights close to 1µm as required for the intended device.

Acknowledgements

The authors would like to acknowledge SFI NAP (National Access Program) and Tyndall National Institute for device fabrication and testing facilities.

References

1. Tilmans, H.A.C. and et al., *MEMS for wireless communications: 'from RF-MEMS components to RF-MEMS-SiP'*. Journal of Micromechanics and Microengineering, 2003. **13**(4): p. S139.
2. Lucyszyn, S., *Review of radio frequency microelectromechanical systems technology*. Science, Measurement and Technology, IEE Proceedings -, 2004. **151**(2): p. 93-103.
3. Rebeiz, G.M., *RF MEMS, Theory, design, and technology*. 2003: . John Wiley & Sons
4. Christodoulou, C.G. *RF-MEMS and its applications to microwave systems, antennas and wireless communications*. in *Microwave and Optoelectronics Conference, 2003. IMOC 2003. Proceedings of the 2003 SBMO/IEEE MTT-S International*. 2003.
5. Hill, M. and C. O'Mahony. *Double Metal Two-Gap Tunable Capacitor with Residual Stress*. in *Micromechanics Europe*. 2007. Guimaraes, Portugal.
6. Jun, Z., et al. *Development of a wide tuning range MEMS tunable capacitor for wireless communication systems*. in *Electron Devices Meeting, 2000. IEDM Technical Digest. International*. 2000.
7. De Coster, J., et al. *Variable RF MEMS capacitors with extended tuning range*. in *TRANSDUCERS, Solid-State Sensors, Actuators and Microsystems, 12th International Conference on, 2003*. 2003.
8. Sniegowski, J.J., *Chemical-mechanical polishing: Enhancing the manufacturability of MEMS*. SPIE, 1996. **2879**: p. 104–150.
9. Tilmans, H.A.C. and R. Legtenberg, *Electrostatically driven vacuum-encapsulated polysilicon resonators: Part II. Theory and performance*. Sensors and Actuators A: Physical, 1994. **45**(1): p. 67-84.
10. Hill, M., *Micromachined CMOS Compatible Tunable Capacitors*. 2007, National University Ireland.

IMAGE-BASED MAGNETIC CONTROL OF SELF-PROPELLING CATALYTIC MICRO MOTORS

J. de Vries[1], J. Keuning[2], L. Zondervan[1], S. Misra[2] and L. Abelmann[1]

[1]*MESA+ Institute for Nanotechnology*
[2]*MIRA Institute for Biomedical Technology and Technical Medicine*
University of Twente, Enschede, Netherlands

***Abstract* — This paper describes our work to magnetically steer self-propelled devices which move by catalysis of hydrogen peroxide. We demonstrate manipulation of paramagnetic particles with a diameter of 100 µm to a given setpoint by means of magnetic field gradients, as well as self-propelled movement of gold-platinum rods. We discuss how to reach magnetic torque control of catalytic micro motors.**

***Keywords:* Gold/platinum, self-propelling, micro motors, hydrogen peroxide**

I – Introduction

For many decades people have been working on downscaling the size of machines. The most famous prediction of micro- and nano-scaled machines is probably the lecture of Richard P. Feynman titled "There is plenty of room at the bottom" which he gave on December 29th 1959. Here Feynman described among other things tiny machines that could manipulate the micro- and nano-sized world [1].

One of the biggest problems with such a micro- or nano-sized device is to find a way to power it and to make sure it can be 'refueled' once the power of machine runs out. A solution to this problem is a device that can draw power from its environment. This way the small particle does not have to carry its own power source and 'fuel' can be added to the environment in order to make the device work.

Research has been performed into devices which can move by catalyzing a reaction in a liquid environment [2]. An example of such a reaction is a piece of platinum put into a solution of aqueous hydrogen peroxide. Inside the peroxide the platinum can catalyze a reaction to separate hydrogen peroxide into water and oxygen by the following reaction:

$$2H_2O_2 \rightarrow 2H_2O + O_2.$$

When using only platinum, the device will stay in place. But several groups have successfully created moving devices or 'microswimmers' from gold/platinum rods [3, 2]. One of the principles of movement reported is that the platinum part of the rod catalyses the reaction mentioned above to create oxygen. The oxygen forms into bubbles within the liquid until they reach a critical size. When the critical size is reached the bubble explodes and thrusts the particle in the direction of the gold part as schematically shown in figure 1 [2].

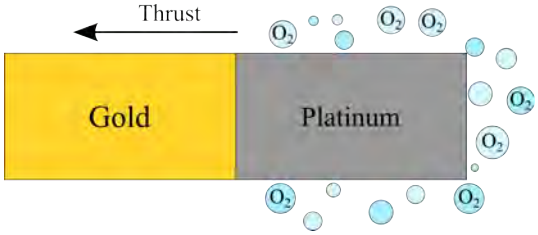

Figure 1: *Schematic view of a gold and platinum rod where the platinum side catalyses the hydrogen peroxide and oxygen bubbles are formed*

Although the self-propelling particles can move through the liquid without external influence, the direction of movement needs to be controlled from the outside world. Since we do not want to add extra mass or volume in the form of electronics or actuators to the device, we choose to add a magnetic part to the particle in order to steer the particles with an external magnetic field. In this paper we discuss our first findings to create such a micro motor and our capabilities to steer micro-sized particles.

II – Magnetic setup

To be able to manipulate the self-propelling micro motors a setup was build which consists of four coils centered around a liquid container with a volume of 10 mm × 10 mm × 2 mm. The particles in the container are imaged by a Sony XCD-X710 1024×768 pixels FireWire camera which is mounted on a Mitutoyo FS70 microscope unit with a Mitutoyo M Plan Apo 2× / 0.055 Objective. The camera is connected to a computer running a program that can track the particles and adjust the magnetic field generated by the coil system. Two software programmed proportional-integral (PI) controllers adjust the current through the coils to steer the particles to the desired location in the camera image shown in figure 2 [4].

The magnetic field supplied by the coils was calculated by means of a finite element model (FEM) [5]. Each coil is represented by a hollow cylinder with a current density corresponding to a current of 1 A running through a coil with approximately 1680 turns. A top down view of the four coil set can be seen in figure 3(a) where a current is applied to the top coil. The variation in color from blue to red shows the strength of the normalized magnetic field, the arrows show its direction. Figure 3(b) shows the y-component of the magnetic field over the length of the liquid container. The field strength in the center of the container is

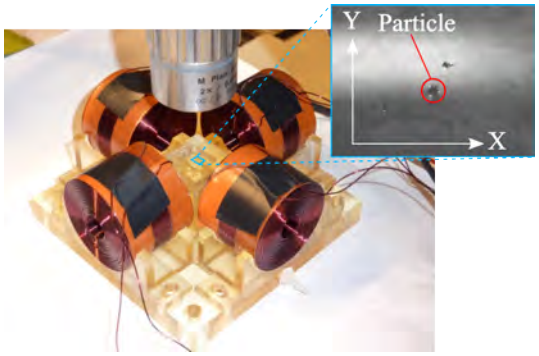

Figure 2: *Image of the magnetic setup with the four coils and the microscope. The inset shows the camera picture with a small cluster of particles*

approximately $3\,\mathrm{kA\,m^{-1}}$.

For the initial test paramagnetic particles are used which consist of iron-oxide in a poly(lactic-acid) matrix with a diameter of approximately 100 µm. The magnetic moment of each particle makes it possible to drag it through the liquid using a magnetic field. This occurs when the force applied by the magnetic field overcomes the drag force created by the particle moving through the liquid. The PI control positions the particle with an accuracy of 7 µm from the setpoint. The maximum attained speed of the paramagnetic spheres was determined to be $235\,\mu\mathrm{m\,s^{-1}}$ [4].

In figure 4 a screen shot of the particle tracker program is shown with a smaller cluster of particles which are manipulated. The green square indicates the region of interest where the particle that is manipulated is located. The pink lines give the direction of the position vectors (x- and y-directions) as outputted by the controller.

The setup enables steering of the particles through the liquid on predefined trajectories with setpoints. When the particle is within approximately 23 µm (10 pixels) from its current setpoint, the next setpoint is given to the controller. As an example, we created a series of setpoints describing a 'figure 8' trajectory. Figure 5 shows the setpoints given to the controller by red circles and the resulting trajectory of the particle cluster by the blue line. As can be seen the cluster of particles closely follows the given setpoints. The speed of the particle cluster was around $122\,\mu\mathrm{m\,s^{-1}}$. The control algorithm was not yet optimized, and higher speeds are certainly possible.

III – Self-propelled particles

To drag the particles through the liquid we applied relatively high fields up to $3\,\mathrm{kA\,m^{-1}}$ because all energy required to move the particle needed to be supplied by the magnetic field. To decrease the required magnetic field we only want to manipulate the direction of movement of the particles in the liquid and use a different source of energy to move the particle. One such possibility is to submerge the particle in its own

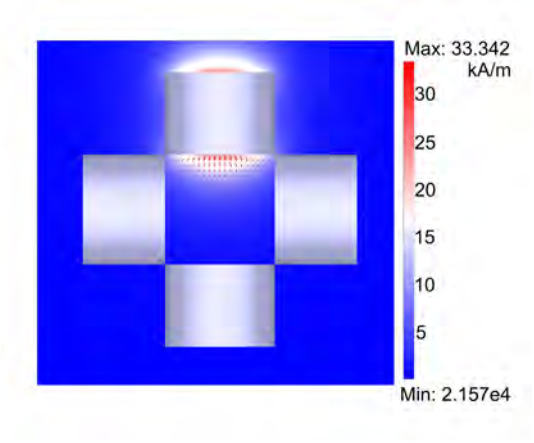

(a) Magnetic field produced by a single coil

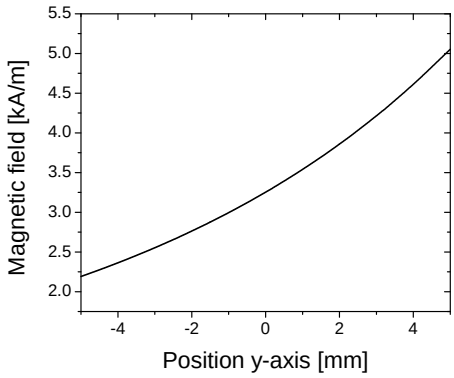

(b) The y-component of the magnetic field produced by a single coil in the liquid container

Figure 3: *Finite element simulation of coil set used for magnetic steering*

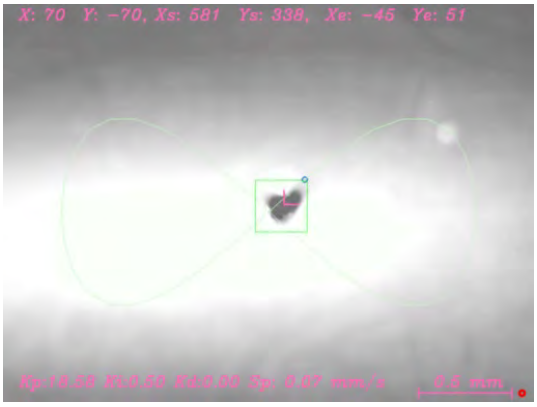

Figure 4: *Screenshot of the particle tracking program where the green square indicates the particles that is manipulated and the pink lines represent the x- and y-position vectors given by the controller output.*

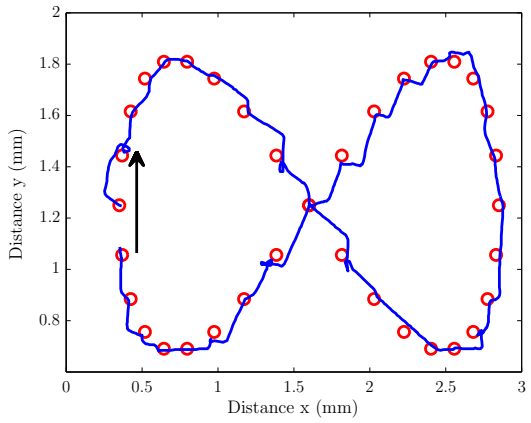

Figure 5: *Comparison the setpoints given to the control software (red dots) and the path of the particles cluster (blue line)*

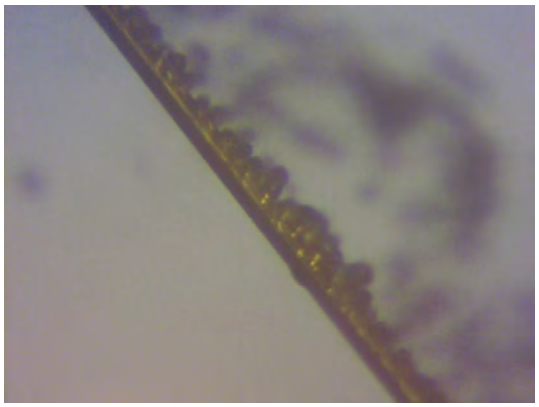

Figure 6: *Piece of gold bondwire with a layer of sputtered platinum in hydrogen peroxide solution where only bubbles are formed on the platinum side*

fuel, much like bacteria. Hydrogen peroxide is one of the simplest systems available, but we imagine future applications of micro-robots in blood streams.

For our first attempt to make a movable 'motor' from gold and platinum we sputtered an approximately 500 nm platinum thin film on a small thread of gold bondwire with a diameter of 50 µm . When the coated gold wire is submerged into a hydrogen peroxide solution bubbles are formed at the platinum surface as can be seen in figure 6. To verify that only the platinum acts as a catalyst a bare piece of gold bond wire is put into the peroxide solution. Indeed, there was no reaction as can be seen in figure 7.

When the platinum surface area is sufficiently large, bubbles will be formed which grow until they leave the wire. The recoil will propel the micro motor in the opposite direction. When a small piece of the platinum/gold wire was put into the hydrogen peroxide solution, movement could be seen from the particle in the setup. There was irregular movement in the path of the particle which was most likely caused by mechanical vibrations of the table and brownian motion due to heating of the liquid by the microscope light source.

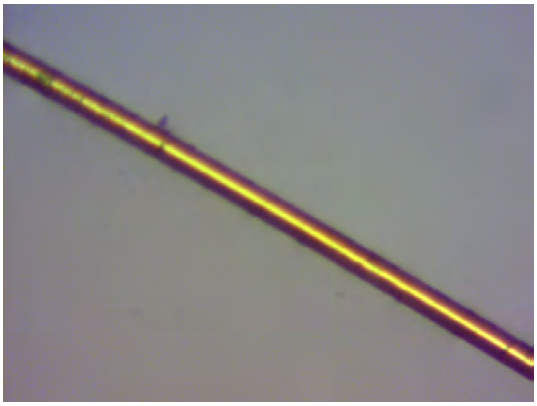

Figure 7: *Piece of bare gold wire in hydrogen peroxide solution where no bubbles are formed on the surface*

Figure 8: *Schematic view of the gold wire coated by platinum where only bubbles are formed on the platinum surface*

The result can be seen in figure 9. Here three subsequent frames are shown where the particle can be seen moving relative to the surface of the water container.

For such a 'bubble propulsion' mechanism to work it is important to have a suitable shape to decrease fluid drag. The drag force is proportional to the area of the particle perpendicular to the direction of movement. A large surface area thus results in a large drag on the micro motor and inhibits movement. In our first attempt the gold wire was covered with platinum on the side instead of the end as shown schematically in figure 8, which decreases the ability of the micro motor to move.

IV – Conclusion

We have shown that we can manipulate the position of paramagnetic particles with a diameter of 100 µm with an accuracy of 7 µm from a desired setpoint using a magnetic setup. A setup of two proportional integral control loops makes it possible to drag the particles through the liquid to a given position or along a given trajectory.

A gold wire was coated with platinum using a sputtercoater to create a self-propelled micro motor. When a small part with a length of approximately 300 µm of the gold/platinum wire was put into hydrogen peroxide solution a large number of bubbles were formed and the wire moved through the liquid. Due to the large number of bubbles formed on the surface it was not possible to see whether the wire actually moved in the direction of gold side as expected. The fluid drag is proportional to the area of the wire perpendicular to the direction of movement therefore the shape shown schematically in

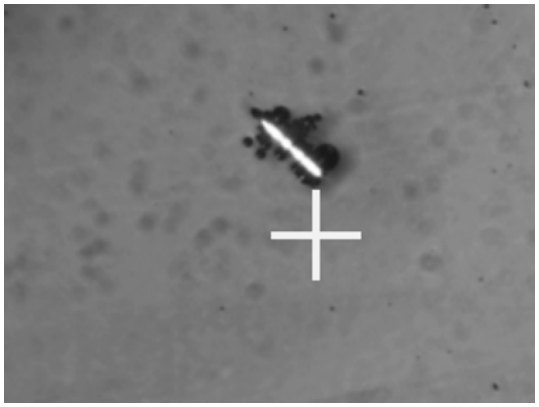

(a) Frame 1

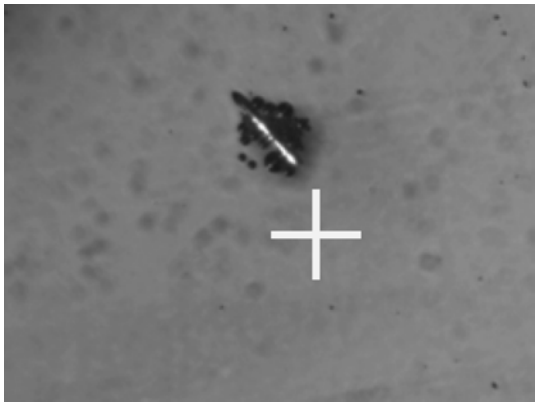

(b) Frame 2

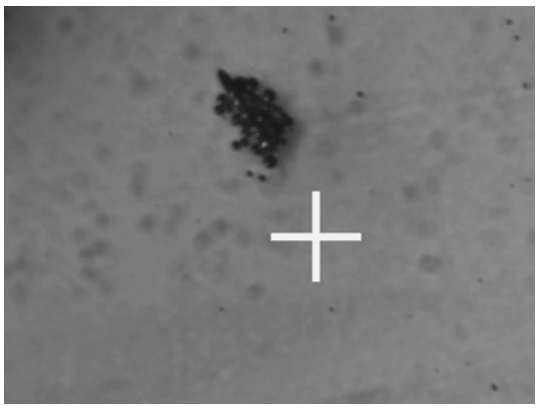

(c) Frame 3

Figure 9: *Three subsequent camera frames showing the movement of the gold/platinum rod in hydrogen peroxide solution. The cross has the same position in each frame and acts as a reference*

figure 1 would be more suitable than the shape shown in figure 8 for linear movement.

V – Future work

Our next step is to create a small rod of gold and platinum where the tip of the rod is coated with platinum. Due to the decreased area of the wire perpendicular to the direction of movement, we expect this shape to be more beneficial for linear movement then the side coated gold wire. The use of an additional magnetic layer should enable control of the direction of movement of this rod by applying a magnetic torque. In this way we separate control and propulsion, so the required external magnetic field can be considerably smaller.

References

[1] R. P. Feynman. There's plenty of room at the bottom. *Microelectromechanical Systems, Journal of*, 1(1):60–66, 1992.

[2] Tihana Mirkovic, Nicole S. Zacharia, Gregory D. Scholes, and Geoffrey A. Ozin. Fuel for thought: Chemically powered nanomotors out-swim natures flagellated bacteria. *ACS Nano*, 4(4):1782–1789, 2010. PMID: 20420469.

[3] Rustem F. Ismagilov, Alexander Schwartz, Ned Bowden, and George M. Whitesides. Autonomous movement and self-assembly. *Angewandte Chemie*, 114(4):674–676, 2002.

[4] Jasper D. Keuning, Jeroen de Vries, Leon Abelmann, and Sarthak Misra. Image-based magnetic control of paramagnetic microparticles in water. *Under review*.

[5] *Comsol Multiphysics*.

COMPOSITION DEPENDENCE OF MECHANICAL AND PIEZOELECTRIC PROPERTIES OF PULSED LASER DEPOSITED $Pb(Zr,Ti)O_3$ THIN FILMS

H. Nazeer[1], M.D. Nguyen[1], L.A. Woldering[1], G. Rijnders[1], M.C. Elwenspoek[1,2] and L. Abelmann[1]

[1]*MESA+ Research Institute, University of Twente, P.O. Box 217, 7500 AE Enschede, The Netherlands*
[2]*FRIAS, Albert-Ludwigs University, Albertstr. 19, 79104 Freiburg, Germany*

***Abstract* — In this contribution we present the compositional dependence of the longitudinal piezoelectric coefficient ($d_{33,f}$), residual stress and Young's modulus of $Pb(Zr_x,Ti_{1-x})O_3$ (PZT) thin films. Pulsed laser deposition (PLD) was used to deposit epitaxial PZT thin films with a $< 110 >$ preferred orientation on silicon cantilevers. By using PLD, excellent piezoelectric properties of the PZT were observed which makes it an exciting piezoelectric material for the development of actuators and highly sensitive sensors. Our investigation of the compositional distribution of the piezoelectric coefficient ($d_{33,f}$) for 250 nm thick films shows a maximum value of 93 pm/V for x=0.52. The static deflection of the cantilevers, measured after the deposition of PZT thin films was used to determine the residual stress for various compositions. The observed trend in the residual stress of PZT thin films is attributed to the varying coefficient of thermal expansion for different compositions. The Young's modulus of the PZT thin films was determined by measuring the flexural resonance frequency of the cantilevers both before and after the deposition. The Young's modulus increases for the zirconium rich PZT compositions, which is in agreement with the trend observed in their bulk ceramic counterparts.**

Keywords: **Cantilevers, residual stress, resonance frequency, Young's modulus, $d_{33,f}$, PZT, PLD.**

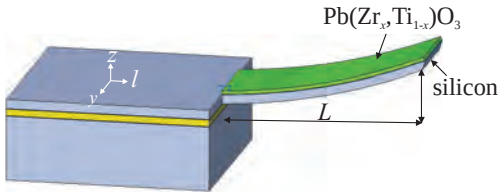

Figure 1: *Schematical representation of a cantilever fabricated from a silicon on insulator wafers. The upward static deflection is due to the tensile residual stress in the PZT thin film that was deposited on the cantilever.*

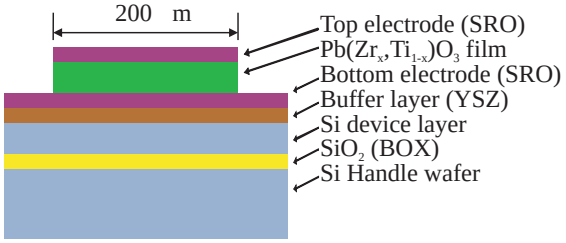

Figure 2: *Illustration of a PZT thin film between top and bottom electrodes. PZT capacitors are needed to measure the longitudinal piezoelectric coefficient. The thickness of the PZT film is 250 nm. The thickness of both the SRO electrodes and YSZ is 100 nm each.*

I – Introduction

The need for highly sensitive sensors and powerful actuators led the micro electromechanical systems (MEMS) industry to explore different materials in the micro- and nano domains. Excellent piezoelectric and ferroelectric properties of $Pb(Zr_x,Ti_{1-x})O_3$ (PZT) thin films makes it an extremely interesting material for the MEMS community [1]. To make PZT suitable for different types of applications, the composition of this material can be controlled by changing the Zr/Ti ratio [2]. To do so, a better understanding of the piezoelectric as well as the mechanical behaviour of PZT thin films of various compositions is needed. Recently, excellent ferroelectric properties have been obtained by using PZT deposited by pulsed laser deposition (PLD) [3]. The compositional dependence of the piezoelectric and mechanical properties of such PLD-PZT thin films is investigated experimentally in this work. To this end, micrometer sized measurement devices are employed. Our investigation focuses on three properties. Youngs modulus of PZT was determined accurately by using the shift in measured resonance frequencies of micro cantilevers [4, 5]. Deflections of the cantilevers as shown in Figure 1 were used to determine the residual stress in the PZT thin films. Piezoelectric coefficient ($d_{33,f}$) was determined by using PZT thin film capacitors, see Figure 2.

II – Fabrication

A dedicated SOI/MEMS fabrication process was used to fabricate 3 µm thick silicon cantilevers. The length of these cantilevers varies from 250 µm to 350 µm in steps of 10 µm with a fixed width of 30 µm. Deep reactive ion etching (DRIE) was used to etch the cantilevers on the device layer of (001) single crystal silicon on insulator wafers and to release the cantilevers from the handle wafer. The buried oxide was etched by using vapours of hydrofluoric acid. The released cantilevers were inspected and characterized by scanning electron and optical microscopy, see Figure 3.

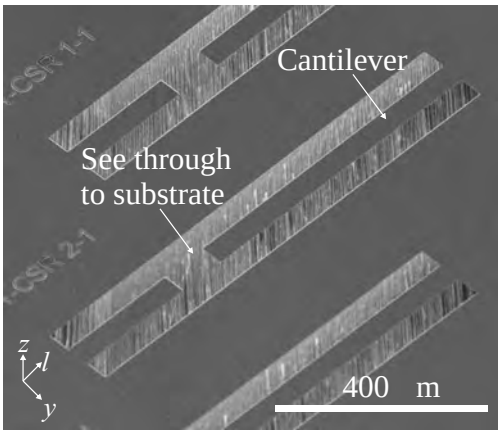

Figure 3: *Scanning electron micrograph of the fabricated cantilevers. Cantilevers were fabricated from a 3 μm thick silicon device layer. Length varies from 250 μm to 350 μm in steps of 10 μm with a constant width of 30 μm.*

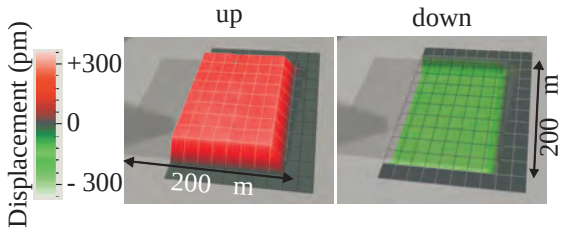

Figure 4: *Scanning laser-Doppler vibrometer measurements of a 250 nm thick $PbZr_{0.52}Ti_{0.48}O_3$ film. By applying an 8 kHz and 6 V peak to peak ac-voltage and measuring the maximum displacement of the top electrode, the piezoelectric coefficient ($d_{33,f}$) was measured.*

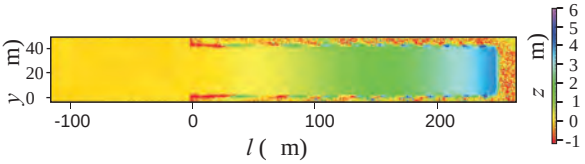

Figure 5: *White light interferometry measurements of the static deflection of a 250 μm long cantilever after deposition of the $PbZr_{0.52}Ti_{0.48}O_3$ thin film. Length and width of the cantilever are represented by l and y. Parameter z represents the transverse deflection of the cantilever.*

PLD was used to deposit 10 nm thick buffer layers of yttria-stabilized zirconia (YSZ) and strontium ruthenate (SRO) and 100 nm thick PZT on fabricated cantilevers. For the piezoelectric coefficient ($d_{33,f}$) measurements, capacitors with in-plane dimensions of 200x200 μm^2 were fabricated on silicon. Starting with the deposition of 100 nm thick buffer layers of YSZ and bottom electrodes of SRO, the 250 nm thick PZT films were deposited followed by the deposition of a 100 nm thick top electrodes of SRO. All these films were deposited using PLD. Different Zr/Ti compositions of $Pb(Zr_x,Ti_{1-x})O_3$ (x=0.2, 0.3, 0.4, 0.52, 0.6 and 0.8) were deposited on separate samples. These samples were then used to investigate the compositional dependence of the piezoelectric and mechanical properties of the PZT thin films.

III – Experimental Details

The orientation of the deposited PZT thin films was analyzed by θ-2θ x-ray diffraction (XRD) scans (XRD, Bruker D8 Discover) with a Cu Kα cathode in the BraggBrentano geometry. Two different types of samples, cantilevers and capacitors, were analyzed separately to determine the preferred orientation of the PZT thin films. X-ray diffraction measurements were performed for all the compositions of PZT thin films that were used in this study.

The piezoelectric coefficient ($d_{33,f}$) was determined by measuring the piezoelectric displacement of the PZT thin film capacitors. This displacement was measured by a MSA-400 micro system analyzer scanning laser-Doppler vibrometer. An 8 kHz and 6V peak to peak ac-voltage was applied on the top and bottom electrodes. The voltage results in the displacement of the PZT thin film that was measured by the displacement of the top electrode. The 2D scan of the top electrode in Figure 4 shows the piezoelectric response of the 200x200 μm^2 $PbZr_{0.52}Ti_{0.48}O_3$ film with a thickness of 250 nm. The measurements were conducted for all compositions of the PZT using identical structures.

The residual stress in different compositions of the deposited PZT thin films were determined by measuring the static deflection of the cantilevers using white light interferometry of the MSA-400 micro system analyzer. The profile of the cantilevers that was measured before the deposition of the PZT thin films was straight. The white light interferometer measurement of the 250 μm long cantilever deposited with $PbZr_{0.52}Ti_{0.48}O_3$ is shown in Figure 5. From this measurement we obtained the maximum deflection of the free end of the cantilever as shown in Figure 6. This information was used to calculate the curvature of the cantilevers for residual stress determination using using Stoney's equation (1) [6].

$$\sigma_f = \frac{1}{6}\frac{E_s t_s^2}{R t_f}, \quad \text{with} \quad R = \frac{L^2}{2\xi} \quad , \qquad (1)$$

the symbols σ, E, t, L, R and ξ are the residual stress, Young's modulus, thickness, length, radius of curvature and deflection, respectively. Subscripts 's' and 'f' denote the silicon and PZT thin film.

To determine the Young's modulus of PZT thin films, the resonance frequency of the cantilevers was measured by using a MSA-400 micro system analyzer scanning laser-Doppler vibrometer. Due to the addition of the PZT thin film on the cantilevers, the resonance frequency was changed, as expected. Measurements of resonance frequencies were conducted both before and after the deposition of the PZT thin films for cantilevers of varying length and for different compositions.

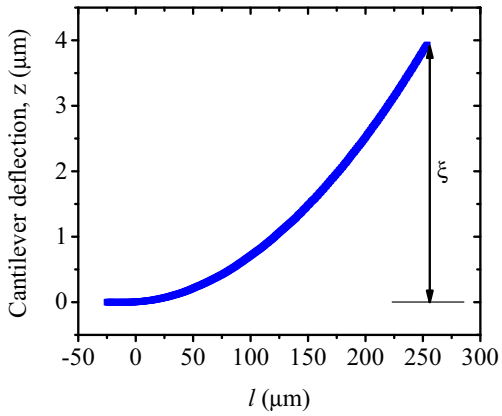

Figure 6: *Profile of the cantilever deflection after the deposition of PZT (x=0.52). A Maximum upward displacement ξ of the free end of the cantilever of almost 4 μm can be clearly seen from the image at l=250 μm.*

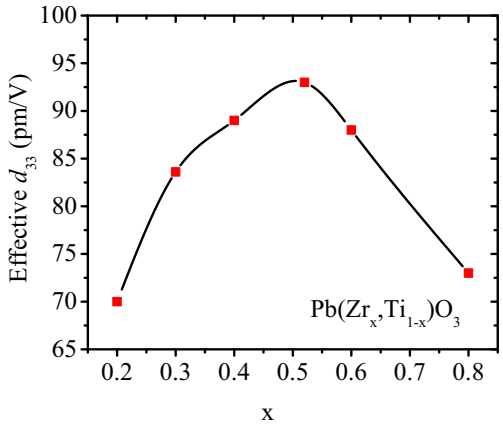

Figure 8: *The effective longitudinal piezoelectric coefficient ($d_{33,f}$) of different compositions. Based on our measurements we find the maximum value of $d_{33,f}$ for x=0.52. The lines are guides to the eye.*

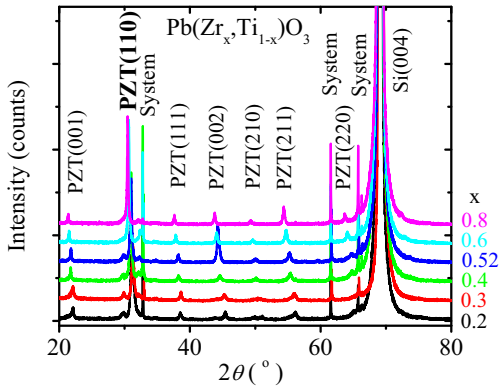

Figure 7: *Measured x-ray diffraction patterns of the pulsed laser deposited $Pb(Zr_x,Ti_{1-x})O_3$ thin films, plotted for different compositions. The PZT films display a preferred (110) orientation.*

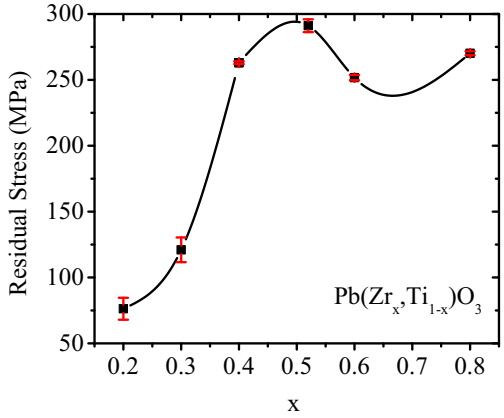

Figure 9: *Compositional distribution of the residual stress in the PZT thin films. Residual stress in the PZT thin film increases with the increasing Zr. content. The lines are guides to the eye.*

IV – Results and Discussion

The mechanical and piezoelectric properties of PZT thin films are dependent on film orientation. For instance, reference [7] discusses the dependence of the residual stress on film orientation. To confirm the orientation of our deposited PZT, we performed X-ray diffraction (XRD) measurements on samples of different compositions. Results reveal that PZT thin films grow with a (110) preferred orientation, see Figure 7.

Figure 8 shows the piezoelectric coefficient ($d_{33,f}$) values for PZT thin films as a function of composition. Clearly, a strong dependence of the piezoelectric coefficient ($d_{33,f}$) on the PZT composition is observed. This dependence shows the same trend as the bulk PZT ceramic counterparts [8]. In particular, the maximum value of piezoelectric coefficient ($d_{33,f}$) of 93 pm/V was observed at x=0.52. This observation is in accordance with the piezoelectric response that is reported in literature for PZT thin films obtained by a sol-gel method [9]. We measured a high ($d_{33,f}$) value of 123 pm/V at film thickness of 1 μm and x=0.52 composition, whereas 72 pm/V is reported for sol-gel PZT at that thickness [9].

The residual stress in PZT thin films of various compositions were found¡ to be tensile and strongly dependent on the film composition, as is shown in Figure 9. For Ti rich compositions of x=0.2 and 0.3, the value of residual stress is small compared to the Zr richer compositions of x=0.4 and above. The tensile residual stress in the PZT thin films increases upto x=0.52 with increasing zirconium content for our measured set of compositions. For x higher than 0.52 we find slightly reduced values for the residual stress. We suspect that this slight reduction may be related to the coefficient of thermal expansion of these compositions. For PZT ceramics, an increase in residual stress for increasing Zr content is attributed to an increase of the thermal expansion coefficient with increasing zirconium content [10]. The maximum value of the residual stress was found to be 291 MPa with a standard error of ± 5 MPa for

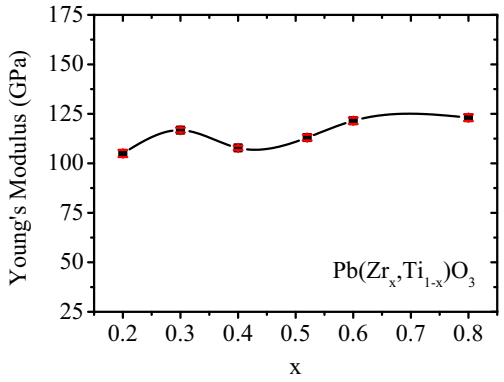

Figure 10: *Zr/Ti composition dependence of Young's modulus of the PZT thin films plotted as a function of Zr. content (x) in $Pb(Zr_x,Ti_{1-x})O_3$ thin films. The lines are guides to the eye.*

the PZT composition with the maximum piezoelectric coefficient ($d_{33,f}$) (x=0.52).

The Young's moduli for PZT thin films with different compositions was determined and plotted in Figure 10. The Young's modulus value for the composition with the maximum $d_{33,f}$ (x=0.52) was found to be 113.5 GPa with a standard error of $\pm$ 1.5 GPa. We observed an increase in the Young's modulus for the Zr rich composition, which is in agreement with published data for PZT ceramics [8].

V – Conclusions

We investigated the Zr/Ti composition dependence of the effective longitudinal piezoelectric coefficient ($d_{33,f}$), the residual stress and the Young's modulus of $Pb(Zr_x,Ti_{1-x})O_3$ thin films. These PZT films were grown on micromachined silicon cantilevers using pulsed laser deposition. This process yields a (110) preferred orientation for all compositions studied in this work.

Compositional distribution measurements of the piezoelectric coefficient ($d_{33,f}$) shows that the maximum value of $d_{33,f}$ was observed at a composition of x=0.52. Compared to sol-gel, our PLD deposited PZT has a 70% higher $d_{33,f}$ value at equal film thickness.

We studied the effect of the Zr/Ti composition on the residual stress of PZT, which was found to be tensile for all the measured Zr/Ti compositions. A maximum residual stress of 291 MPa with a standard error of $\pm$ 5 MPa was measured for the $Pb(Zr_{0.52},Ti_{0.48})O_3$ thin film. The tensile residual stress in the films increases with increasing zirconium content.

The Young's modulus of film with different compositions was determined. The Young's modulus for the composition with maximum $d_{33,f}$ (x=0.52) was found to be 113.5 GPa with a standard error of $\pm$ 1.5 GPa. We observed an increase in the Young's modulus value for the Zr rich composition which is in agreement with the published data for the PZT ceramic [8].

Acknowledgements

The authors gratefully acknowledge the support of the SmartMix Program (SmartPie) of the Netherlands Ministry of Economic Affairs and the Netherlands Ministry of Education, Culture and Science. The authors also thank M.J. de Boer for etching, R.G.P. Sanders for laser Doppler vibrometer measurement, J.G.M. Sanderink and H.A.G.M. van Wolferen for assistance with SEM.

References

[1] B. Piekarski, M. Dubey, E. Zakar, R. Polcawich, D. DeVoe, and D. Wickenden. *Integr. Ferroelectr.*, 42:25–37, 2002.

[2] D. Isarakorn, D. Briand, P. Janphuang, A. Sambri, S. Gariglio, J.-M. Triscone, F. Guy, J.W. Reiner, C.H. Ahn, and N.F. De Rooij. *Smart Mater. Struct.*, 20(2):025015, 2011.

[3] M. D. Nguyen, H. Nazeer, K. Karakaya, S. V. Pham, R. Steenwelle, M. Dekkers, L. Abelmann, D. H. A. Blank, and G. Rijnders. *J. Micromech. Microeng.*, 20:085022, 2010.

[4] H. Nazeer, L. A. Woldering, L. Abelmann, M. D. Nguyen, G. Rijnders, and M. C. Elwenspoek. Influence of silicon orientation and cantilever undercut on the determination of the youngs modulus of thin films, accepted for publication in *Microelectron. Eng.* (2011), doi:10.1016/j.mee.2011.01.028.

[5] H. Nazeer, M. D. Nguyen, L. A. Woldering, L. Abelmann, G. Rijnders, and M. C. Elwenspoek. Determination of the youngs modulus of pulsed laser deposited epitaxial pzt thin films, *submitted*, 2011.

[6] J-A. Schweitz. *J. Micromech. Microeng.*, 1(1):10–15, 1991.

[7] S. Corkovic, R.W. Whatmore, and Q. Zhang. *J. Appl. Phys.*, 103(8):084101, 2008.

[8] B. Jaffe, W.R Cook, and H. Jaffe. *Piezoelectric Ceramics, 1971*. Academic Press, London, 1971.

[9] S-H. Kim, J-S. Yang, C.Y. Koo, J-H. Yeom, E. Yoon, C.S. Hwang, J-S. Park, S-G. Kang, D-J. Kim, and J. Ha. *Jpn. J. Appl. Phys.*, 42:5952–5955, 2003.

[10] G. Shirane, K. Suzuki, and A. Takeda. *J. Phys. Soc. Jpn.*, 7(1):12–18, 1952.

SU 8 BASED MICROFLIUDIC DEVICE FOR BIOPROCESS CONTROL IN MICROTITER PLATES

A. Buchenauer, W. Mokwa, U. Schnakenberg

RWTH Aachen University, Institute of Materials in Electrical Engineering 1, Sommerfeldstr. 24, Aachen, Germany

***Abstract* — Microbioreactors are expected to accelerate the development of biochemical processes by offering both parallelization and process control. Up to now, most microbioreactors have not implemented a controlled dispensing of nutrient solutions. Therefore, we present a microbioreactor with an integrated SU 8 based microfluidic device, which is capable of dispensing fluids for pH control as well as highly viscous substrates. The influence of the membrane material on the pump volume is studied in dispensing experiments. The results correlate well with the simulation of the membrane deflection inside the pump chamber using a simple linear material model. Dispensing experiments with glycerol solutions show that the integrated pumps supply almost constant volumes of approx. 151 nl up to fluid viscosities of 109 mPas.**

Keywords : **Microbioreactor, Microfluidic device**

I - Introduction

Biotechnological processes are a key technology in the synthesis of high-grade chemicals and pharmaceuticals [1]. Efficient production processes have an essential influence on the product cost and thus on its commercial success. The efficiency of production processes is determined during the development phase by the selection of biocatalysts, either enzymes or microorganisms, and the process conditions [2]. But the development of biocatalytical processes is often time-consuming. The reason is the necessity to first identify a suitable biocatalyst and then to find the process parameters for an efficient expression of the biocatalyst [2].

Since the number of screening experiments may amount to several thousand, microtiter plates (MTP) and related measurement technologies have recently attracted a lot of interest [3]. Methods for online monitoring of important process parameters are available especially for MTPs as well as for shake flasks [4-6].

But in most small scale shaken vessels, processes can hardly be influenced and are therefore mostly limited to batch mode. This makes a comparison to industrial fermenters difficult. In contrast, larger experimentation systems as bench-scale fermenters in the range of 0.5 l to 5 l provide full process control, but they lack high throughput, as they are limited to serial processing. Additionally they consume large amounts of culture media.

Since the established methods for process development either lack process control and thus comparability to industrial scale fermenters on the one hand or sufficiently high throughput on the other hand, new experimental platforms have to be developed to enable a fast and cost-efficient process evaluation [7]. Automated fermentations in the submilliliter scale with an integrated online monitoring and fluid supply are regarded as a promising approach to overcome this restriction in process development.

Several approaches for microbioreactors have been reported in literature and are reviewed in [2,7-10]. Up to now, only batch fermentations have been realized in this scale of reaction volume. The most advanced microbioreactors integrate functionalities for fluid handling, sensing or process control. But controlled feeding with nutrient solution is still not integrated in highly parallel microbioreactors, although this is a standard in industrial fermenters.

Although MTPs are an established standard for high-throughput experimentation, they are hardly used as basis for microbioreactors. Thus, their benefits as existing non invasive online monitoring techniques for almost all relevant process parameters, well-known gas transfer characteristics in shaken operation and proven comparability with large scale processes have not been capitalized so far.

Since MTPs represent an ideal basis for microbioreactors, the aim of this work is to equip them with microfluidic devices, which allow fed-batch process in a high degree of parallelization with a high flexibility in experimental design. Such microbioreactors will speed up the development of fermentation processes by achieving a high throughput under highly application relevant conditions during early design phases.

In this paper the microbioreactor concept, the fabrication process and the dispensing characteristics of SU 8 based microfluidic devices are presented. The characterization concentrates on the controlled dispensing using an integrated pump. The dispensing is evaluated for fluids of different viscosities ranging from water to an 85% glycerol solution, because fluids with similar viscosities are used as substrates in fermentation processes.

II – Materials and Methods

A. Microbioreactor

The microbioreactor consists of three main components: The MTP, the microfluidic device and the valve membrane (figure 1). The negative photoresist SU 8 was chosen as construction material for the microfluidic device, because transparency for the optical measurements in combination with a sufficient chemical stabili-

ty and mechanical durability are required. The MTP is a commercially available 48 well MTP (m2p-labs, Aachen, Germany). The microfluidic device is attached to the bottom of the MTP and covers six rows with six wells each. Within one row, it connects the two reservoirs with the four wells.

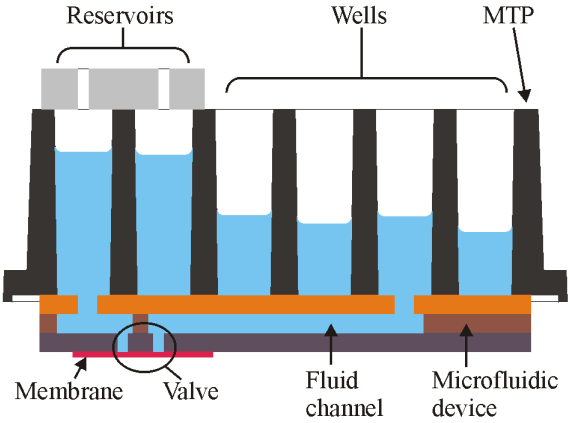

Figure 1: *Schematic cross section of the micro bioreactor consisting of the MTP and the microfluidic device. A detail of the valve is shown in figure 2.*

The fluid flow is controlled by pneumatically actuated valves, which are shown in figure 2. A valve membrane covers two through holes, which are blocked, if a pneumatic pressure of approximately 60 kPa is applied. The valve is opened, if the valve pressure is reduced to ambient pressure. Then the pressurized fluid is able to deflect the membrane and to flow towards the reservoir. The polydimethylsiloxane (PDMS) gasket seals the externally controlled pneumatic pressure.

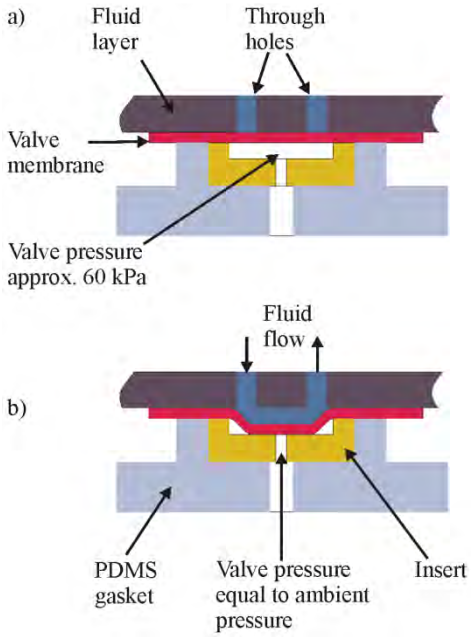

Figure 2: *Cross section of a valve with the PDMS gasket and a brass insert, which provides a defined membrane deflection. a) Open state, b) closed state.*

The three-layer microfluidic device has a thickness of approximately 420 µm. The fluid channels are approximately 118 µm wide and 130 µm high. The fabrication process the connection to external control valves is described in [11]. A detail of the valve array is shown in figure 3.

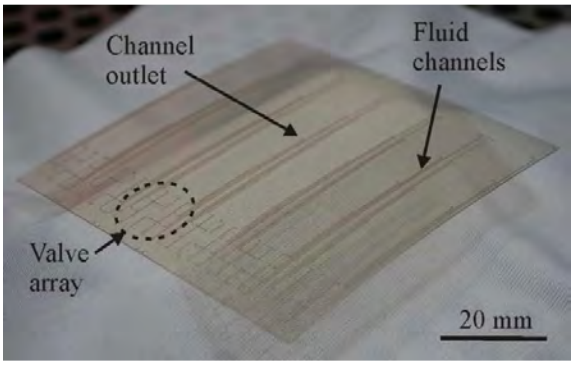

Figure 3: *The three-layer microfluidic device made of SU 8 before being bonded to the MTP. A detail of a valve array is shown in figure 4.*

The valve array is located below the reservoirs, where they do not interfere with the optical measurements, which are carried out through the bottom of the transparent wells. Each reservoir is connected to one inlet valve, a pump chamber and four outlet valves, which control the fluid flow to the wells (figure 4). The cylindrical chambers of the brass inserts shown in figure 2 have diameter of 2 mm. Their depth is 50 µm in case of inlet or outlet valves and 100 µm in case of pump chambers. Fluids are pumped by at first opening the inlet valve and the pump chamber, which are then filled by the pressurized fluid. Then the inlet valve is closed and the outlet valve to a certain well is opened subsequently. The pump chamber is emptied by applying an increased pneumatic pressure. After the outlet valve has been closed the complete pump chamber volume has been supplied to the well and the next pump cycle can be initiated.

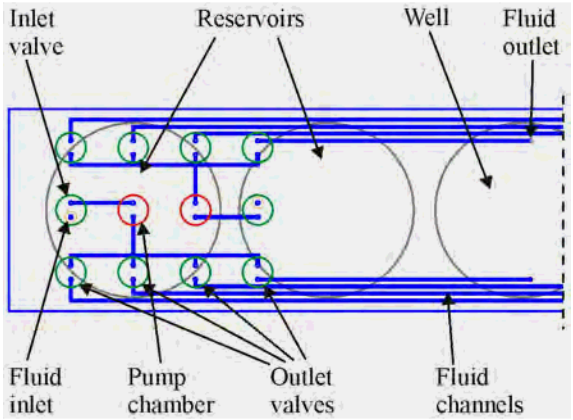

Figure 4: *Layout of the valve array showing the two independent channel systems with one inlet valve, one pump chamber and four outlet valves, each.*

B. Characterization of pump volumes

As indicated in figure 2, the valve membrane is not able to fill the complete insert, as the side wall is perpendicular to the bottom. Therefore, it is assumed that the membrane thickness, the material properties and the

reservoir pressure have a significant influence on the pump volume. Hence, the pump volumes are evaluated with three different membranes. The first is a 15 µm thick low density polyethylene (PE) membrane, the second is a 4 µm thick polypropylene (PP) membrane and the third is a 4 µm thick polycarbonate (PC) membrane (all purchased from Goodfellow). The reservoir pressures are varied within the range of 5 kPa to 45 kPa. The valve pressure remains constant at 60 kPa. The dispensing into each well is repeated 2000 times and afterwards the amount of water has been determined by weighing.

The measured pump volume is compared with the displaced volume resulting from the membrane deflection, which is calculated in a FEM simulation. A two dimensional, rotational symmetric model consisting of axis symmetric shell elements (element type Shell209) and contact elements (element types Conta172 and Targe169) was setup in Ansys (Ansys, Inc.). The membrane is clamped with a fixed support at the outer edge of the membrane and the bending is suppressed at the axis of symmetry. The membrane is loaded with the reservoir pressure. The gasket insert is modeled via contact elements, whose movement is suppressed. The material properties are obtained from the manufacturer data [12]. Elastic moduli of 200 MPa for the PE membrane, 2 GPa for the PP membrane and 2.2 GPa for the PC membrane are used. The contact between the gasket insert and the membrane involves a coefficient of friction of 0.25. The analysis type is steady state and the analytical model is adapted to alterations in shape during the solution process. After the solution, the volume that is enclosed between the deflected membrane and the initial state is calculated from the node displacements.

Finally, the pump volumes of glycerol solutions are evaluated using a PP membrane. The utilized concentrations are 20%, 40%, 60%, 85% and 99.5%. The corresponding viscosities at room temperature are approximately 1.76 mPas, 3.72 mPas, 10.8 mPas, 109 mPas and 1281 mPas, respectively [13]. The reservoir pressure is set to 20 kPa and the valve pressure to 60 kPa.

III - Results and Discussion

The measured and the simulated pump volume of the PE membrane increase continuously with the reservoir pressure (figure 5). At a reservoir pressure of 15 kPa the pump volume is 147.8 nl. The smallest relative difference between the measured and the simulated pump volume of 5.6% is found at a reservoir pressure of 30 kPa. The following increase in pump volumes up to 262.3 nl at 45 kPa is not found in the simulation. This increase is due to a beginning leakage of the outlet valve, when the pneumatic pressure is reapplied to the inlet valve. Then the sum of membrane pretension and external pressure result in a fluid pressure, which is large enough to open the outlet valve partly. In the simulation, the membrane touches the bottom of the pump chamber insert at a reservoir pressure of at least 15 kPa.

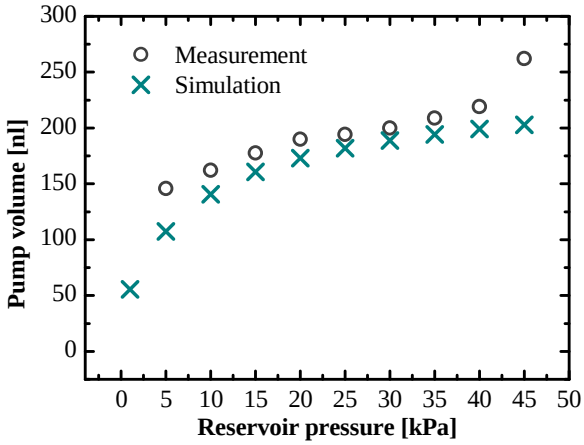

Figure 5: *The pump volume measured using a PE15 membrane depending on the reservoir pressure. The simulated membrane deflection shows a minimal deviation of 11.2 nl, corresponding to 5.6%, at a reservoir pressure of 30 kPa.*

Within the range of reservoir pressures from 10 kPa to 35 kPa, the simulated pump volumes of the PP membrane agree well with the course of the measured pump volumes (figure 6). Here, the simulated pump volumes are in average 6.3 nl larger than the measured ones. This relates to an average difference of 4.8%. In FEM simulations, the reservoir pressure 30 kPa is the smallest regarded pressure, at which the membrane does not touch the pump chamber insert.

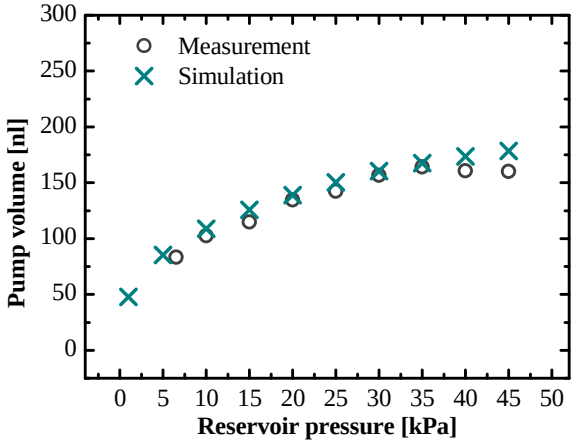

Figure 6: *The pump volume attained with a PP4 membrane depending on the reservoir pressure. The simulated pump volumes are in average 6.3 nl larger than the measured ones, corresponding to an average difference of 4.8%.*

The measured pump volume of the PC membrane continuously rises with an increasing reservoir pressure, until a reservoir pressure of 25 kPa is reached (figure 7). Here, the experimentally determined pump volume is 162.5 nl. Then the pump volume remains almost constant up to a reservoir pressure of 40 kPa. At a reservoir pressure of 50 kPa, the pump volume rises to 360 nl due to the aforementioned leakages. Between reservoir pressures of 30 kPa and 35 kPa, the membrane touches the bottom of the pump chamber.

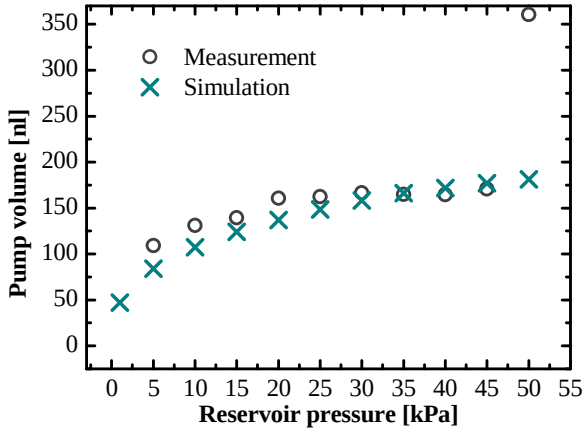

Figure 7: *The pump volume of a PC4 membrane depending on the reservoir pressure. The difference between measured and simulated pump volumes is less than 11% at reservoir pressures of 15 kPa to 45 kPa.*

The pump volumes for glycerol solutions with concentrations of 20% to 85% are between 147.4 nl and 156.6 nl (figure 8). Considering the standard deviations of 5.6 nl to 9.4 nl, theses pump volumes are comparable to those of the pump experiments with water. Just the pump volume attained with the 99.5% solution of 129.8 nl is significantly smaller than that of the other four solutions.

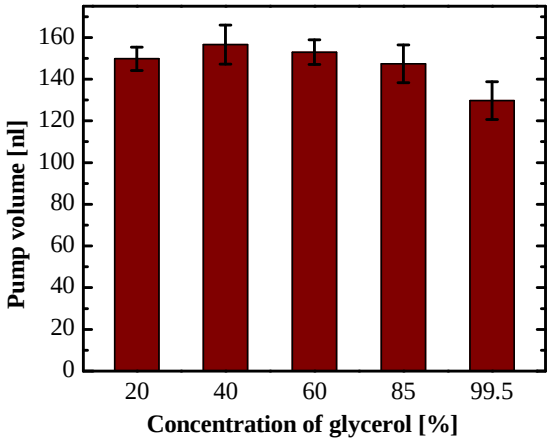

Figure 8: *The pump volumes attained with glycerol solutions in concentrations of 20% to 99.5%. The measurements have been carried out with a PP4 membrane and a reservoir pressure of 20 kPa.*

IV – Conclusion

The pump volume can be approximated by the pressure dependant deflection of the pump chamber membrane using a simple linear material model. This is illustrated by the small differences between measured and simulated volumes of typically less than 11% in relevant reservoir pressure ranges. The investigated membrane types show different courses at increasing reservoir pressures. The PE membrane increases continuously, while the PP membrane provides almost constant pump volumes at pressures from 35 kPa to 45 kPa. The PC membrane offers an even wider range of almost constant pump volumes, which extends from 25 kPa to 40 kPa. These varying courses result from the higher membrane stiffness of the PP and the PP membrane compared to the PE membrane. The remaining differences may be caused by plastic deformations and different stress-strain characteristics. Since the PC membrane provides the smallest changes in pump volume at varying reservoir pressures, it is the best of the three membranes for the described microbioreactor.

The described microbioreactor provides a reliable dispensing of defined volumes of highly viscous solutions as they are commonly used in fermentation experiments. From pure water to 85% glycerol solutions (viscosities of 1 mPas to 109 mPas) can be dispensed in almost constant units of in average 151.7 nl. The standard deviations typically correspond to 4.4%, which is in an acceptable range for fed-batch fermentations of microorganisms.

Acknowledgment

The work was supported by the German Federal Ministry of Education and Research (BMBF), grant 0313811A MRSBio.

References

[1] A. Schmid, J.S. Dordick, B. Hauer, A. Kiener, M. Wubbolts and B. Witholt, *Nature*, vol. 409, 6817, pp 258-68, 2001

[2] G.J. Lye, P. Ayazi-Shamlou, F. Baganz, P.A. Dalby and J.M. Woodley, *Trends in Biotechnology*, vol. 21, 1, pp 29-37, 2003

[3] H.F. Zimmermann, *Chemie Ingenieur Technik*, vol. 77, 4, pp 426-8, 2005

[4] M. Samorski, G. Muller-Newen and J. Buchs, *Biotechnology and Bioengineering*, vol. 92, 1, pp 61-8, 2005

[5] L. Tolosa, Y. Kostov, P. Harms and G. Rao, *Biotechnology and Bioengineering*, vol. 80, 5, pp 594-7, 2002

[6] F. Kensy, G.T. John, B. Hofmann and J. Buchs, *Bioprocess and Biosystems Engineering*, vol. 28, 2, pp 75-81, 2005

[7] D. Schäpper, M.N.H.Z. Alam, N. Szita, A.E. Lantz and K.V. Gernaey, *Analytical and Bioanalytical Chemistry*, vol. 395, 3, pp 679-95, 2009

[8] S. Kumar, C. Wittmann and E. Heinzle, *Biotechnology Letters*, vol. 26, 1, pp 1-10, 2004

[9] P. Fernandes and J.M.S. Cabral, *Biocatalysis and Biotransformation*, vol. 24, 4, pp 237-52, 2006

[10] M. Micheletti and G.J. Lye, *Current Opinion in Biotechnology*, vol. 17, 6, pp 611-8, 2006

[11] A.Buchenauer, W.Mokwa, U.Schnakenberg, *Proc.MME 2009 20th MicroMechanics Europe Workshop*, Toulouse, pp. C30-1 - C30-4, 2009

[12] Goodfellow, *Material properties - polymers*, http://www.goodfellow.com/PDF/TAB302G.pdf, 2011

[13] J.B. Segur and H.E. Oberstar, *Industrial and Engineering Chemistry*, vol. 43, 9, pp 2117-20, 1951

AN IN-PLANE CANTILEVER FOR WALL SHEAR STRESS MEASUREMENT

N.J. Allen[1,2], D.B. Sims-Williams[2] and D. Wood[2]

[1](now at) Aircraft Research Association Ltd., Manton Lane, Bedford, MK41 7PF, UK
[2]School of Engineering and Computing Sciences, Durham University, South Road, Durham, DH1 3LE, UK

***Abstract* — A sensor capable of measuring small shear stresses in wind tunnel applications is presented. The sensor utilises an in-plane cantilever concept for shear stress measurement, designed to minimise intrusiveness into the airflow and allow easy incorporation into wind tunnel test models. The sensor operates independently of input voltage, and can measure <1 Pa shear stresses with a sensitivity of 8.6 mV/V·Pa. Altering the geometry of the sensor has a direct effect on the sensitivity and so can be used to adapt the sensor for different applications.**

***Keywords:* strain gauge, SU8, shear stress, cantilever**

I - Introduction

The accurate measurement of wall shear stress is important for many technical applications. Knowledge of both the magnitude and direction of the flow are essential for the optimisation of aerodynamic surfaces. There are numerous existing methods of measuring wall shear stress, each with their own strengths and weaknesses.

The advent of MEMS techniques have allowed the revision of some of these conventional techniques to improve performance, as well as to allow new devices to be constructed. Hot film sensors have been adapted by thermally isolating the wire using a vacuum cavity beneath the sensor [1] and raising the wire above the surface [2]. However these sensors are still unable to identify reversing flows.

MEMS fabricated skin-friction balances are on a much smaller scale than those previously manufactured; however they remain complex to produce and integrate into test models.

Our previous work [3] introduced the SU8 and nichrome-based device shown here, and the results demonstrated an excellent sensitivity for shear stress measurement. This paper explores the operating parameter space of the device, as well as linking the results with Computational Fluid Dynamics (CFD) and non-linear Finite Element Analysis (FEA) modeling predictions.

II - Experimental Details

The sensor presented here has been designed to allow for high sensitivity measurements while having minimum intrusiveness into the airflow. Additionally, the sensor is surface-mounted and therefore allows easy incorporation into test articles for wind tunnel testing. It was also intended that the sensor should not have the same response to flows in opposing directions in order to allow reversing flow to be identified.

A. Principle of Operation

Figure 1 shows an in-plane cantilever with an integrated strain gauge which is used to measure the pressure-induced deflection, and which can be calibrated to the wall shear stress over the surface on which the sensor is mounted.

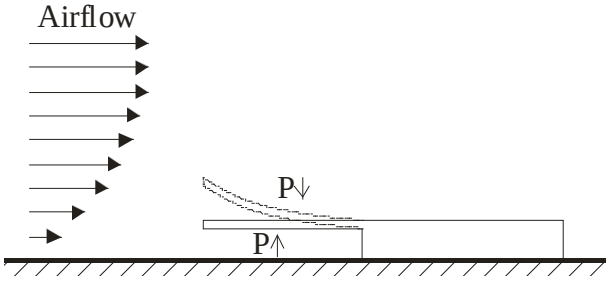

Figure 1: *Sensor operation in an airflow.*

When a flow passes over the sensor, a region of high pressure is created under the cantilever as the local flow stagnates. When the device is deflected there will also be a low pressure region on the top surface. The resulting pressure differential causes the cantilever to deflect upwards. This deflection is measured by the integrated strain gauge and is a function of the local near wall velocity, and hence of the wall shear stress. The length of the sensor in the streamwise direction provides good sensitivity whilst minimising the projection of the device in the wall normal direction. This provides a fundamental advantage over devices which project up from the surface, as these devices must trade sensitivity against the capture of near wall conditions and against minimisation of intrusiveness.

B. Device Fabrication

The cantilever sensors and integral resistors were made from SU8 and nichrome respectively. SU8 has stable mechanical properties after cross-linking, and nichrome has both a high gauge factor (relative to other metals) and a low temperature coefficient of resistivity (TCR). The combination of these two materials offers a good degree of flow sensitivity while minimising temperature-induced changes.

The meander resistor is on the undersurface of the cantilever and this is connected to a Wheatstone bridge incorporated into the body of the device, which in turn serves to further minimise the effects of temperature

variation. The four contact pads required for electrical connections are also in the body of the device. The resistors and contact pads can be seen in figure 2. The sensors were fabricated on a silicon substrate and then released. More complete details on the fabrication process have been published previously [3].

Cantilevers were constructed in a range of dimensions. The lengths of the cantilever were 2, 3 or 4 mm and the width was either 400 or 600 μm. All the cantilevers had a thickness of 12 μm. The resistors had a nominal resistance of approximately 5 kΩ, a length of 12.65 mm, a thickness of 125 nm and a width of 40 μm.

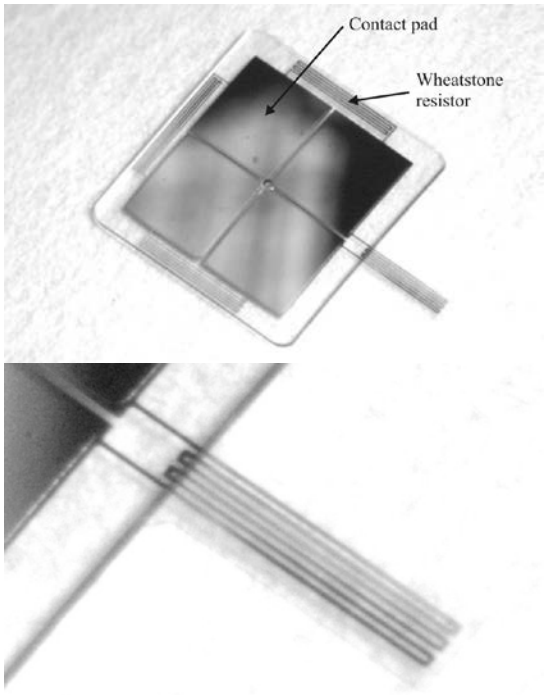

Figure 2: *a) the complete sensor including cantilever, bond pads and bridge circuit; b) the sensing element, which is 2 mm long and 600 μm wide.*

The fabrication process introduces a stress gradient into the polymer. Through careful selection of processing parameters, this stress gradient could be controlled in order to produce a small initial upward deflection at the tip of the cantilever. The degree of curvature varied depending on the length of the cantilever; the tip deflection ranging between <10 μm for the shortest cantilevers and approximately 150 μm for the longest cantilevers.

C. Prediction of Cantilever Response

Simulations were used to aid in device design. The cantilever undergoes a relatively large strain when subjected to an airflow and so predicting its response requires the coupling of both CFD and FEA approaches. Measured material parameters were also required from mechanical testing of example devices.

Previous mechanical testing [3] has shown the Young's modulus of the composite cantilevers to be 1.45 GPa and, for a 2 mm long, 400 μm wide cantilever, the response to tip deflection was 9.6×10^{-7} (mV/V)/μm. This equates to a gauge factor of the NiCr resistor of 1.8. This is slightly lower than the bulk gauge factor of NiCr, but is in the range that could be expected for a thin film of this metal.

CFD was carried out using Ansys Fluent in order to predict the pressure difference between the top and bottom surfaces of the device for a range of cantilever deflections and boundary layer conditions. With the measured value of Young's modulus, non-linear FEA was performed using Strand7 to calculate the deflection which would occur for a range of pressure differences. By identifying intersections between the CFD and FEA results it was possible to obtain the predicted cantilever equilibrium deflection for a range of device designs and boundary layer conditions.

The measured gauge factor for the NiCr then allowed the change in resistance of the strain gauge to be predicted from the FEA strain data at each condition. The resulting prediction for a 2 mm long and 400 μm wide cantilever at a fixed location on a flat plate is shown in figure 3. This response is primarily related to the changing dynamic pressure but also incorporates the changing boundary layer profile with Reynolds number. The cantilever output is throughout presented as the mV imbalance produced across the Wheatstone bridge relative to the excitation voltage applied to the bridge.

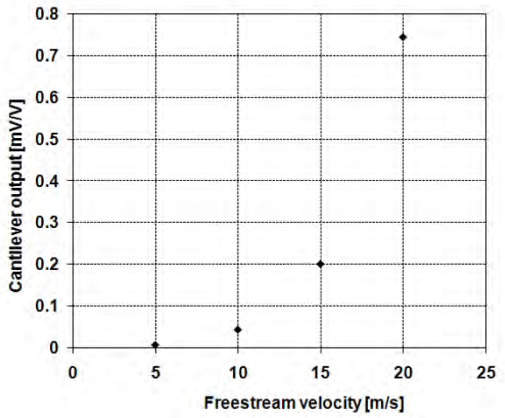

Figure 3: *Predicted response of a typical cantilever.*

D. Thermal Effects

There is a possibility that the heat dissipation in the resistor caused by the measurement technique will interfere with the measurement itself. In addition, the airflow over the sensor would cool the device.

A CFD simulation in Fluent was used to assess the temperature reached by the sensor at different velocities and for varying excitation voltages. The exposed surfaces of the sensor had a temperature applied to them and the heat flux was then obtained from the CFD simulation. Since the heat loss generated by resistive heating could be calculated, it was possible to establish, by an iterative process, the temperature of the sensor at a given velocity for a known excitation voltage.

This analysis confirmed that, even with zero flow passing over the sensor, the impact of resistive heating

on sensor output was negligible. At a freestream velocity of 20 m/s, for an excitation voltage of 1 V, the temperature rise of the sensor was found to be approximately 0.4 K. The NiCr resistor had a low TCR of 150 ppm/K, producing a potential measurement error of 0.003 mV/V. This is more than two orders of magnitude below the sensitivity in the intended mode of operation.

E.Wind Tunnel Testing

The wind tunnel setup is shown in figure 4. The sensors were mounted on a flat aluminum plate in a 0.5 x 0.5 m wind tunnel. The tunnel has a maximum velocity of 21 m/s and the turbulence intensity of the flow is <0.25%. The leading edge of the mounting plate was machined to a knife edge in order to prevent the flow from separating. The sensor was mounted at a position on the plate before transition occurred, where the boundary layer remained laminar and steady-state measurements were taken.

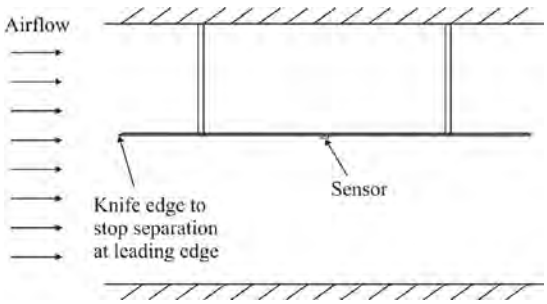

Figure 4: *Schematic of wind tunnel set-up.*

A Preston tube was mounted parallel to the sensor on the plate in order to provide a reference shear stress. A pitot-static tube was also mounted in the wind tunnel to measure the freestream conditions. Both the Preston tube and pitot-static tube were connected to Sensortechnics 103LP10D-PCB pressure transducers.

The sensor's Wheatstone bridge was connected via thin enamel-coated copper wires in twisted pairs, and then through coaxial cables to the data acquisition system and power supply. The output from the pressure transducers was also connected to the same data acquisition system. A National Instruments NI-DAQPad 6015 unit allowed voltage measurements with μV resolution.

III - Results and Discussion

A. Cantilever Length and Width

The response of 400 μm width cantilevers of varying lengths is shown in figure 5. It can be seen that the sensor response increases with increasing length, with the most sensitive cantilever giving ~3 mV/V for a shear stress of 0.35 Pa. The shortest cantilevers have an approximately second order response which is due to the deflection upwards into the airflow. This has the effect of the sensors seeing a larger force and is more pronounced with a greater shear stress. However, the longer cantilevers deflect to such an extent that they bend back over the body of the sensor, which is a non-optimal effect.

The response of typical 2 mm long cantilevers with widths of 400 and 600 μm is shown in figure 6. The difference in response between the two different width cantilevers is small, although the narrower cantilevers were found to have a marginally greater response. First order effects suggest that the sensitivity should be independent of width (since both pressure force and cantilever second moment of area scale almost linearly with width). The increased sensitivity at decreased widths might be attributed to an aerodynamic edge effect but it is more probably attributable to the fact that the wider cantilevers had a slightly smaller degree of initial deflection than the narrower ones. This is because the initial deflection is caused by the stress interaction at the interface between the SU8 and nichrome, and the nichrome does not extend the full width of the cantilever in the wider structure. This would suggest that using a narrower cantilever would be beneficial as it does not have an adverse effect on the sensitivity of the device, and would have greater spatial resolution and reduced impact on the flow.

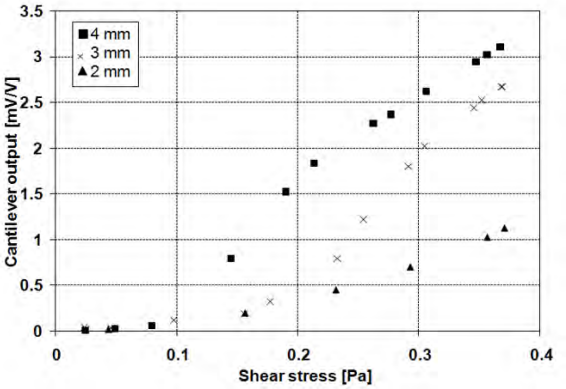

Figure 5: *Measured effect of cantilever length on response.*

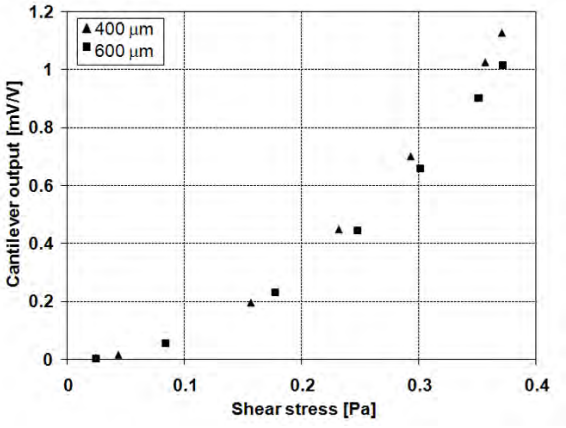

Figure 6: *Measured effect of cantilever width on response.*

B. Excitation Voltage

The effect of the excitation voltage was tested on a 4 mm long cantilever. It can be seen in figure 7 that there is no discernible change, which confirms the conclusions of the CFD analysis that thermal effects were not significant.

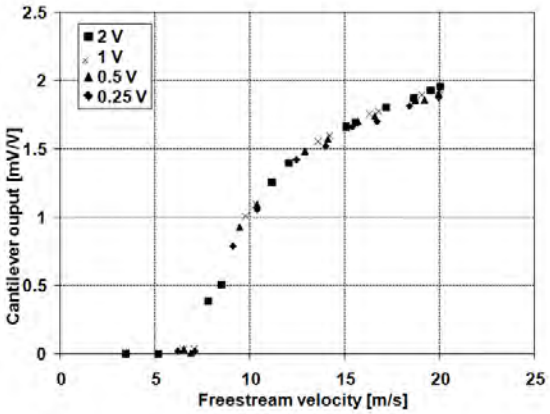

Figure 7: *Measured effect of excitation voltage on response.*

C. Axial Position

The response of a 4 mm long sensor tested at a range of free stream velocities at two different axial positions on the flat plate is shown in figure 8. This shows that the sensor can measure shear stress independently of the thickness and shape of the boundary layer, and means that calibration in one type of boundary layer will give consistent results when moved.

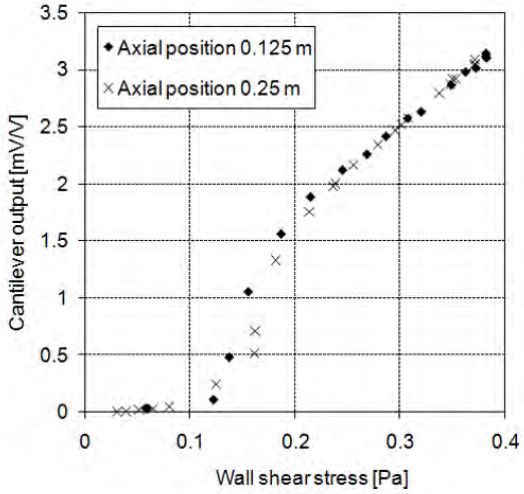

Figure 8: *Response to change in boundary layer thickness.*

D. Comparison of Wind Tunnel, CFD and FE Results

The comparison of results from CFD and FE modeling with experimental data for 2 mm long cantilevers is shown in figure 9. There was good fundamental agreement of the experimental results with the data from modeling. Variations in the data are probably attributable to geometry idealisations in the CFD simulations and possibly due to the effects of the internal stress distributions not being included in the FE model.

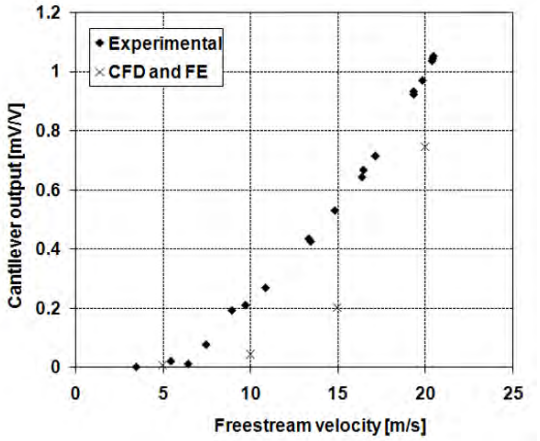

Figure 9: *Comparison of experimental and CFD and FE data.*

IV - Conclusion

A new method of measuring shear stress has been demonstrated which allows the measurement of wall shear stress with a high degree of sensitivity. For the most sensitive cantilever, a response of 3 mV/V for a shear stress of 0.35 Pa is demonstrated, as shown in figure 5. The device design minimises intrusiveness of the sensor into the boundary layer. The range of measurement can be altered depending on the length of the cantilever and a prediction method has been developed to aid device design. The sensor is unaffected by alterations in the excitation voltage and, due to the low thermal coefficient of resistivity and Wheatstone bridge, has little susceptibility to variations in temperature.

Acknowledgements

This work was funded by One North-East (project SP/507 – Enabling Technologies to Support the Knowledge Economy), and the authors would like to thank ONE for their support.

References

[1] M. Sheplak, V. Chandrasekaran, A. Cain, T. Nishida and L.N. Cattafesta, *AIAA Journal* 40 (6), pp. 1099-1104, 2002.

[2] J. Chen, J. Zou and C. Liu, *15th IEEE MEMS Conference*, Las Vegas, January 20-24, pp. 332-335, 2002.

[3] N.J. Allen, D. Wood, M.C. Rosamond and D.B. Sims-Williams, *Eurosensors XXIII*, Lausanne, September 6-9, *Procedia Chemistry* 1, pp. 923-926, 2009.

ELASTOCAPILLARY FOLDING OF THREE DIMENSIONAL MICRO-STRUCTURES USING WATER PUMPED THROUGH THE WAFER VIA A SILICON NITRIDE TUBE

A. Legrain, J.W. Berenschot, R.G.P. Sanders, K. Ma, N.R. Tas and L. Abelmann

Transducers Science and Technology Group, MESA⁺ Research Institute, University of Twente, P.O. Box 217, 7500AE Enschede, The Netherlands

***Abstract* — In this paper we present the first investigation of a batch method for folding of three-dimensional micrometer-sized silicon nitride structures by capillary forces. Silicon nitride tubes have been designed and fabricated using DRIE at the center of the planar origami patterns of the structures. Water is brought to the structures by pumping the liquid through the wafer via those tubes.**

Isolated micro-structures were successfully folded using this method. The potential of this technique for batch self-assembly is discussed.

***Keywords:* Micro-fabrication, elasto-capillarity, self-assembly, origami, three-dimensional, micro-structures**

I – Introduction

An important part of the research in the field of MEMS is nowadays focused on fabrication of three-dimensional (3D) systems [1]. It is well-known that the miniaturization of electronic elements becomes more and more difficult approaching fundamental limits. The third dimension presents a promising option to achieve much higher component densities.

The fabrication of 3D MEMS is difficult because of the inherent two-dimensionality of projection photo lithography [2]. Being primarily based on micro-machining, 3D structures are essentially an extension of 2D patterns obtained by means of lithography. Therefore the height, and complexity, of 3D structures is very limited. Self-assembly is seen to be an encouraging method to overcome these problems [1].

As we recently showed [3, 4, 5], capillarity is a very effective mechanism to achieve the folding of micrometer sized planar structures into 3D shapes. It was demonstrated that 3D micro-objects of silicon nitride could be fabricated starting from planar geometries on which a tiny water droplet was deposited. Surface tension of the deposited liquid induces the out-of-plane rotation of infinitely stiff wings connected to each other by flexible hinges.

Microfabrication inspired on origami, the Japanese paper folding art, can combine the conventional parallel micro-fabrication with the creation of complicated 3D structures [6, 7, 8]. Structures assembled so far using elasto-capillarity have been folded after deposition of a tiny droplet of water using a manually controlled hollow fiber [3, 4, 5]. That method is adequate for experiments carried out in a laboratory, but obviously not for potential industrial applications.

One of the options to provide batch folding of structures is to implement a central tube into the structures and pump water parallel through the wafer towards the structures. By selectively adding or retracting the water, one could nicely control the folding with the pump. Furthermore, the central position of the tube would ensure a good distribution of the liquid over the structures.

The work introduced here aims at the first experiment of folding isolated micro-structures using liquid pumped from backside. The micro-machining of silicon nitride structures patterns along with the preliminary folding experiments are presented in this paper.

II – Design and fabrication

Figure 1 presents a cross-section of the micro-structures during their folding by pumping water through the wafer. The structures are made with stiff flaps connected to each other by flexible hinges. The central plate is connected to a tube which passes completely through the wafer as represented in figure 1a. All elements of the structure are made of silicon nitride.

The size of the flap is in the 50-200μm range, the radius of the tube is 34μm. The folding occurs with the evaporation of water once the pumping has stopped, as represented in figure 1b and c. Figure 2 presents the main steps of the fabrication of the structures

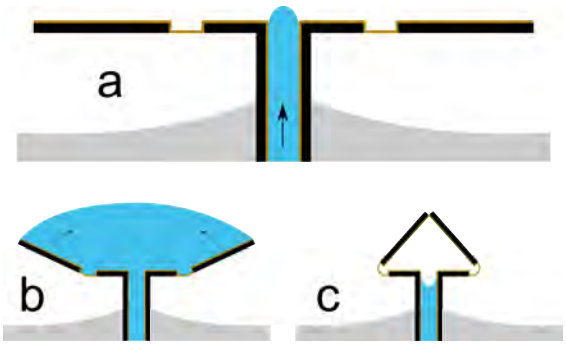

Figure 1: *Folding principle. Water is pumped through the wafer via the central tube (a). The liquid overflows over the structures and the pumping is stopped. The water tends to reduce its liquid-air interface and induces the rotation of the flaps (b). Once the water is evaporated, the flaps stick together and the structure stays closed (c).*

In order to reduce the length of etching through the

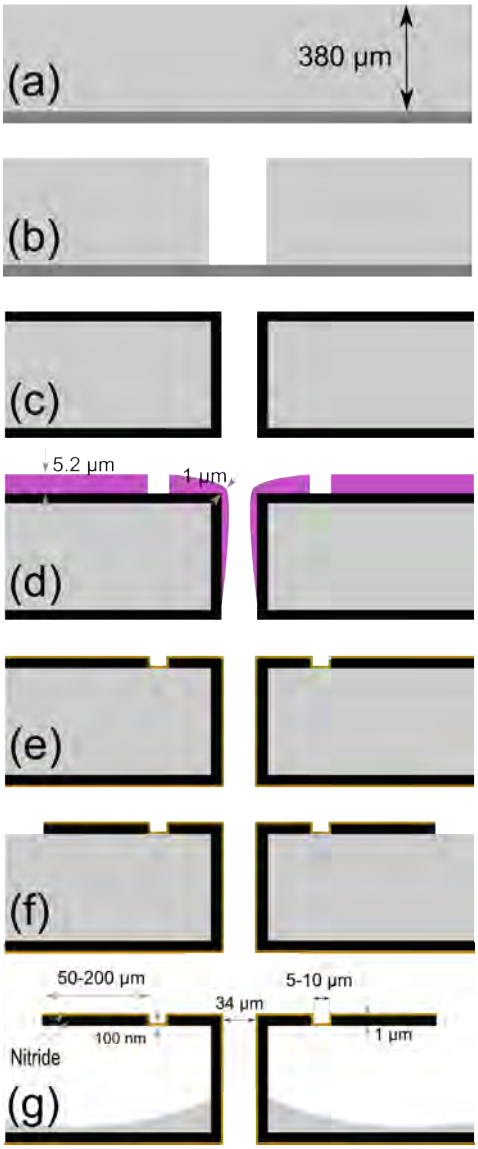

Figure 2: *Main steps of the process. See text for description of the steps.*

wafer and make the future pumping easier, a thin (110) wafer is selected (380 μm thick). Then a foil is applied on the bottom-side of the wafer (a). This foil is temporary needed for the subsequent DRIE step through the entire wafer (b). It acts as an etch stop and prevents leakage of the helium backside cooling, ensuring a stable temperature control of the wafer during the etching process. As a foil we use a DuPont MX500 polymer film [9]. The DRIE is performed using an ADIXEN AMS100SE machine using a Bosch recipe.

After removal of the foil using a reactive oxygen plasma, a 1 μm layer of silicon nitride is grown all over the wafer, including inside the hole, by LPCVD (c). Then, a lithography step follows to define the location of the flexible hinges (d). In order to protect the edges at the intersection between the tubes and the structures patterns, particular attention must be paid to the lithography steps of the process. Otherwise, this intersection is attacked during the subsequent etching step and the silicon nitride patterns are not tethered anymore.

For this purpose, we used a relatively thin photo-resist (OiR 907-35). The wafer is spun at slow speed (2000 rpm) to provide a 5.2 μm thick layer of photo-resist. After verification, it appears that the outer limits of the tubes are protected with about 1 μm of photo-resist as represented in step (d) of the process. This layer is thick enough to protect the edges during etching of the silicon nitride.

Openings are created by a dry SiN etching step (RIE). After stripping the photo-resist in oxygen plasma and in HNO_3, a 100 nm silicon nitride layer is deposited (e). This thin layer defines the flexible hinges which enables the structures to fold. Then another lithography step is performed to define the overall geometry of the structures. Once the edges are well-protected, the silicon nitride can be etched using a dry etching step (RIE) (f). At this time of the process, several origami-like patterns of structures (boxes, tetrahedrons, pyramids) are defined on top of the wafer. Finally, the last lithographic step is performed and the peripheral flaps are freed by under-etching the silicon in dry SF_6 gas etcher (g). The specific design parameters are given in figure 2 (g).

III – Fabrication results

Figure 3a represents a SEM photograph of an isolated tube surrounded by trenches in the first silicon nitride layer. This picture has been taken after the definition of folding locations, figure 2 (e). One can see in figure 3b the characteristic shape of the scallop due to the Bosche recipe used for the creation of the tube. Moreover, there is no discontinuity between the planar pattern and the tube thanks to the spinning of a 907-35 photo-resist layer at low rotation speed during the preceding lithography step as discussed in the previous section.

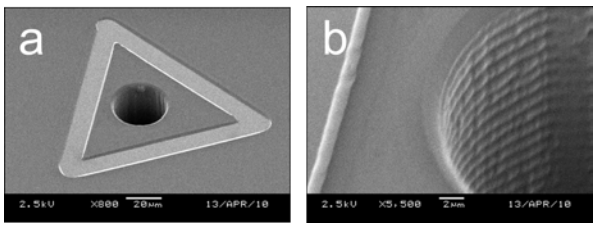

Figure 3: *SEM picture of a silicon nitride tube through the wafer after step (d) in figure 2. At the end of the process, this will become a pyramidal pattern (a). Close up of the central part (b).*

Figure 4a shows an origami pattern of a cube resting on its silicon nitride tube after the under-etching of the silicon substrate (figure 2 step (f)). Figure 4b is a close up view of the fixed central part. Thanks to the use

of a thick enough photo-resist layer the pattern is still attached to the tube. We can also clearly observe the thin hinges along with the thicker flaps. The tube has a diameter of 34μm, the length of the side of the flaps is 60μm.

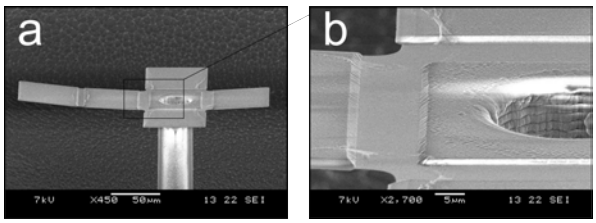

Figure 4: *SEM picture of a silicon nitride origami pattern resting on a silicon nitride tube (a). Close up of the central part (b).*

Figure 5 represents an overall view of a group of micron-sized patterns of boxes. The structures are ready to be folded at the same time.

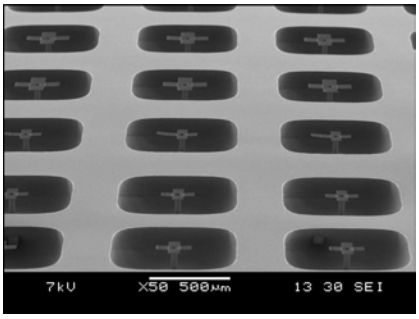

Figure 5: *SEM picture of the frontside of an array of unfolded structures. The holes in the centre can just be distinguised.*

IV – Folding experiments

A. Experimental details

When filling the tubes, the edge between the tube and the planar pattern forms a barrier, since at this point the radius of curvature of the surface of the water is the lowest. This induces a Laplace pressure, defined as Δp=P_l-P_v where P_l is the pressure of the liquid and P_v is the pressure of the vapor, in this case the air [10]. The overpressure Δp needed to overcome the edge is given by:

$$\Delta p = \frac{2\gamma}{R} \simeq 10 \text{ kPa} \quad (1)$$

where γ=72 mN/m is the surface tension of water at 25°C and R is the radius of the curvature of the surface at the edge. Since the radius of the tube is in the sub-millimeter range, the radius of the curvature of the surface can be considered in first approximation of the same order of magnitude as the radius of the tube ($R \simeq 34\mu m$). A pump capable to apply this overpressure is therefore required for the experiments. Moreover, pumping must be precise to avoid the structure to be submerged. Indeed, once the water gets over the edge, the Laplace pressure is much lower and the flow of water could become uncontrollable.

Thus, a high precision syringe pump has been used for our preliminary experiments. Small pulses of pumping can be realized with this pump. A fiber connects the pump to the bottom of a plate with a 0.8mm hole at the center. The sample is placed on this support and an accurate positioning system permits to perfectly align a structure with the fiber. A small silicone o-ring is placed between the sample and the fiber to ensure a watertight connection. The sample is fastened using a u-shaped clamping tool surrounding the structure.

B. Results

As expected, the water emerges out of the tube but a large amount of liquid comes out once the edge is overcome. However, even if the droplet is one order of magnitude bigger than the structure, it still remains on the silicon nitride pattern. Thus, the water does not overwhelm the substrate and the folding occurs after evaporation of the liquid. Once the flow stops and the volume of the droplet stabilizes, small volumes of water (5-10 nL) can be added by actuating the pump.

Figure 6 shows a long structure which has been folded using this setup. This new method of assembly is a considerable improvement for our research. Indeed, there is no deviation of the folding anymore due to the manual deposition of the water since the holes are designed precisely in the center of the structures. Furthermore, from now on the folding sequence can be studied more in depth by adding small volumes of water on demand.

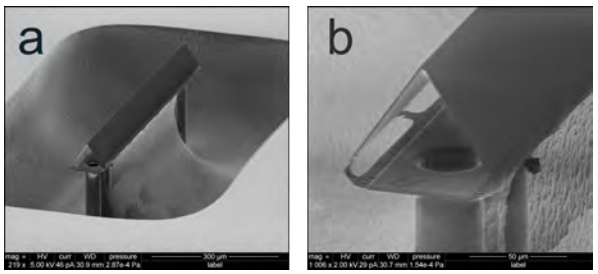

Figure 6: *SEM pictures of a long symmetric structure folded by pumping water through the tubes. An overview (a) and a close-up of one of the extremities (b).*

V – Conclusion

It is possible to fabricate silicon nitride plates connected to a long silicon nitride tube which traverses the thickness of a wafer. One of the most critical process steps is to protect the outer limits of the tubes with a rel-

atively thin layer of photo-resist. This can be achieved by spinning the resist at low rotation speed.

Isolated three-dimensional micron-sized structures can be successfully folded using the surface tension of water pumped through the tubes from the backside of the wafer. As has been theoretically and experimentally shown, the critical point of the assembly is to pump the water out of the tubes to form droplet on the structure. The overpressure required to overcome this barrier can cause an uncontrolled flow once the droplet starts to form.

VI – Recommendations

Future work will have to address the issue of uncontrolled flow. By reducing the capacitance of the pumping system and better control over the applied pressure, unwanted flow might possibly be reduced.

For batch fabrication, the pressure needs to be identical in all tubes over the wafer, which will put stringent demands on the fluidic system. Nevertheless, this new method of assembly is promising, also for all fields of research where the behavior of liquid over surfaces is studied. The fact that the water is brought exactly where the holes have been designed and that small volume of water can be added on demand provides a strong advantage.

Acknowledgments

We wish to acknowledge the contribution of Joost van Honschoten to this work. The main theme of this publication is based on his original ideas. We commemorate his passion for science and for the subject of elasto-capillarity specifically.

References

[1] K. Ariga, J P. Hill, M V. Lee, A. Vinu, R. Charvet, and S. Acharya. Challenges and breakthroughs in recent research on self-assembly. *Sci. Technol. Adv. Mater.*, 9:96 pp., 2008.

[2] Madou. *Fundamentals of Microfabrication*. CRC Press, New York, 1997.

[3] J. W. van Honschoten, J. W. Berenschot, T. Ondarçuhu, R. G. P. Sanders, J. Sundaram, M. Elwenspoek, and N. R. Tas. Elastocapillary fabrication of three-dimensional microstructures. *Appl. Phys. Lett.*, 97:0141031–0141033, 2010.

[4] J. W. van Honschoten, J. W. Berenschot, R. G. P. Sanders, N. R. Tas, and M. Elwenspoek. Fabrication of three-dimensional microstructures using capillary forces. In *Proc. of MicroMechanics Europe (MME), 115*, 2009.

[5] J. W. van Honschoten, A. Legrain, J. W. Berenschot, L. Abelmann, and N. R. Tas. Microassembly of three dimensional tetrahedra by capillary forces. In *24th IEEE International Conference on Micro Electro Mechanical Systems*, pages 288–291, Cancun, Mexico, january 2011.

[6] C. Py, P. Reverdy, L. Doppler, J. Bico, B. Roman, and C. N. Baroud. Capillary origami: Spontaneous wrapping of a droplet with an elastic sheet. *Phys Rev Lett*, 98(15):156103, 2007.

[7] T. G. Leong, A. M. Zarafshar, and D. H. Gracias. Three-dimensional fabrication at small size scales. *Small*, 6(7):792–806, 2010.

[8] M. Boncheva, S A. Andreev, L. Mahadevan, A. Winkleman, D R. Reichman, M G. Prentiss, S. Whitesides, and G M. Whitesides. Magnetic self-assembly of three-dimensional surfaces from planar sheets. *Proc. Natl Acad. Sci.*, 102:3924–3929, 2005.

[9] www.dupont.com. *DuPont Mx5000 Series - Data Sheet and processing information*.

[10] P. G. de Gennes, F. Brochard-Wyart, and D. Quéré. *Capillarity and Wetting phenomena Drops, Bubbles, Pearls, Waves*. Springer, 2004.

SIMULATING THREE DIMENSIONAL SELF-ASSEMBLY OF SHAPE MODIFIED PARTICLES USING MAGNETIC DIPOLAR FORCES

Laurens Alink [1], G.H. (Mathijs) Marsman [1], Léon A. Woldering [1] and Leon Abelmann [1]

[1] *Mesa+ Institute for Nanotechnology, University of Twente, The Netherlands*

***Abstract* — The feasibility of 3D self-assembly of milli-magnetic particles that interact via magnetic dipolar forces is investigated. Typically magnetic particles, such as isotropic spheres, self-organize in stable 2D configurations. By modifying the shape of the particles, 3D self-assembly may be enabled. The design of the particles and the experimental setup are presented. The magnetic configurations of simple particle arrangements are obtained via energy minimization in simulations. The simulations show that a 3D configuration can become energetically favourable over 2D configurations, if the shape of the particle is modified.**

***Keywords:* 3D self-assembly, magnetism, dipolar forces, anisotropic particles, energy minimization**

I – Introduction

Microfabrication techniques are currently based on top-down lithography and therefore inherently two dimensional (2D), or at best very restricted in the third dimension. Fabrication by means of three dimensional (3D) self-assembly will open up a wide range of new applications, such as new types of (smart) supermaterials with interesting optical, mechanical, electrical and magnetic properties [1]. On the long term, we envision 3D electronics as an answer to atomic limits emerging at the end of Moore's law progress [2].

In this paper, we focus on 3D self-assembly driven by dipolar magnetic forces. Particles that interact by dipolar forces only, typically assemble in 2D configurations preferably [3]. Our approach to overcome this limitation is to enable 3D magnetic self-assemblies by clever design of the shape of the particles. In order to have accurate control over the shape, this approach is investigated using millimeter sized particles. Some simple configurations of milli-magnetic particles are shown in figure 1. We investigate the stability of such simple configurations by means of simulations and extend into non-spherically shaped particles.

Figure 1: *Photographs of simple configurations of toy magnets ('neocubes') with a diameter of 4 mm. All the configurations are stable, except for the two rightmost configurations; when the magnets are forced in one of these meta-stable configurations, they readily rearrange when touched.*

II – Setup and particle design

There are four distinct elements that play a role in all self-assembly systems: (I) the particles, (II) binding forces, (III) driving forces and (IV) the environment. In our case these elements are the following: The particles are millimeter sized plastic shells, which are fabricated by 3D-printing. This fabrication technique allows the shape to be to be controlled in an arbitrary fashion. The particles contain an embedded hard magnet. Consequently, magnetostatic forces are the main binding force. In this case, magnetostatic forces are also driving the self-assembly. To enhance the (random) motion of the particles, a turbulent flow will be induced in the liquid by means of agitation. All experiments will be carried out in an aqueous environment. We intend to have the particles hover, *i.e.*, neither sink nor float in the liquid, thus enabling self-assembly without constraints by the bottom or side walls of the beaker. Therefore, for neutral buoyancy, the density of the liquid will be matched with the density of the particles by dissolving NaCl in the water. The designated experimental setup is schematically depicted in figure 2a.

The milli-magnetic particles are neodymium magnets enclosed in a 3D-printed shape, see figure 2b. The used magnets are off-the-shelf neodymium disc magnets. These magnets have their magnetization oriented along their axis. The design specifications the particles are listed in table 1. The particles are designed such that the maximum magnetic force between two particles is slightly larger than the net downward force in water. In this way, the particles can bond magnetically, but weak bonds can still be broken by supplying energy via the turbulently flowing water. Furthermore, we closely match the density of the particles (1.3 kg/L) and the liquid (1.2 kg/L). Therefore, the downward force will be tuned to a small value. For the first test experiments, the particles have a spherical shape.

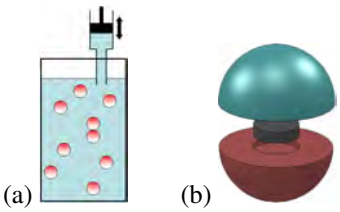

Figure 2: *(a) Schematic drawing of the experimental setup. Shown are the beaker, which contains the liquid with the milli-magnetic particles, and the inlet to which an agitation pump can be connected. (b) Exploded view of a milli-magnetic particle. Shown are the neodymium magnet and the 3D-printed plastic encapsulation, which consist of two half-spheres; their difference in color allows to identify the 'North' and 'South' pole of the particle.*

Table 1: *Design specifications of the particle. In the effective density of the particle, the density and volume of the neodymium magnet and plastic shell are taken into account. The magnetostatic force that is listed here, is the maximum magnetostatic force that two particles can exert on each other [4].*

property	dimension
particle radius, r	5 mm
magnet radius	2 mm
magnet height	1 mm
effective density particle	1.3 kg/L
saturation magnetization, M_s	1.2 T/μ_0
magnetostatic force, F_m	8.3 mN
gravitational force	6.8 mN
net downward force in water	1.7 mN

III – Simulation procedure

The preferred magnetic configuration (that is, the orientations of the magnetic moment of the particles) is found by minimizing the magnetostatic energy of the configuration dynamically. For simplicity, the particles are treated as dipoles. Only the torques on the dipoles are considered and not the forces. In other words, the positions of the particles are fixed in the simulations and the particles can only lower their energy via rotation. We determined stable positions of the particles by using the observed configurations of the neocubes in figure 1 as a guide.

The magnetostatic energy of a single dipole in a magnetic field is given by

$$U = -M\mathbf{m}\cdot\mathbf{B}, \tag{1}$$

where $M = M_s V_m$ is the magnitude of the dipole moment, with V_m the volume of the particle's magnet; $\mathbf{m}$ is the unit vector in the direction of the dipole moment and $\mathbf{B}$ is the magnetic field at the position of the dipole.

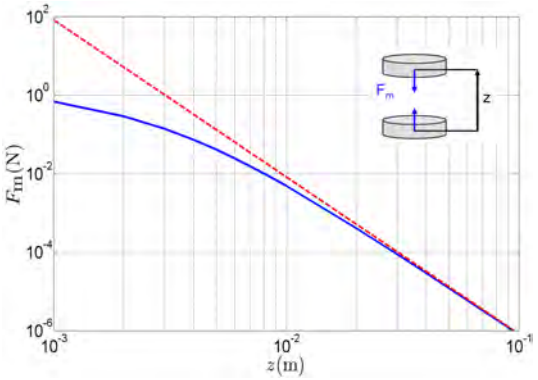

Figure 3: *Force between two cylindrical magnets with a common axis, as a function of center to center separation. The cylinders have an axial magnetization and dimensions as listed in table 1. The exact solution [4] (solid line) and dipole approximation (dashed line) are shown.*

This magnetic field is caused by the other dipoles in the system. The field of a single dipole is given by

$$\mathbf{B} = \frac{\mu_0}{4\pi}\frac{1}{|\mathbf{r}|^3}\left(3\hat{\mathbf{r}}(\mathbf{m}\cdot\hat{\mathbf{r}}) - \mathbf{m}\right), \tag{2}$$

where $\mathbf{r}$ is the distance between the dipole and the point where the field is evaluated and $\hat{\mathbf{r}}$ is the unit vector from the dipole to this point. The magnetostatic force acting on a dipole can be obtained by

$$\mathbf{F} = -\nabla U. \tag{3}$$

In figure 3, the forces between two dipoles are compared with the forces between cylindrical shaped magnets. At large distances, the dipole approximation is accurate. However, the approximation is less accurate at distances that are comparable to the size of the cylindrical shaped magnets. Therefore, the accuracy of the simulations can be improved by taking the exact fields into account for nearest neighbour particles.

The total magnetostatic energy of a configuration of particles can be obtained by summing the energies of all the dipoles in the system.

The magnetostatic energy is minimized by allowing the dipole moments to rotate in the direction of the net field via

$$\frac{\Delta\mathbf{m}}{\Delta t} = -\alpha\,\mathbf{m}\times(\mathbf{m}\times\mathbf{H}), \tag{4}$$

with $\mathbf{H} = \mathbf{B}/\mu_0$. After each iteration step Δt, a new configuration of the dipole moments is calculated with its resulting field. The damping factor α is manually adjusted to optimize simulations speed while maintaining convergence. The simulation is stopped after 10000 steps, or when the change in the total magnetization is below a certain tolerance:

$$\sum_{n=1}^{N} |\Delta\phi_n| + |\Delta\theta_n| < 10^{-5}\ \text{rad}, \tag{5}$$

where N is the number of dipoles in the configuration and ϕ and θ are the angles defining the direction of dipole moment; $\Delta\phi$ and $\Delta\theta$ are the changes of these angles in a single time step.

The energy does not necessarily converge to a global minimum. Therefore, the simulations are repeated several times, with random initial dipole moments, to find the magnetic configuration with the lowest energy.

IV – Results and discussion

The energies corresponding to the simple configurations in figure 1 have been simulated first. The distance between two neighbouring particles in these configurations is $2r$. Table 2 shows the final magnetization state of the simple configurations and the corresponding energies. The energies scale with M^2. The configuration with the lowest energy for $N = 3$ is the 'line' configuration in 3.a. For $N = 4$ the 'ring' configuration in 4.b has the lowest energy.

Table 2: *Magnetic configurations and normalized magnetostatic energies after energy relaxation; in all configurations the dipoles are positioned in plane, except for the 3D configuration 4.d*

configuration		magnetostatic energy U/M^2 J$(Am^2)^{-2}$
3.a		−0.85
3.b		−0.75
4.a		−1.31
4.b		−1.34
4.c		−1.28
4.d		−1.00

Configuration 4.c and the 3D configuration 4.d, have higher energy, as was expected from our experience with the neocubes.

A. energy barriers

The energy barrier between configuration 3.a and 3.b has been investigated, see figure 4. The trajectory is parametrized by angle θ, which is defined in the figure. For each θ, the lowest energy state is found via the simulations. Both the 3.a and 3.b configurations correspond to a minimum in the energy landscape. This means that these configurations are stable. The maximum energy is attained for $\theta = 105°$. For the 4-dipole system, two trajectories are considered. In the first trajectory, an in-plane path from configuration 4.b to 4.c is parametrized. The energy corresponding to this trajectory is given in figure 5. At $\theta = 120°$, $U(\theta)$ has a local maximum. Therefore, the configuration of 4.c is not stable. This is in correspondence with the observed meta-stable behaviour of the neocubes in this configuration.

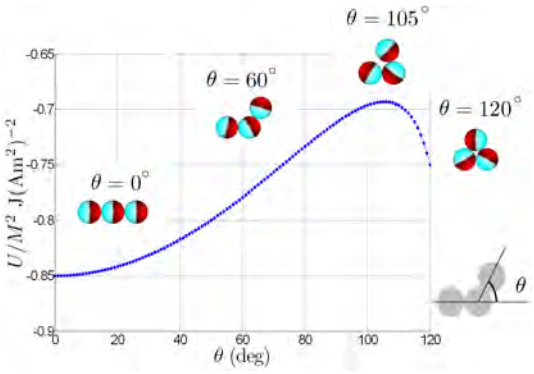

Figure 4: *Trajectory in the energy landscape of a 3-dipole system; the energy is plotted against θ, which is defined in the lower right. The insets show the configuration of the particles for various θ, after minimization of the energy.*

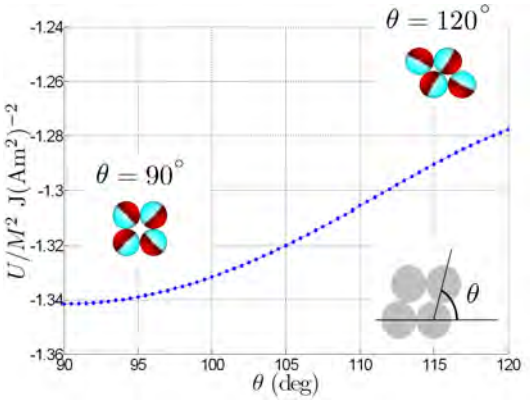

Figure 5: *The in-plane trajectory in the energy landscape of a 4-dipole system. The energy is plotted against θ, which is defined in the lower right inset. The magnetic configurations after energy minimization for $\theta = 90°$ and $\theta = 120°$ are also shown.*

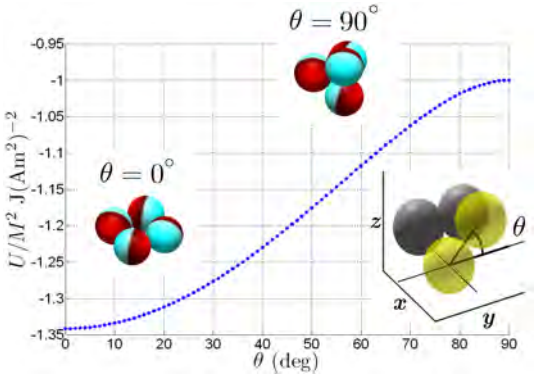

Figure 6: *The out-of-plane trajectory in the energy landscape of a 4-dipole system. The energy is plotted against θ, which is defined in the lower right inset. The magnetic configurations after energy minimization for $\theta = 0°$ and $\theta = 90°$ are also shown.*

The second trajectory is a path from configuration 4.b to 4.d. The final configuration is '3D', since the dipoles move out of the plane. The energy and the parametrization are given in figure 6. The energy attains a maximum at $\theta = 90°$, so the 3D configuration is only meta-stable. This is again in correspondence with the behaviour of the neocubes.

B. shape modifications

From figure 6 we conclude that the 3D configuration with 4 dipoles is not stable. In this paragraph it is investigated whether this 3D configuration can be made stable by modifying the shape of the particles. Moreover, if the energy of the 3D configuration can be reduced in this way, the 3D configuration might become energetically favourable over the 2D configurations.

Figure 7 illustrates a possible shape modification; the particles have been indented at three positions. With such a modification, the top particle can be positioned closer to the 3 bottom particles. This results in a lower

Figure 7: *Illustration of a shape modification. The unmodified particles (left drawing) can be indented to allow a closer packing of the spheres (right drawing). The exploded view (center drawing) shows the indentations and the vertical trajectory (line) of the top particle.*

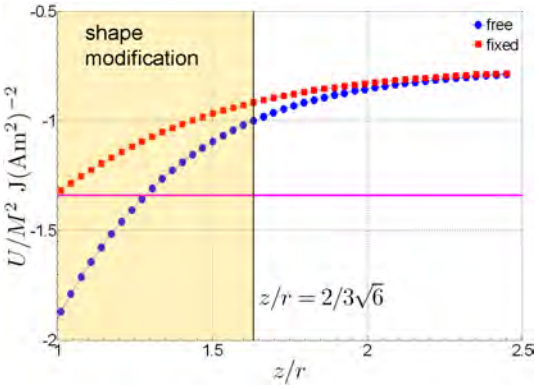

Figure 8: *Energy versus z position of the top dipole in the 3D configuration with 4 dipoles. In the 'free' case (circles) all dipoles were free rotate their dipole moment during the energy minimization; in the 'fixed' case (squares), the moment of the top dipole was fixed the z direction during the energy minimization. The shaded area indicates the region where the shape of the particles needs to be modified. The horizontal line indicates the energy of the 4-dipole ring configuration.*

energy.

The effect of this shape modification is investigated by simulating a trajectory. The 3 bottom dipoles are configured in a ring, with their centers in the *x*-*y* plane. The top particle moves vertically in the $-z$ direction, as illustrated in figure 7. At each position the energy is minimized and $U(z)$ is obtained, where z is the distance between the center of the top particle and the *x*-*y* plane. At $z/r = 2/3\sqrt{6}$ the top particle touches the bottom particles if the particles have their unmodified spherical shape. To allow a smaller z, the shape of the particles must be modified. Figure 8 shows the energies versus z/r that are obtained for two situations. In the first situation, all dipole moments are free to rotate. In the second situation, the magnetization of the top particle is fixed in the z direction. This is of interest, because the modification of the particles defines a preferred orientation of the dipole moment. However, the constraint of having preferred orientations of the dipole moments can be resolved by designing particles that contain magnets which are free to rotate with respect to the shell.

The energies of the two cases are compared with the 4-dipole ring configuration (4.b. in Table 1), since this is the 2D configuration with the lowest energy. In case that the top particle has a fixed magnetization in the z-direction, the energy is always larger than the energy of the ring configuration (horizontal line in figure 8). However, in the case where all particles are free to rotate their dipole moments, the energy is lower than the ring configuration if $z/r \leq 1.25$. Therefore, for particles with a rotatable magnet and a modified shape, the 3D configuration is preferred over the 2D configurations.

V – Conclusions

A 3D self-assembly system using milli-magnetic particles has been designed. The design allows the particles to hover freely in salt water.

The magnetostatic energies of simple particle configurations are obtained via simulations by dynamic minimization of this energy. The simulated energy barriers are in correspondence with the behaviour of the neocubes. Still, the accuracy of the simulations can be improved by taking into account the cylindrical shape of the magnets. In future experiments, the obtained energy barrier for the 3-dipole system might be validated.

Our simulations show that for 4-dipole systems a 2D configuration is energetically favoured over a metastable 3D structure. However, further simulations indicate that by modifying the shape of the particles it is possible to obtain stable 3D configurations. We will now focus on proving this exciting result experimentally. Furthermore, we will investigate the magnetic self-assembly of more intricate 3D architectures by clever design of the shape of the constituent particles.

References

[1] Miko Elwenspoek, Leon Abelmann, Erwin Berenschot, Joost van Honschoten, Henri Jansen, and Niels Tas. Self-assembly of (sub-)micron particles into supermaterials. *J. Micromech. Microeng.*, 20(6):064001, 2010.

[2] L. Abelmann, N. Tas, E. Berenschot, and M. Elwenspoek. Self-assembled three-dimensional nonvolatile memories. *Micromachines*, 1:1–18, 2010.

[3] John A. Pelesko. *Self assembly - The Science of Things That Put Themselves Together*. Chapman & Hall/CRC, 2007.

[4] David Vokoun, Marco Beleggia, Ludek Heller, and Petr Sittner. Magnetostatic interactions and forces between cylindrical permanent magnets. *Journal of Magnetism and Magnetic Materials*, 321(22):3758 – 3763, 2009.

NOISE ANALYSIS OF A MICRO-G PULL-IN TIME ACCELEROMETER

R.A. Dias[1], R.F. Wolffenbuttel[2], E. Cretu[3] and L.A. Rocha[1]

[1]*Universidade do Minho, Instituto de Polímeros e Compósitos, Guimaraes, Portugal*
[2]*Delft University of Technology, Dept. Microelectronics and Computer Eng., Delft, The Netherlands*
[3]*University of British Columbia, Electrical and Computer Engineering, Vancouver, Canada*

***Abstract* — Pull-in time based accelerometers present very high resolutions. One of its most important features is the detection capability bottleneck due to the MEMS structure thermal-mechanical noise rather than the measurement/transduction mechanism. A study of the intervenient noise sources is presented in this paper. MEMS structures fabricated on the SOIMUMPs process were used and a relatively high noise was measured, which, considering the analysis performed, was attributed to environmental vibrations that should be prevented in future experiments. The analysis supports the low-noise characteristics of the pull-in time accelerometer.**

***Keywords :* Pull-in time, Accelerometer, Noise**

I - Introduction

The concept of an accelerometer based on pull-in time has been previously introduced in [1]. The underlying principle is the high sensitivity of the pull-in time to external forces in electrostatically operated micromechanical damped devices [2, 3]. The pull-in transition, in a specific range of actuation and damping conditions, is characterized by a meta-stable (slow movement) region. The duration of this stage is affected by the presence of very small forces, and so is the overall pull-in time. This characteristic has been used in [4] to measure and characterize the mechanical-thermal noise in MEMS devices.

A block diagram of the time-based accelerometer is shown in Fig. 1. A parallel-plates microstructure, with separate sensing and actuation electrodes, is actuated by a square wave generator, with the inertial mass being pulled-in and released repeatedly. The step voltage must be slightly higher than the pull-in voltage to induce a significant dynamic pull-in transition duration, $V_{step} = \alpha V_{pi}$, $1 \approx \alpha > 1$. A front-end readout circuit converts the capacitive changes of the microdevice to a voltage which, when compared to a known threshold, allows the detection of the pull-in event completion. Meanwhile, the time elapsed from the beginning of the actuation (rise of the square wave) to (nearly) full displacement of the inertial mass (readout circuit output reaching the voltage threshold) is measured.

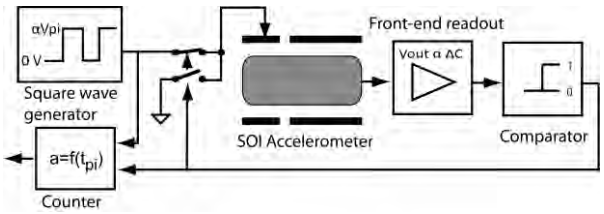

Figure 1. *Microaccelerometer block diagram.*

The pull-in time changes when the accelerometer undergoes external acceleration in the direction as the inertial mass movement (either sense). If the acceleration has the same sense as the pull-in movement, pull-in occurs faster, otherwise pull-in time is longer.

The changes in capacitance are quite large (considering nearly full gap displacements), and therefore the capacitive readout specifications are low in terms of resolution and noise which is a competitive advantage to the conventional direct transduction and signal processing in the electrical domain approach.

Since the non-mechanical noise is set primarily by the resolution of the time measurement, the pull-in time accelerometer concept is expected to have the mechanical-thermal noise as the dominant noise source, hence there is a huge potential for the realization of high sensitivity, low-noise accelerometers.

Since noise is a key feature in this approach, a study of the noise sources affecting the system was performed. The following sections present an overview of the fabricated structures characteristics and the noise analysis.

II – MEMS Structures Modeling and Fabrication

The MEMS structures (Fig. 2) used for the pull-in time measurements were designed and fabricated on the SOI micromachining process offered by MEMSCAP – SOIMUMPS [5]. The design comprises different sets of parallel-plates capacitors for sensing and for actuation, symmetrically placed on each side and 4 bi-folded springs supporting the inertial mass.

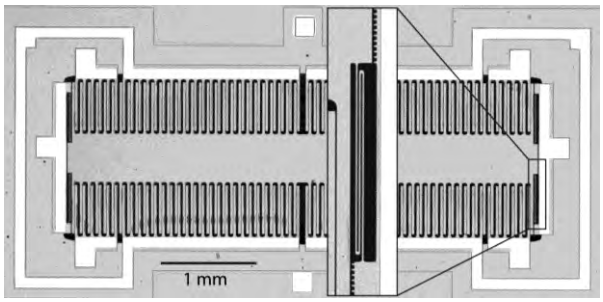

Figure 2: *Microscope picture of the evaluated micro-structure.*

Table 1 presents the main design parameters obtained through analytical and numerical modeling of the microstructure (considering pressure of 10^5 Pa and temperature of 300 K). Matlab was used for the analytic modeling, with a full dynamic model being implemented on Simulink that includes squeeze-film damping with border and rarefaction effects [6]. The pull-in voltages were calculated using a numerical method described in [7], which accounts for the nonlinear behavior of the electrostatic and mechanical domains.

Table 1: *Accelerometer design parameters*

Device Parameters		Value
Mass (m)		0.249 mg
Mechanical spring (k)		3.33 N/m
Zero-displacement gap (d_0)		2.25 µm
Natural resonance frequency (f_0)		582 Hz
Zero-displacement actuation capacitance		0.66 pF
Zero-displ. sensing capacitance (C_{d0})		2.53 pF
Damping coefficient (b)	gap=d_0	1.76 mNs/m
	gap=$2/3d_0$	2.88 mNs/m
Mechanical-thermal noise gap=$2/3d_0$		2.8 µg/√Hz
Pull-in voltage (V_{pi})		2.916 V
Nominal pull-in time (t_{pi})		10.2 ms

III – Noise Analysis

All measurements were obtained using a readout circuit (seen in Fig. 3) based on a charge amplifier to detect the capacitive changes. Its output was acquired using a NI USB-6281 data acquisition board (DAC) (625 kHz sampling frequency) and the data was then processed on Matlab to obtain the pull-in times. All experiments were performed under ambient pressure and temperature.

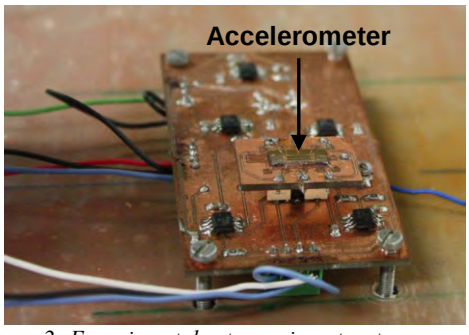

Figure 3. *Experimental setup: microstructure mounted on the front-end readout circuit.*

Initially, the pull-in voltage was measured and a value of 2.931 V obtained. Next, the MEMS structure was actuated with a square wave with voltage $V_{step} = \alpha V_{pi}$, α=1.01 and pull-in times were measured at 0 g. From the measurements, a mean nominal pull-in time of 10.2 ms was retrieved which is in satisfying accordance to the expected values. The pull-in time measurements were performed at a frequency of 50 pull-ins per second and standard deviation of 100 µs was observed in the measurements. This pull-in time noise, given a sensitivity of 0.26 µs/µg (modeled and measured), corresponds to an acceleration noise of approximately 400 µg. In order to understand the roots of this noise level, the analysis of each noise source is presented in the next subsections.

A. Mechanical-Thermal Noise

The random movement (Brownian motion) of the gas molecules surrounding the mechanical structure leads to random fluctuations in the energy transfer between structure and damping gas [8]. This mechanical-thermal noise corresponds to an equivalent acceleration noise spectral density of [8][9]:

$$a_{noise} = \frac{\sqrt{4k_B T b}}{9.8m} \quad (g/\sqrt{Hz})$$

where m is the mass of the movable structure, k_B is the Boltzman's constant, T is the temperature in Kelvin, and b is the damping coefficient in N.m/s. If a constant temperature is considered, the equivalent acceleration noise is only dependent on the proof mass and the damping coefficient.

Since the metastable region occurs at a gap value of $2/3\ d_0$, the damping coefficient can be linearized at this gap in the (low) frequency range of interest [10]. The computed linearized damping coefficient for the fabricated structure, at a gap size of $2/3\ d_0$, is b=2.88 mNs/m. Thus, an equivalent acceleration noise of a_{noise} =2.8 µg/√Hz is obtained. This method for determining the white noise floor due to damping, as well as the damping theory supporting it, has been previously validated by experimental white noise measurements on parallel plates MEMS devices [4].

Frequencies higher than $2/t_{pi}$ are integrated during operation, and therefore only frequencies below $2/t_{pi}$ are present during the full pull-in movement. Operation with $V_{step} = 1.01 \times V_{pi}$, yields a t_{pi} of 10.2 ms and therefore the bandwidth of interest is $BW = 2/t_{pi} \approx 200$ Hz. At this bandwidth, the mechanical-thermal noise contribution is $N_b = 2.8\ \mu g/\sqrt{Hz} * \sqrt{2/t_{pi}\ Hz} \approx 40\ \mu g$.

B. Readout Circuit Noise

The front-end amplifier of the readout electronics has an input noise density specification of 2.5 nV/√Hz. Considering an operation bandwidth of 1 MHz results in a total noise of the readout circuit of about 2.5 µV.

The total pull-in time is obtained by measuring the time elapsed from the moment the square signal is

applied, until the structure passes through about 75% of the gap. At 75% of the gap the voltage change rate is higher than 300 µV/µs, which allows disregarding the front-end readout electronic noise.

The NI USB-6281 board used allows a 625 kHz sampling frequency which corresponds to a time resolution of 1.6 µs. To facilitate data processing, a sampling frequency of 150 kHz was used instead, which translates to a time measurement resolution of about 7 µs. Higher resolutions are possible but this DAQ measurement uncertainty is already much lower than the measured noise level. Since this uncertainty in the pull-in time measurement can be interpreted as readout noise, for a given sensitivity of 0.26 µs/µg, the resolution of 7 µs corresponds to a readout circuit noise contribution of N_r = 27 µg.

C. Actuation Voltage Source Noise

The actuation voltage was provided by using the analog output of the same DAC. The analog output, with a 500 kHz update rate, was monitored with a high resolution multimeter and a standard deviation of 68 µV was found. Since the pull-in time is highly dependent on the actuation voltage, simulations and experiments were performed to evaluate the influence of this variance, and the actuation voltage noise in general, on the pull-in time.

Noise with different values at a 500 kHz bandwidth was added to the actuation voltage and the pull-in time noise was measured (Fig. 4). Linear curve fitting was applied to the experimental data and it was found that the pull-in time noise varies linearly with the actuation voltage noise, for actuation voltage noises above approximately 30 mV, according to the function t_{pi_noise} (µs) = 2.8 × V_{step_noise} (mV)+50 (R^2=0.987 correlation factor). For lower actuation voltage noise, the data does not follow the linear trend and the t_{pi} noise does not reduce below 100 µs. This suggests that the measured noise floor (100 µs) is not due to the actuation voltage noise.

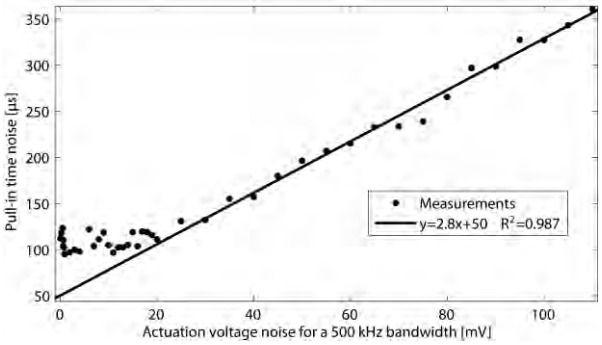

Figure 4: *Measured t_{pi} rms noise using actuation voltages with added rms noise. The data was fitted excluding the actuation voltage rms noise values below 30 mV and yielded a correlation factor R^2= 0.987.*

To better understand these results, several actuation voltage noise values were introduced in the Simulink dynamic model. The resulting t_{pi} noise values showed a linear dependence on the actuation noise following the expression t_{pi_noise} (µs) = 3.02× V_{step_noise} (mV). According to these values, the actuation voltage noise of 68 µV yields a t_{pi} noise of 0.20 µs, which corresponds to N_a = 0.20 µs / 0.26 µs/µg = 0.8 µg acceleration noise due to actuation voltage noise.

D. Total Noise

The total noise is a contribution of all the noise sources existing in the microsystem $N_t^2 = N_a^2 + N_b^2 + N_r^2 + N_{ext}^2$, assuming an external noise contribution (N_{ext}). Given a sensitivity of 0.25 µs/µg, the measured noise of 100 µs corresponds to a total acceleration noise of N_t=400 µg. If one considers the noise sources calculated in the previous sections, N_a = 0.8 µg, N_b = 40 µg, and N_r = 27 µg, the external noise contribution can be found:

$$(400ug)^2 = (0.8\ \mu g)^2 + (40\ \mu g)^2 + (27\ \mu g)^2 + (N_{ext})^2$$

$$\Rightarrow N_{ext} = 397\ \mu g$$

This external noise was attributed to environmental disturbances since no measures were taken to isolate the experimental setup from building vibrations. The magnitude of these external vibrations is in reasonable accordance with values found in literature [11, 12].

In addition to these calculations, the readout circuit noise, the mechanical-thermal noise and the assumed-environmental noise were subtracted to the measured values for increased actuation voltage noise (isolating the actuation voltage noise) and the results were compared to the expected actuation voltage noise dependence obtained with the analytic model (Fig. 5). The linear fitting of both series show approximately the same slope, and good correlation factors, which supports the conclusions taken concerning the actuation voltage noise and the presence of external environmental noise.

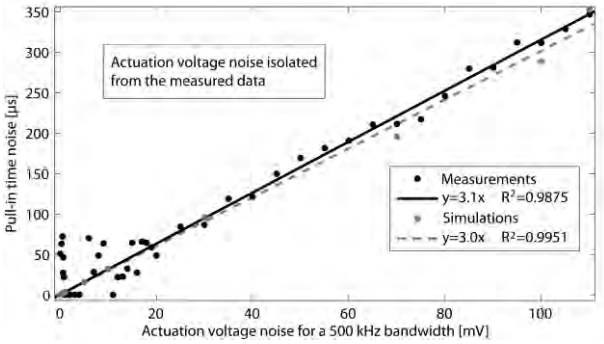

Figure 5: *Comparison between experimental and modeled results for pull-in time noise as a function of the actuation voltage noise.*

IV – Discussion and Conclusions

A study of the noise sources present on a µg accelerometer based on pull-in time measurement was performed in this paper. The response of the fabricated

devices is in agreement with the simulations obtained with the dynamic model implemented in Simulink.

The measured noise floor is much higher than expected and this was attributed to environmental vibrations, due to the poor vibration isolation of the measurement setup. This situation made impossible to measure the expected mechanical-thermal noise of 2.8 μg/√Hz which is very close to the state-of-the-art accelerometers noise found in literature (0.23 μg/√Hz [13], 1.6 μg/√Hz [14] and 0.85 μg/√Hz [15, 16]). Further experimental work needs to be performed in a more controlled environment (to reduce the environmental noise), in order to evaluate the low noise specifications of the accelerometer.

While the readout circuit does not significantly affect the noise performance, care must be taken regarding the actuation voltage. The DC stability of the actuation voltage source is a very important factor on the performance of the device. The structure is actuated with $V_{step}=\alpha V_{pi}$. For $\alpha = 1.01$, the t_{pi} change rate is -0.5394 s/α. If a pull-in voltage of 2.931 V is considered, the change rate is 0.5394/2.931 =0.184 μs/μV. This means that a relatively small DC drift (in the order of magnitude of a few microvolt), yields a significant t_{pi} change. Methods to compensate this aspect, by means of closed-loop control, need to be considered to minimize this effect.

In comparison to the traditional approach of high-resolution capacitive accelerometers found in literature, the main advantage is the huge potential of the measurement method in terms of resolution.

The pull-in time accelerometer relies on a time measurement which can be performed with a very high resolution by simply using a fast clock: for instance if a 100 MHz frequency is used, the resolution of the time measurement will be 10 ns. Given a sensitivity of 0.26 μs/μg, this would correspond to approximately 40 ng input referred noise.

Since a time measurement is performed, rather than just direct transduction of capacitance into acceleration, increasing the measurement resolution only requires a faster clock of the time counting mechanism (to detect smaller changes in the pull-in time). The capacitance change in the gap of interest is very large (pF) and the voltage increase at the front-end readout circuit output is straight-forward to detect. Thus, the requirements of the front-end readout circuit are very low since there is no need to detect small capacitance variations as in the case of the traditional capacitive approach. For instance, the accelerometer presented in [13] (noise of 0.23 μg/√Hz) needs a sensitivity of 35 aF/μg. These specifications for the readout circuits are much more demanding in terms of circuit design and implementation, than the measured sensitivity of 0.26 μs/μg presented in this paper.

The main disadvantages of the current implementation are the non-linear response and the low dynamic range. Nevertheless, both the linearity and the dynamic range can be improved by an effective use of the differential pair of electrostatic actuators. Techniques to compensate the nonlinearities and dynamic range using electrostatic forces are currently being studied. The presented accelerometer can find applications in tilt control, platform stabilization, space applications, structural monitoring, seismography, and others.

References

[1] R. A. Dias, E. Cretu, R. F. Wolffenbuttel and L.A. Rocha, *Procedia Engineering*, vol. 5, pp. 1075-1078, 2010.

[2] L.A. Rocha, L. Mol, R.F. Wolffenbuttel and A. Lage, *Eurossensors XXII*, pp. 1565–1568, 2008.

[3] L.A. Rocha, E. Cretu and R.F. Wolffenbuttel, *J. Micromech. Microeng.* 14, pp. S37-S42, 2004.

[4] L.A. Rocha, E. Cretu and R.F. Wolffenbuttel, *J. Micromech. Microeng*. 15 pp. S30-S38, 2005.

[5] A. Cowen, G. Hames, D. Monk, S. Wilcenski and B. Hardy, *SOIMUMPS Design Handbook*. Rev. 6.0. MEMSCAP Inc., Crolles, 2009.

[6] L.A. Rocha, E Cretu and R.F. Wolffenbuttel, *J Microelectromech Syst* 15, pp. 69-83, 2006.

[7] L.A. Rocha, E Cretu and R.F. Wolffenbuttel, *J Microelectromech Syst* 13, pp. 69-83, 2004.

[8] T.B. Gabrielson, *IEEE Trans. Electron Devices*, 40, pp. 903-909, 1993.

[9] M. Lemkin and B.E. Boser, *IEEE J. Solid-State Circuits* 34, pp. 456–468, 1999.

[10] L.A. Rocha, E. Cretu and R.F. Wolffenbuttel, *NSTI-Nanotech 2004* 2, pp. 271-274, 2004.

[11] Y. Cao and H. Xia, *International Conference on Mechanic Automation and Control Engineering (MACE)*, pp.1850–1853, 2010.

[12] O. Hunaidi, J.H. Rainer and G. Pernica, *Second International Symposium - Transport Noise and Vibration*, pp. 103-108, 1994.

[13] R. Abdolvand, B.V. Amin and F Ayazi, *J. Microelectromech. Syst.* 16, pp. 1036–1043, 2007.

[14] J. Chae, H. Kulah and K. Najafi, *J. Microelectromech. Syst.* 13, pp. 628–635, 2004.

[15] Y. Dong, M. Kraft and W. Redman-White, *J. Micromech. Microeng*. 16, pp. S54–S60, 2006.

[16] H. Külah, J. Chae, N. Yazdi and K. Najafi, *IEEE J. of Solid-State Circuits* 41, pp. 352–361, 2006.

DESIGN OF A POLYMER 3D-THERMAL ACCELEROMETER

C.S. Silva[1], M.F. Cerqueira[1], J.F. Ribeiro[2], L.M. Gonçalves[2], A.J. Pontes[1] J.C. Viana1[1] and L.A. Rocha[1]

[1] *Institute for Polymers and Composites/I3N, University of Minho, Guimarães, Portugal*
[2] *ALGORITMI, University of Minho, Guimarães, Portugal*

***Abstract* — A completely new approach for the fabrication of 3-axis thermal accelerometers is presented in this paper. Microinjected polystyrene micro-parts are assembled with active polyimide membranes enabling the construction of an innovative polymer based thermal accelerometer. The use of polymers (polystyrene and polyimide) with low thermal conductivities improves the overall power consumption of the thermal accelerometer and enables a simple and low-cost fabrication process (no clean room infrastructure required).**

***Keywords :* Polymer microtechnologies, 3-axis accelerometer, microinjection, thermal accelerometer**

I - Introduction

The increasing availability of micromanufacturing technologies is paving the path to a new class of systems, extremely small (Microsystems) that incorporate novel functionalities and are supporting new applications and services. The work presented in this paper introduces the design and preliminary fabrication results of a polymer based 3D thermal accelerometer. The potential advantages of using polymer technologies to microfabricate a thermal accelerometer are twofold: on one hand the infrastructure for polymer microfabrication is gradually becoming available and has the potential for high throughput and low manufacturing costs and on the other hand the large variety of available materials (with good electrical, mechanical and thermal properties) can contribute to the improvement of current state-of-the-art on thermal accelerometers based on Integrated Circuit (IC) technology.

Research efforts on thermal accelerometers have traditionally been initiated, justified and supported due to the potential for better reliability (there are no movable parts), better integration (fully compatible with IC fabrication processes) and stability [1-3]. Convective micro thermal-accelerometers were introduced in the 90's as an alternative to proof mass-based mechanical accelerometers and despite the claimed advantages, the success of these devices has been hampered by the relatively high power consumption (high thermal losses) and the difficulty to fabricate monolithically integrated 3-axis accelerometers. More than a decade passed until 3-axis thermal accelerometers were demonstrated [4]. Nevertheless, they require a complex fabrication process followed by an extra external stimulus to place the z-axis transduction element, which strongly limits the process repeatability.

Since the detection principle in thermal accelerometers is based on air convection, where the hot spot created by a heater is differentially measured by two temperature sensors, the readout electronics required are very simple. Thus, the simplicity of the design suggests that this type of accelerometers can benefit from the microfabrication techniques already available at the polymer industry [5]. The combination of responsive materials, polymer substrates, micromoulding fabrication and new sensor design methodologies promise to enable the next generation of smart systems – low cost high performance polymer sensors.

Even if convective thermal accelerometers present several advantages when compared to piezo and capacitive accelerometers [5], their market penetration is very low and there is just one company using IC technology that delivers these devices [6]. The main limitations of available thermal sensors are related to the power consumption, low bandwidth and unavailability of 3D monolithic silicon accelerometers: silicon is a very good thermal conductor, which increases thermal losses and consequently the power consumption; the thermal sensors are usually based on platinum thermistors with a large thermal capacitance that reduces the sensor bandwidth; standard IC technology does not allow the design of 3D thermal accelerometers.

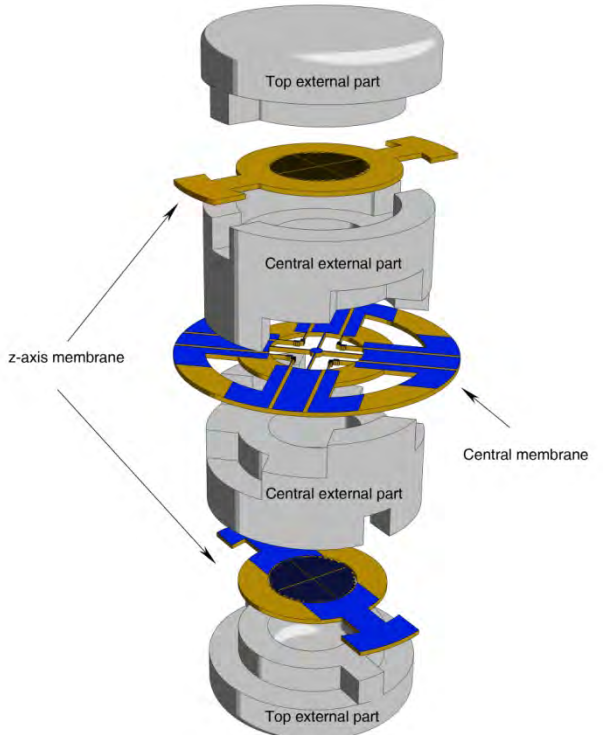

Figure 1*: Drawing of the 3-axis thermal accelerometer showing the main device parts and assembly configuration.*

The proposed 3D polymer accelerometer can therefore overcome some of the existing limitations:

- Power consumption: polymers are very bad thermal conductors contributing to a decrease in heat losses.
- 3D integration: available polymer micromoulding techniques make it easy to construct complex 3D geometries that can be used for the construction of a 3D thermal accelerometer.

This paper is divided in 5 sections. After introduction, the details of the 3D thermal accelerometer are presented. Next, considerations related to material selection are described followed by an explanation of the fabrication process. Finally some conclusions are drawn.

II - 3D Thermal Accelerometer

The proposed 3-axis accelerometer is depicted in Figure 1. The accelerometer comprises an external supporting structure composed of 4 microinjected polymer parts (two identical top parts and two identical central parts) and three polymeric membranes (two identical z-axis membranes and a central membrane). The microinjected parts provide the mechanical support for the active elements that are placed on the membranes (the heater and the temperature sensors). The concept is simple and enables the realization of a 3-axis thermal accelerometer based on polymeric materials.

When current is applied to the heater, the surrounding medium (in this case air) is heated and if no acceleration is presented the thermal sensing par elements measure the same temperature due to symmetry (see Figure 2a).

a)

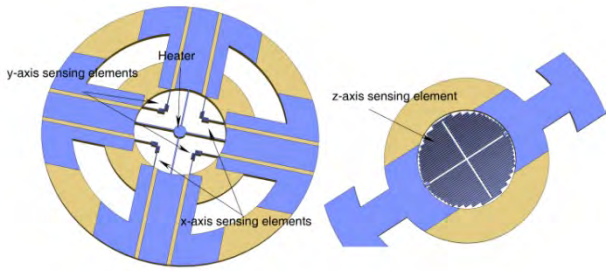

b)

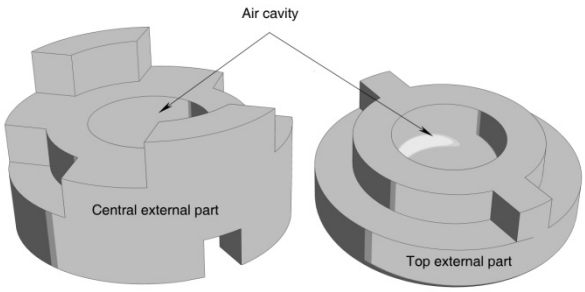

Figure 2*: Main components of the accelerometer. a) Central and top membranes and b) external parts.*

When acceleration is present, free-convection occurs and there are temperature differences proportional to the acceleration. While misalignments on the X-Y sensing elements will be small and are only due to non-idealities on the membrane fabrication process, larger misalignments on the Z-axis membrane are expected. Therefore, if the Z-axis resistors are designed to occupy the full available area as shown in Fig. 2a, it guarantees that the area subject to temperature differences during operation remains the same in both top membranes. This design strategy assures that large misalignments between central and top membranes (that are likely to occur) will not compromise device performance.

III – Material Selection

Material selection is an important part for any manufactured product but when polymers are used it is absolutely vital. When choosing the right material for the application one has to consider both the details of the design to suit the characteristics of the material and the limitations of the production process. Polymers come in a bewildering variety. There are hundreds distinct generic types and the number of different grades of polymeric materials available to the designer now approaches 50000 or more. During the design of any injection moulded part, the designer should maximize the functionality of the part while minimizing the use of material. The external parts (Fig. 2b) are essential to provide mechanical support and to guarantee the necessary operation conditions and therefore the main specifications are:

- Polymer grade must be suitable for microinjection moulding. Typically, it should be easily processable, supporting high shear rates and having a high Melt Flow Index (MFI greater than 20 $cm^3/10$ min).
- Low shrinkage (e.g., less than 0.5%)
- Good dimensional stability: low coefficient of thermal expansion (less than $10x10^{-5}$ $ºC^{-1}$).
- Low thermal conductivity (between 0.1 and 0.2 $W.m^{-1}.K^{-1}$).
- The material must have anti-static properties (volumic resistivity superior than $15x10^{15}$ Ohm.cm) avoiding accumulation of electrical charges.
- The part design should guarantee hermetically sealed cavities. The polymer components are to be bounded by an adhesive.

Since microtechnologies are necessary for the implementation of the active elements, the main specifications for the membrane material are:

- Compatible with thin film deposition techniques.
- Support temperatures until 350ºC.
- Low thermal conductivity (below 0.2 $W.m^{-1}.K^{-1}$).
- Planar geometry control (suitable for lithography and etching).

The materials selected for both the external parts and the membrane, taking into account these specifications, were polystyrene, for the external parts, and polyimide (Kapton®) for the membranes.

Regarding the active elements (heater and thermal sensors), and due to the simplicity of the process (only one deposition required), e-beam physical vapour deposited aluminum was selected.

IV – Fabrication Process

The full fabrication process includes three distinct phases: the microinjection of the external parts, the fabrication of the membranes, and a final assembly process. The three stages are discussed in detail in this section.

A. Microinjected External Parts

Microinjection is a relatively new technology, which appears as variant of the technique of conventional injection moulding [8]. One of the main challenges associated with microinjection is simply the physical size of the parts: while the size range on conventional injection parts is generally of the order of centimeters to meters, in micromoulding the sizes are of the order of micrometers to millimeters and it is possible to produce microparts with mass less than 1 µg [9].

The design and manufacture of moulds for microinjection are one of the main challenges of the process, and the importance of the tool increases exponentially with the decreasing size of the part (due to reduced tolerances and manufacturing processes characteristics). The concepts and methods of conventional mould design must therefore be adopted/changed to the process of micromoulding technology. Moulds used in microinjection of microparts and microcavities are usually produced by metal inserts, which are mounted in the main frame of the mould. The inserts used in this work (Fig. 3) were fabricated using micromilling and the type of steel used was steel 1.2311: this steel is easy to machine and polish and allows productions up to 250000 cycles of abrasive thermoplastics.

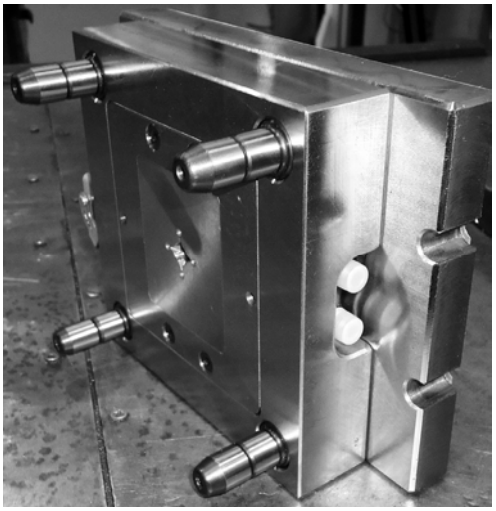

Figure 3*: Insert for the fabrication of the accelerometer external parts.*

Parts were microinjected using a Boy 12 A/M machine. The full injection cycle for the external parts takes 42s. Fabricated external parts are shown in Fig. 4 and quality control of the fabricated microparts reveals that the measured dimensions are in agreement with the designed geometry (Fig. 5).

a)

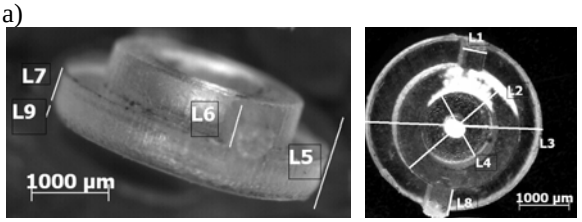

b)

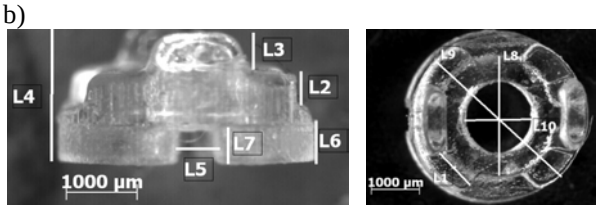

Figure 4*: Details of microinjected a) top and b) central parts*

B. Membranes

The process to fabricate the membranes, including the active elements, uses two masks only (one to define the membrane geometry and the other for the aluminum bond pads). The process starts with a polyimide substrate, 50 µm thick. Next, SU8 resin is spin-coated on both sides and is patterned on one of the sides (first mask). The SU8 photoresist is used as mask for the etching of the polyimide (KOH, ethanol and H_2O are used as the etchant). After stripping the SU8, aluminum is deposited using e-beam physical vapor deposition followed by a patterning step (second mask) to fabricate the active elements of the thermal accelerometer: the heater and the temperature resistors. Figure 6 shows polyimide membranes after the etching process (prior to aluminum deposition).

a)

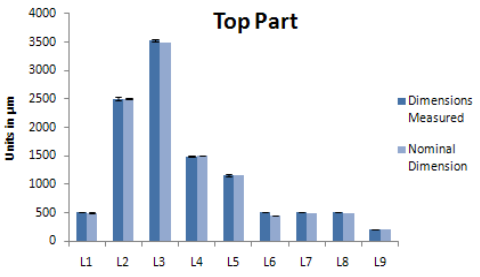

b)

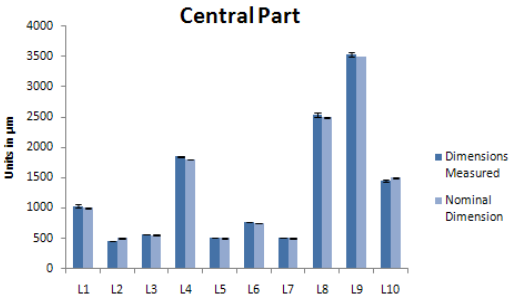

Figure 5*: Dimensions quality control of a) top and b) central parts.*

The membrane fabrication process is relatively simple, but still requires optimization. Dimensional control during polyimide etching is still being optimized (this step is very important for proper heater and thermal resistors definition).

C. Assembling

The final processing step is the accelerometer assembling as depicted in Fig. 1. This process can be fully automated if an automatic pick-and-place machine is used. The mold for the external parts was conceived to enable the simultaneous manipulation of the four parts (Fig. 7) and therefore by careful design of the membranes masks, it is possible to devise a simple automated process (taking a few steps) for the assembling of the accelerometer. During assembly, adhesive is used to create permanent connections between the polymer parts and to create a contained air volume for device operation. Ultraviolet light curing plastic bonding adhesives are being investigated.

The advantages of the proposed approach are the simplicity, the extremely low-cost of the fabrication process used and the possibility to fabricate 3-axis accelerometers.

a)

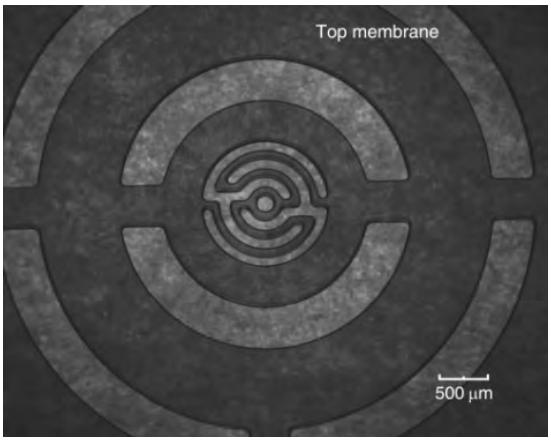

b)

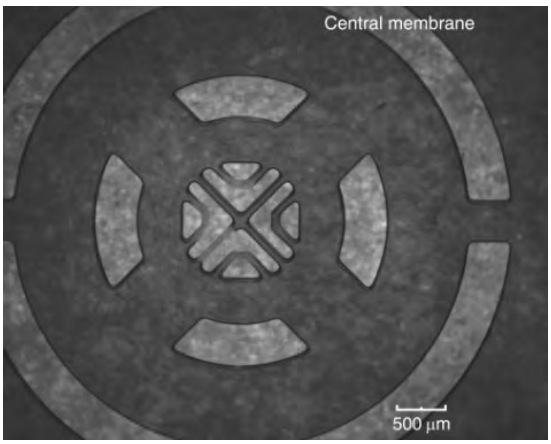

Figure 6*: Top and central membranes after polyimide etching.*

V - Conclusion

This work introduces a novel approach for the design and manufacturing of a thermal accelerometer based on polymers. The proposed design and fabrication process for the accelerometer is innovative in the sensors field and enables the realization of 3-axis accelerometers.

Polymeric microparts have already being successfully fabricated, while the active membranes fabrication process still requires further optimization. On-going work is focusing on the geometry control of polyimide etching, and fully assembled thermal accelerometers are expected soon.

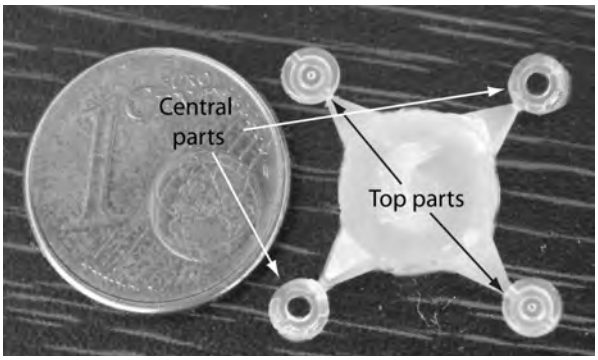

Figure 7*: Microinjected parts.*

Acknowledgments

This work is supported by FEDER through COMPETE and national funds through FCT – Foundation for Science and Technology in the framework of the project PTDC/EEA-ELC/099834/2008.

References

[1] A.M. Leung, J. Jones, E. Czyzewska, J. Chen and M. Pascal, *Technical Digest of Int. Electron Device Meeting (IEDM97)*, pp. 899–902, 1997.

[2] V. Milanovic, E. Bowen, M.E. Zaghloul, N.H. Tea, J.S. Suehle, B. Payne, and M. Gaitan, *Appl. Phys. Lett.*, Vol. 76(4), pp. 508–510, 2000.

[3] S. Billat, H. Glosch, M. Kunze, F. Hedrich, J. Frech, J. Auber, H. Sandmaier, W. Wimmer, and W. Lang, *Sensors Actuators A*, Vol. 97–98, pp. 125–130, 2002.

[4] A.H. Ma and A.M. Leung, *IEEE Sensors Conference*, pp. 1492-1495, 2008.

[5] O. Rotting, W. Ropke, H. Becker, C. Gartner, "Polymer microfabrication technologies", *Microsystem Technologies* 8, pp. 32–36, 2002.

[6] F. Mailly, A. Giani and A. Boyer, *Springer* US, 2006.

[7] http://www.memsic.com/memsic/.

[8] M. Heckele and W.K. Schomburg, *J. Micromech. Microeng*, 14, pp. R1–R14, 2004.

[9] B.R. Whiteside, M.T. Martyn and P.D. Coates, *Plastics, rubber and composites*, vol. 32, pp. 231-239, 2003.

ELECTRODEPOSTION OF COPPER INTO PCB VIAS UNDER MEGASONIC AGITATION

S. Costello[1], D. Flynn[1], R.W. Kay[1], M.P.Y. Desmulliez[1], N. Strusevich[2], M.K. Patel[2], C. Bailey[2], A.C. Jones[3], M. Bennet[3], D. Price[4], R. Habeshaw[5], C.Demore[5] and S. Cochran[5]

[1]*Heriot-Watt University, School of Engineering and Physical Sciences, Edinburgh, EH14 4AS, UK.*
[2]*University of Greenwich, School of Computing and Mathematical Sciences, Old Royal Naval College, Park Row, London, SE10 9LS, UK.*
[3]*School of Chemistry, University of Edinburgh, King's Buildings, Edinburgh, EH9 3JJ, UK.*
[4]*Merlin Circuit Technology Ltd, Hawarden Industrial Park, Manor Lane, Deeside, CH5 3QZ, UK.*
[5]*IMSaT, Dundee University, Wilson House, Wurzburg Loan, Dundee Medipark, DD2 1FD, UK.*

***Abstract* — In this paper we present progresses made into understanding the improvement of the quality of electroplated copper PCB vias submitted to megasonic agitation. Depleted ion concentration in high aspect ratio vias leads to voids and incomplete deposition of copper in PCB vias and through silicon vias. This paper presents the improved quality of electrodeposited copper in microvias with height-to-width aspect ratio (AR) of up to 8:1.**

***Keywords :* Electrodeposition, electroplating, megasonic agitation, acoustic streaming, aspect ratio.**

I – Introduction

The unabated consumer demand for smaller, smarter and lighter portable electronic systems is pushing the miniaturisation and increased wiring density of printed circuit boards (PCBs) and microelectronic chips. The stacking of an increasing number of (thinned) die in microelectronic systems or cheaper alternative techniques for multilayer PCBs require new assembly methods, of which TSVs and high AR blind vias are strong contenders.

Traditional techniques used in the filling of through-hole and blind vias used in mainstream multilayer PCBs have reached their limitations in terms of void free high aspect ratio copper deposition [1]. This bottleneck has driven the introduction of alternative approaches for high density interconnects (HDI) such as sequential build up (SBU) technologies incorporating microvias [2]. Figure 1 displays a schematic representation of the various types of microvia incorporated within SBU for HDIs.

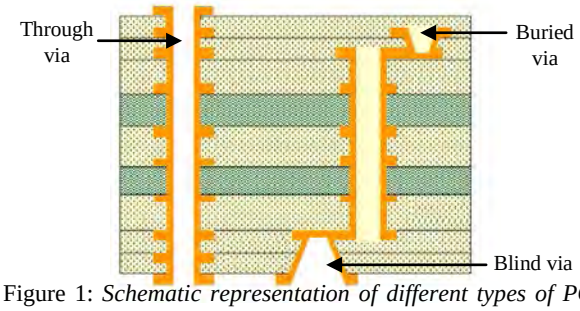

Figure 1: *Schematic representation of different types of PCB vias*

Conductive filled microvias enable further package densification by facilitating via in pad and stacked vias designs. Filled vias are typically produced by solder printing, also called plugging, or by the electrodeposition process [3]. Electrodeposited copper via filling offers several advantages over via plugging. Solid copper filled vias are inherently reliable and have higher conductivity than organic or conductive pastes; gains are realized in manufacturing productivity as densification and electrical connectivity is established in one step; and copper electroplating is a technology already well known and extensively used in PCB fabrication [4].

The unintended formation of voids is however the critical issue with the electrodeposition of vias with aspect ratios greater than 1.5:1 as shown in figure 2 [5].

Figure 2: *Voids in electroplated copper through via.*

Insufficient transport of ions from the bulk of the electrolyte solution into the ion depleted recesses of the via decreases the growth rate and quality of the deposited metal at the bottom of the via. This problem is further compounded by the strong uneven distribution of the current field lines at the mouth of the via, leading to uneven plating and finally void or stream formation. A 'pinching' effect can also be observed when plating occurs rapidly around the mouth the via where the ions are plentiful causing the deposited copper to close over the mouth of the via.

To overcome this limitation, this article proposes to use acoustic streaming of ions within the electrolyte as a means of improving ion transport into vias and enhanc-

ing the uniformity of the deposition. An increase in aspect ratio would reduce the number of laminate PCB layers required in SBU, improving densification and reducing cost. In addition, fully plated vias would be capable of supplying more current [6], improve thermal dissipation and enhanced accuracy impedance matching in high frequency applications.

This paper presents a Design of Experiments (DOE) that examines the influence of megasonic agitation and cathodic current density on the electrodeposition of copper into PCB through-hole vias.

II - Experimental Details

The experiments have been conducted in a 60 litre polypropylene tank. The anode and cathode are vertically aligned on opposite sides of the tank with the transducer positioned directly opposite the cathode at a distance of 1cm. The transducer consists of a 4 by 4 inch wide PZT crystal plate contained in a laser welded container. The transducer is powered by a Sonosys(TM) generator operating at 1MHz with maximum output power of 500W.

The electrolyte used, SLOTOCOUP CU 110, is produced by Schloetter and contains the common constituents for copper deposition, namely; 10% sulphuric acid 300 g/l copper sulphate, 0.1% HCL and 0.05% of organic brighteners. A starter additive performs a wetting action on the cathode to enable uniform electroplating. The inclusion of the further additive, SLOTOCOUP CU 114, leads to grain refinement, stress relief and increased deposition uniformity.

For all of the experiments described within this work the transducer is aligned parallel to the cathode. Through via in PCB samples are used to characterise the influence of megasonic agitation and average current density on the electrodeposition of Cu within high aspect ratio vias.

The electrodeposits induced by Direct Current (DC), with and without megasonic agitation have been compared. The parameters investigated are summarized in table 1. The megasonic power is restricted to a maximum of 250W to limit heating effects within the electrolyte solution. A Design of Experiment (DOE) is employed to compare the influence of varying cathodic current densities and megasonic power levels.

Table 1: *Experimental parameters investigated.*

Megasonic Power (W)	Current Density (A/dm^2)		
	Expt. 1	Expt. 2	Expt. 3
0	1	2	4
100	1	2	4
250	1	2	4

During the DOE, the background conditions kept constant are: concentration of metal salts, conductive salts and buffering agents, concentration of impurities, electrolyte temperature, electrolyte pH, plating cell geometry, composition and condition of the anode, anode/cathode surface area ratio, the nature and condition of the substrate as well as its conductive seed layer. In order to minimize the variation over time of the background conditions, all experiments were carried out in quick succession.

III - Results and Discussion

To examine the results of the deposition process, the PCB samples are diced and the cross-section of the vias are examined. Via filling performance can be characterised by a number of different standards. Percentage of via fill (% VF) and "dimple depth" (D), defined in figure 3, are perhaps the most commonly used to quantify via filling performance [1]. The Relative Deposition Thickness (RDT) is another performance metrics [7]. RDT is defined as the ratio of the fill thickness and the copper thickness plated on the board surface. Figure 3 indicates the parameters used in the various via filling assessment techniques.

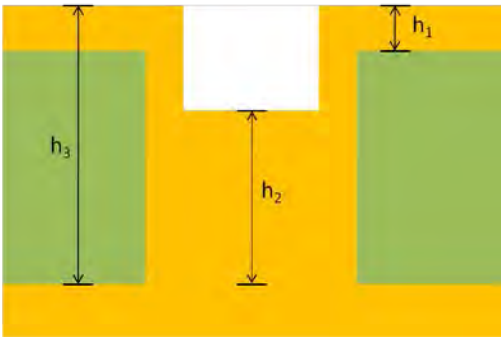

Figure 3: *Schematic of a via cross-section. VF = (h_2/h_3)*100%, D = (h_3-h_2) and RDT = (h_2/h_1)*

A desirable high RDT value indicates that h_1, the thickness of copper deposited within the microvia, is high and the thickness of copper deposited on the PCB surface is low. However, even for relatively high RDT values resulting from successful bottom-up filling of deep microvias, build-up of copper on the surface of the PCB can be excessive. Expensive post-processing stages such as mechanical polishing are required that inhibit the subsequent creation of fine circuit traces.

The PCB, shown below in figure 4, was designed and fabricated for the through via plating trials. The diameter of the via ranges from 200µm to 800µm by increment of 100µm. The PCB is 1.6mm thick and each via has a Cu seed layer, as shown in the cross-section in figure 4.

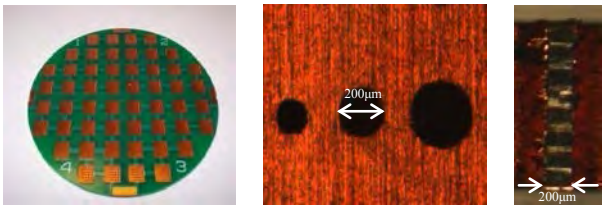

Figure 4: *PCB wafer with through-vias*

White light interferometry analysis indicated that the deposit thickness on the surface of the PCB declines towards the entrance of the via, as shown in figure 5. The result suggests a reduction of the pinching effect near the via opening through the use of megasonic agitation.

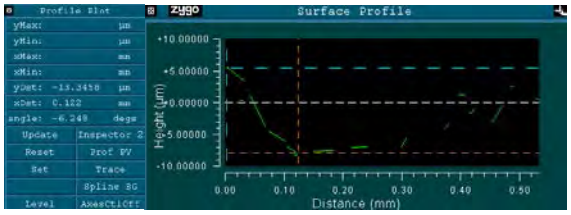

Figure 5: *Zygo analysis of Cu electrodeposit with megasonic agitation on the surface of the PCB. The image highlights that the surface topology of the Cu dips towards the centre of the via.*

Figure 6 displays the results of DC deposition within the 800µm diameter prior to being completely filled with Cu. The agitation is induced by 100W of megasonic power. The cross-section of the via reveals a conformal electroplating result with an even distribution of Cu on the sidewalls of the hole.

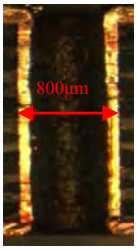

Figure 6: *800µm diameter through vias with conformal Cu deposition produced by 4 A/dm² DC and 100W megasonic power.*

Figure 7 shows through vias with 500µm diameter openings filled with void free copper. The measured deposition rate of Cu is 5% larger than the rate provided by the guidelines from the manufacturers, therefore, megasonic agitation is assumed to have a negligible influence on the deposition rate. The parameters used for the sample displayed in figure 7 were 4 A/dm² current density and 250W megasonic power. Acoustic streaming has enabled the filling of a 3.2:1 aspect ratio via. In comparison, with the same current density and no acoustic agitation leads to via pinching and void formation in the via, as shown in figure 8.

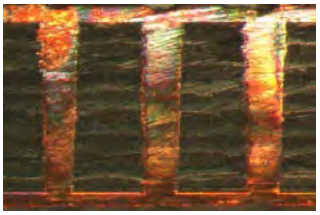

Figure 7: *500µm diameter through vias filled with void free copper with DC 4A/dm² and 250W megasonic power*

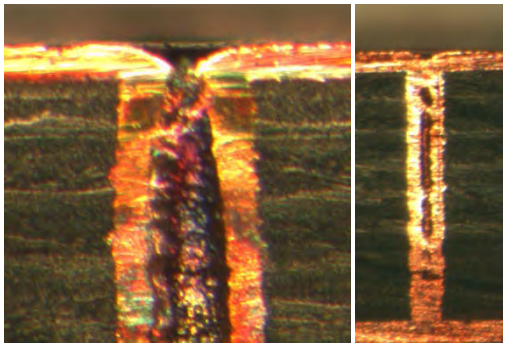

Figure 8: *Pinching effect and void formation within the via induced through current crowding and ion depletion, respectively using DC 4A/dm²*

VI – Conclusions

In summary, low current density DC deposition, with megasonic agitation achieved optimal performance. Figure 9 displays the maximum aspect ratio, 8:1, attainable with the test PCB.

Figure 9: *200µm diameter via filled with void free Cu using DC deposition and megasonic agitation.*

The quality of the via fill is summarised in table 2. The best quality via fill in this experiment is achieved using a current density 1 A/dm^2 and 250 W megasonic power. Megasonic agitation homogenises the concentration gradient of ions around the via opening which would result otherwise in a pinching effect under normal electroplating conditions. Megasonic agitation also assists ion transportation into the microvia to ensure continuous electroplating without voids.

Table 2: *Summary of via filling performance for 200µm diameter via*

Power (W)	Current Density (A/dm^2)								
	1			2			4		
	VF%	D	RDT	VF%	D	RDT	VF%	D	RDT
100	98	02	11	98	0.2	11	96	0.4	10
250	99	0.1	12	98	0.2	12	97	0.3	10

Further work is required to establish absolute maximum aspect ratio attainable using megasonic agitation.

The effect of varying the current waveform used to achieve successful electrodeposition in higher aspect ratio microvias is also to be investigated. Future work also includes investigations into the use of megasonic agitation to improve electrodeposition in TSV's.

References

[1] M. Lefebvre, 'Next Generation Electroplating Technology for MicroviaFilling', PCB I-connect 007,2008 http://www.pcb007.com/pages/zone.cgi?a=44582

[2] N. Matsui, 'Market trends of sequential build-up (SBU) printed wiring boards (PWB) in Japan', Vol. 27, pp15-18, 2001, ISSN 0305-6120

[3] M. Suppa, 'The process and pastes for the via hole plugging of HDI PCBs', pp 25-31, 2008, DOI 10.1108/03056120810848761.

[4] J-H. Lau, C. Chang, 'An overview of microvia technology', Circuit World 26, pp. 22–32, 2000.

[5] J. G. Kaufmann, M.P.Y. Desmulliez, Y. Tian, D, Price, M. Hughes, N. Strusevich, C. Bailey, C. Liu and D. Hutt 'Megasonic agitation for enhanced electrodeposition of copper', Microsyst Technol, Vol. 15, pp. 1245–1254, 2009, DOI 10.1007/s00542-009-0886-2

[6] M. H. Rashid, 'Power electronics handbook: devices, circuits, and applications', 2nd edition, pp.1-15, 2007.

[7] W-P. Dow, M-Y. Yen, S-Z. Liao, Y-D. Chiu and H-C., Huang, 'Filling mechanism in microvia metallization by copper electroplating', Electrochimica Acta, Vol. 53, pp. 8228–8237, 2008.

MICROPHYSICAL CHARACTERIZATION OF MICROMACHINED GaN/Si BASED STRUCTURES USED IN ACOUSTIC AND PHOTONIC DEVICES

A. Cismaru[1], A. Müller[1], G. Konstantinidis[2], M. Purica[1], F. Comanescu[1], A. Dinescu[1], A Stavrinidis [2],A. Stefanescu[1], T.Kostopoulos[2]

[1] *IMT-Bucharest, 32 B, Erou Iancu Nicolae str., 077190 Bucharest, Romania*

[2] *FORTH-IESL-MRG Heraklion, PO Box 1527, Crete, Greece*

e – mail: alina.cismaru@imt.ro

Abstract — **The paper presents the microphysical characterization of thin GaN membranes obtained by micromachining of GaN/Si. The analysis is targeted to contribute towards a better knowledge of the technological limits for manufacturing reliable GaN membrane supported devices like FBARs (Film Bulk Acoustic Resonators) or backside illuminated UV photodetectors. Analysis has been performed using SEM (scanning electron microscopy), optical profile characterization using the WLI (white light interferometry) technique and micro Raman spectroscopy stress.**

1. Introduction

The increase of the frequency of operation is now a demand for many electronic devices and often represents a serious technological challenge. Micromachining technologies are pushed to their limits in order to obtain very thin but at the same time reliable GaN membranes able to support FBARs operating in the X-band frequency range or higher. The same demand is valid for backside illuminated UV photodetectors manufactured on GaN membranes. In the latter case, a very thin membrane is necessary to insure minimum absorption of the light.

Filters working at frequencies below 2 GHz, based on SAW and FBAR piezoelectric resonators have been intensively used in mobile phones. A lot of new applications have imposed the need for higher frequencies [1]. The frequency for the 4G mobile phones is not yet established, but it seems that it will be higher. Wireless local area networks (WLAN) for high speed computer interconnections work in the vicinity of 5 GHz; which is another area of potential application for FBARs and SAWs based resonators and filters.

Highly oriented thin AlN and GaN layers deposited on substrates such as high resistivity silicon allows for compatibility with conventional semiconductor fabrication technologies as well as more "exotic" ones such as MEMS and nanolithography. GaN offers the additional advantage of monolithic integration with passive, but more importantly with active circuit elements including high electron mobility transistors (HEMTs). Micromachining techniques can be used to manufacture thin, high quality self-sustainable membranes. For FBAR devices, the thinner the membrane, the higher the operating frequency. The first GaN based FBAR resonator, realized on a 2.2 μm thin GaN membrane and working at 1.3 GHz, has been reported by the authors ([2]-[3]). Recently we have reported a FBAR structure manufactured on GaN/Si working at 6.3 GHz [4], supported by a 0.5μm thin membrane. For even higher frequencies membranes thinner than 0.5 μm must be realized. Another interesting application of micromachined GaN based devices is that of UV photodetectors [5, 6]. Since a membrane supported UV photodetector is basically used for backside illumination [7], a very thin GaN membrane is necessary to minimize light absorption. Up to now the morphological analysis of GaN micromachined structures has been undertaken only by a small number of groups. This paper presents the microphysical characterization of very thin GaN membranes used for FBAR structures. This analysis is necessary since, in order to achieve higher operating frequency, the thickness of the membrane must be drastically reduced which in turn is critical for the reliability of the device. The analysis has been performed using scanning electron microscopy (SEM), optical profile characterization employing the WLI (White Light Interferometry) technique and micro-Raman characterization

2. Test FBAR structures

Different test structures have been fabricated from the same wafer, together with real FBAR structures. The epitaxial structure was obtained from NTT AT Japan. The 0.3 μm thin GaN layer was grown on a high resistivity (111) oriented silicon

wafer. A buffer layer 0.2 µm thin based on AlN and AlGaN layers (the exact composition and thickness of these layers are unspecified by the provider) was grown between the GaN layer and the silicon substrate. The fabrication and topology of the FBAR structures were similar to those presented in [4]; the main difference was that this time the thickness of the backside floating metallization(Mo), deposited on the bottom of the membrane was reduced from 50nm to 20 nm. This has as effect the increasing of the resonance frequency from 6.3 GHz to 7.8 GHz. The FBAR structures are fed by means of coplanar waveguide transmission lines (planar structures with the signal line surrounded by symmetrical ground planes). The cross section of the structure is presented in Fig 1. The thickness of the top metallization was 40nm (Mo). The pads metallization was Ti/Au 5/500nm thick. Also other test structures were processed: (a) a structure containing only the membrane with backside metallization and (b) a FBAR structure with top electrodes and backside metallization.

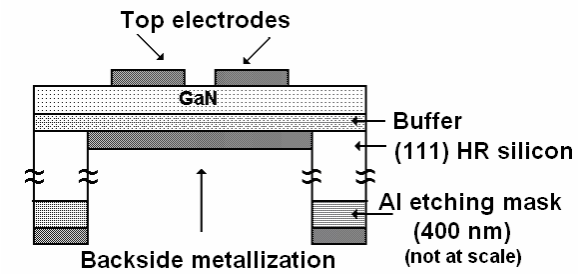

Figure 1 Cross section of FBAR structure

3. SEM analysis of the structures

A qualitative morphological analysis of the FBAR structures was performed using Scanning Electron Microscopy (SEM). In Fig. 2 the tilted view with respect to the electron beam direction of the top of the series connection of the FBAR structures is depicted. It is evident that the structures are deflected and the center of the membrane is lower than the "periphery". The stress in the membrane is compressive. A SEM photo of the bottom of the FBAR series structure is presented in Fig 3. The backside surface of the 0.5 µm thin membrane and the 150 µm deep etched walls are clearly visible. When the accelerating voltage is increased from 5kV to 30kV, the patterned top side metallization of the structures become also visible through the 0.5 µm thin membrane.

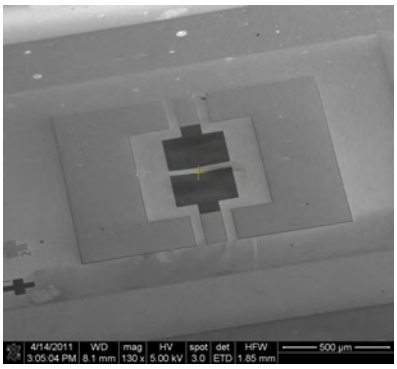

Figure 2. Top SEM photo of series connection (5 kV accelerating voltage)

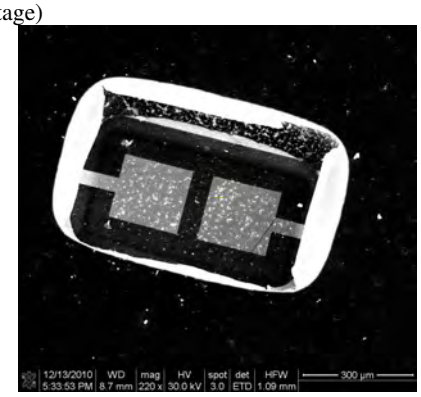

Figure 3. SEM picture of FBAR bottom side (bottom view of two electrodes through GaN thin membrane, (30 kV accelerating voltage)

4. Deflection analysis of thin membranes

The deflection of the thin GaN/buffer membranes was analyzed using a White Light Interferometer (WLI) – Photomap 3D from Fogale. The white light interferometry is the most convenient technique for surface analysis. The optical view of the sample is converted to an elevation map using interferogram processing techniques. The height of each pixel is determined independently from each other with nanometer accuracy, in a single scan. The GaN thin membranes as well as the FBAR structures manufactured on the 0.5 µm thin membranes were examined.

The 3D topography of the GaN thin membrane with backside metallization (20 nm Mo thin film) is presented in Fig. 4, where the light blue area marked with "A" indicates the effect of the backside metallization of the GaN thin membrane. The one dimensional (1D) characterization of the membrane deflection has been done through the dash line for the GaN thin membrane (see Fig.4). The 1D optical profile characterization is presented in Fig. 5. According to the white light interferometry technique, the minimum deflection is called h and represents the distance between the minimum of maximum deflection with respect to the absolute minimum. The maxi-

mum deflection is called H and represents the distance between the maximum deflection with respect to absolute minimum. The maximum deflection for the membrane area with backside metallization is H = 3.20 μm and the minimum deflection is h = 1 μm.

The 3D topography of the FBAR structure (manufactured on 0.5 μm GaN thin membrane) is presented in Fig. 6, where the light blue area marked with "A" indicates the effect of the topside metallization of the electrodes on the thin GaN membrane. The one dimensional (1D) characterization of the membrane deflection has been marked through the dash line for the series connection FBAR structure (see Fig.6). The 1D optical profile characterization is presented in Fig. 7. In this case, the maximum deflection is H = 3.80 μm and the minimum deflection is h = 0.70 μm.

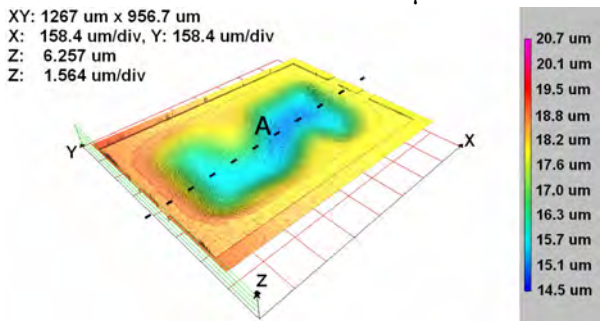

Figure 4. 3D topography of the membrane area (0.5 μm GaN plus buffer thin membrane)

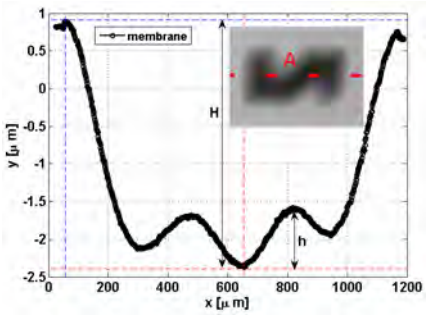

Figure 5. Optical profile of the membrane area with 20 nm Mo thicknesses of backside metallization (0.5 μm GaN plus buffer thin membrane)

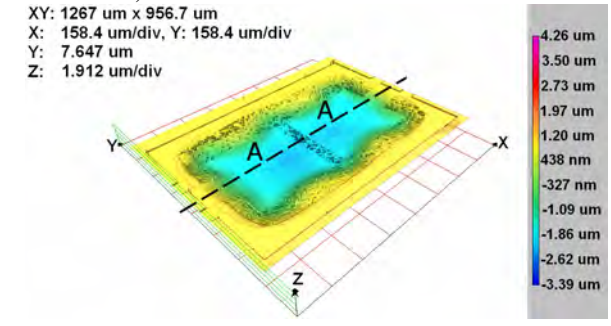

Figure 6. 3D topography of the FBAR structure in the membrane area (0.5 μm GaN plus buffer thin membrane)

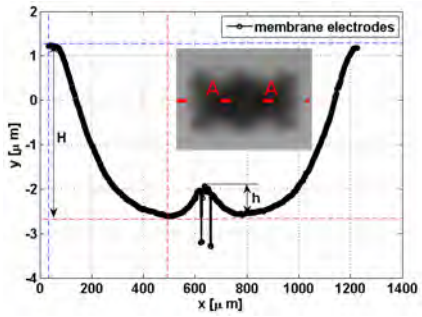

Figure 7. Optical profile of the FBAR structures in the membrane area with 40 nm Mo thicknesses of electrodes metallization(0.5 μm GaN plus buffer thin membrane)

The changes (higher maximum deflection) in the membrane deflection with topside metallization (Fig. 7) in comparison with the membrane without topside metallization (Fig. 5) are explained by the deposition of Mo topside metallization which introduces a tensile stress and the membrane is curved in the opposite direction.

5. Micro Raman spectroscopy stress measurements

Micro-Raman scattering is used to quantitatively characterize the in-plane stress in the fabricated suspended microstructures. The E_2 high mode in the Raman spectra is used because it has been proven particularly sensitive to biaxial stress in GaN films.

There is a linear relationship between the biaxial stress σ_{xx} and E_2 (high) Raman shift [8, 9]: $\Delta\omega = K\sigma_{xx}$. with the K value of 4.3 cm^{-1}/GPa [8].

Raman spectra were acquired in backscattering geometry using LabHR 800 spectrometer from Horriba, at 632 nm laser excitation through a confocal microscope (the beam diameter is 1 μm). The free-stress frequency value of 568 cm^{-1} for bulk crystal GaN was reported in [10] and was used as reference in this work. Raman spectra have been measured on different regions of the FBAR structures having the membrane thickness 0.5μm (0.3 GaN μm +0.2μm buffer). The measurements are presented in Fig 8 and a blowup of the results in Fig 9. The measurement performed on unreleased region of the structure (point A) has evidenced the line at 569.3 cm^{-1} which corresponds to the GaN layer. In fig 8 the low intensity lines corresponding to the buffer (composed from AlN and AlGaN layers) are also visible. The high intensity line corresponding to the silicon substrate is visible in the measurements for the point A. The compressive residual stress of 300 MPa in the unreleased region (point A) is low,

proving the good stress compensation created with an optimum buffer layer structure during the growth of GaN/Si. The stress decreases on the GaN membrane, reaching the minimum value at the center, (70MPa, point B) and values of 180-220 MPa at the membrane corners (points C, D). The stress remains still compressive. The stress on the membrane centre was about 75% lower than on bulk GaN/Si structure. Similar results have been obtained also for structures manufactured on 0.7µm thin GaN/Si membranes.

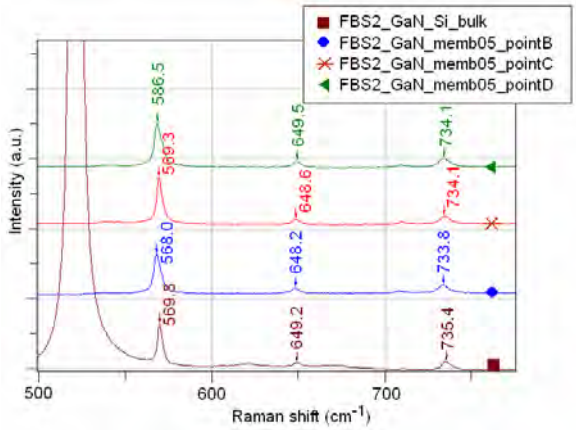

Figure 8. Raman shift for the different regions of the FBAR structures manufactured on the 0.5µm thin membrane

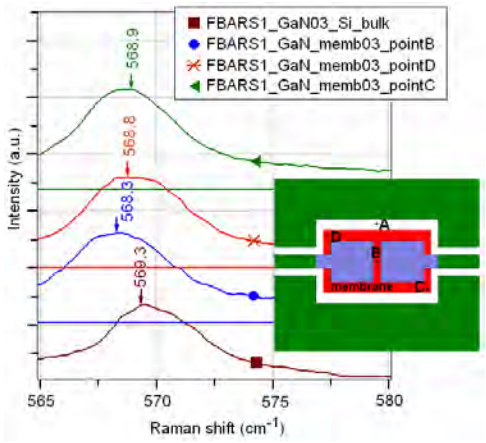

Figure 9 Blow-up of the Raman shift for the different regions of the FBAR structures manufactured on the 0.5µm thin membrane

The decrease of the stress with 87% in released GaN membranes compared with the GaN/Si regions in the close vicinity of the membrane have been recently reported [11]. Also spectacular reduction of the stress in micromachined GaN structures has been also reported in [12-13].

The relative low values of the residual stress explains the excellent behavior of these very thin membranes used as support for devices and circuits and make possible further reduction of the thickness.

6. Conclusions

GaN membranes, used in microwave and optical devices manufacturing have been analyzed. The deflection was estimated using SEM and white light interferometry. The membrane deflection was low enough even for the 0.5 µm thin membranes. Micro Raman spectroscopy performed on FBAR experimental structures has evidenced a compressive residual stress of 300 MPa in the unreleased region and a reduction with about 75% of the stress in the GaN membrane regions, were the silicon under the GaN/Si structure has been removed.

We believe that further reduction of the GaN membrane thickness can be performed without any major influence on the device reliability.

Acknowledgement

The authors Alina Cismaru and Alexandra Stefanescu acknowledge the support of the SOPHRD under the contract number POSDRU/89/1.5/S/63700.

References

[1] R. Lanz, P. Muralt, *IEEE Trans. on UFFC*, 52, 936, 2005

[2] A. Muller et.al. *Superlatices & Microstructures*, vol 40, 426, Oct. 2006

[3] D. Neculoiu, G. Konstantinidis, et.al. , *Int Microwave Symp. Digest, IEEE MTT-S*, 877, 2007

[4] A. Muller, D. Neculoiu, G. Konstantinidis et. al. *IEEE Electron Device Letters,* 30, 799, 2009

[5] A. Müller, G. Konstantinidis et.al. Applied Optics, 47, 1453, 2008

[6] A. Müller , G. Konstantinidis et. al, *Microelectronics Journal*, 40, 319, 2009.

[7] P. Malinowski et.al. *IEEE Electron Device Letters*, 30, 1308, 2009

[8] S. Tripathy, S. J. Chua, P. Chen, and M. L. Miao, *J. Appl. Phys*. 92, 3503, 2002

[9] M. Wagner, F. Bechstedt, *Appl. Phys. Lett*. 77, 346, 2000.

[10] P. Perlin,et.al, *Phys. Rev. B* 45, 13307 1992

[11] Jianan Lv et al. *IEEE Electron Device Letters*, 30, 1045, 2009

[12] Z. Yang et al. *Appl. Phys. Lett.*, 88, 041913,2006

[13] Y. Wang, T. Sasaki, T. Wu, F. Hu and K. Hane, *J. Micromech. Microeng*., 21 (3), 2011

A 3D CHAOTIC MICROFLUIDIC MIXER

Cătălin Mihai Bălan[1], Marioara Avram[1], Andrei Avram[1], Guolin Xu[2], Rhensheng Deng[2] and Ciprian Iliescu[2]

[1] *Micro- Nano- fluidics Laboratory, National Institute for Research and Development in Microtechnologies, Bucharest, Romania*
[2]*Institute of Bioengineering and Nanotechnology, Singapore*

***Abstract* - In this paper we propose a 3D passive microfluidic mixer fabricated using a silicon-PDMS structure. The fabrications of the silicon chip and of the packaging process are detailed within the paper. The 3D pressure-driven flow in the mixing chamber (packed with microspheres) is simulated using the FLUENT CFD commercial package. The code computes the isothermal laminar flows of the Newtonian working fluids, with double precision and with 10^{-10} convergence criterion.**

Keywords: *Microfluidic Mixes, 3D porous chaotic mixing, silicon-plastic structure, CFD, diffusion by convention.*

I - Introduction

It is a well-known fact that miniaturization is the recent trend in analytical chemistry, biochemical and life sciences [1]. The scaling-down of the conventional macro scale process takes advantage of high surface-volume ratio and enables smaller volumes, less waste, higher efficiency and accuracy. Recent research involves cell cultures on microfluidic platforms [2], cell cultures that can be used for drug screening applications [3] an essential aspect in the implementation of new drugs and pharmaceutical compounds. Drug screening processes in microfluidic systems requires exposure of the cell cultures to a gradient of drug concentration [4]. In order to achieve this aspect, perfect mixing process (uniform distribution of the drug in the cross section of the microfluidic channel) is required. The mechanism of mixing two fluids in microscale channels is very different from macroscale ones. The flow in microchannels is always laminar because of the small Reynolds number. As turbulence and secondary flows are absent, mixing at micro scale occurs primarily because of molecular diffusion at the interface between the fluids [5].

In order to enhance mixing performance in microfluidic devices, two types of designs are used [6]: (*i*) passive mixers to induce transverse flows because of the interaction of the main stream with specifically designed channel geometries [7-9], and (*ii*) active methods to produce transverse flows by applying oscillating forces within the channel [10-13]. The passive mixing process relies on diffusion or on chaotic advection [6, 14]. These mixers can be further categorized by the arrangement of the mixed phases: with parallel laminar flows, serial laminar flows, injection, chaotic advection and droplet. Active micromixers use the disturbance generated by an external field in order to enhance the mixing process. Thus, active mixers can be categorized by the types of external disturbance effects such as pressure, temperature, electrohydrodynamics, dielectrophoretics, electrokinetics, magnetohydrodynamics and acoustics [6]. The integration of active micromixers in a microfluidic system for cell cultures can be challenging and expensive. In contrast, the passive micromixer does not require external devices (except those used in fluid delivery) and can be more easily integrated in such systems.

Here we report a passive 3D chaotic micromixer, and its fabrication technique. The filter element consist of a cubic structure (1mm x 1 mm x 1mm), filled with 100µm glass microspheres. The microspheres are use to enhance the diffusion by convection. The inlet of the fluid is at the one of the cube's corner while the exit is at opposite corner (on the main diagonal). Numerical simulation shows that a good volume mixing process requires placing of 4 mixing elements in series. The fabrication process consists off patterning using classical photolithography and deep RIE processes of a silicon die (with aligned microfluidic channel patterns on the both sides of the die and etch-through holes). This silicon die is placed between two PDMS sheets (200µm-thich). The mixing in the microfluidic device was tested using water with color dots.

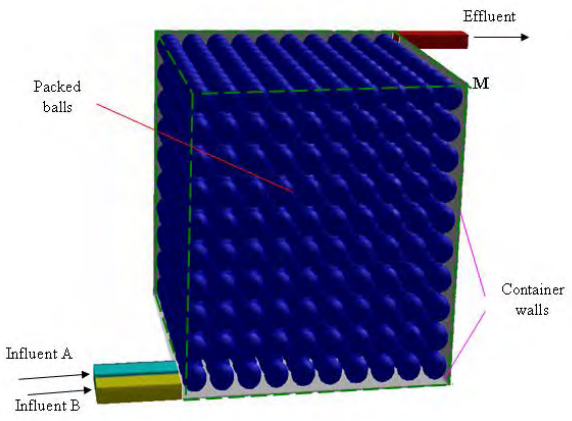

Figure 1: The arrangements of the microspheres inside the mixing chambers (1140 spheres, working volume - 1 mm^3).

II – Device Structure

The structure of the main mixing element was previously described. In a real micromixer (see Figure 2a) the spheres are not arranged in an uniform manner, but more in a chaotic one. The passive mixing elements (microspheres) create in this way, a "*porous*" structure inside the mixing chambers. The architecture of the device is illustrated in Figure 2a. The main element is a 1mm-thick silicon die on which the microfluidic network is imprinted. The microfluidic network consists of microfluidic channels (performed on the both sides of the die), via holes connections (that brings the fluid from the bottom

circuit to the top chip), inlet /outlet connection holes and the mixing containers. In order to seal this microfluidic network two PDMS cover sheets are bonded on the both sides of silicon die.

This microfluidic structure of the silicon chip is illustrated in detail in Figure 2c. The steps in the etch-through inlet/outlet holes are performed for achieving a good alignment between the chip and the microfluidic connector.

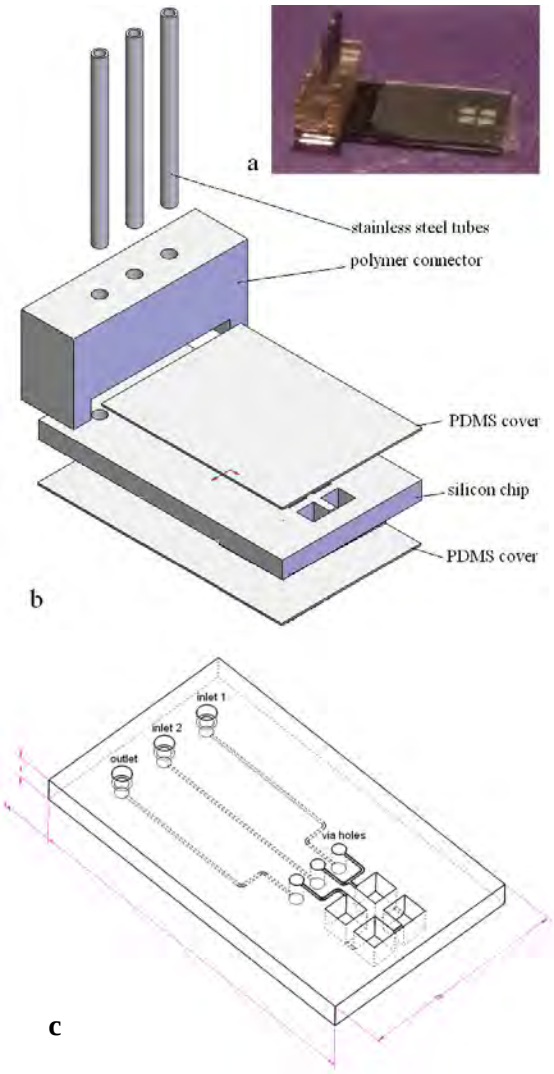

Figure 2: (a) Image with microfluidic mixer, (b) 3D exploded view with the architecture of the microfluidic mixer, (c) detail view of the silicon chip.

III – Analytical Consideration and Simulations

For an incompressible fluid flow, the governing equations for mass conservation and momentum can be expressed as follows:

$$\nabla \cdot \mathbf{u} = 0 \qquad (1)$$

$$Re(Sh_i \frac{\partial u}{\partial t} + grad\,\mathbf{u} \cdot \mathbf{u}) = -grad\ p + \Delta \mathbf{u} \qquad (2)$$

For the numerical computation of the mixing process, in parallel is solved also the diffusion equation for a concentration field *c* expressed as:

$$Pe(Sh_d \frac{\partial c}{\partial t} + grad\,c \cdot \mathbf{u}) = \Delta c \qquad (3)$$

where $Re = \rho RU/\eta$ is the Reynolds number, $Pe = RU/D$ is the Péclet number, $Sh_i = R/(Ut_i)$ and $Sh_d = R/(Ut_d)$ being the corresponding Strouhal numbers.

The expressions (2) and (3) are non-dimensional, scaled with space dimension *R*, the average velocity ($U = U_0$), momentum characteristic time $t_i = \rho R^2/\eta$, and the diffusivity characteristic time $t_d = R^2/D$ (here η is the dynamic viscosity, ρ is the mass density and *D* is the diffusion coefficient, all these material parameters are being considered constant within the flow field). The ratio between the two time scales (t_d/t_i) defines the Schmidt number, $S_c = \eta/(\rho D)$, one of the most important parameter which can characterizes the diffusion process in a viscous fluid [6].

Since the Reynolds number corresponding to the simulated conditions is less than 1, the flow is considered laminar, steady and three-dimensional. In order to examine the mixing effect, a user-defined-scalar (UDS) is introduced which has concentrations of 1 and 0 in influents A and B, respectively. The diffusion coefficient of the UDS is set at as low as 10^{-20} kg/m·s, which can effectively eliminate the mass transfer by diffusion. By solving the coupled transport equations of continuity (1), momentum (2) and UDS (3), the distribution profiles of pressure, velocity and UDS concentration can be determined. An analysis on the UDS profile can reveal the quality of fluid mixing in the mixer.

In our trial calculations, we examined the influence of influent flow rate, sphere packing method and inlets allocation on the device performance. It is found that the mixing effect increases slightly with decreasing flow rate. With its possible application in cell culture in mind, a flow rate of 1 µl/min was chosen for the two influents in the final simulation. On the other hand, the simple cubic packing method was adopted because it offers the best mixing effect compared to the hexagonal and the faced center packing. We also tested various allocation methods of the two inlets (for example, both in the middle of one wall, each in opposite corners, etc.), and the one shown in Figure 1 gives the best mixing effect.

It can be seen from Figure 3a that the UDS concentrations at Inlets A and B are 1 and 0, respectively, as specified by the boundary condition. On the outlet plane, however, it has a value between 0 and 1, decreasing gradually from one side to the opposite side. Note that the UDS diffusion is already excluded, so the uniform UDS distribution on the outlet plane must be the result of convective transport, or, in other words, the mixing of the two fluids. The more uniform UDS profile, the better fluid mixing in the mixer. However, the relatively non-uniform UDS distribution at the outlet plane in Figure 3a shows that the mixing effect of a single mixer may not be sufficient for certain applications. To solve this problem, we connect several such mixers in series, with the effluent from one mixer flowing into the inlet of the subsequent mixer. Figure 3b shows an example of four-mixers-in-series, where fluid mixing occurs in each mixer, and the UDS distribution on the outlet plane is

much more uniform than that for a single mixer. To quantitatively evaluate the mixing effect, the standard deviation and span (defined by the maximum minus the minimum) of UDS concentration at the outlet plane was calculated.

A smaller deviation (or a narrower span) corresponds to a more homogeneous effluent and a better mixing effect in the mixer. As shown in Figure 4, the mixing effect is greatly improved when the mixer increases from 1 to 2, but the improvement is less significant with further increasing number of mixers. In a practical application, the number of mixers to be used may be determined by the requirement of fluid mixing quality.

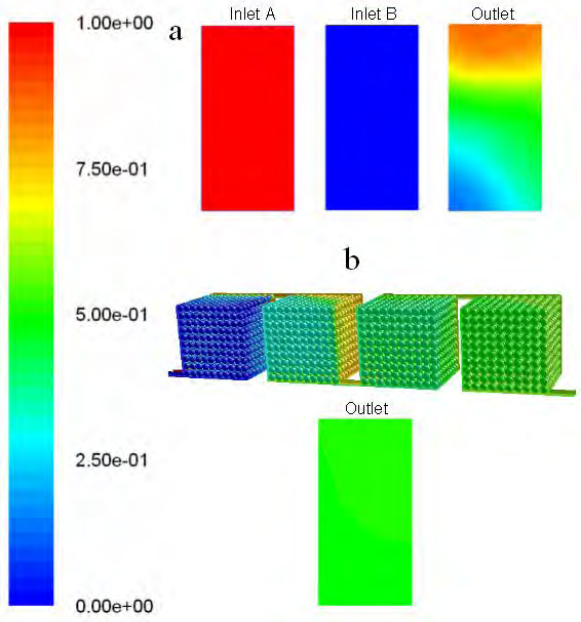

Figure 3: (a) The distribution of UDS concentration on the inlet and outlet planes for a single mixer. (b) The distribution of UDS concentration in the mixers and on the outlet plane for a four-mixers-in-series device.

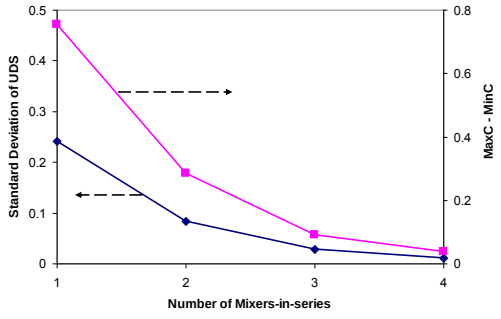

Figure 4: The standard deviation and maximum span of the UDS concentration on the outlet plane for different number of mixers-in-series.

From the UDS distribution in Figure 3b, one may notice that not all the spheres are efficiently used for fluid mixing. The spheres far away from the inlets and outlet (for example, those near the corner denoted by M in Figure 1) may be in contact with one fluid only, thus they do not contribute to the mixing of two fluids. It is possible to modify the container shape from purely cubic to a more appropriate shape in order to save the "*wasted*" spheres. However, the fabrication process of such shaped container may be so complicated that it does not worth the effort.

In some applications, the liquid volume needed to fill the mixer may be important. For example, if a blood sample is used, it will be desired that a minimum volume is used. In the current mixer, the spheres take up about 54.4% of the container space, which means that the fluid "trapped" in the mixer can be significantly reduced. Using a smaller sphere size may further decrease the priming volume, although the outlet dimension should be reduced accordingly in order to retain the spheres.

IV – Fabrication Process

A. Fabrication of the silicon chip

The fabrication process of the silicon die is illustrated in Figure 3 and involves four deep RIE etching processes (two for each side of the wafer) and four lithographic processes involving two masking layers (thick photoresist and PECVD-SiO_2) deposited on each side of the wafer. The thick photoresist masks were used to pattern etch-through holes patterning while the PECVD-SiO_2 masks was used for the definition of the microfluidic channels.

A 1mm-thick double-side polished silicon wafer with <100> crystallographic orientation and resistivity of 1-100 Ωcm was cleaned in a piranha solution (H_2SO_4 /H_2O_2 in ratio 2:1) at 120^0C for 20 minutes followed by rinsing in DI water and spin dried. 1μm-thick SiO_2 layers were deposited on both sides of the silicon wafer (Figure 5a) using a PECVD reactor (SPTS, USA) at a deposition temperature of 300ºC in low frequency mode (380MHz) RF using a power of 700W, from pure SiH_4 and N_2O (flow rates of 50sccm and 400sccm respectively) at a pressure of 450Pa (deposition rate of 400nm/min). Classical photolithographic process (using 2μm-thick AZ7220 positive photoresist) was used for the definition of the mask required for the patterning of the SiO_2 layers. The dry-etching process of the SiO_2 layers (Figure 5b) was performed in a RIE etcher (SPTS) using CHF_3 and O_2 (40sccm/4sccm), at a pressure of 90mTorr, and a power of 150W. In the next step (Figure 5c) a 12μm-thick photoresist mask (AZ9260-from Clariant)- mask with the design of through-holes - was aligned and applied over the SiO_2 mask. The thickness of the photoresist layer was required by the depth of the deep RIE process that will be performed in the next step. A classical Bosch process (using SF_6/C_4F_8) performed on an ICP deep RIE (Alcatel AMS 100) was used for anisotropic etching of a depth of 450μm. The photoresist mask was removed in an ultrasonic bath using NMP (N-Methyl-2-pyrrolidone) remover and a short deep RIE process (through SiO_2 mask) was used for definition of microfluidic channel on one side of the wafer (Figure 5d). A 300 nm-thick TEOS layer was deposited on a PECVD reactor (SPTS) on the generated surface using DRIE process as protection and etch-stop layer. In a similar manner, the other side of the Silicon wafer was processed: first using a thick photoresist mask (that defines only etch through holes) a 450μm depth was etched in silicon (Figure 5e) and further, after removing of the photoresist mask the microfluidic channels were etched (Figure 5f). For these

steps, the processed silicon wafer was temporary bonded with wax on a dummy silicon wafer. To de-bond the dummy wafer, it was kept on a hotplate at 110ºC and later cleaned in an ultrasonic NMP tank. The PECVD - SiO_2 and TEOS layers –used in the previous steps as mask or protection layer – was removed in a classical BOE (buffered oxide etch) solution. In order to generate a hydrophilic surface of the microfluidic structure a 150 nm thick thermal SiO_2 layer was grown using a classical dry oxidation process in an oxide furnace (Tystar, USA) at 1000ºC for 1h 30 min (Figure 5g). Finally the wafer was diced in individual chips using dicing saw equipment (DISCO 3350).

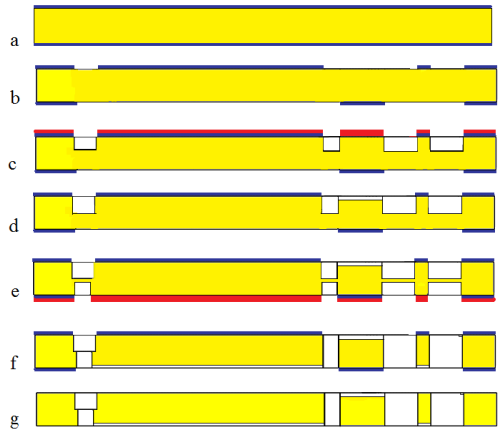

Figure 5: *Main steps of the fabrication process of the silicon chip: (a) deposition of PECVD SiO_2 layer, (b) patterning of SiO_2 layer, (c) 1st deep RIE process through a photoresist mask, (d) 2nd deep RIE process (after removing the photoresist mask), (e) 3rd deep RIE process, (f) 4th deep RIE process, (g) Removing of the oxide mask and thermal oxidation.*

B. Packaging and testing

The sealing of the microfluidic channel was performed using a 100µm-thick PDMS foil. The PDMS sheet was activated in O_2 plasma before bonding. A first bonding process was performed between silicon chip and PDMS cover. For an improved adhesion the bonding was performed on a hot plate at 70^{O}C. In the next step the glass beads (100µm- diameter) were placed in the "*mixing container*" and using a razor blade the excess beads were removed.

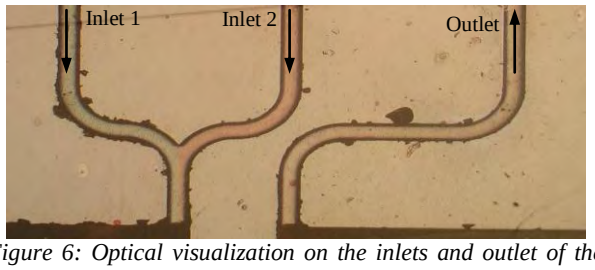

Figure 6: Optical visualization on the inlets and outlet of the chip micromixer.

A second bonding process between the silicon chip and a similar PDMS cover assure the sealing of the microfluidic chip. The microfluidic connector was fabricated using a polymer-printing machine Eden 350 (3D solutions, France). The inlet/outlet holes etched on silicon chip (with a diameter of 0.7mm and a depth of 0.5mm) easily allows in positioning of the connector.

The image with the assembled chip is presented in Figure 2a and a detailed view of the inlets and outlet is seen in Figure 6. A preliminary test was made with diluted dyes. The visual results are showing a good mixing process. A future experimental work will involve a fluorescence spectroscopy procedure to quantify the mixing process at the outlet.

IV – Conclusion

The hydrodynamic behavior in a micromixer with a "*porous*" structure formed by spheres was simulated in a 3D configuration. The simulations performed with the use of a UDS procedure shows good results when several mixing chambers are connected in serial. The fabrication process of silicon chip and packaging method of the micromixer have been detailed within the paper. Preliminary results performed with diluted dyes are showing a good mixing process enhanced by the presence of the spheres.

Acknowledgements

This project is funded by the SOP-IEC, O.2.1.2, Project (Microfluidic Factory for "Assisted Self-Assembly" of Nanosystems), No.209, ID 665.

References

[1] J. West, M. Becker, S. Tombrink, A. Manz, Micro total analysis systems: Anal. Chem. 80/12, 4403-4419, 2008

[2] M. Ni, et al, *Int. J. Molecular Sciences* 10/12, 5411-5441. 2009

[3] S. Zhang, et al, *Biomaterials*, **32/4,** 1229-1241, 2001.

[4] Y. C. Toh, C. Zhang, J. Zhang, Y. M. Khong, S. Chang, V. D. Samper, D. van Noort, D. W. Hutmacher and H. Yu *Lab on a Chip*, 7 302-309. 2007

[5] D. Broboană, C.M. Bălan, T. Wohland, C. Bălan, *Chem. Eng. Sci.*, 66, 1962-1972, 2011.

[6] N.T. Nquyen and Z. Wu *J. Micromech. Microeng.* vol. 15, R1-R16, 2005.

[7] J. Branebjerg, P. Gravesen, J.P. Krog, C.R. Nielsen, *IEEE Micro Electro Mechanical System (MEMS)*, San Diego, USA, pp. 441-446, 1996.

[8] R.H. Liu, M.A. Stremler, K.V. Sharp, M.G. Olsen, J.G. Santiago, R.J. Adrian, H. Aref, and D.J. Beebe, *J. Microelectromech Syst*, vol. 9, pp. 190-197, 2000.

[9] A.D. Stroock, S.K.W. Dertinger, A. Ajdari, I. Meyic, H.A. Stone, G.M. Whitesides, *Science*, vol. 295, pp. 647-651, 2002.

[10] F. Bottausci, I. Mezic, C.D. Meinhart and C. Cardonne, *Philos Trans R Soc Lond A Math Phys Eng Sci*, vol. 362, 1001-1018, 2004.

[11] J. Deval, P. Tabeling and C.M. Ho, *IEEE Micro Electro Mechanical System (MEMS), Las Vegas, USA*, 36-39, 2002.

[12] Y.K. Lee, J. Deval, P. Tabeling and C.M. Ho, *IEEE Micro Electro Mechanical System (MEMS), Interlaken, Switzerland*, 483-486, 2001.

[13] R. Lu, K. Ryu and C. Liu, *J. Microelectromech Syst*, 11, 462-469, 2002

[14] T. M. Squires and R. S. Quake, *Reviews of Modern Physics*. **77**, 977-1026, 2005.

USING DIFFRACTION TO DETECT DEFLECTION OF THE CANTILEVERS IN AN ARRAY

O. Pjetri[1], W. W. Koelmans[1], L. Abelmann[1], M. H. Siekman[1], and M. C. Elwenspoek[1,2]

[1]*Transducers Science and Technology, MESA+ Institute for Nanotechnology, University of Twente, Enschede, the Netherlands*
[2]*Freiburg Institute for Advanced Studies (FRIAS), Albert-Ludwigs-Universität Freiburg, Freiburg im Breisgau, Germany*

***Abstract* — We present an optical technique to detect cantilever deflection of an array using Fraunhofer diffraction patterns. Application areas include probe-based data storage. Intensity profiles of different cantilever arrays are captured on a CCD camera and compared with our model. These measurements are in excellent agreement with the Fraunhofer theory, less than 3% deviation is found. Each cantilever can either be deflected by a fixed amount or undeflected. Based on noise measurements on our setup and intensity patterns simulations, we predict that this method allows the measurement of** 1 nm **deflections in an array of six cantilevers with an SNR of 35dB.**

***Keywords* — Cantilever array, diffraction, optical readout, probe storage**

I – Introduction

Cantilever arrays are used in many applications like probe-based data storage [1], probe based nano-lithography and nano-manufacturing. In many cases feedback of the cantilever position is needed. A common way to achieve this is by integrating a sensor on every cantilever like piezoelectric [2], thermal [3] and magnetoresistive. These techniques present complexity of fabrication and constrains on the cantilever design. Optical readout on the other hand is separated from the array, does not put any constrains on the fabrication and cantilever design, and is simple to incorporate.

Sensing of cantilever deflection using diffraction patterns was first introduced by [4], by fabricating a grating inside a cantilever which creates a diffraction pattern. Later, this technique is extended to parallel operation and capturing on separate detectors [5]. We present a new scheme where the cantilevers themselves form an optical grating so that the state of deflection of each cantilever within the array determines the diffraction pattern, as is shown in figure 1. We consider the situations where the cantilevers can only be in two states: undeflected or deflected by a fixed amount.

Detection of the diffraction patterns can be performed by comparing measured patterns with calculated patterns stored in a look-up table. This is, however, not the most efficient way. In [6], fast, low complexity detection algorithms are presented to retrieve the state of the cantilevers from the measured intensity profiles. In this paper we focus on the experimental verification and quantification of the change in the diffraction patterns.

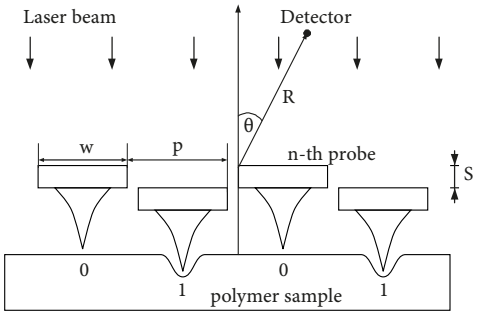

Figure 1: *Schematic of the optical readout using Fraunhofer diffraction patterns. A line shaped laser beam illuminates the array. The reflected light from the cantilevers will give rise to a diffraction pattern which is captured by a CCD camera. Small deflections of the cantilevers will result in different intensity patterns.*

II – Theory

When coherent laser light is focused on the array, the phase of the reflected light waves depends on the amount the cantilevers are deflected. This change in phase results in a different interference on the screen thus changing the intensity pattern. To be in the Fraunhofer region it must hold: $F \ll 1$, where F is [7]:

$$F = \frac{a^2}{R\lambda} \tag{1}$$

where a is the radius of the aperture, λ the wavelength and R the distance between the array and the camera. Because the thickness of the line shaped beam incident on the array is much smaller than the length of the cantilevers, we consider the one dimensional Fraunhofer integral. The equation of the intensity profile on the camera is then given by:

$$I(x) = I(0)\, sinc^2\left(\frac{qw}{2}\right)\left|\sum_{n=0}^{N-1} e^{-i(2ks+qnp)}\right|^2 \tag{2}$$

where $I(0)$ is the irradiance at the center of the screen with no cantilever deflected, s the deflection, k the wavenumber, w the cantilevers width, p the cantilevers period, n the cantilever index and $q = \frac{kx}{R}$ with R being be the distance between the array and the screen where the diffraction pattern is measured while x represents the coordinate on the screen.

A. A figure of merit for diffraction patterns

In order to quantitatively evaluate the difference between two intensity patterns, a figure of merit is proposed based on the area between two intensity profiles,

$$\Delta I_{\mathrm{P}} = \sqrt{\frac{\int_{\text{profile}} \left[I_{\mathrm{P1}}(\theta) - I_{\mathrm{P2}}(\theta)\right]^2 \mathrm{d}\theta}{\int_{\text{profile}} I_{\mathrm{P1}}(\theta)^2 \mathrm{d}\theta}} 100\% \qquad (3)$$

where I_{P1} and I_{P2} are the two intensity profiles to be compared.

III – Experimental

A schematic of the setup is shown in figure 3. The spot from a laser diode with a wavelength of 635 nm and 3 mW power is expanded five times using a beam expander. This expanded beam is then passed through a rectangular shaped aperture of 15 mm width and 10 mm height. The resultant beam is focused on the array by a cylindrical lens with a focal length of 200 mm. This way all cantilevers are illuminated by a line-shaped coherent beam of 15 mm wide and 80 µm thick. Because the laser spot is not exactly at the tip end of the cantilever, the measured deflection is smaller than the deflection at the tip.

The diffraction pattern created by the reflected light from the array is reflected by a second prism onto another cylindrical lens with a focal length of 60 mm and rotated 90° with respect to the first lens. The diffraction pattern is then projected onto a CCD camera positioned in the back focal plane of the second lens. By placing the image plane in the back focal plane of the lens, the Fraunhofer diffraction pattern can be observed independently of the distance between the array and the lens: the image plane is placed effectively at infinity [8]. Using a lens has several advantages: the size of the diffraction pattern can be tuned with the focal length of the lens and also the optical path can be shortened using a lens with a shorter focal length. The camera has a resolution of 2048x1536 pixels and a pixel size of 5 µm.

The cantilever array is mounted on two slip-stick motors on top of each other: one allows the adjustment of the roll-angle of the array and the other allows the course positioning in the z-direction (normal to the sample surface).

Measurements were performed with arrays without tips as these are easier to fabricate. Because this method is based on the phase shift introduced by the difference in height of the reflective surface of the cantilevers, it is very important that the cantilevers thickness be as uniform as possible and that their surface be as coplanar as possible. The cantilevers are etched out of the device layer of a SOI wafer, which therefore determines the uniformity of the reflecting surface height of the cantilevers. The fabrication process is similar to that described in [9], with exclusion of the steps that define the tips. A SEM photo of an array with four cantilevers, 14 µm wide, 250 µm long and 3 µm thick, is shown in figure 2.

In order to deflect certain cantilevers in an array, a medium was fabricated consisting of a silicon wafer

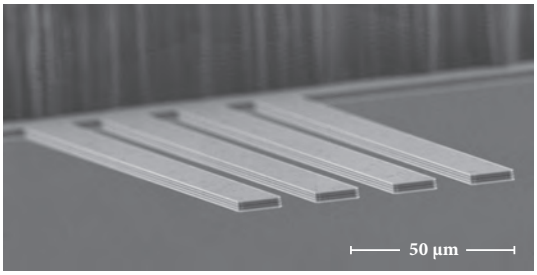

Figure 2: *Scanning electron micrograph of an array with four cantilevers* 15 µm *wide and a pitch of* 25 µm *used to measure the patterns shown in figure 4, 7 and 6*

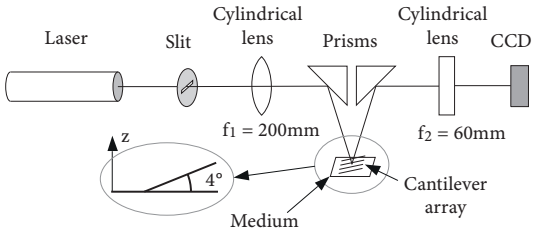

Figure 3: *Schematic of the setup used to measure diffraction patterns. An expanded laser beam is first passed through a rectangular shaped aperture and then focused by a cylindrical lens on the array. The second cylindrical lens projects the diffraction pattern on a CCD camera.*

with etched pits of varying size in order to match the cantilevers width and pitch. The medium is mounted on a *xyz* stage used for fine positioning. By moving the medium in the z-direction, certain cantilevers are deflected when they touch the medium, while others fall into the pits, thus remaining undeflected.

A. Analyzing CCD images

In the recorded CCD images the angle of diffraction, which is approximately equal to x/R (with x and R being defined in equation 2), is oriented horizontally. The captured images are averaged over 200 lines in the vertical direction in order to minimize the influence of dust and particles. After this averaging, low pass filtering is performed to remove high spatial-frequency noise. All the post-processing of the images is done in MatLab software.

IV – Results

A. Diffraction patterns with no cantilever deflection

Our first experiment was performed in order to check the accuracy of our model. To avoid aberrations, the second lens in the optical path ($f_2 = 60\,\mathrm{mm}$) was removed. The CCD camera was placed at a distance of 70 mm from the array. An array with five cantilevers was used having a width of 14 µm and a pitch of 20 µm. The array is not in contact with the medium underneath so that all cantilevers are undeflected. The measured in-

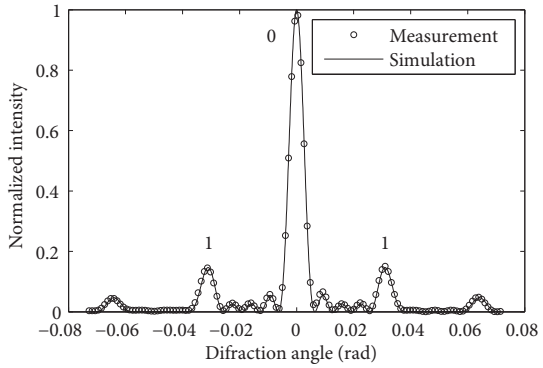

Figure 4: *Calculated and measured intensity profile of the diffraction pattern created by an array of five undeflected cantilevers. The numbers near the maxima indicate the zeroth- and first-order maxima. The ΔI_P between theory and measurement, as defined in equation 3 is 3%.*

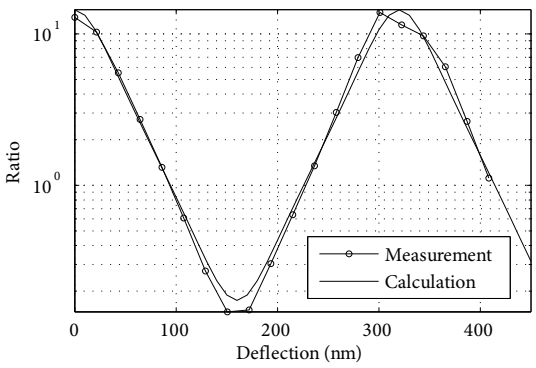

Figure 5: *The ratio of the amplitudes of the zeroth mode maximum to the first mode maxima as function of deflection for an array of N = 3 with the two side cantilevers bended. The measurements are in good agreement with the model.*

tensity profile and calculated are shown in figure 4. The error of fit according to equation 3 is smaller than 3%, showing the measurements are in excellent agreement with theory.

B. Introducing cantilever deflection

In the next set of experiments we introduce cantilever deflection. Here we use an array of three cantilevers 30 µm wide and a pitch of 40 µm where the outer two cantilevers are deflected by the same amount. With increasing deflection, the zeroth-order maximum decreases while the first-order maxima increase (figure 4). The ratio of the zeroth-order and first-order maxima is used as a measure of cantilever deflection. Figure 5 shows the calculated and measured ratio as a function of deflection. These measurements are in good agreement with theory for deflections up to 440 nm. Furthermore, figure 5 shows that the sensitivity of this technique changes based on the deflection point around which the cantilevers are operating. Maximum sensitivity is achieved when the cantilevers are operating around a deflection bias of 30 nm and lowest sensitivity when operating around 159 nm (1/4 λ).

C. Offset in deflections

We illustrate the effect of biasing using an array of four cantilevers having a width of 14 µm and a pitch of 25 µm. The outer right cantilever is deflected in steps of 50 nm. The deflection at the center of the spot is calculated to be 23 nm. For this array and deflected cantilever, we calculated the most sensitive biasing point to be 1/4 λ. First we measure two intensity profiles with 22 nm biasing. These two profiles for $h = 22$ nm and $h = 45$ nm are shown in figure 6. The calculated ΔI_P for this pair is found to be 17.6%. Next, we measure another pair with 136 nm biasing: $h = 136$ nm and $h = 159$ nm. These two patterns are shown in figure 7. ΔI_P in this case is calculated to be 32.2%. This is a factor 1.83 better compared to the case where 22 nm biasing was used.

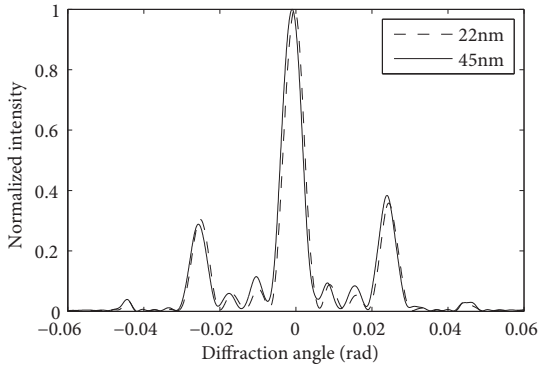

Figure 6: *Two normalized diffraction intensity profiles created by an array of four cantilevers with its outright cantilever bent at* 22 nm *and* 45 nm*. The ΔI_P as defined in equation 3 for this pair is 17.6%.*

D. Noise measurement

In order to give a quantitative evaluation of the capability of this technique, noise measurements were performed on an array with six cantilevers, 19 µm wide and 30 µm pitch. A hundred patterns were measured with one second interval and 9 ms exposure time giving a bandwidth of 111.1 Hz. The patterns were corrected for drift. Noise amplitude for each measurement was calculated using equation 3 with I_{P1} being the measured intensity profile and I_{P2} the calculated profile. The standard deviation of $\Delta I_P(n)$ is a measure for the noise level.

The signal amplitude of the same array is calculated with the outer right cantilever deflected at 159 nm and 160 nm. We use equation 3 with I_{P1} and I_{P2} being the simulated intensity profiles of the two deflections. Together with the noise level calculated above, this leads to an SNR of 35dB.

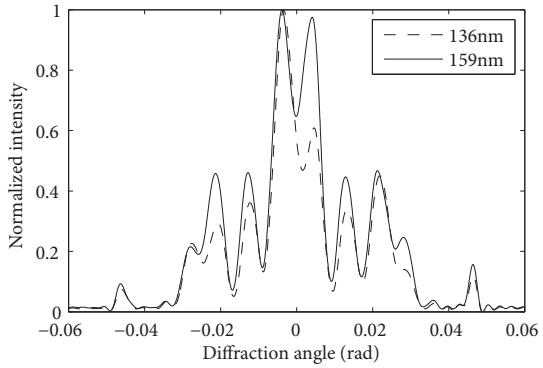

Figure 7: *Two normalized diffraction intensity profiles created by an array of four cantilevers with its outer right cantilevers bent at* 136 nm *and* 159 nm*. The* ΔI_P *as defined in equation 3 for this pair is 32.2%.*

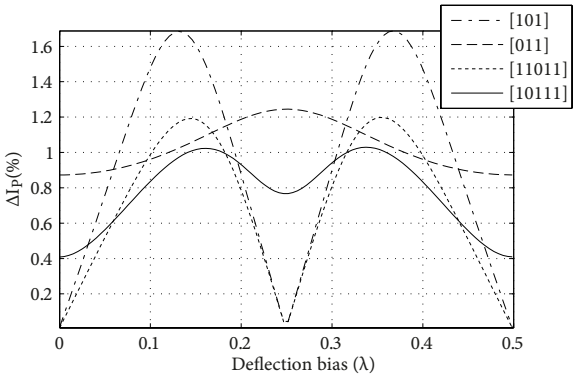

Figure 8: *Simulated* ΔI_P *for* 1 nm *deflection at different offsets for different cantilever arrays. "1" and "0" represent undeflected and deflected cantilevers respectively. Sensitivity differs per array and per set of deflected cantilevers.*

V – Discussion

Measurements show that diffraction patterns are very sensitive to cantilever deflection. Sensitivity can be increased by biasing the cantilevers at a certain deflection. The simulations in figure 8 show that the exact amount of bias for optimal performance differs per array and also per set of cantilevers that are deflected. Instead of a CCD camera, a photodiode array could be used to increase bandwidth and resolution resulting in faster and more accurate measurements.

We expect thermal noise to be negligible compared to shot noise, especially with increasing laser power. Moreover, when used in information storage, the cantilevers will be supported by the sample where the data is stored, further reducing thermal noise.

VI – Conclusion

In this work we show that parallel optical readout of cantilever arrays can be achieved by analyzing the diffraction patterns created by such arrays when illuminated by a line shaped laser beam. The diffraction pattern obeys the one-dimensional Fraunhofer theory. Noise measurements on our setup and intensity profile simulations predict that a 1 nm deflection of individual cantilevers can be detected with a SNR of 35 dB, in a bandwidth of 111 Hz.

Sensitivity can be improved by biasing the cantilevers deflection. The exact amount of bias for optimal performance differs per array and also per set of cantilevers that are deflected. For an array of four cantilevers, with the outer right cantilever deflected, we measured a signal improvement of a factor 1.83 when the cantilever is biased by 136 nm.

References

[1] A. Pantazi *et al.*, "Probe-based ultrahigh-density storage technology," *IBM J. Res. Dev.*, vol. 52, no. 4-5, pp. 493–511, 2008, doi:10.1147/rd.524.0493.

[2] C. S. Lee, H.-J. Nam, Y.-S. Kim, W.-H. Jin, S.-M. Cho, and J. uk Bu, "Microcantilevers integrated with heaters and piezoelectric detectors for nano data-storage application," *Appl. Phys. Lett.*, vol. 83, no. 23, pp. 4839–4841, 2003, doi:10.1063/1.1633009.

[3] W. P. King, T. W. Kenny, K. E. Goodson, G. Cross, M. Despont, U. Durig, H. Rothuizen, G. K. Binnig, and P. Vettiger, "Atomic force microscope cantilevers for combined thermomechanical data writing and reading," *Appl. Phys. Lett.*, vol. 78, no. 9, pp. 1300–1302, 2001, doi:10.1063/1.1351846.

[4] S. R. Manalis, S. C. Minne, A. Atalar, and C. F. Quate, "Interdigital cantilevers for atomic force microscopy," *Appl. Phys. Lett.*, vol. 69, no. 25, pp. 3944–3946, 1996.

[5] T. Sulchek, R. J. Grow, G. G. Yaralioglu, S. C. Minne, C. F. Quate, S. R. Manalis, A. Kiraz, A. Aydine, and A. Atalar, "Parallel atomic force microscopy with optical interferometric detection," *Appl. Phys. Lett.*, vol. 78, no. 12, pp. 1787–1789, 2001, doi:10.1063/1.1352697.

[6] J. Van Honschoten, H. W. De Jong, W. W. Koelmans, T. P. Parnell, and O. V. Zaboronski, "Information storage and retrieval for probe storage using optical diffraction patterns," *submitted*, 2011. [Online]. Available: http://arxiv.org/abs/1104.0871

[7] E. Hecht, *Optics*. Addison-Wesley, 2002.

[8] F. Träger, *Springer Handbook of Lasers and Optics*. Springer, 2007.

[9] W. W. Koelmans, T. Peters, L. Abelmann, and M. C. Elwenspoek, "Fabrication of cantilever arrays with tips for parallel optical readout," in *Proc. Micromechanics and Microsystems Europe*, Enschede, The Netherlands, 26-29 Sept. 2010.

Charge accumulation in double-layer dielectric for Capacitive RF MEMS Switch

Gang Li, Yingge Wang and Xuyuan Chen

Faculty of Science and Engineering, Vestfold University College, P.O.Box-2243, N-3103 Tonsberg, Norway
Email: Gang.Li@hive.no, Xuyuan.Chen @hive.no

Abstract— **SiO_2/Si_3N_4 double-layer dielectric stacks, instead of single dielectric layer, have been investigated to mitigate charge accumulation in the dielectric for the purpose of high reliable capacitive microelectromechanical switch. Two kinds of multi-dielectric-layers with two different thickness ratios are structured, and SiO_2 single-layer dielectric structure are also fabricated for comparison. The charge injection kinetics in the dielectric layer has been investigated by performing C-V measurements on metal-insulator-semiconductor (MIS) capacitor structure instead of an actual switch. When bias voltage is applied, compared with charge injection situation in single dielectric layer, some charge injection dependent parameters, such as the tunneling effective masses, injection barriers and the electric field across the dielectric, will be probably modified by using the double-layer dielectric due to the heterojunction formation. The changes of these parameters will definitely cause the change of the charge injection behaviors in the switch dielectric. In general, the experiment results show that low charge accumulation has been achieved by using double-layer dielectric stacks. The experiment results further show that the charge accumulation behaviors varied greatly with the different thickness ratio of Si_3N_4 to SiO_2. With same positive dc bias voltage for charge injection, we found that net negative charge accumulated in the thin-oxide MNOS structure and net positive charge accumulated in the thick-oxide MNOS structure as the electron injection is suppressed by the thick oxide. It can be anticipated that the charge accumulation in the switch dielectric can be minimized by optimizing the thickness ratio of double-layer dielectric.**

Index Terms - RF MEMS switch; Charge accumulation; Double-dielectric layer; C-V measurement

I. INTRODUCTION

RF MEMS capacitive switches are expected to be a very promising technology for many microwave and wireless applications since they can provide low loss, low-power consumption, high linearity and quality factor [1, 2]. However, the reliability problem is still one of the important limitation factors which present a research challenge for the industrialization of these devices. It is well known that the deposited dielectric films used in RF MEMS capacitive switches, typically SiO_2 and Si_3N_4, contain large density of traps associated with dangling bonds. The lifetime of these switches is believed to be adversely affected by charge trapping in the dielectric. These accumulated charges in the dielectric will cause the metal bridge to be partially or fully pulled down, degrading the on-off ratio of the switch. . In spite of huge effort has been made from many research groups worldwide for more than a decade to develop robust RF MEMS switches, little information is available in the literature providing a fundamental solution to this problem [3-6].

Charge accumulation will probably happen in the dielectric where high voltage is required. In our previous work [7], we described the charge injection and their trapping in the dielectric follow a modified Fowler-Nordheim tunneling model, which is applied to a triangular barrier and takes place when the barrier thickness is relatively large [4]. Based on the tunneling model, some important parameters will influence the charge injection behaviors of the dielectric under high applied voltage, such as the effective masses of the tunneling carriers, injection barrier and the electric field in the dielectric.

In this work, for the aim of control of the charge accumulation, double-layer dielectric structures instead of single dielectric layer were proposed to be used as the dielectric layer in capacitive RF MEMS switches. In order to optimize the charge accumulation in the dielectric, double-layer dielectric structures were designed with different thickness ratio of Si_3N_4 to SiO_2, on the condition that the total dielectric thickness was fixed to 300 nm. By measuring and analysing the capacitance versus voltage (*C-V*) curves of MIS structures, the charging kinetics of the dielectrics can be characterized before and after charge injection.

II. EXPERIMENTS

A. Sample preparation

In our experiment, charge accumulation in the dielectric layer was investigated by using MIS capacitor structure instead of an actual capacitive RF MEMS switch. Three MIS capacitor devices have been designed as shown in Figure 1. The dimension of the test MIS structure is designed according to the measurement range of the measurement setup. For each device, both the silicon dioxide and silicon nitride films were fabricated by using Plasma Enhanced Chemical Vapour Deposition (PECVD) technique. The thickness of each insulate layer was about 3000Å in total. Then Al metal electrodes with a circular area of 2.25×10^{-4} cm^2 were sputtered by means of photolithography.

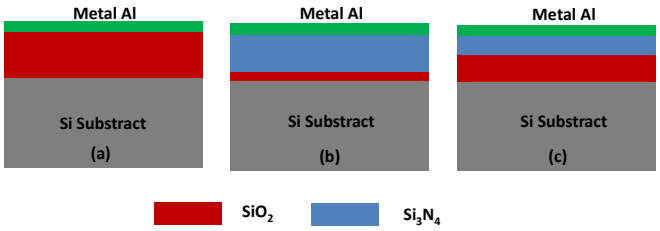

Fig. 1 Schematic cross-sectional views of the three MIS capacitor devices with different dielectric structures: (a) SiO_2=300nm, (b) Si_3N_4/SiO_2=250nm:50nm and (c) Si_3N_4/SiO_2=100nm:200nm.

B. CV measurements

It is well known that charge accumulation in the dielectric of MIS structure can be evaluated by *C-V* measurement. Flat band voltage (V_{FB}) of the *C-V* curve, as a function of the total amount of the space charges in the dielectric, provides information on how many charges are trapped in the dielectric of the MIS structure. The shifts of *C-V* curves after the dc bias towards the left or right indicate that the net positive or negative charges injected into the dielectric. In the experiments, the bottom of silicon substrate is held at the prober station chuck and all samples were measured in air ambient and at room temperature, the MIS samples were first biased with dc bias stress, so that charges can be injected into the dielectric films. Then, the high-frequency *C-V* measurements were performed immediately charge injection. All measurements took place in a probe station of the Faraday shielded box. By comparing the measured *C-V* curves before and after charge injection, the dynamic process of dielectric charging can be analysed.

III. RESULTS AND DISUSSION

The *C-V* curves had been measured on all the samples by performing a voltage sweep from -20 to 20 V with frequency of 100 kHz. Before applying the dc bias to the MIS device, same *C-V* measurement on a virgin MIS device was carried out twice to make sure if the sweep voltage will cause charge injection in the dielectric.

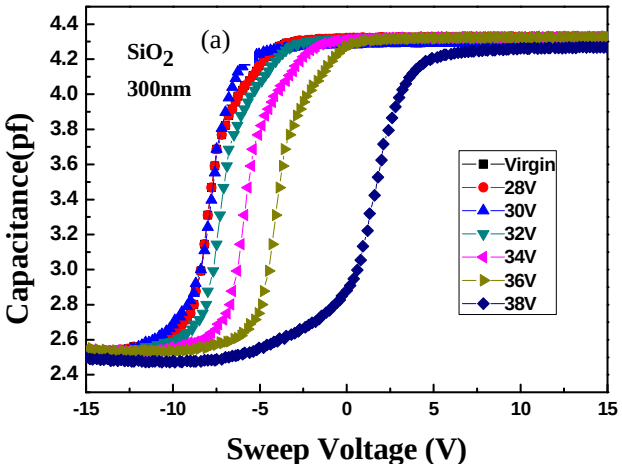

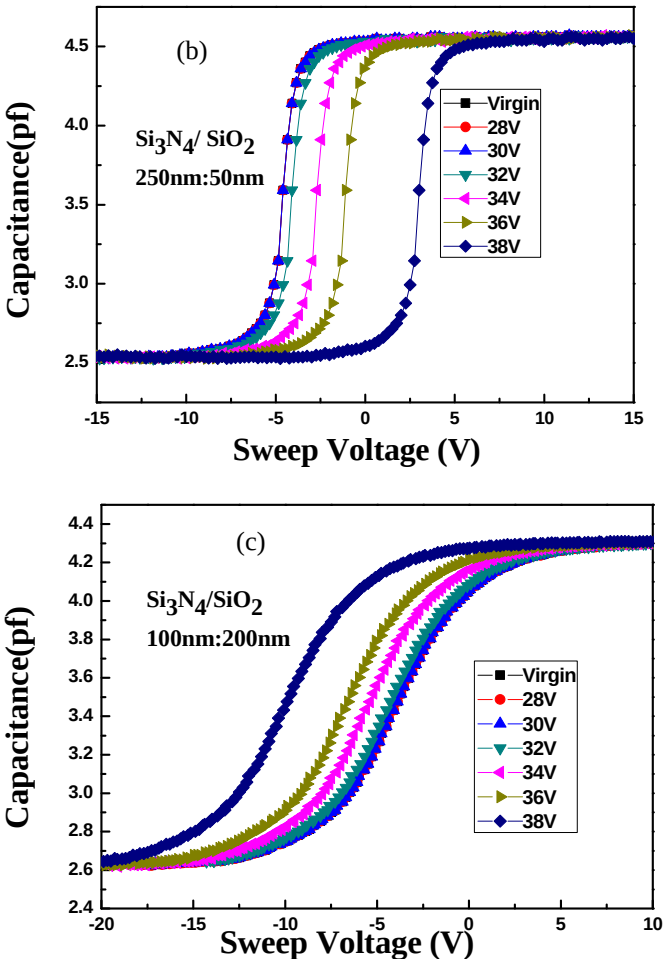

Fig. 2 *C-V* curves respectively measured on the three MIS devices before and after the charge injection: (a) MOS device, SiO_2=300nm, (b) thin-oxide MNOS device, Si_3N_4/SiO_2=250nm:50nm and (c) thin-oxide MNOS device, Si_3N_4/SiO_2=100nm:200nm. The applied DC voltages to metal electrode of MIS devices are −28, −30, 32, 34, 36 and 38 V, respectively.

In all our experiments, the dc bias is applied to the metal electrode of the MIS devices for one minute. After each positive DC bias, the C-V measurement was immediately performed. In fig 2(a)-2(c), the *C-V* curves were respectively measured from the three designated MIS devices before and after each DC voltage stress.

It can be seen two different charge injection behaviours by analysed the experiment results shown in Fig. 2. First, as shown in fig. 2(a), when a small positive voltage (say 28 and 30 V) is applied to the metal electrode of MOS device, no obvious V_{FB} shift can be found between the *C-V* curves measured before and after each dc bias stress, it indicates few charges accumulated in the dielectric of the MOS device. Similarly, when the same small positive voltage is applied to either thick-oxide MNOS device or thin-oxide MNOS device, as shown in fig. 2(b) and (c), the same results can be found in both devices as that in MOS device. On the contrary, when larger positive voltage (say 32 V or above) is applied, as shown in fig. 2(a)-(c), the obvious V_{FB} shifts indicate some charges were accumulated in the

dielectric of all the three devices. The above results can be explained as the following.

For a given dielectric layer, a critical electric field will exist, which determine whether the charge carriers tunnelling will take place. When the applied critical electric is lower than the critical electric field, no obvious charge tunnelling will happen. That's why almost no obvious V_{FB} shift can be found in all the three devices under small bias voltage such as 28 and 30V. Once the electric field is over the critical electric field, charge tunnelling probability depends exponentially on the equivalent thickness, the equivalent thickness will decrease as the applied voltage increase, obvious charge injection can be observed [7]. Therefore, obvious V_{FB} shifts were found at the applied voltages of 32, 34, 36 and 38V, respectively.

Second, when a larger positive voltage (say 32 or above) is applied to the metal electrode of MOS device, as shown in fig. 2(a), the *C-V* curve shifts to right side of the original one along the voltage axis, which indicates that net negative charges were accumulated in the silicon nitride film of MOS device. Similarly, when a larger positive voltage is applied to the metal electrode of thin-oxide MNOS, as shown in fig. 2(b), the same results can be found in the thin-oxide MNOS device as that in MOS device. For this case, the amount of net charges and their polarity is mainly attributed to the injection of charges with same polarity as the potential of the Si substrate.

However, different experiment result was found in thick-oxide MNOS device. When a larger positive voltage is applied, shown in fig. 2(c), the shift of *C-V* curves to the right side of the original one in the MOS and thin-oxide MNOS devices did not happen in the thick-oxide MNOS device, the *C-V* curve shift to left side of the original one in thick-oxide MNOS device. This result indicates net positive charges instead of negative charges were accumulated in the dielectric layer of the thick-oxide MNOS device. In this case, the amount of net charges and their polarity is mainly attributed to the injection of charges with same polarity as the potential of the Al electrode.

In fact, the mechanism governing the sign of net accumulated charge in the dielectric under a bias voltage stress is still not clear yet. According to the theory in Reference [8] and [9], if a large positive bias is applied to the metal electrode of MIS structure for an extended period, two aspects will contribute to the ΔV_{FB} shift, electrons are injected from the semiconductor and further to be captured by the traps in the dielectric, at the same time, holes injected from the gate to the dielectric, would also contribute to ΔV_{FB}. However, electron injection from the silicon substrate is dominant under positive bias stress, most of holes injected from the gate would be neutralized by electrons under positive bias stress, as a result, do not contribute to the ΔV_{FB} shift. Similarly, holes injection from the silicon substrate is dominant charge injection mechanism under negative bias stress.

The results in the MOS device show that electron injection from the silicon substrate is dominant under positive bias stress, which is therefore the evidence of the theory in Ref. 8 and 9. However, the opposite result in thick-oxide MNOS device shows holes injection from the metal electrode is dominant under positive bias stress. As we described in our previous work, charge injection process follows a modified Fowler–Nordheim tunnelling charge injection model, where the effective masses of the tunnelling carriers, injection barrier and the electric field in the dielectric for charge injection are the important parameters which will influence charging properties in the dielectric under high applied voltage. When a positive voltage is applied to the metal electrode of MOS device, as shown in fig.3, the potential barrier of silicon nitride for holes injection form Al electrode is higher than the electrons injection from silicon substrate, e.g., the barrier height for holes tunnelling at the Al/SiO_2 interface φ_h=2.4eV and barrier height for electrons tunnelling at the Si/Si_3N_4 interface φ_e=2.0eV [10]. Therefore, the net negative charges accumulated in MOS device is possibly attributed to the lower potential barrier of SiO_2 for electron injection than that for hole injection under positive bias stress.

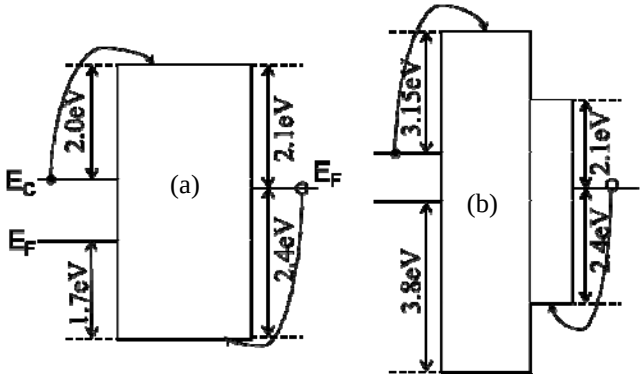

Fig. 3. Energy diagram of MIS device at zero bias voltage applied to the metal electrode of (a) MOS device, (b) thick-oxide MNOS device.

As the dielectric layer was changed from single to double, the potential barriers for electron injection from silicon substrate will be probably changed even under same bias voltage, for MNOS device, as shown in fig.3, the barrier height for holes tunnelling at the Al/Si_3N_4 interface φ_h=2.4eV while barrier height for electrons tunnelling at the Si/SiO_2 interface φ_e=3.15eV [10]. Furthermore, the electric field in silicon nitride and silicon oxide will be also changed due to the different dielectric constants of the two dielectric films. In the thick oxide double-layer dielectric structure, the large tunnelling barrier of the thick oxide layer act as an effective blocking layer to suppress electron injection from the silicon substrate, as a result, the net positive charges accumulated in thick-oxide MNOS device, which was different from that in MOS device.

However, the different charge injection result in thin-oxide MNOS device, where electron injection from the silicon substrate is dominant under positive bias voltage, which can be explained in terms of the changes of electric field and charge injection barriers. (1) As the thickness ratio of Si_3N_4

to SiO_2 changes, the electric fields both in silicon nitride and silicon oxide will also change, e.g., when the applied voltage and total thickness are fixed, the electric field in silicon nitride will increase with the thickness ratio of Si_3N_4 to SiO_2. (2) In addition, it is reported that the potential barrier of a given dielectric for charge carriers tunnelling will be influenced by the thickness [11] and composition of the dielectric [12], the potential barrier of thin silicon oxide for electron injection is possibly lower than the thick silicon oxide. Due to the lower potential barrier and electric field of thin silicon oxide, net negative charges were therefore accumulated in thin-oxide MNOS device under positive bias voltage.

To study the bias voltage dependence of charge injection, we plotted the flatband shift (ΔV_{fb}) as a function of the magnitude of bias stress, while the DC bias voltage is applied to the metal electrode. The measured results are shown in Figure 4.

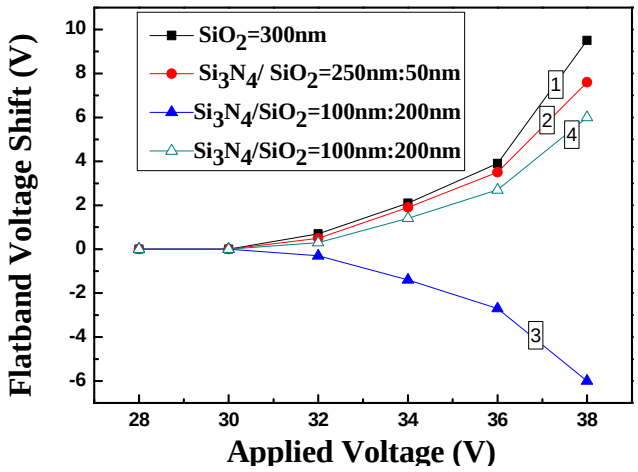

Fig. 4 Flatband voltage shift as applied voltage for three MIS devices (1 is the ΔV_{fb} of C-V curve measured from the MOS device, 2 is the ΔV_{fb} of C-V curve measured from the thin-oxide MNOS device, 3 is the ΔV_{fb} of C-V curve measured from the thick-oxide MNOS device, and 4 is the absolute value of ΔV_{fb} of C-V curve measured from the thick-oxide MNOS device).

It can be found that the flat band voltage shift increases as applied voltage increase, which indicates the total number of injected charges increases with applied voltage across the dielectric. These results confirm again that the charge injection depends nearly exponentially on the applied voltage for a given dielectric [7].

Furthermore, as shown in Fig. 4, for the MOS device, the V_{FB} shift to the right side away from the original one is about 0.7 V when 32 V is applied, and the V_{FB} shifts of 2.1, 3.9 and 9.5V are respectively measured when 34, 36 and 38 V are applied. For thin-oxide MNOS device, the corresponding V_{FB} shift equals 0.5, 1.9, 3.5 and 7.6V, respectively. In contrast, for the thick-oxide MNOS device, the corresponding V_{FB} shifts to the left side of the original one are -0.3, -1.4, -2.7 and -6.0 V. Clearly, less charge accumulation was found in the double dielectric layers because the shift of the C-V curves measured from the MNOS device is clearly smaller than that in MOS device at same bias voltage (32, 34, 36 and 38V).

IV. CONCLUSIONS

In double-layer dielectric stacks, when bias voltage is applied, some charge injection dependent parameters, e.g., the tunneling effective masses, injection barriers and the electric field across the dielectric, will be probably modified by varying the thickness ratio of Si_3N_4 to SiO_2. The changes of these parameters will definitely cause the change in the quantity of injected charges into the dielectric from both top and bottom interfaces. As a result, the charge injection behaviors in the dielectric would be influenced. Therefore, it is shown that charge accumulation levels in both the thick and thin oxide MNOS structures are lower than that in single layer. It is further shown that positive bias voltage at metal electrode would lead to net negative charge accumulation in the thin-oxide MNOS structure while net positive charge accumulation in the thick-oxide MNOS structure as the electron injection is suppressed by the thick oxide. The significant results confirm that the sign of charge accumulation in the dielectric could be controlled by varying the thickness ratio of double-layer dielectric stacks. This indicates that low charge accumulation can be achieved by using double-layer dielectric stacks to improve switch reliability.

ACKNOWLEDGMENT

This work was supported by China Scholarship Council.

REFERENCES

[1] J. J. Yao, “RF MEMS from a device perspective”, J. Micromech. Microeng. Vol.10, pp. R9, 2000.

[2] David Mardivirin, Stanis Courrèges, Aurelian Crunteanu, Arnaud Pothier, Pierre Blondy, Fabio Coccetti and Robert Plana, “Evidence of Successive Fowler-Nordheim and Frenkel-Poole Conductions in Si3N4 Based RF-MEMS Capacitive Switches”, Proceedings of the 40th European Microwave Conference, 28-30 September 2010, Paris, France.

[3] Gang Li, Haisheng San, and Xuyuan Chen, “Charging and discharging in ion implanted dielectric films used for capacitive radio frequency microelectromechanical systems switch” , J. Appl. Phys. 105 124503 (2009).

[4] C. L. Goldsmith, J. Ehmke, A. Malczewski, B. Pillans, S. Eshelman, Z. Yao, J. Brank and M. Eberly, “Lifetime characterization of capacitive RF MEMS switches”, IEEEMTT-S Int. Microwave Symp. Digest, pp. 227, 2001.

[5] W. Merlijn, van Spengen, R. Puers, Robert Mertens and Ingrid De Wolf, “A comprehensive model to predict the charging and reliability of capacitive RF MEMS switches”, J. Micromech. Microeng. Vol.14, pp.514-521, 2004.

[6] M. Exarchos, V. Theonas, P. Pons, G. J. Papaioannou, S. Melle, D. Dubuc, F. Cocetti, and R. Plana, “Investigation of charging mechanisms in Metal-Insulator-Metal structures”, Microelectronics Reliability. Vol.45, pp.1782-1785, 2005.

[7] Gang Li and Xuyuan Chen, "Modified Fowler-Nordheim tunnelling for modelling charge injection in Si3N4 of MIS structure ", submitted to Appl. Phys. Lett.

[8] K. Lehovec, C. H. Chen, and A. Fedotowsky, "MNOS charge versus centroid determination by staircase charging", IEEE Trans. Electron Devices. 25, 1030 (1978).

[9] Agarwal, A.K.; White, M.H., “New results on electron injection, hole injection, and trapping in MONOS nonvolatile memory devices”, IEEE Trans. Electron Devices. 32, 941 (1985).

[10] A.V. Vishnyakov, Yu.N. Novikov, V.A. Gritsenko, and K.A. Nasyrov, "The charge transport mechanism in silicon nitride: Multi-phonon trap ionization", Solid-State Electronics 53, 251 (2009).
[11] C Y Ng, T P Chen and C H Ang, "Dependence of barrier height and effective mass on nitrogen concentration at SiOxNy/Si interface and gate oxide thickness", Smart Mater. Struct.15, (39) 2006
[12] M. Vetter, "Surface passivation of silicon by rf magnetron-sputtered silicon nitride", Thin Solid Films 337, (118)1999.

TOWARDS IN-SITU TEM ANALYSIS OF PLD $Pb(Zr,Ti)O_3$ THIN FILM MEMBRANES

O. Sardan Sukas[1], J. W. Berenschot[1], M. J. de Boer[1], M.D. Nguyen[2], M. van Zalk[2] and L. Abelmann[1]

[1]*MESA+ Institute for Nanotechnology, University of Twente, Enschede, the Netherlands*
[2]*SolMateS BV. Enschede, the Netherlands*

***Abstract* — In this paper, a novel technique for fabricating Transmission Electron Microscopy (TEM) chips for investigating structural and piezoelectric properties of Pulse Laser Deposited (PLD) Lead Zirconium Titanate (PZT) thin films is presented. The method involves silicon-on-insulator (SOI) wafer technology together with deep reactive ion etching (DRIE) and highly selective etchants.**

This study is unique in the sense that it will facilitate in-situ characterization of the PLD PZT membranes during actuation. As well as PLD PZT, the proposed method can be applied to a variety of materials by proper selection of the etchants and tuning of the process parameters.

Being a critical step of the process sequence, the deposition profile of the PZT layer on the Lanthanum Nickel Oxide (LNO) seed layer is characterized prior to fabrication. The results reveal that the PLD process is not conformal and the thickness of the LNO/PZT layer is different on surfaces with different topographies.

***Keywords:* Lead Zirconium Titanate (PZT), Pulsed Laser Deposition (PLD), Transmission Electron Microscopy (TEM) Membrane, In-situ Analysis**

I - Introduction

Piezoelectric materials are used in a wide variety of applications in the field of microelectromechanical systems (MEMS) including sensors [1] and actuators for various purposes [2].

Lead zirconium titanate (PZT) is the most commonly used piezoelectric material due to its excellent ferroelectric and piezoelectric properties [3]. A number of different methods are used for PZT deposition [4-7]. Among these, pulsed laser deposition (PLD) is a promising technique since it enables deposition of PZT thin films with superior piezoelectric and ferroelectric properties [8, 9].

Characterization of the crystal structure becomes rather important at nano-scale since it has a great influence on the material properties. Although there are efforts for more advanced in-situ TEM experiments [10-12], the TEM studies carried out on PZT thin film membranes are mostly cross-sectional, for which preparation of the samples is rather demanding [13, 14].

In this paper, the method for fabricating TEM chips with a PLD PZT thin film membrane will be presented. The chips fabricated using this method will enable investigation of the PZT membranes from the top, through their thickness. Top view TEM has many more advantages than cross-sectional TEM, such as the possibility of determining the crystal size, revealing the diffraction patterns perpendicular to the plane and observing grain boundaries, crystal defects and such. Moreover, there is no need for modifying or damaging the structure to be investigated. Most importantly, the chips fabricated during this study will enable in-situ investigation of the membranes during actuation.

II – Design

A. Chip Design

The designed chips should be able to fit into a standard TEM holder, where the length of the diagonal should be smaller than ~3.05 mm. The chip geometry is selected to be a square with a side length of 2.1 mm, accordingly.

There exist 20 μm-wide rectangular grooves through the device layer, which define the chip boundaries. Matching grooves are also present at the backside until the half thickness of the carrier wafer, in order to ease the cleavage of individual chips.

Square membranes are located at the center of each TEM chip. Side lengths of these membranes vary in the range from 5 μm to 50 μm in order to investigate the effect of the size on different properties of the membranes, such as the internal stress.

Top and bottom electrodes as well as their contact pads are included in some designs in order to enable actuation of the membranes, even during TEM investigation, using a specially designed holder with electrical connections.

At the center of each individual chip, there is a 100 μm-diameter circular hole through the bottom of the wafer until the LNO bottom electrode.

B. Process Design

As well as the chip itself, the techniques to be used and the process parameters should be carefully designed in order to accomplish the fabrication of the TEM chips successfully.

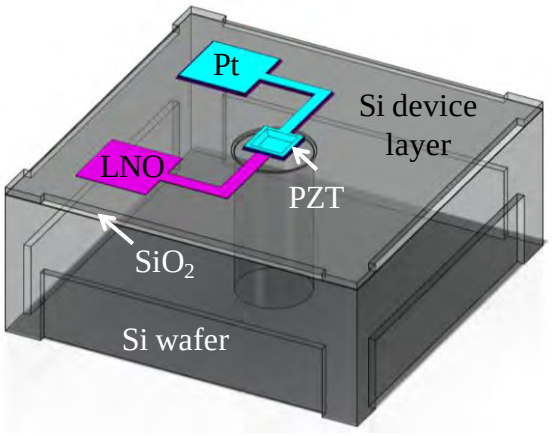

Figure 1*: Schematic illustration of the TEM chip.*

Initially, the carrier wafer should be selected considering the most critical process steps. Rather than a standard silicon wafer, an SOI wafer is used in this process. The main reason behind this is to take advantage of the buried oxide layer as an etch-stop during the through DRIE etching of the holes from the backside. Hence, the effect of any non-uniformity during this step is eliminated.

Moreover, by stopping at the buried oxide layer rather than the membrane itself, both this layer and the device layer will provide strength to the membrane. Hence, fracture of the thin film membranes due to the pressure difference during etching in a DRIE system with helium backside-cooling will be prevented.

One final advantage of the SOI wafer is that, any variation in the size of the membranes can be eliminated by defining their location by etching rectangular grooves into the silicon device layer from the top, prior to the deposition of the thin film membrane. However, the device layer should not be etched through to maintain the strength during the backside etch. Furthermore, the deposition profile of the PZT layer inside the grooves should be carefully investigated in order to account for any discontinuity of the thin film at the corners or possible short-circuits.

Selection of the top and the bottom electrodes are also rather important. A metal (e.g. platinum) top electrode can easily be realized through a straightforward lift-off process after deposition and patterning of the PZT layer. However, realization of the bottom electrode is more critical, having an influence over the properties of the grown PZT layer. Furthermore, it should be possible to pattern the PZT layer selectively from the bottom electrode. Considering the above issues, LNO is selected as the bottom electrode since it is electrically conducting, it serves an excellent seed layer for PZT deposition and it can be etched selectively from the PZT layer using an HCl-based solution [15].

As briefly mentioned above, the through etching of the holes from the backside is carried out using a DRIE system, which exerts a limitation on the size of the through-holes. For a more uniform etch profile, the diameter of the holes is selected to be equal to each other and 100 µm as stated in the previous section. Furthermore, the front side of the wafer should be properly protected during etching.

III- Fabrication

For the fabrication of the TEM chips, 4-inch SOI wafers with <100> orientation are used (Figure 2(a)). The thicknesses of the device and the silicon dioxide layers are 10 µm and 0.5 µm, respectively.

As a first step, 20 µm wide grooves defining the chip boundaries are etched by DRIE through the thickness of the device layer until the buried oxide layer is reached (Figure 2(b)). Following this step, the wafers are coated with a 100 nm-thick low-stress LPCVD silicon nitride layer, which is then patterned on the front side to serve as a mask for anisotropic wet etching of the device layer in a in a KOH solution at 75°C (Figure 2(c)).

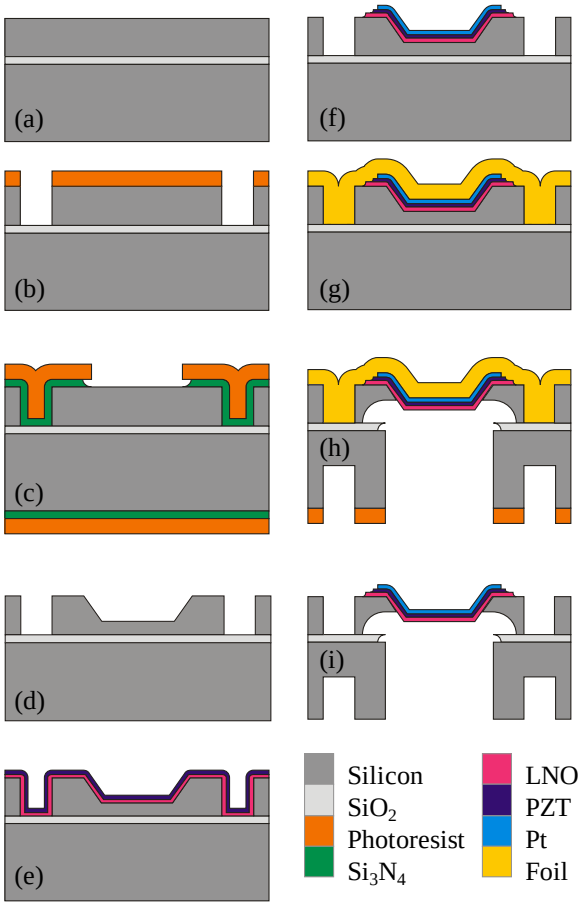

Figure 2*: Fabrication sequence for the TEM chips with PLD PZT membranes.*

The purpose of the anisotropic wet etch step is to define the position and size of the membrane windows (Figure 2(d)). Then, the nitride mask is removed in a phosphoric acid solution at 180 °C and a 20 nm/100 nm-thick LNO/PZT layer is deposited by PLD at 600 °C on the front side of the wafer [16] (Figure 2(e)).

After patterning the LNO bottom electrode) and the PZT layer using HCl- and BHF/HNO_3-based solutions, a 20 nm platinum top electrode is deposited and patterned by a lift-off process (Figure 2(f)).

As the processing of the front side is accomplished, it is coated with a protective foil (DuPont MX 5020) in order to prevent any damage on the PZT layer and the electrodes (Figure 2(g)). 100 µm diameter holes were etched through by DRIE of the carrier wafer [17], BHF (1:7) etching of the silicon oxide layer and isotropic plasma etching of the remaining device layer, respectively (Figure 2(h)). During the DRIE of the carrier wafer, the 20 µm-wide grooves, similar to those defining the chip boundaries are also etched in order to facilitate cleaving of the chips. As the holes are completely etched through the thickness of the carrier wafer, these grooves will be etched only until the half thickness due to the aspect ratio dependent etching (ARDE) effect [18]. Finally, the protective foil is removed (Figure 2(i)) and the chips are cleaved individually from the carrier wafer, glued and wire bonded to a specially designed TEM holder and investigated inside a TEM.

IV –Experimental Work

A. Introduction

In order to investigate the step coverage of the PLD PZT thin films on inclined surfaces and corners, 20 nm/100 nm LNO/PZT layers were deposited on (100) silicon wafers with KOH etched rectangular grooves and v-grooves (Figure 3). Note that, the silicon dioxide layer used as a mask during the etching of the rectangular grooves was not removed in order to investigate the quality of the PZT layer grown on this layer and understand the degree of step coverage during the PLD process.

B. X-ray Diffraction (XRD) Analysis

Results of the XRD analysis performed on the deposited layers reveal that the deposited film is a good quality PZT film, which is a mixture of (100) and (110) directions (Figure 4).

C. The Deposition Profile

High resolution scanning electron microscope (HR-SEM) images showing the cross-section of the samples reveal that the deposition not conformal and the PZT layer grow in a columnar fashion (Figure 4(a-d)). Thickness values for the layers deposited on different surfaces of the grooves are summarized in Table 1.

Comparison of the Surfaces: For both samples, thickness of the PZT layer on the side walls is roughly equal to the thickness of the top layer multiplied by the cosine of the angle between the two planes –(100) and (111)- as follows:

$$t_{Side} = t_{Top} \cdot \cos 54.7° \qquad (1)$$

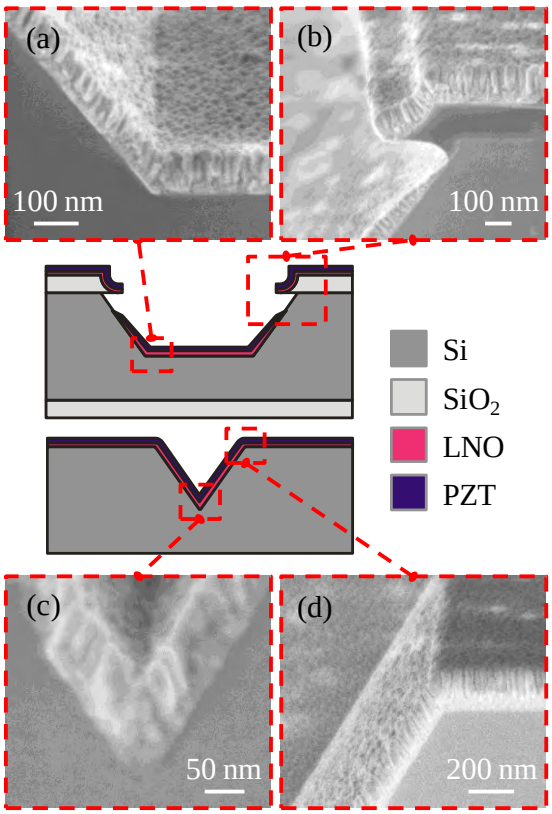

Figure 3: *Cross-section of the samples with (top) rectangular and (bottom) v-shaped grooves. Insets show HR-SEM images of the LNO/PZT layers on different surfaces of the grooves.*

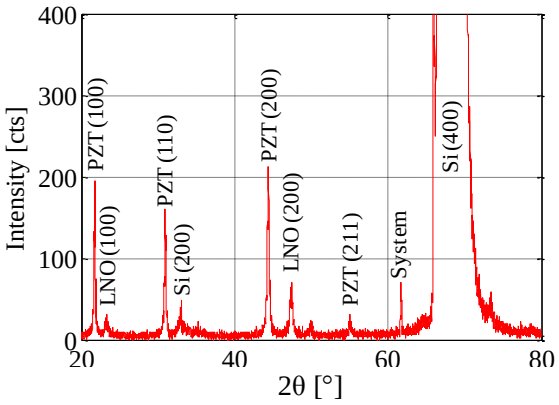

Figure 4*: XRD spectrum of the LNO/PZT thin film deposited on the (100) silicon surface.*

Table *1*: *Thickness of LNO & PZT layers on different surfaces of the grooves.*

	Rectangular grooves		V-grooves	
	LNO	PZT	LNO	PZT
t_{Top} [nm]	30.9	99.3	70.3	108.9
t_{Side} [nm]	20.7	57.1	42.2	63.2
t_{Bottom} [nm]	26.4	79.2	-	-
t_{Tip} [nm]	-	-	40.3	81.5

The relation given in (1) indicates that the film density on the sidewall is identical to that on the top.

Although expected to be the same, the thickness of the PZT layer on the bottom surface of the rectangular grooves is 20% less than those at the top surface. The reason for this may be that, the amount of material entering the groove and reaching the bottom surface is less since part of the target flux is blocked by the sidewalls. This should be further investigated by checking if there is a thickness gradient along the sidewalls.

Comparison of the Corners: The PZT layer is continuous at the bottom corners of the rectangular grooves, as well as the tip of the v-grooves (Figure 3 (a&c)). The ratio t_{Top}/t_{Tip} for a v-groove is similar to the ratio t_{Top}/t_{Bottom} for a rectangular groove.

The PZT layer is also continuous at the top corners of the v-grooves (Figure 3(d)). However, there is a discontinuity between the layers on the top and the sidewalls of the sample with the rectangular grooves as a result of the shadowing due the overhanging silicon dioxide layer (Figure 3(b)). Rather than having a sharp ending exactly under the silicon dioxide edge, the thickness of the PZT layer slowly decreases and finally approaches to zero towards the middle of the overhanging part.

D. The Growth Direction

Comparison of the Surfaces: PZT columns grow along the normal direction of the top and bottom surfaces, which have (100) orientation (Figure 5). However, the directions of the PZT columns on the sidewalls having (111) orientation vary from the <111> direction by an angle, α. This angle varies between 20-35° for individual columns.

Comparison of the Corners: PZT columns grow randomly along a direction between the normal direction of the intersecting surfaces, both at the top and the bottom corners.

V - Conclusion

A novel method for fabricating TEM chips for investigation of PLD PZT thin film membranes is presented. The proposed method enables in-situ characterization of thin film membranes of different materials inside a TEM.

TEM chips are designed considering the space requirements of a TEM and enabling characterization of different properties of the thin films. Furthermore the fabrication sequence is designed carefully in order to eliminate any size variation, non-uniformity or damaging of the membranes.

Having a critical importance for the final experiments, the deposition profile of the PZT layer on the LNO seed layer was investigated prior to fabrication. The results seem promising since the deposited layer is continuous both at the sidewalls and the corners and the thickness is well-controlled. However, the deposition is not conformal, the thickness of the layers on different topographies is varying and discontinuities occur at the shadowed regions.

Acknowledgements

The LNO/PZT layers are supplied by SolMateS BV, Enschede, the Netherlands. The authors would like to thank M. A. Smithers for the HR-SEM images.

This project is supported by the Smart Mix Program (Smart Pie) of the Netherlands Ministry of Economic Affairs and the Netherlands Ministry of Education, Culture and Science.

D

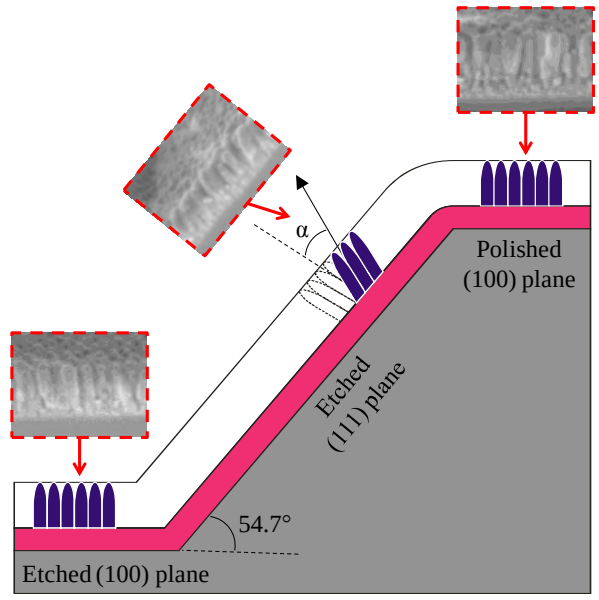

Figure 5*: Growth direction of the PZT columns on different surfaces of the grooves.*

References

[1] K. Yamashita, H. Katata, M. Okuyama, H. Miyoshi, G. Kato, S. Aoyagi, and Y. Suzuki, *Sensors and Actuators A: Physical*, vol. 97, pp. 302-307, 2002.

[2] H. Kueppers, T. Leuerer, U. Schnakenberg, W. Mokwa, M. Hoffmann, T. Schneller, U. Boettger, and R. Waser, *Sensors and Actuators A: Physical*, vol. 97, pp. 680-684, 2002.

[3] B. P. Zhu, D. W. Wu, Q. F. Zhou, J. Shi, and K. K. Shung, *Applied Physics Letters*, vol. 93, pp. 012905-012905-3, 2008.

[4] V. N. Hung, L. V. Minh, B. T. Huyen, and N. D. Minh, in *Journal of Physics: Conference Series*, 2009, p. 012063.

[5] T. J. Zhu, L. Lu, and M. O. Lai, *Applied Physics A: Materials Science & Processing*, vol. 81, pp. 701-714, 2005.

[6] T. Hata, S. Kawagoe, W. Zhang, K. Sasaki, and Y. Yoshioka, *Vacuum*, vol. 51, pp. 665-671, 1998.

[7] E. Tokumitsu, S. Ueno, R. I. Nakamura, and H. Ishiwara, *Integrated Ferroelectrics*, vol. 7, pp. 215-223, 1995.

[8] D. Akai, M. Yokawa, K. Hirabayashi, K. Matsushita, K. Sawada, and M. Ishida, *Applied Physics Letters*, vol. 86, p. 202906, 2005.

[9] M. D. Nguyen, H. Nazeer, K. Karakaya, S. V. Pham, R. Steenwelle, M. Dekkers, L. Abelmann, D. H. A. Blank, and G. Rijnders, *Journal of Micromechanics and Microengineering*, vol. 20, p. 085022, 2010.

[10] A. Lei, D. H. Petersen, T. J. Booth, L. V. Homann, C. Kallesoe, O. S. Sukas, Y. Gyrsting, K. Molhave, and P. Boggild, *Nanotechnology*, vol. 21, p. 405304, 2010.

[11] J. F. Creemer, F. Santagata, B. Morana, L. Mele, T. Alan, E. Iervolino, G. Pandraud, and P. M. Sarro, in *MEMS 2011*, Cancun, Mexico, 2011, pp. 1103-1106.

[12] B. Morana, F. Santagata, L. Mele, M. Mihailovic, G. Pandraud, J. F. Creemer, and P. M. Sarro, in *MEMS 2011*, Cancun, Mexico, 2011, pp. 380-383.

[13] D. Kaewchinda, T. Chairaungsri, M. Naksata, S. J. Milne, and R. Brydson, *Journal of the European Ceramic Society*, vol. 20, pp. 1277-1288, 2000.

[14] Y. Liu, R. Wang, X. Guo, and J. Dai, *Materials characterization*, vol. 58, pp. 666-669, 2007.

[15] T. Kobayashi, M. Ichiki, R. Kondou, K. Nakamura, and R. Maeda, *Journal of Micromechanics and Microengineering*, vol. 18, p. 035007, 2008.

[16] M. D. Nguyen, J. M. Dekkers, and G. Rijnders, in *EUROSENSORS XXII*, Dresden, Germany, 2008, pp. 810-813.

[17] H. V. Jansen, M. J. Boer, S. Unnikrishnan, M. C. Louwerse, and M. C. Elwenspoek, *Journal of Micromechanics and Microengineering*, vol. 19, p. 033001, 2009.

[18] H. Jansen, M. de Boer, and M. Elwenspoek, 1996, pp. 250-257.

DESIGN OF NONLINEAR SPRINGS FOR MEMS VIBRATION ENERGY HARVESTING APPLICATIONS

Ngoc-Han T Tran, Son D Nguyen, Einar Halvorsen

Department of Micro and Nano Systems Technology, Vestfold University College, Norway

***Abstract* —This paper investigates a method for designing nonlinear springs for MEMS electrostatic energy harvesters. The method to determine the geometry of the springs is illustrated in detail. The performance of the nonlinear harvester is then analyzed with both narrow and broad band excitations. The results show that a higher output power and a substantially enlarged bandwidth are obtained by using a proper choice of nonlinear spring.**

***Keywords :* MEMS, Energy Harvesting, Nonlinear springs, Wide-bandwidth**

I – Introduction

Vibration-based micro energy harvesters basically consist of a spring-mass-damper system. The maximum power is achieved if the resonant frequency of the transducer matches the frequency of the ambient vibration. Any mismatch will lead to a significant decrease in the scavenged power. This limitation of resonant vibration harvesters restricts their capability in real applications because environmental vibration spectra exhibit a range of frequency [1]. There are many proposed solutions to overcome this limitation such as tuning of the resonant frequency or widening the bandwidth of the harvester [2]. Nonlinear springs have been exploited as a promising solution to extend the bandwidth of the energy harvester. Ramlan *et al* [3, 4] investigated two non-linear mechanisms for energy harvesting: a nonlinear bistable spring that can enhance power and a specific type of hardening springs that broadens the frequency response in one direction. Spreemann *et al* [5] introduced a magnetic spring instead of conventional one to produce a nonlinear restoring force. Burrow *et al* [6] presented a nonlinear energy harvester with a nonlinearity generated by the addition of magnetic reluctance forces. These devices were all piezoelectric or electromagnetic.

For electrostatic vibration energy harvesters, Tvedt *et al* [7] demonstrated by experiments that a considerable bandwidth was obtained for a device with nonlinear mechanical suspension and argued that design of nonlinear springs are particularly suited for electrostatic harvesters fabricated with high aspect ratio micromachining. This was further supported by numerical investigations [8] and one type of nonlinear-spring-based energy harvester was successfully fabricated and characterized by Nguyen *et. al* [9]. A difficulty with this approach was the lack of a systematic approach to the spring design that made necessary several finite element method (FEM) assisted design iterations.

In this paper, we present a systematic way to design nonlinear springs with similar characteristics to that in [9]. The method is based on previous methods to generate bistable mechanisms [10] and allows varying the spring characteristics from linear to bistable behavior.

II – Spring Design and Modeling

This work considers the electrostatic energy harvesters having two asymmetric overlap varying transducers. Figure 1 shows the schematic model including mechanical and electrical parts. The mechanical part consists of an inertial mass *m*, mechanical damping *b*, and the spring suspension while the electrical part includes out-of-phase variable capacitors C_1 and C_2, load resistors R_{L1} and R_{L2}, parasitic capacitances C_p and C_{pL}, and a bias V_e.

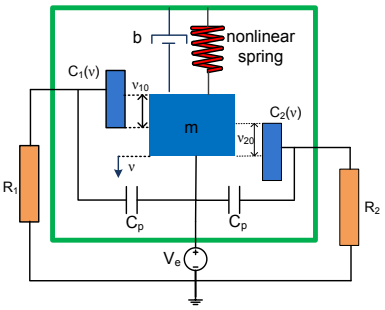

Figure 1: *Schematic model of energy harvester including mechanical and electrical parts*

The nonlinear springs are constructed by choosing a shape in the stress-free state that corresponds to the deformed shape of an initially straight and uniform beam. To find the unstressed shape of the nonlinear spring, a straight spring is clamped at one end and the other end is guided as shown in Figure 2. The constraints are no rotation and no horizontal movement at the tip.

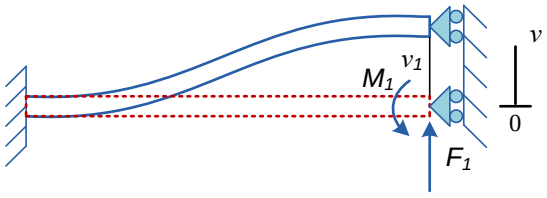

Figure 2: *Deformed spring from a linear one*

For a given initial displacement v_1, the vertical displacement v at the position x is given, as a first approximation, by Euler-Bernoulli theory as

$$v = \frac{v_1}{L^2} x^2 \left(3 - \frac{2x}{L} \right) \qquad (1)$$

where L is the length. This shape is chosen as the unstressed shape of the nonlinear spring.

III – Simulations

A. *Linear stiffness constraint*

Figure 3 shows the step by step procedure to create the layout for nonlinear springs. It is also the flow chart for calculating the stiffness of the springs.

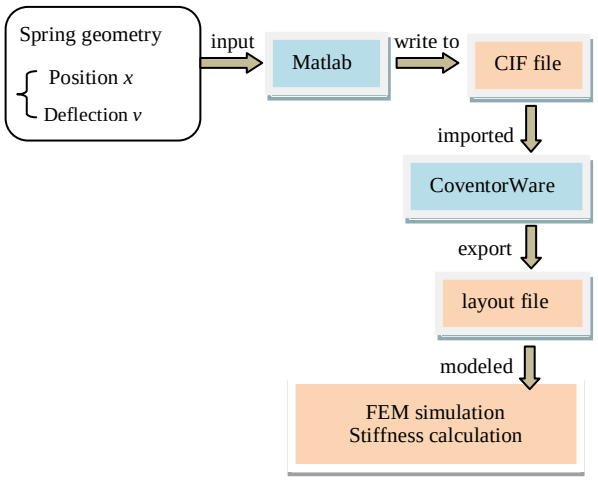

Figure 3: *Flow chart of generating the layout and for calculating the stiffness of the nonlinear springs*

A set of the coordinates (x,v) for the beam axis is calculated from (1) and written into a Caltech Intermediate Format (CIF) file using Matlab. Then this file is imported into CoventorWare to build the mask. From here FEM calculations may proceed to calculate the stiffness.

By varying the vertical displacement v_1, we can generate a set of spring shapes. For a given beam cross section and length, the procedure results in different linear stiffness values for the different springs. With very different stiffness values, the devices would work in very different frequency ranges. Normally one would design for a certain frequency range and in any case, it is reasonable to compare devices working at least approximately in the same frequency range. We therefore need to constrain the linear stiffness. This can be accomplished by varying the length L together with v_1.

Using the method of [10], we can find the relation between L, v_1 and with the vertically applied force F for the curved beam. The assumption for the approximation is that the angle Θ_0 made by the tangent to the initially deformed spring with the horizontal axis at the center of the spring is small.

The vertical displacement is given by

$$\hat{\Delta}_v \approx \hat{H} - \frac{2}{3}\hat{L}_S{}^2\theta_0 - \frac{8}{45}\hat{L}_S{}^7\theta_0{}^3 \qquad (2)$$

where $\hat{H} = \frac{v_1}{L}$, $\hat{L}_S \approx \frac{1}{2}\left(1+\sqrt{1+\frac{12}{5}\hat{H}^2}\right)$

and θ_0 is the angle at the center after the force F is applied to the spring. It is given by

$$\theta_0{}^3 + \alpha\theta_0 + \beta = 0 \qquad (3)$$

The coefficients α and β are calculated from (4) and (5)

$$\alpha = \frac{15}{4}\frac{-10\hat{r}^2 + \hat{L}_S{}^2 - \hat{L}_S}{\hat{L}_S{}^5\left(\hat{L}_S - 2\right)} \qquad (4)$$

$$\beta = \frac{65}{16}\frac{\left(12\hat{H} + \hat{P}_v\pi^2\hat{L}_S{}^3\right)\hat{r}^2}{\hat{L}_S{}^8\left(\hat{L}_S - 2\right)} \qquad (5)$$

where $\hat{P}_v = F / P_E$, and $P_E = \pi^2 EI / L^2$

For a given linear stiffness and for a given initial displacement, the length of the spring can be calculated from (2).

Our work investigates four different springs having four different initial displacements (10, 20, 32 and 50µm). Other parameters are the same as in [9] such as the spring height of 15µm and the width of 300µm. We chose the linear stiffness k_{linear} = 485N/m as the nominal linear stiffness for all. Thus, the lengths of the four springs are correspondingly estimated.

There is a certain mismatch between the analytical approximation of the linear stiffness and a FEM calculation for the same spring. Therefore an adjustment in length and recalculation in FEM is necessary until a sufficiently small deviation from the desired stiffness is reached. The final results are shown in Table 1

Table 1 *Spring lengths after numerical calculation and their corresponding linear stiffness values output from FEM*

Spring name	**10**	**20**	**32**	**50**
Length (µm)	832	1080	1380	1725
Linear stiffness (N/m)	496	474	472	511
Stiffness deviation (%)	2.27	2.27	2.28	5.36
Undamped resonant frequency (Hz)	597	583	582	605

Figure 4 shows the force as a function of displacement obtained in FEM calculation for the four springs. The linear spring stiffness is also plotted to compare.

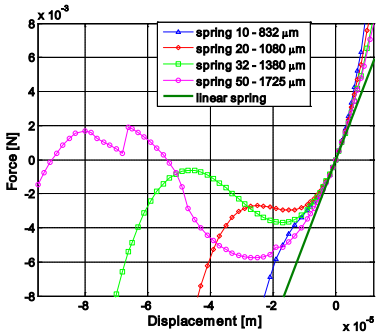

Figure 4: *Force versus displacement for four springs with different initial displacements and lengths*

When the displacement has positive values, all the springs have a larger force than the linear spring, i.e. become stiffening. As we see the smaller initial-displacement and the shorter a spring is, the stiffer it is for positive displacements. For instance, spring 10 is the stiffest compared to others. Otherwise, if the displacements are negative, all of them become softer than the linear case and each has a different response to the force. This dissimilarity between two sides constitutes the asymmetric characteristic of the springs: one side of

the spring is stiffening and the other softening. For the highest initial displacement (spring 50), bistable behavior can be observed. The other varieties are nonlinear but do not show bistability.

B. *Equivalent circuit model*

Electrostatic energy harvesting is made possible by the coupling between the mechanical and the electrical domains as described by the following equations

$$m\ddot{v} + b\dot{v} + F_r + F_e = ma \tag{6}$$

$$V_{L1/L2} = \frac{q_{1/2}}{C^T_{1/2}(v)} + V_e \tag{7}$$

where m, $\dot{v}$ and $\ddot{v}$ are respectively the proof mass, its velocity and its acceleration. F_e is the electrostatic force and F_r is the spring force obtained from FEM and can be fitted to a polynomial form

$$F_r = \sum_{i=1}^{7} k_i v^i \quad . \tag{8}$$

The parameters listed in Table 2 are based on the structures fabricated and characterized in [9]. In the following we compare simulation results for harvesters sharing these parameters but differing in the nonlinear spring force (8). In the case of spring 50 under high acceleration, the proof mass vibrates out of the overlap. To avoid this, the initial finger overlap of spring 50 was increased to 50µm for transducer 1 and 140µm for transducer 2.

Table 2: *Parameters used for simulations*

Parameters	Value
Proof mass, m	35.25 mg
Mechanical damping, b	2.53x10^{-4} Ns/m
Bias voltage, V_e	28.4 V
Parasitic capacitance of transducer 1, 2 $C_{1p/2p}$	3.17 pF
Number of capacitor fingers on each transducer, N_g	128
Gap between fingers, g_0	15 µm
Structure thickness, t_f	300µm
Initial finger overlap of transducer 1, v_{10}	50 µm (spring50) 35 µm (the rest)
Initial finger overlap of transducer 2, v_{20}	140 µm (spring50) 100 µm (the rest)

IV - Results and Discussion

A. *Sinusoidal excitation*

Linearly increasing frequency sweeps (up-sweeps) and linearly decreasing frequency sweeps (down-sweeps) with the sweep rate 2.667Hz/s are simulated. Figure 5 shows the peak-peak output voltage of transducer 2 at various excitation amplitudes 0.062, 0.088, 0.110 and 0.135g. The output power is evaluated at optimal load resistances.

For frequency up-sweeps, the responses of the four springs and the compared one in [9] are almost the same. For down-sweeps, spring 20 and 32 always give higher peak output voltage and bandwidth at a low acceleration 0.062g. For further increasing acceleration, spring 32 and 50 are more pronounced in giving higher output power and bandwidth response, compared with the others.

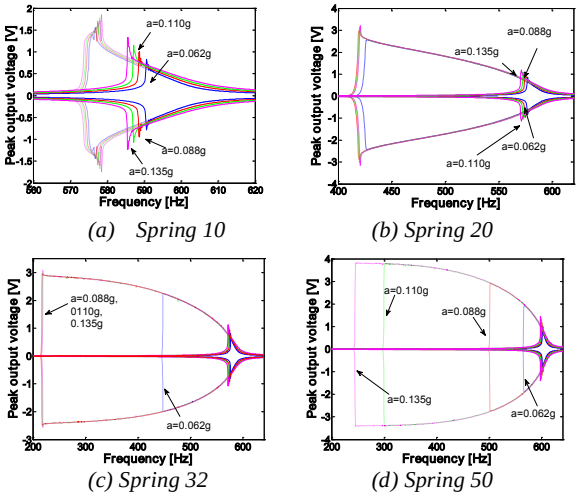

(a) Spring 10 (b) Spring 20

(c) Spring 32 (d) Spring 50

Figure 5: *Peak-peak output voltage on transducer 2 as a function of frequency for up-sweeps (solid curves) and down-sweeps (dotted curves) at levels of excitation 0.062, 0.088, 0.110 and 0.135g*

In Figure 6, traces for all devices are shown for the same acceleration amplitude in order to compare the output bandwidth and voltage. The bandwidth for spring 32 and 50 are approximately equal, but the output voltage of spring 50 is larger. The output bandwidth and voltage of the spring 20 are both smaller than those of springs 32 and 50. Spring 10 doesn't show any advantage in this comparison.

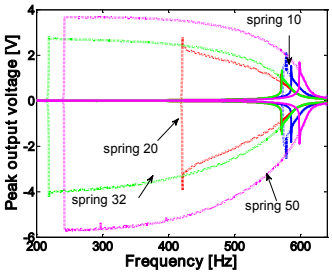

Figure 6: *Peak output voltage versus frequency at acceleration of 0.135g*

B. *Broadband excitations*

Taking the load optimized by simulations, the average output power is investigated over a range of acceleration power spectral densities (PSDs) as shown in Figure 7. The linear spring is also simulated for comparison. This linear spring is assumed to be built in a symmetric structure that has the same initial overlapping in both transducers. The average output power is obtained from four random input signal files for five springs.

The output power increases with increasing acceleration, but at different rates with different springs. Consider the average output power at excitation levels of 7.0x10^{-4} and 8.0x10^{-4} g^2/Hz for all springs in Table 3. Compared to the linear spring, all three springs 20, 32 and 50 can enhance output power. Spring 32 is the best, 1.34 times in case of 7.0x10^{-4} g^2/Hz more than the linear spring, and 1.29 times in case of 8.0x10^{-4} g^2/Hz.

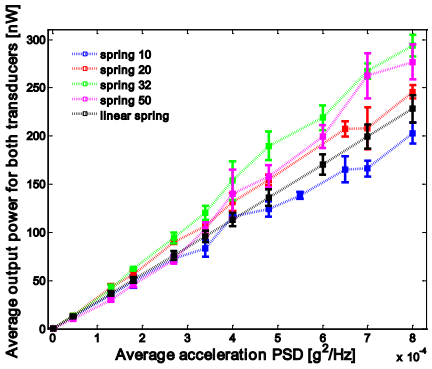

Figure 7: *Average output power as a function of average acceleration PSD using optimal load at 4.8x10^{-4}g^2/Hz*

Table 3: *Average output power of all springs at 7.0x10^{-4} and 8.0x10^{-4} g^2/Hz using optimal load at 4.8x10^{-4}g^2/Hz*

	Average output power (nW)				
Excitation level (g^2/Hz)	Spring 10	Spring 20	Spring 32	Spring 50	*Linear* Spring
7.0x10^{-4}	166.3	207.88	267.43	262.66	*199.35*
8.0x10^{-4}	203.08	246.00	293.95	276.85	228.26

Figure 8 shows the output PSDs for four springs at various excitation levels. The excitation level is selected from low to high to investigate the bandwidth of the harvester from the linear regime and to the nonlinear regime.

At a very small acceleration (1.5x10^{-6} g^2/Hz), the spectra are very narrow for all four springs since the harvester works in the linear spring regime. Their peaks are roughly at the undamped resonant frequency (approximately 590Hz). For increasing excitation levels, the widening bandwidth of spring 20 and 32 occurs rapidly. For further increases, the bandwidths of all cases are increased. Spring 20, 32 and 50 tend to expand bandwidth toward lower frequency from the undamped resonant frequency. Spring 10 has also that widening but at rather small acceleration (4.6x10^{-5} g^2/Hz). Then, it broadens toward higher frequency at higher excitation levels. Then it behaves as a hardening spring.

The 3dB-bandwidth of the harvester for the four nonlinear springs is depicted in Figure 9. As discussed, spring 20 gives a high PSD over a range of large frequencies so that it apparently has a huge bandwidth. The results do not confirm this expectation. The reason is that when increasing the acceleration, the highest peak increase simultaneously with the broadening of the flat portion of the spectrum. The bandwidth calculations may capture the peak. The largest variation in bandwidth is seen for spring 32 and 50. The reason is similar to the spring 20 case. The bandwidth of spring 10 is continuously increasing with increasing acceleration.

V – Conclusion

We have introduced a systematic way to create a nonlinear spring for energy harvesters. With the new design, both output voltage and bandwidth can be enhanced under both narrow and broadband excitations. Considerable power and bandwidth improvement over the linear case can be obtained.

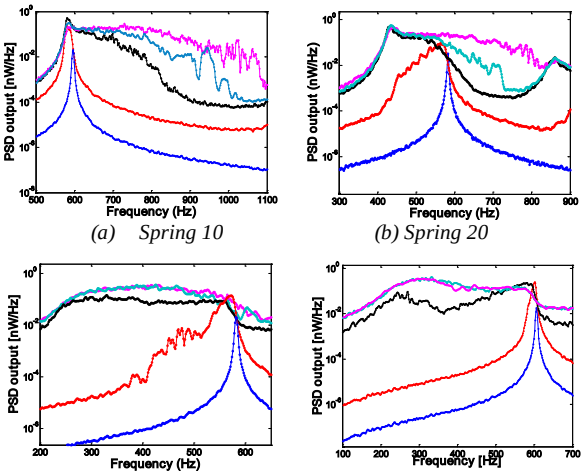

(a) Spring 10 *(b) Spring 20*

(c) Spring 32 *(d) Spring 50*

Figure 8: *PSD output as a function of frequency at excitation of 1.5x10^{-6}, 4.6x10^{-5}, 3.4x10^{-4}, 7.0x10^{-4} and 8.0x10^{-4} g^2/Hz (from inner to outer)*

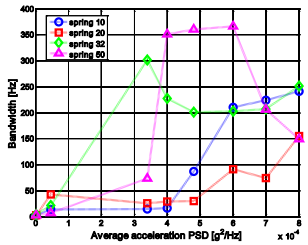

Figure 9: *3dB-bandwidth versus average acceleration PSD for all springs*

Acknowledgment

The author would like to thank Cuong Phu Le for his useful suggestions and discussions.

References

[1] E. K. Reilly, L. M. Miller, R. Fain, and P. Wright, *Technical Digest PowerMEMS*, Washington DC, USA, pp. 312-315, Dec. 1-4, 2009.

[2] D. Zhu, M. J. Tudor, S. P. Beeby, *Measurement Science and Technology*, vol. Volume 21, pp. 022001, Jan. 1, 2010.

[3] R. Ramlan, *et al.*, *Nonlinear Dynamics*, vol. 59, pp. 545-558, 2010.

[4] R. Ramlan, PhD thesis, Uni. of Southampton, 2009.

[5] D. Spreemann, B. Folkmer, Y. Manoli, *Eurosensors XX*, Göteborg, pp. 17-20, Sep. 2006

[6] S. G. Burrow, Clare, L.R, *Electric Machines & Drives Conference*, Antalya, pp. 715 - 720, May 3-5, 2007.

[7] L. G. W. Tvedt, D. S. Nguyen, E. Halvorsen., *Journal of Microelectromechanical Systems*, vol. 19, p. 305, 2010.

[8] D. S. Nguyen, E. Halvorsen, *PowerMEMS*, Leuven, Belgium, pp. 331-334, Nov 30 – Dec 3, 2010.

[9] D. S. Nguyen, E. Halvorsen, G. U. Jensen and A. Vogl, *Journal of Micromechanics and Microengineering*, vol. 20, pp. 125009, Nov. 2010.

[10] S. Krylov and Y. Bernstein, *Sensors and Actuators A: Physical*, vol. 130-131, pp. 497-512, 2006.

DESIGN AND REALISATION MICROFLUIDIC STOCHASTIC MIXERS INTEGRABLE IN BIOANALYTICAL SYSTEMS

Z. Fekete[1,2], E. G. Holczer[1,2], E. Tóth[3], K. Iván[3], P. Fürjes[1]

[1]*Research Institute for Technical Physics and Materials Science - MFA, H-1525 Budapest P.O. Box 49, Hungary*
[2]*Budapest University of Technology and Economics, H-1111 Budapest, Műegyetem rkp. 3., Hungary*
[3]*Pázmány Péter Catholic University, H-1083 Budapest, Práter str. 50/a, Hungary*

***Abstract* — The present work is intended to describe the design aspects of microfluidic structures applicable to dilute and transport analyte solutions to the sensing areas of biosensors. The behaviour of different chaotic mixer structures were analysed by numerical modeling and experimentally to determine their efficiency. The characterized microstructures were realised by micro-fabrication in polydimethilsiloxane and integrated into real microfluidic transport systems and biological analyte was applied to verify their practical performance.**

The final goal of this work is to design, develop and realize reliable and robust microfluidic systems which are applicable for cost-effective sample transport and still containing some simple sample preparation functions, such as mixing or dilution to ensure homogeneous concentration distribution of the species along the fluidic channels.

***Keywords:* stochastic mixing, microfluidics, bioanalytical systems, modeling, PDMS, SU-8**

I - Introduction

The manipulation of fluids (e.g., biological samples) in analytical systems is a key issue in terms of the final applicability of these devices. In novel analytical microsystems the sample manipulation is executed by complex micro-fluidic structures, which can perform the main sample preparation tasks such as mixing, dilution, transportation, and separation; all of these complex tasks are realized in a single integrated structure. The miniaturization effort enables, for example, the acceleration of low-cost clinical tests by largely decreasing sample amount needed for a single test and realizing High-Throughput (HT), quick and cost effective analytical systems. Complex fluidic devices integrating active and passive micro-systems, as well as combining silicon micromechanics and polymer technology can be applied for fast, low cost and intelligent sample control at the microscopic scale.

Important function of the fluidic structure is the dilution and complete mixing of the biological sample with an adequate buffer solution. Without complete mixing and dissolution the reproducibility of the measurements can be insecure due to the inhomogeneous concentration distribution of the species along the fluidic channels. Therefore, great care has to be taken when choosing the channel length and the mixing efficiency per unit length. Finite Element Modeling was applied to find an optimum structure which gives proper mixing in a reasonable time.

The mixing is a gradient driven transport process decreasing the inhomogenity of particle distribution, temperature and phases. Several possible mixing strategies can be found in macroscale as molecular diffusion, turbulent diffusion, advection and Taylor-dispersion. Turbulent flow can not be built up in microscale due to the dominant viscosity, so the mixing possibilities are limited in this case. [1, 2] Due to the small dimensions of the microfluidic systems usually the flows are laminar and the component streams mix only by diffusion, creating a dynamic diffusive interface with predictable geometry. Advection could be generated by the fluid flow, resulting in a chaotic distribution of the molecules. The Taylor-dispersion is an advection generated by the gradient of the molecular velocity. The chaotic advection could be and ideal mixing method in the case of the microfluidics considering stable and laminar flow also.

II – Experimental

Three different mixer structures were characterized and realised by polymer micromachining technology as presented in Figure 1. The staggered blocks realised in the T-mixer (b) can generate vortexes with higher Reynolds number which run through the laminar stream distribution inducing transversal flow in the fluidic channel. The Herring-Bone type chaotic mixer structure (c) was also analysed. For reference a simple T-mixer structure (a) was implemented.

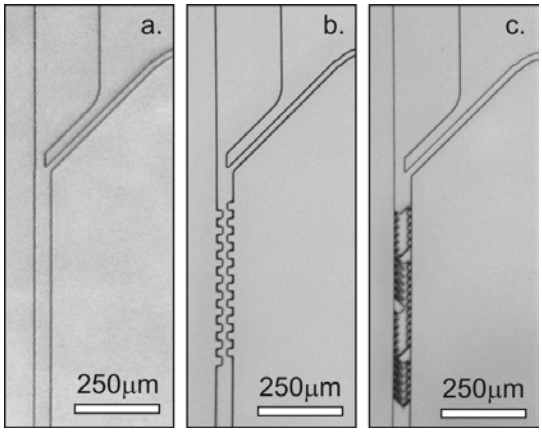

Figure 1: *The realised mixer structures: T-mixer (a), T-mixer staggered blocks (b) and Herring-Bone type (c) chaotic mixers.*

The critical parts of the transport microfluidics were analysed by Finite Element Modeling to characterize their properties and behaviour. The COMSOL Multiphysics code was applied to simulate the different microfluidic structures by numerically solving the Navier-Stokes and diffusion equations. To describe the efficiency of a mixer structure the concentration distribution evolved at the outlet of the channel system was compared to the ideal mixing situation. For the calculations the parameters of the 0,1mM/mL human serum albumin solution and 1μL/min flow rate were applied as initial boundary conditions (for each model). The modeled concentration distributions evolved in the Herring-Bone type mixer (b) and the reference T-mixer (a) are schematically presented in Figure 2.

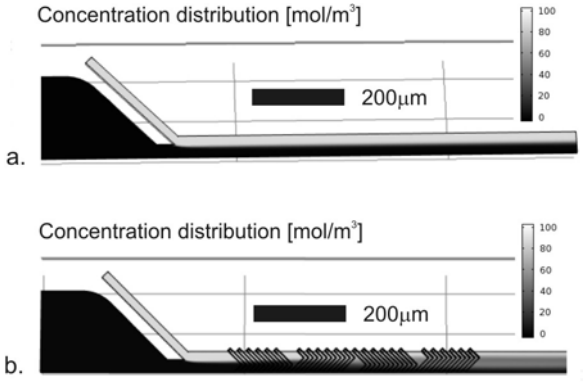

Figure 2: *Modeled concentration distribution evolved at the center surface of the reference T-mixer (a) and the Herring-Bone type mixer (b).*

Among the polymer materials one of the most attractive candidates to realize simple micro-fluidic systems is polydimethylsilixane (PDMS) is also well suited for mass production, since it can be replicated from photoresist microstructures serving as replication masters [3].

The PDMS is a silicon based organic polymer: $(H_3C)_3[Si(CH_3)_2O]_nSi(CH_3)_3$ which is absolutely feasible to form microfluidic structures in bioanalytical applications due to its reliable geometric transfer, flexibility, transparency, biocompatibility and price. It could support both the large scale production and fast prototyping. PDMS has absolutely simple formation method by moulding, polymerizing on a pre-structured moulding form and peeling from.

To create microfluidic structures in PDMS the SU-8 epoxy based negative photoresist was applied as moulding replica developed by a special multilayer technology. The fluidic channels with the reservoirs and the fluidic inlets and Herring-Bone mixer structure were formed by different SU-8 layers as Figure 3 presents. The channel width was chosen to 50 μm, the depth was determined by the SU-8 technology (according to the 20 μm layer thickness of the SU-8 2015 photoresist). The sealing of the channel structure was solved by low temperature bonding after oxygen plasma treatment.

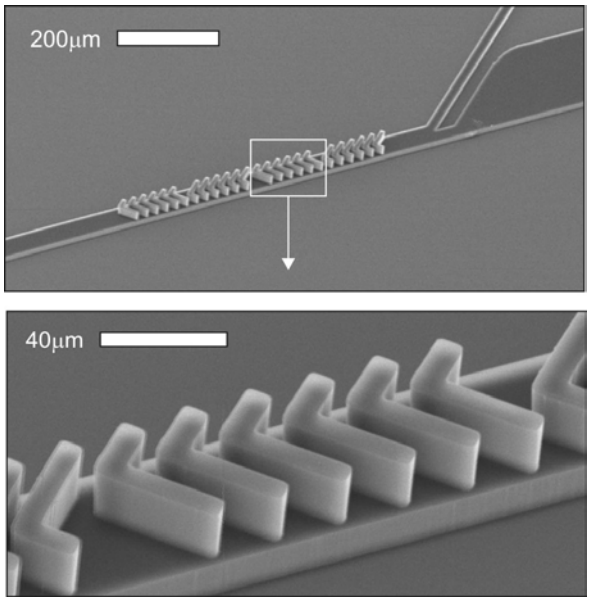

Figure 3: *SU-8 moulding replica for the Herring-Bone type mixer structure fabricated by 3D multilayer technology.*

The results of the simulations were verified by using fluorescent human serum albumin diluted in phosphate buffered salt solution. The channel surfaces were blocked by bovine serum albumin against the non-specific binding of the test proteins.

III – Results and discussion

The mixing efficiencies of the different structures were characterized by the evolving concentration distributions in the specific microfluidic components.

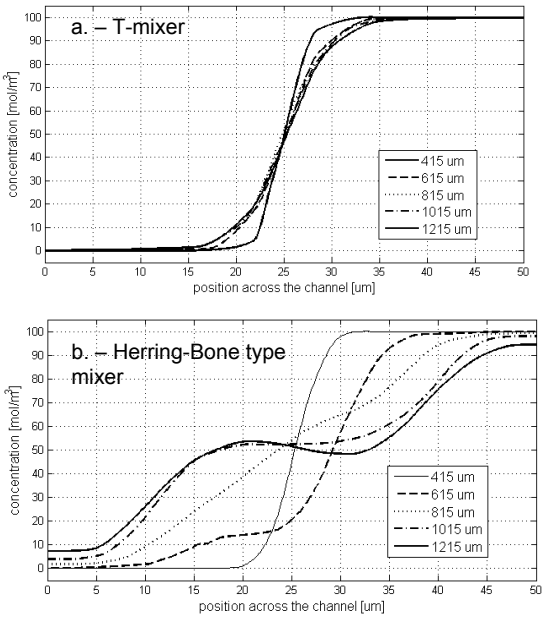

Figure 4. *Concentration distributions of the analyte in the centreline of different surface slides (distances from the inlet indicated) of the mixer structures: a. T-mixer, b. Herring-Bone type mixer*

Figure 4 clearly demonstrates the mixing behaviour of the Herring-Bone type and the simple reference T-mixers. The performance of the giving mixer can be characterized by the homogeneity of the concentration distribution of the target species (HSA in our case) in the cross-section of the fluidic channels.

According to the model calculations the Herring-Bone mixer and the T-mixer staggered blocks presented highest mixing efficiency as concluded in Figure 5. The curves in this diagram show the difference between the evolved and the ideally mixed concentration distribution on the outlet surface considering 1mm channel length in case of the different structures. It was clear that the two chaotic mixers are the most applicable structures and these are to be integrated in the transport fluidic system.

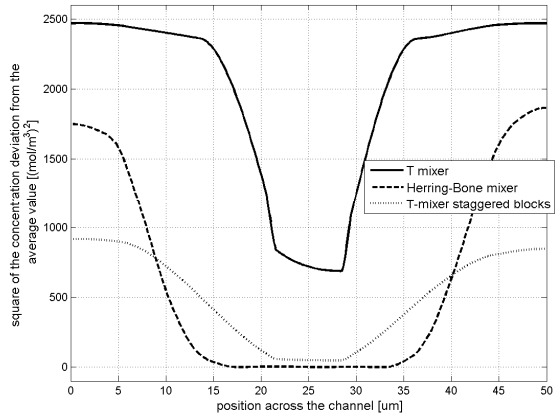

Figure 5. *Comparison of the mixing efficiencies demonstrated by the square of the concentration deviation from the average value calculated on the outlet surface.*

The experimental results are in adequate accordance with the model calculations, as the HSA concentration distributions in the microfluidics show in Figure 6.

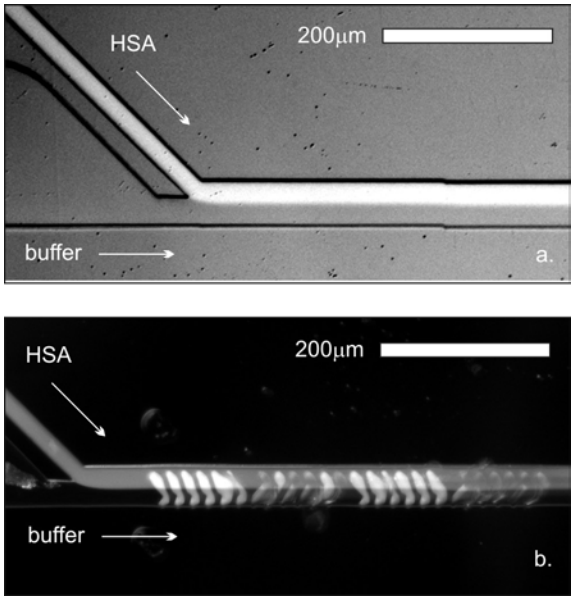

Figure 6: *The mixing of fluorescent HSA and buffer solutions in the Herring-Bone type (b) and the reference T-mixer (a).*

IV - Conclusion

Different microfluidic structures applicable for analyte manipulation in bioanalytical systems were characterized by numerical modeling, and experimentally also. According to the preliminary expectations considering the sample transport and adequate mixing condition the fluidic layouts were designed consisting different advanced chaotic mixer systems. The microfluidic structures were realised in PDMS polymer utilizing an improved 3D multilayer SU-8 technology for moulding replica formation. The verification of the numerical results was performed by fluorescent imaging applying fluorescent labeled human serum albumin solution. The fluidic behaviour of the chaotic mixer structures were demonstrated in details and their applicability in complex sample preparation systems was proved accordingly.

Acknowlegdements

The partial supports of the European Commission through the seventh framework program FP7-ICT4-P3SENS (248304) and the János Bolyai fellowship of the Hungarian Academy of Sciences (recipient: Péter Fürjes) are gratefully acknowledged.

The significant efforts of Magda Erős and Margit Payer in micromachining technology and Levente Illés in scanning electron microscopy are also acknowledged.

References

[1] Andrew J. deMello, Control and detection of chemical reactions in microfluidic systems – Review Article, Nature 442, 394-402 (2006)

[2] A.D. Stroock, S.K.W. Dertinger, A. Ajdari, I. Mezic, H.A. Stone and G.M. Whitesides, Chaotic mixer for microchannels, Science, Vol. 295, pp. 647–650 (2002)

[3] L. Gervais and E. Delamarche, Toward one-step point-of-care immunodiagnostics using capillary-driven microfluidics and PDMS substrates, Lab Chip 9, 3330-3337 (2009)

DESIGN, MANUFACTURING AND PACKAGING OF A MICRO ULTRASONIC TRANSDUCER FOR MEDICAL APPLICATIONS

J.H.G. Ng[1], R.T. Ssekitoleko[2], D. Flynn[1], M.P.Y. Desmulliez[1], C.E.M. Démoré[3] and S. Cochran[3]

[1]*MIcroSystems Engineering Centre (MISEC), Heriot-Watt University, Edinburgh EH14 4AS, Scotland, UK*
[2]*Department of Bioengineering, University of Strathclyde, Glasgow, G4 0NW, Scotland, UK*
[3]*Institute for Medical Science and Technology (IMSaT), University of Dundee, Dundee DD2 1FD, Scotland, UK*

***Abstract* — In this paper we present an innovative manufacturing and 3-dimensional packaging of a miniaturized ultrasonic transducer for medical applications. A spirally rolled-up flexible circuit was employed for interconnection of a linear transducer array in a needle size footprint. Photolithography, precision dicing and low temperature conductive bonding are amongst the technologies under investigation for the realization of this high frequency ultrasound device.**

***Keywords :* Linear Array Transducer, High Frequency Ultrasound, 3D Packaging**

I - Introduction

High resolution ultrasound using high frequency transducer arrays has applications in diagnostic imaging and guiding surgical procedures. Operating frequency above 30 MHz is required to improve image quality for medical ultrasound imaging with less than 100 µm feature resolution. This paper concerns the development of sensitive high frequency transducers with fine-scale element dimensions, housed in a package of an intervention tool such as a biopsy needle for inserting through the human skin to allow for easier *in vivo* pathology. Microfabrication of such devices are challenging due to the constraints implied by the construction of the ultrasound device; these include the maximum processing temperature of the piezoelectric ceramic material, the acoustic impedance of materials, and the design of the package which might affect the ultrasonic beam forming and focusing.

For example, a linear transducer array operating at 30MHz, requires element pitch (electrode + gap) equal to the imaging wavelength, 50µm, thereby requiring definition of element electrodes with a width of 25µm or less. A high number of elements, for instance 128, are desired for image scans over a wide area. Fine pitch bonding and high density interconnection normally used in the microelectronics industry is required to realize the next generation of ultrasound devices.

Research in incorporating ultrasound transducers at the tip of surgery guidance needles [1] and catheters [2] has been carried out for some time. Single element transducers have a fixed focus and a limited image depth of field; beamforming for a movable focus and an enlarged depth of field can be achieved electronically by arrays of transducers [3]. Efforts in constructing arrays transducers at the tip of a catheter of 3 mm inner diameter have been carried out recently [4]. These types of arrays transducers require high density and small pitch interconnections. Furthermore, a new piezoelectric ceramic single crystal material, lead magnesium niobate – lead titanate (PMN-PT), is becoming more popular for higher sensitivity imaging owing to its properties of high piezoelectric coefficient and electromechanical coupling factor [5-6]. PMN-PT has a maximum processing temperature of 60ºC without depoling which is important for its piezoelectric properties. This adds another obstacle to choosing the manufacturing and packaging technologies currently in use in industries including wire bonding and flip chip bonding which usually require temperatures of 120ºC and above. Thus, the design of a manufacturing process incorporating fabrication technologies from different fields has been investigated that capitalizes on our previous work on SU-8/TiO_2 composite, flexible circuits, powder blasting, and precision dicing [7].

Reduction in the number of process steps and the processing time has been taken into careful considerations in this new design. The reduction of the footprint devoted to interconnects is enabled by a flexible fan-out distribution layer spirally rolled up within the needle. This technique replaces the conventional lateral stacking approach found in silicon IC chip packaging where Through Silicon Vias (TSVs) are created, filled and aligned for each layer in the stack. The device structure and the construction steps of the arrays transducer are first described. The fabrication issues of this process are then discussed. Finally, a working prototype following the proposed construction process flow is presented.

II - Device Structure

The element electrodes are patterned on the surface of the active piezoelectric layer of the device, which comprises 55µm pillars of piezoelectric ceramic, lead zirconate titanate (PZT-5H), with a 90µm pitch and embedded in an epoxy matrix, forming a piezocomposite. PZT-5H was used instead of PMN-PT for the prototype due to cost whilst new bonding methods for reducing the processing temperatures are still being investigated. The piezocomposite layer is sandwiched between an acoustic matching layer and an acoustic absorbing backing layer as shown in Figure 1. The matching layer allows efficient acoustic energy transfer into the tissue. The backing layer is a dense, acoustically lossy material behind the piezoelectric layer that provides damping for the piezoelectric resonator and allows a short pulse to be transmitted forward from the array. It also prevents reflection from the bottom of the

transducer as well as providing structural support. This is especially beneficial for providing resistance to mechanical and thermal shocks when high power ultrasound is used for therapeutic applications. The thickness of these acoustic layers and the element pitch size for 15, 25 and 50MHz operating frequencies considered for prototypes are listed in Table 1. These are based on PMN-PT active layer and the matching layer is 15% alumina filled epoxy by volume.

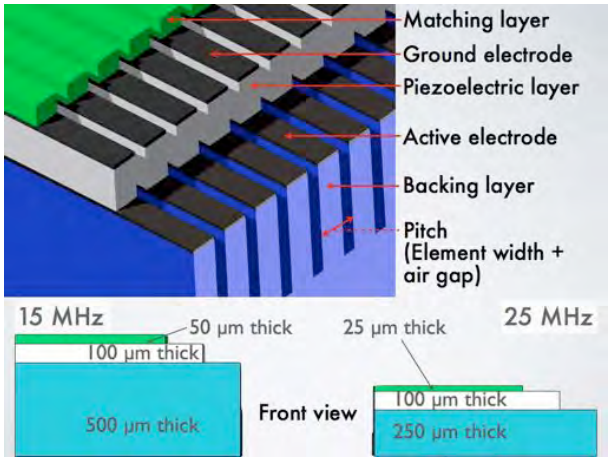

Figure 1*: Structures of the 15MHz and 25MHz linear array transducers. Top shows a 3D view of the arrangement of the layers. Bottom shows a front view illustrating the thickness of the layers.*

Table 1: *Layer thickness and pitch size for the linear array transducer at 15, 25 and 50MHz frequencies.*

Layer	15MHz	25MHz	50MHz
Piezocomposite (μm)	100	80	40
Matching (μm)	50	27	14
Backing (μm)	500	250	200
Pitch (element width + gap in μm)	100	60	30

In the current design, the matching layer, piezocomposite layer and backing layer adopt a staggered configuration as shown in Figure 1. The active electrodes are exposed on the top face of the backing layer and the ground electrodes are exposed on the top face of the piezocomposite layer. A fan-out flexible circuit is then attached to the active electrodes which, in turn, can be spirally rolled up along the long axis of the needle as shown in Figure 2. By using this configuration, only one or two strips of flexible circuit strips are needed for for connecting up to 128 elements in the linear array. If two strips are needed, they will be rolled up side by side forming an interlaced strand.

Since it is important to have a high level of control of beam quality and focus for the precise volume of tissue to be imaged or ablated, mechanical and electrical cross talks must be minimized. The air gaps in between the elements as shown in Figure 1 inhibit any undesired waves propagation in the piezocomposite layer generated from electric field spreading from individual element electrodes. Electrical cross talk can be further minimized by introducing an unconnected metal track in between each active connection in the high density fan-out flexible circuit strips.

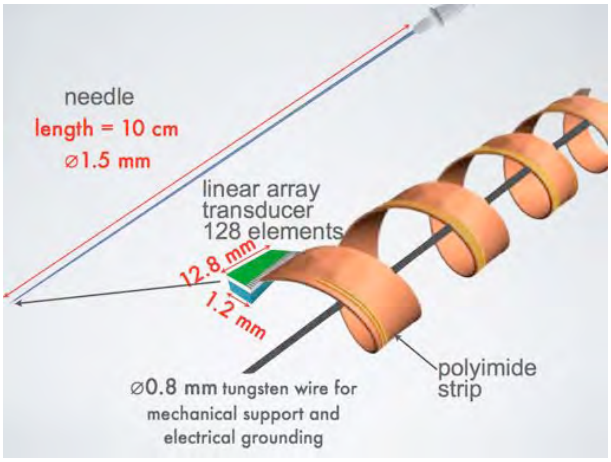

Figure 2*: Schematic diagram illustrating the interconnection between the transducer at the tip to the other end of a needle by a spirally rolled-up polyimide based flexible circuit.*

III - Fabrication Methods and Prototype

A. The layers in the transducer

A layer of 1-3 composite was manufactured by the common “dice and fill” technique whereby a mechanical dicing saw (Loadpoint MicroAce) is used to cut kerfs into a piece of bulk piezoceramic, the kerfs being subsequently backfilled with epoxy [8]. A slow spindle speed of 10,000 rpm and a low feed rate < 0.2 mm/s were used in order to prevent damage whilst dicing the fine pillars. Flatness in each of the matching layer, the piezoelectric layer and the backing layer is very important in preventing interference with wave propagation. A Logitech lapping and polishing machine was used to lap after each time epoxy was poured and cured. Figure 3 shows the piezocomposite layer after lapping.

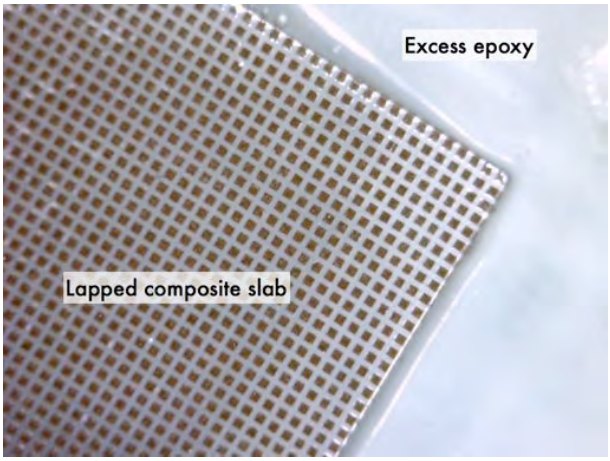

Figure 3*: Image of a lapped composite slab consisting of diced ceramic pillars of 50 x 50μm and a kerf of 30μm which has been filled with epoxy.*

For the active electrodes, a titanium layer was deposited onto the piezocomposite layer by physical vapour deposition as a first trial. A problem found was that the piezoelectric material became depoled by the temperature rise during the metal vapour evaporation. It was then decided that the electrodes would be formed on the backing layer instead as shown in Figure 1. However this means that the backing layer would need to be bonded to the piezocomposite layer by another interlayer material.

Epoxy dispersed with alumina particles was casted on top of the piezocomposite layer to form the matching layer. Silver paint was used to form ground electrodes in between the matching layer and the piezocomposite layer. After lapping, the sample was released from the carrier and flipped over for casting the backing layer using epoxy dispersed with tungsten particles.

By making use of an interlayer bonding material, it was decided that the matching layer and the backing layer are to be cured and lapped on individual carriers separate from the piezocomposite layer. This allows higher curing temperatures that shorten curing time as well as saving time in flipping over the sample and preparing the layers in a serial manner. However, releasing the thin matching layer from a carrier requires delicate care.

The elements were defined by dicing after all the layers and the flexible circuits had been assembled.

B. Flexible circuits

Since the polyimide flexible circuit is directly bonded to the linear array elements, the line width and spacing of the copper tracks on the polyimide strip is a limiting factor for the pitch size possible on the transducer. Photolithography using a dry film photoresist (Ordyl) was applied to a copper clad polyimide laminate. The copper thickness was 18 µm and the polyimide was 25 µm. These thicknesses give fairly good integrity for rolling up the circuit. Cupric chloride was used as the etching solution which provides a fast etch rate. Using this setup, moderate feature size as shown in Figure 4 can be produced reliably without defects. The produced line width and gap are 114 µm and 157 µm, respectively, from an original dimension of both 125 µm at the design stage. These deviations can be attributed to the curing chemistry of the dry film photoresist which generally has a lower feature resolution than liquid photoresist, the development chemistry, the 40µm thick dry film, the thickness of the copper and the etch rate as well as additives and other conditions in the etching chemistry. Further experiments using the current setup indicate that a pitch (linewidth + gap) of 125µm is achievable. Work is underway to run trials for a 100µm pitch in order to produce a 15MHz transducer.

In addition, other brands of dry film photoresist that allow high resolution down to 30µm pitch are either in R&D stage or already in the market. Samples of those are being sourced in order to produce higher frequencies transducers.

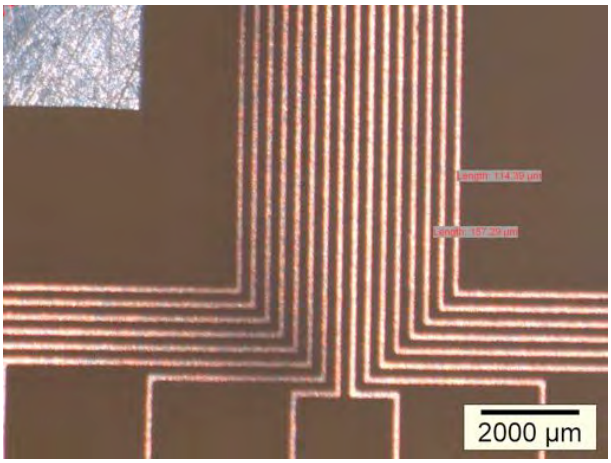

Figure 4: *Microscope image of a flexible circuit fabricated by photolithography.*

C. Bonding

As already mentioned earlier, an interlayer conductive bonding material is to be used to assemble the matching and the backing layers to the piezocomposite layer. Isotropic conductive adhesive (ICA) commonly used as a solder replacement can be blanket coated and partially cured on the matching and the backing layers individually first. Then the two layers can be bonded to sandwich the piezocomposite layer by a low temperature technique in order to avoid depoling of the piezoelectric material.

As for bonding the flexible circuit on to the backing layer with active electrodes exposing from the staircase arrangement as shown in Figure 1, anisotropic conductive film (ACF) is considered. ACFs achieved anisotropic electrical conduction in the z-axis by deforming the metal particles dispersed in the film using the appropriate temperature and pressure. It is important that a minimum contact pitch area is provided to allow for sufficient amount of metal particles to be in contact within the contact area. Testing of a fine pitch type ACF for bonding is underway.

Alternatively, since dicing is carried out through the whole transducer assembly, which includes the flexible circuit, to define the elements by create air gaps, ICA could be used for bonding without the anisotropic connection requirement.

D. First prototype

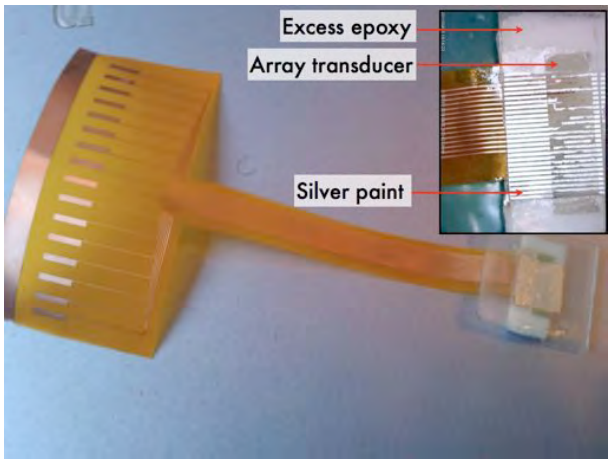

Figure 5: *Photograph of the first prototype assembled. Inset shows the connection between the flexible circuit and the linear array transducer.*

A prototype has been manufactured as presented in Figure 5. Excellent alignment was achieved between the copper tracks on the flexible circuit and the dicing blade for defining the elements as shown in Figure 6. Impedance analysis measurement revealed that the assembled transducer operates at 5.8 MHz as shown in Figure 7.

Further iterations of prototypes with higher element count, reduced pitch size, and extended fabrication details together with the results from the transducers in-water testing will be presented at the conference.

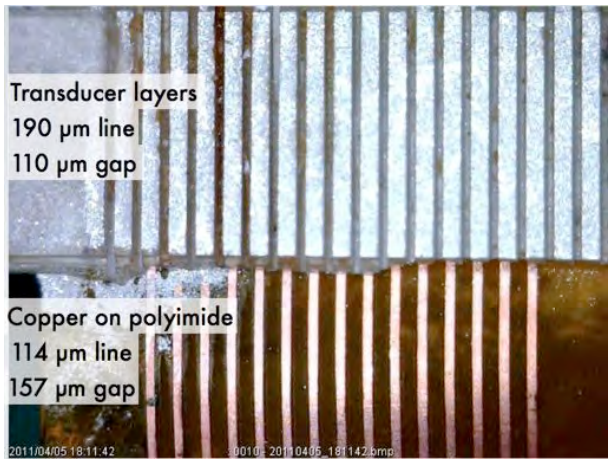

Figure 6: Image of the diced linear array aligned to the copper tracks on the flexible circuit.

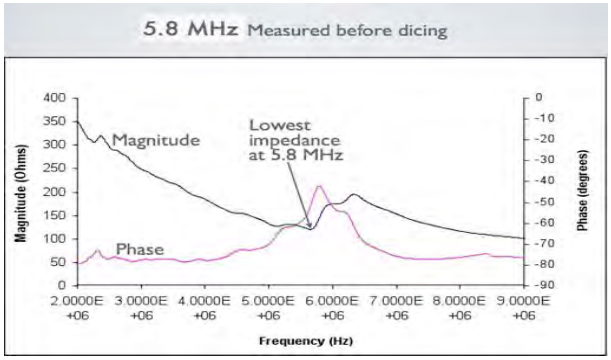

Figure 7: *Preliminary impedance measurements.*

IV - Conclusion

A new and simple approach in realizing a miniaturized linear array transducer has been presented which partially meets the challenges of interconnection in a very narrow and ultra high aspect ratio footprint with the potential of achieving high frequencies. The limiting factors for manufacturing small pitch arrays identified through the process flow are: (i) photolithography on flexible substrates, (ii) contact area allowed for bonding between the flexible circuits and the active electrodes, and (iii) rupture of the fine width element during dicing. In addition, the proposed processing steps are upscalable, suitable for wafer-level manufacturing.

References

[1] Q. Zhou *et al.*, "Design and fabrication of PZN-7%PT single crystal high frequency angled needle ultrasound transducers," *IEEE Trans Ultrason Ferroelectr Freq Control*, 55, pp. 1394-1399, 2008.

[2] M. Makuuchi, G. Torzill, and J. Machi, "History of intraoperative ultrasound," *Ultrasound in Medicine and Biology*, 24, pp. 1229-1242, 1998.

[3] J. M. Cannata, J. A. Williams, Q. Zhou, T. A. Ritter, and K. K. Shung, "Development of a 35-MHz piezo-composite ultrasound array for medical imaging," *Ultrasonics, Ferroelectrics and Frequency Control, IEEE Transactions on*, 53, pp. 224-236, 2006.

[4] D. Stephens *et al.*, "Multifunctional catheters combining intracardiac ultrasound imaging and electrophysiology sensing," *IEEE Trans Ultrason Ferroelectr Freq Control*, 55, pp. 1570-1581, 2008 Jul.

[5] K. C. Cheng, H. L. W. Chan, C. L. Choy, Q. Yin, H. Luo, and Z. Yin, "Single crystal PMN-0.33 PT/epoxy 1-3 composites for ultrasonic transducer applications," *Ultrasonics, Ferroelectrics and Frequency Control, IEEE Transactions on*, 50, pp. 1177-1183, 2003.

[6] X. Jiang, K. Snook, A. Cheng, W. S. Hackenberger, and X. Geng, "Micromachined PMN-PT single crystal composite transducers -- 15-75 MHz PC-MUT," IEEE International Ultrasonics Symposium, 2008.

[7] J.H.-G. Ng *et al.*, "Progress towards the development of novel fabrication and assembly methods for the next generation of ultrasonic transducers," Electronics System Integration Technologies Conference, Berlin, September 13-16, 2010.

[8] K. A. K. H. P. Savakas, And R. E. Newnham, "PZT-epoxy piezoelectric transducers: A simplified fabrication procedure," *Materials Research Bulletin*, 16, pp. 677-680, 1981.

A HIGH OPEN-CIRCUIT VOLTAGE GALLIUM NITRIDE NUCLEAR BETAVOLTAIC MICROBATTERY

Zai-Jun Cheng[1], Hai-sheng San[1], Zhi-Hong Feng[3], Bo Liu[3], and Xu-Yuan Chen [1,2,*]

[1]*Pen-Tung Sah Micro-Nano Technology Research Center, Xiamen University, Xiamen 361005, Fujian, People's Republic of China*
[2]*Faculty of Science and Engineering, Vestfold University College, P.O. Box 2243, N-3103 Tønsberg, Norway*
[3]*Science and Technology on ASIC Laboratory, Hebei Semiconductor Research Institute, Shijiazhuang 050051, Hebei, People's Republic of China*

***Abstract* —A high open-circuit voltage betavoltaic nuclear microbattery based on Gallium nitride (GaN) p-i-n homojunction was demonstrated. Under the irradiation of a 4×4 mm^2 planar solid ^{63}Ni source with an activity of 2 mCi, the open-circuit voltage of the fabricated single 2×2 mm^2 microbattery reaches as big as 1.62 V which is the record value reported for betavoltaic batteries with ^{63}Ni source, the short-circuit current density was measured as 16 nA/cm^2 and the conversion effective of 1.13% was obtained. The experimental results suggest that the GaN betavoltaic microbattery is an attractive candidate as power supply for microelectromechanical system (MEMS) devices.**

Keywords: **Betavoltaic microbattery, Gallium Nitride, Direct energy conversion**

I - Introduction

With the rapid development of MEMS technology, there is an ever-increasing demand for micro-scale energy systems to power the majority of MEMS devices such as remote MEMS sensors and implantable medical MEMS chips which are required for long-term operation. For powering such MEMS devices, fossil fuels and chemical batteries are only a limited lifetime solution due to the requirement of periodic recharge or replacement. Microscale radioactive power sources are getting more and more attractive as the energy source for powering MEMS devices because of their high energy density, long life time and insensitivity to environment and temperature. To convert radioactive decay energy into electric power, one promising technique is direct energy conversion (DEC) method using a semiconductor p-n diode in which electrons and holes are generated by beta stream from radioisotope source [1]. Taking into lifetime, energy density, and safety account, ^{63}Ni seems the most suitable radioisotope source which radiates pure beta particles of maximum value of 66.7 kev, and has long half life (100 years).

The operation principle of a betavoltaic microbattery is similar to that of a photovoltaic microbattery. In betavoltaic cells, electron-hole pairs are generated in the semiconductor by beta electrons from the radioactive source (average energy of 17.1 Kev for ^{63}Ni) instead of the photons. In comparison with a photon exciting an electron-hole pair, a beta particle can create tens of thousands of electron-hole pairs. Along the beta particles moving trajectory, the carriers generated in the depletion region and the n or p region near the depletion boundary with width less than the carrier diffusion length can be collected. As a result, the decay energy of beta particle is harvested and converted into electrical energy.

Semiconductor p-n diodes for conversion of beta radiation into electrical power were firstly suggested in the 1950s [2]. In the latest decade, several betavoltaic batteries based on Silicon (Si) and Silicon carbide (SiC) have been reported [3-8]. Theoretical analysis shows that efficiency of betavoltaic conversion increases with the increase of the band gap of semiconductor [9]. To compare with Si (band gap of 1.12 eV) and SiC (band gap of 2.3~3.3 eV), the wide band gap semiconductor of GaN (3.4 eV) is a more attractive choice for creating the betavoltaic microbattery. In addition, GaN has also the advantage of higher radiation resistance. However, no fabricated GaN p-n diode betavoltaic microbattery has been reported so far. To date only two research groups have reported their theoretical design and efficiency calculations for GaN-based betavoltaic microbattery [10, 11].

In our previous work, we have reported the design optimization and experimental fabrication of GaN p-n diode for betavoltaic microbattery [12]. The GaN diodes were grown by low-pressure metal-organic chemical-vapor deposition (MOCVD). For MOCVD p-type GaN, the difficulties are to grow p-type GaN layer with high quality, enough thickness, and high doping concentration. The range of doping concentration for p-type GaN is limited to 1~5×10^{17} cm^{-3}. For MOCVD n-GaN, the difficulty is to obtain lightly doped n-type GaN layer. Nominally undoped GaN grown on sapphire substrate shows an n-type conductivity (n>5×10^{16} cm^{-3}) due to residual impurities [13, 14]. These difficulties result in a very narrow depletion region in the GaN p-n diode, only a small part of generated electron-hole pairs can be collected, thus the power output of fabricated betavoltaic microbattery is far less than expected.

To improve the performance of the GaN diode betavoltaic microbattery, it is necessary to investigate how to produce the GaN diode with a wider depletion region which can collect as many as possible radiation generated carriers. In this work, GaN p-i-n homojunction is designed. For the growth of i-GaN

layer, process of compensation doping has been developed in which an acceptor impurity of Fe is added to the nominally undoped GaN layer, we are able to achieve lightly doped ($n=1\times10^{15}$ cm^{-3}, measured by Hall effect) i-GaN layer with the thickness of 1200 nm. Because the depletion region of the GaN p-i-n homojunction extends across the whole i-GaN layer, much more excited electron-hole pairs can be collected than in GaN p-n diode, thus the outputs of the betavoltaic microbattery will be improved significantly.

II - Experimental Details

The p-i-n GaN structure were grown on 2-inch c-plane sapphire (Al_2O_3) substrates using a MOCVD reactor system. Firstly a 20-nm thick low temperature GaN nucleation layer was grown as the buffer layer to stop the propagation of defects arising from lattice mismatch between sapphire and the followed GaN epitaxial layer. Then a 600-nm high-quality undoped GaN layer was grown. Finally, the p-i-n structure consisting of a 1000-nm Si-doped n-type GaN, a 1200-nm Fe-doped i-GaN, and a 50-nm Mg-doped p-type GaN was grown subsequently. After the growth, the wafers were annealed at 750 °C for 25 minutes in N_2 ambient to activate Mg dopant. An X-ray diffraction (XRD) was performed to determine the crystal quality of GaN epitaxial layers by measuring the full width at half maximum (FWHM) of the symmetric (002) low angle diffraction peaks of the rocking curve.

For fabricating GaN betavoltaic microbattery on the planar p-i-n GaN wafer, firstly the p-type GaN layer was patterned and etched using an inductively coupled plasma (ICP) etching system to expose the n-type GaN layer for preparing the ohmic contact on n-type GaN. Then, the sample was dipped in HCl：HNO_3 (3：1) for 300 seconds to remove native oxide layer on the exposed n-type GaN. Next, an electron-beam evaporator was used to deposit the contacts consisting of Ti/Al/Ti/Au (26/230/8/80 nm), annealed at 550 °C for 45 seconds in an N_2 ambient. As the fourth step, the Ni/Au (8/10 nm) layers were deposited to form a current spreading layer on the top p-type GaN layer, annealed at 470 °C for 120 seconds in a nitrogen-oxygen mixture (N_2：O_2=2:1) ambient. Finally, the 100×100 μm^2 pads consisting of Ni/Ag/Au (100/100/200 nm) were deposited on the p-current spreading layer for external contacts. The size of the fabricated single microbattery is 2×2 mm^2. In order to characterize the performance of ohmic contact to p-type and n-type GaN, a Transfer Length Measurement (TLM) method was used [15]. A series of Ti/Al/Ti/Au-n-type GaN and Ni/Au-p-type GaN contacts separated by various distance were deposited together with the preparation of the n- and p-type GaN electrodes, and the size of metal-GaN contacts is 200 µm long and 200 µm wide, the interspacings between the contacts were changed from 15 to 50 µm with 5 µm interval.

The p-i-n GaN betavoltaic microbattery was characterized by using Keithley Model 4200-SCS

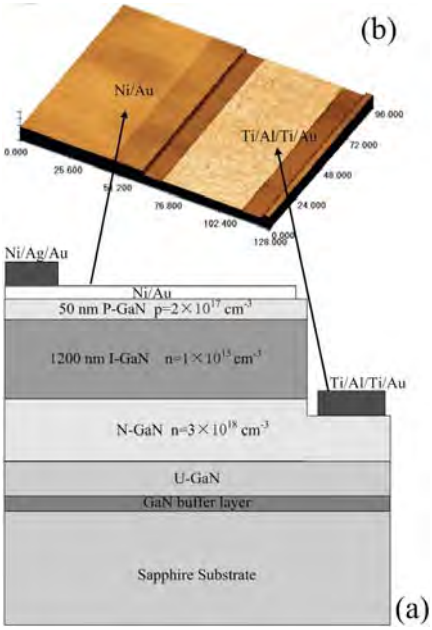

Figure 1: *Schematic structure of the GaN p-i-n betavoltaic microbattery (a) and the laser scanning confocal microscope image of fabricated Ohmic contact electrode (b).*

Semiconductor Characterization System. The measurements were made under dark and room temperature conditions in a Faraday cage. The ^{63}Ni beta source used in this experiment was a 4×4 mm^2 solid plate with the activity of 2 mCi, supplied by China Institute of Atomic Energy.

III - Results and Discussion

Figure1 (a) shows the typical device structure with detail of its each epitaxial layer, the laser scanning confocal microscope image of partial fabricated device is shown in Figure1 (b). Figure2 shows the XRD rocking curve (ω-scan) for (002) peaks of the grown GaN layers, since the dislocation density decreases with the decrease of XRD FWHM, the narrow FWHM value of 280 arcsec presents that the achieved GaN epilayer have excellent crystalline quality.

Figure3 shows the TLM characteristics of the Ni/Au-p-type GaN and Ti/Al/Ti/Au-n-type GaN contacts. Probes are applied to neighboring pairs of contact and the resistance between them is measured by

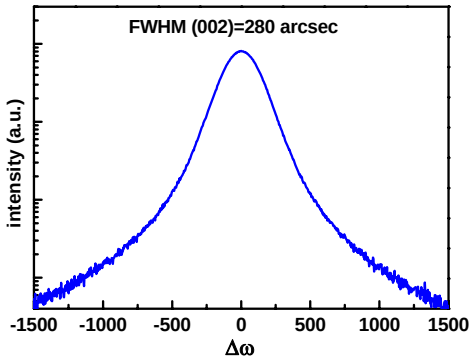

Figure 2: *The symmetric (002) low angle diffraction peaks of rocking curve for GaN p-i-n epilayer.*

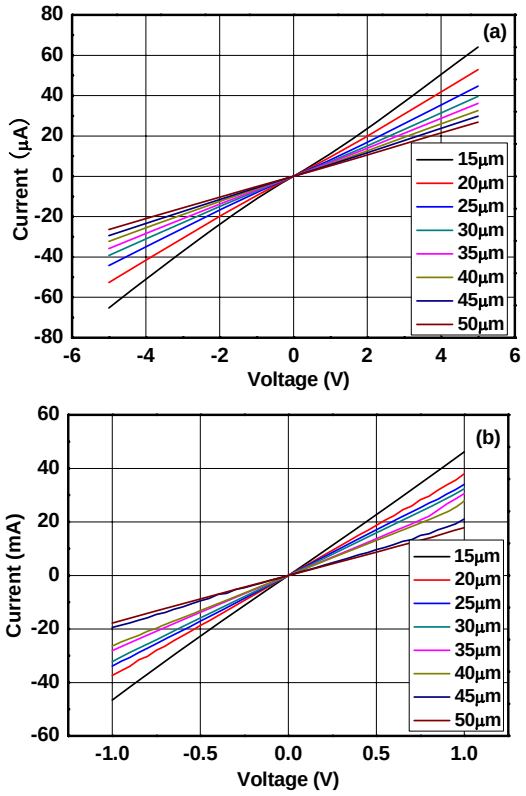

Figure 3: *I-V curves between 200×200 μm contacts with different spaces for (a) p-GaN metal contact using Ni/Au (b) n-GaN metal contact using Ti/Al/Ti/Au.*

applying scanning voltages across the contacts and measuring the resulting currents. It can be seen that both the p-type and n-type contacts exhibit a linear current-voltage (I-V) characteristic, which indicates the perfect Ohmic contact performance of metal electrodes both on the P-type and N-type GaN layer. The specific contact resistivity (ρ_c) was evaluated to be $2\times10^{-1}\ \Omega\,cm^2$ for Ni/Au-p-type GaN and $1\times10^{-4}\ \Omega\,cm^2$ for Ti/Al/Ti/Au-n-type GaN.

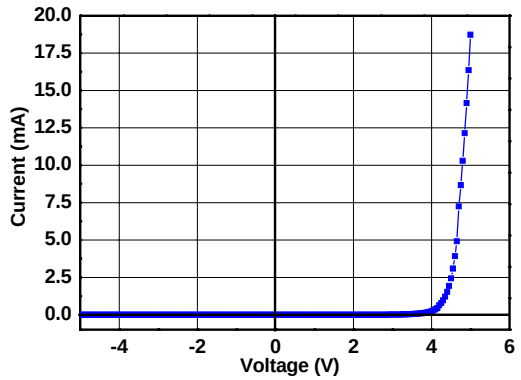

Figure 4: *Dark I-V characteristics of the microbattery without irradiation.*

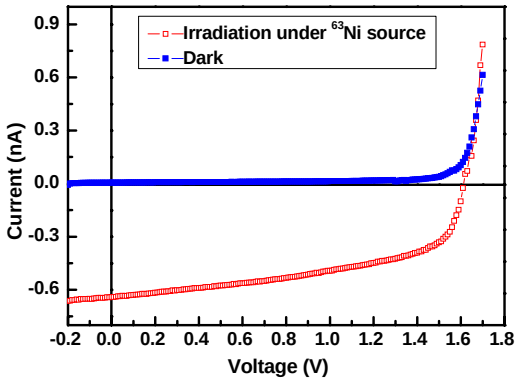

Figure 5: *I-V characteristics of the microbattery under the ^{63}Ni irradiation of 2mCi.*

Figure 4 is the dark I-V characteristic of the microbattery measured without irradiation. It can be seen that the fabricated GaN p-i-n device has a very good p-n junction performance. The leakage currents at 0 V and -5 V are at the level of 10^{-16} A and 10^{-10} A respectively. The turn-on voltage of the microbattery is approximately 3.9 V. The low leakage current and high turn-on voltage are typical for wide band gap semiconductor p-i-n diode structures.

Figure 5 shows the I-V curve of the microbattery under the irradiation of ^{63}Ni source. As shown in Figure 5, under the irradiation of a 4×4 mm^2 planar solid ^{63}Ni source with an activity of 2 mCi, the microbattery exhibits an open-circuit voltage (V_{oc}) as high as 1.62 V, which is much higher than the reported values. The reported maximum value of V_{oc} for Si-based and for SiC-based betavoltaic batteries with ^{63}Ni source is 0.115 V [3] and 0.72 V [5], respectively. The measured voltage at the peak power is 1.33 V, leading to a filling factor (FF) of 0.55. Assuming the illuminated area is equal to the area of the microbattery (2×2 mm^2), only 0.5-mCi ^{63}Ni-beta effective irradiation is received by the microbattery, resulting in the short-circuit current (I_{sc}) of 640 pA, or, the short-circuit current density (J_{sc}) of 16 nA/cm^2 obtained. No degradation of the performance was observed over a period of 5 months.

Energy conversion efficiency of radiation energy into electrical power is a key parameter for performance of betavoltaic microbattery. The conversion efficiency η can be defined as the following equation:

$$\eta = \frac{P_{out-\max}}{P_{source}} = \frac{FF \times V_{oc} \times I_{sc}}{3.7\times10^{7} \times \Phi \times E_{avg} \times e} \times 100\% \quad (1)$$

where $P_{out\text{-}max}$ presents the maximum output power of the microbattery, P_{source} presents the radiation power of the source, Φ is the source activity (mCi), E_{avg} is the average beta energy of the isotope (keV), and e is the electron charge (C). With Eq. (1), for the GaN-based betavoltaic microbattery fabricated in this work, the conversion efficiency of 1.13% is obtained.

"High efficiencies" of 6% and 4.5%±0.3% for SiC-based betavoltaic batteries had been reported by M.V. S. Chandrashekhar et al [5] and C. J. Eiting et al [8]. In M.V. S. Chandrashekhar et al's article, P_{source} of the 1mCi-^{63}Ni source was measured by using a

picoammeter in a Faraday cup, which equals 1.54 pA×V_{mean} (V_{mean} =17.1 kV corresponds to the average energy of a beta particle form ^{63}Ni). However, using Eq. (1), the conversion efficiency of M.V. S. Chandrashekhar et al's SiC-based betavoltaic cells is recalculated and equals 1.52% which is comparable with our results. In C. J. Eiting et al's article, the value of P_{source} for their 230 mCi-^{33}p source was calculated as 12.4% of the total power produced in the source. However, using Eq. (1), the conversion efficiency equal to 0.56% is obtained for their microbattery, which is half of our result.

IV - Conclusion

We have demonstrated a high open-circuit voltage betavoltaic microbattery based on GaN p-i-n homojunction. GaN epitaxial layers were grown by a MOCVD system on the 2-inch *c*-plane sapphire substrates. By using intentional doping with Fe as the compensation of residual donors in undoped GaN layer, we successfully epitaxially grew a thick (1200 nm) and lightly doped ($n=1\times10^{15}$ cm^{-3}) intrinsic layer for betavoltaics. Under the irradiation of a 4×4 mm^2 solid plate ^{63}Ni source with an activity of 2mCi, the betavoltaic microbattery with dimension of 2×2 mm^2 exhibits a short-circuit current of 640 pA, an open-circuit voltage of 1.62 V, and the efficiency of 1.13% for conversion of irradiation energy into electrical power. The results suggest that the wide-band gap semiconductor of GaN is a high potential candidate for the long-life betavoltaic microbattery. The high open-circuit voltage is very important for the microbattery to be used directly as power supply for electrostatically actuating MEMS devices.

Acknowledgements

This work was supported by the National Natural Science Foundation of China (No. 51075344) and Natural Science Foundation of Fujian Province of China (No.2010J01015)

References

[1] A.G. Kavetsky, S. P. Meleshkov, and M. M. Sychov, in Polymers, Phosphors, and Voltaics for Radioisotope Batteries, edited by K.E.Bower, Y. A. Barbanel, Y. G. Shreter, and G. W. Bohnert (*CRC Press, Boca Raton*, FL, 2002), pp.38.

[2] Rappaport, *Phys. Rev.* 93, pp. 246-247, 1954.

[3] Hang Guo, and Amit Lal, *Proceedings of the 12th International Conference on Solid State Sensors, Actuators and Microsystems, Transducers'03 Conference*, Boston, pp.36-39, 2003.

[4] Rajesh Duggirala, Steven Tin, and Amit Lal, *Proceedings of the 14the International Conference on Solid-State Sensors, Actuators and Microsystems, Transducers'07 Conference*, Lyon, France, pp.279-282, 2007.

[5] MVS Chandrashekhar, Christopher I. Thomas, Hui Li, M.G. Spencer and Amit Lal, *Appl. Phys. Lett.* 88, 033506, 2006.

[6] Hang Guo, Hui Yang and Ying Zhang, *MEMS 2007*, Kobe, Japan, pp. 867-870, 2007.

[7] Wei Sun, Nazir P. Kherani, Karl D. Hirschman, Larry L. Gadeken, Philippe M. Fauchet, *Adv. Mate.*, 17, pp. 1230-1233, 2005

[8] C.J. Eiting, V. Krishnamoorthy, S. Rodgers, and T. George, *Appl. Phys. Lett.* 88, 064101, 2006.

[9] V.M. Andreev, in Polymers, Phosphors, and Voltaics for Radioisotope Batteries, edited by K.E.Bower, Y.A.Barbanel, Y.G.Shreter, and G.W.Bohnert (*CRC Press*, Boca Raton, FL, 2002) pp. 48.

[10] Christiana Honsberg, William A. Doolittle, Mark Allen, Chris Wang, Proceedings of *the 31st IEEE Photovoltaics Specialis Conference*, Orlando Florida, 2005.

[11] M. Mohamadian, S. A. H. Feghhi, H. Afariadeh, Proceedings of the *7th WSEAS International Conference on Power Systems*, Beijing, China, pp. 247-250, 2009.

[12] Zaijun Cheng, Haisheng San, Yanfei Li, Xuyuan Chen, Proceedings of *the 2010 5th IEEE International Conference On Nano/Micro Engineered and Molecular Systems*. Xiamen, China, pp. 575-579, 2010.

[13] D. C. Look and P. J. Molnar, *Appl. Phys. Lett.* 70, 3377, 1997.

[14] M. G. Cheong, K. S. Kim, C. S. Oh, N. W. Namgung, G. M. Yang, K. Y. Lim, E. K. Suh, K. S. Nahm, H. J. Lee, D. H. Lim, and A. Yoshikawa, *Appl. Phys. Lett.* 77, 2557, 2000.

[15] J. S. Foresi and T. D. Moustakas, *Appl. Phys. Lett.* 62, No. 22, 1993.

DYNAMIC PERIODS TANDEM GRATING FOR SPECKLE REDUCTION

Xu Dang, Zhaomin Tong, Guangmin Ouyang, Nan Feng, Dong Yang, M. N. Akram, K. Y. Wang, and X. Y. Chen
Faculty of Science and Engineering, Vestfold University College, N-3103 Tonsberg, Norway

***Abstract* — In this paper we discuss a motionless diffractive optical element for speckle reduction: dynamic period tandem grating. The dynamic period could be realized by combining several driving electrodes together to form a new electrode to have more diffractive patterns. It was designed based on finite-element method simulations and the speckle noise can be reduced to 14% according to the theory.**

Keywords: **Speckle reduction, PDMS, Tandem Grating, MOEMS**

I – Introduction

Laser is characterized as long lifetime, power saving, compact, and high resolution illumination source which is essential in display technology. While offering such advantages it has limited applicability due to speckle effects which degrade the image quality. Speckle is induced by the light scattering and interference of coherent radiation from a screen with roughness of optical wavelength. In order to keep the image quality in laser illumination, the reduction of speckle is highly desirable. The fundamental theory of speckle formation, its statistical properties, and despeckle methods are described thoroughly in [1]. Considerable efforts have been made to minimize the speckle in display systems with laser source, to list a few, a moving diffuser placed at the image plane [2], dynamic Hadamard phase patterns inside each detector resolution pixel at the intermediate image plane [3], partially coherent beams [4], and a stationary phase plate based on the Barker or another binary phase code at the intermediate image plane [5]. When a mechanically vibrating element is used, such as those in [2, 3], a motor is needed to provide fast vibration or rotation. This can be difficult for practical implementation and decreases the system's reliability. When a laser array is used, as in [4], the illumination optics is complicated and the cost increases. The methods based on binary phase code [5] are only applicable in line-scan projectors.

In this paper we are going to discuss a dynamic diffractive optical element (DOE). With the dynamic period driving by different biased electrodes, independent diffractive pattern number increases helping in speckle reduction.

II – Dynamic period tandem gating design

A. Design principle

In this work the speckle reduction is based on averaging the intensity of N uncorrelated speckle patterns during the integration time of the detector, which is around 30 ms for human eyes. The contrast of the "speckle" image serves as the measure of speckle intensity which is defined as the ratio of the standard deviation of the intensity fluctuation and the mean intensity. Under the most favorable condition, where all the N independent speckle configurations have equal mean intensities, the contrast is reduced to $1/\sqrt{N}$

A diffractive optical element (DOE) with static period shown in Fig. 1, has been studied in [6]. The DOE consists of three electrically controlled gratings. Each grating can be switched "on" and "off" independently by specific biasing. In the "off" state, the incident light is reflected at the angle of the total internal reflection (TIR), while in the "on" state a phase grating in the form of periodical relief is generated, which splits light into several diffraction orders. When one or several gratings are actuated, the incoming light is split into a multitude of diffraction orders. There are maximum diffraction patterns $M=2^m$ for a DOE with m gratings [6]. In our work we are going to improve the DOE from static period to dynamic period in order to increase the maximum number of the diffractive patterns.

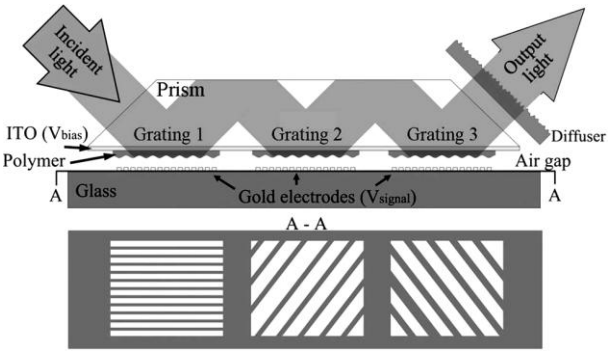

Fig. 1. Schematic drawing of the dynamic DOE. Picture at bottom shows the orientation of electrodes in each grating. The dimensions are not to scale. [6]

For the dynamic period DOE, the width of electrodes to make the diffractive period can be modulated electrically, which means each grating has more than two states. Therefore, incoming light can be split with much higher diffraction orders. The design of the dynamic period DOE is realized by combining several electrodes together to form a new electrode. An example is illustrated in Fig.2. Each individual electrode is designed with the width of 10μm. By biasing the electrodes with designed potential patterns, DOE consisting of gratings of different periods can be achieved. As shown in Fig.2, where the dark and grey colors represent the positive and negative biased electrodes respectively, we have formed a DOE of 40μm as the diffractive period at the left side (4 electrodes form one period), and of 60μm at the right side (6 electrodes form one period). In the case of three gratings configuration

shown in Fig.1, if every grating could change their period among 40μm and 60μm, then each grating can be switched "on" with 40μm or 60μm diffractive period, and "off" independently by applying voltage. Therefore, maximum number of diffraction patterns can reach $M=3^m$ for a DOE with m gratings. As the result of the simple mathematics, when we increase the number of modulated diffractive periods to q, then the maximum number of diffraction patterns for this DOE with m grating will be $M = (q+1)^m$.

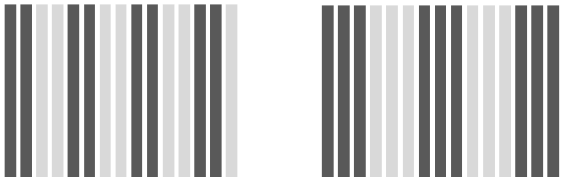

Fig. 2. Schematic drawing of the dynamic periods. Picture in the left side shows two electrodes combined mode, picture in the right side shows three electrodes combined mode.

B. Method to control the combination of electrodes

By controlling every electrode of each grating individually to build up a dynamic period DOE is unrealistic because we need about 900 electrodes to form one grating in the real case. A method has been developed to handle this problem, which is described in details hereafter. Shown in the Fig.3 as example, the vertical lines are grating electrodes which are grouped in three (3a), four (3b), and five (3c) with the same bias in order to change the grating period. When the bias is defined as 0 for negative and 1 for positive, the bias configuration for all grating electrodes is given in table 1, in which the columns are the index of the grating electrodes subsequently. The rows are the biasing configurations for forming different periods. From this table, we find that the columns as the bias configurations are a periodic change of the binary 000 to 111 for three dynamic periods. Therefore, only 8 independent bias inputs are required to bias all grating electrodes for realizing the designed bias configurations. As shown in figure 3, the horizontal lines isolated from the vertical lines are the 8 bias inputs which are defined by the binary number from 000 to 111. The interconnection for the bias inputs and the grating electrodes can be determined following table 1, as presented by the black dots in figure 3. From table 1, the bias configurations for the three grating periods are obtained as depictured in table 2.

Now we can explicitly demonstrate the formation of the grating periods by coloring the electrodes in figure 3, where the electrodes of blue color are biased positively and of yellow color are biased negatively. Following table 2, the colored grating electrodes clearly show that we have achieved three different periods.

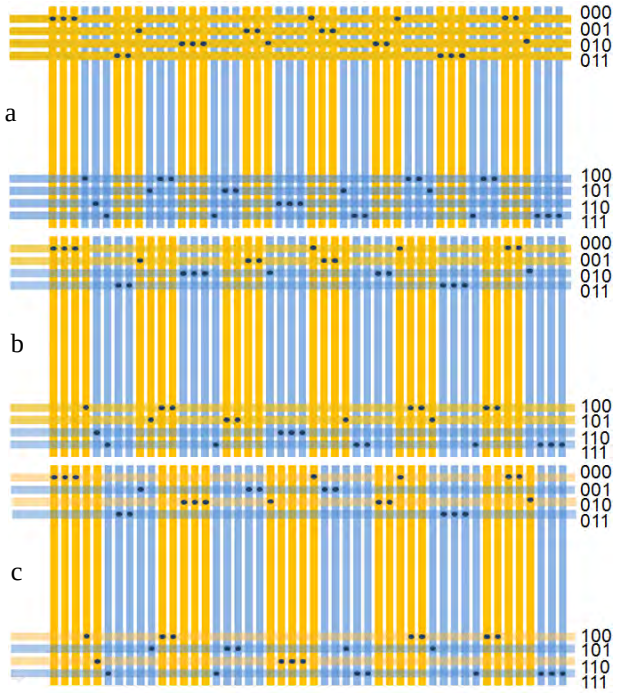

Fig. 3. Schematic drawing of the method to realize 3/4/5 electrodes combination

Table 1. Binary digital array, from the 1st column to the 120th column

0	0	0	1	1	1	0	0	0	1	1	1	0	0	0	1	1	1	0	0
0	0	0	0	1	1	1	1	0	0	0	0	1	1	1	1	0	0	0	0
0	0	0	0	0	1	1	1	1	1	0	0	0	0	0	1	1	1	1	1

1st to 20th

0	1	1	1	0	0	0	1	1	1	0	0	0	1	1	1	0	0	0	1
1	1	1	1	0	0	0	0	1	1	1	1	0	0	0	0	1	1	1	1
0	0	0	0	0	1	1	1	1	1	0	0	0	0	0	1	1	1	1	1

21st to 40th

1	1	0	0	0	1	1	1	0	0	0	1	1	1	0	0	0	1	1	1
0	0	0	0	1	1	1	1	0	0	0	0	1	1	1	1	0	0	0	0
0	0	0	0	0	1	1	1	1	1	0	0	0	0	0	1	1	1	1	1

41st to 60th

0	0	0	1	1	1	0	0	0	1	1	1	0	0	0	1	1	1	0	0
1	1	1	1	0	0	0	0	1	1	1	1	0	0	0	0	1	1	1	1
0	0	0	0	0	1	1	1	1	1	0	0	0	0	0	1	1	1	1	1

61st to 80th

0	1	1	1	0	0	0	1	1	1	0	0	0	1	1	1	0	0	0	1
0	0	0	0	1	1	1	1	0	0	0	0	1	1	1	1	0	0	0	0
0	0	0	0	0	1	1	1	1	1	0	0	0	0	0	1	1	1	1	1

81st to 100th

1	1	0	0	0	1	1	1	0	0	0	1	1	1	0	0	0	1	1	1
1	1	1	1	0	0	0	0	1	1	1	1	0	0	0	0	1	1	1	1
0	0	0	0	0	1	1	1	1	1	0	0	0	0	0	1	1	1	1	1

101st to 120th

Table. 2. Binary digital array

Biasing electrodes index	Biasing level (0 and 1 represent negative and positive biasing respectively)		
000	0	0	0
001	0	0	1
010	0	1	0
011	0	1	1
100	1	0	0
101	1	0	0
110	1	1	0
111	1	1	1
Biased electrodes configuration	3electrodes grouping biased	4electrodes grouping biased	5electrodes grouping biased

III Design simulation for diffractive patterns

We use commercial available software ZEMAX to simulate optical geometry. A schematic drawing of simulation model with 2 gratings is shown in Fig.4. The resulting diffractive patterns are exhibited in Fig.5.

In the case with 3 dynamic-period-gratings and each grating has diffractive periods of 36μm (grouping three electrodes), 48μm (grouping four electrodes), and 64μm (grouping five electrodes), theoretically we can get the maximum number of the diffractive pattern $M=(3+1)^3=64$.

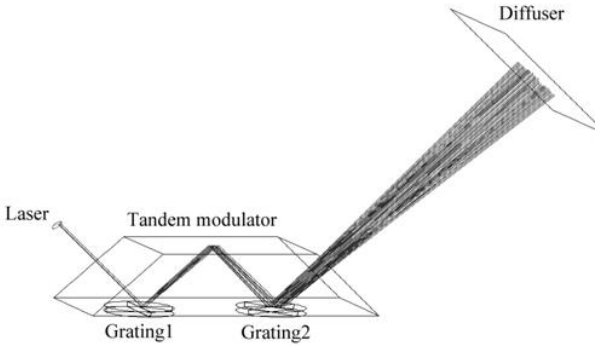

Fig. 4. Simulation model in ZEMAX

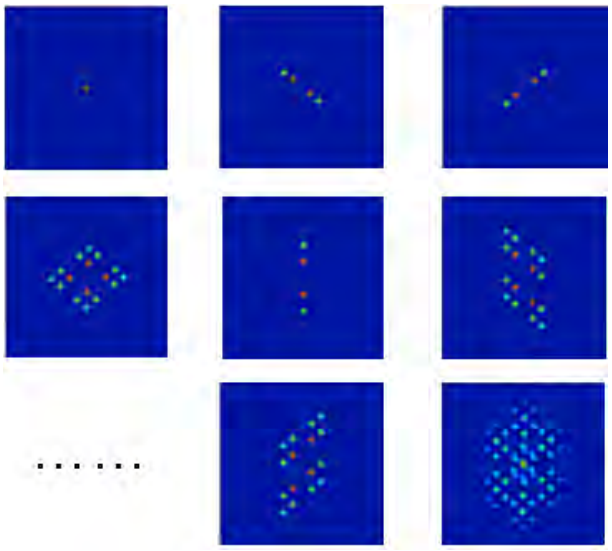

Fig. 5. Example of the simulation result in ZEMAX

However, these 64 patterns are not fully independent due to the partially overlap of the light spots in the different patterns which leads patterns dependent. For the speckle contrast reduction, the independent patterns number should be simulated and calculated.

IV Independent patterns for speckle reduction introduced by the dynamic period DOE

The general expression for the speckle contrast C in a system with the diffractive DOE and the light homogenizer was derived in [7], and presented as,

$$C=\sqrt{\frac{M+K+1}{MK}+\frac{K^2+K}{M^2K^2P^2}\sum_{m=1}^{M}\sum_{\substack{n=1,\\ n\neq m}}^{M}\left[\iint_{S_{RPP}}\sqrt{I_{RPP}^{(m)}(x,y)\cdot I_{RPP}^{(n)}(x,y)}\,dxdy\right]^2}$$

where C is speckle contrast, M the number of diffraction patterns, K the number of lens resolution elements within eye resolution element, P the intensity of the diffraction patterns, $I_{RPP}^{(m)}(x,y)$ the light intensity at the position of (x,y) in the diffraction pattern of number m. Using Matlab, the reduced speckle contrast by M diffractive patterns can be simulated. By substituting the simulation result in to $C=1/\sqrt{N}$, we can determine the fully independent diffractive patterns introduced by the designed dynamic period DOE.

A summary of the simulation results is shown in Table 3. We see that three gratings, each of which is with 3 different periods, will deliver the maximum number of the fully independent patterns. The major reason for this is because four or more gratings will result in a stronger spatially overlapping of light spots in the different diffractive patterns. For our specific designed grating electrodes of 8um width separated by 2 um, we also find that the way of grouping electrodes has significantly influence to the number of fully independent patterns. The best way of grouping electrodes for sufficient speckle reduction is grouping 3, 4, and 5 neighbouring electrodes for the three different periods, which gives 49.04 fully independent patterns and reduced speckle contrast to 14.3%.

Table. 1. Independent Pattern Number Simulation Summary

					Independent value *N*		Speckle Contrast	
Total gratings	Electrodes	Diffraction periods (μm)			Simulation result	Theoretic value	Simulation result	Theoretic value
3	1	100			6.872	8	0.38	0.35
	2/3	66	100		23.43	27	0.21	0.19
	1/2/3	33.3	66.7	100	38.9	64	0.16	0.125
	2/3/4	48	72	96	39.41	64	0.16	0.125
	2/3/4	50	75	100	37.45	64	0.16	0.125
	3/4/5	36	48	60	45.9	64	0.15	0.125
	3/4/5	48	64	80	49.04	64	0.143	0.125
	3/4/5	54	72	90	48.49	64	0.144	0.125
	3/4/5	60	80	100	43.225	64	0.152	0.125
	4/5/6	53.4	66.7	80	43.34	64	0.152	0.125
	4/5/6	60	75	90	42.33	64	0.154	0.125
	6/7/8	60	70	80	31.7	64	0.179	0.125
4	1	100			14.5	16	0.263	0.25
	2/3	66.7	100		21.12	81	0.217	0.111
	2/3/4	50	75	100	26.08	256	0.196	0.063
5	1	100			13.93	32	0.268	0.177

V. Design for the fabrication process

PDMS, a kind of electrical active polymer, is used for fabricating the dynamic gratings [6]. The process flow of fabricating dynamic period tandem grating driving circuit is present by the schematic plot shown in Fig.6. Explain in detail, in step a) the 1st metal layer was sputtered on glass wafer. In step b) 1st metal layer was patterned to form electrodes. In step c) Si_3N_4 layer was deposited by PECVD as isolating layer and was patterned to form connection via holes. On the isolating layer, a photo resist layer was patterned to protect driven electrodes working area as shown in d). In step e), 2nd metal layer was sputtered and was pattern to form driving input electrodes in step f).

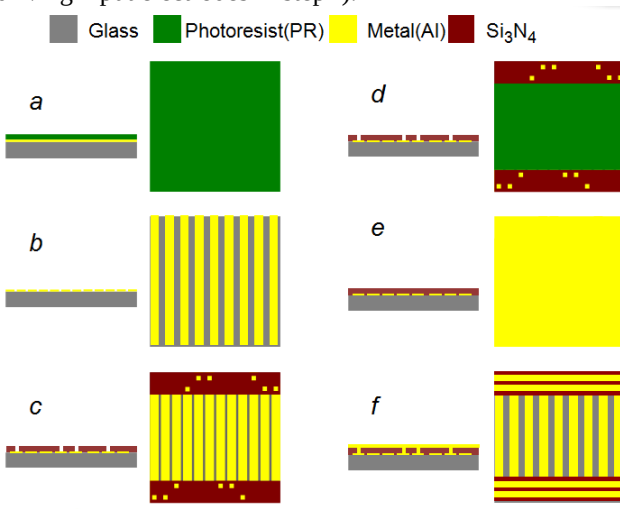

Fig.6 Schematic drawing of the fabrication process to realize multi layers driving circuit

IV - Conclusion

The dynamic period DOE for speckle reduction has been designed. A novelty electrical driving scheme is demonstrated. The designs have been simulated using ZEMAX and MATLAB for optimized speckle reduction. 14% speckle contrast has been achieved with the optimized design, i.e., the dynamic period DOE which consists of three gratings each of which has three different diffractive periods. The process flow for fabricating the DOE has proposed.

References

[1] J. W. Goodman, Speckle Phenomena in Optics: Theory and Applications (Roberts, 2007).

[2] S. Lowenthal and D. Joyeux, J. Opt. Soc. Am. 61, 847 (1971).

[3] J. I. Trisnadi, Opt. Lett. 29, 11 (2004).

[4] S. An, A. Lapchuk, V. Yurlov, J. Song, H. Park, J. Jang, W. Shin, S. Karagpoltsev, and S. Yun, Opt. Express 17, 92 (2009).

[5] M. N. Akram, V. Kartashov, and Z. Tong, Opt. Lett. 35, 444 (2010).

[6] Guangmin Ouyang, OPTICS LETTERS Vol. 35, No. 17 (2010)

[7] Vladimir Kartashov and Muhammad Nadeem Akram, "Speckle suppression in projection displays by using a motionless changing diffuser," JOSA A, Vol.27, pp.2593-2601, 2010

[8] G. Ouyang, K. Wang, M. N. Akram, and X. Chen, Proc. SPIE 7426, 742604 (2009).

[9] G. Ouyang, K. Wang, L. Henriksen, M. N. Akram, and X. Y. Chen, Sens. Actuators A 158, 313 (2010).

Integration of meso- and nano-scale objects by capillary assembly and adhesive transfer

Cyrill Kuemin[1,2], Lea Nowack[1,2], Cathrein Hueckstaedt[1,2], Emanuel Loertscher[1], Antje Rey[1,3], Nicholas D. Spencer[2], Heiko Wolf[1*]

[1]*IBM Research – Zurich, Säumerstr. 4, 8803 Rüschlikon, Switzerland*
[2]*Laboratory for Surface Science and Technology, Department of Materials, ETH Zurich, Wolfgang-Pauli-Strasse 10, 8093 Zürich, Switzerland*
[3]*Nanotechnology Group, Department of Mechanical and Process Engineering, ETH Zurich, Tannenstrasse 3, 8092 Zürich, Switzerland*

The special properties of micro- and nanoscale objects, such as metal and semiconductor nanoparticles, nanowires, nanotubes, or functionalized polymer particles make them promising building blocks for novel optical, electronic, or biosensing devices. Often, these small objects are prepared as colloidal suspensions or can be dispersed in a liquid to form a stable suspension. Thus, the fabrication of devices requires methods for efficient and accurate integration of particles from the liquid phase onto a solid surface. More complex device architectures may, in addition, entail the selective assembly of several different types of small objects at pre-defined locations or demand an assembly with the correct orientation when such objects are non-spherical.

We describe a technique that uses a combination of capillary assembly and printing with elastomeric stamps to fabricate defined particle arrays with high yield and accuracy. Capillary assembly is performed from an aqueous colloidal suspension onto a patterned template. The template is a silicone elastomer replica of a 3D-structured silicon master. In a subsequent transfer step, the assembled particles are printed onto the target substrate.

During capillary assembly, the meniscus of a colloidal particle suspension is dragged over the 3D-structured elastomer template (Figure 1)[1]. Particles get trapped and positioned at predefined geometric features of the template by capillary forces. The actual deposition process during capillary assembly is very sensitive to the geometry of the assembly traps. By going beyond particle deposition into simple holes, to fabricating templates with arrays of posts of specific shape and geometry instead, it was possible to assemble sub-micrometer polymer particles in a size-selective manner (Figure 2)[2].

Even non-spherical nano-objects, such as gold nanorods, lend themselves to capillary assembly in sparse arrays with single-particle resolution. In order to obtain high assembly yields, it is essential to reach high particle concentrations in a narrow zone directly at the meniscus (the accumulation zone). At a given colloid concentration, this can be achieved by controlling the temperature of the colloid and thus the evaporation rate at the meniscus. Under optimized conditions, assembly yields of more than 90% could be reached (Figure 3)[3].

When using short linelets (shallow holes with dimensions close to those of the nanorods) as assembly sites it is possible to control the position as well as the orientation of the assembled nanorods (Figure 4). Thus, these rod-shaped nanoparticles could be positioned in large numbers with unprecedented accuracy.

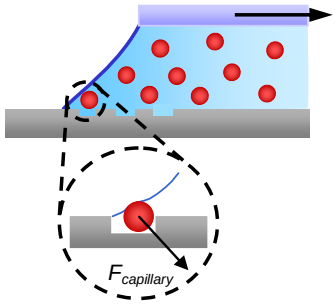

Figure 1: Schematic view of the capillary assembly step. The template consists of a patterned silicone elastomer. The meniscus of the colloidal particle suspension is dragged over the template, filling topographical structures with particles.

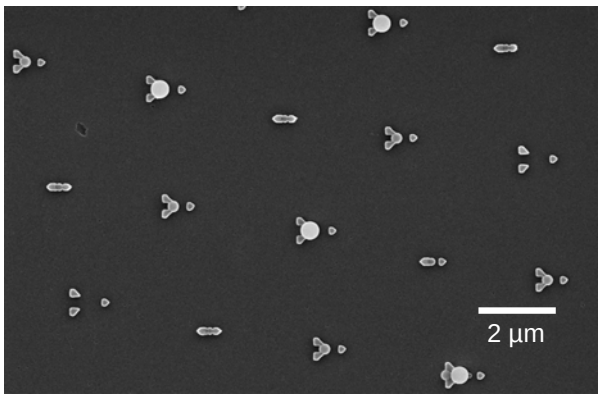

Figure 2: Scanning electron microscope (SEM) image of polystyrene spheres of different sizes, assembled sequentially into their corresponding assembly sites on a PDMS template.

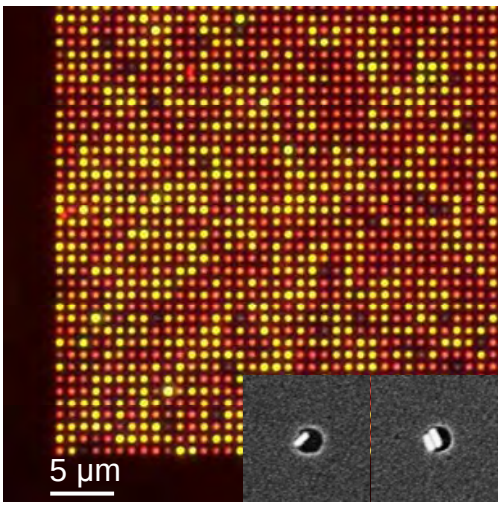

Figure 3: Dark-field optical micrograph of 25 nm x 74 nm Au nanorods assembled onto an elastomer template consisting of an array of circular holes (120 nm diameter, 40 nm deep). The inset shows SEM images of individual holes filled with Au nanorods.

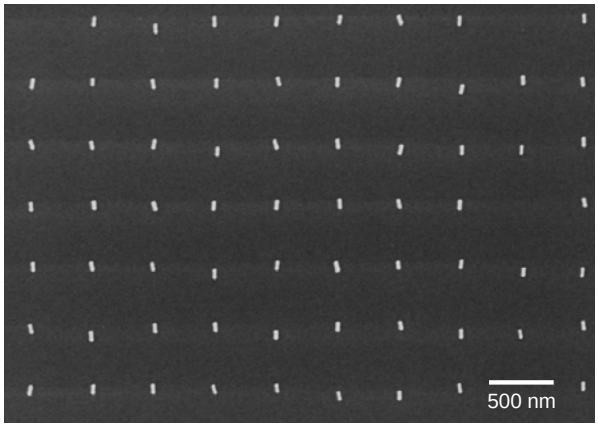

Figure 4: SEM image of an array of Au nanorods (25 nm x 80 nm) printed onto a Si substrate from a template with 37-nm deep linelets (50 nm x 120 nm) acting as assembly sites.

References

[1] Malaquin, L.; Kraus, T.; Schmid, H.; Delamarche, E.; Wolf, H. "Controlled Particle Placement through Convective and Capillary Assembly" Langmuir **2007**, *23*, 11513-11521

[2] Kuemin, C.; Hueckstaedt, K. C.; Lörtscher, E.; Rey, A.; Decker, A.; Spencer, N.D.; Wolf, H. "Selective Assembly of Sub-Micrometer Polymer Particles" *Adv. Mater.* **2010**, *22*, 2804-2808

[3] Kuemin, C.; Stutz, R.; Spencer, N.D.; Wolf, H. "Precise Placement of Gold Nanorods by Capillary Assembly" *Langmuir* **2011**, *27*, 6305-6310

HIGH PERFORMANCE THERMAL IMAGING FPA BASED ON SI/SIGE QUANTUM WELL THERMISTORS IN COMBINATION WITH NOVEL 3D WAFER LEVEL INTEGRATION CONCEPTS

T. Kvisterøy[1]

[1]*Sensonor Technologies AS; Horten, Norway*

***Abstract* — A new 3D integration concept for the fabrication of uncooled infrared bolometers using low temperature oxide-oxide wafer bonding to transfer the detector material from a sacrificial carrier wafer to a CMOS ROIC wafer has been developed at Sensonor. The legs supporting the bolometer pixels and connecting them to the ROIC are built underneath the pixel membrane. Mono crystalline Si/SiGe quantum wells with high TCR and low 1/f noise are used for temperature sensing. A second wafer level bonding step, based on Cu-Sn solid liquid inter diffusion soldering, are used for the vacuum encapsulation of the FPA.**

***Keywords :* Heterogeneous 3D integration, Quantum well thermistor, Non-conductive transfer bonding, Wafer level vacuum encapsulation, SiGe, MEMS, Micro bolometer, FIR focal plane array**

I - Introduction

Bolometers are detectors that convert a minute temperature change induced by incoming electromagnetic radiation into a measurable electrical signal. The uncooled infrared bolometers usually refer to resistive micro bolometers in which the temperature change is converted into a resistance change that can be measured and interpreted as image information. The progress achieved in the last years in the area of uncooled infrared bolometer technology has made it possible to reach performance levels that previously were only possible with cooled infrared photon detectors. Most of the reported uncooled bolometers are fabricated by building up a focal plane array (FPA), consisting of a multitude of pixels, directly on top of the pre-manufactured read out integrated circuit (ROIC) using thin layer deposition and patterning. This monolithic integration is limited to materials and processes that are compatible with the CMOS "substrate". Processing temperatures above 400-450°C are prohibited and therefore the choices for the infrared sensitive material (the thermistor) are limited to materials that can be obtained by processing at such low temperatures. Vanadium oxide (VOx) and amorphous silicon (α-Si) are examples of such monolithically integrated bolometer materials. VOx has demonstrated good performance, but it is a somewhat exotic material and difficult to make. Amorphous silicon is compatible with CMOS fabrication, but it exhibits inferior material characteristics to VOx resulting in more modest detector performance.

II – Technology

A novel noncooled micro bolometer, SB100, has been developed at Sensonor. It uses Si/SiGe quantum wells as temperature sensitive material. See Figure 1.

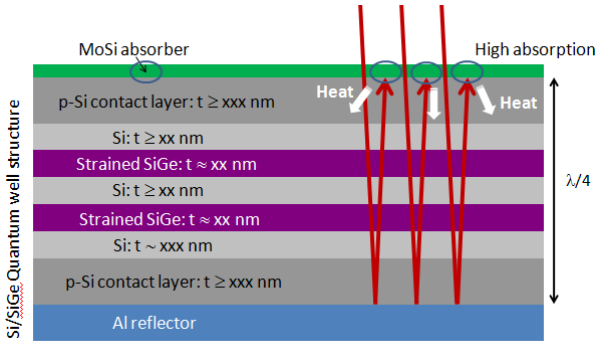

Figure 1*: Si/SiGe Quantum Well thermistor structure*

The thermistor material is transferred from a handle wafer to the CMOS wafer by low temperature oxide-oxide wafer bonding. Transfer bonding allows the use of high quality crystalline material for the temperature sensing. The pixel definition is completed after the removal of the sacrificial carrier wafer by deposition and etching processes that are compatible with the pre-fabricated ROIC. See Figure 2.

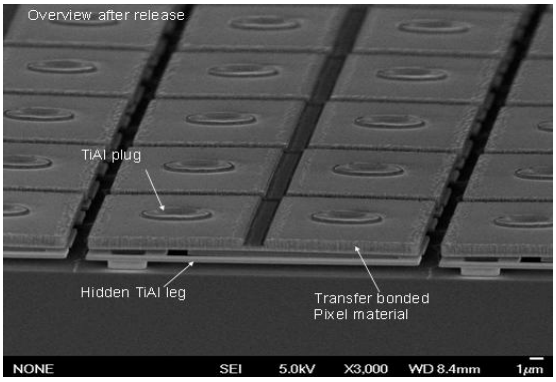

Figure 2*: Released Si/SiGe Quantum Well thermistor pixels with supporting legs underneath*

The advantage of this heterogeneous 3D integration resides in the improved performance of the thermistor layer and consequently of the FPA. High TCR (higher than 3% / K) and low 1/f noise together with an optimized pixel design lead to improved bolometer performances compared to those of existing devices. The legs that connect the pixels to the ROIC are fabricated prior to the transfer bonding and they are therefore situated

under the pixels enabling high fill factors. The pixels are subsequently released by anhydrous vapor HF of the sacrificial oxide layer. Finally the ROIC wafer containing the released FPA is bonded in vacuum with a silicon cap wafer providing the needed low pressure and hermetic encapsulation at low cost. Antireflection coatings and a thin getter layer are deposited on the cap wafer prior to bonding. See Figure 3.

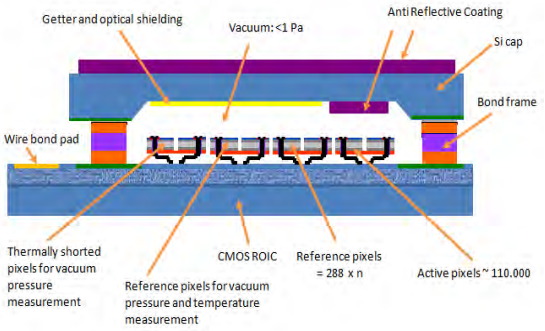

Figure 3*: The SB100 wafer level packaged micro bolometer-with Si/SiGe Quantum Well thermistor pixels*

II – Micro bolometer function

The SB100 consists of 384*288 pixels. It converts the projected LWIR (Long Wave IR) image to a digital data stream of image frames. No part of the SB100 is thermally controlled. The SB100 is intended used with a dedicated controller (FPGA or digital ASIC) acting as a provider of FPA configuration data as well as video frame readout timing master and frame data receiver on a per-line basis. The controller is assumed to implement per-pixel image correction functions based on static correction terms and relative temperature data from the SB100. To aid dynamic NUC (Non Uniformity Correction) the use of a mechanical shutter is assumed. See Figure 4.

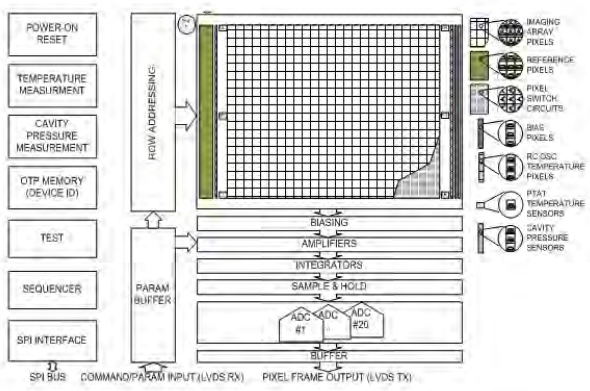

Figure 4*: SB100 micro bolometer functional block diagram*

TRIAXIAL ACCELEROMETER FABRICATED USING THE MULTI MEMS PROCESS WITH A DEEP REACTIVE ETCHING AS ADDITIONAL STEP

Luca Petricca[1], Christopher Grinde [1], Craig Lowrie[2] and Per Ohlckers.[1]
[1]*Vestfold university College; IMST, Borre, Norway*
[2]*Heriot-Watt University; MISEC, Edinburgh, Scotland*

***Abstract* — In this paper we present a micro-machined silicon accelerometer for monitoring post surgery heart's motion. The accelerometer has been fabricated by using the MultiMEMS multiproject wafer foundry process. In addition to the standard process, it has been used an extra deep reactive ion etching step, finalized to etch simultaneously 3 µm, 23 µm and 400 µm tranches. With the size of 4.2x2x1.5 mm3, the final device is small enough to be pulled out trough the patient chest few days after the surgery without re-operate the patient.**

***Keywords: Ischemia*, 3-D accelerometer, Multi project wafer, MultiMEMS, DRIE**

I - Introduction

One possible problem associated with heart bypass surgery is the risk for ischemia. Ischemia is mainly a post operative condition and it consists on a blood supply reduction that leads to tissue damages or malfunction. Recently it has been demonstrated that monitoring the heart motion can be used for early detection of it [1-3]
Accelerometers attached to the epicardium (the outer layer of heart tissue) can provide a precise measurement of the heart wall motion and thus revealing ischemia in the beginning stage.
The accelerometer should be removed within a few days after the bypass operation without extra surgery. In order to do this, the accelerometer and its biocompatible package, must be small enough to be pulled out of the patient chest trough the surgery stitches. The maximum device size must fit into a cylinder of 2.5 mm diameter and 5 mm height. Despite even smaller accelerometer are already present on the market (e.g.[4]), they in general require extra circuitry in close proximity of them that makes them inconvenient for such application. Here we present concept, design, fabrication and initial measurements of a piezo-resistive accelerometer build for such specific application that does not require any extra components nearby it.

II - Experimental Details

A. Working Principle

The 3-D accelerometer here presented consist of two similar 2-D accelerometers rotated by 90 degree each other (Figure 1). Each 2-D accelerometer is able to sense one in plane acceleration (X or Y axis) and one out plane acceleration (Z- axis). In this way we have a full 3-D acceleration sensor with a measurement redundancy on z-axis.

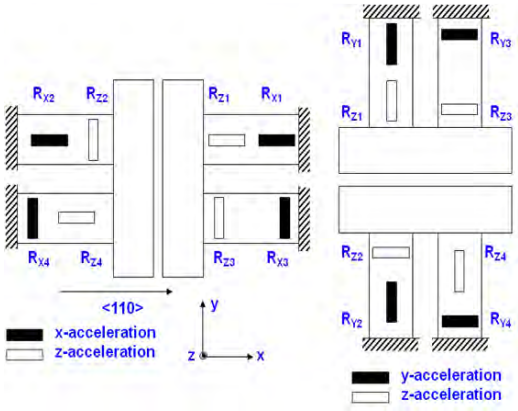

Figure 1 : 3D Accelerometer overview: consist of two similar 2-D accelerometer rotate by 90 degree each other.

The sensing elements consist of 16 buried piezo-resistors to form 4 Wheatstone bridges (Figure 1): one for X axis, one for Y axis and two for Z axis (redundant).
The mass displacement will create a resistance variation ΔR of the piezoresistive elements proportional to the stress as shown in (1) [5]:

$$\Delta R = R\left(\pi_L \sigma_L + \pi_T \sigma_T\right) \qquad (1)$$

Where σ_L and σ_T are the longitudinal and transversal stresses respectively, while π_L and π_T are the longitudinal and transversal piezo- resistive coefficients.

During in plane acceleration (X or Y axis) the masses tend to bend in accord to Figure 2, while during out of plane acceleration the masses will displace in accord with Figure 3.

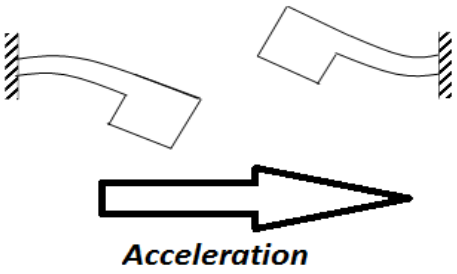

Figure 2 : Masses behavior during in plane acceleration

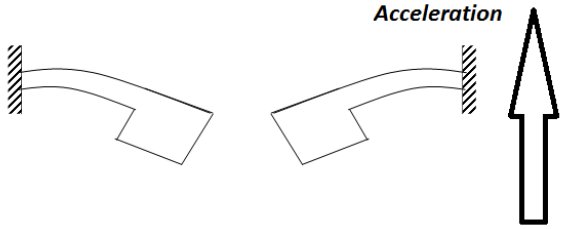

Figure 3 : Masses behavior during out of plane acceleration

The resistor position and orientation (Figure 1) together with the applied stress will determine an imbalance of the Wheatstone bridge proportional to the acceleration applied.

For example in the situation illustrated in Figure 3 the Wheatstone bride sensing Z acceleration is reported in Figure 4 (a). It is possible to see that both R4 and R1 tend to increase their value while R3 and R2 decrease their value.

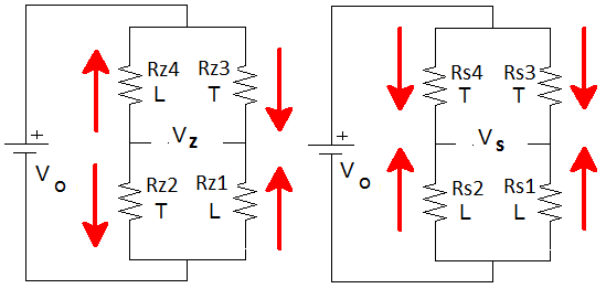

Figure 4: Wheatstone Bridge for Z-axis (a) and Y-X axis (b) sensing when subject to out of plane acceleration shown in Figure 3 (up arrow indicate an resistance increasing while letter L and T mean respectively Longitudinal and Transversal)

In this situation the bridge is not anymore balanced and the signal V_z coming out from Z-axis Whetstone Bridge is:

$$\begin{aligned} R_{Z1} &= R + \Delta R \\ R_{Z2} &= R - \Delta R \\ R_{Z3} &= R - \Delta R \\ R_{Z4} &= R + \Delta R \end{aligned} \qquad (2)$$

$$V_z = V_O \frac{(R+\Delta R)(R+\Delta R)-(R-\Delta R)(R-\Delta R)}{(R+\Delta R+R-\Delta R)(R-\Delta R+R+\Delta R)} =$$

$$= V_O \frac{\Delta R}{R} \qquad (3)$$

We can see the voltage V_z is proportional to the applied stress, and thus to the acceleration.

However, if we repeat the calculation for X- (or Y-) bridge Figure 4 (b), we find that:

$$\begin{aligned} R_{S1} &= R + \Delta R \\ R_{S2} &= R + \Delta R \\ R_{S3} &= R - \Delta R \\ R_{S4} &= R - \Delta R \end{aligned} \qquad (4)$$

$$V_S = V_O \frac{(R+\Delta R)(R-\Delta R)-(R+\Delta R)(R-\Delta R)}{(R+\Delta R+R-\Delta R)(R+\Delta R+R-\Delta R)} =$$

$$= 0 \qquad (5)$$

Where the subscript "S" represent either of X-bridge or Y-bridge (same situation).

The output signal V_S is equal to 0 since the piezoresistor variation in the bridge is symmetrical keeping the bridge balanced. This means that in case of out of plane excitation in only the z-axis bridge will give a signal proportional to the acceleration.

We can easily extend this demonstration to in-plane excitation (Figure 2). In this case we will find that the Z-axis bridge will not give any signal, while the X-bridge (or Y-bridge, depending on which 2D accelerometer we are considering) will give an output signal proportional to the in plane acceleration.

B. Process Used

The device has been fabricated by using the Multi-MEMS MPW process as described in [6-7].

C. Design

It is desirable to have equal sensitivities for all three axes. To achieve this with beam-mass accelerometers as described here, it is important to locate the center of gravity of the masses such that it is equal for all for both the in-plane and the out-of-plane directions.

With reference to Figure 5, it means that the distance L_b must equal L_z (where cg is the center of gravity of the mass).

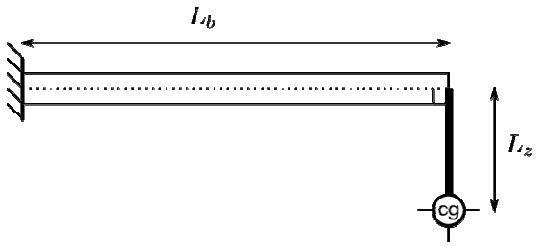

Figure 5: Sketch of the center of gravity (cg) position in beam-mass system.

One way to achieve this is by using a folded mass design as illustrated in Figure 6 which allows positioning the center of gravity of the mass at the beginning of the beam.

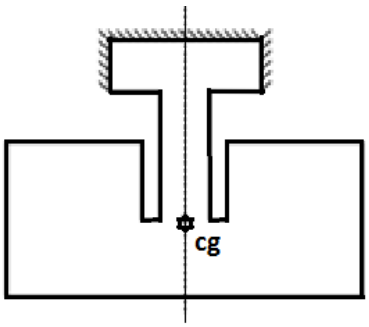

Figure 6: Folded mass design: (where cg is center of gravity)

If the mass walls were perfectly vertical, the distance Lz would be exactly half of wafer thickness. However, due to the wet bulk etching process (anisotropic), the dominating plane of the mass wall will be the 111} plane and thus the position of the center of gravity in z-direction is shifted towards the top surface of the mass (Lz <200 µm).

The total size of the device is around 4.2mm x 2 mm, small enough to satisfy the application requirements discussed in the introduction paragraph.

III - Results and Discussion

A. Visual inspection

A top view micrograph of the fabricated device is included in Figure 7.

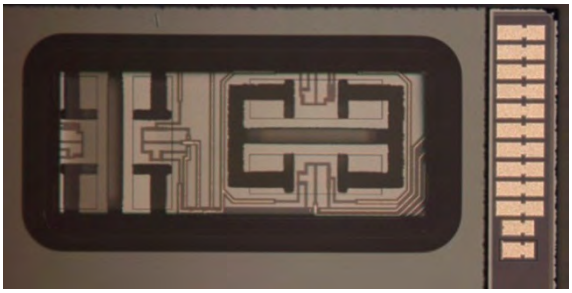

Figure 7: Accelerometer top view. It is possible to recognize the two 2-D accelerometers rotated by 90° each other. Image got by using optical microscope

Figure 8 shows one picture of the device with back illumination. By using this technique it was possible to observe that the masses are completely released and they are supported only by the beams. Furthermore, it is also possible to notice their extent and location (in yellow) that are in the expected place (no mask miss alignments). Another observation that must be done regards the corner of the devices. Indeed in the four corner regions it seems that the silicon is not completely etched; however further inspection have permitted to conclude that the no-released corned is only a optical effect due to the curvature of the glass etched region present on top of the device.

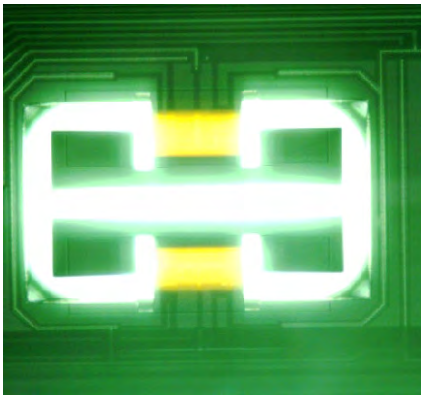

Figure 8 Back-illuminated accelerometer's picture. We can notice that the masses are completely released. The yellow areas are the beam regions.

B. measurements set up

The encapsulated devices have been tested by using a custom made set up as illustrated in Figure 9. It compares the signal from the accelerometer with that of a reference accelerometer. The signals are amplified and data acquired with a Digital acquisition board (DAQ) from National Instrument. The same board has also been used for piloting the shaker. Both for the reference accelerometer and for the testing accelerometer were supplied with 5V.

The core of the amplification circuits was one INA101 instrumental amplifier, with gain set to 94 by using external discrete resistors mounted on a custom PCB.

More detailed information regarding the equipment used is reported in *TABLE I.*

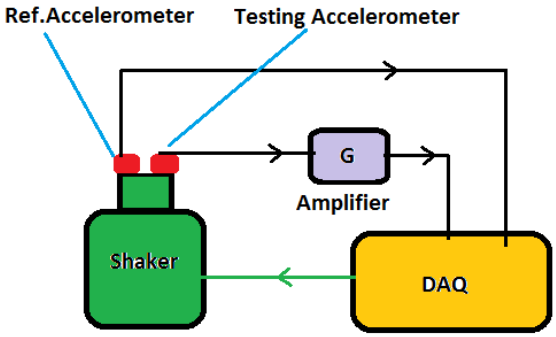

Figure 9: Set up representation. The signal coming out from the accelerometer has been acquired by using a Digital Acquisition Board. The same DAQ has also been used for generating the control-signal for the shaker.

TABLE I: Set up equipments: description

Device	Model
Shaker:	Bruel and Kjaer Vibration Exciter Type 4809
Power amplifier of the shaker	Bruel and Kjaer Power Amplifier Type 2706
Reference acce-	Analog Devices ADLX320

lerometer	dual-axis accelerometer
Accelerometer amplifier	INA101 instrumental amplifier with gain set to 94
DAQ	National Instrument
Power Supply 1	ITT Instruments AX 322 metrix twin supply (±15V for amplifier card)
Power Supply 2	GW Laboratory DC Power Supply Model: GPS-3030 (+5VDC for Wheatstone Bridges)

C. Measurement results

Due to the small signal levels and to mechanical stability problems of the set up system, the sensitivity was calculated only in z-direction. The excitation frequency of the shaker was set to 100 Hz.

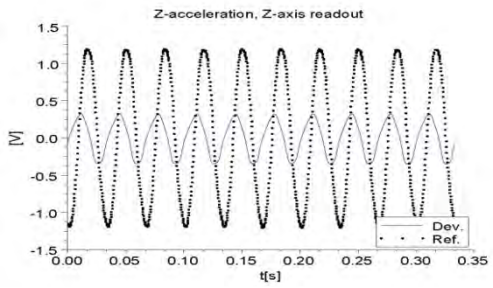

Figure 10: Signals from reference accelerometer (red sinus) and testing accelerometer (white sinus)

Figure 10 shows the signals (in red the reference accelerometer, while in white the testing accelerometer). The calculated sensitivity is around ~0.04mV/V/g in Z axis read-out during z axis motion. Furthermore, Figure 11 shows the cross axis sensitivity for the z-axis bridge (Z axis read-out during x axis excitation).

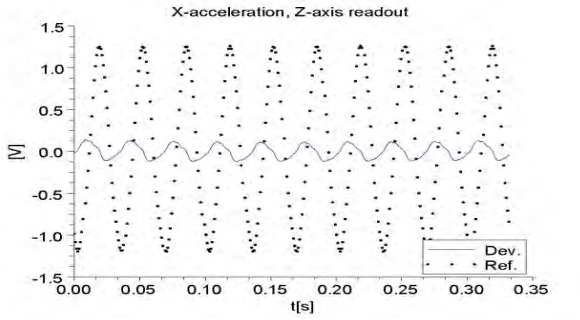

Figure 11: Cross axis sensitivity for z axis signal. In red the reference accelerometer signal, while in white the testing accelerometer signal

We can notice that the there is a phase shift of about 90º. The phase shift between the test accelerometer and the reference accelerometer is due partly to the capacitive sensing principle of the reference accelerometer, but also due to differences in signal conditioning with bandwidth filtering introducing different phase shifts for the output from the amplified test accelerometer and for the reference accelerometer.

IV - Conclusion

A tri-axial accelerometer has been fabricated using the MultiMEMS Foundry Process. The small size of the device (4.2mm x 2mm) and the absence of external components nearby it, make it suitable for the post surgery heart monitor application.

Both the visual inspection and the initial measurements demonstrate the device perform as expected. In the future work we will improve the measurement set up, increasing the mechanical stability of the system and trying to further reduce external noise. By doing this we expect that will be possible to run a full characterization of the device.

References

1. Elle, O.J., et al., *Early recognition of regional cardiac ischemia using a 3-axis accelerometer sensor.* Physoilogical Measurments, 2005. **26**: p. 429-440.
2. Halvorsen, S., et al., *Feasibility of a three-axis epicardial accelerometer in detecting myocardial ischemia in cardiac surgical patients.* Journal of Cardiovascular Surgery, 2008. **136**: p. 1496-1502.
3. Halvorsen, P.S., et al., *Detection of myocardial ischemia by epicardial accelerometers in the pig.* British Journal of Anasthesiology, 2008. **102**(1): p. 29-37.
4. (2010) VTI Technologies CMA3000 Series. http://www.vti.fi/en/products/accelerometers/consumer_electronics/cma3000_series/.
5. Stelzer, O.N.T.a.E.L., *Piezoresistive Properties of Silicon Diffused Layers* Journal of Applied Physics **Volume 34**(Issue 2).
6. P. Ohlckers, L.P., C. Grinde, *A silicon micromachined triaxial accelerometer using the multimems mpw process with additional deep reactive ion etching as post-processing*, in *MME2010*. 2010.
7. Grinde, C., et al., *Two clover-shaped piezoresistive silicon microphones for photoacoustic gas sensors.* Journal of Micromechanics and Microengineering,, 2010. **20**.

GSM/GPS/INS SYSTEM FOR URBAN RAILWAY MONITORING BASED ON MEMS INERTIAL SENSORS

Emil Iontchev[1], Ivaylo Simeonov[2], Rosen Miletiev[2]

[1]*Higher School of Transport "T. Kableshkov" 158 Geo Milev Street, Sofia, Bulgaria*
[2]*Faculty of Telecommunications at Technical University of Sofia, 8 Kl. Ohridski Blvd, Sofia, Bulgaria*

***Abstract* — The measurement and valuation of the tramway (horizontal or vertical offset and surpass) are the main tasks of the section which is responsible for the tramway support, control and safety. The current paper suggests GSM/GPS/INS system which is capable of real-time monitoring and record of the tramway status. The system also may analyze the tramway condition and sends the data via GSM network to the database. The gathered statistic allows collecting information of the tramway condition for a long period of time. It also may alarm if the tram acceleration overcomes the defined limit and the tram stability may be decreased. The dangerous points of the tramway may be marked and colored on the map in the control center. These points of the tramway have to be repaired immediately or the system may alarm the tram drivers to prevent dangerous situations. The low cost GPS receivers, GSM transceivers and MEMS inertial sensors allow creating low cost measurement system, which could be installed on each vehicle.**

Keywords : **MEMS sensor, tram railway**

I - Introduction

The safety and comfort motion of the urban trams is defined by the condition of the tramway and the dynamic interaction between the rails and vehicle. The tram operations influence over the rail parameters, so the rail deviation is increased from their initial position. The rail faults which depend from the geometry may be defined as periodic, non-periodic or custom ones. The rail faults also conduct to the vibration generation jointly with the tram wheels. If the generated vibration forces are periodic ones and their frequency is close to the natural frequencies of the tram, then the vibrations lead to the cyclic deformations of the railways.

The tram reaction of these deformations is strongly individual and it is not proportional to the deformation size. It depends from the vehicle specific characteristics, railway deformation length and the tram speed.

The measurement of the railway current condition may be accomplished with specialized motor cars [1] and the railway geometry may be analyzed according to the measurements. This procedure requires expensive motor cars and often the railway condition is evaluated according to the manual railway measurements. The correlation between the obtained valuation and the generated forces is inadequate, but the passenger comfort depends from the dynamic forces. This is the reason to develop and evaluate the measurement systems, which are capable to measure the dynamic reactions between the railway and the tram.

The first main parameter of the dynamic reaction is the movement noise. The measurement of the generated noise is based on the microphone dynamics and this method is often used to determinate the wave wear of the rails [2]. The European standard EN3095 [3] defines the permissible levels of the generated noise from the railway roughness.

The second parameter is defined as dynamic forces, which effect on the wheel pair axes. The publication [4] proves that the amplitude of the generated dynamic forces is highly correlated to the railway roughness.

The measurement of these forces is accomplished by the strain gauges, which are stick on the wheel [6] or translation sensors and tens meters on the rails [7]. The force amplitude calculation is described in the European standard EN14363 [8]. Their amplitude is used as a criterion for valuation of the railway safety and its loading capacity.

The third parameter is defined as vertical and horizontal accelerations and tram angular rate. The acceleration amplitudes are used as an index to control the rail failures. The acceleration measurements are accomplished by linear or angular rate accelerometers, which are installed on the tram or on the rails [9]. This method gives the valuation of the combined roughness of the rails and the wheels. In these systems [10] the roll value is also measured to obtain the accelerations which are caused by the varied rail level.

II - Experimental Details

The low cost of the GPS receivers and MEMS inertial sensors allows developing low cost measurement systems, which may be installed on the trams to ensure real-time monitoring of the railway condition. The measurement system is a single complete device which is supplied from the motor car electrical system. Its internal structure is described at our previous paper [11] and the main system components are shown at Figure 1.

The main system component is recognized as a three axes linear accelerometer LIS3LV02DQ, produced by ST, and combined GPS receiver and GSM module TELIT GE863-GPS. The measurement data are stored as a binary numbers in an external memory card. The measurement system is installed on the terminal clam and is firmly fixed to ensure proper transfer function between the rails and the system. The integrated GSM module transmits the GPS data to the server to realize real-time monitoring of the tram position. The acceleration data are not transmitted via GSM network due to

their high volume but they could be analyzed directly in the device to detect the critical points. The detection of the critical point may be transferred to the server to point the railway fault positions.

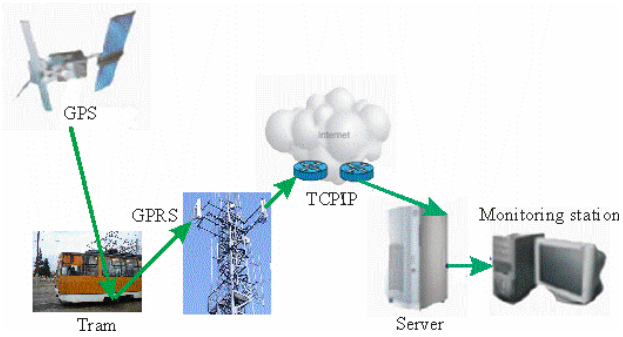

Figure 1: *Components of the measurement system*

The obtained measurement data are firstly read from the SD card. During this operation the digital data are converted to the corresponding acceleration data, because the SD card stored the data in a raw format (binary one) to ensure a maximum capacity. Secondly the acceleration integral valuation is calculated for the chosen tramway length. The sections with the biggest acceleration values are separated and shown on the graphics. These sections are analyzed further at the time and frequency domain. The block diagram of the processing algorithm is shown at Figure 2. The described functions are realized in the MATLAB environment.

The connection between the acceleration values and the frequencies are defined according to relation [12]:

$$\frac{d^2}{dt^2}x(t) \leftrightarrow (j2\ f)^2 X(f), \qquad (1)$$

where $x(t)$ - the accelerometer shift in the time domain, $X(f)$ - Fourier transform of the $x(t)$ vector.

The highest shifting is generated at the frequency band 0÷10Hz, therefore the measurement data are filtered by low pass filter. This procedure is accomplished by Low_fft_filter_f function.

The values of the terminal clam shifting are calculated by numerical integration [13]. The critical point in the numerical integration is connected with the null bias offset value and variation of the accelerometer output data [14]. This bias offset is removed by the second-order high pass IIR filter, which is realized by the Hi_pass_modif_f function. The raw accelerometer data contains a high frequency noise, which is generated by the vibration profile. This noise is removed by a wavelet transformation [15].

The vertical shock movements of the tramway are generated by the non-linear suspension elements. The described functions Fft_spgrama_f, WP_spgrama_f, ACF_fft_draw_f realize a window Fourier transformation, wavelet packet and parametric spectrum analysis respectively to calculate the data spectrograms. The RMS and peak values may be also calculated by the Rms_func and Pk2pk_f functions respectively. The acceleration threshold is defined by the RMS statistic parameters. If the acceleration of the analyzed point overcomes this threshold, then the point geographic coordinates are stored separately. As the point analyze is accomplished then all critical points are shown on the map. This information is directed to the railway company for an inspection.

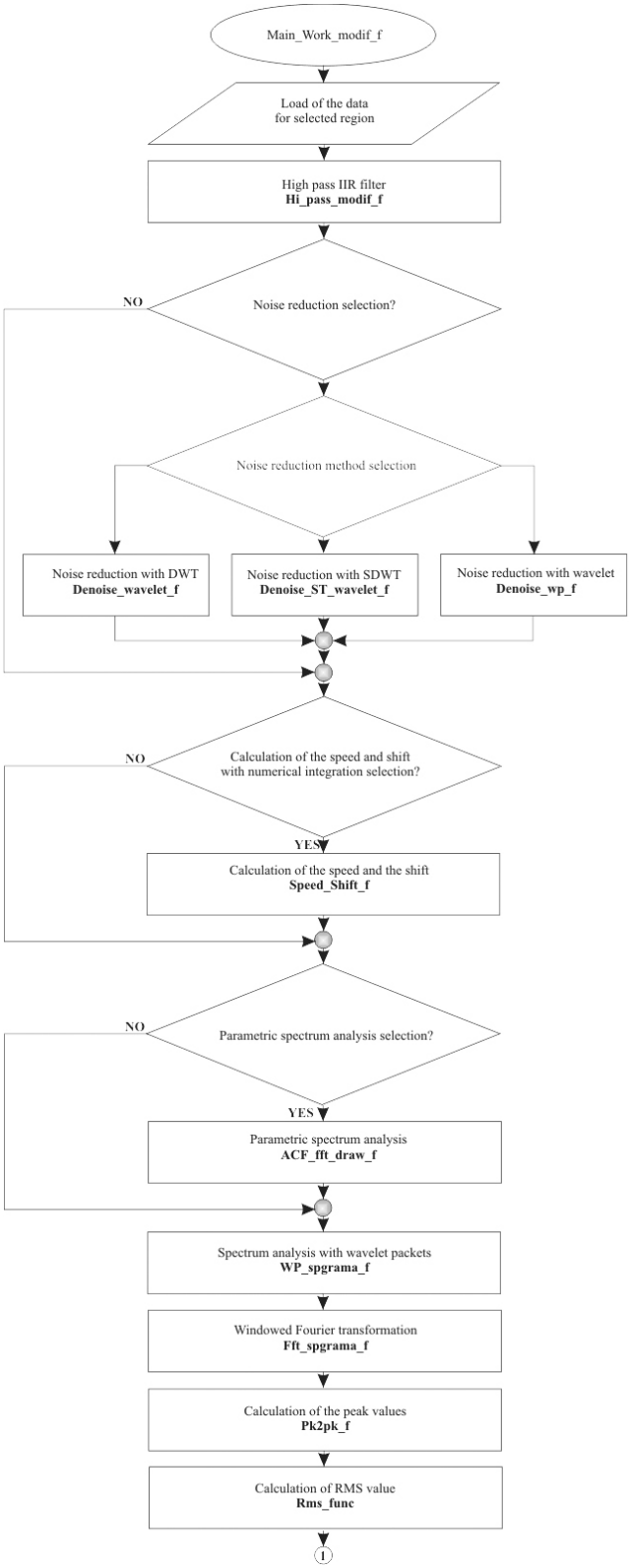

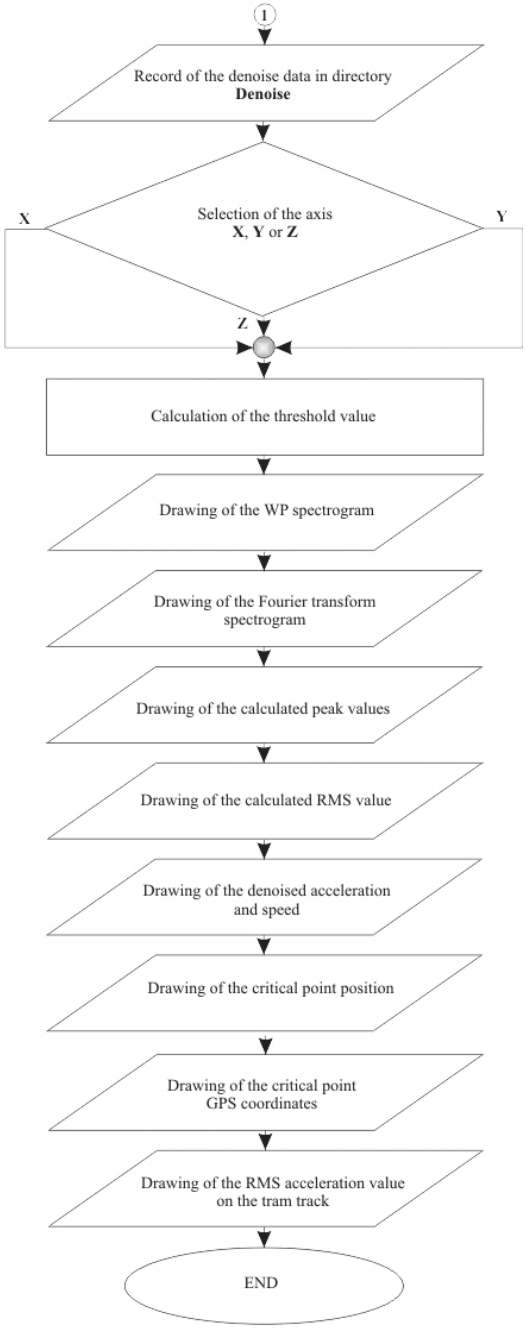

Figure 2: *Data processing algorithm*

III - Results and Discussion

The experimental data are collected using the described measurement system, which is installed on the 6-axes tram motor car T6M 400. Its suspension consists from three carts: power ones (I and III-rd) T65 and supporting one (II-nd cart) type $T_{sp}65$. The carts consist of two-stage spring suspension (cylindrical springs) and the H-shaped open type cart frame.

The experimental data are collected from the two tram transitions for each direction – forward and reverse. The railway critical points are detected by the described algorithm and are shown at Figure 5. The results from the accomplished analysis are shows below as follows:

- Figure 3 represents all critical points;
- Figure 4 represents the critical points for each direction separately;
- Figure 5 represents a wavelet spectrogram for the first tram transition;
- Figure 6 represents a wavelet spectrogram for the second tram transition;
- Figure 7 represents windowed Fourier analysis.

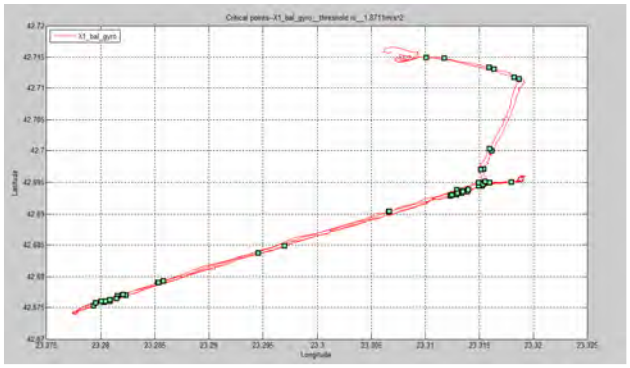

Figure 3: *Visualization of the tramway critical points*

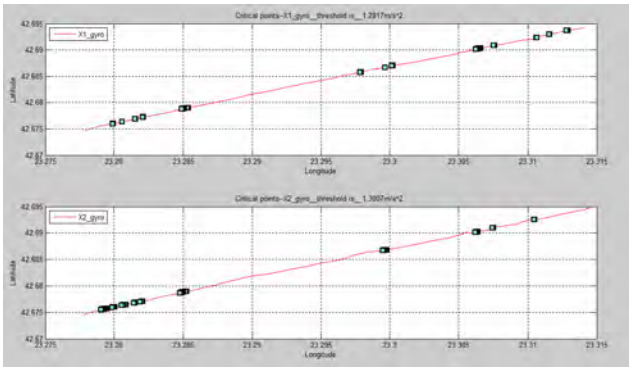

Figure 4: *Visualization of the railway critical points for each direction*

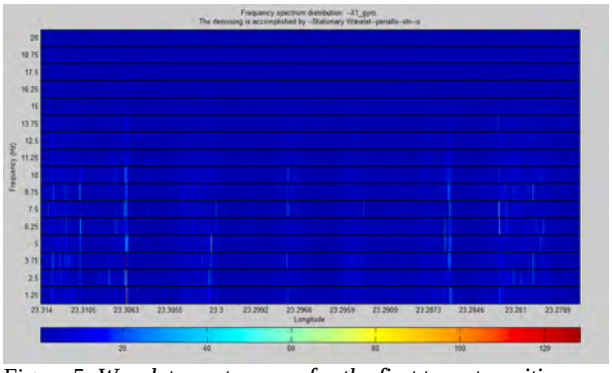

Figure 5: *Wavelet spectrogram for the first tram transition*

Since the GPS receiver accuracy is approximately equal to 2÷5 meters, the inspected railway length has to be extended to 10m at the both directions. The distribution of the peak values related to the tram speed is shown at Figure 8. It is clearly visible that the acceleration peak values have not been correlated to the highest speed and are generated by the railway roughness. The speed values are divided with coefficient 2.0638 to ensure best visualization of the results.

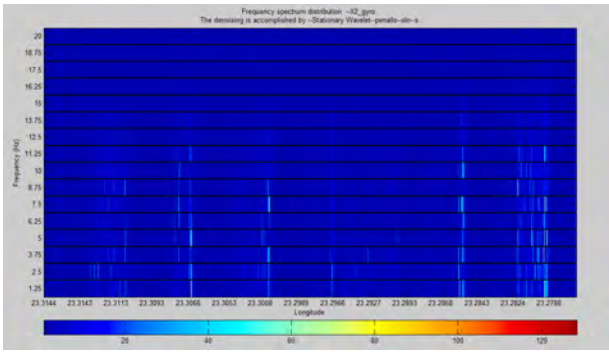

Figure 6: *Wavelet spectrogram for the second transition*

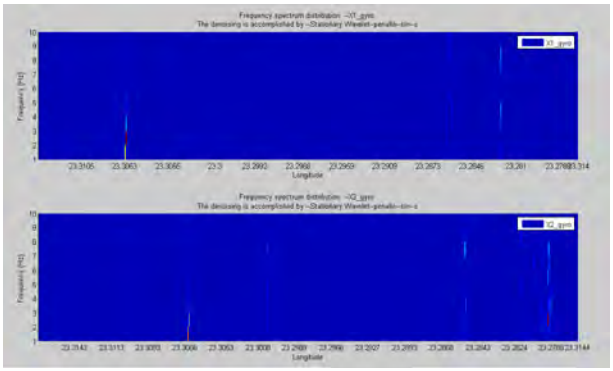

Figure 7: *Fourier transformation spectrogram of the acceleration data*

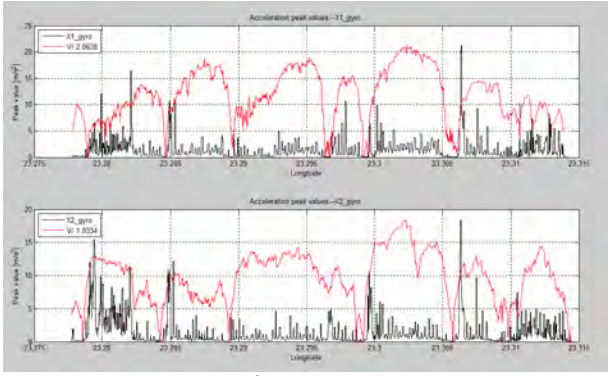

Figure 8: *Distribution of the acceleration peak values and tram speed*

IV - Conclusion

The current paper discusses the GSM/GPS/INS measurement system which is capable to detect railway faults and transfers the critical point positions to the server to alarm for the tramway dangerous places. The proposed analysis algorithm and the obtained experimental data from the tram motor car show the system ability to detect the tram faults in a real-time and to fulfill the transport safety levels.

V - Acknowledgement

This paper was prepared and supported by the National Fund under contract number No.DTK02/2-2009.

References

[1]. E. Sackl, The EM-SAT 120 Track Survey Car, an integrated part of the track geometry data base of the Austrian Federal Railways ÖBB, *Railway Technical Review*, 2/2004, pp.39-43

[2]. Y. Hayashi, T. Kojima, H. Tsunashima and Y. Marumo, Real time fault detection of rail way vehicles and tracks, *Railway Condition Monitoring* 2006, pp. 20-25

[3]. European Standard EN ISO 3095:2005: *Railway Applications—Acoustics—Measurement of Noise Emitted by Railbound Vehicles*, August, 2005.

[4]. Hawari, H. M., Murray, M. H., Correlating track forces and track profile, *Conference on Railway Engineering* CORE2006.

[5]. Jan Spännar, A new approach of assessing rail roughness, *The Swedish Railway Administration*, Banverket

[6]. Per Gullers, Lars Andersson, Roger Lunden, High-frequency vertical wheel–rail contact forces—Field measurements and influence of track irregularities, *Elsevier Wear* 265, 2008, 1472–1478

[7]. Yoshihiro Suda, Hisanao Komine, Kosuke Matsumoto, Yasunobu Endo, Takuji Nakai, Masuhisa Tanimoto, Feedback friction control between wheel and rail by detecting yaw moment of wheelset, *Elsevier, Wear* 265 (2008) 1512–1517

[8]. EN 14363, Railway applications – *Testing for the acceptance of running characteristics of railway vehicles – Testing of running behaviour and stationary tests*, 2005.

[9]. E. Verheijen, A survey on roughness measurements, *Journal of Sound and Vibration* 293 (2006), pp 784–794

[10]. H. Tsunashima, T. Kojima, Y. Marumo, A. Matsumoto and T. Mizuma, Condition monitoring of railway track and driver using in-service vehicle

[11]. Iontchev E. Iv. , Rossen Miletiev R. G., Event data recorder for land vehicles and cargo, *V International scientific conference "Trans–Mech–Art–Chem"* 2008, MIIT, pp 91-93

[12]. Openheim A., Whilski A., Yung – Signals and systems, Sofia, *Technics*, 1993

[13]. John H. Mathews, Kurtis D. Fink, Numerical Methods Using MATLAB, Third Edition, *Prentice Hall*, Upper Saddle River, NJ 07458

[14]. Yonchev E, Miletiev R. Arnaudov R. Algorithm for signal processing from an accelerometer measuring dynamics of interaction vehicle-railway track. *Machines, technologies, materials, International virtual journal*, ISSN 1313-0226, ISSUE 8-9 / 2010, pp. 25-28

[15]. Misiti Michel, Misiti Yves, Oppenheim Georges, Poggi Jean-Michel, Wavelet Toolbox™ 4, User's Guide, *The MathWorks, Inc.*, 1997-2009, p.1-27, p.1-39, p.6-100

FABRICATION OF AN ARRAY OF SILICON MICROSCALES FOR THE MONITORING OF CHEMICAL PROCESSES

M. Lacolle[1], I.R. Johansen[1], D. Wang[1], S. Moe[1], H. Sagberg[2], S. Clausen[3], A. Karlsson[4] and D. Akporiaye[4]

[1]*SINTEF ICT, MiNaLab, Oslo, Norway*
[2]*GasSecure, Oslo, Norway*
[3]*SINTEF ICT, Optical Measurement Systems and Data Analysis, Oslo, Norway*
[4]*SINTEF Materials and Chemistry, Process Chemistry, Oslo, Norway*

***Abstract* — We present the fabrication and demonstration of a two-dimensional array of scales micromachined in silicon. Each scale consists of a platform suspended by a spring. The mass on each scale is measured from a distance by a camera, which is imaging the fringe pattern that arises from optical interference in the gap under each spring scale. A diffractive lens at the bottom of the gap separates the fringe signal from unwanted reflections and directs this signal towards the camera. When a mass deflects a scale down, the gap narrows and the fringe pattern is getting tighter. Operation at temperatures as high as 700 C was demonstrated, which makes the device useful for the monitoring of high temperature chemical processes.**

Keywords : microscale, optical MEMS, diffraction.

I – Introduction

Some chemical processes can be monitored by measuring the mass of a recipient containing a liquid in a reaction with a gas, which is called gravitometry. Often this occurs in a reaction chamber or reactor, at high temperatures, where traditional methods for reading the position of a micromechanical sensor cannot be used (such as piezoresistors or electrostatic readout).

In this article, we demonstrate an array of microscales that can be read out optically and at a distance from the microscales themselves. The electronic component (consisting in this case of a light source and a camera) are placed outside the reaction chamber where the microscales are placed. This way the chamber can be warmed to several hundreds of degrees C without impairing the functioning of the electronics. Furthermore, such an optical readout setup can be realized with off-the-shelve components.

Another difficulty associated with operation at high temperatures is that bimorph stress will bend micromechanical structures consisting of several layers of different materials. This has the adverse effect of displacing the scale platforms, giving a wrong readout of the mass on each scale. To solve this problem we have fabricated a structure consisting exclusively of silicon and silicon oxide.

II –Operation principle

The construction consists of two parts with different functionalities: a mechanical part that is micromachined in a silicon-on-insulator wafer, and an optical part that is micromachined on a standard wafer. The two wafers are bonded together by means of high temperature fusion bonding.

The mechanical part of the scale consists of a centre platform, suspended by an annular spring, as shown in Figure 1. Each scale has an axial symmetry, and the spring is simply a thinner silicon torus around the platform. Increasing the mass placed on a platform bends the annular spring as the platform moves down. The optical wafer consists of 2-level diffractive lens etched in silicon. The optical wafer was thinned in some parts just under the scales, in order to limit the attenuation of light through silicon. The back of the spring is separated from the diffractive lens by a 8 µm gap, in order to allow vertical deflection of the platform-spring structure.

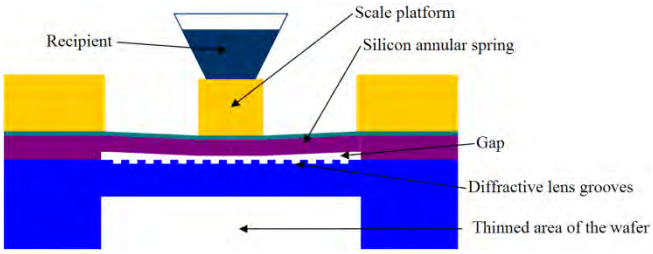

Figure 1. The different parts of a scale element: The optical wafer is shown in blue. The mechanical wafer consists of three layers, a 300 µm thick silicon substrate (yellow), a thin oxide layer (green) and a 35 µm thick silicon device layer (purple).

The basic principle is that increasing the mass in a recipient moves the underneath platform down, causing a progressive reduction of the gap situated under the scale platform and its spring. The principle for optical readout is very similar to that used to read the position of the microphone membrane described in [1].

Basically, the gap acts as a Fabry-Perot cavity where optical interference occurs. The light intensity reaching the camera from a place just under a scale depends on 1) the intensity of the light reflected by the Fabry-Perot cavity at this location and 2) the diffraction efficiency of the diffractive lens, both of which changes with the gap length. Thus the camera sees a fringe pattern consisting of concentric rings under each scale. This simple optical setup ensures a good contrast in the images, thanks to the diffractive Fresnel lens that separates the fringe signal from unwanted reflections and directs it off-axis towards the camera. When the scale platform moves

down, the gap gets narrower in the middle of the scale, and the density of the rings increases, as illustrated in Fig. 2.

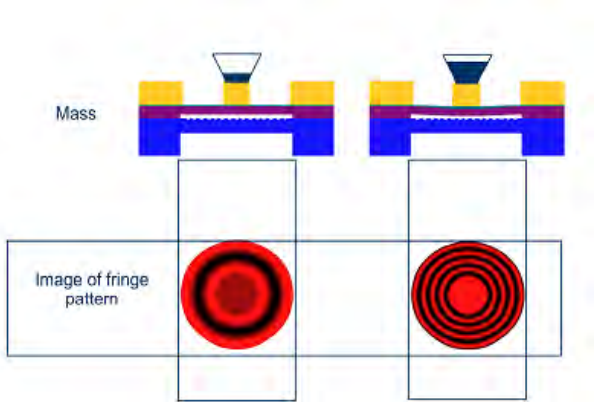

Fig. 2. The left scale has a low mass on top of it, and the annular spring is little bent. The scale shown on the right is loaded with a higher mass, bending the spring more and resulting in a fringe pattern underneath consisting of tighter rings.

III – Measurement setup

The measurement setup consists of a reaction chamber enclosing an array of recipients, each standing on its own scale, as shown in Fig. 3. A 4x4 scale array fabricated in silicon can be seen in Fig. 4. The vertical deflection of the scales is measured optically, by imaging the fringe pattern under each scale. The scale array is lit by a quasi-monochromatic light source, such as a LED. The fringe patterns are imaged by a camera, which is placed outside the reaction chamber. The camera can either be a standard and relatively inexpensive CCD, but for operation at temperature higher than 400° C, we will see that an InGaAs camera is required. Note that the light source and camera "see" the scale array through a window as they are placed outside the high temperature chamber.

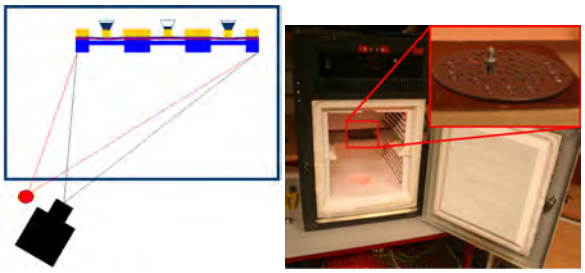

Fig. 3. Measurement setup (left): The light source is shown as a red dot, just over the camera, under the reaction chamber. The actual setup was enclosed in an oven with an opening under (right), and the scales were loaded with objects of known mass (such as the screw in the picture).

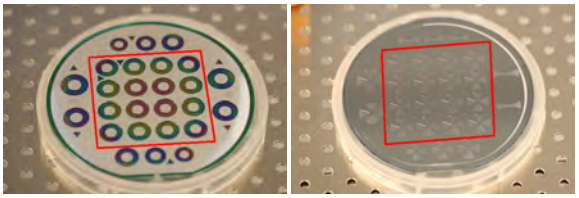

Fig. 4. Pictures of the fabricated devices: On the mechanical side (left), the scale platforms can be seen as circular areas enclosed by annular springs, while on the optical side (right), parts with a clover shape of the wafers were thinned. The red parallelepipeds represent the 4x4 scale array, while the structures outside were for test purposes only, and will be sawed away in a final version of the device.

IV – Fabrication

We have fabricated arrays of micro scales with a pitch of 13 mm, so that 16 scales fit on a 4-inch wafer, as seen in Fig. 4. If more scales are needed, it is possible to increase the wafer size or to assemble several sawed wafers side by side.

The array of scales were fabricated using fusion bonding of two silicon wafers, a silicon-on-insulator wafer on which was implemented the mechanical part of the scale, and a standard silicon wafer with the optical function of the device. The process was a combination of dry etches with different depths, in addition to the fusion bonding itself.

The micromachining process can be seen in Fig. 5. The mechanical wafer is a Silicon-on-Insulator wafer consisting of a 380 µm silicon substrate (shown in yellow in the figures) and a 43 µm silicon device layer (purple in the figure). Between the two silicon layers there is a 5 µm thick buried oxide layer. The optical wafer is a standard 300 µm thick double-sided polished silicon wafer. The first step of the process is to etch, using Reactive-Ion-Etching (RIE) technique, a gap under each scale. This gap defines the length of the Fabry-Perot cavity when no mass is present on the scale, and was chosen to be 8 µm. In parallel, the diffractive Fresnel lens is etched on the surface of the optical wafer, also using RIE. The two wafers are then bonded together with fusion bonding, which consist in aligning and pressing the two wafers in contact, before annealing the stack at 1050º C. The next step is to etch with deep RIE the substrate of the mechanical wafer, in order to define the platform of the scale. The resulting platform is suspended by the thinner device layer, which acts as a spring. Finally, the optical wafer is thinned to 100 µm using deep RIE. Not the whole area under the scale is thinned, but rather a clover shaped area, in order to keep as much structural strength as possible to the wafer stack, while giving a reasonably large "window" for imaging the fringe pattern under the scale.

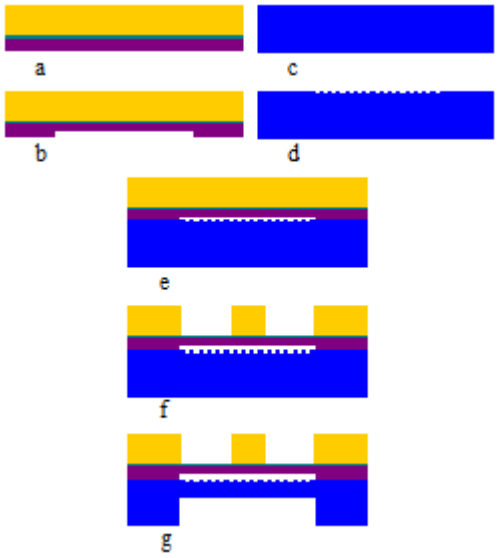

Fig. 5. Fabrication of the scale, seen as the cross-section of one scale element. Dimensions are not to scale. (a) The mechanical wafer. (b) Dry etching of a 8 µm gap in the device layer. (c) The optical wafer is a standard double-side polished wafer. (d) The diffraction pattern is dry etched onto the surface of the optical wafer. (e) The two wafer are aligned and bonded. (f) Deep Reactive Ion Etch defines the scale platform and spring area. (g) Thinning of the optical wafer with Deep Reactive Ion Etch.

V – Experimental results

A. Measurement using a CCD camera

In a first experiment, we used a CCD silicon camera to image the fringe pattern at the backside of the scale array. An image of the backside of the whole scale array can be seen in Fig. 6. The light source consisted of a halogen lamp connected to a fibre bundle, whose other end acted as a point source for illumination of the backside of the scale array. A band pass filter centred at 1067 nm was used to reduce the bandwidth of the illumination to 20 nm. The illumination wavelength was chosen to be at the edge at the silicon bandgap, so that light was still able to propagate without too much attenuation through the thinned parts of the optical wafer (100 µm thick), while remaining in the wavelength region where the CCD is sensitive to light. A wavelength of 1067 nm might not be ideal for this purpose, but was the closest available wavelength without having to order a custom filter.

Unfortunately, when the temperature of silicon increases, the edge of the bandgap moves towards longer wavelengths. We obtained good images of the fringe pattern at 200°C, even through the whole thickness of the optical wafer (ca. 300 µm), and at up to 400°C through the 100 µm thinned parts of the optical wafer. But above 400°C, transmission through silicon was too low to be able to extract the fringe pattern from the background noise. This is illustrated in Fig. 7.

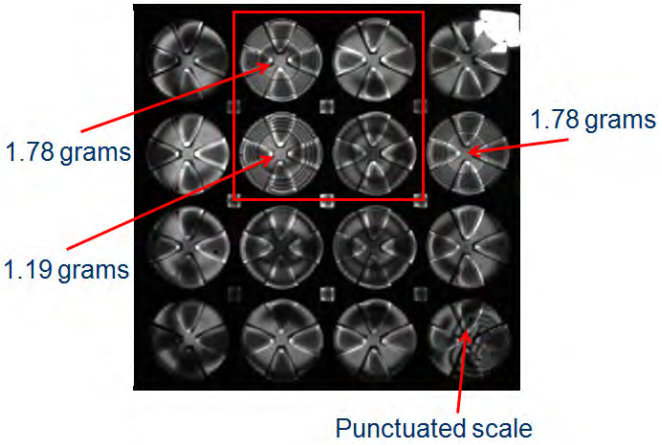

Fig. 6. Backside of the scale seen from the CCD camera, with different weights placed on several scales.

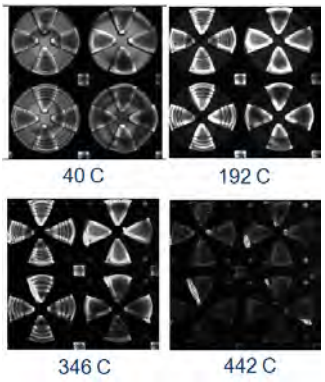

Fig. 7. A subset a 4 scales seen as temperature is increased from 40 ℃ to over 400 ℃.

An automated program was used to count the number of fringes under each scale. The basic principle is to extract intensity curves from cross-sections of the fringe pattern, and to count the number of peaks and valleys. Such a measurement is shown in Fig. 8, where a mass of 2.38 grams gave 9 rings, that were counted with a resolution of 5 pixels per period. Only counting the number of peaks and valleys gives only a limited precision of the mass measurement. This can be improved by measuring, in addition, the lateral position of the peaks and valleys, even though this was not implemented in this experiment.

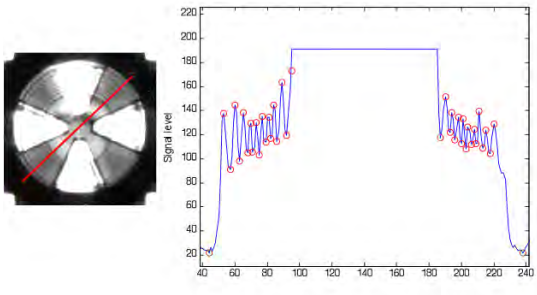

Fig. 8. Automated measurement of the number of rings in the fringe pattern under a scale. The signal level along the red line is plotted on the right graph.

In order to investigate the linearity and the cross talk between neighbouring scales, we have taken images of a

subset of four scales while varying the mass on one of them, as shown in Fig. 9. We observed in the images taken no visible cross talk between neighbouring scales. In addition, the relation between the number of rings and the mass placed on a scale showed a good linearity, as shown in Fig. 10.

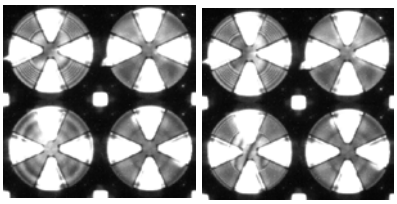

Fig. 9. Subset of four scales, with a constant weight of 1.78 grams on the upper left scale and a varying weight on the lower left scale: 0.55 grams (left) and 3.34 grams (right).

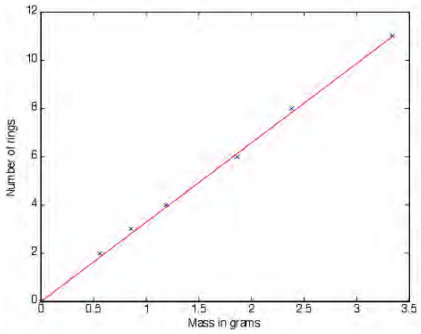

Fig. 10. Number of rings counted manually versus mass of objects.

B. High temperature measurement using an InGaAs camera

In order to increase the maximal temperature at which the fringe pattern can be imaged, we have used an InGaAs camera and an illumination at 1330 nm. This wavelength is not absorbed by silicon, while detected by the NIR-sensitive camera.

Because of the available camera lens, we had to place the scale array much closer to the camera lens (25 cm instead of the designed 40 cm) to be able resolve the rings in the fringe pattern. As a result, the diffractive lens was not focusing light on the camera aperture for all scale elements, and only light from parts of the scale array could be observed at the same time, as can be seen in Fig- 11. This problem could easily be solved by using an appropriate camera lens with higher magnification.

With the InGaAs camera, fringe patterns could be observed at temperatures as high as 700º C. However, the contrast of the fringe becomes lower as temperature increases, because the heating elements of the oven produce a large background signal that extends in the NIR-region as the temperature increases. This background signal can be measured by turning off the illumination of the scale array, and then subtracted from the images obtained with the illumination on. But at roughly 700º C, the camera was saturated by the background light and the fringe pattern became invisible.

Fig. 11. Image of the fringe pattern taken with an InGaAs camera.

Another possible limitation in the temperature at which the scale array can be operated, is mechanical stability. Because the structures consist of several layers of silicon and silicon oxide, with different thermal expansion coefficients, bimorph forces build up as temperature increases, with the result of bending the structures on the wafer. As a consequence, the position of the scale platform is modified, and thus the observed fringe pattern. This phenomenon can clearly be seen in Fig. 11, where the number of rings decreases from 4 at 490º C to 2.5 at 700º C. A possible solution to this problem is to calibrate each scale at different temperatures. But a more ideal solution would be to attenuate the bimorph forces by reducing further the number of layers the scale array consists of. In our construction, we had an aluminum layer on top of the scale array, which was used as a mask for Deep Reactive Ion Etching of the scale platform. This layer could easily be removed at the end of the scale array processing. Similarly, there is an oxide layer on top of the annular springs, which also could easily be removed.

VI - Conclusion

We have fabricated and demonstrated an array of microscales that is read out optically from a distance and that can be operated at high temperatures. We have implemented a method that derives the scale deflection by counting the number of circular fringes under each scale. This method shows good linearity from 0 to 3.5 grams. We have not observed crosstalk between neighbouring scales. Using a standard CCD camera, we could operate the scale up to 400ºC. At higher temperatures, the silicon structure under the scales becomes opaque for short wavelengths and a near-infrared-sensitive camera must be used to be able to see the fringes. Using an In-Ga-As camera we demonstrated operation at up to 700ºC. At such high temperatures, both the thermal stability of the structures and the thermal emission from the chamber gradually degrade the performance of the system.

References

[1] H. Sagberg, A. Sudbø, O. Solgaard, K.A.H. Bakke, I.R. Johansen, IEEE Photonics Technology Letters, vol. 15, pp. 1431-1433, 2003.

ETCHING BURIED OXIDE AT THE BOTTOM OF HIGH ASPECT RATIO STRUCTURES

A. Summanwar[1], N. Lietaer[1]

[1]*SINTEF ICT, Department of Microsystems and Nanotechnology, Oslo, Norway*

***Abstract* — Plasma based dry etching is a key process widely used in micro-fabrication today. In this article, we look at the challenges involved in the anisotropic etching of buried SiO_2 layers at the bottom of high aspect ratio structures on SOI wafers. We present our etch results that show the limitations of using a process with radio frequency (RF) substrate bias. This is followed by results obtained with a newly developed dielectric etch process based on a pulsed low frequency (LF) bias which makes it possible to etch through even relatively thick buried oxide layers. Finally we present an application in which this newly developed process was used.**

***Keywords:* Plasma etching, DRIE, Dielectric charging, SOI, Notching, High Aspect Ratio**

I - Introduction

High aspect ratio structures in silicon play an important role in many MEMS devices and are also finding a growing number of applications in other semiconductor devices. Dry anisotropic etching using high density plasmas is a key technology that is widely used for etching high aspect ratio structures in silicon. However there are several well-known phenomena that lead to non-uniformities in etch rates during deep silicon etching such as the aspect ratio dependence of the etch rate (ARDE), and loading effects (both micro-loading and macro-loading). To overcome these non-uniformities, silicon-on-insulator (SOI) substrates are often employed for fabrication of MEMS devices in order to ensure a uniform etch depth for all structures, by using the buried oxide (BOX) as an etch stop layer.

When etching high aspect ratio structures and stopping on the BOX layer, a well-known phenomenon that occurs is notching. Notching is the lateral etching of the sidewalls of the silicon structures, in the region near the interface between the silicon device layer and the BOX layer as shown in figure 1. When the BOX layer gets exposed to the plasma, it gets charged by the positive ions flux that is directed towards the substrate. Due to the charging of the BOX layer, the ion trajectories are distorted causing ions to be deflected towards the sidewalls of the etched structure [1]. This leads to undesirable lateral etching of the structures in the silicon device layer which could cause problems in the subsequent fabrication steps or hamper the performance of the devices.

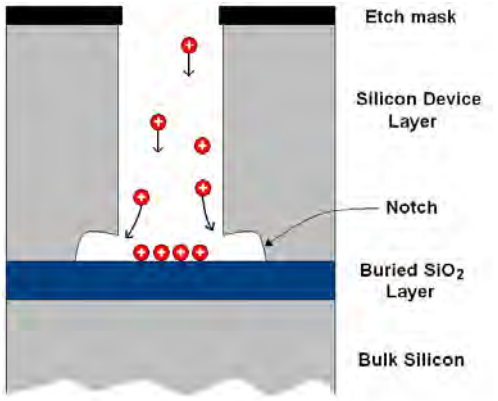

Figure 1*: Notching phenomenon resulting from the charge buildup on the buried oxide layer*

A similar notching phenomenon results when one attempts to etch through the BOX layer at the bottom of high aspect ratio structures. An additional challenge when etching buried SiO_2 in such structures is the fact that the etching of SiO_2 layers in general requires a relatively high amount of energetic ion bombardment [2]. Due to the charge buildup on the BOX layer and consequent ion deflection, the amount of energetic ion bombardment at the bottom of high aspect ratio structures is considerably reduced as compared to the top surface of the wafer, which results in a significantly lower etch rate.

In this article we report the results of our experiments to find a solution to etching through the BOX layer at the bottom of high aspect ratio structures. We then present an application where this etch process has been used successfully to fabricate MEMS devices with through silicon vias (TSVs) in the SOI substrates.

II - Experimental Setup

All experiments reported here were performed on an Alcatel AMS200 SE I-Productivity etch tool. This is a so-called downstream etch tool which is built to run a switched etch process such as the BOSCH deep reactive ion etch (DRIE) process [3]. However, it is also possible to run continuous etch processes such as dielectric etch or isotropic silicon etch, making it a very versatile tool for micro-fabrication. Figure 2 is a simplified functional illustration of the tool. The upper portion of the tool is a high density inductively coupled plasma (ICP) source. It consists of a ceramic cylinder into which various process gases (typically SF_6, C_4F_8 and O_2) are introduced. RF power from a generator is applied to a coil antenna wound around the ceramic cylinder to create a plasma. A diffusion chamber lies below the plasma

source. It is here that various ions and radicals from the plasma react with the substrate to be processed.

The substrate is electrostatically clamped onto the substrate holder. The temperature of the substrate holder is regulated by a system consisting of an external chiller unit and resistive heaters. Thermal conductivity between the substrate and the substrate holder is achieved by a flow of Helium gas between the back-surface of the substrate and the substrate holder, which is used to regulate the substrate temperature during processing.

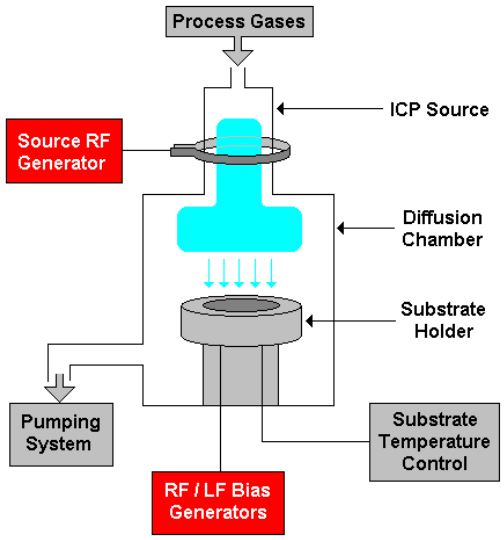

Figure 2*: Simplified functional illustration of the plasma etch tool used in the experiments*

To accelerate ionic species from the plasma sheath towards the wafer it is possible to apply an electrical bias on the substrate to be etched. In this way, the energy of ionic species arriving at the substrate is controlled independently of their flux. The biasing can be achieved either by applying RF power (13.56 MHz) or LF power (100 KHz to 460 KHz) from independent substrate bias generators. If LF bias is used, it is also possible to pulse the bias "ON" and "OFF" or between a High and Low value.

The substrates used in these experiments were all 100 mm diameter SOI wafers with a nominal thickness of 340 µm. Two types of wafers were used: The first type had a 43 µm thick device layer and a 0.5 µm thick BOX layer and the second type had a 40 µm thick device layer and 2 µm thick BOX layer. An aluminium layer (0.7 µm thick) was patterned and used as the hard-mask for dry etching. On all the wafers test structures in the form of trenches with a width of approximately 7 µm and a length of 70 µm were etched down to the BOX layer using the BOSCH process. The trenches had an aspect ratio of approximately 5:1. The goal of the experiments was to develop an etch process to etch through the BOX layer at the bottom of the trenches while keeping the etch-profile as straight as possible.

III - Results

A. Etch results on wafers with a 0.5µm BOX layer

In the first set of experiments the SOI wafers had a 43 µm thick device layer and a 0.5 µm thick BOX layer. After the trenches were etched in the silicon device layer, a standard dielectric etch recipe (Recipe RF1) which uses RF substrate bias was used as a starting point for the BOX etch. Process parameter details of this recipe are mentioned in Table 1. An etch time of 5 minutes was used, which would be sufficient to etch more than 2 µm SiO_2 on the top surface of the wafer.

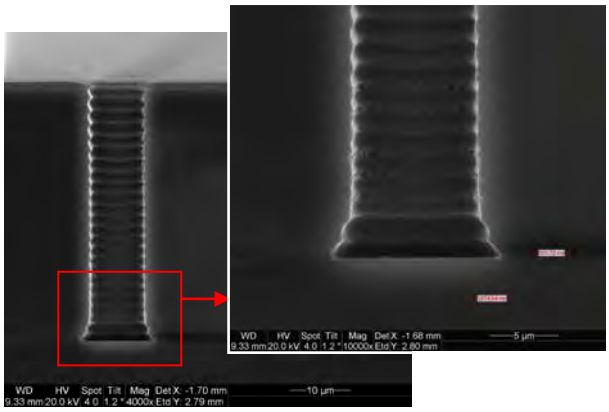

Figure 3*: Etch results obtained with a standard dielectric etch process (Recipe RF1) on a SOI wafer with 0.5µm thick BOX.*

Figure 3 shows SEM cross-sections of the etch result. It appears that virtually no buried oxide was etched. We also see a considerable amount of notching at the bottom of the device layer (> 1.8 µm on each side). We know that the notching resulting from the device layer etch (BOSCH process) was less than 0.7 µm. Thus during the BOX etch, the width of the notch increased by more than 1 µm.

In an attempt to increase the energy of the ions arriving at the BOX layer, a new recipe was developed (Recipe RF2) with double the applied RF substrate bias power, half the process pressure and half the C_4F_8 gas flow as compared to Recipe RF1.

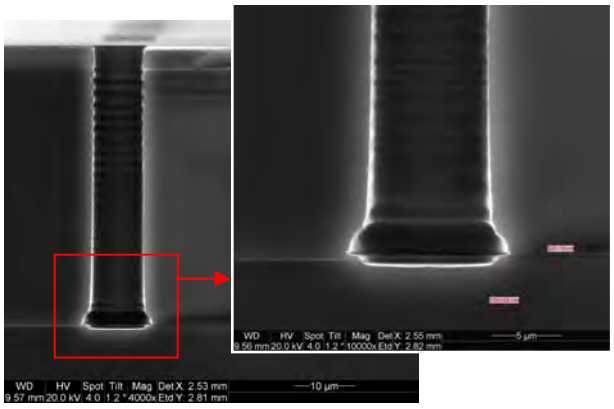

Figure 4*: Etch results obtained with Recipe RF2 on a SOI wafer with 0.5µm thick BOX.*

Figure 4 shows the etch result for Recipe RF2 with an etch time of 8 minutes. It is clear that significantly increasing the ion energy made it possible to etch through the BOX layer. Notching is still a problem, even though it is slightly reduced (to about 1.6 µm on each side).

B. Etch results on wafers with a 2µm BOX layer

In the next set of experiments the SOI wafers had a 40 µm thick device layer and a 2 µm thick BOX layer. At first we attempted to etch through the BOX layer using Recipe RF2 that was successfully used to etch a 0.5 µm BOX layer. However in this case, even after a relatively long etch time of 14 minutes, very little of the BOX layer was etched. Figure 5 shows SEM images of the etch result. Near the bottom corners of the trenches only about 170 nm of the BOX layer was etched while at the centre of the trenches no BOX was etched at all. In fact in the centre of the trenches we observe a build up of polymer residues on top of the BOX layer. We also see a very significant amount of notching (> 3.6 µm on each side) which was unacceptable for our application.

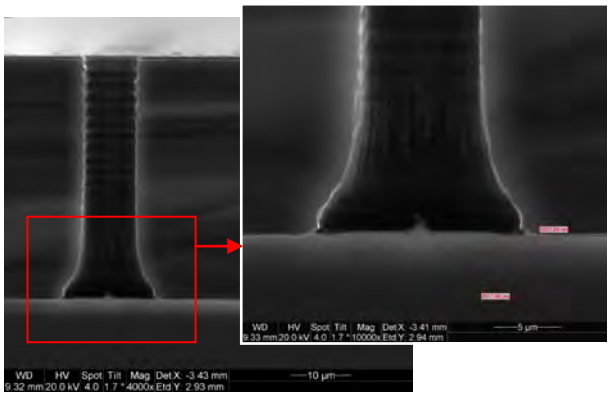

Figure 5*: Etch results obtained with Recipe RF2 on a SOI wafer with 2µm thick BOX.*

Another limitation that became apparent was that due to the high energy ion bombardment onto the wafer, the aluminium hard-mask eroded rapidly. As only about 150 nm of the aluminium mask was left, it was difficult to increase the etch time further.

As it became clear that a RF substrate biasing scheme had its limitations, we experimented and developed a new etch process (Recipe LF1) based on a pulsed LF substrate biasing scheme instead of RF biasing. Figure 6 shows the etch results obtained after 35 minutes of etching with this process. It is evident that pulsed LF biasing made it possible to etch through the 2 µm thick BOX layer. The amount of notching is also very little (< 0.7 µm on each side). In fact keeping in mind that we already had up to 0.7 µm of notching after the device layer etch itself, the increase in notching due to this BOX layer etch is insignificant. In addition, only approximately 270 nm of the aluminium mask was consumed.

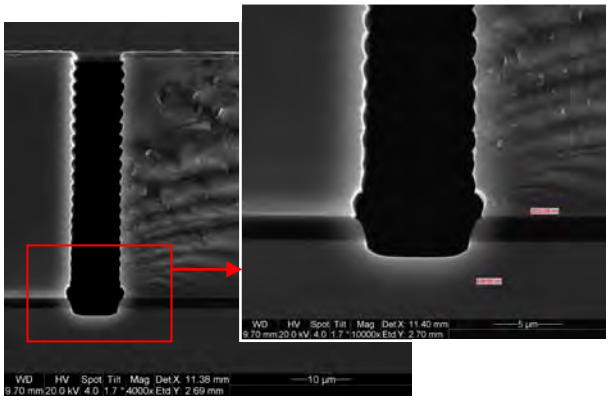

Figure 6*: Etch results obtained with Recipe LF1 on a SOI wafer with 2µm thick BOX.*

More detailed process parameters for each etch recipe are given in Table 1.

Parameter	**Recipe RF1**	**Recipe RF2**	**Recipe LF1**
Source power	2800 W	2800 W	2800 W
C_4F_8 gas flow	50 sccm	25 sccm	25 sccm
Pressure	0.6 Pa	0.3 Pa	0.3 Pa
Substrate-holder temperature	20 °C	20 °C	20 °C
Substrate bias power	100 W (RF 13.56 MHz)	200 W (RF 13.56 MHz)	100 W (LF 200 KHz, pulsed)

Table 1: *Process parameter details of the etch recipes*

Table 2 gives a summary of various etch rates measured for each process. Although for these experiments an aluminium hard mask was used, the etch rate of a commonly used positive photoresist (HiPR 6512) was also measured for all the etch processes in order to give an idea about the selectivity of a photoresist mask.

Parameter	**Recipe RF1**	**Recipe RF2**	**Recipe LF1**
Avg. etch rate of top surface SiO_2 (nm/min)	456	609	202
Avg. etch rate of 0.5 µm BOX layer (nm/min)	~0	~167	~120
Avg. etch rate of 2.0 µm BOX layer (nm/min)	~0	~0	~105
Avg. photoresist etch rate (nm/min)	310	526	115
Avg. aluminium etch rate (nm/min)	12.3	38.9	7.8

Table 2: *Summary of etch rates for all etch processes*

IV - Discussion

The experimental results show that the use of a RF substrate bias leads to charging of the BOX layer, causing ion trajectories inside the trenches to diverge towards the sidewalls of the trenches. This results in lateral etching of the silicon device layer leading to notch formation. Another consequence of the charging is that it reduces the ion bombardment onto the BOX layer which significantly reduces the etch rate.

Although pulsed LF biasing has been used to limit notching in deep silicon etching [4,5], to our knowledge its use in etching of the BOX layer has not been reported in literature until now. The use of a pulsed LF bias addresses the root cause of the problem which is the charging of the BOX layer. The 'ON' time of the pulses provide enough ion energy to etch the BOX layer while the built-up charge gets enough time to discharge during the 'OFF' time of the pulses

V - Application

Fragile MEMS structures are usually protected from the environment by bonding a capping wafer to the device wafer. As opposed to using lateral interconnects at the interface between the cap wafer and the device wafer, the use of vertical TSVs significantly simplifies the mounting of the components and it also results in the smallest geometry. Figure 7 shows a schematic cross-section of a MEMS accelerometer that was fabricated as part of the European ENIAC Joint Undertaking project JEMSIP-3D. The newly developed pulsed LF bias etching process made it possible to successfully fabricate TSVs through the SOI wafer.

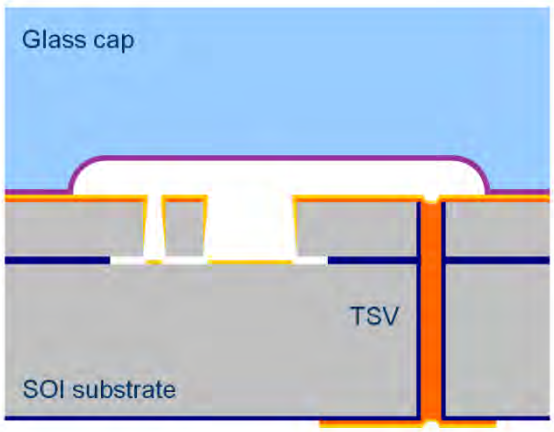

Figure 7*: A schematic crosss-section of a MEMS accelerometer with TSV through the SOI wafer.*

Using a via-first approach, TSVs were first created on the SOI wafers followed by the fabrication of the MEMS devices. Plasma etching was extensively used for fabricating both the TSVs and the MEMS structures. For creating the TSVs, three consecutive anisotropic etch steps were performed using an aluminium hard-mask. First the silicon device layer was etched using the BOSCH DRIE process, followed by dry etching of the 2 µm BOX layer using the LF bias etch process. This enabled us to minimize the notching at the bottom of the device layer which would have led to void formation in the vias at a later stage in the processing. Finally, another multi-step BOSCH DRIE process was used to etch through the silicon handle wafer. The vias were then isolated with thermal oxide and made conductive by filling them with heavily doped polysilicon. More details regarding the fabrication process of the TSVs and MEMS devices are available in another article [6].

VI - Conclusion

In this article, we have looked at the challenges involved in the anisotropic etching of buried SiO_2 layers at the bottom of high aspect ratio structures. We have shown that for this purpose a dielectric etch process using RF bias has significant limitations: very low etch rate, notching issue, and low selectivity to the etch mask. The root cause of the problem is the charging of the BOX layer which causes ion trajectories to diverge towards the sidewalls of the high aspect ratio structures. We have successfully developed a new dielectric etch process using pulsed LF bias which addresses the problem and makes it possible to etch through even relatively thick buried oxide layers. This new process has been applied successfully for the fabrication of through silicon vias in a MEMS application.

Acknowledgements

This work was supported by the European ENIAC Joint Undertaking project ID:120016 JEMSIP-3D.

References

[1] G.S. Hwang, K.P. Giapis: On the origin of the notching effect during etching in uniform high density plasmas, *J. Vac. Sci. Technol. B*, vol. 15, no. 1, pp.70-87, 1997

[2] D. L. Flamm, V. M. Donnelly: The design of plasma etchants, *Plasma Chem. Plasma Proc.*, vol. 1, no. 4, pp. 317-363, 1981

[3] F. Lärmer, A. Schilp: Method of anisotropically etching silicon, Patent US 5501893

[4] F. Lärmer, A. Urban: Challenges, developments and applications of silicon deep reactive ion etching, *Microelectronic Engineering*, vol. 67-68, pp.349-355, 2003

[5] J. Hopkins et al: Method and apparatus for etching a substrate, Patent US 6187685

[6] N. Lietaer, A. Summanwar, T. Bakke, M. Taklo, P. Dalsjø: TSV development for miniaturized MEMS acceleration switch, *2010 IEEE International 3D Systems Integration Conference (3DIC), Munich, Germany*, 2010

CMUT ARRAYS WITH POLYSILICON BOTTOM ELECTRODES AND NANOMETER PRECISION CAVITY GAPS

J. Due-Hansen[1], K. Midtbø[2], E. Poppe[1], A. Summanwar[1], G.U. Jensen[1], L. Breivik[1], D. T. Wang[1]

[1]*SINTEF ICT, Department of Microsystems and Nanotechnology, Oslo, Norway*
[2]*NTNU, Department of Electronics and Telecommunication,Trondheim, Norway*

***Abstract* — A fabrication process for an array of capacitive micromachined ultrasound transducers (CMUTs) has been developed. The CMUTs have a targeted gap of 60 ± 5 nm, and a bottom electrode made from doped polysilicon. To obtain good reliability and uniformity both across the wafer surface and from wafer to wafer, a process for dry silicon etching was developed and is presented in this paper. During processing, the bottom polysilicon electrode surface roughness increased during thermal processing, so that the final values were incompatible with the targeted 60 nm gap of the CMUT. A process for doping and annealing that resulted in a final polysilicon roughness of 1 nm rms was developed, and is presented in this paper.**

***Keywords :* CMUT, ultrasound, dry etch, RIE, polysilicon, surface roughness, uniformity**

I - Introduction

Ultrasound is a popular technique for medical imaging, and is used in applications ranging from obstetrics to gastroscopy and cardiology [1]. Ultrasound provides high portability and low price per examination, and does not apply ionizing radiation. The size and the scanning frequencies of an ultrasound transducer depend on the targeted application. Frequency ranges from 2 to 10 MHz are commonly used for diagnostic imaging outside the body.

Capacitive micromachined ultrasound transducers (CMUTs) enable the fabrication of miniaturized ultrasound transducers using technologies applied for micro electromechanical systems (MEMS). CMUTs have been fabricated by surface micromachining [2] and bulk silicon technology [3,4].

We are developing a fabrication process for an improved version of a previously published CMUT array, fabricated by wafer bonding [5,6]. The improved CMUT array will have CMUTs with nanometer gaps. Elements of the array can be electrically addressed by hermetic through-wafer vias, developed at SINTEF [7].

The fabrication process poses several challenges. The challenges include the realization of conductive and hermetic through-wafer vias, hermetic sealing by fusion bonding of features only 1.1 µm wide, bonding of a surface that is polished by chemical mechanical polishing (CMP), and reliable and repeatable fabrication of vertical gaps of 60 ± 5 nm.

For process-specific reasons, doped polysilicon was the preferred material for the bottom CMUT electrode, constituting the bottom of the vertical gap. The literature reports Atomic Force Microscopy (AFM) on doped polysilicon material showing that surface roughnesses of 9.9 to 16.3 nm rms may occur, depending on thermal treatment, doping source, and degree of doping of the layer [8,9]. These measured roughness values are non-negligible compared to the 60 nm gap height of our CMUT devices. In addition, there are challenges in developing a dry silicon etching process that produces 60 nm gaps with high precision and good uniformity across the whole surface of a wafer with diameter 100 mm.

This paper presents the development of a suitable dry etch process and feasible solutions to avoid intolerable polysilicon surface roughness, resulting in repeatable and uniform high-precision gaps of the CMUT array.

II – CMUT Design and Fabrication

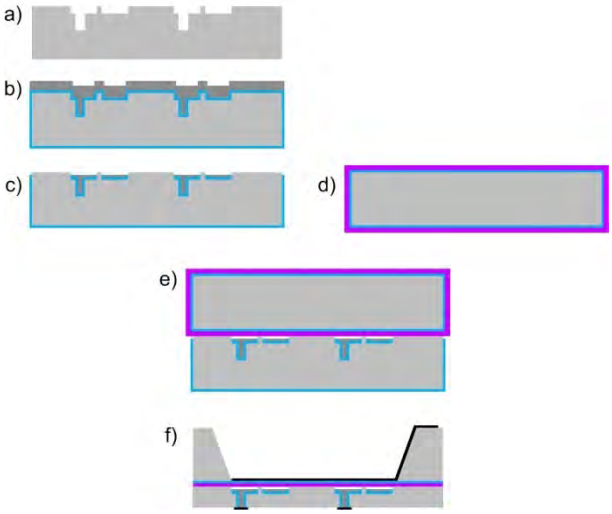

Figure 1*: Fabrication process for CMUT arrays. Silicon material is light grey, blue is SiO_2, dark grey is polysilicon, purple is Si_3N_4, and the black areas are aluminium.*

Figure 1 outlines the fabrication process for the CMUT arrays. The arrays are made from bonding top and bottom wafers. First, the through-wafer vias and the areas for the CMUT elements were dry etched in the bottom wafer (a). Thermal SiO_2 was grown for electrical isolation, and the vias were filled with polysilicon, that was doped using $POCl_3$ as phosphorus source (b). The wafer surface was then polished by chemical mechanical polishing (CMP) to obtain a surface roughness suitable for wafer bonding. The 60 nm deep cavities of the CMUTs were realized by etching of polysilicon and SiO_2 (c).

The membrane materials of SiO_2 and Si_3N_4 were grown and deposited on the top wafers (d) before bonding the two wafers together (e). After bonding, the bulk silicon of the top wafer was etched away, leaving only the membrane of SiO_2 and Si_3N_4 in the CMUT areas. The bottom wafer was thinned to expose the through-wafer vias. Aluminium was deposited and patterned on both sides of the wafer, to complete the fabrication process of the CMUT arrays (f).

The arrays contain 9216 individual CMUTs. Groups of four CMUTs form an element. Each element is connected to one through-wafer via, and groups of 36 through-wafer vias are connected to one bond pad. There are 64 bond pads to be electrically addressed.

Key features of the CMUT elements are listed in Table I. The targeted resonance frequency was 30 MHz in fluid, which implies a resonance frequency of 60 MHz in air.

Table 1: *Physical parameters of the CMUT and array.*

Dimension	Size
Membrane radius [µm]	5.7
Cavity pitch [µm]	12.5
Separation between cavities [µm]	1.1
Bottom electrode radius [µm]	4
Cavity height [nm]	60
Membrane	
- LPCVD Si_3N_4 [nm]	100
- SiO_2 [nm]	50
- Al [nm]	300
Outer dimension full array [mm^2]	0.9 × 1.6

III - Experimental

A. Investigation of polysilicon surface roughness

Four silicon wafers, named S1 – S4, with thermal SiO_2 were used for the experiments. Wafer S1 had 0.4 µm of deposited polysilicon, which was doped employing a $POCl_3$ deposition process yielding a sheet resistance of 3 Ω/□ in crystalline silicon. Wafers S2 – S3 were polysilicon deposited in three runs, with thicknesses 0.8 µm, 1.0 µm, and 1.0 µm. After each deposition, the polysilicon was doped employing a $POCl_3$ deposition process yielding a sheet resistance of 20 Ω/□ in crystalline silicon. Wafer S4 had 0.7 µm polysilicon which was doped employing a $POCl_3$ deposition process yielding a sheet resistance of 20 Ω/□ in crystalline silicon. The polysilicon of wafer S4 was polished and thinned to 0.5 µm by CMP. The CMP was performed at Fraunhofer ISiT [10]. An overview of the wafers is given in Table 2.

During doping, the wafers were subjected to thermal processing. Wafer S1 was exposed to 1000°C for 170 minutes. Wafers S2 – S3 were exposed to 900°C for 30 minutes for each doping process, i.e. three times. After doping, wafer S3 was annealed for 48 hours at 1050°C in N_2. Wafer S4 was exposed to 900°C for 30 minutes and 1050°C for 3 hours prior to CMP and dry etching. After CMP and etching, wafer S4 was annealed for 2 hours at 1050°C.

Table 2: *Overview of wafers for investigation of polysilicon surface roughness and sheet resistance.*

Wafer ID	Poly thickness [µm]	Sheet resistance in crystalline silicon
S1	0.4	3 Ω/□
S2 – S3	0.8 + 1.0 + 1.0	20 Ω/□
S4	0.7, thinned to 0.5	20 Ω/□

The surface roughness before and after thermal processing was investigated by a FEI Quanta 600 FEG scanning electron microscope (SEM) and white light interferometry using a Zygo New View 6300. The uniformity of a wafer was calculated as $100\times(1 - \Delta h/h_{av})$, where Δh was the difference between the maximum and minimum measured etch depth and h_{av} was the average etch depth of each wafer. Sheet resistance was measured by a Veeco FPP5000 four-point probe.

B. Development of dry etching process

The etching process was based on C_4F_8 and was intentionally tuned for low etch rate in order to control the depth of 60 nm. The targeted etch time was in the order of 30 seconds. The etch process was developed on test wafers before it was applied on 9 process wafers, named C1 – C9. After etching, the etch depth was measured by white light interferometry using a Zygo New View 6300 on 5 measurement points (up, down, left, right and middle) on each wafer. An AMS200 I-Productivity (Alcatel) machine was used for the dry etching processes.

IV - Results

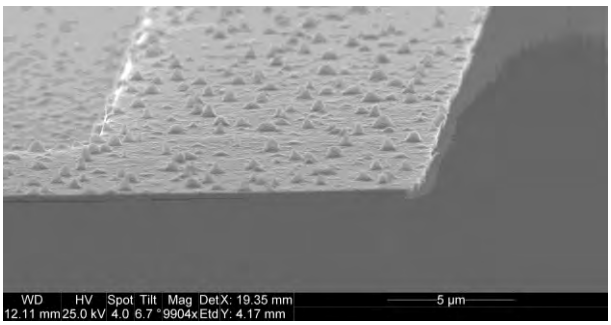

Figure 2: *SEM picture of the surface of wafer S1 after doping including thermal treatment.*

Figure 2 shows the surface of wafer S1 after doping and thermal processing. Sharp fins protruding from the surface of the 0.4 µm thick polysilicon film are clearly seen. Figures 3 and 4 show the surfaces of wafers S2 and S3, respectively. No significant difference could be seen in the surface roughness of wafer S2, which was not annealed, and wafer S3, which did receive the additional anneal for 48 hours at 1050°C in N_2. Measurements of the surface roughness and sheet resistance

of wafers S2 – S4 are listed in Table 3. The measurements support the visual impression that there was no significant difference in surface roughness of wafers S2 and S3. The surface roughness of wafer S4, which was polished by CMP, was significantly lower. This measurement is also supported by the SEM picture of wafer S4, seen in Figure 5. Figure 5 also shows the dry etched cavities in the polysilicon surface. No difference in surface roughness between the etched and un-etched areas could be observed. Figure 6 shows a 3D plot of a Zygo measurement of the surface topography of a polysilicon area on wafer S4 after annealing at 1050°C for 48 hours.

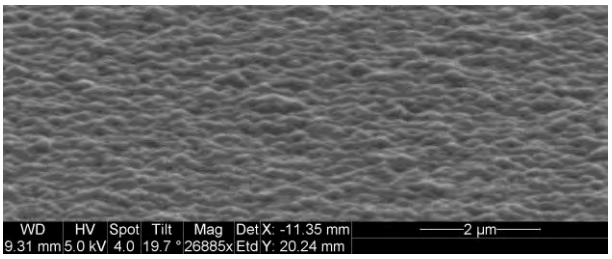

Figure 3*: SEM picture of the surface of wafer S2 after doping including thermal treatment.*

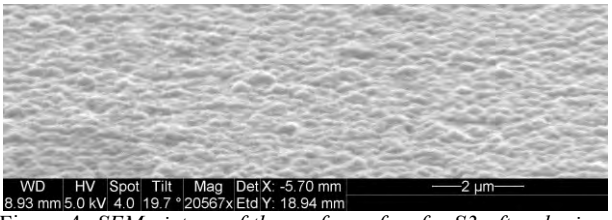

Figure 4*: SEM picture of the surface of wafer S3 after doping including thermal treatment.*

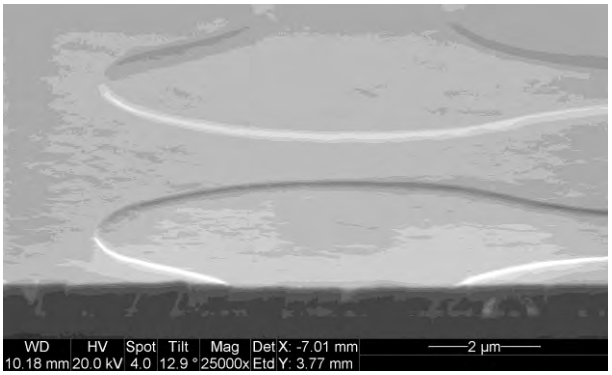

Figure 5: *SEM picture of the surface of wafer S4 after doping including heat treatment, CMP, dry etching of 60 nm gaps and thermal anneal.*

Table 4 lists the mean and standard deviation of the five measured cavity depths and the calculated uniformity for each of the process wafers C1 – C9. The mean and standard deviation of the nine means was 59.2 ± 3.9 nm. Figure 7 is an image of the final, working CMUT array with 9216 CMUTs.

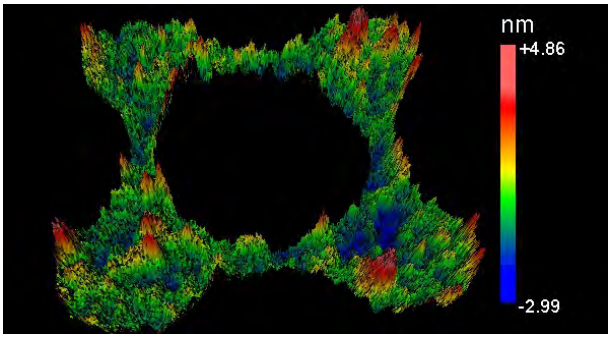

Figure 6: *3D plot of the Zygo measurement of the surface topography of the bottom polysilicon electrode of four CMUTs on wafer S4 after final anneal at 1050°C for 2 hours.*

Table 3: *Measured values for surface roughness and sheet resistance of polysilicon before and after annealing for 48 hours at 1050°C (wafers S2 and S3), and before and after dry etching and anneal for 2 hours at 1050°C (wafer S4). Wafer S4 was polished by CMP.*

Wafer ID	Surface roughness [nm] rms		Sheet resistance [Ω/□]	
	Before	After	Before	After
S2	8.7	-	15.9	-
S3	-	8.9	-	4.0
S4	1.0	1.0	57	22

Table 4: *Mean and standard deviation of the five measured cavity depths and calculated uniformity on process wafers C1– C9.*

Wafer ID	Mean [nm]	Standard deviation [nm]	Uniformity [%]
C1	55.0	0.7	3.6
C2	61.7	1.1	4.7
C3	54.8	0.8	3.7
C4	63.1	0.3	1.1
C5	54.8	0.8	3.7
C6	62.6	1.0	4.0
C7	56.2	0.8	3.6
C8	62.4	1.0	3.5
C9	63.1	0.3	1.0

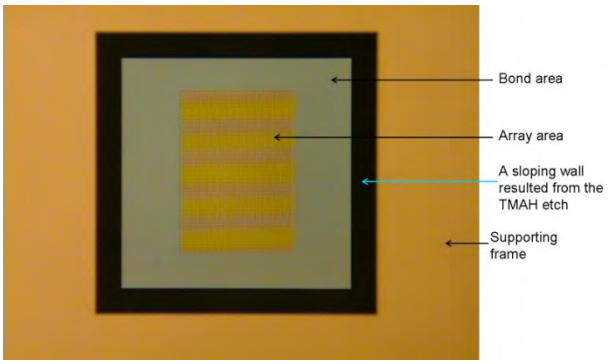

Figure 7: *Final, working CMUT array with 9216 individual CMUTs.*

V - Discussion

Figure 2 shows that polysilicon that is doped to a level that results in a sheet resistance of 3 Ω/□ in crystalline silicon, has a high surface roughness. This result is in agreement with the work of Lin et al [8]. According to Hegde et al [9], the surface roughness could be related both to the high level of doping, and to the use of $POCl_3$ as phosphorus source.

Figures 3 and 4 shows that the surface of three polysilicon layers that each was doped by a process yielding 20 Ω/□ in crystalline silicon, had similar surface roughness before and after an anneal for 48 hours at 1050°C in N_2.

Figure 5 and Table 3 show that the polysilicon that was doped by a process yielding 20 Ω/□ in crystalline silicon, polished by CMP and dry etched, had a surface roughness of 1 nm rms. It is likely that the doping could be somewhat increased while still keeping a surface roughness at the same level. However, doping levels giving 3 Ω/□ in crystalline silicon, are expected to result in high surface roughness of polysilicon surfaces.

Because of the grain structure of polysilicon, identical doping processes are expected to give different sheet resistances in crystalline silicon and polysilicon. The final sheet resistance may depend on film thickness, doping and deposition parameters as well as subsequent thermal processing. Table 3 shows that three repetitions of polysilicon deposition and doping that would give a sheet resistance of 20 Ω/□ in crystalline silicon, resulted in a sheet resistance of 15.9 Ω/□ in polysilicon before annealing, and 4.0 Ω/□ in polysilicon after annealing. The low sheet resistance obtained resulted in good electrical contact from the bottom CMUT electrode to the backside aluminium contact, through the through-wafer via.

The means and standard deviations listed in Table 4 show that the etching process gave very uniform depths across each wafer, and that the targeted depth of 60 ± 5 nm was achieved. The standard deviation of the nine mean depths of 3.9 nm indicates that the developed process had a high wafer-to-wafer uniformity.

According to literature, the etch depth uniformity is typically dependent on gas flow rate, pressure in the plasma chamber [11], and the total wafer area to be etched [11, 12]. Low pressures in the plasma chamber will increase the uniformity [11]. Early publications on uniformity across the wafer of dry etch processes typically reported ± 5% for wafers with 150 mm diameter mm [13]. The measured variations on the presented process wafers C1 – C9 ranged from 1.0% to 4.7 %, indicating that the developed process resulted in high uniformity, even for the targeted etch depth of 60 nm.

VI – Conclusion

A dry etching process that realizes etch depths of 60±5 nm uniformly and repeatably has been developed and tested. A polysilicon doping process that yields a sheet resistance of 4.0 Ω/□ without compromising the surface roughness has been developed and tested. The two processes are key processes that enable the fabrication of CMUT arrays suitable for applications in for instance intravascular cardiology and gastrointestinal imaging.

Acknowledgments

The authors wish to thank Kari Schjølberg-Henriksen for preparation of the manuscript and Lars Geir Whist Tvedt for assistance with Zygo measurements. The work was partly funded by the Norwegian Research Council.

References

[1] R.W. Prager, U.Z. Ijaz, A.H. Gee, and G.M. Treece, *Proc. Inst Mech Eng, part H: J Eng Medicine*, 224, pp. 193 – 223, 2009.

[2] Ö. Oralkan, S.T. Hansen, B. Bayram, G.G. Yaralioglu, A.S. Ergun, and B.T. Khuri-Yakub, *Proc. IEEE Ultrason Symp*, 1, pp. 399 – 402, 2004.

[3] A. Logan and J.T.W. Yeow, *IEEE Trans Ultrason Ferroelectr Freq Control*, 56, pp. 1074 – 1084, 2009.

[4] X. Zhuang, I.O. Wygant, D.S. Lin, M. Kupnik, Ö. Oralkan, and B.T. Khuri-Yakub, *IEEE Trans Ultrason Ferroelectr Freq Control*, 56, pp. 182 – 192, 2009.

[5] K. Midtbø, K. Schjølberg-Henriksen, M.M.V. Taklo, A. Rønnekleiv, *Proc. Electrochem. Soc.* PV 2005-02, pp. 288 – 294, 2005.

[6] K. Midtbø, A. Rønnekleiv and D.T. Wang, *Proc. IEEE Ultrason Symp*, 1, pp. 934 – 937, 2006.

[7] N. Lietaer, A. Summanwar, T. Bakke, M.M.V. Taklo, P. Dalsjø, *Proc. IEEE 3D Syst. Integr. Conf., 3DIC*, Article number 5751457, 2010.

[8] D-S Lin, X. Zhuang, S.H. Wong, A.S Ergun, M. Kupnik, B.T. Khuri-Yakub, *Proc. IEEE Ultrason Symp*, pp. 523 – 526, 2007.

[9] R.I. Hegde, W.M. Paulson, P.J. Tobin, *J. Vac Sci Technol B*, 13(4), pp. 1434 – 1441, 1995.

[10] Fraunhofer ISiT, Fraunhoferstraße 1, 25524 Itzehoe, Germany.

[11] A.A. Ayón, K-S Chen, K.A. Lohner, S.M. Spearing, H.H. Savin, M.A. Scmhidt, *Mat Res Soc Symp Proc* 546,pp. 51 – 61, 1999.

[12] A. Kornblit *et al*, *Proc. Electrochem. Soc.* PV 2004-09, pp. 11 – 24, 2004.

[13] T. Pandhumsoporn, L. Wang, M. Feldbaum, P. Gadgil, M. Puech, P. Maquin, *Proc SPIE Int Soc Opt Eng*, 3328, pp. 93 – 101, 1998.